Some studies of laser doppler anemometry in wet steam

Foster, Stephen John

SOME STUDIES OF LASER DOPPLER ANEMOMETRY IN WET STEAM

STEPHEN JOHN FOSTER B.Sc.

Department of Engineering
University of Durham

A thesis submitted for the degree of
Doctor of Philosophy
of the University of Durham

December 1985

Dedicated to

my Parents

DECLARATION

The work contained in this thesis has not been submitted elsewhere for any other degree or qualification and that unless otherwise referenced it is the author's own work.

ABSTRACT

This study concerns the use of counter based laser Doppler anemometry in a wet steam flow of variable wetness fraction. Velocity measurements across the flow were made under different steam conditions. Comparison was made with a theoretical profile based upon a simple flow analysis.

A small radial turbocharger was used as a means of extracting enthalpy homogeneously from a dry superheated flow of steam using the compressor as a brake. The wetness fraction of the exhaust was estimated using measured values of the thermodynamic properties. A laser extinction method was used to determine the number concentration and mean radius of the water droplets acting as natural scatterers in the wet steam.

A laser anemometer was designed which made use of the properties of a propagating gaussian beam to produce a small probe volume. This was required to reduce the number of water droplets likely to be present simultaneously in the measuring volume. Good Doppler signals were obtained and these have been presented for a range of wet steam conditions.

A computer model was developed to predict the scattering of laser light through wet steam. Results have shown that this can be accurately modelled using a particle size distribution function. The program written to perform the simulation takes into account both single and multiple scattering events. The parameters used for the distribution

function required a knowledge of the wetness fraction and so provided a useful means of checking the estimate based upon the thermodynamic measurements.

It has been demonstrated that the ability to obtain Doppler signals from the wet steam can be predicted by computation of the signal-to-noise ratio for the medium. Good results were obtained for the wet steam conditions under investigation.

ACKNOWLEDGEMENTS

I would like to express my gratitude to the following organisations. To NEI Parsons Ltd for their financial support during the research and for permission to publish this thesis. To Holset Engineering for providing the turbocharger (and a replacement) used in this research and their enthusiastic staff whose help was invaluable. To Laser Systems Ltd who bailed me out of a very difficult position when my laser burned out.

I am indebted to my supervisor, Dr. C.F. King, for his advice and endless encouragement during the research and his dedication in the preparation of this thesis. I would also like to thank Dr. A.W. Brinkman who provided the inspiration for much of the theoretical treatment in this research.

Thanks are due to the following personnel at Durham University. To the technicians Bill, Terry, Dave, Kevin and Peter for their help in the manufacture of the hardware and to Ray and Mike for stoking the boiler. To Lesley for having devoted countless hours in typing this thesis.

Thanks are also due to the following personnel at NEI Parsons Ltd. To Norman the photographer whose artwork was superb. To Ed who so willingly reproduced some of the diagrams with perfection and to Mike for his careful proofreading.

Special thanks are due to Mr. W. Worthy of Gateshead Technical College who assisted in the manufacture of some of the more difficult hardware. Finally I would like to acknowledge the patience of my wife, Sue, during this research and her help in proofreading this thesis.

LIST OF FIGURES

Figure No.	
2.1	TYPICAL TURBINE PROBES
2.2	METHODS OF WETNESS FRACTION MEASUREMENT
2.3	BASIC LIGHT EXTINCTION APPARATUS
2.4	LAYOUT OF LIGHT EXTINCTION METHOD
2.5	GROWTH OF WATER DROPLET RADIUS
2.6	LOCATION OF OPTICAL PROBE IN MODEL TURBINE EXHAUST
2.7	MEASURED LIGHT ATTENUATION THROUGH A NOZZLE
2.8	DROPLET RADII VARIATION WITH PRESSURE AND EXPANSION RATE
2.9	VARIATION IN THE NUMBER OF DROPLETS WITH PRESSURE
2.10	MEASUREMENTS OF WATER DROPLET SIZE USING THE MIE THEORY
2.11	SCATTERING EFFICIENCY FACTOR AGAINST SIZE PARAMETER
2.12	LAYOUT OF OPTICAL PROBE
2.13	MEASURING STATIONS FOR PROBE TRAVERSES
2.14	LOCATION OF LIGHT EXTINCTION PROBE AT EXIT OF FINAL STAGE
2.15	LAYOUT OF STEAM TUNNEL
2.16	LAYOUT OF LDA OPTICAL SYSTEM
2.17	RELATIONSHIP BETWEEN MEAN VELOCITY AND LASER POWER
2.18	TYPICAL DOPPLER SIGNAL TRACE (1)
2.19	TYPICAL DOPPLER SIGNAL TRACE (2)
2.20	SPECTRUM OF DOPPLER SIGNAL
2.21	COMPARISON OF VELOCITIES DERIVED FROM PITOT TUBE AND LASER ANEMOMETER
3.1	THE GAUSSIAN INTENSITY DISTRIBUTION FOR A TEM_{00} LASER
3.2	NOTATION USED FOR THE FOCUSING OF A LASER BEAM THROUGH A SINGLE LENS.
3.3	VARIATION OF THE BEAM PARAMETER WITH BEAM RADIUS
3.4	GROWTH OF BEAM RADIUS AS A FUNCTION OF d_2/f_F
3.5	THE WAIST-WAIST RELATIONSHIP FOR A GIVEN LENS SYSTEM
3.6	VARIATION OF INPUT WAIST POSITION WITH OUTPUT WAIST POSITION FOR A GIVEN BEAM PARAMETER
3.7	BEAM EXPANSION AS A FUNCTION OF WAIST TO LENS SPACING FOR A GIVEN BEAM PARAMETER AND LENS
3.8	A SIMPLE 2:1 BEAM EXPANDER USING A DIVERGING AND CONVERGING LENS
3.9	THE BEAM EXPANDER USED IN THIS RESEARCH

Figure No.

4.1	SIMPLE REFERENCE BEAM ARRANGEMENT
4.2	SIMPLE DUAL BEAM ARRANGEMENT
4.3	VIEW OF LDA SYSTEM USED IN THIS RESEARCH
4.4	VIEW OF THE OPTICAL SYSTEM SHOWING THE FOLDING OF THE LASER BEAM
4.5	A DUAL BEAM ANEMOMETER USING A DIFFRACTION GRATING
4.6	PRINCIPLE OF DETECTING THE SCATTERED LIGHT FROM THE PROBE VOLUME
4.7	WATER DROPLET CONCENTRATION IN WET STEAM FOR A RANGE OF PRESSURES
4.8	THE PATH OF THE LASER BEAM THROUGH THE THREE LENS SYSTEM
5.1	SIZE CATEGORIES OF WATER DROPLETS AND PROCESSES THEY ARE INVOLVED IN
5.2	GROWTH OF A NEAR-CRITICAL WATER DROPLET AT VARIOUS PRESSURE LEVELS
5.3	WATER DROPLET CONCENTRATION IN WET STEAM FOR A RANGE OF PRESSURES
5.4	PRESSURE DISTRIBUTION ACROSS A LAVAL NOZZLE
5.5	GEOMETRY OF THE EXPERIMENTAL LAVAL NOZZLE
5.6	NOTATION USED FOR A TURBOCHARGER
5.7	USE OF A TURBOCHARGER ON THE EXPERIMENTAL RIG
5.8	TURBINE PERFORMANCE CHARACTERISTIC
5.9	TURBINE EFFICIENCY CHARACTERISTIC
5.10	COMPRESSOR PERFORMANCE MAP
6.1	LAYOUT OF EXPERIMENTAL STEAM FACILITY
6.2	PROPOSED LOCATION ON TOP OF CONDENSER
6.3	ESSENTIAL FEATURES OF THE LUBRICATION SYSTEM
6.4	COMPRESSOR PERFORMANCE MAP SHOWING RUNNING CONDITIONS
6.5	TURBINE PERFORMANCE CHARACTERISTIC SHOWING RUNNING CONDITIONS
6.6	THE POSSIBLE PASSAGE OF OIL FROM THE JOURNAL BEARINGS INTO THE EXHAUST
6.7	VARIATION OF INLET MACH NUMBER WITH MASS FLOW RATE
6.8	VARIATION OF EXHAUST MACH NUMBER WITH MASS FLOW RATE
6.9	THE STEADY FLOW ENERGY EQUATION
6.10	FLOW CHART FOR CALCULATING THE DRYNESS FRACTION
6.11	VARIATION OF STEAM WETNESS WITH TURBINE SPEED
6.12	STEAM EXPANSION SHOWN ON A MOLLIER CHART
7.1	ANGULAR PATTERNS OF SCATTERED INTENSITY FROM PARTICLES OF THREE SIZES

Figure No.

7.2	MULTIPLE SCATTERING, OR RESCATTERING OF ONCE SCATTERED LIGHT
7.3	THE SCATTERING GEOMETRY IN THREE-DIMENSIONS
7.4	EXAMPLE OF COMPUTED SINGLE SCATTERING PHASE FUNCTION
7.5	SCATTERING EFFICIENCY FACTOR AGAINST SIZE PARAMETER
7.6	PARTICLE SIZE DISTRIBUTION
8.1	THE MONTE CARLO TECHNIQUE
8.2	A SIMPLE PLANE-PARALLEL ATMOSPHERE
8.3	ILLUSTRATING THE PRINCIPLES OF INVARIANCE
8.4	ILLUSTRATING ALL THE TERMS OF THE REFLECTION COEFFICIENT
8.5	ILLLUSTRATING ALL THE TERMS OF THE TRANSMISSION COEFFIENCT
8.6	METHOD OF DOUBLING FOR THE TRANSMISSION COEFFICIENT
8.7	METHOD OF DOUBLING THE REFLECTION COEFFICIENT
8.8	THE SUITE OF MULTIPLE SCATTERING PROGRAMS
8.9	BREAKDOWN OF THE MAIN PROGRAMS
8.10	GENERATION OF THE PLOTFILES
8.11	COMPARISON BETWEEN THE PHASE FUNCTIONS - HAZE - M
8.12	COMPARISON BETWEEN THE PHASE FUNCTIONS - WET STEAM MODEL
8.13	TRANSMISSION COEFFICIENT FOR 0 DOUBLINGS
8.14	REFLECTION COEFFICIENT FOR 0 DOUBLINGS
8.15	ANGLE CONVENTION USED FOR COMPUTING THE TRANSMISSION AND REFLECTION COEFFICIENTS
8.16	TRANSMISSION COEFFICIENT FOR ANGLE OF INCIDENCE OF 32.4^{o}
8.17	TRANSMISSION COEFFICIENT FOR ANGLE OF INCIDENCE OF 62.1^{o}
8.18	COMPARISON BETWEEN THE PHASE FUNCTIONS - 24 STEPS
8.19	COMPARISON BETWEEN THE PHASE FUNCTIONS - 12 STEPS
8.20	TRANSMISSION COEFFICIENT FOR 10 DOUBLINGS
8.21	REFLECTION COEFFICIENT FOR 10 DOUBLINGS
8.22	TRANSMISSION COEFFICIENT FOR 20 DOUBLINGS
8.23	REFLECTION COEFFICIENT FOR 20 DOUBLINGS
8.24	TRANSMISSION COEFFICIENT FOR 30 DOUBLINGS
8.25	REFLECTION COEFFICIENT FOR 30 DOUBLINGS
8.26	MODIFIED GEOMETRY FOR THE LDA COMPUTATIONS
8.27	GEOMETRY USED TO COMPUTE THE SNR
8.28	SCATTERING GEOMETRY TO INCLUDE THE DETECTION OPTICS
8.29	FLOW CHART TO CALCULATE THE SNR
8.30	CONE OF DETECTION

Figure No.

8.31	SIGNAL-TO-NOISE RATIO FOR A GIVEN DETECTOR POSITION
9.1	PRINCIPLE OF MEASURING THE EXTINCTION OF THE LASER BEAM
9.2	VARIATION OF LASER LIGHT EXTINCTION WITH TURBINE SPEED
9.3	FLOW CHART TO CALCULATE N AND rp FROM THE EXTINCTION MESUREMENT
9.4	PLOT TO SHOW THE COINCIDENCE OF MEASURED N AND rp WITH THE THEORETICAL VALUES
9.5	CORRECTION FACTORS FOR THE TRANSMISSION LAW AGAINST OPTICAL DEPTH
9.6	VARIATION OF CORRECTION FACTOR WITH SIZE PARAMETER
9.7	VARIATION OF ERROR IN THE USE OF THE TRANSMISSION LAW WITH SIZE PARAMETER
9.8	GEOMETRY FOR PREDICTING THE DISTRIBUTION FO DIFFUSELY TRANSMITTED LASER LIGHT
9.9	LAYOUT OF EXPERIMENT TO MEASURE THE DIFFUSELY SCATTERED LASER LIGHT
9.10	VARIATION OF "ALPHA" WITH RATIO OF GAMMA DISTRIBUTION RADII
9.11	VARIATION OF COEFFICIENT "a" WITH VALUES OF "ALPHA"
9.12	COMPARISON BETWEEN PREDICTED AND EXPERIMENTAL DIFFUSE INTENSITY FOR Y = 0.01
9.13	COMPARISON BETWEEN PREDICTED AND EXPERIMENTAL DIFFUSE INTENSITY FOR Y = 0.019
9.14	COMPARISON BETWEEN PREDICTED AND EXPERIMENTAL DIFFUSE INTENSITY FOR Y = 0.04
9.15	COMPARISON BETWEEN PREDICTED AND EXPERIMENTAL DIFFUSE INTENSITY FOR Y = 0.047
9.16	THE SCATTERING PHASE FUNCTION TYPICAL OF RAYLEIGHT SCATTERING
9.17	LOCATION OF VELOCITY MEASURING STATIONS IN THE RIG
9.18	MEAN VELOCITY PROFILES ACROSS A FLOW OF WET STEAM
9.19	COMPARISON BETWEEN PREDICTED AND EXPERIMENTAL PROFILES
9.20	DEVELOPMENT OF A FLOW PROFILE ALONG A PIPE
9.21	SCATTERING PHASE FUNCTIONS FOR LARGE PARTICLES
9.22	CORRESPONDING SIZE DISTRIBUTION FUNCTIONS
9.23	THE VARIATION OF PREDICTED SNR ACROSS THE FLOW AT 4% WETNESS
9.24	THE VARIATION OF PREDICTED SNR ACROSS THE FLOW AT 4.7% WETNESS

Figure No.

9.25 THE VISIBILITY FACTOR WITH PARTICLE SIZE
9.26 THE RATIO OF SNR IN FORWARD AND BACKSCATTER WITH SCATTERING PARTICLE SIZE

LIST OF PLATES

Plate (i)	LDA in Wet Steam - Layout of the Experimental Facility.
Plate (ii)	Typical Doppler Signals Obtained from a Water Flow.
Plate (iii)	Showing the Probe Volume formed by the Focused Laser Beams in a Flow of Dry Steam.
Plate (iv)	The Spectral Response Characteristics for Various Types of Photocathode.
Plate (v)	The LDA Optical System - Beamsplitter Module.
Plate (vi)	The LDA Optical System - Mask used for the Coarse Alignment of the Beamsplitter.
Plate (vii)	The LDA Optical System - Detection Optics and Photomultiplier Tube Assembly.
Plate (viii)	Typical Doppler Signals Obtained from a Flow of Wet Steam of 3% Wetness.
Plate (ix)	Typical Doppler Signal Obtained from a Wet Steam Flow of 2.3% Wetness.
Plate (x)	Expanded Doppler Signal Obtained from a Wet Steam Flow of 2.3% Wetness.
Plate (xi)	Showing the Intersection of the Laser Beams in a Flow of Wet Steam of 3% Wetness.

a	constant in the Gamma size distribution function.
A	cross-sectional area (m^2).
ALPHA	constant in the Gamma size distribution function.
a_e	equilibrium speed of sound (ms^{-1}).
a_f	frozen speed of sound (ms^{-1}).
a_n, b_n	Mie series coefficients independent of angle.
An(y)	factor in the Mie series containing functions of argument y.
b	constant in the Gamma size distribution function.
B	constant
C	velocity of gas flow (ms^{-1}).
c	mean velocity of gas flow (ms^{-1}).
C_p	specific heat capacity at constant pressure ($KJkg^{-1}K$).
C_{scat}	scattering cross-section (m^2).
D_{EXH}	diameter of exhaust of turbine (m).
d_m	diameter of the measuring volume (m).
D_m	diameter of the measuring section of the rig (m).
dp	mode diameter in a particle size distribution (m).
d_{ph}	diameter of the probe volume (m).
D_T	diameter of turbine wheel (m).
e	unit of electronic charge (C).
f	focal length of lens (m).
F	total incident light flux in arbitray units.
Δf	bandwidth of processing electronics (Hz).
G	gain of photodetector.

ΔGi	change in Gibbs free enthalpy (KJ/kg).
GAMMA	constant in the Gamma size distribution function.
h	specific enthalpy ($KJkg^{-1}$).
H	total enthalpy (KJ).
h_c	Plancks constant (Js).
i_1, i_2	complex Mie amplitude functions for vertically and horizontally polarised light.
i_c	mean photodetector output current. (μA).
i_d	mean dark current (μA).
i_N	rms noise current (μA).
I (I_o)	intensity (initial value) (Wm^{-2}).
$J_n(x)$	Bessel function of argument x.
k	propagation constant = $2\pi/\lambda$ (m^{-1}).
K	Boltzmann constant. (JK^{-1}).
k_e	isentropic exponent for an equilibrium mixture.
k_f	isentropic exponent for a vapour phase.
Kn	Knudsen number.
ℓ	molecular mean free path length (m).
$\bar{l}$	length (m).
ℓ_m	length of measuring volume (m).
l_M	total length of expanded measuring section for the rig (m).
m	complex refractive index.
$\dot{m}$	mass flow rate (kgs^{-1}).
$\dot{m}_{ch}$	choked mass flow rate (kgs^{-1}).
M	Mach number.
M_∞	free stream Mach number.
n(r)	number of scattering particles of radius r.

N	number concentration of scattering particles or water droplets (m^{-3}).
N_{kg}	specific number of scattering particles/water droplets (kg^{-1}).
$N_{i}.eq$	equilibrium number of molecular clusters in a mass of gas. (m^{-3}).
N_T	turbine speed (rev s^{-1}).
P	static pressure (Nm^{-2}).
P_o	stagnation pressure (Nm^{-2}).
p_r	pressure inside a water droplet of radius r (Nm^{-2}).
p_s	saturation vapour pressure of a vapour (Nm^{-2}).
$p(\cos\theta)$	single scattering phase function.
$P_l(x)$	ordinary legendre polynomial in x of order l.
$P_l^m(x)$	associated legendre polynomial in x of order l, degree m.
Pm	power meter reading (mW).
$\dot{P}$	expansion (s^{-1}).
POW	power (W).
Q	rate of heat loss (KJs^{-1}).
Q_{scat}	scattering efficiency of a particle.
r	radius of a particle (m).
r_{crit}	critical radius of a water droplet (m).
r_p	mode radius in a particle size distribution (m).
r_I	initial radius of nucleated water droplet (m).
R	specific gas constant ($KJkg^{-1}K$).
R_{ec}	recovery factor.
R_e	Reynolds number.
S	Supersaturation ratio.

PLEASE NOTE:

For a given scattering particle of radius r_p:

$$Q_{scat}(r_p) = C_{scat}(r_p)/\pi r_p^2$$

S_1, S_2	dimensionless components of the Mie scattering amplitudes.
T	thermodynamic temperature (K).
T_o	stagnation temperature (K).
T_∞	full steam temperature (K).
ΔT	degree of subcooling (K).
u	object distance (m).
v	image distance (m).
V	velocity of a particle (ms^{-1}).
W	work output (J).
W_e	Weber number.
W_l	l^{th} value of weighting function.
w(z)	beam radius as a function of distance z (m).
w_L	beam waist radius at lens surface (m).
X	dryness fraction
Δx	fringe spacing
Y	dimensionless complex argument, $m\alpha$, of function An.
Y	wetness fraction.

Greek Symbols

α	Mie size parameter ($= 2\pi r/\lambda$).
α_b	intersection angle of laser beams (degrees).
α_d	constant in the Gamma size distribution function.
β_{scat}	extinction coefficient for a polydispersion (m^{-1}).
$\delta\omega$	elementary solid angle for scattering on a volume element at a point in space.
δ	small element of a quantity.

γ	ratio of specific heats
λ	wavelength of illuminating radiation (m).
λ_g	thermal conductivity (Wm^{-2}).
μ, μ_o	cosines of the local zenith angle for diffuse and incident radiation in planetary physics.
μ_D	dynamic viscosity (Nsm^{-2}).
ν	specific volume (m^3kg^{-1}).
ν_D	Doppler frequency (ms^{-1}).
θ	zenith angle between the incident and scattered waves in two dimensions.
Θ	zenith angle between the incident and scattered waves in three dimensions.
Ω	solid angle of 4π of all space around a point (steradians).
ϕ	azimuth angle.
ℓ	density (kgm^{-3}).
σ	surface tension of water (Nm^{-1}).
σ_b	standard deviation of a gaussian distribution.
σ_{ext}	extinction coefficient for a monodispersion (m^{-1}).
σ_{abs}	absorption coefficient (m^{-1}).
σ_{scat}	scattering coefficient (m^{-1}).
τ	optical thickness.
$\tau_n(\theta), \pi_n(\theta)$	angle dependent coefficient in the Mie Series.
ω_r	slip velocity between droplets and vapour phase (ms^{-1}).

Subscripts

a	air
B	referring to the bearings.

C	referring to the compressor.
d	referring to Gamma distributions.
D	referring to the optical detector.
f	liquid phase.
fg	phase transition.
g	gaseous phase.
i	inlet.
o	initial values.
q	quantum
st	referring to steam.
r	referring to a water droplet.
s	saturated.
T	referring to the turbine.
W	referring to the Wilson point.
1	referring to compressor intake.
2	referring to compressor exhaust.
3	referring to turbine inlet.
4	referring to turbine exhaust.

Superscripts

-	mean value.
'	saturated liquid or first order scattering.
''	saturated vapour or second order scattering.
'''	referring to third order scattering.

PLEASE NOTE:

Any reference to rp and dp in the text should be read as r_p and d_p respectively.

CONTENTS

	Page
ABSTRACT	(i)
ACKNOWLEDGEMENTS	(iii)
LIST OF FIGURES	(v)
LIST OF PLATES	(x)
PRINCIPAL NOTATION	(xi)
CHAPTER 1 : INTRODUCTION	1
1.1 Some background to the research	1
1.2 Objectives of the research	3
1.3 The layout of the Chapters in this thesis	6
CHAPTER 2 : LITERATURE REVIEW OF INSTRUMENTATION FOR WET STEAM	9
2.1 The principles of instrumentation for wet steam	9
2.2 An introduction to optical measurements	13
2.3 A review of optical extinction methods	16
2.4 The application of laser Doppler anemometry to wet steam flows	19
CHAPTER 3 : THE THEORY OF PROPAGATING GAUSSIAN BEAMS	36
3.1 An introduction to gaussian optics	36
3.2 A review of fundamental work	38
3.3 The general formulae for a propagating gaussian beam	39
3.4 The effects of diffraction limiting upon the propagation of laser beams	43
3.5 A design characteristic for gaussian beams	44
3.6 A computer program to trace the path of a gaussian laser beam along an optical axis	46
CHAPTER 4 : THE DESIGN AND PERFORMANCE OF THE LDA OPTICAL SYSTEM	48
4.1 Introduction and Objectives	48
4.2 Description of the LDA optical system	54
4.2.1 The transmission optics	54
4.2.2 The collection system	58
4.3 Design of the transmission optics	64
4.3.1 Introduction	64
4.3.2 Matching the transmission optics to the geometrical requirements	66
4.3.3 To produce a tiny probe volume	68

Page

4.4 The alignment procedure for the transmission optics 72
4.5 The performance of the optical system 74

CHAPTER 5 : SOME ELEMENTARY WET STEAM THEORY 81

5.1 Introduction 81
5.2 Basic Wet Steam Theory 83
5.2.1 The structure of wet steam 83
5.2.2 The process of nucleation 87
5.3 A classical method of generating a wet steam flow 92
5.3.1 Introduction 92
5.3.2 The classical method of generating wet steam 94
5.4 Some other properties of wet steam flows 96
5.4.1 Droplet deformation and break up 96
5.4.2 The property of relaxation 97
5.4.2.1 The thermal relaxation of wet steam 98
5.4.2.2 Inertial relaxation of the water droplets within the steam 101
5.4.3 The velocity of sound in wet steam 102
5.5 A technique using a turbocharger to generate a wet steam flow 104
5.5.1 Introduction 104
5.5.2 The turbocharger non-dimensional parameters 106
5.5.3 The turbine and compressor performance characteristics 107
5.5.4 Selection of a turbocharger 108

CHAPTER 6 : DESIGN AND PERFORMANCE OF THE WET STEAM RIG 111

6.1 Introduction and Objectives 111
6.2 Description of the wet steam experimental facility 113
6.3 A review of the instrumentation required 117
6.3.1 For the temperature measurement 117
6.3.2 For the pressure measurement 118
6.3.3 Measurement of the air and steam massflow rates 118
6.3.4 Measurement of the turbine shaft speed 119
6.4 Commissioning of wet steam rig 120
6.4.1 The problem of optical access into the steam 120
6.4.2 Water drainage in the measuring section 121
6.4.3 The lubrication system 122
6.5 Generating the wet steam flow 123
6.5.1 Introduction to the method 123
6.5.2 The performance of the compressor 124
6.5.3 The performance of the turbine 125

Page

6.5.4 Method of calculating the quality of the wet steam 128
6.5.4.1 Qualitative outline of the method 128
6.5.4.2 Detailed procedure for the calculations 130
6.5.4.3 Results of the calibration of the wet steam 133
6.5.4.4 An assessment of the errors in the wet steam calculation 137

CHAPTER 7 : DEVELOPMENT OF THE LIGHT SCATTERING MODEL 140

7.1 Introduction 140
7.2 Principle characteristics of scattering 142
7.2.1 Nature of the scattering process 143
7.2.2 Types of scattering 145
7.2.3 Scattering by many particles 146
7.2.4 Bulk extinction 148
7.3 The single scattering phase function 150
7.3.1 Introducing the Mie solution 151
7.3.2 Geometry of scattering in three dimensional space 153
7.3.3 The basic Mie scattering formulae 157
7.3.4 To compute the single scattering phase function 159
7.3.4.1 Computation of the Mie formulae 160
7.3.4.2 The extension of the phase function to polydisperse systems 163
7.3.4.3 Exponential size distribution function 165
7.3.5 The scattering efficiency function 166
7.4 Discussion 168

CHAPTER 8 : DEVELOPMENT OF THE MULTIPLE SCATTERING MODEL 170

8.1 Introduction 170
8.2 The problem of Multiple Scattering 173
8.2.1 A review of the methods of treatment 174
8.2.1.1 The Monte Carlo technique 174
8.2.1.2 The doubling method 177
8.2.2 The determination of the multiple scattering of radiation by the doubling method 178
8.2.2.1 Some basic definitions 179
8.2.2.2 The principles of invariance for a plane parallel atmosphere 180
8.2.2.3 The basic transmission and reflection functions for the initial double layer 183
8.2.2.4 Physical interpretation of these formulae 185
8.2.2.5 Reduction of the transmission and reflection coefficients 187

Page

8.2.2.6 To obtain the expressions for the first double layer 192
8.2.2.7 The method of doubling to very large depths 195
8.3 The computational method used in evaluating the multiple scattering formulae 197
8.3.1 Qualitative outline of the method 198
8.3.2 Representing the phase function 200
8.3.3 To generate the scattering data file 201
8.3.4 Evaluating the terms for the initial layer 205
8.3.5 To check the results of the program 210
8.4 To estimate the SNR for a two phase medium 215
8.4.1 Derivation of the general signal-to-noise formula 215
8.4.1.1 Noise mechanisms in photomultipliers 215
8.4.1.2 The basic SNR relationship 216
8.4.2 Adaptation of the scattering geometry for the experimental rig 219
8.4.3 Derivation of the practical formulae for the SNR in an LDA system 222
8.4.4 Computation of the SNR and results 225

CHAPTER 9 : RESULTS AND DISCUSSION 228

9.1 The form of the results 228
9.2 Measurements of the light extinction to determine N & rp values 233
9.2.1 Outline of the method 233
9.2.2 Results of the extinction measurement 236
9.2.3 Discussion of the results 239
9.3 Prediction of the polar distribution of diffuse light intensity 245
9.3.1 Introduction 245
9.3.2 Measurement of the diffuse light intensity 247
9.3.3 Method of predicting the diffuse light intensity using the multiple scattering simulation program 248
9.3.4 A comparison between experimental and predicted distributions of diffuse light intensity 253
9.3.5 A discussion of the predicted and experimental distributions 255
9.4 Using LDA to obtain velocity profiles across the flow of wet steam 257
9.4.1 Outline of the method 257
9.4.2 The velocity profiles and a theoretical fit using simple pipe flow analysis 259
9.4.3 Discussion 263
9.5 A prediction of the SNR at the photodetector and a comparison with experimental results 270
9.5.1 Introduction 270
9.5.2 Results 273

Page

9.5.3 Discussion 278

CHAPTER 10 : CONCLUSIONS 283

10.1 The design of a laser Doppler anemometer 283
10.2 The generation of wet steam using a turbocharger 284
10.3 The optical extinction method of determining the scattering characteristics of wet steam 286
10.4 The polar variation of the diffusely scattered light intensity by multiple scattering 289
10.5 The use of laser Doppler anemometry in wet steam 291
10.6 The prediction of the SNR of the Doppler signals obtained from the wet steam 294
10.7 Suggestions for further research 297

REFERENCES

APPENDIX A : LISTING OF PROGRAM "TSCAT"

APPENDIX B : THE FORM OF THE DISTRIBUTION FUNCTION

FIGURES

PLATES

1. INTRODUCTION

1.1 Some background to the research

The last two decades have seen significant advances in the design and manufacture of large electrical generating equipment. In an effort to maintain the competitiveness of their products, manufacturers have pursued research programmes in the search for new ideas and techniques. On-load condition monitoring of the steam turbine and the electrical generator has received growing interest.

The steam turbine acts as a prime mover for the electrical generator in power stations and research continues worldwide into improving the efficiency of the turbines. Attention has been directed towards the low pressure steam turbine in particular, of which there are at least two in a 350-1200 MW turbine generator set, where there is room for improvement in its efficiency. It is during expansion through the final stages of a low pressure steam turbine that the steam is subcooled to such a degree that condensation takes place. The steam is now said to be wet and research is continuing into predicting the effects of wet steam upon the efficiency of these final stages.

Wet steam exists as an equilibrium mixture of dry steam and water, the water phase being constituted by fine fog droplets typically of the order of 0.1 μm in radius (68) and of number densities of 10^{12}-10^{18} m^{-3}. In the steam turbine deposition and condensation of these droplets on the blade surfaces leads to the formation of rivulets of water.

This water is torn from the trailing edges of the stationary blades and breaks up into droplets of 100-500 μm in radius. Droplets of this size impinge on the leading edges of the moving blades and serious blade erosion can occur. Not only is the durability of these blades affected but also the aerodynamic efficiency of the final stages. The development of suitable and reliable instrumentation is therefore a very important aspect in the study of wet steam and any new instrumentation techniques influence the rate at which new knowledge is gained.

Measurements have been made of the wetness fraction and mean fog droplet size by inserting an optical probe into the steam turbine whilst on load (69). Optical techniques are based upon the measurement of the extinction of a light source by the fog the amount of which can be equated to the scattering properties of the fog. The two major problems associated with any optical measurement technique are suitable optical access into the wet steam flow and the possibility of severe extinction by the fog.

NEI Parsons Ltd wish to expand their range of optical research techniques and in particular would like to investigate the viability of laser Doppler anemometry (LDA) for making velocity measurements in wet steam flows using the nucleated water droplets as seeding particles. LDA has the distinct advantage that it is non-intrusive to the flow and optical access can be made via a good quality window.

Collaboration with the University of Durham began in October 1982 when the author embarked upon a research project dedicated to the application of a laser anemometer to a variable quality wet steam flow.

1.2 Objectives of the research

The main objective of this research was to supply NEI Parsons Ltd with a summary of the potential use of LDA as a means of making velocity measurements in wet steam flows and its limitations. The company already possesses a Photon Correlator based LDA system and the approach at Durham University was to apply a Counter based system to the problem. A comparison of the use of both systems under the same operating conditions would provide useful information on the applicability of LDA systems to wet steam flows. LDA in wet steam has been investigated by other researchers (14) (15) but this research represents the first serious attempt by this company.

At the onset of the research no hardware existed and the following objectives were set:

1. To design and manufacture a laser Doppler anemometer system for making velocity measurements including the light detection optics.
2. To generate a wet steam flow of a variable and predictable wetness fraction, consistently and reliably.

3. To investigate the use of the LDA system in the wet steam produced in the experimental facility at Durham University.

4. If the preliminary investigations were successful then the LDA system was to be adapted to make velocity measurements in an experimental steam turbine at NEI Parsons Ltd.

The first of these presented few problems and the final design for the anemometer was successful and the detections optics performed well. The second task, however, proved to be the most formidable and really tried the author's knowledge of wet steam. In order to attempt to model the conditions likely to be present in an experimental steam turbine, it was decided to use a turbomachine at Durham to extract enthalpy homogeneously from the wet steam and a commercial turbocharger was tried. Another research contract had just been initiated at Durham University with Holset Engineering Ltd and initial discussions with this company proved encouraging. Some very approximate calculations were carried out with their help and on the basis of these an experimental rig was fully commissioned. The rig was calibrated so that the wetness fraction could be estimated from the speed of the turbine in the turbocharger.

It must be emphasized that this thesis is not concerned with an in depth study of the nucleation processes involved in condensing steam flows but some appreciation of

its behaviour was required in order to able to interpret some of the results.

Some good results were obtained with the laser anemometer in six steam conditions with wetness fractions of 1.0, 1.9, 2.3, 3.0, 4.0 and 4.7% respectively. The Photon Correlator system was not functioning when it was required at Durham and so no comparison was made between the two systems. Due to delays in manufacturing of the experimental rig at Durham University and the failure of a laser tube, time did not permit any work to be continued on an experimental steam turbine. But the results obtained at Durham do provide NEI Parsons Ltd with a conclusive piece of research which can form the basis of continued development towards a fibre-optic anemometer.

In order to provide a theoretical content to the research the process of light scattering was studied and applied to the transmission of a laser beam through fogs such as wet steam flows. A computer program was written which would predict the polar intensity distribution of both direct and diffusely scattered light derived from a computation of single and multiple scattering events. A close agreement was obtained between the predicted distribution of diffusely scattered light and experimental values taken at each wet steam condition. The great benefit of this program was that it could be applied to the transmission of light of any wavelength and polarization through any particulate medium. The program was adapted to

predict the signal-to-noise ratio of the Doppler signals obtained from the steam and quite a good agreement was obtained with the ability to make velocity measurements under certain conditions.

1.3 The layout of the Chapters in this thesis

This thesis has been organised into ten distinct Chapters each Chapter uniquely defining a particular aspect of the research.

Chapter 2 is concerned with a literature review of instrumentation techniques developed for wet steam and concentrates upon optical methods of droplet sizing and wetness fraction determination. All previously published work on the application of LDA to wet steam flows has been reviewed.

Chapter 3 is concerned with the propagation of gaussian laser beams through a lens system and the formulae which govern the size and location of the focused laser beam waist at any given point in the system. These formulae have been presented in a form that can be used directly to design an effective optical system.

Chapter 4 covers the design of the LDA optical system used in this research. Various criteria have to be adopted when designing an anemometer for making velocity measurements in wet steam and this Chapter describes the steps that were taken to produce a useful design.

Chapter 5 is the first of two concerned with the subject of wet steam and the generation of a variable

quality wet steam flow. This Chapter covers the theory of equilibrium mixtures of dry steam and water and the classical methods of generation through Laval type nozzles. The relationships governing the production and growth of nucleation centres and the subsequent growth of the fog droplets upon continued expansion have been presented. The concept of the Wilson point is introduced as being an important thermodynamic condition during the process of nucleation in expanding steam flows. An introduction is made to the use of a small radial turbocharger to extract enthalpy from a supply of dry superheated steam.

The design and commissioning of a wet steam rig is described in Chapter 6. The expansion process through the turbocharger is plotted on a Mollier chart for each of the wet steam conditions produced. The wetness fraction is shown to be estimated from local thermodynamic measurements.

Chapters 7 and 8 are concerned with the development of a light scattering model to predict the polar intensity of the diffusely scattered components of laser light as it passes through a medium of wet steam. Chapter 7 deals with the physics of the light scattering process and the development of a computer program to predict the single scattering phase function based upon the well known Mie theory. Chapter 8 discusses a method to take into account the multiple scattering of light in optically thick media. The computation of the diffuse light intensity is shown to

be a valid means of confirming the estimates of the wetness fraction.

Chapter 9 discusses the use of LDA in wet steam and the determination of the velocity profiles across the measuring section of the experimental facility. A general results section is incorporated which summarizes the computer simulation for the diffuse light intensities and comparison with experimental data.

Finally Chapter 10 presents the conclusions to the research and lays down recommendations for further research and development.

2. LITERATURE REVIEW OF INSTRUMENTATION TECHNIQUES USED IN WET STEAM

2.1 The principles of instrumentation for wet steam

The development of suitable and reliable instrumentation for measurements in wet steam has largely determined the rate at which new knowledge can be accumulated on the nucleation process and the formation of water droplets of a size that lead to the concentrated erosion of the turbine blading. The basic parameters of a wet steam flow for which instrumentation has been developed are:

(i) Steam pressure, steam temperature, velocity and direction over the flow field.

(ii) Distribution of the steam wetness and coarse water.

(iii) The size distribution of the fog droplets and coarse water droplets, and their relative velocities.

Wet steam in equilibrium can be considered, in an ideal situation, as a mixture of a dry vapour phase and a wet phase present as a suspension of fine fog droplets typically of the order of 0.1 μm in radius after the process of nucleation (71). In practice, due to the effects of coagulation, deposition and drooling from the trailing edges of blading, there also exists a distribution of coarse water droplets which have been established as the principal cause of turbine blade erosion (77). In an attempt to combat

erosion and losses in aerodynamic efficiency due to the presence of the two phases in the flow, engineers in both the CEGB and the various major turbine manufacturers throughout the world, have developed instrumentation techniques. These techniqueshave first been proven in experimental turbines (61) (62) and, in some cases, experimental nozzles (70) whence they have developed for use in large operational steam turbine generating sets (86).

For measurement of the parameters in (i) probes have been developed to determine total pressure and total temperature but suffer from the perennial problem of access into an operational machine. Permanently attached installations have often been unreliable and it has been preferable in many cases to use long probes which are inserted into the turbine via accurately positioned guide tubes. A range of probes typically used in wet steam turbines is shown in figure 2.1 and applications of these are discussed in (71). All the probes shown have been developed to require minimum calibration. Probe (a) can be rotated to obtain the flow direction (yaw angle) by nulling static pressures on each side of the disc and total pressure is obtained from the Kiel probe. The symmetry of the disc and the Kiel probe ensure the measurements are independent of the pitch angle. The probe in (b) is used in conjunction with probe (a) and is set at the measured yaw angle and nulled to determine the pitch angle. The inherent accuracy of these probes far outweighs the disadvantage of using more

than one probe to measure the conditions required.

Several methods of wetness fraction measurement of varying accuracy, complexity and applicability have been devised. The selection of an appropriate method depends on the form of the liquid phase (71) (i.e. coarse water or fog). An example of a probe to measure the coarse wetness fraction has been developed by one of the turbine manufacturers (88) and is inserted into the steam space between the blades through guide tubes. The most common methods of measuring fog wetness fraction are the throttling calorimeter and the heating method.

The throttling method is well known and references can be found in many older texts on steam. The principle of the method is to transfer a sample of the steam by an isentropic expansion from a wet to a superheated state. The enthalpy H_2 can be determined from pressure and temperature measurements p_{02} and T_{02} of the superheated vapour. The wetness Y of the original sample can then be obtained from

$$Y = \frac{Hg_1 - H_2 - q/m_s}{hfg_1} \qquad (2.1)$$

where Hg_1 is the total enthalpy of saturated steam at the sample pressure P_1 and q is the heat lost from the sample of steam of mass m_s. The problems of obtaining a representative sample are common to almost all of the thermodynamic methods of wetness measurement. The particular problems with throttling, however, are due to

errors arising from heat loss and incomplete mixing following expansion. Adequate insulation and a sufficient size of sample can reduce heat loss errors to acceptable proportions. A practical limit to the application of the system occurs at low pressures as shown in figure 2.2. The pressure P_{o2} of the expanded sample is usually determined by the temperature of available cooling water for an auxiliary condenser, a typical minimum value being ~20 m bar. To promote heat transfer a minimum final superheat of at least 20^0C is necessary and from figure 2.2 the corresponding lowest pressure, P_{o1}, of a 10% wet sample would be ~10 bar.

The heating method is a little more flexible and a wet steam sample is electrically heated until superheated. The heat required to dry the sample is detected by a rise in steam temperature downstream of the heater. The wetness fraction may be calculated from.

$$Y = \frac{(H_2-H_1)_s}{h_{fg1}} - \frac{\delta q}{\dot{m}_{st}\, h_{fg1}} \qquad (2.2)$$

where δq is the heat input rate to make the sample mass flow rate $\dot{m}_{st}$ become dry saturated.

In recent years (1965 on) optical instrumentation techniques have become more widely used. They offer a very high potential accuracy and a simple optical and mechanical arrangement which can be easily transported. Most of the techniques developed make use of the intensity distribution of scattered light as predicted by the Mie theory. As this

research is dedicated towards the assessment of a totally non-invasive flow measuring technique for wet steam using laser optics, the development and application of optical methods for measurement of the steam parameters, N, r_p and Y will be reviewed in detail.

2.2 An introduction to optical measurements

Optical techniques are well established for the measurement of the size of light scattering particles whose diameter is of the same order as the wavelength of the illuminating light. They are effective for measurements in suspensions of scattering particles because of the phenomenon of electromagnetic scattering. The electromagnetic scattering by particles of up to a few wavelengths in diameter produces an angular distribution of intensity, or scattering pattern, that systematically evolves in shape and complexity with an increasing particle size (6).

The subject of electromagnetic scattering by spherical particles was studied in 1908 by Mie (54) who solved Maxwell's electromagnetic wave equations for plane waves incident on homogeneous spheres. The method of solution adopted by Mie consisted of expressing the incident wave in terms of spherical waves centred at the scattering sphere, fitting the appropriate boundary conditions and solving the differential equation for the amplitude of the resultant scattered wave (50). As such it is the analytical solution of the problem since it uses a formal theory and classical

mathematical analysis for an idealized sphere. For the purpose of scattering research, both in colloidal suspensions or in the atmosphere, the Mie solution has proved to be the most successful. It is a general solution which may be reduced to describe the scattering by both very small and very large particles. More recent authors such as Liou (59) and Kerker (54), have adopted the Mie theory and used their own interpretation of the complicated formulae involved to present a simpler argument. Apart from different notation and a more general approach to the solution, the practical formulae are similar. Extensive tables of the Mie scattering amplitude functions are available such as those of Penndorf (74) which, to a large extent, alleviate the necessity to study the Mie solution in detail.

Based upon the Mie theory, optical methods offer some potential for accurate measurement of the size of fog droplets present in wet steam flows without the need for calibration. The suitability of the Mie theory for this type of application has been confirmed by Gucker and Egan (46) who have shown that the scattering patterns for individual liquid droplets agree with the Mie theory in minute detail. Several methods of optical measurement have been developed based upon the Mie theory which rely upon two specific principles (i) angular scattering of the incident light beam and (ii) the total scattering of the beam, more commonly referred to as total extinction.

Method (i) uses some feature of the scattering pattern such as depolarization, the polar intensity variation or the angular position of the maximum intensity. The approach adopted in (11) was to record the angular variation of polar intensity. The size of the scattering particle is deduced by comparing the measured position of the intensity distribution minima with Mie theory values for the wavelength of the illuminating light used.

The extinction method (ii), on the other hand, involves the measurement of the attenuation of light as it passes through a particulate atmosphere. The essentials of any extinction apparatus are shown in figure 2.3. The extinction method has two main advantages which result from the principle of measuring the unscattered part of the incident beam of light.

(a) It is less prone to errors due to multiple scattering. It must be emphasized here that "less prone" does not mean that errors due to multiple scattering are insignificant. It has been shown by Deepak et. al (17) (18) that the influence of multiple scattering upon the transmission behaviour of light beams through fogs can be severe if insufficient care is taken. However, provided that the scattering particles are small and in the order of 0.1 μm in radius, then the basic transmission laws can be used

with accuracy to large optical depths. Because this method may be unaffected by multiple scattering, it can cope with a greater range of number densities of scattering particles.

(b) A simpler optical system can be employed and a less sensitive photodetector will be required since the intensity measurements are made only along the path of the illuminating beam.

It is therefore not surprising to find that the extinction method has provided the most widely applied means of making measurements of the size of fog droplets in wet steam.

2.3 A review of optical extinction methods

The steam wetness in the flow at the low pressure end of steam turbines can lead to damage of the blading. It is mainly for this reason that the subject of steam wetness has attracted so much attention by the users and manufacturers of steam turbines. Over the years instrumentation has been developed to give turbine designers information on the parameters which effect the state of expanding wet steam and the processes which lead to concentrated erosion of the turbine blading. The light extinction technique has been one of the more successful methods of measuring the mean water droplet size, number concentration and the corresponding wetness fraction.

Gyarmathy (47) developed a device capable of measuring the extinction of laser light through low pressure steam fogs. The fogs were produced in a Laval nozzle in one experiment while in another experiment the fog in the exhaust casing of a model turbine was studied. Gyarmathy concentrated his investigation on the events that take place between the formation of the fog and the action of the erosive water. A clearer understanding of the size of the mean water droplet at different rates of expansion and its corresponding rate of growth was required. In the model steam turbine used in the experiments, the fog droplet size was expected to be of the order of 0.1 μm. Such small droplets could not be observed individually (e.g. by capturing or by short time photography). The light extinction method was therefore chosen for determining the sizes of these sub-micron droplets. In order to develop a theory of light transmission through the fog, Gyarmathy made the following assumptions:

(i) All droplets have a uniform size,

(ii) This size lies in the range of Rayleigh, scattering ($r_p < \lambda/2\pi$ or $r_p < 0.1\ \mu m$ if red light is used) and,

(iii) The mean distance between the droplets is much larger than their diameter.

Using the theory of light scattering and the Lambert-Bouguer transmission law the mean fog droplet radius can be expressed as

$$r_p = \frac{\lambda}{2\pi} \cdot \left[\frac{\rho_f \cdot \nu_{st}}{Y} \cdot \frac{(m^2+2)}{(m^2+1)} \cdot \frac{\lambda}{4\pi l} \cdot \ln\left[\frac{I_o}{I}\right] \right] \qquad (2.3)$$

In this equation ν_s and Y are given by the thermodynamic state of the wet steam, ρ_f, m and λ are known constants and l is defined by the experimental set-up. It is the intensity ratio I/I_o which is measured by the extinction technique. All the extinction measurements were made downstream of the Wilson point, i.e. at locations where the local wetness (Y) was greater than the wetness precipitated at the Wilson line (Y_w). From the measured fog droplet radius r_p, the radius r_w of the fog droplets immediately after the completion of spontaneous condensation can be calculated as:

$$r_w = r_p \sqrt[3]{\frac{Y_w}{Y}} \qquad (2.4)$$

This equation assumes that the number of fog droplets per unit mass of steam remains constant between the points of fog formation and measurement. The apparatus used by Gyarmathy is shown in figure 2.4. Using a 15mW Helium-Neon laser, the beam was split into a measuring beam (M) and a reference beam (R) which can be alternately interrupted by a chopper disc. The measuring beam passes through the steam to a mirror and returns through the steam to the beamsplitter. Its reflected part falls on the photocathode of a photomultiplier tube whose output current is proportional to the incident light intensity. Figure 2.4(b)

shows the probe used to conduct the light extinction measurements inside the exhaust casing of the model turbine.

Measurements made in the Laval nozzle with an expansion rate $\dot{P}$ of $1000s^{-1}$ (corresponding to an initial wetness Y_w of 0.03) yielded the results of figure 2.5. The curve starting at r_w indicates the variation of the fog droplet radius along the nozzle as calculated by the following equation

$$r_p(\ell) = r_w \sqrt[3]{\frac{Y(\ell)}{Y_w}} \qquad (2.5)$$

The variation of fog droplet size is, within the experimental scatter, in good agreement with the growth corresponding to the increase in wetness.

For the measurements in the turbine, the probe was inserted into the exhaust casing as shown in figure 2.6. The fog droplet size was measured optically at several inlet temperatures. Gyarmathy found that decreasing the inlet temperature resulted in an optically denser steam (given by lower I/I_o) with the water droplets becoming larger. This was caused by a shift of the Wilson point towards higher pressures. Owing to uncertainties in the inlet temperature measurements it was not, however, possible to infer the exact position of the Wilson point with respect to the turbine stages.

Gyarmathy showed that the growth of fog droplets could be predicted accurately and used a Laval nozzle to prove the light extinction device. The most difficult practical

problem that was experienced was found to be the varying light scattering effectiveness of the dirt layers formed on the windows into the flow. Furthermore the scattering effectiveness of these layers could vary quite significantly with time. The problem was overcome by making the fog disappear and reappear in very quick sequence by shutting and opening the exit of the nozzle and registering the intensity signals on an oscilloscope.

Petr (75) carried out similar measurements to Gyarmathy but only in a Laval nozzle. In particular the tests were performed for three expansion rates of 2000, 5000 8000s^{-1} over a pressure in the Wilson region of 0.4-1.5 bar. Gyarmathy showed that the concentration and size of the nucleated droplets in a wet steam flow depended on the pressure and expansion rate in the Wilson region. This observation was largely confirmed by Petr in his experiments. An example of the measured static pressure and the light intensity attenuation through the nozzle for an expansion rate of P = 2000s^{-1} is shown in figure 2.7. It can be seen that the value of I/I_o at the point where spontaneous condensation occurs is:

$$(I/I_o)_{(1)} = 1 - \delta(I/I_o)_{(1)} \qquad (2.6)$$

Petr points out that the decrease in $\Delta\,(I/I_o)_{(1)}$ was probably due to partial condensation on dust particles or inevaporated water droplets coming from the steam supply to the nozzle. The light intensity due only to spontaneous

condensation was therefore found to be approximately

$$(I/I_o) = (I/I_o)_{(2)} + \delta(I/I_o)_{(1)} \qquad (2.7)$$

Figure 2.8 shows the average fog droplet size measured at the end of spontaneous condensation, this size being dependent upon the pressure P_w (in the Wilson region) and the expansion rate $\dot{P}$. The effect of multiple scattering for an expansion rate of $\dot{P} = 2000s^{-1}$ is shown together with experimental droplet sizes obtained by Gyarmathy. Petr did notice the existence of multiple light scattering phenomena which caused a deviation from the Lambert-Beer law of transmission. This was particularly noticeable at light intensity attenuation values of less than 0.74. Similar measurements made on Sulpher emulsion gave an approximate correction of the error caused by multiple scattering.

The average droplet sizes calculated by this method were found to be approximately 25-60 per cent greater than the values obtained by Gyarmathy as shown in figure 2.8. Petr argues that in any analysis the following should be taken into account:

(i) Influence of the chemical composition of the steam affecting the surface tension of the droplets.

(ii) The presence of non-condensing gases and

(iii) Turbulence.

The discrepancy in the experimental values cannot be explained satisfactorily because information on the above

was not available.

Petr also concluded that as the expansion rate increases and the pressure in the Wilson region decreases, there is a decrease in the average size of fog droplet, shown in figure 2.8, but an increase in the number of droplets, as shown in figure 2.9. For a given wetness fraction this would be expected from a geometrical consideration.

The optical method of droplet sizing developed at C.E.R.L. by Walters (85) differs from that of Gyarmathy and Petr in that values of wetness fraction and droplet size were obtained simultaneously from measurements of the scattering properties of the wet steam flow over a wide spectral range. This method and associated optical system was specifically chosen for eventual use in a probe for measurements in turbines (86). The method used in (75) was simple to apply but did not appear to be very accurate, Petr quoting an error of up to 30 per cent in the measured size. In the investigations of (47) and (75) the extinction was measured at one incident wavelength from which the droplet size was deduced using a wetness fraction estimated from pressure measurements assuming the flow to be in a thermodynamic equilibrium at the end of condensation. In spite of the measurements made, Walters (86) observes that the method cannot be considered to be applicable to full size machines when the distribution of wetness fraction cannot be estimated accurately.

The method used by Walters (85) involves measuring the extinction by the flow of wet steam of a beam of light at many wavelengths. The droplet size and wetness fraction are then determined from the correspondence of the measured spectral turbidity with the Mie theory. At about the same time instrumentation techniques were being developed by the turbine manufacturers a similar method was applied by McAllistair (60), (61). Both authors successfully applied the instrument and it has since proved to have high potential accuracy (86).

The light extinction system employed by Walters is shown in figure 2.3. It basically consists of a 75w Xenon light source and two collimating lenses. A series of 18 interference filters were employed to give evenly spaced discrete wave numbers over the spectral range 310nm $\leqslant \lambda \leqslant$ 800nm. McAllistair (62) used 9 interference filters covering the 414 nm to 843 nm range of wavelengths. The larger the number of filters used the more accurate was the droplet sizing as will be shown. The essential difference between the work of Walters and McAllistair is that in the former, extinction measurements were carried out in a Laval nozzle of variable geometry whereas in the latter, droplet sizing was actually performed in an experimental HP turbine. The principle of measurement used by both authors was very similar and was based upon the following argument. The Lambert-Bouguer law of light transmission is given by

$$\frac{I}{I_o} = e^{-\sigma_{ext} \cdot \ell} \qquad (2.8)$$

If there is negligible slip between the phases it can be shown (see section 9.3) that

$$\frac{I}{I_o} = \exp\left[\frac{-3}{2} \cdot \frac{Q_{scat}}{d_p} \cdot \frac{Y}{1-Y} \frac{\rho_s}{\rho_f}\right] \qquad (2.9)$$

assuming that the wetness fraction is known. If the wetness fraction is not known but needs to be measured then:

$$\frac{I}{I_o} = \exp\left[-\frac{3}{2} \cdot \frac{Q_{scat}}{d_p} \cdot w_y\right] \qquad (2.10)$$

where

$$w_y = \left(\frac{Y}{1-Y}\right) \frac{\rho_s}{\rho_f} \text{ and } Y = \frac{w_y \cdot \nu_s}{\nu_f + w_y \cdot \nu_s} \qquad (2.11)$$

From equations (2.8) and (2.9) the extinction coefficient is given by

$$\sigma_{ext} = \frac{3}{2} \cdot \frac{Q_{scat}}{d_p} \cdot w_y \qquad (2.12)$$

The transmissivity of the wet steam was measured using a photocell. The sizing of the fog droplets was achieved by measuring I/I_o at the wide range of wavelengths and superimposing a plot of log (I_o/I) against the wave number $\nu = \pi/\lambda$ on a similar plot of $Q_{scat}(\alpha)$. At the point at which the curves match, the mean fog droplet diameter is found from the correspondence of the logarithmic abscissae

with $\alpha = \pi d_p/\lambda$ and $\nu = \pi/\lambda$. The graph obtained in (62) is shcwn in figure 2.10. An exact fit of the experimental curve is obtainable only for a monodispersion of water droplets in the fog. For example McAllistair found that the curve (b) in figure 2.10 fitted the Mie scattering efficiency curve of figure 2.11 at a range of α of α = 3.5 to α = 7.85. Selecting a value of λ_1 say 0.6 μm gives from figure 2.10 a value of α_1 = 5.26 and hence $Q_{scat\ 1}$ = 3.72. Since $\alpha_1 = \pi d_p/\lambda_1$ then:

$d_p = 5.26 \times 0.6/\pi = 1.0\mu m.$

The same procedure was adopted for the curves (a), (c) and (d). At this same wavelength $\sigma_{ext\ 1} \cdot \ell$ = 4.91 which in conjunction with the densities of the vapour and liquid phases at the local thermodynamic conditions gave a corresponding value for the wetness fraction from equation (2.11).

Walters concludes (85) that for fog droplets smaller than 0.1 μm in diameter, optical measurement by light extinction becomes progressively less accurate for two reasons:

(a) The rate of change of Q_{scat} (α) becomes very small as seen from figure 2.11 for α = 1.22. (Corresponding to d_p = 0.1 μm).

(b) The relatively weak extinction by water droplets of this size makes accurate turbidity measurements more difficult.

Measurements in wet steam turbines have been made by inserting an optical probe and traversing along a blade passage or across an exhaust section. One type of probe has already been discussed (47) but this device was not used to take light extinction measurements in the rotor areas. Walters et al (86) describe an optical probe that obtained the fog droplet size and wetness fraction of flows in large operational LP steam turbines. Mean droplet diameters were found to be in the range 0.2-0.4 μm and could be measured to an accuracy of ±5% and the wetness fraction to within ±6%. The technique uses the Mie scattering theory and is described in detail in (85).

The main constraint on the design of any probe is that it should be of 25.4 mm in diameter so that it can be inserted and withdrawn from the turbine on load by means of valve guided tubes installed in the L.P. casing. In general on the C.E.G.B. machines four or five of these tubes are used so that a full survey of the flow in the final wet steam stages can be made with radially traversing probes. Several 500-660 MW machines have been equiped in this way and have been described by Moore and Sculpher (69).

Figure 2.12 shows the optical probe and light input unit as used in (86). It differs from that of (47) because it has been purposely designed to fit into the tiny blade passages of turbines on load as opposed to an experimental machine. This probe proved to be very easy to use in the operational turbines, only a few minutes being required to

obtain a full set of transmission data at each traverse position. Figure 2.13 shows the location of the traverse positions on operational turbines and figure 2.14 shows the location of an optical probe with respect to the rotor blading and the direction of traverse. Vibration tests carried out at C.E.R.L. on the probe head ensured that there was no risk to the moving blades on insertion of the device.

The validity of the data provided by the probe (86) was demonstrated by a very close agreement between the measured extinction of the wet flows in the turbine and that given by the Mie theory. The significance of this is that it showed that the water droplets involved were effectively monodisperse so the effective size could be determined accurately by identifying the spectral variation of their light extinction with the Mie theory prediction for a single droplet of known size.

2.4 The application of laser Doppler anemometry to wet steam flows

For flow investigations through most turbomachines, laser Doppler anemometry has been a standard tool for a considerable time (34). Such investigations have often been widely published with the result that significant advances in its use and the sophistication of the processing electronics have been made. However, very little has been published on the application of this technique to a condensing flow of steam. It is this type of flow that is encountered in the final stages of a low pressure steam

turbine as used in power generation. These stages contribute to the power output to an extent that a better understanding of the complex flow patterns will reduce specific fuel consumption.

Modern optical methods in wet steam have largely been concerned with the determination of the size of the water droplets in the steam. Prominant workers in this area have already been reviewed in section 2.3. The only research into the use of LDA in wet steam has been confined to the efforts of three groups of workers, Decuypère et al (15), Crane et al (14) and Wittig et al (89). Decuypère et al were involved with the investigation of the flow of superheated steam expanding at supercritical pressure ratios such that spontaneous condensation occured. Velocity measurements were made, using LDA, at the leading and trailing edges of model turbine blades mounted on a cascade in a specially designed wind tunnel. The tunnel is shown schematically in figure 2.15 and will be referred to in the following description.

The work of Decuypère was not so much intended to assess the feasibility of LDA as an instrument technique for use in wet steam itself, as the ability of the LDA system to study the flow of steam around the blade surfaces which as it happened was at the onset of nucleation. As such the nucleated water droplets existing in the test section were only of the order of $10^{-3}\mu m$ in radius. With droplets of this size no signals of significant signal-to-noise ratios

could be generated regardless of how much laser power was available. Unusual as this was for wet steam, a seeding technique was required. Decuypère provided suitable seeding by placing a small nozzle in the settling chamber of the tunnel as shown in figure 2.15. A jet of water was presented to the steam in the direction of the flow. Very soon after the settling chamber, the jet of water disintegrated into water droplets of different sizes. The droplets were not entirely monodisperse due to the way that they were generated, but were mainly in the size range 1-2μm. At this size they were able to follow the streamlines of the flow (71) without any appreciable deviation and slip. At low laser power, only the light scattered by the larger droplets exceeded the detection level of the processing electronics used. When the laser power was increased (up to 1400 mW) then the very small droplets did succeed in producing acceptable Doppler signals. Decuypère admits that the seeding technique requires refinement particularly regarding the position of the water nozzle. The use of water droplets as artificial seeding was preferable for technical reasons as follows. Quartz silica windows were used for optical access into the test section of the tunnel. Any solid seeding particles constituted a risk of damage to the very expensive windows over a certain time and oil would ultimately have caused precipitation on the windows necessitating frequent dismantling of the test section for cleaning.

The optical layout of the single component anemometer used by Decuypère is shown in figure 2.16. The laser beam passes through a cover and retarder plate (two $\lambda/4$ birefringent plates mounted coaxially, relative rotations of which rotate the plane of polarization of the beam relative to the source) before being split. The two beams were then expanded and focused to form an intersection volume containing 15μm fringes by a 500 mm focal length lens. It is important to emphasize at this stage that the optical system employed by Decuypère did not have to be as rigorously designed as those systems of Crane (14) and Foster (36), (38). This was due to the fact that in the test section of Decuypère's steam tunnel, spontaneous condensation was ony just occuring. If it was an equilibrium wet steam flow that Decuypère needed, then the velocity measurements would have been repeated downstream of the cascade where larger 0.1μm, and possibly larger still, water droplets would have existed in very large numbers. Since, therefore the density of seeding particles was not of any importance in this research, a larger intersection volume could be afforded. No severe attenuation was encountered in the test section around the cascade simply because the nucleated water droplets were not large enough to extinquish the laser beams significantly by scattering.

On-axis detection of the scattered light from the seeding particles was not used in order to avoid scattering from reflections of the incident laser beams on the windows.

Steam velocities were obtained over the blade profile in the cascade and very high laser powers were used. Figure 2.17 shows the relation between the mean velocity measured and the laser power required to give a Doppler signal of consistent quality.

A similar feasibility study was carried out in the Westinghouse Steam Tunnel by Wittig et al (89). Transonic velocity measurements were made in a wet steam cascade, but in contrast to the work of Decuypère, Wittig tested the feasibility of LDA in a fully nucleated wet steam flow up to several per cent wetness. The wet steam used in the experiments was produced by expansion through a nozzle, this being the so called classical method as reviewed in Chapter 5.

The Doppler signals produced from within the wet steam cascade in this work are shown in figure 2.18. The size of the signal indicates that only relatively small diameters of water droplets were present which in turn suggests that the droplets did not originate on surfaces but had actually formed in the flow. The signal trace of figure 2.18 also indicates a fairly uniform particle size. It is interesting to compare this signal with that of Plate (ix) which is the signal obtained by the author in his research. As can be seen in this photograph there is a continuous background signal of very low intensity and two levels of higher intensity signals. The water droplet distribution in the wet steam generated by the author consisted of nucleated

water droplets in the order of 0.1μm in radius together with a much smaller number of larger droplets due to water leakage from the bearings of a turbocharger and drooled from the walls of the test section. The significance of these observations will be discussed in detail in Chapter 9 but the trace has been referred to here for the purposes of comparison. By expanding the signal trace of figure 2.18, obtained by Wittig et al, as shown in figure 2.19, the Doppler frequency shift was determined and the local velocity calculated.

Difficulties were encountered due to poor signal quality on the suction side of the blades in the cascade. In this region the water droplets present in the flow were very small since the larger droplets were flung towards the pressure side of the flow passage. The very large concentration of the smaller particles would constitute a dense fog that would have almost certainly provided severe attentuation for the laser beams. Wittig repeated the measurements with a turbine in the system which resulted in a noticeable change in the particle distribution which became narrower. The flow was much foggier than in the previous tests and this resulted in a continuous signal being generated, an observation which is consistent with the experience of the author.

Wittig et al concluded that LDA techniques can be successfully applied to the velocity measurement of subsonic, transonic and supersonic flows of wet steam

through cascades. It is emphasized that extreme care should be taken in the signal processing as the particle size and velocity differences within the blade passages of the cascade are considerable and the particle trajectories do not necessarily follow the streamlines. Measurements made by these workers have indicated that droplet sizes in the low micron range are required for accurate velocity measurements, a result which is consistent with that of other workers (30).

Crane et al (14) have adopted a different approach to the question of whether LDA is a feasible measuring technique in wet steam. The direct evaluation of the efficiency of a large, low pressure condensing steam turbine requires measurement of velocity distributions in two-phase flows at speeds of between 100 and 600ms^{-1} and wetness fractions up to about 10%. The simplest form of traversing instrument for site use cannot give sufficiently accurate results in two phase flows due to uncertainties in interpreting the results. It is with this in mind that the LDA technique was tried and comparisons made between the velocities measured by the LDA and pitot tube. The measurements were made in the steam tunnel described in (70). The flows used ranged in speed from 50-200 ms^{-1} and in wetness fractions from 0.005 to 0.05, at static pressures between 0.06 and 0.30 bar. The anemometer used was a conventional dual beam type as described in (71). An Argon-ion laser capable of delivering from 60 to 240 mW of power

was used together with an EMI 9558B photomultiplier. The calibration factor of the anemometer was 0.338 MHz $m^{-1}s$. Crane used spectrum analysis as a method of signal processing due to the poor signal-to-noise ratio and the high Doppler frequencies (i.e. 68 MHz at 200ms^{-1}). Figure 2.20 shows the spectrum of a typical Doppler signal as recorded on an X-Y plotter. The position of the base line in the figure indicates a high level of background noise as the vertical scale is linear in power. As an indication of the signal-to-noise ratio, this was less than one by observation in figure 2.20. In fact Crane has concluded that, referred to the bandwidth of the spectrum, The signal-to-noise ratio is about 0.5, a figure which apparently did not vary significantly with a fourfold change is laser power. The optimum laser power that was achieved in Crane's work was about 60 mW.

Figure 2.21 shows the comparison between velocities of the wet steam flow measured by LDA and the pitot tube as obtained by Crane et al. These results were valid for wetness fractions up to 0.05. Agreement to within 2% was obtained which meant that velocity measurements in fog flows were possible by laser Doppler anemometry. A theoretical treatment by Drain (23) suggests that a reference beam optical system with coherent light detection would be advantageous with the concentrations of scattering particles that are typical of wet steam flows. According to theory, the fringe type anemometer deteriorates rapidly. However,

no work has been published on the use of this alternative method in wet steam. Indeed one of the disadvantages of the reference beam method is that the collection efficiency of the detection optics is limited by the so called coherence condition (24) of detection. In applications where the levels of scattered light containing the Doppler signal are very low anyway due to attenuation in wet steam, then the tendency is to favour the fringe type of optical system because of the large aperture that may be used (this is the so called non-coherent detection) in the detection optics. In wet steam flows this advantage may outweigh the extra sensitivity and better signal-to-noise ratio that may be offered by the reference beam anemometer. However, as far as the investigation of wet steam flows in concerned, the use of reference beam systems has yet to be investigated.

There is one conclusion that all researchers engaged in the use of LDA in wet steam seem to share. The accuracy of laser anemometer measurements at higher wetness fractions (i.e. > 0.03) will clearly depend upon the degree of slip between the velocity of the droplets and the steam flow, and large errors could result if signals are detected from the larger droplets that may be present. An error of this nature cannot be predicted as a function of the wetness fraction, since this quantity does not provide information on the distribution of the water droplet size and corresponding number density.

3. THE THEORY OF PROPAGATING GAUSSIAN BEAMS

3.1 An introduction to gaussian optics

In almost all LDA applications the laser is operated in its fundamental transverse mode. The spatial mode produced by a gas laser is determined by its construction and the type of gas present in the tube. In particular it is dependent upon the mirror radii within the cavity, the limiting aperture within the cavity and the wavelength of operation. The most desirable mode is the fundamental or TEM_{oo} mode which is characterized by a gaussian power distribution across the beam. The intensity distribution of a gaussian laser beam may be described by the following relation:

$$I = I_o \exp\left[-\frac{1}{2}\left(\frac{w}{\sigma_b}\right)^2\right] \qquad (3.1)$$

and is illustrated in figure 3.1. This mode of operation provides the smallest beam diameter and divergence angle. It can be focused to a single spot and it is this feature which makes it most desirable in LDA.

A distinction should be made here between the conventional geometrical laws of light propagation and those referred to as gaussian. The geometric object image relationship given by:

$$\frac{1}{u} + \frac{1}{v} = \frac{1}{f} \qquad (3.2)$$

is known classically as Newton's imaging formula. It

applies to the path of light rays propagating along an optical axis. Under certain conditions, the gaussian laser beam behaves in quite a different manner from that expected by equation (3.2) when the geometric laws no longer apply.

The designer of an LDA optical system requires a complete knowledge of gaussian optics in order to optimize the design to yield best results. One of the dominant features of a gaussian beam is that once brought to a focus, the beam radius passes through a minimum known as the waist of the beam. At a beam waist the wavefronts are plane and this has important implications in LDA (12). The relative size of this waist is dependent upon the geometry of the actual optical system and the size and position of the unfocused waist. Further, depending upon the size of this beam waist, the position of the focused waist may or may not be predictable from equation (3.2).

This chapter presents the fundamental relationships governing the focusing of gaussian laser beams. The laser anemometer that is to be used for making velocity measurements needs to have a very small probe volume. This is due to the high number concentration of water droplets (seeding particles) likely to be present in the flow. Reducing the dimensions of the probe volume will reduce the number of droplets passing simultaneously through the probe volume. In order to design an anemometer with a small probe volume, the relationship between the focused waist at the intersection of the two laser beams and the unfocused waist

from the laser must be established. A computer program has been written which plots the profile of a laser beam through a lens system and this is demonstrated as a useful design tool.

3.2 A review of fundamental work

Two authors have dominated the scene over the last decade and the results of their work have since been utilized by many LDA workers (84). The work of Kogelnik (55) has attempted to characterize the gaussian laser beam. In particular some basic formulae have been derived which relate the size and the position of a laser beam waist to the geometry of the two mirror resonating cavity of the laser itself. The results of the theoretical treatment are absolutely fundamental since they have established that an ideal lens system leaves the tranverse field distribution of a laser beam mode unchanged. In practice this means that an incoming fundamental gaussian beam will emerge from the lens as a fundamental beam. Similarly a higher order mode remains a mode of the same order after passing through the lens system. Kogelnik's work, however, does not provide practical information which would help the designer.

The treatment of Dickson (21) does provide some useful relationships. An expression for the amplitude of a propagating laser beam of a given power and wavelength is derived. Dickson shows that the intensity variation of the beam remains gaussian from the lens to any plane to the right of the lens so long as the lens aperture does not

truncate the beam. The relevance of these formulae will now be discussed from the point of view of designing the optical system for the laser anemometer.

3.3 The general formulae for a propagating gaussian beam

The radius of a gaussian beam is conveniently defined as that radius at which the intensity of the beam is $^1/e^2$ times the intensity at its centre (and hence the amplitude of the beam is $^1/e$ times the amplitude at w = 0). This means that 86.5% of the available beam power is contained within one standard deviation either side of w = 0.

The formulae of most interest in a single lens system are those relating the $^1/e^2$ radius of a propagating gaussian beam to the input waist, lens focal length, lens to waist spacing and the distance from the lens to the plane of interest. The single lens system is assumed to be non-truncating. According to Dickson, the safe truncation condition is when the radius of the physical aperture is at least twice the $^1/e^2$ radius of the gaussian beam at the aperture.

Referring to the single lens system in figure 3.2, Dickson shows that the beam is fully characterized by the following expression

$$w = w_o \cdot \frac{d_2}{d_1} \cdot (1+(f_F^2/d_1^2))^{-\frac{1}{2}} \left(1+\frac{d_1^4}{f_F^2} \cdot (1+f_F^2/d_1^2)^2\right.$$

$$\left. \times \left(\frac{1}{d_2} - \frac{1}{f} + \frac{1}{d_1(1+f_F^2/d_1^2)} \right)^2 \right)^{\frac{1}{2}} \qquad (3.3)$$

The parameter f_F, often referred to as the beam parameter, is the property associated with the beam at each waist and determines the way in which that waist is focused by any subsequent beams. Figure 3.3 shows the variation of f_F with beam waist size for two different laser wavelengths, typical of lasers used in LDA systems. Due to the very small difference in magnitude for the two wavelengths, any optical system designed for use with an Argon-ion laser for example will perform almost as well for a Helium-Neon laser.

Equation (3.3) has limited practical use unless it can be reduced to suit particular cases. Dickson has performed this to illustrate some unique properties of gaussian laser beams but only the following have any relevance in this research.

(i) A propagating laser beam when no lens is encountered

This example has been chosen to illustrate the effect of f_F upon the divergence of a laser beam. Setting $d_1 = 0$ and $f = \infty$ in equation (3.3) yields the following:

$$w = w_o \left[1 + (d_2^2/f_F^2)\right]^{1/2} \qquad (3.4)$$

Figure 3.4 shows the percentage growth in beam radius as a function of the ratio (d_2/f_F). For large f_F the beam is slowly diverging whilst for small f_F, the beam rapidly diverges from the waist.

(ii) To find the location of the minimum output waist of the beam

This is the first of the two most important cases for the focusing of gaussian laser beams. Differentiating equation

(3.3) with respect to d_1 and equating to zero yields the following:

$$d_{2min} - f = (d_1-f)\, f^2/[(d_1-f)^2 + f_F^2] \qquad (3.5)$$

which shows that if the input waist is located at the input focal plane, i.e. $(d_1-f) = 0$, then the output waist is located the output plane since $(d_2min - f) = 0$. This is exactly the expression sought when the output waist needs to be located at the lens focal plane. Equation (3.5) may be rearranged to give:

$$\frac{d_{2min} - f}{f} \cdot \frac{f_F}{f} = \frac{(d_1 - f)/f_F}{1+[(d_1-f)/f_F]^2} \qquad (3.6)$$

This is shown plotted in figure 3.5 and gives the output waist to lens spacing as a function of the input waist to lens spacing for a given system and wavelength. In most optical systems, the wavelength of the laser light lies in the range 488-633 mm and the input waist is typically of the order of 0.5 mm. Hence the value of the beam parameter is given as

$$f_F \geqslant 1.25 \text{ m}$$

and the value of $(d_1-f)/f_F$ will be less than unity for almost all systems using a positive lens. This is indicated by the positive slope region of the first and third quadrants in figure 3.5. The meaning of this characteristic may be explained as follows.

In the positive slope region, the two waists are related in a manner which is exactly opposite to that

predicted by equation (3.2). As the input waist moves toward the lens, the output waist also moves toward the lens. Similarly as the input waist moves away from the lens so too does the output waist. If d_1 is increased so that $(d_1-f)/f_F >> 1$ then the output waist will begin to move back towards the lens. Further as $d_1 \to \infty, d_{2min} \to f$, a result expected from geometrical optics. The broken line in figure 3.5 is given by equation (3.2).

(iii) <u>To find the size of the output waist</u>

This is the second of the two most useful formulae for the focusing of gaussian beams. It can be found by first solving equation (3.3) for d_2, viz:

$$d_2 = \frac{f}{(d_1-f)^2+f_F^2} \cdot (d_1(d_1-f)+f_F^2) \pm ((d_1(d_1-f)+f_F^2)^2 - ((d_1-f)^2+f_F^2)\cdot(d_1^2+f_F^2(1-\frac{w_2^2}{w_o^2})^{\frac{1}{2}}))^{\frac{1}{2}} \quad (3.7)$$

This minimum waist, $w_{2\,min}$, occurs when the square root term goes to zero where

$$d_{2min} = \frac{f}{(d_1-f)^2 + f_F^2} \cdot [d_1(d_1-f)+f_F^2] \quad (3.8)$$

which is identical in form to equation (3.5). The square root term vanishes when:

$$r_{2min} = r_o \cdot \frac{f}{[(d_1-f)^2+f_F^2]} \quad (3.9)$$

Equations (3.5) and (3.9) represent the two most useful imaging formulae for gaussian beams relating the size and

location of the focused output waist to the input quantities in a single lens system.

3.4 The effects of diffraction limiting upon the propagation of laser beams.

Dickson has derived the basic expressions for a gaussian beam assuming that the optical system is diffraction limited.

The design of any optical system is complicated by knowing how well any particular lens will perform a given task. There are two separate mechanisms that contribute to a spread of the image. One is lens aberation which can be minimised for the specific application. The other is the so called diffraction limitation which is a physical limitation and must be accepted. In most lens systems aberation effects predominate over diffraction effects. However, the designer should be aware that in certain conditions, aberations can be minimized to the point at which diffraction effects are more significant. Such a lens system is then said to be diffraction limited. It is the point at which no further increase in performance can be achieved unless the aperture is increased.

For all lenses there exists an optimum aperture. Due to cost and size limitations this optimum design may not always be practical. In order to minimise diffraction effects it is preferable to select a lens with a numerical aperture or f-number (focal length of lens divided by the diameter of the lens aperture) of no greater than 4. This

is a widely quoted figure that has been used to design laser optics systems for LDA. For a given focal length lens, the aperture has to satisfy the following conditions:

$$\frac{f}{D_L} \leqslant 4.0 \qquad (3.10)$$

and $$D_L \geqslant 4w_L \qquad (3.11)$$

in order to be within the limit of diffraction and truncation.

3.5 A design characteristic for gaussian beams

Figure 3.5 may be redrawn to show the waist-waist relationship as a function of f/f_F. Equation (3.6) may be rearranged to give:

$$\frac{d_{2min}-f}{f} \cdot \frac{f_F}{f} = \frac{(d_1-f)/f_F}{[1+(d_1-f)/f_F{}^2]} \qquad (3.12)$$

dividing through by f_F/f gives:

$$\frac{d_{2min}-f}{f} = \frac{1}{(d_1-f)/f + f/(d_1-f)\cdot(f_F/f)^2} \qquad (3.13)$$

Figure 3.6 shows the relationship of $(d_{2min}-f)/f$ against $(d_1-f)/f$ for various values of f/f_F. There are two extreme conditions illustrated by the plot. The first refers to the strictly gaussian position of the characteristic where $(d_1-f)/f$ is very small, viz:

$$\frac{d_2-f}{f} \approx \frac{d_1-f}{f} \cdot \left(\frac{f}{f_F}\right)^2 \qquad (3.14)$$

The second asymptote is where the geometric regime occurs when f/f_F is small and hence:

$$\frac{d_2-f}{f} \approx \frac{f}{d_1-f} \qquad (3.15)$$

rearranging the above gives:

$$(d_2-f)\ (d_1-f) = f^2$$

or

$$\frac{1}{d_1} + \frac{1}{d_2} = \frac{1}{f}$$

which is the geometric imaging formula. There are thus two definite conditions for a gaussian beam. For large (f/f_F) the beam behaves in a geometric manner but for very small (f/f_F) gaussian behaviour dominates. At the knee where $f = f_F$, Dickson predicts that for a given lens system the effective focal length is one half of the actual focal length. This is the transition region between the two regimes.

Rearranging equation (3.9) gives:

$$\frac{r_{2min}}{r_1} = \frac{1}{\left[\left(\frac{d_1-f}{f}\right)^2 + \left(\frac{f_F}{f}\right)^2\right]^{1/2}} \qquad (3.16)$$

This is shown plotted in figure 3.7 for the same values of f/f_F. As before there are two asymptotic conditions. The first is where $(d_1-f)/f$ is very small, i.e. for an input waist located at the lens focal plane, and

$$\frac{r_{2min}}{r_1} = \frac{f}{f_F} \qquad (3.17)$$

The degree of expansion of the focused waist is only

dependent upon the ratio of (f/f_F). The second asymptote defines the geometric condition:

$$\frac{r_{2min}}{r_1} = \frac{f}{d_1 - f} \quad \text{when} \quad \frac{d_1 - f}{f} >> \frac{f_F}{f} \tag{3.18}$$

Figure 3.7 is useful as a design characteristic because it predicts what degree of beam expansion can be achieved for a given lens system knowing the input waist size. (Here $f_F = \pi w^2_{input}/\lambda$). Conversely if a given beam expansion is required then a lens can be chosen to suit the desired geometry of the optical system. The characteristic also predicts the maximum expansion that is possible with a given lens system.

3.6 A computer program to trace the path of a gaussian laser beam along an optical axis.

A computer program was written to plot the e^{-2} profile of a laser beam along the axis of an optical system. The purpose of this was not only to illustrate the fundamental relationships governing the propagation of laser beams but also to serve as a useful design tool for LDA optical systems. The program can handle an optical system containing any number or combination of positive and negative lenses. (Dickson's formulae are valid for a negative lens on substitution for f=-f and taking the negative root of the term in the denominator in equations (3.6) and (3.9)).

In this application an anemometer was designed with a very small probe volume and it was with the aid of this

program that this feature was achieved. Many LDA systems use beam expansion in order to present a large input waist to the final transmitting lens thus producing a smaller waist at the focal plane of the lens. Figure 3.8 shows a very simple beam expander using a negative and positive lens. The beam expansion shown is 2:1. Consider as an example the effect of the diverging lens upon the laser beam. The value of f/f_F is very small and so from equation (3.15), near geometric behaviour may be expected. For the second lens f/f_F is large and so gaussian behaviour is dominant which is illustrated by the fact that the output waist distance is equal to the input waist distance. The virtual waist of the first lens must, however, be situated at the input focal plane of the second lens.

Of importance is that a 2:1 beam expansion has been performed within a distance of only $f_2 - f_1 = 50$ mm. However, as will be discussed further in the next Chapter, in this application a minimum waist of 20μm was required in the probe volume. To achieve this using the transmitting lens available required a beam expansion of 16:1. This was achieved within a distance of 270 mm using the lens combination shown in figure 3.9, which shows the actual form of beam expansion used in this research.

4.0 THE DESIGN AND PERFORMANCE OF THE LDA OPTICAL SYSTEM

4.1 Introduction and Objectives

One of the main requirements of this work is to establish whether an LDA based technique is a viable one for making velocity measurements of the water droplets in a wet steam flow. The theory of LDA and its applications is well documented and can be found in several good texts (26) (30), but for completeness, some of the basic principles and the way in which these influenced the final choice of anemometer system will be briefly discussed.

There are basically two main types of LDA configuration, the reference beam mode and the so called dual beam or 'differential Doppler' mode of operation. In any LDA system, laser light is transmitted to the point of interest in the flow. The advantage of using laser light is that it can be focused into a very small volume at the point where the velocity measurement is required. In both modes of operation, the basic principle is the detection of the Doppler shift in frequency of laser light scattered by particles moving in the flow. The presence of particles in the flow is fundamental to the operation of the instrument.

For both the reference beam and the dual beam anemometer, the Doppler shift in frequency is given by

$$\Delta\nu_D = \frac{2V}{\lambda} \sin(\alpha_b/2) \qquad (4.1)$$

The only technique suitable for measuring very small Doppler

shifts uses the principle of heterodyning or beating of two frequencies in a detector with a non-linear response. This can be illustrated by a simple example:

Let $V = 10ms^{-1}$

$\lambda = 500 \times 10^{-9}m$

$\alpha_b = 6^0$

The maximum value of $\Delta\nu_D$ from equation (4.1) is 1.0MHz. However, the frequency of laser light with a wavelength of 500nm is 5×10^{14}Hz. Therefore the percentage frequency shift of the scattered light as a proportion of the original frequency is given by:

$$\frac{1 \times 10^6}{5 \times 10^{14}} \times 100 = 2 \times 10^{-7}\%!$$

The principle of optical heterodyning is used to extract the Doppler frequency from the scattered light. A normal opto-electronic detector is non-linear, and is more frequently referred to as a 'square law detector', since its output is proportional to the square of the electric field of the detected light. This can be illustrated by considering two, time varying electric fields representing the two wavefronts of light to be optically mixed on the surface of the photodetector.

Let $E_1 = E_1 \cos 2\pi\nu t$ and $E_2 = E_2 \cos 2\pi(\nu+\Delta\nu_D)t$

Now i(t) is the output current of the photodetector and is proportional to the mean square of the total electric field,

viz:

$$i(t) = B[E_1 \cos 2\pi\nu t + E_2 \cos 2\pi(\nu+\Delta\nu_D)t]^2 \qquad (4.2)$$

On expanding, and neglecting the higher order frequencies since they are of no interest, then

$$i(t) = B[E_1^2 + E_2^2 + E_1E_2 \cos 2\pi(\Delta\nu_D)] \qquad (4.3)$$

i.e. a d.c. component of $[E_1^2 + E_2^2]$

and a Doppler frequency of $\Delta\nu_D$

This is the principle of optical heterodyning as employed by the detection systems in LDA.

The reference beam mode of operation involves the mixing of scattered light with a reference beam whose intensity is a fraction of the intensity of the laser source. A typical arrangement is shown in figure 4.1. Optical beating takes place on the aperture of the photodetector between the unshifted reference beam and the Doppler shifted beam. Only a small aperture can be used and hence the intensity of the collected scattered light is small. The signal at the output of the photodetector can be increased by increasing the intensity of the reference beam. There is a fundamental limit to the signal-to-noise ratio (24) which is dependent upon the intensity of the scattered light, so that increasing the intensity of the reference beam can lead to no improvement in the signal-to-noise ratio. The big disadvantage of the reference beam technique is that the Doppler frequency is dependent upon the angle of

detection (36).

The differential beam technique is shown in figure 4.2 in which a reference beam is not used. Instead optical heterodyning takes place between two laser beams scattered through different angles. In the most usual arrangement as shown in figure 4.2, two focused beams of equal intensity separated by an angle α_b produce an intersection region. The Doppler frequency detected is independent of the angle of detection. A large detector aperture gives a considerably greater signal than could be obtained by the reference beam technique. It is for these reasons that the differential beam technique was chosen for this work.

The operation of the differential beam anemometer can also be explained by the so called 'fringe model'. This model postulates that interference fringes are produced by the interference of the two monochromatic, coherent laser beams in the intersection region. Indeed if the intersection is projected upon a screen, fringes will be seen because the human eye is a square law detector and interference is taking place upon the surface of the cornea. It is the presence of these fringes upon the surface of the photocathode which produces the modulation of the signal at the output of the photodetector. This model is satisfactory for the purpose of design and analysis of laser Doppler anemometers but confusion can arise if the physics of the detection of the scattered light is not fully understood.

As far as this research is concerned, the question of the applicability of this technique to wet steam flows arises due to two very important factors which are unique to a turbid two phase flow and to wet steam in particular.

(i) There is likely to be a very severe attenuation problem with the laser beams due to extinction by the large number density of water droplets. The total number of scattering particles has been found to be of any order of magnitude up to about 10^{18} m^{-3} depending upon the mean particle size and system pressure, and

(ii) In order to simplify design requirements, it is frequently assumed (71) that for nucleating steam flows a monodispersion of water droplets is produced. In practice, however, other sizes of water droplets are likely to be present due to condensation on solid surfaces, for example. Since the water droplets in the wet steam flow are to act as seeding particles for the LDA, the components of the optical system have to be matched to a given range of particle sizes (32) (33). The choice of particle size to satisfy the matching criteria for optimizing the performance of the instrument, is thus very important.

Whether or not LDA was successful in this application, depended entirely upon whether signals of sufficient strength and quality could be detected from within the wet steam. The original objectives put forward by NEI Parsons Ltd were to make velocity measurements at depths of up to one metre into a wet steam flow. Due to the high values of turbidity and, hence extinction, that are likely even at low wetness fractions, this was rather ambitious. However, due to the exploratory nature of the research, an optical system was designed that would be capable of performing this function, should it have been required to do so.

The purpose of this chapter is to cover the design of such an optical system. Provision was to be made for both forward and backscatter detection and to enable both vertical and horizontal components of the droplet velocity to be measured. From an LDA consideration the beam spacing of the two laser beams before focusing would have to be such as to provide a good calibration factor. The calibration factor refers to the sensitivity of the instrument and is derived from equation (4.1) viz:

$$\frac{\nu_D}{v} = \frac{2}{\lambda} \sin(\alpha_b/2) \qquad (4.4)$$

For the dual beam anemometer used in this work, the value of the calibration factor is 0.25 MHz/ms^{-1}. This means that a seeding particle moving through the intersection region perpendicularly to the bisector of the two beams, as shown

in figure 4.2, with a velocity of $10ms^{-1}$ would produce a maximum Doppler shift in frequency of 2.5 MHz. The calibration factor is useful for matching the Doppler frequencies likely to be produced from the flow to the bandwidth of the processing electronics.

Extensive use is made of gaussian beam theory and the waist-waist relations discussed in the previous Chapter. A very small intersection region is required between the two focused laser beams. This is to reduce the number of seeding particles likely to be present simultaneously in the measuring volume. Since a counting technique was used to process the Doppler signals it was highly desirable to try and obtain discrete Doppler bursts.

4.2 Description of the LDA optical system

In this work, a two beam, or differential, anemometer was used. Basically a laser beam is expanded, split and re-focused to provide an intersection of the two beams within the flow at a point in space at which measurements are to be made. The theory of LDA is well understood and documented and has been covered briefly in the previous section. Only a qualitative description of the function of the individual optical components will be given here. The optical system used is shown in figure 4.3.

4.2.1 The transmission optics

The laser used to provide a monochromatic single mode light source was a Spectra Physics Model 2020 2W Argon-ion laser. This particular laser was capable of providing up to

1400 mW at a wavelength of 514 nm. Laser powers of this order were certainly capable of fulfilling the range of power requirements as discussed in the literature (14) (15). Its minimum lasing power was about 80 mW. Mounted onto the aperture of the laser is a DISA type 55 x 20 Cover and Retarder plate. Although this piece of equipment is specially designed to fit on to the DISA beamsplitter module, an adaptor was made for the unit. In its mount the retarder plate can be rotated through 360 degrees and locked in any position. This component is necessary due to the way in which the laser beam was split and will be discussed later in the section. The beam is folded through 180 degrees by means of two high quality research mirrors each of $\lambda/10$ surface flatness. Each mirror is mounted on a fully adjustable kinematic mount.

Mounted between mirrors M1 and M2 is a 30 mm biconvex lens. As shown in figure 4.4, the mirrors M1 and M2 not only fold the beam 180 degrees with respect to its intial direction of propagation but raise the optical axis of the system by 40 mm.

The second lens, L2, is a biconvex lens with an aperture of about 60 mm. Together with L1, these two lenses serve to expand the diameter of the laser beam in the ratio 16:1. The calculation of this expansion ratio and the correct positioning of these lenses with respect to each other to produce this expansion has been covered in (36). The beam has a parallel sided profile when it leaves lens

L2, and it is this collimated beam which enters the beamsplitter module.

Referring now to the beam splitting process, there are basically two methods commonly used to split a laser beam. Of these the most useful method is to use a rotating diffraction grating. By using a series of masks to stop all but the first two order beams, the two beams of the highest intensity can then be used as the two split beams. In the most common arrangement the laser is actually focused onto the grating. This enables the grating to be used as the beamsplitter in what is a very simple self aligning differential Doppler anemometer. In figure 4.5 a typical arrangement employing a rotating diffraction grating is shown. The two crossed beams in the figure are obtained from the +1 and -1 orders of diffraction which are shifted by $\pm V_G/d_G$, where d_G is the spacing of the grating and V_G is the velocity of the grating at the intersection of the laser beam. The other orders of diffraction are stopped off. The frequency shift imposed on the Doppler beat signal is thus $2(V_G.d_G)$ or, expressed in another way, twice the product of the rotation frequency of the grating and the total number of lines on the grating. This frequency shift is of considerable advantage when making velocity measurements in complex flow structures where flow reversal is likely. Not only can the magnitude of the velocity be measured but so too can its direction given by the sign of the difference between the measured Doppler frequency and the degree of

frequency shift. The second method is simpler in that it does not allow flow reversal to be identified without an external means of shifting frequency. If this is not important then it may be the choice of method for many applications. It requires the use of a beamsplitter cube and usually three mirrors. For lasers of long coherence length (typically of the order of tens of metres) two mirrors may be used. The advantage of using three mirrors is that the optical paths through the beamsplitter are path compensated.

In this application, flow reversal is unlikely in the measuring section in what is essentially a turbulent pipe flow. A beamsplitter cube was therefore chosen with three mirrors as shown in figure 4.3. A beamsplitter cube is much simpler to construct as it does not require the use of an electric motor and power supply as would a rotating diffraction grating system. The input to the beamsplitter module in figure 4.3 is thus an expanded and collimated laser beam which is nominally vertically polarized in the absence of the cover and retarder plate. The beamsplitter requires the polarization vector of the incoming beam to be at 45^0 to the plane of splitting in order for the two split beams to be polarized in the same sense. For a given splitting plane, therefore, the cover plate needs to be rotated to change the sense of the polarization vector of the incoming beam. The beamsplitter module used is shown in Plate (v). The mounting mechanism can be seen from this

photograph. The optical components were mounted on an optical bench to which the special feet were bolted as shown. This type of fixture enabled the quick removal and reassembly of the module and afforded a very rigid structure. The beamsplitter module contains three mirrors and a 50/50 beamsplitter cube. Each mirror is fully adjustable.

Finally the transmitting lens, L3, re-focuses the two colliminated laser beams whose centres are paraxial to the main optical axis. The intersection of the two beams occurs at the lens focal plane. The designed function of the two beam conditioning lenses L1 and L2 and their relationship with the transmitting lens L3 will be discussed in section 4.3.

The optical system and the laser were all mounted on an extended milling machine bedplate. This provided full 3-D traversing and a very rigid foundation for the optics, giving a virtually vibration free movement of the laser and transmission optics.

4.2.2 The collection system

In any LDA system light is scattered in all directions by the seeding particles travelling through the intersection volume. Of direct interest is that light scattered by particles whose direction of motion is perpendicular to the bisector of the two beams. The Doppler shift in frequency of this scattered light carries the velocity information which needs to be collected. The crossover region of the

two focused laser beams is commonly referred to as the intersection volume though it has been called the crossover volume or probe volume by other authors. What is of real importance is the definition of the measuring volume. The measuring volume is defined as that portion of the intersection volume from which light is collected by the collection optics. The scattered light from the intersection volume may be collected at any angle. The subject of light scattering is dealt with in Chapter 7 but it is sufficient at this stage to appreciate that the nature of any light scattering process is a function of the ratio of the particle circumference to the wavelength of the illuminating light. Water droplets typically exhibit high intensities of scattered light in the forward direction, ie in the direction of propagation of the original light. Depending upon the size of the individual water droplets this may be up to three orders of magnitude higher than in other directions. It is for this reason that forward scatter systems are employed where the geometry of the measuring situation permits.

The scattered light needs to be converted into an electric current in order to be processed. For this purpose a photomultiplier tube was used, and many different types of tube are commercially available depending upon the user's requirements. The tube chosen for this work had to meet the following criteria:

(i) The tube photocathode had to be particularly sensitive to a wavelength of 514 nm. Due to the proximity of the collection optics to a very hot turbine casing it was important that the tube had a low response in the near infra-red spectrum. Very low intensity light signals were anticipated from the steam and it was therefore important that every advantage was taken of superior photomultiplier tube designs.

(ii) Finally the tube had to have a low dark current. All photodiodes and photomultipliers show a dark current which increases with applied voltage when no light is received. The dark current refers to the current that flows when the available aperture is closed.

Advice was sought from the manufacturers (63) as to which tube would be best suited to meet the above requirements. The only tube to meet the criteria was the Thorn EMI 9954B. This particular tube has a very high gain of 10^7 with a 2.5 kV power supply and a cathode sensitivity of 75 μA/lumen which is quite high for the range of tubes sensitive to blue-green light. The dark current is specified to be typically of the order of 2nA, (63) and is about the lowest available. The 9954B represented the best compromise of the research requirements. The photocathode

material is Rubydium-Caesium (RbCs) and it is this material that gives the tube its pronounced blue-green response. The spectral response chart that is generally reproduced in the sales brochures is shown in Plate (iv). It can be seen that the Rubydium-Caesium surface has the most pronounced response in the blue-green region and this quickly reduces as the wavelength approaches the visible red region. Its infra-red response is very low. The most commonly used surface in LDA applications is the S20 and extended S20 type. This surface gives a good response over all the visible spectrum. The sensitivity of this surface is not so critical since tubes with this surface would be used in less severe conditions such as collecting scattered light from water flows. In order to minimise electromagnetic interference, e.g. mains hum from the various power supplies in the experimental facility, a screened μ-metal shield was fitted around the photomultiplier tube itself.

The principle of detection of the scattered light is that an image of the crossover region of the beams is focused upon the photodetector surface. Through the well known principle of optical heterodyning (24), the beat frequency, or in this case, the Doppler frequency, provides the rms signal current at the output from the photomultiplier tube. A method is now required to focus the scattered light upon the photodetector surface. Figure 4.6 shows such an arrangement. Scattered light from the intersection volume produced by the anemometer is focused by

a lens onto a pinhole. The pinhole acts as a spatial filter to remove optical noise from the focused light before it impinges on the photocathode of the tube. Additional spatial filtering, if required, would be provided by the available lens aperture. A typical size of pinhole would be 100 μm in diameter though in this research a 50μm pinhole was most frequently used. The importance of the size of pinhole will be discussed further in Chapter 9. A commercial camera zoom lens was chosen for the focusing optics for the following reasons:

(i) The optics used in commercial camera accessories are of a very high quality and when bought off the shelf, they are cheaper than even a single unmounted lens of comparable quality bought as a special order.

(ii) The lens size chosen was an 80-210 mm f4.5 TAMRON zoom lens. This lens offered a wide range of focal lengths and a range of apertures available in half stops down to f32. Such a flexible range of aperture sizes would allow any additional spatial filtering should this be required.

A variable focal length lens enabled the image of the measuring volume on the pinhole to be enlarged or reduced depending upon what was required to improve the signal. The main advantage of a zoom lens, however, was the ability to

control the image size thus providing a means of illuminating the pinhole with only that part of the image containing the cleanest signal.

A special adaptor was made which housed the pinhole mount and which bolted onto the photomultiplier housing. The camera lens was then screwed onto the front end of the mount using an M42 Pentax screw thread mount. The whole assembly is shown in Plate (vii). The pinhole mount was secured between two adjustable stops which enabled the centre of the pinhole to be moved relative to the axis of the scattered light. A X40 microscope objective and a X10 eyepiece were used in order to aid the focusing of the beam intersection upon the pinhole. Even a 50 μm pinhole was quite clearly visible using this arrangement. The eyepiece assembly can be seen on the photograph.

The transmission optics have thus been designed to produce the appropriate size of intersection volume for the application whilst the detection optics are required to optimize the measuring volume. The optics were mounted on a good quality camera tripod for easy location. Due to the minimum focusing distance of the zoom lens of 0.8 m, the detection optics could not be used directly in line with the most intense regions of the scattered light. As shown in figure 4.6, a mirror mounted on a tripod was used to direct light from the intersection volume onto the front of the camera lens. A coarse adjustment of the lens position moved the image of the measuring volume over the pinhole. The

fine adjustment screws could in turn be used to yield the optimum signal strength and quality.

4.3 Design of the transmission optics

4.3.1 Introduction

It was mentioned earlier that a very small probe volume was required in order to try to minimise the potentially high number of water droplets likely to be present simultaneously in the probe volume. Microscopic probe volumes are certainly possible with well designed optics and with a laser operated in the TEM_{oo} mode. Other authors in LDA (56) have produced very tiny probe volumes and have used the simple waist-waist size relationships proposed by Dickson. The same approach will be adopted here in the design of the transmission optics employed in this research.

The design of any optical system for LDA begins with the size required for the measuring volume. It is from here that the measurements will be made and any advantages that have been developed into the transmission optics must be felt here.

From the point of view of the measuring situation, the lower the pressure in the measuring section of the experimental rig, the lower the concentration of water droplets for a given pressure and droplet radius. This is shown in figure 4.7. Before embarking upon a final design for the transmission optics some features of the wet steam need to be considered. The experimental rig will be

discussed in detail in Chapter 6, but it is sufficient to say here that a condenser was used with the experimental rig to condense the exhaust steam. This condenser was normally used in conjurction with a small laboratory steam turbine. When running the turbine at full speed the condenser pressure dropped to about 0.2 bar absolute. The mass flow rate of steam into the turbine under these conditions was about 0.27 kgs^{-1} and was the maximum that the supply would deliver. It was decided to use these conditions as a typical situation. Some estimate of the radius of the water droplets is now required. Measurements taken in the experimental turbines at NEI Parsons (61) suggest that a monodispersion of water droplets of 1μm diameter were present in the exhaust stages, From figure 4.7 at 0.2 bar there may have been up to 10^{12} droplets/m^3 present. These conditions were used to design the optics. It is accepted that these conditions may not be correct, but it is important, however, that some conditions be chosen that are at least based upon some experimental evidence and then optimization of the anemometer could be made when the true wet steam conditions were realized.

The design of the transmission optics will be treated in two sections. The first will consider the way the two beams can be focused to produce a tiny probe volume and the second will concentrate upon the geometrical matching of the anemometer to the range of scattering particle sizes anticipated.

4.3.2 Matching the transmission optics to the geometrical requirements

It has already been emphasized that a correct matching of the LDA optics to the geometry of the measuring situation is important. The most influential of these requirements is concerned with a general relationship between the spacing of the apparent fringes in the probe volume and the size of the individual scattering particles. Various authors (24) (33) have suggested that the particle size should be matched to this fringe spacing according to the following relationship:

$$\sin(\alpha_b/2) \sim \lambda/16\, rp \qquad (4.5)$$

The particles to which the optics were matched lie in the size range:

$$0.1\ \mu m \leq rp \leq 1.0\ \mu m \qquad (4.6)$$

From figure 4.7 a water droplet concentration of between 4×10^{14} and $4 \times 10^{11}\ m^{-3}$ can be expected for the wet steam at 0.2 bar and 1% wetness. Taking a mean particle radius of 0.5 μm, the water droplet concentration is likely to be between $2 \times 10^{12} m^{-3}$ at 1% and $20 \times 10^{12} m^{-3}$ at 10% wetness under these conditions. It is to these conditions that the optics have been matched.

From equation (4.5) the half angle between the two laser beams at the intersection needs to be:

$$\sin \alpha_b/2 = \frac{514 \times 10^{-9}}{16 \times 0.5 \times 10^{-6}}$$

Therefore

$$\alpha_b/2 = 3.68^0$$

where $\lambda = 514 \times 10^{-9}$ m for an Argon-ion laser.

Now the apparent fringe spacing is given by (33)

$$\Delta x = \frac{\lambda}{2\sin(\alpha_b/2)} \qquad (4.7)$$

whence using $\alpha_b/2 = 3.68^0$ gives $\Delta x = 4$ μm.

It is worth commenting upon the choice of particle radius to which the transmission optics have been directly matched. The smaller the value of rp, the larger the required beam spacing in order to reduce the fringe spacing in accordance with equation (4.5). There is a physical limit upon the size of aperture of the transmission lens required, available at reasonable cost. If one lens was to be used to focus the two laser beams then an aperture of at least 130 mm was required between the beam centres for a lens of 1000 mm focal length. However to avoid truncation, Dickson (21) has shown that the available aperture has to be at least twice the $1/e^2$ diameter of the beam. Since the laser beams have been expanded to a $1/e^2$ radius of 8 mm at the lens surface then an aperture of at least 200 mm is required to focus two expanded laser beams whose centres are 130 mm apart, without truncation.

One further matching requirement is that the diameter of the measuring volume (ie that portion of the probe volume

seen by the detection optics) must be smaller than that of the intersection volume in order to avoid detection of the poorer quality signals resulting from the outer regions of the fringe pattern.

It is normally recommended (33) that at least 20% more apparent fringes are produced than are seen by the detection optics in the measuring volume.

4.3.3 To produce a tiny probe volume

When a laser beam is focused by a single lens, the waist radius of the focused beam is given by (21)

$$w_1 = \frac{\lambda f}{\pi w_o} \qquad (4.8)$$

This assumes that the waist is positioned at the focal plane of the lens. The geometry of the probe volume produced by two intersecting beams is shown in figure 4.6. It can be shown that the length of the measuring volume, ℓm is given by

$$\ell m = \frac{4 w_1}{\sin(\alpha_b/2)} \qquad (4.9)$$

whence using (4.8) gives

$$\ell m = \frac{4}{\pi} \cdot \frac{f\lambda}{w_o \sin(\alpha_b/2)} \qquad (4.10)$$

The probe volume may be described by an ellipsoid whose major axis is given by ℓm in equation (4.10) and whose minor axis can be approximated as:

$$\frac{4}{\pi} \cdot \frac{f\lambda}{w_o \cos(\alpha_b/2)} \qquad (4.11)$$

The probe volume can now be totally described as an ellipsoid by the following equation.

$$x^2 + y^2 \cos^2(\alpha_b/2) + z^2 \sin^2(\alpha_b/2) = (w_1)^2 \qquad (4.12)$$

at the $1/e^2$ intensity points.

It can be shown (30) that the volume of such an ellipsoid is given by:

$$V_e = \frac{\pi (2w_1)^3}{3 \sin(\alpha_b/2)} \qquad (4.13)$$

For 2 particles of size rp = 0.5μm to be present simultaneously in the probe volume then:

$$10^{-12} = \frac{\pi (2w_1)^3}{3\sin(\alpha_b/2)}$$

whence w_1 = 20 μm.

For signal detectability using a counter, one mode of the counter requires a minimum of 8 fringes in the measuring volume. From earlier considerations (33), the apparent number of fringes should be at least 10.

Hence the minimum probe volume diameter that is practical is given by:

$$(d_{ph})_{min} = 10 \times \Delta x = 40\mu m$$

and in figure 4.6, d_m = 32μm. The concept of a diameter of the probe volume is simplified by considering the probe volume to be very crudely approximated by a cylinder of length ℓm and diameter d_{ph}.

From equation (4.10), therefore, ℓm can be calculated as being 623μm. The minimum value for the measuring volume is then approximately:

$$V_m \approx \frac{\pi}{4} dm^2 \, \ell m \approx 5 \times 10^{-13} \, m^3$$

Given the measuring situation predicted in section 4.3.1, between 1 and 10 particles of 0.5μm radius may be expected to be present simultaneously in the measuring volume for a range of steam wetness of between 1% and 10%.

The laser beam itself diverges very slightly as it propagates from the laser. Given a typical radius of the beam of 0.6 mm, there is now a problem of reducing this by two orders of magnitude in order to obtain the small size of the probe volume required. The laser beam will have to undergo beam expansion.

The beam expansion technique, used in the transmission optics works by taking advantage of a very useful property of gaussian beams. Figure 4.8 shows the path of a single beam propagating along the optical axis of the three lens system discussed in section 4.1. The relative sizes of the waists w_1, w_2, and w_3 depends upon the relative distances between the three lenses, L1, L2 and L3. In Chapter 3 it was shown that if the input waist of a lens was positioned

at the lens input focal plane, the focused waist would be located at the lens output plane. The distances between the lenses in figure 4.8, were thus equal to the sum of the focal lengths as shown. In this manner the waist sizes were simply related to each other as described by equation (4.8). The beam expansion used the techniques already described in Section 3. A beam expansion ratio of about 16:1 was produced by this arrangement. The focal length and aperture of each lens is shown in figure 4.8 for clarity.

The three lenses provided the necessary beam conditioning to produce the required waist size in the intersection volume. As long as the focused waist of each lens was located in the focal plane of the next then when the beam was split, coincidence of the two waists focused by L3 was assured. The function of each lens may be summarized as follows:-

L3 is the final transmission lens and its focal length is such as to produce the required waist from the expanded input waist. It served to focus two collimated and paraxial beams onto its focal plane. L1 produced a small waist, leaving the beam to rapidly diverge so as to be collimated at the required expanded waist by L2. L1 therefore determined the size of the final waist in the intersection volume, and L2 determined the position of the final waist. L2 and L3 were intended to be be moved in conjunction with each other to ensure that the waist of each beam was coincident at the intersection volume.

4.4 The alignment procedure for the transmission optics

With an optical system which has been manufactured in house, it was essential that every single optical surface was adjustable. Due to manufacturing tolerances even only a very fine adjustment may have been necessary but this still had to be allowed for.

As a result the mirrors and lenses had kinematic mounts which were fully adjustable. The drawback however of having every surface fully moveable was that alignment could often be a tedious and difficult process. With this type of system a method was perfected that allowed a rapid assembly and alignment. Referring to figure 4.3 showing the general layout of the optical system, one of the functions of the mirrors M1 and M2 was to raise the optical axis of the system by 40 mm. It was because of this folding of the beam that alignment was made easier.

In this arrangement the laser was fixed with respect to the bedplate. Thus the lower optical axis was fixed in a similar manner. The large transmission lens was fitted with a mount with limited adjustment. Once adjusted, however, this lens fixed the upper optical axis. This lens was treated with a broad-band anti reflection coating (BBAR) in case backscatter detection was to be employed. Such a coating would minimise stray reflections from the lens to the detection optics. The coating did, however, slightly impede optical alignment as it was mainly through the use of

reflections that the optical system was coarsely aligned.

With the laser power set to about 100 mW and lens L3 in position, mirrors M1 and M2 were inserted. These mirrors were adjusted together until the laser beam was travelling through the centre of L3, at least as far as the eye could tell. At this point, the back reflection of the beam from the back surface of the lens L3 would either be on mirror M2 or elsewhere on the bench. Adjustment now of M2 would bring the weaker reflected beam into coincidence with the transmitted beam. This coincidence of images could then be checked upon the face of M1 and the aperture ring of the laser itself. At this stage the beam was travelling straight through the centre of L3, as confirmed by the use of a mask.

Lens L1 could now be mounted onto the bedplate and its angle adjusted to suit the folding of the beam at this point. The beam would almost certainly be off axis and hence would not be incident upon the centre of the back surface of L3 as before. By a similar method of bringing the new reflection into alignment with the original beam, L1 could be correctly positioned. An identical process was performed with L2 and the beamsplitter module. The intersection of the beams was carried out by projecting the intersection upon a wall using a 20 mm diverging lens. The mirrors on the beamsplitter were adjusted until both beams were coincident. Lens L2 could now be moved relative to L3 until the spot size was at its minimum and the interference

fringes were at their sharpest. A mask was essential for locating the two split beams in their correct plane. The mask that was used throughout the research for general alignment of the optical system is shown in Plate (vi). This was used for those components positioned on the upper optical axis of the system. The central hole was for beam alignment along that axis and the four holes around the periphery were used for setting the plane for the two split beams both horizontally and vertically.

4.5 The performance of the optical system

During the course of this work the hardware was manufactured in several stages. Each stage had to be assembled and fully commissioned in order that the experimental facility performed as well as expected. The most crucial of these stages was the correct alignment and performance of the LDA optical system. Assuming that a wet steam flow could be generated, the success of the research largely depended upon the ability to obtain good quality Doppler signals from the water droplets present in the flow. The correct alignment of any optical system in LDA is important but in this application it was crucial.

It is well known that the visibility of Doppler signals can be optimized with correct alignment of the transmission optics and adequate spatial filtering of the scattered light detected by the collection optics. Provided that the laser beam entering the optical system is split equally and each beam is focused to the same degree, then a

probe volume should be formed which is illuminated with a gaussian intensity distribution of laser light. This can be assumed to be the case since Dickson (21) has shown that for any combination of lenses, a laser beam entering an optical system with gaussian intensity distribution will emerge with the same distribution. The problem here, however, was not whether the intensity conformed to this distribution or not, but whether the two minimum beam radii were:

(a) located in the lens focal plane and,

(b) were fully coincident

If the beam waists were not fully coincident, then non-uniform fringes of a dubious definition would have been produced. Techniques have been developed for locating precisely the position on a beam at which a minimum waist occurs. This has been done by Tridimas et. al (83), who have also provided a means of measuring the size of this waist. However, this is an area of some research in itself and can be time consuming particularly if the transmission optics are to be checked frequently. The problem in this application lay in the fact that a lens of long focal length (f = 1000 mm) as the final transmission lens was used to produce a spot size of only 40 μm diameter. (Measurable only at the $1/e^2$ intensity points of the beam). Due to the geometry of this, the slightest knock on the optical bench could have jolted the mirror mounts on the beamsplitter module. In fact the total mirror movement only had to be about 140 seconds of arc to fully separate the focused

waists. The mirrors needed to be very securely locked in position. A technique for checking the alignment and performance of the optical system was therefore required which was quick, foolproof and would allow the mirrors to be locked. At any time using this same method, the transmission optics could be rechecked and, if necessary, quickly adjusted. There were two methods adopted throughout this work to meet these criteria depending upon the degree of beam realignment and signal optimization that was required.

(i) A projection of the beam intersection upon a plane surface by positioning a small (ie f = 20 mm) diverging lens into the intersection region of the two beams so that the single spot was incident upon its surface. This method showed whether fringes were produced and thus provided a means of coarse adjustment to the probe volume. It was found that so long as some part of each beam was coincident then fringes were produced but were not especially clear. It was only when the spot from one beam was fully covering the spot from the other that the sharp brightly contrasting fringes normally associated with LDA systems were produced. This method was also essential for the correct positioning of the three beam conditioning lenses of figure 4.8.

(ii) The second method required the actual detected Doppler signal and constituted a means of very fine adjustment. It was only via this means that the full effect of any minor adjustments on the optical system could be appreciated. The signal in question was the fully conditioned signal as modified by the Counter Processor and observed on a digital storage oscilloscope. Any adjustment of the transmission optics would have inevitably lead to a slight deformation or shift in the position of the probe volume and had, therefore, to be made in conjunction with a fine adjustment of the pinhole mount.

At this stage in the manufacture and development of the LDA optics, the wet steam rig had not yet fully commissioned. In any case using a wet steam flow as a means of checking the performance of the optics was not realistic. Due to the expected uncertainty of the quality of the Doppler signals from the steam flow, it was essential that the optics were to be tested in a medium other than wet steam. A channel flow containing drinking water was chosen as this medium. Provided that the water was filtered (using, say a 50 μm filter) then classical textbook LDA signals could be produced.

Two examples of these signals are shown in Plate (ii). The first is a typical Doppler burst produced by a single

particle passing through the measuring volume. The second is the capture of a multiple burst given by two particles passing simultaneously through the measuring volume. With clean water as a medium, extremely sharp signals are possible with a very high signal-to-noise ratio. For example the signal trace shown in Plate (ii), was obtained by a particle passing through the measuring volume at a velocity of $0.2\ ms^{-1}$, given by the mean velocity computer on the Counter Processor. Under these flow conditions a data rate of about 2 kHz was obtained and data acceptance was as high as 55%. However, as an indication of the performance of the LDA optics the Plates contain some useful information. Each peak in the signal trace corresponds to an interference fringe as seen by the photodetector. The total number of peaks is approximately 20 which gives a probe volume diameter of about $20 \times \Delta x = 20 \times 4 = 80\mu m$, i.e. about twice that number calculated in section 4.3.3. This could be due to one of several influencing factors:

(i) Due to the form of the intensity distribution in figure 3.1, the apparent size of the laser spot is approximately twice that of the diameter given by the $1/e^2$ intensity points. Due to the transparency of drinking water, the amount of laser power available and the overall design strengths of the optical system, the fringes seen by the photodetector over the distribution outside the $1/e^2$ limits

are of sufficient contrast to generate a signal. Under these ideal conditions, every fringe seen by the photodetector can be located on the signal trace. (This observation will be compared with those signals obtained from the wet steam when such good fringes are not seen by the photodetector and so the number of individual peaks that can be counted in the signal trace is significantly less than 20).

(ii) An alternative possibility is that a probe volume of the dimensions hoped for was not possible due to the effects of spherical abberations upon the performance of the large transmitting lens (L3 in figure 4.3.). Because of the importance of bringing two very small spots together, only one lens was used. Two parallel beams moving paraxially to the optical axis of L3 were focused to a common spot using the one lens. Each beam had a spot sizeofabout 16 mm (at the $1/e^2$ intensity points) at the front surface of the lens. Even though the lens was made with an aperture as large as practicable, each beam was passing through the lens at very near to its outer edge. Ideally a smaller aperture lens (subject to diffraction limiting conditions) should have

been used for each beam, where each beam would pass through its centre. If spherical abberations were responsible for this effect then it is at these outer edges where their effects would have been most pronounced.

It should be noted that ir the signal trace no spatial filtering other than the use of a 100 μm pinhole was used.

5. SOME ELEMENTARY WET STEAM THEORY

5.1 Introduction

As already indicated in Chapter 1, the emphasis of this research was not on a detailed and exhaustive review of methods of generating a wet steam flow, rather it was the analysis of a technique developed for making velocity measurements in wet steam, using the water droplets present in the flow as seeding particles. However, an appreciation of the nature of wet steam and its behaviour is required. This chapter is intended to discuss briefly the fundamental aspects concerning the occurrence of wet steam and some of the useful equations which describe this. The nature of wet steam is complicated by the fact that a theoretical approach can be totally different from the real situation. For example, a simple definition of wet steam might be that it is a mixture of dry steam and water which is in thermal equilibrium between the two phases and the surroundings. This suggests that the water is present as a bulk liquid which is highly unlikely in practice. According to nucleation theory (22) the water is present as a very fine fog or suspension of water droplets. Theory then predicts that these water droplets grow larger by condensation due to expansion or by coagulation due to collisions. Real wet steam can be a very different and unpredictable environment. The essential differences between the real wet steam and well behaved wet steam lie in the processes involved in producing a supersaturated environment in the first instance. One

such method is to extract enthalpy from dry superheated steam and a practical example of this is in the large axial steam turbines used as the prime mover for a turbine-generator set. In thermal power stations it is within the final two stages of a low pressure turbine that the steam nucleates and goes wet. This is a very harsh environment in which the moving turbine blade rows are rotating at 3000 rpm relative to the stationary blade rows. Individual blades can have moving tip speeds of between 520 and 620 ms^{-1} in the final low pressure stages. The water droplets can quickly grow by condensation and coagulation and may well collide with the stationary blades and collect there. Experiments (69), (78) have shown that water films flow over the stationary blades and are stripped off the trailing edge forming large unstable water droplets. These droplets have been measured up to 1500 μm in size. They have been shown (90) to leave the trailing edge of a blade and accelerate to a maximum velocity of about 21 ms^{-1} over a distance of about 25 mm in the blade wake. They are then caught in the main steam flow which has a velocity up to 370 ms^{-1} where they are broken up and rapidly accelerated. These droplets then impact on the moving blades causing erosion. Although this process of formation of large droplets leading to turbine blade erosion has been discussed briefly in Chapter 2, it has nevertheless been quoted here as an example of a process that exists to modify the size of the water droplets present in a turbine. Where during the

intial stages of nucleation a monodispersion of water droplet sizes is produced, very quickly a distribution of droplets sizes may exist due to the various accelerating and viscous forces that exist in such an environment. This chapter will review some of the factors which govern and influence water droplet growth, instability and deformation.

Due to the changing conditions within a steam turbine, the events which lead to erosion and loss in aerodynamic efficiency have encouraged some in depth research into the subject of real wet steam. Methods of producing wet steam in an experimental facility such as a cascade have therefore evolved. This chapter will review the classical method of nucleating a saturated steam flow which does not involve enthalpy extraction. Wet steam that is formed in this way can be said to be well behaved. An introduction will be made to the use of a commercial turbocharger to extract enthalpy from dry superheated steam. This is a novel technique in itself and details will be left to Chapter 6.

5.2 Basic Wet Steam Theory

5.2.1 The structure of wet steam

Wet steam may be thought of as a mixture of dry steam and water. If the total mass of this mixture is M_t and is composed of M_g parts of dry steam and $M_f = M_t - M_g$ parts of water then the following definitions may be made:

$$\text{Dryness fraction, } X = \frac{M_g}{M_t} \qquad (5.1)$$

and

$$\text{Wetness fraction, } Y = \frac{M_f}{M_t} = 1 - X \qquad (5.2)$$

The subscripts f and g denote the liquid and gaseous phases respectively. If this mixture is enclosed adiabatically and kept at constant volume then the two phases will tend to have the same temperature and pressure. This is achieved by partial evaporation from the liquid to the vapour phase or by partial condensation from the vapour to the liquid phase. In this condition the steam and water are saturated. As has already been mentioned, wet steam such as produced by turbines differs considerably from the ideal thermodynamic equilibrium situation. In steam turbines, the following conditions may occur which illustrate the departure from an ideal system.

(i) the various state parameters are subjected to rapid changes during expansion through a turbine which may lead to supersaturation and condensation on moving and fixed surfaces. This means that existing water droplets grow or evaporate or coagulate as they flow around these surfaces. A polydispersion of droplet sizes will soon exist.

(ii) In an ideal system, the steam wetness is present as a fine mist of single sized water droplets. Clearly in the real system this is not the situation.

(iii) The vapour phase itself is not a uniform monomolecular substance but contains submicroscopic sized clusters of condensed molecules. As will be seen in the next section, nucleation or spontaneous condensation may occur.

(iv) In a steam turbine there may be relative motion between the phases. For water droplets up to about 5μm in radius, the degree of slip between the phases is normally negligible (71), but for larger droplets such as those torn off from the trailing edge of the fixed blades, the slip can be substantial. Due to their relatively high inertia, these droplets are subjected to high accelerating forces. These forces can overcome the surface tension forces within the droplet which reduce progressively as the volume of the droplet increases. The droplet becomes unstable and breaks up into tiny fragments of unequal size (73).

The behaviour of wet steam under given flow conditions is largely determined by the size distribution of the water droplets present and by the total amount of steam that has been condensed, given directly by the wetness fraction.

Figure 5.1 is a general guide and shows some of the processes that exist in the real steam turbines in which

water droplets of a given size dominate (71). It must be emphasized that although initial nucleation of water droplets is shown, under conditions of rapid expansion in steam turbines these droplets very quickly grow into the category of fine and coarse fogs.

For the ideal situation, a very simple relation can be derived which expresses the concentration of water droplets under given conditions. Being an ideal system, it is necessary to assume that the wetness fraction, Y, is known, all the water droplets have the same radius and are uniformly distributed in space. The mass of a water droplet is then given by:

$$m = \frac{4}{3} . \pi r^3 \rho_f \qquad (5.3)$$

and the specific number of droplets is then given by:

$$N_{kg} = \frac{Y}{m} = \frac{3Y}{4\pi\rho_f r^3} \qquad (5.4)$$

For a wetness fraction of less than 0.2, the volume occupied by unit mass of wet steam is given by $\nu' \approx X\nu''$. The number concentration of droplets. (i.e. the number per unit volume) is then given by:

$$N = \frac{N_{kg}}{X\nu''} \equiv \frac{3Y}{4\pi\rho_f r^3 X\nu''} \qquad (5.5)$$

The variation of droplet concentration can be plotted for a given droplet radius and pressure (given by ν'', the

specific volume of the vapour phase). This is shown in figure 5.3 for a range of operating pressures. It is interesting that the specific number of droplets is very nearly linearly dependent upon the operating pressure. It is due to this fact that the wet steam present in the measuring section of the experimental rig was kept at as low a pressure as practicable. The fewer the number of water droplets that are flowing simultaneously through the probe volume of the LDA system, the more likely it becomes that discrete bursts of Doppler signal will be detectable.

Basically the bulk of water droplets that are likely to exist in the wet steam produced by large steam turbines may be categorized into two main groups:

(i) fine fogs in which r_p = 0.01-0.2μm and N $\approx$ 10^{18}-10^{15}kg^{-1}

(ii) coarse fogs in which r_p = 0.5-10μm and N ~ 10^{14}-10^{10}kg^{-1}.

These are typical values.

5.2.2 The process of nucleation

According to the kinetic theory of ideal gases, the molecules of the water vapour are in a continuous disorderly motion. Their speeds of flight are statistically distributed according to Maxwell's law. Among the many collisions that occur constantly with these molecules, there is a probability that those travelling at low enough velocities will meet. Intermolecular cohesion forces may cause them to form a cluster of two, three or more

molecules. It is these submicroscopic clusters of molecules that form the nucleation sites for a supersaturated vapour. However, to take this approach a little further, for a cluster of i molecules there exists an expression for the equilibrium number of i molecule clusters in a given vapour under given conditions. This is familiar to statistical thermodynamics and is given by Boltzmann's law as:

$$N_i \,.\, eq = N_m . \exp\left(\frac{-\Delta G_i}{kT}\right) \qquad (5.6)$$

ΔG_i is the change in Gibbs free enthalpy when a number i of molecules is converted into a cluster of i molecules. The magnitude of ΔG_i and its variation with i is strongly dependent upon the value of supersaturation in the vapour.

When an initially saturated vapour becomes supersaturated the formation of these clusters begins. Some of the clusters will grow beyond what is known as the critical droplet size to become stable sizes. This process is called nucleation or spontaneous droplet formation. Before discussing what is meant by the critical droplet size it is pertinent to establish the process of nucleation and to consider post nucleation effects.

The nuclei that emerge from the nucleation process as stable droplets will grow further by condensation of the vapour phase on their surface and by coagulation with other droplets. The rate of condensation from the vapour phase on a droplet is governed by the rate at which latent heat can

be carried away from the surface into the cooler vapour. Essentially the rate of growth of the droplets is dependent upon the rate of subcooling of the vapour phase. This in turn is a function of the rate of decrease in pressure of the steam flow as given by an expansion rate:

$$\dot{P} = \frac{-1}{p} \frac{dp}{dt} \qquad (5.7)$$

the negative sign acting as a reminder that it is a decrease in pressure that is being referred to. It is this parameter which controls the growth rate of water droplets and their final size in an expansion process. It is of particular relevance in methods used to produce ideal wet steam flows for fundamental research work. The ideal flows referred to here are those generated by the convergent - divergent nozzle. This method will, however, be discussed further in section 5.3.

The concept of a critical droplet size has been mentioned in the context of the process of nucleation. It is of particular significance to nucleation theory because a water droplet above this size will become stable and grow, but below this size it will tend to evaporate. Because the vapour pressure of a convex surface is larger than a plane one (it must be due to surface tension forces) water droplets tend to evaporate in saturated steam. The vapour pressure of a water droplet is given by the Kelvin-Helmholtz equation as:

$$P_r = P_s(T_r) \exp.\left(\frac{2\sigma}{r\rho_f RT_r}\right) \qquad (5.8)$$

This expression is valid if the vapour can be assumed to be an ideal gas. If the water droplet is surrounded by a supersaturated vapour atmosphere so that $p=p_r$ and $T_g=T_r$, then it is in thermal equilibrium with the vapour. The equilibrium is unstable because the smaller droplets where $P_r>P$, tend to evaporate. Conversely those larger water droplets in which $P_r>P$ tend to grow. For a given ratio of p_s/p, known as the supersaturation ratio(S), the radius of the unstable droplet, or critical droplet size, is given by

$$r_{crit} = \frac{2\sigma/\rho_f . RT_g}{\ln S} \qquad (5.9)$$

For significant degrees of supersaturation (i.e. $S \geqslant 1{\cdot}2$), r_{crit} is of the order of 10^{-9}m, ie 0.001μm (71). Water droplets of this size would contain typically about one hundred molecules of water.

Gyarmathy (71) has derived an expression for the rate of growth of critical water droplets. This is given by

$$\dot{r} = \frac{dr}{dt} = \frac{\lambda_g}{\rho_f . \Delta h_{fg}} \cdot \frac{1-r_{crit}/r}{r + 1.59\bar{\ell}} \cdot \Delta T \qquad (5.10)$$

This is relatively meaningless in the above form but is useful when computing droplet growth curves. A few growth curves computed from equation (5.10) have been reproduced in

figure 5.2 for completeness (71). The main features of droplet growth as highlighted by figure 5.2 are the following:

(i) Droplet growth is lower at low pressure than at high pressure.

(ii) The growth of droplets is limited while the individual droplet size is still near the critical value,

(iii) A tenfold increase in diameter (ie 1000-fold increase in mass) can occur in a matter of microseconds. This fact is apparent even at low pressures.

The description of the main process involved in nucleation of wet steam is nearly complete. It has already been mentioned that the formation of nucleation sites and subsequent growth of water droplets is governed by the expansion rate given in equation (5.7)

$\dot{P}$ is essentially a measure of the rate of decrease of pressure as a steam flow expands. This is not to be confused with equation (5.10) which describes the rate of growth of water droplets once they have reached their critical size. In all nucleating gas flows there is a thermodynamic condition corresponding to the maximum supersaturation (or subcooling) before spontaneous condensation occurs. The condition at which this occurs is known as the Wilson point. For a given expansion process it can be found experimentally and can be linked with the expansion

parameter of equation (5.7). Various Wilson points can be plotted on a Mollier chart for steam obtained with expansions starting from different initial conditions in the dry superheated region. A Wilson line may then be drawn through the various Wilson points. Experimentally for steam turbine blading with an expansion parameter of 5000 s^{-1} (given by equation (5.7)), the Wilson lines have been found (22) (71) to lie in a range corresponding to 2.9-3.3% equilibrium wetness. Any wetness values outside this range are generally thought to be in error due to wet inlet flow conditions. In other words the range of wetness values quoted above are considered typical for large axial steam turbines.

5.3 A Classical method of generating a wet steam flow

5.3.1 Introduction

In section 5.1 some reference was made to the fact that wet steam has been produced in situations other than in large steam turbines in order to conduct fundamental research into its behaviour and to study the flow of wet steam around turbine blade sections such as found in model turbine cascades (15).

'Wet steam' of a description can be generated by several methods. The use of inverted commas here is intended to emphasize that real wet steam is considered to exist only in steam generating plant and in steam turbines. Basically there are two methods in which wet steam has been produced.

(i) Dry superheated steam can be expanded through a convergent - divergent nozzle known as a Laval nozzle. This method is the so called classical method.

(ii) Decuypere et. al (15),have used water droplets in a superheated steam flow in order to study the flow of 'wet steam' around turbine blading in a model. Water droplets of a known size and concentration were sprayed into the steam flow. The reason for doing this was that suitable sized seeding particles were required for an LDA measurement system. Decuypere's measurements of velocity around the blade profiles were made in the subcooled steam at the onset of nucleation. The size of the fog droplets present were so small, in the order of 0.001μm, that they quite simply did not scatter sufficient of the laser light to yield detectable Doppler signals. This particular application of LDA to steam flows has already been discussed in section 2.3.

The next section of this Chapter is therefore intended to review the so called classical method of generating a wet steam flow as it has formed the basis for much experimental work. Since this method has not been adopted in this research, the review will be spared much detail and it will

serve only as a means of comparison with the technique chosen for this work.

5.3.2 The classical method of generating wet steam

Laval nozzles are basically convergent - divergent channels in which a gas or vapour flow is accelerated from subsonic to supersonic speed. Spontaneous condensation is manifested by a change of pressure distribution as compared to the dry superheated flow at the inlet of the convergent section. The sequence of events that takes place in the Laval nozzle is shown in figure 5.4. Superheated dry steam is expanded from a constant inlet stagnation pressure P_{0t} to a back pressure P_B. This pressure is sufficiently low to ensure shock free supersonic flow. It is assumed that the inlet stagnation temperature remains constant throughout the expansion. The dotted line in figure 5.4. shows the pressure distribution an all superheated isentropic expansion. The steam in this condition is behaving as a gas. Of significance, however, is the change in pressure shown in figure 5.4. as the line BC. Nucleation and fog formation takes place once the point of supersaturation corresponding to the Wilson point has been reached. The rate of formation of condensation nuclei has been shown (71) to be negligible for a supercooling of $\Delta T < 30^0C$. This is a very useful guide figure because at the Wilson line it can be shown similarly that $\Delta T > 30^0C$ and the number of nuclei is very large. The sudden change in

pressure during the expansion through the nozzle outlet may be explained by the following process. Nucleated water droplets which have grown and lie in the size range 0.05-1.0 μm in radius have a number density typically of the order $10^{17} - 10^{13}\ m^{-3}$. The total surface area of water for this concentration and size of droplets is typically of the order $100\text{-}5000\ m^2.m^{-3}$. This represents a very large surface area and is the reason why the small water droplets tend to remain in thermal equilibrium. The heat transfer from an equivalent film of water of this surface area would be significant. When spontaneous condensation occurs, some of the latent heat of vaporization is carried away from the surface of water droplets into the slightly cooler vapour. (The surrounding vapour is still expanding and thus cooling). This results in a warming of that vapour and an increase in local pressure and local temperature. The bump in pressure is more commonly referred to as a condensation shock (70).

The number density of the nucleated water droplets may be given by the following expression.

$$N = N_m \exp\left(\frac{-4\pi r_I^2.\sigma}{3kTg}\right) \qquad (5.11)$$

where

$$r_I = \frac{2\sigma T_s}{\rho_f.h_{fg}.\Delta T} \qquad (5.12)$$

N, here, represents the number density of nuclei formed at any degree of supercooling ΔT. As can be seen from its exponential relationship, N has a very strong dependence

upon ΔT.

Experimental nozzles of the type (70) shown in figure 5.5 are designed to incorporate a varying throat height and divergence angle. The nozzles A-E as shown were selected by the authors to give a progressively decreasing rate of expansion, as expressed by the expansion parameter of equation (5.7), at any given static pressure. At positions in the nozzle where supersaturated expansion from the inlet conditions produced a Mach number of 1.2, the expansion rate varied from $3160s^{-1}$ for nozzle A to $460s^{-1}$ for nozzle E. According to nucleation theory different degrees of supersaturation may be expected before condensation in each nozzle. This would lead to different sizes of nucleated water droplets in each case.

This technique has been the most frequently reported for generating spontaneous condensation in a steam flow under laboratory conditions. A considerable number of experiments employing this technique have been performed (49) (70) (75). However the technique used in this research was concerned with the homogeneous extraction of enthalpy from superheated dry steam and will be introduced in section 5.5.

5.4 Some other properties of wet steam flows

5.4.1 Droplet deformation and break up

The stability of a water droplet moving through a two phase flow depends upon the ratio of the aerodynamic pressure forces trying to deform it and the surface tension

forces trying to make its shape spherical. This ratio is usually expressed by the Weber number (73).

$$We = \frac{\rho_g \cdot \omega_r^2 d_p}{\sigma} \qquad (5.13)$$

At low values of We, a water droplet will remain nearly spherical. This occurs with a slow relative speed (or minimum slip) to the steam flow or with a small droplet diameter d_p. A water droplet exposed to a high We flow is quickly deformed and fragmented. Droplet break-up has been the subject of numerous experimental investigations, (73), (78). These investigations have been confined to the study of water droplets torn from the trailing edges of blades in large steam turbines. Under these conditions a critical Weber number has been found experimentally to be of the order of 20 (73).

5.4.2 The property of relaxation

When some property of a medium, say ϕ' is displaced from its equilibrium value, ϕ_o', and restoration to equilibrium occurs at a finite rate, the substance is termed a relaxing medium (71). The simplest of such systems is defined by the proportionality.

$$\frac{d\phi'}{dt} \alpha (\phi' - \phi_o') \qquad (5.14)$$

The system may be more fully characterised by the constant of proportionality to give

$$\frac{d\phi'}{dt} = \frac{-1}{\tau}(\phi' - \phi_o') \qquad (5.15)$$

where τ is known as the relaxation time or time constant. Integrating equation (5.15) with time gives the well known exponential form of decay of ϕ to equilibrium, viz:

$$\frac{\phi' - \phi_o'}{\phi_1' - \phi_o'} = e^{-t/\tau} \qquad (5.16)$$

where ϕ_1' is the initial displacement value.

From the point of view of assessing the performance and running characteristics of the wet steam experimental rig in Chapter 6, it would be useful to have an indication of the state of equilibrium within the working section of the rig. For this purpose equation (5.16) will be used to define the thermal relaxation for the wet steam flow and the inertial relaxation of those water droplets in the flow.

5.4.2.1 The thermal relaxation of wet steam .

A mixture of water and steam is displaced from thermodynamic equilibrium if the temperature of the vapour phase differs from that of the water droplets. Thermal equilibrium is restored by a change of phase, the latent heat that is transferred bringing the temperature of the vapour phase towards the saturation temperature. This can be expressed further by a derivation of the thermal relaxation time for a wet steam flow.

If the water droplets are immersed in supersaturated steam at a temperature T_g, where $T_g < T_s$, the rate of return

to thermal equilibrium is determined by the rate of transfer to the steam of the latent heat released by condensation of some of the vapour phase on the surface of the droplets. The water droplets will thus grow in size.

Assuming that this process occurs at constant pressure, the rate of enthalpy increase of the steam may be written as

$$C_{pg}\,(1-Y)\,\frac{dT_g}{dt} \approx N\pi\, d_p^{\,2},\ \alpha_L \cdot (T_s - T_g) \qquad (5.17)$$

where it is assumed that the rate of enthalpy reduction due to the decrease in the proportion of vapour is small. Gyarmathy (71) has shown that the best heat transfer coefficient for small water droplets in wet steam is given by:

$$\alpha_L = \frac{2\lambda g}{dp}\left(\frac{1}{1 + 3.18\,Kn}\right) \qquad (5.18)$$

where the Knudsen number is also defined as

$$Kn = \frac{1.5\mu}{dp\rho_g}\cdot\left(\frac{1}{RT_g}\right)^{1/2} \qquad (5.19)$$

Combining equations (5.4), (5.15) and (5.17) gives the rate equation as

$$\frac{dT}{dt} = -\left(\frac{Y}{1-Y}\right)\cdot\frac{12\lambda_g}{d_p^{\,2} C_{pg}\,\rho_f\,(1+3.18Kn)}\,(T_g - T_s) \qquad (5.20)$$

Comparing equation (5.20) with equation (5.15) allows the thermal relaxation time to be defined as:

$$\tau_T = \left(\frac{1-Y}{Y}\right) \frac{d_p^2 C_{pg} . \rho_f (1+3.18Kn)}{12\lambda g} \qquad (5.21)$$

The above equation suggests that the thermal relaxation time for wet steam is not particularly sensitive to the pressure and temperature of the steam over the normal range of conditions found in steam turbines. A value can be calculated for some very typical conditions found in steam turbines. In the exhaust section of a low pressure turbine where the pressure is less than atmospheric then the following values for the parameters in equation (5.21) can be assumed:

$$C_{pg} \approx 1.9 \times 10^3 \text{ J/Kg.K}$$

$$\rho_f \approx 1.0 \times 10^3 \text{ kgm}^{-3}$$

$$\lambda_g \approx 0.024 \text{ Jm}^{-1}\text{s}^{-1}\text{K}$$

$$\mu \approx 1.0 \times 10^{-5} \text{ N.s m}^{-2}$$

which for a wet mixture of wetness fraction 10%, say, containing a monodispersion of water droplets of diameter 1.0μm, say, would give $\tau_T \approx 60 \ \mu s$. To put this into perspective the time for a flow of steam to pass through one blade row of the turbine would be approximately 200μs and so within the blade rows thermal relaxation is likely. A comparison will be made in Chapter 6 between these and the corresponding conditions for a turbocharger running with steam.

5.4.2.2 Inertial relaxation of the water droplets within the steam.

Another form of non-equilibrium occurs in a wet steam flow when the velocities of the vapour and liquid phases are not equal. Drag forces of the steam on the water droplets in the flow will tend to reduce the velocity of the steam relative to the droplets according to the equation of motion.

$$\left(\frac{\pi}{6} d_p \rho_f\right) \frac{dC}{dt} = D \qquad (5.22)$$

This drag force may be expressed in terms of a drag coefficient C_D where

$$D = \frac{\pi dp^2}{4} \cdot \frac{\rho_g (C-V)^2}{2} C_D \qquad (5.23)$$

where $V < C$. According to Gyarmathy (71) for small $|C - V|$ then

$$C_D = \frac{24\mu}{|C - V| . \rho g . d} \left(\frac{1}{1+2.7Kn}\right) \qquad (5.24)$$

Combining the above equations (5.22), (5.23) gives:

$$\frac{dc}{dt} = -\frac{1}{\tau_I} (C - V)$$

Whence the inertial relaxation time may be defined as

$$\tau_I = \frac{d_p^2 . \rho_f . (1+2.7Kn)}{18\mu} \qquad (5.25)$$

Using the same values for the parameters as for the calculation of the thermal relaxation time gives $\tau_I \sim 5\mu s$.

The inertial relaxation time is considerably less than the thermal equivalent. From equation (5.21) and (5.25) the ratio of τ_T/τ_I can be expressed as:

$$\frac{\tau_T}{\tau_I} = \left(\frac{1-Y}{Y}\right) 1.5 \frac{C_{pg}.\mu}{\lambda g} \qquad (5.26)$$

The Prandtl number of the vapour phase is given by $Cpg.\mu/\lambda g$ and its value here is approximately 0.85. It is for all intents and purposes independent of pressure and temperature. The above ratio is therefore dominated by the degree of wetness of the steam.

5.4.3 The velocity of sound in wet steam

A flow of wet steam of variable quality was produced by a turbocharger in the experimental rig used in this research. The Mach number of the wet steam in the exhaust was an important design and experimental parameter as will be shown in Chapter 6. In order to be able to estimate its value, some knowledge of the velocity of the sound in wet steam was required.

An adiabatic one dimensional compressible flow is said to be choked when the flow velocity equals the speed of sound at a nozzle throat. The flow in the converging section is then totally insensitive to changes downstream of the throat and the mass flow rate remains fixed at a constant maximum value provided conditions upstream remain constant. A physical explanation of this is that small

disturbances propagate at the speed of sound and hence cannot pass upstream through the throat of the nozzle. A two phase flow, however, is not so simple to treat and presents a problem. The speed of sound varies with the dispersion of the liquid phase and also with the frequency of the sound wave itself. Very high frequency disturbances moving through a medium containing large water droplets propagate at the frozen speed of sound viz:

$$a_f = (K_f P/\rho_g)^{1/2} \qquad (5.27)$$

The frozen speed of sound is defined as the speed of sound in the vapour phase. It implies that all interaction with the liquid phase is frozen. Alternatively very low frequency waves moving through a medium containing small water droplets propagate at the equilibrium speed of sound, viz:

$$a_e = (K_e.P/\rho)^{1/2} \qquad (5.28)$$

This implies that during the passage of the sound wave the two phases remain in equilibrium with zero slip. For low pressure steam (<1 bar absolute), typical values of K_f and Ke are 1.32 and 1.12 respectively (92). The equilibrium speed a_e depends upon the wetness fraction but the ratio a_e/a_f is usually very close to 0.9. For most practical purposes, however, either equation (5.27) or equation (5.28) may be used to calculate the acoustic velocity of sound in a wet steam flow.

5.5 A technique using a turbocharger to generate a wet steam flow

5.5.1 Introduction

One of the objectives of this research was to produce a wet steam flow of a variable and predictable quality. Further it was to be of a great advantage if the quality of the wet steam could be produced in a consistent manner. This was essential if an LDA technique was to be developed to make velocity measurements on the water droplets present in the flow. Such consistency would require a careful calibration of the rig used to generate the wet steam. In order to try and model the wet steam conditions that prevail in the penultimate stage of a wet steam turbine, a small turbomachine was sought. This machine would be required to extract a known amount of enthalpy homogeneously from a given supply of superheated steam. The use of such a machine is being introduced in this chapter because it provides a direct comparison between two completely different methods of generating a wet steam flow. On the one hand is the so called classical method which provides a predictable wet steam flow based upon a predetermined rate of expansion and hence cooling of the flow. On the other is the use of a small radial turbomachine to extract enthalpy from the inlet steam. An unmodified commercial engine turbocharger was tried for such a purpose. A turbocharger consists basically of a radial flow turbine and compressor stage mounted on the same shaft. Normally the turbocharger

is mounted between the exhaust manifold and inlet manifold of an internal combustion engine. The engine exhaust gases are used to drive the turbine at high speed and the compressor serves to increase the mass flow rate of the fuel/air mixture before entering the combustion chamber. This enhances the performance of the engine. In this application the turbine was driven by the supply steam and braked by the compressor stage.

The use of a turbocharger to generate wet steam is totally novel. In fact the running of the turbine stage on steam is different in itself and because steam is not a medium for which the machine was originally designed. No work has yet been published concerning the use of a turbocharger for such a purpose. It does offer the advantage that being a single stage machine, it is likely to produce a monodispersion of water droplet sizes. Optical extinction measurements made through the wet steam suggested that the bulk extinction was caused by water droplets of about 0.1μm in radius. This would indicate that there has been only one source of nucleation during the expansion through the turbine stage. This chapter is intended to discuss how the turbine characteristics may be modified for use with steam.

The author had no experience of the operation of turbochargers at the onset of this work. Consequently the choice of a suitable turbocharger was rather arbitrary but some indication of the processes that were involved in the selection of such a machine will be given in this Chapter.

5.2.2 The turbocharger non-dimensional parameters

For a turbine and compressor combination, the conventional way of defining the subscripts for the inlet and exhaust of each machine is shown in figure 5.6. As with all turbomachines a complete set of performance characteristics for machines of the same geometry may be obtained by use of the non-dimensional parameters. Table 5.1 shows the six non-dimensional parameters which are frequently used for turbochargers. The speed, N_T, is the same for both the turbine and the compressor wheel. For an air/exhaust gas mixture the manufacturers assume constant values for R and γ. Thus in practice they tend to be ignored and the engine manufacturers tend to use a simplified version of the non-dimensional parameters shown in Table 5.1. These are

$$\frac{\dot{m}\sqrt{To_1}}{Po_1} \quad , \quad \frac{Po_2}{Po_1} \quad , \quad \frac{N_T}{\sqrt{To_1}} \qquad \text{for the compressor} \qquad (5.29)$$

and

$$\frac{\dot{m}\sqrt{To_3}}{Po_3} \quad , \quad \frac{Po_3}{P_4} \quad , \quad \frac{N_T}{\sqrt{To_3}} \qquad \text{for the turbine} \qquad (5.30)$$

In this research the turbocharger was driven with dry superheated steam therefore R and γ could not be ignored. These are very different for steam than for air and must be taken into account. Any performance characteristics for the turbine will be valid for the parameters of equation (5.30) but will require some modification for steam.

	Temperature Change	Pressure Ratio	Speed Parameter	Mass Flow Parameter	Efficiency	Cp/Cv
COMPRESSOR	$\frac{\Delta To}{To_1}$	$\frac{Po_2}{Po_1}$	$\frac{N_T D_C}{\sqrt{RTo_1}}$	$\frac{\dot{m}_c \sqrt{\gamma RTo_1}}{Po_1 D_C^2}$	η_C	γ
TURBINE	$\frac{\Delta To}{To_3}$	$\frac{Po_3}{Po_4}$	$\frac{N_T D_T}{\sqrt{RTo_3}}$	$\frac{\dot{m}_{st} \sqrt{\gamma RTo_1}}{Po_3 D_C^2}$	η_T	γ

Table 5.1 THE NON-DIMENSIONAL PARAMETERS FOR A TURBOCHARGER

Consider first the non-dimensional mass flow parameter. Written out formally it is the same for both steam and air and is

$$\frac{\dot{m}_a\sqrt{\gamma_a R_a To_{3a}}}{Po_3 \; D_T^2} = \frac{\dot{m}_{st}\sqrt{\gamma_{st} R_{st} To_{st}}}{Po_{3st} D_T^2} \qquad (5.31)$$

rearranging equation (5.31) gives:

$$\frac{\dot{m}_a\sqrt{To_{3a}}}{Po_{3a}} = \frac{\dot{m}_s\sqrt{To_{3st}}}{Po_{3st}} \cdot \sqrt{\frac{R_a}{R_{st}}} \cdot \sqrt{\frac{\gamma_{st}}{\gamma_a}} \qquad (5.32)$$

This is what would normally be plotted on a characteristic supplied by a turbocharger manufacturer. If the performance characteristic is to be modified for steam then equation (5.32) must be rearranged to give:

$$\frac{\dot{m}_s\sqrt{To_{3st}}}{Po_{3st}} = \frac{\dot{m}_a\sqrt{To_{3a}}}{Po_{3a}} \cdot \sqrt{\frac{R_{st}}{R_a}} \cdot \sqrt{\frac{\gamma_a}{\gamma_{st}}} \qquad (5.33)$$

Similarly for the non-dimensional speed parameter, this can be modified to give:

$$\frac{N_T}{\sqrt{To_{3st}}} = \frac{N_T}{\sqrt{To_{3a}}} \cdot \sqrt{\frac{R_{st}}{R_a}} \cdot \sqrt{\frac{\gamma_{st}}{\gamma_a}} \qquad (5.34)$$

5.5.3 The turbine and compressor performance characteristics

In order to fully characterize the performance of a turbocharger, plots were required which incorporated a pressure ratio parameter, speed, mass flow rate and efficiency. Two sets of turbine performance characteristics

and a compressor map were supplied with the Holset H1a turbocharger used in this research. The turbine maps were modified in a manner discussed in the previous section. Figure 5.8 shows the mass flow parameter plotted against the speed parameter for given pressure ratios for the turbine. This map is the modified version of the manufacturers map for air, and was used throughout the work to assess the performance of the turbine whilst operating with steam. Figure 5.9 shows the efficiency characteristic for the turbine, again modified for steam from the manufacturers original data. The compressor map required no modification as the operating medium was air. Figure 5.10 shows a reproduction of the original manufacturer's compressor map. This map was used initially to test whether the compressor was running according to specification and that all the instrumentation used in the rig was performing satisfactorily. The full commissioning of the wet steam rig including a rigorous testing of the turbine and compressor will be treated in Chapter 6.

5.5.4 Selection of a turbocharger

To the best of the author's knowledge no serious attempt has been documented as to the use of a turbocharger to generate a wet steam flow. Much of the initial work deciding which turbocharger was to be used was done on a trial and error basis and consequently the basic design of the wet steam rig was not particularly involved. The author has, however, gained considerable operating experience of

the turbocharger during the research and the choice made proved to be encouraging.

Some attempt was made to quantify the design requirements before approaching the manufacturer. The only equipment in the laboratory that used a steam supply was an experimental turbine used for demonstration purposes. The running conditions of this machine were used as a guide because when the turbine was running close to its maximum speed the mass flow rate of steam into the blading was the maximum that the steam supply was capable of providing. This gave an indication of the limitations of the available steam supply and condensing equipment. Any turbocharger chosen had to run within these limits.

The experimental turbine was run at the maximum speed the supply could meet. The inlet pressure was 4.5 bar (gauge) and a temperature of 187^{0}C (460k). Under these conditions the steam mass flow rate over the running period was measured as 0.25kg s^{-1}. Assuming that a turbocharger would run under the same conditions then in equation (5.32).

$$\frac{m_a\sqrt{To_{3a}}}{Po_{3a}} \approx \frac{0.25\times 460.0}{4.5}\cdot\sqrt{\frac{488.0}{287.0}}\cdot\sqrt{\frac{1.3}{1.4}}$$

$$\approx 1.44$$

A mass flow parameter of 1.44 for air would be equivalent to about 1.2 for steam which would just be possible with the H1a turbine that was offered by the manufacturer. A compressor stage was arbitrarily chosen to match the

turbine. If this particular turbocharger had turned out to be unsatisfactory then different options would have been offered. The H1a turbocharger did perform well once commissioned and did generate a wet steam flow. Its use is shown schematically in figure 5.7. The effect of using a turbocharger with a different geometry is unknown and both time and prevailing priorities did not permit an investigation into this aspect.

6. DESIGN AND PERFORMANCE OF THE WET STEAM RIG

6.1 Introduction and Objectives

This chapter is concerned with the commissioning of the wet steam facility. The commissioning involved not only the running of the turbine but also an assessment of how the rig would produce wet steam of a known and predictable quality. The answer to the question as to whether sufficient specific enthalpy would have been extracted from the inlet supply steam to provide the necessary degree of subcooling (ΔT_s) for the steam to nucleate, will be given. The subject of subcooling and nucleation has already been covered in Chapter 5.

The second section of this Chapter is concerned with the description of the experimental facility. A colour photograph of the laboratory helps to locate the various components and to provide an appreciation of the physical layout. Successive sections are concerned with the various aspects of the commissioning. One of the biggest practical problems overcome was that of optical access into the rig. At the onset of the work it was envisaged that very severe problems would be experienced with the steaming up of the windows. In practice they remained clear when equilibrium conditions were reached. During transitory operation e.g. when changing the speed of the turbine, a temporary deposition and condensation of water droplets on the inside of the windows did occur. But this condition cleared after a short period of time. The instrumentation has been

covered briefly in so far as the interpretation of readings were concerned. The method of calculating the amount of enthalpy extracted from the system is also presented. The commissioning of the turbine and compressor themselves primarily involved checking whether these machines ran under conditions according to their performance characteristics. These characteristics were kindly provided by Holset Engineering Limited. The turbine performance maps have been modified by a technique as described in Chapter 5. The compressor performance map was valid in its original form as no modification was required. The results of these calibration runs are presented. The various steam conditions are shown plotted on the Mollier diagram for steam. The change in specific enthalpy and specific entropy for each running condition as calculated from thermodynamic measurements are plotted. They agree with the wetness fraction obtained from another set of instrumentation readings. The whole experimental process involved a certain amount of cross-checking of the various techniques. The philosophy adopted throughout was that if the same result could be obtained from at least two different methods, then each individual technique was valid.

The objectives of the experimental wet steam facility may be summarized as follows:

1. To produce wet steam of a known quality (i.e. wetness fraction).

2. To produce this quality steam consistently and in thermal equilibrium with the surroundings.

3. The commissioning process was intended to be able to establish the most effective running conditions. The compressor boost pressure could then be set permanently. Enthalpy extraction would then be a function of turbine speed only.

6.2 Description of the wet steam experimental facility.

All the mechanical hardware for this work had to be designed and installed. The existing steam facility at Durham University included a steam supply and a Sugden oil-fired superheater. The steam generator was capable of delivering about 1000 kg/hr of steam which was essentially a bleed from the site heating and hot water system. This steam supply is used mainly to drive an experimental turbine for student demonstration and laboratory purposes. Additional necessary facilities included an air-pump primed condenser and cooling tower complex. The superheater itself was capable of delivering this quantity of steam at a pressure of 5.5 bar (absolute) and at a temperature of up to 220^{0}C. There was a temperature fluctuation of ±10^{0}C over a ten-minute cycle which was inherent in the system. The cause of this lies almost certainly with the cyclic operation of the thermostat on the superheater. In practice this had no noticeable effect upon the operation of the wet steam rig. Mounted on a section of redundant pipework from the superheater was an old ARCA steam regulator. This formed the supply for a

research project abandoned some time previously.

The measuring section of the rig was a five way crosspiece with three windows. This is shown in figure 6.1. Two windows mounted opposite each other were required for traversing the flow. The window mounted above the working section was intended purely as an observation window. The dimensions of the crosspiece were chosen so as to allow maximum observation of the measuring volume in the steam. The crosspiece was machined from solid in order to achieve the required geometry. Clearly the bore of the measuring section was larger than the exhaust of the turbocharger. An expansion chamber was used as an adaptor. The length of this chamber was chosen according to the criterion: (67)

$$\frac{L_M}{D_{EXH}} \geqslant 20 \qquad (6.1)$$

Hence setting the length, L_M, of the expansion chamber to be at least 20 times the dimension of the diameter, D_{EXH}, of the turbine exhaust should allow sufficient settling time for the flow after the sudden expansion. This relation is valid up to Re ≈ 40000.

The measuring section was originally intended to be mounted directly onto the condenser in a vertical position as shown in figure 6.2. A flanged coupling which was blanked off was already in existence on the condenser. The dimensions of this coupling influenced the final dimensions of the measuring section. However the safety requirements

for the operation of lasers which were prevailing at the time dictated that the laser be used away from the main laboratory. Mounting the measuring section vertically has the distinct advantage that any water which condenses out onto its walls will immediately flow into the condenser. The disadvantages associated with mounting it horizontally in the smaller laboratory were as follows:

(i) Additional lengths of pipework (and lagging) were required to deliver the superheated steam to the turbine. This was done initially via the steam regulator on the superheater. An undesirable pressure drop along this section of pipe was inevitable.

(ii) Steam was taken back to the condenser via a 50 mm bore pipe. Water which condensed on the walls of the rig could not flow away to the condenser. The permanent presence of a pool of water in the measuring section did prove a problem initially but this was overcome at a later stage by preheating the rig with dry superheated steam to minimize the intial condensation on the walls.

Fortunately these disadvantages did not present themselves as insurmountable problems during experimental runs.

Two flexible couplings were used to deliver steam to and take steam away from the rig. On the inlet side a 25 mm

bore industrial steam hose was inserted between the rigid steel pipework entering the laboratory and the inlet flange of the turbine. Similarly a larger 50 mm bore industrial hose completed the connection between the measuring section and the rigid return pipe to the condenser. Use of these hoses had the following advantages.

(i) They allowed easy removal of the turbocharger for inspection and replacement,

(ii) They provided an essential expansion facility for the steam pipework. If these connections were rigid, then problems might have been encountered when the pipework expanded. The weakest joint would have been the turbine casing which might have cracked as a result. Any failure of this nature during a run would have been disastrous.

Lubrication of the turbine bearings was required. Holset Engineering recommended an oil pressure of at least 40 p.s.i. the oil having been preheated to at least 90^{0}C. Figure 6.3 shows the essential features of the lubrication system used for the turbocharger. Beneath the rig was mounted an electrically driven pump and cooler bolted to a rigid frame. The oil sump originally contained about 5 litres of turbine oil. A 1 kW thermostatically controlled heating element was mounted in the sump which took about 75 minutes to heat this quantity of oil to the required temperature. This will be discussed further in section

6.4.3. The steam rig was completely lagged with Armaflex lagging three layers deep. All the pipework was lagged with glass fibre cloth backed lagging held on by metal straps. The entire layout of the rig in the laboratory is shown in Plate (i).

6.3 A Review of the Instrumentation Required

6.3.1 For the temperature measurement

The static temperature of the steam or air flow could not be measured. This is because to measure static temperature requires a transducer travelling at the flow speed and is therefore not practical. However, if the wall of the pipe is well insulated, a measured wall temperature will be nearer the free steam stagnation temperature (flow velocity is zero below the boundary layer). Thus $T_{wall} \approx T_{o\infty}$, and:

$$T_{wall} = T_{\infty} \left[1 + R_{ec} \cdot \left(\frac{\gamma-1}{2}\right) \cdot M^2_{\infty}\right] \qquad (6.2)$$

where the recovery factor R_{ec} is defined as

$$R_{ec} = \frac{T_{wall} - T_{\infty}}{T_{o\infty} - T_{\infty}} \qquad (6.3)$$

T_{wall} was measured hence

$$T_{\infty} = T_{wall} \left[1 + R_{ec} \left(\frac{\gamma-1}{2}\right) \cdot M^2_{\infty}\right]^{-1} \qquad (6.4)$$

But $R_{ec} = \sqrt[3]{Pr}$ for a turbulent boundary layer and since for air, $P_r \approx 0.72$, $R_{ec} \approx 1$. Further for the low velocity exhaust steam flow where $M << 1$, $T_{wall} \approx T_{\infty}$. The wall temperatures for both the air and steam were measured using

Copper-Constantin thermocouples, mounted equi-pitched on the pipe and three readings were taken and averaged. The themocouples were mounted at least 20 pipe diameters downstream of the exhaust in order that any perturbations in the flow would be at a minimum. A series of four thermocouples were mounted around the periphery of the measuring section.

6.3.2 For the pressure measurement

Only the static pressures were measured, a conversion to stagnation quantitites being performed using the compressible flow equations. For the compressor exhaust pressure measurement, three wall tappings were used equi-pitched on the pipe circumference. They were mounted two pipe diameters further downstream from the thermocouples in order to avoid any unnecessary disturbance in the boundary layer that may have been caused by the wall tappings. A Druck 0-7 bar pressure transducer was used to measure P_2. For the steam pressures P_3 and P_4, recently calibrated test pressure gauges were used.

6.3.3 Measurement of the air and steam massflow rates

Both these quantitites were required for the calculations to determine the amount of specific enthalpy extracted from the steam. The mass flow rate of air flowing through the compressor was measured by a bellmouth supplied by the manufacturer. A Bell & Howell pressure transducer (0-200 mbar) was used to measure the drop in static pressure as the rate of mass flow increased. The bellmouth had been

calibrated by the manufacturer and conversion data had been provided but given in cfm and ''H_2O. Using the following equation

$$P_1 \text{ (mbar)} = \frac{249.174 \times . \ 1.0125}{P_{o1} \times 10^5} \qquad (6.5)$$

where x was the height in ''H_2O and the fact that 152 cfm ≡ 0.215 $m^3 s^{-1}$ then the volumetric flow rate culd be measured using the data provided.

The mass flow rate of the steam was measured by monitoring the level of condensate collected in a tank. It was, however, important to allow about ten minutes after turbine speed change for the change in flow rate to appear at the condensate tank.

6.3.4 Measurement of the turbine shaft speed

A very simple yet dependable method of measuring the shaft speed was to use an induction type coil. The turbine shaft was fitted with a two pole permanent magnetic nut. This was factory fitted because the machine had to be balanced. The frequency of the voltage induced in the coil was proportional to the rotational speed of the shaft. The signal voltage was fed into a frequency counter and due to a minimum counting frequency, the range of turbine shaft speeds that could be measured was 400-2500 rps. The coil was mounted directly above the magnetic nut and strapped to the exhaust casing.

6.4 Commissioning of wet steam rig

6.4.1 The problem of optical access into the steam

Three windows were mounted in the measuring section as shown in figure 3.1. The two smaller windows of 120 mm in diameter were mounted using a standard sightglass arrangement (NEI Parsons Ltd.), but the larger 185 mm window has a custom made detectable mount. Before the rig was commissioned it was anticipated that severe misting of the windows would be a problem. This was not the case but one method was tried to provide a solution should this problem have arisen.

A glass coating is commercially available known as HYVIZ a variant of which has been used in aircraft windscreens to prevent icing. A conducting gold film of 0.020" thickness is bonded onto the surface and connection of an electrical supply will heat the glass. On a sample of glass sent by the manufacturer, electrical contact was made using "silver dag" conducting paint. With a current of 3A flowing across the sample, a surface temperatrue of 120^{0}C was reached in several minutes. The greatest drawback, however, was that a 35% attenuation of the laser beam was experienced. Added to this the very high cost of £500 per window meant that it was not really practical.

At this stage it was realized that once the steam had reached an equilibrium condition with the rig, the most serious problem was not misting but deposition of large water droplets onto the inside surface of the windows. The

droplets refracted the laser beam through a wide range of angles. Consequently, achievement of minimum waist coincidence was not always possible. The most effective method of preventing this was to coat the inside surface of each window with domestic washing up liquid. The much lowered surface tension caused the droplets to collapse and form a thin moving film of water across the face of the window. This film of water had no appreciable effect upon the laser beams and the process had to be repeated before each run. Even when a dense fog was present in the measuring section the windows remained clear as can be seen in Plate (xi). The two smaller windows were made from toughened soda lime glass and the larger window was specially manufactured from a borosilicate glass (PYREX) chosen for its non-birefringency.

6.4.2 Water drainage in the measuring section

Plate (xi) shows the path of the two laser beams in the wet steam. It is clear from this photograph that a large amount of water collected in the measuring section. Periodically, though typically after two hours of running, this water had to be drained off. To aid this a tap was fitted to the underside of the five-way crosspiece. The condenser could then be isolated and this water drained very quickly. Care did have to be taken when running from cold because steam remaining in the pipework from the previous run would condense out. A drain was fitted before the turbine inlet allowing the pipework to be completely purged

of water using the steam from the supply.

6.4.3 The lubrication system

During the initial stages of commissioning, the lubrication system posed a number of difficulties. The journal type bearing in the turbocharger has a piston ring seal as shown in figure 6.6. The turbine exhaust pressure varied between 0.1 bar and 0.9 bar absolute and a certain amount of lubricant was forced into the measuring section of the rig. In an engine a little oil in the exhaust is not too critical but in this application an absolutely clean turbine exhaust flow was required and no loss into the rig could be tolerated. Monitoring the level of lubricant in the sump it was estimated that, at a turbine speed of 80000 rpm, approximately three litres of lubricant was lost into the steam flow over a period of three hours. This represented a loss of lubricant of less than 1 $cm^3 s^{-1}$ and although small compared with the steam volumetric flow rate of approximately 0.2 $m^3 s^{-1}$, was sufficient to cause oil droplets to be present in the flow. Under these circumstances, the windows very quickly fouled up with an oil/water emulsion. After consultation with the turbine manufacturer (58) some reduction in the level of smearing was produced by reducing the pressure of the lubricant at the turbine casing. However this only served to increase the wear on the journal at high speeds. Eventually seal wear became important and oil was again forced out of the bearings, this time in larger quantities. It soon became

evident that a loss of lubricant from the bearings was unavoidable and so water was tried on a new machine. Delivered at a pressure of 3 bar (gauge) and pre-heated to a temperature of 90^{0}C, the loss of water was higher at about 2 $cm^{3}s^{-1}$ but at least the deposition by the large water droplets could be dealt with in the manner suggested earlier. There were two main drawbacks of using water as a lubricant

(i) If the machine was left idle for any length of time, the bearings had to be purged with oil. This was to prevent corrosion of the castings and possible seizure.

(ii) The lower viscosity of water meant that the life of the bearings would be greatly reduced. It was, however, perfectly satisfactory during the research period for which it was run for approximately 200 hours. Although no obvious signs of damage were evident after a strip-down the use of water was not anticipated as a long term solution.

6.5 Generating the wet steam flow

6.5.1 Introduction to the method

It was intended to generate a wet steam flow in the measuring section of the rig of a variable wetness fraction. The compressor stage of the turbocharger was used to load the turbine by a varying amount as determined by the setting

of a boost valve on the compressor exhaust. The work done by the compressor in raising the temperature of the air was calculated using measured values of total and static tempertures. Knowing the mechanical efficiency of the bearings enabled the useful work done by the turbine stage to be calculated. An estimate was made for the heat loss in the system after which the system could be described by the steady flow energy equation. The change in specific enthalpy of the dry superheated steam at the inlet, see figure 5.7, could be calculated. The local wetness fraction in the steam was then calculated using local static pressure measurements. Before any calculation could be performed based upon property measurements, it was necessary to ensure that the turbine and compressor were each running according to the performance characteristics of figure 5.8 and 5.10. This will be presented after which the method of predicting the steam wetness fraction will be discussed.

6.5.2 The performance of the compressor

The method used to assess the performance of the compressor stage of the turbocharger was to check whether given running conditions coincided with figure 5.10. There are three parameters which are mapped on the performance chart:

(i) Total-total pressure ratio($P_{o2}:P_{o1}$).

(ii) Volumetric flow rate of cfm (can be converted to m^3s^{-1}).

(iii) Speed in rpm.

The lines of constant efficiency were not required in this research.

Measurement of static pressure, P_2, and the volumetric flow rate of air flowing through the compressor enabled the pressure ratio to be determined for a given shaft speed. (P_{o1} was given by the pressure in the laboratory). In figure 6.4 the operating conditions have been plotted for the shaft speed range 100-1900 rps in discrete steps of 100 rps. A very good coincidence was obtained between (P_{o2}/P_{o1}), the shaft speed and the volumetric flow rate for each speed. In all cases the three parameters coincided within 4% and the compressor stage was judged to be running according to design specifications.

6.5.3 The performance of the turbine

The turbine stage of the turbocharger was primarily designed to be driven by the exhaust gases of an internal combustion engine. Intuitively it may be expected that its performance with dry steam was predictable. To this end the performance characteristics for the turbine were adjusted for steam using the true non-dimensional parameters of the machine. These have been shown in figures 5.8 and 5.9 using R_{st} = 0.488 kJ $kg^{-1}K$ (R_a = 0.287 kJ $kg^{-1}K$) and γ_{st} = 1.3 (γ_a = 1.4). The mass flow parameter, speed parameter and total-static pressure ratio ($P_{o3}:P_4$) for the expansion of the steam through the turbine are shown in Table 6.1 for the range of operating speeds. These quantities were calculated using local measurements and were given by

(i) Turbine mass flow parameter, $\dot{m}_{st}\sqrt{T_{o3}}/P_{o3}$

(ii) Speed parameter, $N_T/\sqrt{T_{o3}}$

(iii) Total-static pressure ratio, P_{o3}/P_4.

It was the variation of (i) and (iii) in figure 6.5 that have yielded some interesting results for the machine. The intersection of the mass flow parameter are quite close and most were found to be within 5%. The problem here was that no plot existed for the Hla turbine operating with an expansion ratio of greater than 3. A certain amount of extrapolation was required to locate the locii of constant mass flow parameter for the higher pressures. However, the operating conditions have been mapped for an exhaust of visibly dry steam and for the wet steam. The mass flow parameter is seen to increase with speed, albeit rather sharply. Some departure from the good coincidence of the operating parameters was experienced at shaft speeds above 1600 rps. The reason for this may have been due to the high Mach numbers that characterized the dry steam flow at the inlet as shown in figure 6.7. At the higher values operation would have been in a region where shock free behaviour could not be guaranteed and hence static pressure measurements may have been unreliable. At the turbine exhaust, however, the converse was true and here compressibility effects were negligible as shown in figure 6.8. Thus the total-static pressure ratios as calculated were likely to be higher than the operating conditions under which a test machine was run to construct the original

characteristic for air.

The transition from dry to wet running conditions appeared to be smooth and the mass flow parameter increased until the flow was choked as given by its maximum value in figure 6.5. As the speed increased the flow remained choked until $N_T/\sqrt{T_{o3}}$ was equal to about 85 after which the mass flow parameter decreased with increasing speed.

This observation may be expressed in terms of the choking mass flow rate through a nozzle in which the flow is choked at the throat. The mass flow rate is then given by the following:

$$\dot{m}_{ch} = A \cdot P_{o3} \cdot \sqrt{\frac{\gamma_{st}}{R_{st} T_{o3}}} \cdot \frac{1}{\left(1 + \left(\frac{\gamma-1}{2}\right)M^2\right)^{(\gamma+1)/\gamma(\gamma-1)}} \quad (6.6)$$

whence on setting M = 1 gives

$$\dot{m}_{ch} = A \cdot P_{o3} \cdot \sqrt{\frac{\gamma_{st}}{R_{st} T_{o3}}} \cdot (\gamma(\gamma-1))/(\gamma+1) \quad (6.7)$$

Assuming that the flow became choked in the inlet pipe to the turbine then the following values relating to the conditions of running at the time may be used:

$N_T/\sqrt{T_{o3}} = 95$, $\dot{m}_{ch} = 0.29 \text{ kgs}^{-1}$ (by measurement)

$\gamma_{st} = 1.3$

$R_{st} = 0.488 \text{ kJkg}^{-1}\text{K}$, $T_{o3} = 397\text{K}$, $P_{o3} = 4.92 \text{ bar}$

giving in equation (6.7), $\dot{m}_{ch} = 0.27 \text{ kgs}^{-1}$ which is in quite close agreement with the measured value.* Thus the flow was not choked at a position corresponding to the maximum mass

*NOTE ON CHOKING

The most likely explanation for the fall of the mass flow parameter in figure 6.5 is that choking must be taking place other than at the inlet, and most probably in the exhaust. If the choking were only occurring at the inlet, then the mass flow parameter would have constant value.

N_T (rps)	$\dot{m}_{st}$ (kgs^{-1})	M_3	M_4	Speed Parameter	Mass Flow Parameter	$\frac{Po\,3}{P\,4}$
1000	0.107	0.77	0.029	49.3	1.06	2.31
1100	0.119	0.80	0.032	54.3	1.04	2.56
1200	0.122	0.75	0.032	58.8	1.13	2.60
1300	0.154	0.85	0.038	63.8	1.19	2.90
1400	0.161	0.79	0.038	69.1	1.23	2.98
1500	0.190	0.83	0.042	74.2	1.26	3.20
1600	0.210	0.82	0.045	79.0	1.29	3.50
1700	0.230	0.810	0.048	84.0	1.29	3.70
1800	0.270	0.89	0.056	89.2	1.27	4.30
1850	0.280	0.89	0.057	91.2	1.22	4.65
1900	0.290	0.99	0.057	95.4	1.17	5.5

Table 6.1 CALCULATION OF NON-DIMENSIONAL PARAMETERS FOR THE TURBOCHARGER

flow parameter.

6.5.4 Method of calculating the quality of the wet steam

6.5.4.1 Qualitative outline of the method

Wet steam was generated in the rig by extracting an amount of enthalpy from a superheated supply of steam on expansion through a turbine. A determination of the change in enthalpy of the steam as it expanded through the turbine involved an intricate set of calculations and a flow chart will be described.

The power developed by the compressor stage was calculated using measured values of T_{o1} and T_{o2} according to

$$POW_C = \dot{m}_a \cdot C_{pa} (T_{o2} - T_{o1}) \qquad (6.8)$$

The manufacturers claim an efficiency of 98% for the journal bearings when used with the recommended grade of lubricant. With water as a lubricant, however, a figure of 92% was taken.

The specific work required in the shaft to the compressor is then given by

$$W_C = \frac{POW_C}{\dot{m}_a} \text{ KJkg}^{-1} \qquad (6.9)$$

And so the useful specific work required from the turbine stage is given by

$$W_T = \frac{W_C}{\eta_B}$$

whence

$$W_T = \frac{\dot{m}_a . C_{pa} . (T_{02} - T_{01})}{\dot{m}_{st} . \eta_B} \qquad (6.10)$$

The steady flow energy equation (SFEE) was then used to calculate the final enthalpy for the exhaust steam. Use of the SFEE required the mean steam velocities the inlet and exhaust and the method for determining these will be discussed in the next section. Given the local static pressure measurements in the measuring section, the values of h_f and h_{fg} could be obtained from the steam tables and so

$$h_c \approx h_{f4} + x h_{fg\,4} \text{ for } Y \leq 0.1$$

whence

$$x = \frac{h_4 - h_{f4}}{h_{fg\,4}} \qquad (6.11)$$

Using this value for the dryness fraction the change in specific entropy was calculated using

$$S_4 = S_{f4} + x S_{fg\,4} \qquad (6.12)$$

Equation 6.11 was used to plot the isentropic expansion across the turbine on a Mollier chart. The final operating point was determined using equation 6.12.

The steam rig was assumed to be a closed system to which the SFEE culd be applied. Such a system is shown in figure 6.9 and the SFEE may be written as

$$Q - W_T = (h_4 - h_3) + \frac{1}{2} . (C_4^2 - C_3^2)$$

whence

$$Q = (h_4 - h_3) + \frac{1}{2}(C_4^2 - C_3^2) + W_T \qquad (6.13)$$

It has been shown how W_T was calculated and h_3 was determined from the measurement of static pressure and temperature at the turbine inlet (i.e. the dry superheated steam where pressure and temperature are two independent properties). C_3 was known in the same way as h_3 since the steam density could be determined and the mass flow rate was known by measurement of the condensate over a period of time. The problem, however, was that h_4 and C_4 could not be directly determined and Q was not known. It was not sufficient to asssume that Q was negligible on the grounds that the rig was lagged. In fact the turbine and compressor castings were not fully lagged and so at the high running temperatures ($< 140^{\circ}C$), the heat transfer to the laboratory must have been considerable. The next section will describe the method used to estimate the heat loss Q and how the exhaust velocity was estimated allowing h_4 to be evaluated from equation (6.13) and hence X in equation (6.11).

6.5.4.2 Detailed procedure for the calculations

The calculation of the specific work output of the turbine is an important step in the determination of the quality of the exhaust steam. From equation 6.13):

$$h_4 = (h_3 - W_T) + \frac{1}{2}(C_3^2 - C_4^2) + Q$$

The term $(h_3 - W_T)$ refers to the enthalpy extraction by the turbine and the second term refers to the change in kinetic energy of the steam at the exhaust relative to the inlet. Q is defined as being positive if flowing into the closed

system. As mentioned earlier to find h_4 required knowledge of the following:

(i) Heat loss to the surroundings i.e. -Q

(ii) Inlet velocity of the steam into the turbine.

(iii) Exhaust velocity of the steam in the rig.

As far as the magnitude of Q is concerned, $Q_{DRY} > Q_{WET}$. This statement refers to the magnitude of the heat loss to the surroundings when the exhaust steam is dry relative to when the exhaust steam is wet. As the exhaust steam goes wet, its temperature and that of the turbine, with which it is in thermal equilibrium, is lowered. The lower this temperature the lower the rate of heat loss that may be expected. The magnitude of Q_{WET} under given conditions can be approximated by the following based upon the Newton law of cooling

$$\dot{m}_{st(WET)}\, Q_{WET} \approx \dot{m}_{st(DRY)}\, Q_{DRY}\left[\frac{\left(\frac{(T_{03}+T_{04})}{2} - T_{01\ WET}\right)}{\left(\frac{(T_{03}+T_{04})}{2} - T_{01\ DRY}\right)}\right] \qquad (6.14)$$

where T_{01} is taken as the ambient temperature in the laboratory. Since pressure and temperature are not independent variables below the saturation line, Q had to be estimated when the exhaust steam was dry. The enthalpy of the exhaust steam could then be determined from the steam tables as for h_3. Q_{DRY} was calculated with the turbine running at 1300 rps, in the following manner.

For

N_T = 1300 rps, $\dot{m}_{st}$ = 0.165 kgs^{-1}, W_T = 89.1 $kJkg^{-1}$

h_3 = 2746.9 $KJkg^{-1}$, h_4 = 2690.1 $KJkg^{-1}$

C_3 = 299.6 ms^{-1}, C_4 = 11.8 ms^{-1}

Hence in equation (6.13)

$$Q_{DRY} = (2690.0-2746.9) \times 10^3 + (89.1 \times 10^3) - \frac{1}{2}(299.6^2 - 11.8^2)$$

Therefore

Q_{DRY} = - 12.5 KJ/kg i.e. flowing outwards

This represented a heat loss of 0.165 x 12.5 = 2.06 kW under DRY conditions.

Now consider the second requirement namely that of calculating the inlet steam velocity. The density of the steam at inlet was provided by the steam tables for a given operating condition. The mass flow rate was measured as described from which the mean inlet velocity was calculated from

$$\dot{m}_{st} = \rho_{st} A_3 \cdot C_3 . \qquad (6.15)$$

and the sonic velocity in the steam from

$$a_{st} = \sqrt{\gamma_{st} \cdot R_{st} \cdot T_3} \qquad (6.16)$$

Knowing these two velocities gave the Mach number of the inlet flow. The inlet static pressure could then be readily converted into an equivalent stagnation pressure by the following relation for compressible flow.

$$P_{o3} = P_3 \cdot (1 + \frac{(\gamma_{st}-1)}{2} \cdot M_3^2)^{\gamma st/(\gamma_{st}-1)} \qquad (6.17)$$

The pressure P_{o3} was required in order to obtain the expansion ratio given on the manufacturers characteristic as total-static pressure ratio (P_{o3}/P_4).

The third and final quantity to be measured was the mean velocity of the exhaust steam. This involved an interative process and is best described with the aid of a flow chart as in figure 6.10. The actual value of M_4 used was determined by a trial and error method. There was no alternative method for calculating M_4 analytically.

Referring to the flow chart, the assumption that $C_3 >> C_4$ was valid because in all cases the velocities were less than 25 ms^{-1}. Thus in the kinetic energy term of the SFEE $\left|\frac{1}{2}\cdot(C_4^2-C_3^2)\right| \approx \frac{1}{2}\cdot C_3^2$ since the Mach numbers in the inlet flows were very high, the equilibrium speed of sound has been used to describe the conditions in the exhaust.

6.5.4.3 Results of the calibration of the wet steam rig

The calculations described in the previous section were performed for turbine speeds in the range 1000-1900 rps in speed increments of 100 rps. The throttle or boost value on the compressor exhaust was adjusted before each set of calibration runs. Once a consistent set of values for the steam quality, and a maximum wetness fraction, was achieved, the throttle setting was left at its final position. The main objective of the calibration procedure was to be able to generate a wet steam flow of a known and variable quality and this has been met. Figure 6.11 shows the variation of steam wetness with turbine speed

and this served as a calibration characteristic for the wet steam facility. A turbine speed of 1850 rps was tried in order to provide an additional experimental condition at the higher speeds. The most important results are those shown plotted on a Mollier chart for steam. Figures 6.12 (a)-(f) show the expansion maps for the turbine running with speeds of 1500, 1600, 1700, 1800, 1850 and 1900 rps respectively, at which a fog was present in the measuring section. In the first three instances the fog was thin and patchy, but in the remaining cases, the fog was particularly thick and presented severe attenuation of the laser beams. Due to the difficulty of producing a complete Mollier chart in sufficient detail to show the isentropic and isenthalpic expansions taking place in the rig, only a small portion could be reproduced here.

In figures 6.12 (a)-(c), the expansion is shown for an estimated steam wetness of 1%, 1.9% and 2.3% respectively. Under these conditions a thin fog was present in the measuring section of the rig.

Nucleation theory predicts (22) and experimental results show (71) that spontaneous condensation does not occur in large axial steam turbines until a condition pertaining to the so called Wilson point is reached during the expansion. This is contrary to the situation here. The turbine of the turbocharger unit is a small radial machine. It has been assumed that enthalpy has been extracted homogeneously from the dry superheated steam by expansion

across the turbine wheel. There are two possible reasons why this radial turbine could have generated the wet steam flow soon after expansion through the saturation line.

(i) The dry steam may not have been expanded homogeneously across the wheel. A small amount of the dry steam may have been subjected to a significant degree of overexpansion as it passed across the wheel passage. The degree of overexpansion would then have been sufficient for the Wilson point to have been reached resulting in the onset of spontaneous condensation. The smaller number of critical fog droplets formed in this manner might account for the thin and patchy fog conditions that were present at the lower speeds. A simple calculation based upon the steady flow energy equation illustrates that the speeding up of the steam flow at local centres in the machine is possible.

Consider the expansion of figure 6.12(a) where Y (estimated) = 0.01. At a speed of 1500 rps, M_4 =0.029 from figure 6.8.

Also $a_{ext} = \sqrt{1.13 \times 0.4488 \times 10^3 \times (87 + 273)}$

$= 427\ ms^{-1}$

$\therefore C_4 = 12.4\ ms^{-1}$

For an area ratio of 3.3 in the measuring section, the mean velocity at exit from the turbine = $135\ ms^{-1}$.

From figure 6.12 (c), the additional enthalpy that needs to be extracted from the inlet steam to reach the conditions corresponding to the Wilson point is ~

50 KJ/kg.

Therefore $\Delta h = 50 \times 10^3$ J/kg.

Equating this to velocity, the flow would need to be accelerated to C_4' where:

$$\frac{1}{2}(C_4'^2 - C_4^2) = \Delta h \qquad (6.18)$$

therefore $C_4' = [50 \times 10^3 \times 2 + 135.0^2]$

whence $C_4' = 343\ ms^{-1}$

an increase over C_4 of ~ 150%.

Overexpansion of this magnitude may be possible. Perhaps the growing interest in the application of turbochargers might encourage further research into the way in which the turbine wheel in the turbocharger extracts enthalpy from the exhaust gases of an internal combustion engine. In any case, this process requires some further investigation.

(ii) The second possibility is that the steam at inlet was not perfectly dry or contained some rust particles from the superheater which would have acted as nucleation centres for the expanding steam flow. It is important to realise that the steam passing through modern steam turbines is very pure and true thermodynamic nucleation may be expected to take place. The steam supply from the superheater in this application did contain visible solid particles which were clearly contaminants of some description.

6.5.4.4 An assessment of the errors in the wet steam calculation

In order to be able to quote the estimated wetness fraction from the thermodynamic measurements, some estimate of its accuracy was required. The approach adopted was to apply a simple error analysis to calculate the worst case error. The SFEE for the system may be written as

$$Q_{DRY} = (h_4 - h_3) + W_T - \frac{1}{2}(C_3^2 - C_4^2) \qquad (6.19)$$

The error in Q_{DRY} will now be estimated using the results of the dry exhaust running conditions of section 6.5.4.2. Each individual term in equation (6.19) will now be considered.

(i) Error W_T, δW_T, has been estimated as follows:

$\eta_B = 0.92 \pm 0.06$ i.e. $\delta\eta_B = \pm 6.5\%$

In equation (6.10), the error in the temperature measurements, T_{o2} and T_{o1} is 0.1%.

Therefore

$$\delta T_o = \frac{0.001 \times (61.3+21.0)}{(61.3 - 21.0)} = 0.2\%$$

The mass flow rate, $\dot{m}_{st}$ was measured by monitoring the level of condensate in a tank. This could be done to 1 mm in 1000 mm, i.e. 0.1%.

Therefore

$$\delta W_T = \delta\eta_B + \delta T_o + \delta \dot{m}_{st} = 6.8\%$$

(ii) Error in $(h_3 - h_4)$, δh was calculated as follows:

Using 4-figure steam tables a linear interpolation was

performed to arrive at the value of specific enthalpy for the given conditions:

$(h_3 - h_4) = 2746.9 - 2690.1 = 56.8$ kJ/kg giving

$$\delta h = \frac{0.01}{56.8} = 0.018\%$$

(iii) Similarly for the velocity terms where interpolation was performed to estimate the density of the steam giving the velocity C_3 or C_4 from continuity. Here :

$\dot{m}_{st} = \rho_s . A_3 . C_3$

Error in $\dot{m}_{st}$ = 0.1% and in density ≈ 0.1% from the steam tables.

Therefore $\delta C \approx 0.2\%$

Thus the error in Q_{DRY}, δ_{DRY}, was estimated as:

$$\delta Q_{DRY} = \frac{0.00018 . (h_3 - h_4)}{|h_3 - h_4|} + \delta W_T + \frac{0.002 . (C_3^2 + C_4^2)}{(C_3^2 - C_4^2)}$$

$$= 1.9 + 6.8 + 0.21$$

Therefore $\delta Q_{DRY} = 8.9\%$

Assume that $\delta Q_{DRY} \approx \delta Q_{WET}$.

Rearranging equations (6.19) to solve for h_4 gives:

$$h_4 = (h_3 - W_T) + \frac{1}{2} . (C_3^2 - C_4^2) + Q_{DRY}$$

Since h_4 and C_4 were not known in the wet region then the above equation becomes

$$h_4 = (h_3 - W_T) + \frac{1}{2} . (C_3^2 - C_4^2) + Q_{WET} \qquad C_3 \gg C_4$$

and this had to be iterated to solve for h_4 and C_4 as given in figure 6.10.

Therefore

$$\delta h_4 = \left[\frac{(0.\ 00018.h_3)+(0.068.W_T)}{|h_3 - W_T|}\right] + \frac{0.002.C_3}{(C_3^2-C_4^2)} + \delta Q_{WET}$$

The second term above is justified since in this case $C_3 >> C_4$. Hence on inserting the values gives for δh_4.

$$\delta h_4 = \left[\frac{(0.00018.\ 2746.9)+(0.068.\ 89.1)}{(2746.9-89.1)}\right] + \frac{(0.002.2.299.6)}{(299.6^2 - 16^2)} + 8.9$$

$$\therefore \delta h_4 = 9.25\%$$

But the value of h_4 was used in figure 6.10 to calculate C_4, so as a worst case situation $\delta C_4 \approx \delta h_4$. Here h_4 was used also to determine X, the dryness fraction (Y=1-X). Hence in this text and in particular in Chapter 9, the exhaust wet steam velocities C_4 and the wetness fraction will be quoted with the following worst case error:

exhaust velocity = $C_4 \pm 10.0\%$

wetness fraction = $Y \pm 10.0\%$.

7. DEVELOPMENT OF THE LIGHT SCATTERING MODEL

7.1 Introduction

The success of a laser Doppler anemometer used in a very turbid medium depends upon the ability to gain suitable optical access into that medium and to produce a signal of sufficient strength and quality to be detectable by the processing electronics.

The detection optics in any LDA system are focused upon the probe volume produced by the intersection of two laser beams in the medium, and scattered light from the seeding particles moving through the measuring volume impinges upon the photodetector cathode. It is therefore the scattered light which contains the Doppler frequency information and it is this which is extracted from the total signal by means of optical heterodyning on the photodetector surface. In order to be able to assess, on a theoretical basis, the performance of an LDA system as used in a flow of wet steam, it was decided to construct a model of the turbid medium. The objective was to be able to estimate the magnitude of the signal that could be obtained under different operating conditions. Due to the high number densities of seeding particles (i.e. water droplets) in wet steam flows and hence the small mean distances between particles, not only single scattering events are taking place. Light which has already been scattered in one direction by one seeding particle may be rescattered in a different direction by another and this process need not be

limited to just two scattering particles.

A method is therefore required which will predict not only that light scattered by the particles moving through the measuring volume which constitutes the signal, but also that light which has been diffusely transmitted by further multiple scattering through the medium. This diffusely transmitted light is incoherent and contains no useful information. It does, however, increase the level of background light at the expense of useful signal intensity and therefore constitutes much increased phase noise. The signal-to-noise ratio of the signal obtained from the medium thus becomes badly affected as the proportion of diffuse light increases with seeding particle density. The relationship between the decrease in useful signal and increase in the diffusely transmitted light can be expressed as a change in the signal-to-noise ratio for a given turbid medium. The treatment of this, however, is beyond the scope of this chapter and has been confined to Chapter 8.

This Chapter will concentrate upon the prediction of the polar intensity distribution of scattered light due to a beam of light striking a seeding particle. This intensity distribution can be expressed as a series of phase relationships between the scattered and incident waves. The formal solution to a numerical evaluation of these relationships was first proposed in 1908 by Mie (50) and it was upon the basis of his fundamental work that the well known Mie intensity functions (54) have been documented.

Many workers throughout this century have suggested elaborate solutions to the Mie formulae. As the computational power of mainframe computers has increased so has the ingenuity and sophistication of some of the numerical solutions. Several very fast and efficient (20) (60) computer algorithms are available in the literature. All these methods will yield a polar intensity distribution of scattered light for a scattering particle of any size, geometry and refractive index. One computation method to solve the Mie formulae will be presented in this Chapter. Although the program described was not composed by the author, its results have been vital to the author's work.

This Chapter begins by reviewing the basic light scattering process. The formal Mie scattering formulae will be introduced and their significance discussed. The concept of the single scattering phase function will be defined and its relevance to the study of light scattering by particles presented in detail. Finally the computational technique used to solve the Mie formulae and arrive at the single scattering phase function for a particle will be described. Examples will be given for different particle sizes showing the dominant features of the physical scattering process and the way in which they develop for increasing particle size.

7.2 Principle characteristics of scattering

The development of a computer program to model a light scattering process must take into account the different types of scattering that may take place. The scattering of

electromagnetic radiation is a very broad topic. Models exist for various atmospheric hazes, fogs and clouds which may be extended to predict the scattering and extinction of radiation through any turbid medium. It was intended to develop such a model that may be satisfactorily employed to predict the transmission of laser light through a flow of condensing steam.

This section looks at the basic scattering process and considers the several different types of scattering that occur when a light wave is incident upon a particle. This is done first in terms of a single isolated particle and the effects of particle size relative to wavelength are described. The scope is then extended to the case of a group of particles scattering in proximity to each other, thus creating composite effects.

7.2.1 Nature of the scattering process

Scattering is the process by which a particle, or any piece of matter, in the path of an electromagnetic wave continuously abstracts energy from the incident wave and re-radiates that energy into the total solid angle centred at the particle. The particle is thus the point source of this scattered energy. For scattering to occur, it is necessary that the refractive index of the particle be different from that of the surrounding medium. The particle is then an optical discontinuity, or inhomogeneity, to the incident wave. As a result, scattering occurs whenever an electromagnetic wave propagates in a material medium. In

atmospheric physics the particles responsible for scattering lie in the range of sizes from gas molecules to raindrops. For reasons of interest only, the wide ranges of size and concentration of these particles are shown in Table 7.1. About each particle the intensity of the scattered radiant energy, more commonly referred to as the scattered intensity, forms a characteristic three-dimensional pattern in space. If the particle is isotropic, the pattern is symmetrical about the direction of the incident wave. The form of pattern depends strongly upon the ratio of particle size to wavelength of the incident wave. This important fact is illustrated in figure 7.1. In figure 7.1(a) the relatively small particle tends to scatter equally into the forward and back hemispheres. The polar intensity distribution is symmetrical. The particle size would typically be smaller than one tenth of the wavelength of the incident radiation. When the particle is larger as in figure 7.1(b), the overall scattering is greater and is more concentrated in the forward direction. The size of this particle would be of the order of one quarter of the wavelength. For a still larger particle as in figure 7.1(c), the overall scattering is even greater. Most of it is now concentrated in a forward lobe and secondary maxima and minima appear at various angles. This form of polar plot will be most familiar to workers employing LDA techniques for flow measurement in either water or artificially seeded gas flows. Further increases in

TYPE	RADIUS (μm)	CONCENTRATION (cm^{-3})
Air Molecule	10^{-4}	10^{19}
Aitken Molecule	10^{-3}-10^{-2}	10^{4}-10^{2}
Haze Particle	10^{-2}- 1	10^{3}-10
Fog Droplet	1 -10	100 -10
Cloud Droplet	1 -10	300 -10
Raindrop	10^{2}-10^{4}	10^{-2}-10

Source McCartney (64)

Table 7.1 PARTICLES RESPONSIBLE FOR ATMOSPHERIC SCATTERING.

particle size produce patterns of even greater complexity as illustrated by Gardavsky (43). In all cases the exact form of the pattern is influenced by the relative refractive index, that is the ratio of the refractive index of the particle to that of the medium surrounding the particle. There are other characteristics relating to the state of polarization of the scattered radiation. Even if the incident radiation is unpolarized, the scattered radiation is polarized to some extent. The type and degree of polarization depends on the optical properties of the particle, the polarization of the incident radiation and the direction in which it is observed. When the particle is isotropic, the scattered intensity referred to a particular polarization is a function of particle size, particle relative refractive index and the wavelength of the incident radiation. These are the three parameters of scattering.

7.2.2 Types of scattering

When the particle is very much smaller than the wavelength, the scattering process is known as Rayleigh scattering after its investigation by Lord Rayleigh in 1871. Scattering of this type varies directly as the second power of the particle volume and inversely as the fourth power of the wavelength.

For particle diameters greater than about one tenth of the wavelength as shown in figure 7.1(c), Rayleigh theory is inadequate to explain the scattering effects. For greater complexities in the polar plots in the figures, the theory

developed in 1908 by Mie is required for their explanation. The advantage of the Mie theory is that it is expressed as a mathematical series embracing all particle sizes which reduces to the Rayleigh expression. Every particle in the atmosphere is in fact a Mie scatterer, even those of great relative size, such as raindrops illuminated by visible light. For this work the Mie formulae have been employed to compute the polar intensity distribution for a given particle size. A computer model based upon these will thus be able to cope with a very wide range of particle sizes due to the general nature of the Mie theory.

7.2.3 Scattering by many particles

When the average separation distance is several times the particle radius, each particle is considered to scatter independently of all the others. This is independent scattering and the relations for a medium containing N scattering particles are simplified. The intensity scattered by the medium is N times that scattered by a single particle and the energy removed from the original beam is also N times that removed by a single particle. This simple proportionality holds only if the radiation to which each particle is exposed is essentially the light of the original beam.

Each particle is also exposed to light scattered by the other particles, whereas the light of the original beam may have suffered extinction by the other particles. With single scattering no account is taken of the fact that each

particle in a scattering volume is exposed to and also scatters a small amount of light already scattered by the other particles. This light, very weak by comparison with that of the direct beam, reaches a given particle from many directions. This process is shown in figure 7.2. Some of the light that has been first scattered may be re-scattered one or more times before emerging from the scattering volume. This is called secondary or multiple scattering. The important fact here is that although multiple scattering has little effect on the total amount of light removed from the direct beam, it may significantly alter the composite pattern of scattered intensity due to all the particles. This characteristic of multiple scattering can be illustrated by figure 7.1(c). If the polar intensity distribution here is overlaid with a multitude of similar but far weaker patterns with all orientations in space, the composite intensity distribution exhibits fewer and smaller variations in intensity as a function of angle. It will, however still retain the principle features of the original distribution. In the extreme condition, as with a very turbid medium, all sense of the direct beam is lost and the scattered light will reach an observer rather uniformly from all directions. This tendency is typical of a dense fog.

Multiple scattering does not involve new physical problems. The assumption of independence, which states that each water droplet may be thought to be in free space exposed to light from a distant source, holds true whether

the source is the incident beam or another droplet. However, finding the intensities both inside and outside the medium is a difficult mathematical problem. It has been treated in many texts (10) and is the subject of radiative transfer.

Concluding this section, a simple test for the absence of multiple scattering is to double the concentration of particles in the sample under test. If the scattered intensity is doubled then only single scattering is important. The intensity of a beam passing through the sample is reduced by extinction to $e^{-\tau}$ of its original value. τ is the optical depth of the sample along this line. If $\tau < 0.1$ single scattering prevails. For $0.1 < \tau < 0.3$ (50) a correction for multiple scattering may be necessary. For larger optical depths, multiple scattering becomes a very important factor. It may not prevent a determination of the scattering properties of a single particle, but will certainly make interpretation less clear. Multiple scattering becomes significant when the optical depth is not small in all directions through the sample medium.

7.2.4 Bulk extinction

When a beam of light traverses a turbid medium, the incident beam experiences attenuation. This attenuation is called extinction. In general

extinction = scattering + absorption

Absorption, however, is not present in significant quantities for water droplets illuminated by visible radiation. All further reference to attenuation by extinction will imply that bulk extinction through a medium is by scattering only. The extinction of a light beam through a turbid medium along the line of incidence may be given by

$$\frac{I}{I_o} = e^{-\tau} \tag{7.1}$$

This is Bouguer's exponential law of attenuation, more often referred to as the Lambert-Bouguer, or the Beer-Bouguer-Lambert law. The extinction coefficient may be defined as:

$$\tau = \sigma_{ext} \cdot \ell \tag{7.2}$$

and the optical depth may be rewritten as

$$\tau = \sigma_{scat} \cdot \ell \tag{7.3}$$

since in general

$$\sigma_{ext} = \sigma_{scat} + \sigma_{abs} \tag{7.4}$$

and absorption is neglected. The scattering coefficient is a measure of the total energy intercepted and scattered from the incident beam of light. It must relate to the number of scattering particles in the medium and the scattering properties of each individual particle. For a monodispersion this may be written as

$$\sigma_{scat} = NC_{scat} \tag{7.5}$$

or $$\sigma_{scat} = NQ_{scat}\pi r_p^2 \tag{7.6}$$

so that for a monodispersion equation (7.1) becomes

$$\frac{I}{I_o} = \exp.\,[-NQ_{scat}.\pi\, r_p^2.\ell] \tag{7.7}$$

Similarly for a polydispersion, equation (7.7) may be adjusted to give

$$\frac{I}{I_o} = \exp.\left[\sum_{i=r_{min}}^{i=r_{max}} N_i\, Q_{scat\,i}\, \pi\, i^2.\ell\right] \tag{7.8}$$

The extinction law is almost totally independent of whether single scattering or multiple scattering is predominant since it is a measure of the total energy removed from the beam by scattering.

7.3 The single scattering phase function

Scattering by particles whose radius is greater than about 0.03 times the wavelength of the incident light is called Mie scattering. Starting with small particles, as the particle size relative to the wavelength increases, there is a gradual transition from Rayleigh to Mie scattering. Broadly this is characterized by

a) A complicated dependence of scattered light intensity upon the angle of observation. The degree of complexity increases with particle size relative to the wavelength.

b) An increasing ratio of forward scattering to backscattering as the particle size increases. This results in the growth of the forward lobe as shown in figure 7.1(c).

c) Little dependence of scattering upon wavelength when the particle size relative to wavelength is large. In atmospheric physics the white appearance of clouds and a blue sky typify the two extremes of particle scattering.

The Mie theory has been covered in detail in several good texts (50) (54) and recent tabulations of the Mie coefficients are available (74). It is therefore not intended to discuss the Mie theory in depth but merely to illustrate the practical formulae. The formulae are restricted to monodispersions in order to present the essentials of the theory most simply. The relevant formulae relate to the two angular intensity distribution functions that are the essence of Mie theory.

7.3.1 Introducing the Mie solution

Scattering is caused by the interaction between electromagnetic waves and the electric charges that constitute matter. Very simply, when a particle is illuminated by an incident wave it is set into oscillation. This gives rise to secondary electric and magnetic waves known as partial waves which combine in the far field to produce the scattered wave.

These partial waves are represented in the Mie theory by successive amplitude terms in a slowly converging series whose squared summation gives the scattered intensity at a particular angle of observation. Because the size of the particle is comparable to a wavelength, the phase of the primary wave is not uniform over the particle resulting in phase differences between the various partial waves. Where the partial waves combine to form the scattered wave, for example on a detector surface, interferences occur between the partial waves caused by these phase differences. These interferences depend upon the wavelength of the incident light, the size and refractive index of the particle and the angular location of the detector. Sharp variations in scattered intensity are experienced when the detector aperture is moved to various observation angles. The distribution and angular dependence of this scattered intensity is described by the phase function. In general the phase function may be approximated by an expansion of a series in legendre polynomials of the form

$$p\ (\cos\ \theta) = \sum_{\ell=0}^{\infty} w_{\ell} . P_{\ell}\ (\cos\ \theta) \qquad (7.9)$$

and is referred to in the context of the scattering geometry introduced in the next section. In practice the series on the right hand side is a terminating one with only a finite number of terms. More formally the phase function may be defined as the rate at which energy is being scattered into

a solid angle $d\omega$ and in a direction inclined at an angle θ to the direction of incidence of an incoming beam of light. It may be written as

$$\int p(\cos\theta)\frac{d\omega}{4\pi} = 1 \qquad (7.10)$$

and is normalised to a spherical distribution hence the term 4π in the above expression. A concept known as the albedo of single scattering measures the effectiveness of scattering relative to extinction. For either a monodisperse or a polydisperse distribution of scattering particles this albedo is defined by

$$\bar{\omega} = \frac{Q_{scat}}{Q_{scat} + Q_{abs}} \qquad (7.11)$$

or the ratio of the amount of flux scattered to that scattered and absorbed. Equation (7.10) may be rewritten to include the albedo viz:

$$\int p(\cos\theta)\frac{d\omega}{4\pi} = \bar{\omega} \leq 1 \qquad (7.12)$$

Thus the general case differs from the case of pure scattering only in the fact that the phase function is not normalised to unity.

7.3.2 Geometry of scattering in three dimensional space

Before continuing with the present theory and adapting it to the treatment of the multiple scattering problem it is

essential to define and describe a coordinate system. It is upon this geometry that further work will be centred.

Figure 7.3 shows the general ccordinate system in three dimensional space. Referring to this figure it is required to find the scattering angle Θ in terms of the angle of incidence, the angle of emergence and the corresponding azimuth angles. It is convenient to define the scattering angle as

$$\Theta = f\ (\mu,\ \phi,\ \mu_o,\ \phi_o) \tag{7.13}$$

where $\mu = \cos\theta$ and $\mu_o = \cos\theta_o$ $(-1 \leqslant \mu,\ \mu_o \leqslant 1)$

Taking unit vectors then from the dot product

$$OQ\ .\ OR = |OQ|\ .\ |OR|\ .\ \cos\Theta \tag{7.14}$$

$$\text{Therefore}\ \frac{OQ\ .\ OR}{|OQ|\ .\ |OR|} = \cos\Theta \tag{7.15}$$

Now if

$$OQ = \alpha i + \beta j + \gamma k$$

$$OR = \delta i + \omega j + \sigma k$$

$$\text{then}\ \ OQ\ .\ OR = \alpha\delta + \beta\omega + \gamma\sigma \tag{7.16}$$

Therefore

$$OQ = \sqrt{(\alpha^2 + \beta^2 + \gamma^2)} = 1 \tag{7.17}$$

$$\text{and}\quad OR = \sqrt{(\delta^2 + \omega^2 + \sigma^2)} = 1 \tag{7.18}$$

Hence a substitution of equations (7.16), (7.17) and (7.18)

into equation (7.15) gives

$$\cos\theta = \frac{\alpha\delta + \beta\omega + \gamma\sigma}{\sqrt{(\alpha^2+\beta^2+\gamma^2)}\,\sqrt{(\delta^2+\omega^2+\sigma^2)}} \qquad (7.19)$$

Now for unit vectors $\sqrt{(\alpha^2+\beta^2+\gamma^2)} = \sqrt{(\delta^2+\omega^2+\sigma^2)} = 1$

Therefore $\theta = \cos^{-1}(\alpha\delta + \beta\omega + \gamma\sigma)$ (7.20)

Consider the vector OR:

$$OR' = OR \sin\theta$$

Therefore

$$\delta = OR' \sin(180-\phi)$$
$$= OR' \sin\phi$$
$$= \sin\theta \sin\phi$$

$$\omega = -OR' \cos(180-\phi)$$
$$= OR' \cos\phi$$
$$= \sin\theta \cos\phi$$

$$\sigma = OR \cos\theta$$
$$= \cos\theta$$

Similarly for α, β, γ whence:

$$\alpha = \sin\theta_o \sin\phi_o$$
$$\beta = \sin\theta_o \cos\phi_o$$
$$\gamma = \cos\theta_o$$

On substitution of the above into equation (7.20) gives:

$$\Theta = \cos^{-1}\left[\sin\theta\sin\phi\sin\theta_o\sin\phi_o + \sin\theta\sin\theta_o\cos\phi_o\cos\phi + \cos\theta_o\cos\theta\right] \qquad (7.21)$$

This can be quickly checked by setting $\phi_o = \theta_o = 0$ then $\Theta = \cos^{-1}(0+0+\cos\theta) = \theta$ which is the expected result. Any of the complicated formulae describing the angular scattered distribution of radiation, whether it be as a result of single or multiple scattering processes, requires integration over all angles. Gaussian integration is often used because it is both quick and efficient for this type of problem. Because of this it is convenient to use the cosine of all angles since the integrand can only have the limits $(-1,1)$.

Thus set $\mu = \cos\theta$ and $\mu_o = \cos\theta_o$ as before so that equation (7.21) becomes

$$\cos\Theta = \mu_o\mu + \sin\theta\sin\theta_o\left[\sin\phi\sin\phi_o + \cos\phi_o\cos\phi\right]$$

$$= \mu_o\mu + \sin\theta\,\sin\theta_o\left[\cos(\phi-\phi_o)\right]$$

Now $\sin\theta = (1-\cos^2\theta)^{1/2} = (1-\mu^2)^{1/2}$

and $\sin\theta_o = (1-\cos^2\theta_o)^{1/2} = (1-\mu_o^2)^{1/2}$

Therefore

$$\cos\Theta = \mu_o\mu + (1-\mu_o^2)^{1/2}\,(1-\mu^2)^{1/2}\cos(\phi-\phi_o) \qquad (7.22)$$

which is the form used on expanding the phase function in terms of cosines of the scattering angles. This is an important relation as it serves greatly to simplify the complicated formulae for the multiple scattering problems.

7.3.3. The basic Mie scattering formulae

As previously mentioned the angular characteristics of Mie scattering for all particle sizes and wavelengths are expressed by two intensity distribution functions.

The light scattered at any angle Θ may be treated as consisting of two components polarized perpendicular and parallel to the plane of polarization. The components are proportional to two intensity distribution functions i_1 and i_2 respectively. For a spherical particle the functions are given by:

$$i_1(\alpha,m,\Theta) = |S_1|^2 = \sum_{n=1}^{\infty} \frac{2n+1}{n(n+1)} |(a_n \pi_n + b_n \tau_n)|^2 \qquad (7.23)$$

$$i_1(\alpha,m,\Theta) = |S_2|^2 = \sum_{n=1}^{\infty} \frac{2n+1}{n(n+1)} |(a_n \tau_n + b_n \pi_n)|^2 \qquad (7.24)$$

Each intensity function is the sum of an infinite series. The full mathematical treatment is available in several good texts (50) (54). S_1 and S_2 are the dimensionless complex Mie amplitudes of the scattered waves observed as intensities $I_\perp(\Theta)$ and $I_{11}(\Theta)$. The complex functions a_n and b_n give the amplitudes of the electric and magnetic components of the scattered wave respectively (20). The values of a_n and b_n are found from the Ricatti-Bessel functions (20) whose arguments derive from the particle characteristics α and m but are independent of the observation angle θ. Extensive tables of these functions have been published covering a wide range of particle sizes and refractive indices (74) (80).

PLEASE NOTE:

$I_\perp$ and I_{11} are the components of the scattered intensity polarized perpendicularly and parallel to the scattering plane.

The functions π_n and τ_n in equations (7.23) and (7.24) depend only on the angle Θ and involve the first and second derivatives of legendre polynomials having order n and argument cos Θ. The computation of these functions is given by Deirmendjian (20), van de Hulst (50), and Kerker (54). The next section is concerned with the treatment of Deirmendjian since this has been referred to in order to produce the computer program.

It is worth mentioning the operational use of these functions. When the particle is illuminated by plane polarized light whose electric vector is perpendicular to the plane of observation, so that the polarization angle ϕ is 90 degrees, the intensity of the scattered light is given by

$$I_{\perp}(\Theta) = E_{\perp} \frac{\lambda^2}{4\pi^2} \cdot i_1 \qquad (7.25)$$

There is thus no i_2 component in this plane. The intensity of each scattered component is in units of $\lambda^2/4\pi^2$ when the incident light has unit irradiance.

When the particle is illuminated by plane polarized light whose electric vector is parallel to the plane of observation so that $\phi = 0$, the intensity is given by:

$$I_{\parallel}(\Theta) = E_{\parallel} \cdot \frac{\lambda^2}{4\pi^2} \cdot i_2 \qquad (7.26)$$

Here there is no i_1 component.

Finally when the particle is illuminated by unpolarized (eg white) light represented by two electric vectors of equal magnitude perpendicular and parallel to the plane of observation but having no coherent relationship, the scattered light consists of two incoherent components according to

$$I(\theta) = \frac{1}{2}[I_{\perp}(\theta) + I_{\parallel}(\theta)] = E \cdot \frac{\lambda^2}{4\pi^2} \cdot \left(\frac{i_1+i_2}{2}\right) \qquad (7.27)$$

However, in this work only equation (7.25) will be employed as the laser light source is polarized in this manner.

Using the values a_n and b_n from equation (7.23), the scattering efficiency factor may be defined as:

$$Q_{scat}(m,\alpha) = \frac{2}{\alpha^2} \sum_{n=1}^{\infty} (2n+1)\left(|a_n|^2+|b_n|^2\right) \qquad (7.28)$$

7.3.4 <u>To compute the single scattering phase function</u>

This requires some adaptation of the Mie intensity functions to machine computation. Their evaluation depends upon the accurate computation of a_n and b_n which are functions of m and α only, and of the angular coefficients π_n and τ_n which are functions of μ (= $\cos\theta$) only. This process will be discussed briefly together with an example of the scattering phase function as computed by such a program.

The program was originally written for a polydispersed distribution of droplet sizes, however it still computed a

single scattering phase function. It was developed for the study of atmospheric scattering of sunlight through dust storms in Nigeria (7) and has since been used for various solar energy studies. The extension from monodisperse to polydisperse systems, that is to particles of identical optical constants but differing in size only, follows naturally from any discussion on the Mie theory. The converse is also true however, namely that given a computation that refers to a polydispersal, a monodisperse system may be approximated by selecting the distribution of particle sizes carefully.

7.3.4.1 Computation of the Mie formulae

The Mie intensity functions have been successfully computed by Brinkman (7) and it was this program which was to be used as the basic component of the solution to the multiple scattering problem. The program is listed in Appendix A and comment statements have been included to explain the process step by step. The program utilizes the reduced formulae developed by Deirmendjian.

Very briefly, the Mie coefficients of equation (7.23) may be rewritten in the form

$$a_n(m,\alpha) = \frac{\dfrac{A_n(y)}{m} + n/\alpha)\ \mathrm{Re}\{w_n(\alpha)\} - \mathrm{Re}\{w_{n-1}(\alpha)\}}{(A_n(y) + n/\alpha)\ w_n(\alpha) - w_{n-1}(\alpha)} \qquad (7.29)$$

and

$$b_n(m,\alpha) = \frac{(m\,A_n(y) + n/\alpha)\ \mathrm{Re}\{w_n(\alpha)\} - \mathrm{Re}\{w_{n-1}(\alpha)\}}{(mA_n(y) + n/\alpha)\, w_n(\alpha) - w_{n-1}(\alpha)} \qquad (7.30)$$

where in general

$$w_n(\alpha) = \sqrt{\frac{\pi x}{2}} \cdot [J_{n+1/2}(\alpha) + (-1)^n i\, J_{-n-1/2}(\alpha)] \qquad (7.31)$$

and results from a substitution of the Ricatti-Bessel functions. For example:

$$W_1(\alpha) = \frac{w_o(\alpha)}{\alpha} - W_{-1}(\alpha)$$

$$= \sqrt{\frac{\pi\alpha}{2}} \cdot [J_{3/2}(\alpha) - i\, J_{-3/2}(\alpha)]$$

$$W_2(\alpha) = \frac{3}{\alpha} w_1(\alpha) - w_o(\alpha)$$

$$= \sqrt{\frac{\pi\alpha}{2}} \cdot [J_{5/2}(\alpha) + i\, J_{5/2}(\alpha)]$$

using the recurrence relation:

$$w_n(\alpha) = \frac{2n-1}{\alpha} \cdot w_{n-1}(\alpha) - w_{n-2}(\alpha) \qquad (7.32)$$

Further, the coefficients A_n may be generated by

$$A_n(y) = \frac{J_{n-1/2}(y) - n/y\, J_{n+1/2}(y)}{J_{n+1/2}(y)} \qquad (7.33)$$

$$A_n(y) = -n/y + \frac{J_{n-1/2}(y)}{J_{n+1/2}(y)} \qquad (7.34)$$

where

$$A_o(y) = \frac{J_{-1/2}(y)}{J_{1/2}(y)} = \cot y$$

and $y = m\alpha$

The angular coefficients π_n and τ_n are generally defined in terms of legendre polynomials and their derivatives. By using certain recurrence relations between these polynomials and their derivatives, it can be shown (20) that the coefficients can also be generated by their own recursion without actual reference to the legendre polynomials. Hence we have:

$$\pi_n(\theta) = \cos\theta \cdot \frac{2n-1}{n-1} \cdot \pi_{n-1}(\theta) - \frac{n}{n-1}\pi_{n-2}(\theta) \qquad (7.35)$$

and

$$\tau_n(\theta) = \cos\theta\,[\pi_n(\theta) - \pi_{n-2}(\theta)] - (2n-1)\sin^2\theta \cdot \pi_{n-1}(\theta) + \pi_{n-2}(\theta) \qquad (7.36)$$

with $0 \leq \theta \leq \pi$

and $\pi_o(\theta) = 0 \qquad \tau_o(\theta) = 0$

$\pi_1(\theta) = 1 \qquad \tau_1(\theta) = \cos\theta$

$\pi_2(\theta) = 3\cos\theta \qquad \tau_2(\theta) = 3\cos 2\theta$

which can easily be programmed for machine computation. They are shown in subroutines "CROSSS" and "INTENS" within the listing of program "TSCAT" in Appendix A. An example of a computed phase function from this program is shown in

figure 7.4. The ratio of forward to backscatter is in the order of three decades and is typical of a water particle of 0.5 μm radius being illuminated by laser light of the wavelength 514.5 nm.

7.3.4.2 The extension of the phase function to polydisperse systems

The extension from monodisperse to polydisperse systems, that is to particles of identical optical constants but differing in size only, is a natural progression from any discussion on the Mie theory. When a turbid medium contains scattering particles distributed in discrete sizes, the quantities N, $p(\cos\theta)$ and Q_{scat} will be replaced by the corresponding summations, with the latter two properly weighted by the number of particles in each size range. The total number of particles per unit volume is given by the integral:

$$N = \int_{r_1}^{r_2} n(r)\, dr \qquad (7.37)$$

assuming that the distribution may be represented by a continuous function of the radius within any given range of interest $r_1 \leq r \leq r_2$. Here, $n(r)$ is a continuous and integrable function defined within the range, representing the partial concentration per unit volume and per unit increment of the radius r. It is more convenient to define the distribution function $n(r)$ in terms of the Mie size parameter α ($\alpha = 2\pi r/\lambda$), thus introducing the wavelength λ as an independent

parameter. Equation (7.37) may then be written as:

$$N = \frac{\lambda}{2\pi} \int_0^\infty n(\alpha).d\alpha$$

$$= k^{-1} \int_0^\infty n(\alpha).d\alpha \qquad (7.38)$$

where $n(\alpha)$ has the same form as $n(r)$ after the change of variable. For a monodispersion the scattering efficiency, Q_{scat} is usually defined (see section 7.2.4), by setting

$$\sigma_{scat}(N,\alpha) = N\pi r^2 Q_{scat}(\alpha) \qquad (7.39)$$

for a medium containing N particles of radius r (hence size parameter of $2\pi r/\lambda$) per unit volume of space. Substituting (7.38) into (7.39) gives:

$$\beta_{sca}[\lambda, n(\alpha))] = \pi k^{-3} \int_0^\infty \alpha^2 n(\alpha) Q_{scat}(\alpha).d\alpha \qquad (7.40)$$

for a polydispersion.

Further, for a monodispersion, Deirmendjian defines a dimensionless quality $P_j(\theta)$ where

$$P_j(\theta) = \frac{4i_j(\theta)}{\alpha^2 Q_{scat}(\alpha)} \quad j=1,2 \qquad (7.41)$$

where $P_j(\theta)$ $j = 1,2$ refers to the normalised scattering phase function for vertically and horizontally polarized incident light respectively. Only $P_1(\theta)$ is of interest here, however. Multiplying the numerator and denominator of (7.41) by $\pi k^{-3} n(\alpha)$ and integrating separately gives

$$P_j(\theta) = \frac{4\pi}{\alpha^3 Q_{scat}} \int_0^\infty n(\alpha)\, i_j(\theta)\, d\alpha \quad j=1,2 \qquad (7.42)$$

for a polydispersion. This is the form of distribution for which "TSCAT" evaluates the phase function.

7.3.4.3 Exponential size distribution function

A function much used for model dispersions in atmospheric studies of scattering is the one proposed by Deirmendjian. It has the form:

$$n(r) = a r_p^{\alpha_d} \exp(-b r_p^{\gamma}) \qquad (7.43)$$

where a, b α_d and γ are positive constants. It is referred to as the modified Gamma distribution. Because it has four adjustable constants, it can be fitted to various models of haze, cloud and even rain. It is hoped that it will also prove a useful model for a distribution of nucleated water droplets in wet steam given a careful selection of constants. Basically the four values have the following significance:

a is a scaling coefficient

α_d essentially controls narrowness, ie large α_d narrow distribution

γ controls skewness and $\gamma=3$ for a symmetric distribution

$$b = \frac{\alpha_d}{\gamma r_p^{\gamma}}$$

PLEASE NOTE:

Any reference to rp and dp in the text should be read as r_p and d_p respectively.

The determination of the above constants is shown in Appendix B for a known distribution. To illustrate the versatility of the function in scattering applications, Table 7.2 lists some well known documented size distributions (20). An example of the Gamma distribution parameters for wet steam are also shown for comparison. Of significance is the wide range of distribution parameters that the function can handle.

The Gamma distribution that was used in "TSCAT" to produce the phase function is shown in figure 7.6. The values of the constants are given below the curve. The main features of this characteristic are the rate at which the number concentration decreases for particle sizes away from the mode radius and the very narrow particle size range that is plotted. This particular size distribution is probably the best approximation to a monodispersion that can be obtained with this type of function given the wet steam conditions.

7.3.5 The scattering efficiency function

The two parameters of wavelength and particle size jointly determine the distribution of phase over the particle. It has been assumed that the particle is spherical which is very nearly true for a fog particle. The ratio of particle size to wavelength is expressed by the dimensionless size parameter α, defined by

$$\alpha = \frac{2\pi r}{\lambda} \qquad (7.44)$$

DISTRIBUTION TYPE	N	a	r_p	α	b	γ	$n(r_p)$
HAZE M	100 cm^{-3}	5.3×10^4	0.05μm	1	8.94	½	360.9cm^{-3} μm^{-1}
RAIN M	1000 m^{-3}	5.3×10^5	0.05μm	1	8.94	½	3609cm^{-3} mm^{-1}
HAZE L	100 cm^{-3}	4.98×10^6	0.07μm	2	15.12	½	446.6cm^{-3} μm^{-1}
RAIN L	1000 m^{-3}	4.98×10^7	0.10μm	2	15.12	½	4466m^{-3} mm^{-1}
HAZE H	100 cm^{-3}	4.0×10^5	0.10μm	2	20.0	1	541.4cm^{-3} μm^{-1}
FAIL H	10 m^{-3}	4.0×10^4	0.10μm	2	20.0	1	54.14m^{-3} cm^{-1}
CUMULUS CLOUD, C1	100 cm^{-3}	2.37	4.0μm	6	$^3/_2$	1	24.09cm^{-3} μm^{-1}
CORONA CLOUD, C2	100 cm^{-3}	1.085×10^{-2}	4.0μm	8	$^1/_{24}$	3	49.41cm^{-3} μm^{-1}
DOUBLE CORONA CLOUD, C4	100 cm^{-3}	5.56	4.0μm	8	$^1/_3$	3	98.82cm^{-3} μm^{-1}
WET STEAM	$4.4 \times 10^{14} m^{-3}$	1.18×10^{73}	0.14μm	57.6	12707.3	3	$4.4 \times 10^8 cm^{-3}$ m^{-1}

Source: Deirmendjian(20)

Table 7.2 SOME WIDELY USED SIZE DISTRIBUTION MODELS

which is essentially the product of the wave constant and the particle radius. All particle scattering is strongly dependent upon α. The most important governing factor of Mie scattering is neither the absolute value of particle size nor the absolute value of wavelength. It is the ratio of the two as expressed in equation (7.44). The effect of increasing the wavelength is to make the particle appear smaller. A fog particle with a radius of 0.5μm can be considered quite large when illuminated by white light of an approximate wavelength of 0.55 μm. But that same particle becomes relatively small for an infra-red wavelength of 10μm. At an extreme, a raindrop having a radius of 1000μm appears large to the infra-red but relatively small to a radar wavelength in the cm region.

Corresponding to the great range of relative sizes is an even greater range and diversity of scattering characteristics.

The total scattering cross-section C_{scat} is defined as the cross-section of an incident wave acted on by the particle having an area such that the power flowing across it is equal to the total power scattered in all directions. Values of the total scattering cross-section cover a wide range, greater than the corresponding range of geometric cross-sections. The two are related by the efficiency factor Q_{scat} more often referred to as the scattering coefficient or Mie coefficient. It is quite simply the ratio of the scattering to the geometric cross-section.

PLEASE NOTE:

For a given scattering particle of radius r_p:

$$Q_{scat}(r_p) = C_{scat}(r_p)/\pi r_p^2$$

This ratio defines the efficiency with which the particle totally scatters the light. Figure 7.5 shows the variation of Q_{scat} with α for a water droplet. These values are as computed by Penndorf (1956). When α is very small, the value of Q_{scat} is very much less than unity, and the particle scatters far less incident flux than would be intercepted by its geometric cross-section. As α increases Q_{scat} runs to a maximum value of nearly 4 and asymptotically converges in a damped oscillatory manner to a value of 2. A curious feature of the plot in figure 7.5, is the ripples of high frequency and small amplitude superimposed on the larger scale variations. These minor oscillations have no noticable effects on particle scattering for the particle sizes of interest here. They do, however, have theoretical interest for the study of dipole resonances (50). This explains why many texts (59) concerned with the subject of particle scattering depict $Q_{scat}(\alpha)$ as a smoothly varying function. A significant fact emerging from figure 7.5, is that a water droplet scatters most efficiently when its radius is approximately equal to the wavelength of incident light.

7.4 Discussion

The essential features of the light scattering process by particulate media have been described and a general scattering geometry introduced. It has been emphasized that for very turbid media such as a nucleated wet steam flow a treatment of light scattering through such a medium by an

analysis using the single scattering phase function is insufficient. However the treatment has been confined to single scattering events. The numerical technique described in section 7.3.4.1 has been transformed into a file "TSCAT" by Brinkman (7), the listing of which is in Appendix A. This program has been used because the results will be used to model the multiple scattering process by a technique which relies only upon a detailed knowledge of the single scattering phase function. It has been demonstrated in this Chapter that the phase function may be predicted accurately for any particle size, geometry and refractive index. The formulae used in the computational process are very general in nature and in the limit will give a good result for Rayleigh scattering for those particles whose dimensions are very small compared to the wavelength of incident light. The full Mie solution becomes evident for particles greater than about $\lambda/2$ as shown in figure 7.1. The problem of multiple scattering and its treatment will be the subject of Chapter 8.

PLEASE NOTE:

For a given scattering particle of radius r_p:

$Q_{scat}(r_p) = C_{scat}(r_p)/\pi r_p^2$

8. DEVELOPMENT OF THE MULTIPLE SCATTERING MODEL.

8.1 Introduction

The previous chapter has served to introduce the basic concepts of light scattering and to discuss the development of the computer program "TSCAT". This program calculates all the required parameters completely to define the polar intensity distribution of scattered light. It must be emphasized at this stage that this program can handle scattering particles of any size and refractive index and can take into account the effect of incident light of any polarization and wavelength. The flexibility of this program is important to the next stage of development.

It will be shown in this chapter that the biggest problem in highly turbid media, such as nucleating steam flows, is that any studies involving single particle scattering soon become inaccurate. In turbid media with large optical depths the effects of multiple particle scattering can become significant, and even dominant. Multiple scattering processes have already been outlined in Chapter 7. There it was pointed out that the total effect of multiple scattering upon light propagating through a turbid medium may be thought of as a summation of the effects brought about by each individual single scattering event. It would be very useful, therefore, if a method could be developed which would compute the effects of multiple scattering using a detailed knowledge of the single scattering phase function. In particular a method is

required which can predict the diffusely scattered light both transmitted through a turbid medium and reflected back out of that medium. Several methods have been tried by various authors and these are reviewed in section 8.2.1.

The method chosen for this work is that which was originally developed by van de Hulst (50) but more recently adopted and published by Hansen (48). In his paper, Hansen discusses a technique for computing the transmission and reflection coefficients for diffusely scattered light. However, precise details of the computing method are not given. Section 8.2.2 derives the fundamental equations for the coefficients which are quoted by Hansen. An attempt has been made to reduce the equations for the transmission and reflection coefficents in such a way as to allow a computation method to be developed. Hansen does quote some fast execution times for his computer simulation program. This means that he has succeeded in significantly reducing the complexity of the formulae. This section highlights the author's attempt at doing the same.

Having reduced the terms the next stage is to write the computer program to evaluate them. Section 8.3 is concerned with the development of such a program and some of the techniques which were used to reduce the execution time.

The detection of diffuse light constitutes background noise and it is the effect of this that will reduce the effective quality of the Doppler signals.

Some studies have already been conducted by several authors to evaluate the signal strength of fringe type laser Doppler systems. Computer models have been developed by Adrian and Earley (2), Deepak (16) and Meyers and Walsh (65) . In each case, the evaluation of LDA performance has been done using the Mie scattering theory. An attempt has also been made to predict the signal-to-noise ratio. All the authors have used very fundamental concepts to develop their computer models. During this research a computer model has been developed to evaluate the effects of multiple scattering. The question was therefore asked "Can the single scattering phase function program be used in conjunction with the multiple scattering program to yield an estimate of the signal-to-noise ratio of a given two phase medium?". Section 8.4 discusses a method used to develop a relationship for the dependence of the signal-to-noise ratio of signals obtained from the medium upon the two intensity distributions produced by "TSCAT" and the multiple scattering program. Essentially what is computed for the medium is the ratio of direct single scattered light to the strength of the diffusely scattered light in a given direction. This is not intended to be an all embracing formula in that it includes all the effects of a scattering process in an LDA situation. It does, however, include the most important and influential parameters. It takes into account the conversion of the integrated scattered light energy, incident upon the photocathode of a detector

surface, into electrical energy and an expression is derived which also includes the influence of the photodetector characteristics. This expression is intended to give an estimate of the signal-to-noise ratio (SNR) of the signals obtained from a turbid medium as seen by the processing electronics. Values of the SNR will be computed for various stations across the measuring section of the wet steam rig and a comparison will be made in Chapter 9 between these computed values and the relative difficulty in obtaining good data rates and validation rates from the flow, when using a counter processor.

8.2 The Problem of Multiple Scattering

In a flow of nucleating steam, the optical depth of the turbid medium across a measuring section of diameter 200 mm will, in almost all cases, be greater than 0.3. Consequently in calculation of the transmission through optically thick media, the effects of higher order scattering must be taken into account (50). The water droplets present will not only be scattering the direct light upon them from the incident beam but also that scattered light incident upon them from other particles. This is called multiple scattering as defined in section 7.2.3. The subject of radiative transfer (10) is concerned with the solution to this problem. Many procedures have been developed to include multiple scattering effects in radiative transfer calculations. These techniques include Monte Carlo methods (9) (76) and the doubling method (48)

(51). However, the Monte Carlo method is based upon a statistical approach and the underlying physics of the photon-particle interactions is completely hidden. In the doubling method, the medium is divided into slabs so that in each slab only single scattering occurs. This method, on the other hand, does not take into account the physics of the multiple scattering process. The two methods represent the most widely used although recently other techniques have been tried (19) (93).

The extent to which these methods have been used will be briefly discussed. One method will be chosen to develop a computer model to predict the pattern of diffusely scattered radiation through a turbid medium. In particular the transmission and reflection coefficients will be evaluated for an incident light beam of known intensity. Some test conditions will be considered to test the accuracy of the computer simulation.

8.2.1 A review of the methods of treatment

8.2.1.1 The Monte Carlo technique

Monte Carlo simulation techniques have been used in recent years to study radiative transfer in the atmosphere and the oceans. In the atmosphere it has been applied to the study of low visibility conditions in the presence of atmospheric aerosols such as dust, smoke and fog (9). Scattering of laser radiation by such aerosol clouds, being basically a multiple scattering process, is very difficult to predict. The advantage of the Monte Carlo

method here is that it can handle strange geometries as well as inhomogeneities. In the study of oceanography, biological researchers have resorted to lidar techniques to observe and study various research problems (76). Variations in time and space of important biological parameters present a formidable obstacle for the researcher using conventional shipboard measurement techniques. A technique is needed for interpreting the accuracy of lidar system measurements over a wide range of environmental conditions, as well as for various boundary conditions and source or sensor geometries. Again, the Monte Carlo technique presents a model which is well suited to these conditions.

The use of the Monte Carlo method to treat the effects of multiple scattering on the propagation of light through a turbid medium has some advantageous features deriving from its simplicity. However, the biggest disadvantage of the method lies in the length of time necessary to obtain reliable results. Often, all calculations have to be repeated if the parameters defining the medium or the geometry of the propagation problem have to be varied.

The most widely used version of this technique is described by Burscaglioni (9). The basic process is shown in figure 8.1. A cylindrical light beam is assumed to propagate in the x direction. A receiver of area A is placed at a distance D from the source S. Considering only a homogeneous medium for simplicity, the extinction coefficient may be represented by σ_{ext}. A simple Monte

Carlo procedure would consist of following the broken path of a photon emitted by the source S, initially in the x-direction.

A random number generating routine would be used to determine the length of each straight part given the extinction coefficent of the medium. By analogy, the routine may be considered to determine the angle in space for each scattering event, given the scattering properties of the medium. This would normally be represented by the phase function. By repeating the procedure a sufficient number of times, the fraction of the emitted power, received at R, is evaluated by counting the photons whose paths arrive in the area of the receiver.

The random procedure is employed to determine the positions of the points P_1, P_2 ... P_m where the first, second ... n^{th} scattering events occur. For each of these points, for example point P_k, the probability function is evaluated. This is the probability that the photon will be received by the elemental area of the receiver at P_R without encountering any further scattering. This probability is defined as:

$$P_R = \frac{\Delta A}{2} p (\cos \theta_k) e^{-\sigma_{ext} \cdot r} \qquad (8.1)$$

where r is the distance between P_R and P_ℓ.

By following this procedure, each single photon path is used to study the effects of the different order of scattering. It is for this reason that the technique has

been referred to as the method of "photon histories" by some authors.

The manner in which the process is extended and adopted is dependent upon the circumstances in each individual application. As the technique is not going to be used in this work, it is therefore beyond the scope of this text to discuss it.

8.2.1.2 The doubling method

Although this method has been less widely used recently, it still represents a valid means of treating the multiple scattering problem. The doubling method was first used by van de Hulst to provide rapid and accurate results for the problem of diffuse reflection from a turbid medium. A development by Hansen (48) eliminated the need for numerically solving an equation of transfer for the entire medium. If the transfer equation could be solved for a layer of such small optical thickness ($\tau_o \sim 2^{-25}$), then the transmission and reflection functions for that layer could be approximated by the Mie scattering phase function. If this solution could then be used to obtain solutions for layers of thickness $2\tau_o$, $4\tau_o$, $8\tau_o$ etc., then considerable computing time could be saved. Hansen has applied such a doubling method to the study of spectral scattering by clouds in which the phase function is strongly peaked in the forward direction. Hansen describes a computing method which is capable of giving fast and accurate results for all optical thicknesses. A similar method has been used by

Irvine (51) based upon van de Hulsts' initial work.

The computer program developed for this research will handle any phase function. This is because earlier it was stated that one of the objectives of such a method was to predict the polar intensity distribution of diffusely transmitted and reflected light using a "detailed knowledge of the single scattering phase function". By virtue of this, the phase function for any two phase or particulate medium can be used as an input to a more general program developed by the author to perform the necessary further computation.

The main advantage of the doubling method in this application is its speed and relatively high accuracy. Provided that the turbid medium can be represented by a large number of parallel sided optical slabs (albeit of very small thickness), then the doubling method is ideal. For awkward geometries or in cases where the medium constants are varying, then the Monte Carlo method is highly preferable for reasons explained. In this work, however, the doubling method has been chosen. A turbid medium of wet steam is homogeneous and is a relatively simple application of this method. Furthermore the scattering geometry is conventional as shown in figure 7.3.

8.2.2 The determination of the multiple scattering of radiation by the doubling method

In order to provide a little background theory for deriving the transmission and reflection coefficients, it

would be useful to discuss the so called principles of invariance (10). Since the turbid medium is to be subdivided into a very large number of layers of finite thickness, each with parallel faces, the medium is hereafter referred to as a plane-parallel atmosphere. In addition to deriving a few basic quantities this section will also establish the sign convention to be adopted throughout the treatment.

The equations for the transmission and reflection coefficients can then be formulated for the initial layer. Once this has been done the actual method of doubling will be discussed.

8.2.2.1 Some basic definitions

Consider a plane-parallel atmosphere consisting in its simplest form of two layers as shown in figure 8.2. Let the intensity of radiation diffusely reflected in the direction (μ, ϕ) be denoted by $I(0;\mu,\phi)$ $(0 \leq \mu \leq 1)$ and let the intensity diffusely transmitted in the direction $(-\mu, \phi)$ below the surface $\tau = \tau_1$ be denoted by $I(\tau;-\mu, \phi)$. The sign convention adopted here is that the inward direction to the layer is negative and the outward direction, positive.

These reflected and transmitted intensities can be expressed in terms of a scattering function:

$$S(\tau;\mu,\phi;\mu_o,\phi_o)$$

and a transmission function

$$T\ (\tau;\mu,\phi;\mu_o,\phi_o)$$

in the forms:

$$I\ (0,\ \mu,\ \phi) = \frac{F}{4\mu}\ .\ S(\tau_1;\mu,\phi;\mu_o,\phi) \qquad (8.2)$$

and

$$I\ (0;\ -\mu,\ \phi) = \frac{F}{4\mu}\ .\ T(\tau_1;\mu,\phi;\mu_o,\phi)$$

which leads to the more formal definitions.

The reflection coefficient may be defined as the proportion of the incident radiation that is diffusely reflected from the direction (μ_o, ϕ_o) into the direction (μ, ϕ) at a given optical thickness. The transmission coefficient may similarly be defined as that proportion of the incident radiation that is diffusely transmitted from the direction ($-\mu_o$, ϕ_o) into the direction (μ,ϕ).

To further distinguish between the outward ($0 \leqslant \mu \leqslant 1$) and the inward ($0 \leqslant \mu \leqslant -1$) directed radiations, let:

$I(\tau;\mu,\phi)$ where ($0 \leqslant \mu \leqslant 1$) be reflection

and

$I(\tau;-\mu,\phi)$ where ($0 \leqslant \mu \leqslant -1$) be transmission

8.2.2.2 <u>The principles of invariance for a plane parallel atmosphere</u>

(a) The intensity $I(\tau;\mu,\phi)$ at any level τ results from the reflection of the reduced incident flux and the diffuse radiation

$I(\tau;-\mu',\phi')$ $(0\leq\mu'\leq 1)$ incident on the surface at τ by the atmosphere of optical thickness $(\tau_1 - \tau)$ below τ.

This is illustrated in figure 8.3(a). Some of the radiation will be scattered directly from the surface as a result of the incident radiation. However, due to the incidence of diffuse radiation on the surface, a proportion of this will be scattered due to the layer of thickness $(\tau_1 - \tau)$ in the direction (μ, ϕ). This can be expressed mathematically as

$$I(\tau:\mu,\phi) = \frac{F}{4\mu} \cdot e^{-\tau/\mu_o} \cdot S(\tau_1-\tau:\mu,\phi:\mu_o,\phi_o)$$

$$+ \frac{1}{4\pi\mu}\int_0^1\int_0^{2\pi} S(\tau_1-\tau:\mu,\phi;\mu',\phi')I(\tau_1:-\mu',\phi')\,d\mu'd\phi' \qquad (8.3)$$

(b) The intensity $I(\tau;-\mu,\phi)$ at any level τ results from the transmission of the incident flux by the atmosphere of optical thickness τ above the surface τ and the reflection by this same surface of radiation $I(\tau_1;\mu',\phi')$ $(0\leq\mu\leq 1)$ incident on it from below. This is illustrated in figure 8.3(b) and is expressed mathematically as .

$$I(\tau:-\mu,\phi) = \frac{F}{4\mu} \cdot T(\tau:\mu,\phi:\mu_o,\phi_o) +$$

$$\frac{1}{4\pi\mu}\int_0^1\int_0^{2\pi} S(\tau:\mu,\phi:\mu',\phi').I(\tau:\mu',\phi')\,d\mu'd\phi' \qquad (8.4)$$

(c) The diffuse reflection of the incident radiation by the entire atmosphere is equivalent to the reflection by the part of the atmosphere of optical thickness τ, above the level τ, and the transmission by this same atmosphere of the diffuse radiation $I(\tau;\mu',\phi')$ $(0\leq\mu'\leq1)$ incident on the surface τ from below.

This is illustrated in figure 8.3(c) and can be expressed mathematically as:

$$\frac{F}{4\mu}.S(\tau:\mu,\phi:\mu_o,\phi_o) = \frac{F}{4\mu}.S(\tau:\mu,\phi:\mu_o,\phi_o) + e^{-\tau/\mu}.I(\tau:\mu,\phi)$$

$$+\frac{1}{4\pi\mu}\int_0^1\int_0^{2\pi} T(\tau:\mu,\phi:\mu_o,\phi_o).I(\tau:\mu',\phi')\,d\mu'd\phi' \qquad (8.5)$$

which on substitution for $I(\tau_1;\mu,\phi)$ and $I(\tau;\mu',\phi')$ will yield the full expression.

(d) The diffuse transmission of the incident radiation by the entire atmosphere is equivalent to the transmission of the reduced incident flux and the diffuse radiation $I(\tau;-\mu',\phi')$ $(0\leq\mu'\leq1)$ incident on

the surface τ by the atmosphere of optical thickness $(\tau_1-\tau)$ below τ.

This is illustrated in figure 8.3(d). The mathematical expression for this may be written as:

$$\frac{F}{4\mu}.T(\tau:\mu,\phi:\mu_o,\phi_o) = \frac{F}{4\mu}.e^{-\tau/\mu_o}.T(\tau_1-\tau:\mu,\phi:\mu_o,\phi_o) +$$

$$e^{-\tau_1/\mu}.I(\tau_1-\tau:-\mu,\phi)+\frac{1}{4\pi\mu}\int_0^1\int_0^{2\pi}T(\tau_1-\tau):\mu,\phi:\mu',\phi')I(\tau_1:-\mu',\phi')d\mu'd\phi' \quad (8.6)$$

and similarly, on substituting for $I(\tau_1-\tau;-\mu',\phi')$ and $I(\tau_1;-\mu';\phi')$ in equation (8.6) yields the full expression.

8.2.2.6 <u>The basic transmission and reflection functions for the initial double layer</u>

In order to initiate the doubling process the scattering and transmission functions $S(2\tau;\mu,\phi:\mu_o,\phi_o)$ and $T(2\tau;\mu,\phi:\mu_o,\phi_o)$ for the first pair of single layers are required. They may be found by adding the ways in which the diffuse radiation can escape from the double layer

Thus for the reflection (or scattering) coefficient.

$$\frac{F}{4\mu}.S(2\tau:\mu,\phi:\mu_o,\phi_o) = \frac{F}{4\mu}.S(\tau:\mu,\phi:\mu_o,\phi_o)$$

$$+e^{-\tau/\mu}.S(\tau:\mu,\phi:\mu_o,\phi_o).F.e^{-\tau/\mu_o}$$

$$+\frac{1}{4\pi\mu}\int_0^1\int_0^{2\pi}T(\tau:\mu,\phi:\mu',\phi').\frac{1}{4\mu'}.\Sigma_o(\tau:\mu',\phi':\mu_o,\phi_o).d\mu'd\phi'.F.e^{-\tau/\mu_o}$$

$$+e^{-\tau/\mu}.\frac{1}{4\pi\mu}.\int_0^1\int_0^{2\pi}\Sigma_o(\tau:\mu,\phi:\mu',\phi').\frac{T(\tau:\mu',\phi':\mu_o,\phi_o)}{4\mu'}.d\mu'd\phi'.F$$

$$+\frac{1}{4\pi\mu'}\int_0^1\int_0^{2\pi}\int_0^1\int_0^{2\pi} T(\tau:\mu,\phi:\mu'',\phi'').\frac{1}{4\pi\mu''}.\mathcal{E}_o(\tau:\mu'',\phi'':\mu',\phi')$$

$$\times T\frac{(\tau:\mu',\phi':\mu_o,\phi_o)}{4\mu'}\cdot d\mu'd\phi'd\mu''d\phi''.F \qquad (8.7)$$

where:

$$\mathcal{E}_o(\tau:\mu,\phi:\mu_o,\phi_o)=\sum_{n=1,3\ldots}^{\infty}S_n(\tau:\mu,\phi:\mu_o,\phi_o)$$

$$S_1(\tau:\mu,\phi:\mu_o,\phi_o)=S(\tau:\mu,\phi:\mu_o,\phi_o)$$

and a recurrence formula where:

$$S_n(\tau:\mu,\phi:\mu_o,\phi_o)\equiv\frac{1}{4\pi}\int_0^1\int_0^{2\pi}S(\tau:\mu,\phi:\mu',\phi')$$

$$\times\ S_{n-1}(\tau:\mu',\phi':\mu_o,\phi_o).\frac{d\mu'd\phi'}{\mu'} \qquad n>1 \qquad (8.8)$$

This is illustrated in full in figure 8.4.

Similarly an expression may be written down for the transmission coefficient below, and is illustrated in figure 8.5;

$$T(2\tau:\mu,\phi:\mu_o,\phi_o)=T(\tau:\mu,\phi:\mu_o,\phi_o)+e^{-\tau/\mu}.T(\tau:\mu,\phi:\mu_o,\phi_o)$$

$$+e^{-\tau/\mu}.\mathcal{E}_e(\tau:\mu,\phi:\mu_o,\phi_o).e^{-\tau/\mu_o}$$

$$+\frac{1}{4\pi}\int_0^1\int_0^{2\pi}T(\tau:\mu,\phi:\mu',\phi').T(\tau:\mu',\phi':\mu_o,\phi_o).d\mu'd\phi'$$

$$+e^{-\tau/\mu_o}.\frac{1}{4\pi}\int_0^1\int_0^{2\pi}T(\tau:\mu,\phi:\mu',\phi').\mathcal{E}_e(\tau:\mu',\phi':\mu_o,\phi_o)\frac{d\mu'}{\mu'}.d\phi'$$

$$+e^{-\tau/\mu}.\frac{1}{4\pi}\int_0^1\int_0^{2\pi}\mathcal{E}_e(\tau:\mu,\phi:\mu',\phi').T(\tau:\mu',\phi':\mu_o,\phi_o)\frac{d\mu'}{\mu'}.d\phi'$$

$$+\frac{1}{16\pi^2}\int_0^1\int_0^{2\pi}\int_0^1\int_0^{2\pi}T(\tau:\mu,\phi:\mu'',\phi'').\mathcal{E}_e(\tau:\mu'',\phi'':\mu',\phi')\times$$

$$T(\tau:\mu',\phi':\mu_o,\phi_o).\frac{d\mu'}{\mu'}d\phi'\frac{d\mu''}{\mu''}d\phi'' \qquad (8.9)$$

where

$$\Sigma_e(\tau;\mu,\phi;\mu_0,\phi_0) \equiv \sum_{n=2,4,\ldots}^{\infty} S_n(\tau;\mu,\phi;\mu_0,\phi_0)$$

using the same recurrence relation for $S_n(\tau;\mu,\phi;\mu_0\phi_0)$ as before.

8.2.2.4 Physical interpretation of these formulae

At first glance equations (8.7) and (8.9) appear complicated but interpretation is made more clear if their full physical significance is explained. Attention is confined for this purpose to the expression for the reflection coefficient. A similar approach exists for the transmission coefficient.

(a) The first term on the RHS of equation (8.7) is the intensity of the radiation diffusely scattered in the upper layer without interaction with the lower layer.

(b) The second term refers to the radiation which has passed through the upper layer without interaction and is scattered any number of times back and forth between the two layers and passed back out in the direction (μ, ϕ) without any further interaction. Note that for this term there are an odd number of reflections in the summation. This can be compared with the even number of terms in the summation of the

even number of terms in the summation of the third term of the transmission coefficient in equation (8.9).

(c) The third term refers to the proportion of diffuse radiation emerging in the direction (μ, ϕ) after successive interlayer scattering between the lower and upper layers. This radiation has undergone interaction with a scattering particle in the lower layer.

(d) The fourth term refers to a similar process as (c) but scattering has further taken place with a particle in the upper layer,

(e) The fifth and final term refers to that proportion of diffusely transmitted radiation which has undergone particle scattering in both layers as well as some interlayer scattering.

In most cases only the first two terms will be significant unless the medium is particularly optically dense in which case the proportion of directly transmitted radiation is negligibly small when the other terms may become significant.

The degree to which this occurs depends largely upon the albedo and the form of the scattering phase function. There will be in addition to all those terms, a proportion

of the incident radiation which will pass directly through each successive layer and will be attenuated by an amount determined by the bulk extinction coefficient.

8.2.2.5 Reduction of the transmission and reflection coefficients

The formulae for the transmission and reflection coefficients given in equation (8.7) and (8.9) are difficult to handle in the cases of numerical integration. They now need to be greatly simplified.

In the first instance it is convenient to suppose that the expansion of the phase function in ordinary legendre polynomials consists of only a finite number of terms, say N viz:

$$p(\cos\theta) = \sum_{\ell=0}^{N} w_\ell P_\ell(\cos\theta) \qquad (8.10)$$

where w_ℓ (ℓ=0,1,2...N) are a set of (N+1) constants for a phase function of the form below using the result of equation (7.22) in section 7.2.2.

$$p(\mu,\phi;\mu',\phi') = \sum_{\ell=0}^{N} \omega_\ell P_\ell\left(\mu\mu' + (1-\mu^2)^{1/2}(1-\mu'^2)^{1/2}\cos(\phi'-\phi)\right) \qquad (8.11)$$

The ordinary legendre polynomials may be expanded for the argument:

$$\mu\mu' + (1-\mu)^{1/2}\cdot(1-\mu'^2)^{1/2}\cdot\cos(\phi'-\phi)$$

whence from the "addition theorem for spherical harmonics"

(13) the phase function may be rewritten as:

$$P(\mu,\phi:\mu',\phi') = \sum_{\ell=0}^{N} \omega_\ell \cdot \left\{ P_\ell(\mu) \cdot P_\ell(\mu') + 2 \sum_{m=1}^{\ell} \frac{(\ell-m)!}{(\ell+m)!} \cdot P_\ell^m(\mu) \cdot P_\ell^m(\mu') \cos m(\phi'-\phi) \right\} \qquad (8.12)$$

Inverting the summation on the RHS gives:

$$P(\mu,\phi:\mu',\phi') = \sum_{m=0}^{N} (2-\delta_{om}) \left\{ \sum_{\ell=m}^{N} \cdot \omega_\ell^m \cdot P_\ell^m(\mu) P_\ell^m(\mu') \cos m(\phi'-\phi) \right\} \qquad (8.13)$$

where

$$w_\ell^m = w_\ell \frac{(1-m)!}{(\ell+m)!} \quad (l=m \ldots .N \quad 0 \leqslant m \leqslant N)$$

and $\delta_{om} = 1$ for $m = 0$

$\delta_{om} = 0$ for $m > 0$

The phase function has thus evolved from a weighted sum of ordinary legendre polynomials to an enhanced weighted sum of a product of a series of associated legendre polynomials. The purpose of this expansion is to separate the azimuth angles (ϕ and ϕ_o) and to replace them with a series expansion and hence reduce the large integral terms.

According to Hansen (48) a considerable advantage is gained in computing time if the azimuth dependent functions are expanded in a half range fourier series in $(\phi-\phi_o)$. It has already been shown that the phase function may be expanded in cosines of the scattering angle. Hence this gives the series as

$$S(\tau:\mu,\phi:\mu_0,\phi_0) = \sum_{M=0}^{\infty} S^M(\tau:\mu,\mu_0)\cos M(\phi-\phi_0) \qquad (8.14)$$

where

$$S^M(\tau:\mu,\mu_0) = \frac{1}{(2-\delta_{0M})}\int_0^{2\pi} S(\tau:\mu,\phi':\mu_0,\phi_0)\cos M(\phi'-\phi_0)\,d\phi' \qquad (8.15)$$

$\delta_{om} = 0$ if $m \neq 0$ and $= 1$ if $m = 0$

Further, Chandrasekhar (10) approximates the scattering and transmission functions for the single layer to the scattering phase function, viz:

$$S(\tau_0:\mu,\phi:\mu_0,\phi_0) \approx \left(\frac{1}{\mu}+\frac{1}{\mu_0}\right)^{-1}\left\{1-\exp\left[-\tau_0\left(\frac{1}{\mu}+\frac{1}{\mu_0}\right)\right]\right\}p(\mu,\phi:-\mu_0,\phi_0) \qquad (8.16)$$

and

$$T(\tau_0:\mu,\phi:\mu_0,\phi_0) \approx \left(\frac{1}{\mu}-\frac{1}{\mu_0}\right)^{-1}\left\{\exp\left(\frac{-\tau_0}{\mu_0}\right)-\exp\left(\frac{-\tau_0}{\mu}\right)\right\}p(\mu,\phi:\mu_0,\phi_0) \qquad (8.17)$$

where $p(\mu,\phi;\mu_0,\phi_0)$ is normalised to ω, the albedo for single scattering. Concentrating upon the scattering coefficient the formulae may now be reduced further.

Substituting the form of equation (8.16) into equation (8.15) gives:

$$S^M(\tau:\mu,\mu_0) = \frac{1}{(2-\delta_{0M})}\left(\frac{1}{\mu_0}+\frac{1}{\mu}\right)^{-1}\left\{1-\exp\left[-\tau_0\left(\frac{1}{\mu}+\frac{1}{\mu_0}\right)\right]\right\} \times \int_0^{2\pi} p(\mu,\phi':-\mu_0,\phi_0)\cos M(\phi'-\phi_0)\,d\phi' \qquad (8.18)$$

Now substitute the expansion of $p(\mu, \phi'; -\mu_o \phi_o)$ of equation (8.13) in equation (8.16) to give:

$$S^m(\tau; \mu, \mu_o) = \frac{1}{(2-\delta_{om})} \left(\frac{1}{\mu} + \frac{1}{\mu_o}\right)^{-1} \left\{1 - exp\left[-\tau_o\left(\frac{1}{\mu} + \frac{1}{\mu_o}\right)\right]\right\}$$

$$\times \sum_{m=0}^{N} (2-\delta_{om}) \left\{\sum_{\ell=m'}^{N} w_\ell^{m'} P_\ell^{m'}(\mu) P_\ell^{m'}(-\mu_o)\right\}$$

$$\times \int_0^{2\pi} \cos m'(\phi - \phi') \cos m(\phi' - \phi_o) \, d\phi' \qquad (8.19)$$

Note: in equation (8.19) the first m has been changed to m' for clarity. !!

Each independent fourier component has thus been represented by a weighted sum of associated legendre polynomials. Equation (8.19) has been organized into a form to facilitate the next essential step for reduction. The integral term involving the azimuth dependence may be evaluated analytically using the well known trigonometric orthogonality condition (45):

$$\int_0^{2\pi} \cos m'(\phi - \phi') \cos m(\phi' - \phi_o) \, d\phi'$$

$$= 0 \text{ if } m \neq m'$$

$$= \pi \cos m(\phi_o - \phi) = \pi \text{ if } m = m' \neq 0$$

$$= 2\pi \text{ if } m = m' = 0$$

Equation (8.19) may now be rewritten as

$$S^m(\tau; \mu, \mu_o) = (1 + \delta_{om}) \cdot \pi \cdot \left(\frac{1}{\mu} + \frac{1}{\mu_o}\right)^{-1} \left\{1 - exp\left[\left(\frac{1}{\mu} + \frac{1}{\mu_o}\right)\right]\right\} \times$$

$$\sum_{\ell=M}^{N} \omega_\ell^M \cdot P_\ell^M(\mu) \cdot P_\ell^M(-\mu_0) \qquad (8.20)$$

$\delta_{om} = 1$ for $m=0$, $\delta_{om}=0$ for $m>0$

from a similar consideration, noting that the phase function is now $p(-\mu,\phi;-\mu_0,\phi_0)$ the transmission fourier coefficients may be written as

$$T^M(\tau;\mu,\mu_0) = (1+\delta_{0M}) \cdot \pi \cdot \left(\frac{1}{\mu}-\frac{1}{\mu_0}\right)^{-1} \left\{ exp\left(\frac{-\tau}{\mu_0}\right) - exp\left(\frac{-\tau}{\mu}\right) \right\}$$
$$\times \sum_{\ell=M}^{N} \omega_\ell^M \cdot P_\ell^M(-\mu) \cdot P_\ell^M(\mu) \qquad (8.21)$$

Hence the azimuth dependent term has been dropped completely. In practice these equations will provide the initial values for the reflection and transmission functions respectively. Since the exponential terms in brackets involve the differences of nearly equal numbers, some of the accuracy would be lost on a computer. It is better to expand the exponentials in a power series and keep terms through τ_0^2.

Using the Maclaurin expansion of e^x where:

$$e^x = 1 - \frac{x}{1!} + \frac{x^2}{2!} - \frac{x^3}{3!} + \ldots (-1) \frac{x^n}{n!}$$

gives, on the condition that τ_0 is very small (which it is):

$$\left(\frac{1}{\mu}+\frac{1}{\mu}\right)^{-1}\left[1-\exp\left\{-\tau_0\left(\frac{1}{\mu}+\frac{1}{\mu_0}\right)\right\}\right] \approx \left\{\tau_0-\tau_0^2\left(\frac{1}{\mu}+\frac{1}{\mu_0}\right)\right\}$$

and

$$\left(\frac{1}{\mu}-\frac{1}{\mu_0}\right)^{-1}\left[\exp\left(\frac{-\tau_0}{\mu_0}\right)-\exp\left(-\frac{\tau_0}{\mu}\right)\right] \approx \left\{\tau_0-\tau_0^2\left(\frac{1}{\mu}+\frac{1}{\mu_0}\right)\right\}$$

Thus equations (8.20) and (8.21) reduce further to give

$$S^m(\tau;\mu,\mu_0) = (1+\delta_{0m}).\pi.\left\{\tau_0-\frac{\tau_0^2}{2}\left(\frac{1}{\mu}+\frac{1}{\mu_0}\right)\right\} \times \sum_{\ell=m}^{N} \omega_\ell^m.\, P_\ell^m(\mu).\, P_\ell^m(-\mu_0) \qquad (8.22)$$

and

$$T^m(\tau;\mu,\mu_0) = (1+\delta_{0m}).\pi.\left\{\tau_0-\frac{\tau_0^2}{2}\left(\frac{1}{\mu}+\frac{1}{\mu_0}\right)\right\} \times \sum_{\ell=m}^{N} \omega_\ell^m.\, P_\ell^m(\mu).\, P_\ell^m(-\mu_0) \qquad (8.23)$$

where $\delta_{om} = 1$ for $m = 0$, $\delta_{om} = 0$ for $m > 0$

8.2.2.6 <u>To obtain the expressions for the first double layer</u>

An attempt may now be made to rewrite equations (8.7) and (8.9) in a much reduced form in terms of the independent fourier coefficients $S^m(\tau;\mu,\mu_0)$ and $T^m(\tau;\mu,\mu_0)$ for a particular value of m. Again concentrating on the reflection term:

$$S^m(2\tau;\mu,\mu_0)\cos m(\phi-\phi_0) = S^m(\tau;\mu,\mu_0)\cos m(\phi-\phi_0)$$

$$+ e^{-(\tau/\mu+\tau/\mu_0)} \cdot \sum_{n=1,3\ldots}^{\infty} S_n^m(\tau;\mu,\mu_0)\cos m(\phi-\phi_0)$$

$$+ \frac{e^{-\tau/\mu_0}}{4\pi} \cdot \int_0^1 T^m(\tau;\mu,\mu') \sum_{n=1,3\ldots}^{\infty} S_n^m(\tau;\mu',\mu_0)\frac{d\mu'}{\mu'} \int_0^{2\pi} \cos m(\phi-\phi')\cos m(\phi'-\phi_0)\,d\phi'$$

$$+ \frac{e^{-\tau/\mu}}{4\pi} \cdot \int_0^1 \sum_{n=1,3\ldots}^{\infty} S_n^m(\tau;\mu,\mu') T^m(\tau;\mu',\mu_0)\frac{d\mu'}{\mu'} \times \int_0^{2\pi} \cos m(\phi-\phi')\cos m(\phi'-\phi_0)\,d\phi'$$

$$+ \frac{1}{16\pi^2}\int_0^1\int_0^{2\pi} T^m(\tau;\mu,\mu'') \sum_{n=1,3\ldots}^{\infty} S_n^m(\tau;\mu'',\mu') T^m(\tau;\mu',\mu_0)\frac{d\mu'}{\mu'}\frac{d\mu''}{\mu''} \times \int_0^{2\pi}\int_0^{2\pi} \cos m(\phi-\phi'')\cos m(\phi''-\phi')\cos m(\phi'-\phi)\,d\phi' d\phi'' \quad (8.24)$$

But again using the well known orthogonal properties of a trigonometric integral gives:

$$\int_0^{2\pi} \cos m(\phi-\phi')\cos m(\phi'-\phi_0) = \pi\cos m(\phi-\phi_0) \quad \text{if } m\neq 0$$
$$= 2\pi \quad \text{if } m=0$$

and

$$\int_0^{2\pi} \cos m(\phi-\phi'')\cdot\cos m(\phi''-\phi')\cdot\cos m(\phi'-\phi_0)\,d\phi' d\phi''$$
$$= \pi^2\cos m(\phi-\phi_0) \quad \text{if } m\neq 0$$
$$= 4\pi^2 \quad \text{if } m=0$$

Hence

$$S(2\tau;\mu,\mu_0) = S^m(\tau;\mu,\mu_0) + \left(e^{-\tau/\mu} + e^{-\tau/\mu_0}\right)\sum_{n=1,3\ldots}^{\infty} S_n^m(\tau;\mu,\mu_0)$$

$$+\frac{e^{-\tau/\mu_0}}{(2-\delta_{0m})}\cdot\int_0^1 T^m(\tau:\mu,\mu')\sum_{n=1,3\ldots}^{\infty} S_n^m(\tau:\mu',\mu_0)\,\frac{d\mu'}{\mu'}$$

$$+\frac{e^{-\tau/\mu}}{(4-\delta_{0m})}\cdot\int_0^1\sum_{n=1,3\ldots}^{\infty} S_n^m(\tau:\mu,\mu')\cdot T^m(\tau:\mu',\mu_0)\,\frac{d\mu'}{\mu'}$$

$$+\frac{(1-\delta_{0m})}{16}\int_0^1\int_0^1 T^m(\tau:\mu,\mu')\sum_{n=1,3\ldots}^{\infty}(\tau:\mu'',\mu')\,T^m(\tau:\mu',\mu_0)\,\frac{d\mu'}{\mu'}\,\frac{d\mu''}{\mu''} \qquad (8.25)$$

which together with equation (8.22) completes the reduction of equation (8.24). This is the final form of the reflection coefficient for the first double layer.

Similarly the final form of the transmission coefficient may be written as:

$$T^m(2\tau:\mu,\mu_0) = T^m(\tau:\mu,\mu_0)\cdot\left\{e^{-\tau/\mu_0}+e^{-\tau/\mu}\right\}$$

$$+e^{-\tau/\mu}\cdot e^{-\tau/\mu_0}\cdot\sum_{n=2,4\ldots}^{\infty} S_n^m(\tau:\mu,\mu_0)$$

$$+\frac{1}{(4-2\delta_{0m})}\cdot\int_0^1 T^m(\tau:\mu,\mu')\,T^m(\tau:\mu',\mu_0)\,\frac{d\mu'}{\mu'}$$

$$+\frac{e^{-\tau/\mu_0}}{(4-2\delta_{0m})}\cdot\int_0^1 T^m(\tau:\mu,\mu')\sum_{n=2,4\ldots}^{\infty} S_n^m(\tau:\mu',\mu_0)\,\frac{d\mu'}{\mu'}$$

$$+\frac{e^{-\tau/\mu}}{(4-2\delta_{0m})}\cdot\int_0^1\sum_{n=2,4\ldots}^{\infty} S_n^m(\tau:\mu,\mu')\cdot T^m(\tau:\mu',\mu_0)\,\frac{d\mu'}{\mu'}$$

$$+\frac{(1-\delta_{0m})}{16}\int_0^1\int_0^1 T^m(\tau:\mu,\mu'')\sum_{n=2,4\ldots}^{\infty} S_n^m(\tau:\mu'',\mu')\cdot T^m(\tau:\mu',\mu_0)\,\frac{d\mu'}{\mu'}\,\frac{d\mu''}{\mu''} \qquad (8.26)$$

Equations (8.25) and (8.26) are the working equations. Both have lost their azimuth dependence and are therefore easier to integrate.

8.2.2.7 The method of doubling to very large depths

The derivation and reduction of the initial layer formulae has been discussed in section (8.2.2.5). The most common method of extending the transmission and reflection coefficients to very large depths is known as the addition method. If the initial layers are the same small thickness then the procedure may be referred to as the doubling method (48).

Having calculated the coefficients for the first double layer, the relationship between the input radiation to that layer and the diffusely scattered radiation from that layer is uniquely defined. This is the advantage of the doubling method. The complexities of the entire process are concentrated into the initial calculations. The computation for a medium of any optical depth is then relatively straightforward. The doubling process for successive double layers is depicted in figure 8.6. Concentrating on the doubling procedure for the transmission coefficient, this is known for a double layer of optical thickness $2\tau_o$. The manner in which the diffuse radiation will propagate through the next double layer is known. The figure illustrates an example for three distinct angles of incidence and emergence for simplicity. For each incident direction e.g. I_1, there exist three possible diffusely

scattered intensities I_o', I_1' and I_2' in addition to an attenuated direct intensity, $I_1 e^{-\tau/\mu_1}$, in this case.

This diffuse intensity distribution then becomes the incident radiation for the next double layer. Because the distribution is effectively made up of discrete components, each component of the incident distribution may be added to other components in the same direction. Again only three components are considered. The intensity distribution for an optical depth of $\tau = 4\tau_o$ has now been uniquely defined. The lower set of figures show in a similar way how two double layers are extended to four double layers, i.e. an optical depth of $8\tau_o$. This doubling process is repeated until the desired optical depth is reached. It is important throughout to take into account the proportion of direct radiation attenuated by the previous double layer that enters the next double layer in each incident direction.

The reflection coefficient is the same in principle but is slightly more complicated in practice, and is shown in figure 8.7. This is because the proportion of radiation reflected back from the next double layer in each direction is itself diffusely transmitted through the first double layer. This in turn may be reflected back down through the double layer. It is highly unlikely that this component is ever going to be significant in comparison to the first order diffuse transmission and reflection and will be neglected in any further treatment. This is justified for the following reason. At any given double layer or

multiples thereof i.e. $8\tau_o$, $16\tau_o$ etc, the ratio of diffusely scattered radiation to directly transmitted radiation will always be insignificant until the direct beam is so attenuated that it is comparable in magnitude with the intensity of the diffuse distribution. Even at this stage of the process where larger optical depths are encountered, successive diffuse transmission and reflection at each layer interface will be small. In any case, these diffuse intensity distributions will be attenuated due to extinction to negligible proportions either back out through the medium or further forwards into the medium.

Any computation of this process will benefit from representing the angular diffuse intensity distributions at a large number of discrete angles. Provided each component of the diffuse distribution in each direction is added at every doubling and account is taken of the direct components then the distribution will be defined for a medium of a given optical depth. All the possible ways that the radiation could have propagated through that medium will then have been computed.

8.3 The computational method used in evaluating the multiple scattering formulae

When developing a computational means of solving the transmission and reflection coefficients for the initial double layer, it was important to have reduced the formulae as far as possible. During the long development period of the program certain common features became apparent between

the various components of the formulae. These similarities will be discussed in the next section. The computer model will predict the scattered angular intensity distribution of incident radiation through a turbid medium of any optical thickness. Use is made of a program developed by A.W. Brinkman (7) to compute the single scattering phase function for a particle of any size and refractive index illuminated by radiation of any wavelength and degree of polarization. One of the limitations of this program, however, is that it has been developed primarily for polydispersions (20). In the case of nucleating steam a near monodispersal of droplet sizes can be expected as discussed in Chapter 6. However the distribution of droplet sizes required by any polydispersal model can be approximated to that of a monodisperal by making the distribution very narrow and sharply peaked at the mode radius. Finally some test cases will be considered as evidence that the program is behaving as intended. The results will then be compared with experimental data to be discussed in section (9.3.4). The suite of multiple scattering programs is shown in figure 8.8.

8.3.1 Qualitative outline of the method

Due to the relative complexity of the formulae and the variety of debugging problems that would ensue it was decided to break the program up into separate units. Each unit or subprogram would be concerned with the execution of a particular aspect of the problem. This approach would have the following advantages:

1. More computer memory is available to each individual program thereby decreasing the execution time of the overall program.

2. Fault finding becomes easier when the program is broken down into well defined areas each of which has subroutines performing distinct operations.

3. The program will stand the test of time. This method of writing the program should enable the user to remember the intricate details more readily if the program has not been used for many months.

Hansen (48) claims to have developed a computer to predict the transmission and reflection coefficients which will execute in about 400 seconds of cpu time. Allowing for the fact that machines vary in their speed of execution there must be a very fast algorithm to perform the integration routines. One of the biggest single contributing factors that led to a significant decrease in execution time was to set the number of available angles of incidence and emergence for the turbid medium equal to the number of gaussian steps chosen for the integration routines. Hence, for example, if a 6-step gaussian rule was to be applied, only six angles of incidence and six angles of emergence would be considered. However, as suggested by Hansen, at least 48 steps are required to maintain accuracy. A 48-step gaussian rule will provide a resolution of 90/48

degrees which should be sufficient for the purpose of this research. Further, the extra accuracy and resolution afforded by a 96-step rule would not fully justify the enormous memory requirements and a much slower execution time as a result of data storage on a magnetic tape.

The various subprograms are shown in figure 8.8. Program "MS/LOOKUP" generates the required data files containing the legendre and associated legendre polynomials for the main calculations. Program "MS/TRANSM" calculates the transmission and reflection coefficients for the initial double layer. There is a choice of doubling and plotting routines available depending upon what form of plot is required. Programs "MS/PLOTLOG" and "MS/PHASEPLOT" will both perform the interlayer doubling and plot out the results on a log-linear set of axes. The intended use of "MS/PHASEPLOT" will be discussed in section 8.3.5.

8.3.2 Representing the phase function

Following from the discussion in section (8.2.2.5), the scattering phase function may be represented by a weighted series of ordinary legendre polynomials. This is written in the following form:

$$p(\cos\theta) = \sum_{\ell=0}^{\infty} w_\ell P_\ell(\cos\theta)$$

where w_ℓ ($\ell = 0,1,2...N$) are a set of (N+1) constants.

If $p(\cos\theta)$ is continuous (which it is) then at every point of $p(\cos\theta)$ in the interval $-1 \leqslant \cos\theta \leqslant 1$ there will

exist a legendre series expansion as above.

By definition (45) then

$$w_\ell = \frac{2\ell+1}{2} \int p(\cos\theta).P_\ell(\cos\theta).d(\cos\theta)$$

$$w_\ell = \frac{2\ell+1}{2} \int p(\mu)P_\ell(\mu)d\mu \qquad (8.27)$$

The purpose of this is to provide an accurate curve fitting technique to the scattering phase function $p(\cos\theta)$ provided by a totally independent program. Equation (8.27) requires that the values w_ℓ, $\ell = 0,1,2 \ldots N$ are known.

This means that for any scattering phase function computed for any given scattering geometry, a set of values of ω_1 can be produced which completely defines that phase function. All the required information relating to particle size, refractive index and wavelength will be reflected in these values of the weighting function.

A given function $f(x)$ may be represented by a series summation of the following form:

$$\int_{-1}^{1} f(x)\,dx = \sum_{n=1}^{N} c_n f(x) \qquad (8.28)$$

which represents numerical integration through gauss quadrature.

8.3.3 To generate the scattering data file

Consider the second, third and sixth terms of the transmission coefficient in equation (8.26), viz:

(ii) $$e^{-\tau/\mu} \cdot e^{-\tau/\mu_o} \cdot \sum_{n=2,4\ldots}^{\infty} S_n^m(\tau:\mu,\mu_o)$$

(iii) $$\frac{1}{(4-2\delta_{om})} \cdot \int_0^1 T^m(\tau:\mu,\mu') T^m(\tau:\mu',\mu_o) \frac{d\mu'}{\mu'}$$

(iv) $$\frac{(1-\delta_{om})}{16} \cdot \int_0^1 \int_0^1 T^m(\tau:\mu,\mu'') \sum_{n=2,4\ldots}^{\infty} S_n^m(\tau:\mu'',\mu') \times T^m(\tau:\mu',\mu_o) \frac{d\mu'}{\mu'} \frac{d\mu''}{\mu''}$$

Restricting the number of incident and emergent angles μ and μ_o to the number of gaussian steps in the integration greatly reduces the computation of the above terms. These terms have been chosen because they illustrate the range of diffuse angles over which the integration is performed. Not only is there μ' and μ'', but a function of the form $T^m(\tau;\mu_1\mu_o)$ and $S^m(\tau;\mu,\mu_o)$ will have a numerical similarity with functions of the form $T^m(\tau;\mu,\mu')$ and $T^m(\tau;\mu,\mu'')$ and $S^m(\tau;\mu,\mu')$ and $S^m(\tau;\mu,\mu'')$ respectively. Further, due to the orthogonal properties of the associated legendre polynomials,

$T^m(\tau;\mu,\mu_o)$ is equivalent to $T^m(\tau;\mu_o,\mu)$ as is $T^m(\tau;\mu,\mu'')$ to $T^m(\tau;\mu'',\mu)$ etc.

If a look-up table of data is produced then computation of the above terms becomes more efficient.

According to equation (8.26), the independent fourier coefficients consist primarily of a summated series of associated legendre polynomials and a modified weighting function, w_l^m, l=m=0,1,2,...N. It is these parameters which will form the data in such a look-up table.

Program "MS/LOOKUP" generates the required data from any scattering phase function. As shown in figure 8.8, the program requires the use of two independent data files. The first is "SCATDATA" or "PHASEFTN" and contains the scattering phase function data as computed by the Mie scattering formulae in program "TSCAT". The second is "GAUS.ABSWGTS" which contains the gaussian abscissae and coefficents for 4, 6, 12, 24, 48 and 96-step integration (1).

For the associated legendre polynomials there exist the two indices l and m. Because of this there exists a variety of recurrence relations depending upon what is known of the initial conditions.

For fixed degree (l) but varying order (m):

$$P_l^{m+1}(x) = \frac{(2+1)}{(l-m+1)} \circ xP_n^m(x) - \frac{(l+m)}{(l-m+1)} \circ P_{l-1}^m(x) \qquad (8.29)$$

also for fixed m but varying l:

$$P_{l+1}^m(x) = \frac{(2l+1)}{(l-m+1)} \circ xP_l^m(x) - \frac{(l+m)}{(l-m+1)} \circ P_{l-1}^m(x) \qquad (8.30)$$

The look-up table contains these polynomials for an order, degree and argument up to 24, 24, 25 respectively.

To check that the recurrence formulae were being computed correctly, known values for the polynomials of a given argument x were used. The following are an example.

$$P_2^2(x) = \frac{(-1)^2 \cdot 4!}{2^2 \cdot 2!} \cdot (1-x^2)^{\frac{1}{2}} = 3(1-x^2)^{\frac{1}{2}}$$

$$P_4^4(x) = \frac{(-1)^4 \cdot 8!}{2^4 \cdot 4!} \cdot (1-x^2)^2 = 105(1-x^2)^2$$

$$P_{10}^{10}(x) = \frac{(-1)^{10} \cdot 20!}{2^{10} \cdot 10!} \cdot (1-x^2)^5 = 6.54 \cdot 10^8 (1-x^2)^5$$

$$P_{20}^{20}(x) = \frac{(-1)^{20} \cdot 40!}{2^{20} \cdot 20!} \cdot (1-x^2)^{10} = 3.2 \cdot 10^{23} (1-x^2)^{10} \qquad (8.31)$$

These test values were computed from the generating relation

$$P_n^m(x) = \frac{(-1)^m \cdot (n+m)!}{2^n \cdot n!} (1-x^2)^{m/2} \qquad (8.32)$$

This particular look-up table of data is extended to cover arguments of μ' where

$$\mu' = \frac{\mu_o + 1}{2}$$

and will be used for the integration routines in "MS/TRANSM" where a change of variable is required to perform a gaussian integration between the limits of 0 and 1.

The curve fitting as discussed in section 8.3.2 is performed in subroutine "WEIGHT". The main part of this subroutine is concerned with the generation of the ordinary

legendre polynomials. Use is made of the following recurrence relation.

$$P_{l+1}(\cos\Theta) = \frac{(2l+1)\cos\Theta_o \, P_l(\cos\Theta) - lP_{l-1}(\cos\Theta)}{l+1} \qquad (8.33)$$

In agreement with Hansen (48) only 50 terms of this expansion have been taken so that the phase function may be represented by

$$p(\cos\theta) = \sum_{l=0}^{50} w_l . P_l(\cos\theta) \qquad (8.34)$$

8.3.4 Evaluating the terms for the initial layer

The first double layer calculations are formed in program "MS/TRANSM". The first term of equation (8.26) is evaluated by combining and adding the associated legendre polynomial products. The values are stored so that the coefficients for all possible combinations of μ and μ_o are available for the integration routines. This is done in subroutine "TERM1". The second terms for both the transmission and reflection coefficients are not so straightforward. The breakdown of the main multiple scattering programs is shown in figure 8.9.

There are two variations on the second term. The first is a sum of an even series referring to the transmission of radiation after an even number of interlayer reflections. This is given by:

$$\sum_{n=2,4}^{\infty} S_n^m(\tau; \mu, \mu_o) \qquad (8.35)$$

The second is the sum of an odd series referring to the net reflection of radiation after an odd number of interlayer reflections. This is given by:

$$\sum_{n=1,3,5}^{\infty} S_n^m(\tau; \mu, \mu_o) \qquad (8.36)$$

According to Hansen these summations may be truncated at some n=N~5 with the omitted terms replaced by the geometric formula. This is justified because radiation scattered back and forth between the two layers tends towards an isotropic distribution after a number of such scatterings. The ratio of successive terms in the infinite series approaches a constant value.

The recurrence relation for the series of terms is given in equation (8.8). This type of expansion could involve many iterations within an extensive nesting of loops. An attempt was therefore made to evaluate $S_3^m(\tau; \mu, \mu_o)$, $S_4^m(\tau; \mu, \mu_o)$, and $S_5^m(\tau; \mu, \mu_o)$ efficiently.

The approach adopted was to consider a 3-step gaussian integration first of all. This enabled the method to be developed and checked easily. Writing $S_1(\mu_1, \mu_2)$ as S_1^{12} etc, then replacing the integration by sums through gauss quadrature yields the following:

$$S_2^{12} = C_1 S_1^{11} S_1^{12} + C_2 S_1^{12} S_1^{22} + C_3 S_1^{13} S_1^{32}$$

$$S_2^{22} = C_1 S_1^{21} S_1^{12} + C_2 S_1^{22} S_1^{22} + C_3 S_1^{23} S_1^{32}$$

$$S_2^{32} = C_1 S_1^{31} S_1^{12} + C_2 S_1^{32} S_1^{22} + C_3 S_1^{33} S_1^{32}$$

$$S_3^{12} = C_1 S_1^{11} S_2^{12} + C_2 S_1^{12} S_2^{22} + C_3 S_1^{13} S_2^{32}$$

$$S_3^{22} = C_1 S_1^{21} S_2^{12} + C_2 S_1^{22} S_2^{22} + C_3 S_1^{23} S_2^{32}$$

$$S_3^{32} = C_1 S_1^{31} S_2^{12} + C_2 S_1^{32} S_2^{22} + C_3 S_1^{33} S_2^{32}$$

$$S_4^{12} = C_1 S_1^{11} S_3^{12} + C_2 S_1^{12} S_3^{22} + C_3 S_1^{13} S_3^{32}$$

where c_1, c_2 and c_3 are the gaussian coefficients. From the above the full 9 terms of S_1 are required. Writing this out in matrix form gives

$$\begin{bmatrix} S_1^{11} & S_1^{12} & S_1^{13} \\ S_1^{21} & S_1^{22} & S_1^{23} \\ S_1^{31} & S_1^{32} & S_1^{33} \end{bmatrix}$$

but only 3 terms of S_2, viz:

$$\begin{bmatrix} X & S_2^{12} & X \\ X & S_2^{22} & X \\ X & S_2^{32} & X \end{bmatrix}$$

and only 3 terms of S_3:

$$\begin{bmatrix} X & S_3^{12} & X \\ X & S_3^{22} & X \\ X & S_3^{32} & X \end{bmatrix}$$

Writing out S_4 in full gives:

$$S_4^{12} = C_1 S_1^{11} S_3^{12} + C_2 S_1^{12} S_3^{22} + C_3 S_1^{12} S_3^{32}$$

whence on substitution: $S_4 =$

$$C_1 S_1^{11}(C_1 S_1^{11} S_2^{12}) + C_2 S_1^{12}(C_1 S_1^{22} S_2^{22}) + C_3 S_1^{12}(C_1 S_1^{31} S_2^{12})$$
$$+ C_1 S_1^{11}(C_2 S_1^{12} S_2^{22}) + C_2 S_1^{12}(C_2 S_1^{22} S_2^{22}) + C_3 S_1^{13}(C_2 S_1^{32} S_2^{22})$$
$$+ C_1 S_1^{11}(C_3 S_1^{13} S_2^{32}) + C_2 S_1^{12}(C_3 S_3^{23} S_2^{32}) + C_3 S_1^{13}(C_2 S_1^{33} S_2^{32})$$

Hence the result $S_4^m(1,2)$.

The total number of calculations is 3(3+3+3) = 27 instead of a possible 3x3x3x3 = 81.

The method makes use of redundancy which only becomes significant for the higher step integrations. Thus, for example, with 96-step integration, the reduced method would require 96 x (96+96+96) = 27648 calculations instead of a possible 96x96x96x96, i.e. 8.49×10^7, which is effectively a reduction in execution time of the order of 10^3.

Equation (8.36) can then be reduced to:

$$\sum_{n=2,4\ldots}^{\infty} S_n^m(\tau:\mu,\mu_0) = S_2^m(\tau:\mu,\mu_0) + S_4^m(\tau:\mu,\mu_0) + \frac{S_4^m(\tau:\mu,\mu_0)}{\left[1 + \frac{S_4^m(\tau:\mu,\mu_0)}{S_2^m(\tau:\mu,\mu_0)}\right]} \qquad (8.38)$$

taking

$$\frac{S_4^m(\tau;\mu,\mu_0)}{S_2^m(\tau;\mu,\mu_0)}$$

as the geometric ratio and equation (8.37) by a similar process reduces to:

$$\sum_{n=1,3,5\ldots}^{\infty} S_n^m(\tau;\mu,\mu_0) \equiv S_1^m(\tau;\mu,\mu_0) + S_3^m(\tau;\mu,\mu_0)$$

$$+ \frac{S_3^m(\tau;\mu,\mu_0)}{\left[1 + \frac{S_5^m(\tau;\mu,\mu_0)}{S_3^m(\tau;\mu,\mu_0)}\right]}$$

taking

$$\frac{S_5(\tau;\mu,\mu_0)}{S_3^m(\tau;\mu,\mu_0)}$$

as the geometric ratio.

Subroutines "TERM34" and "TERM6" manipulate the results of "TERM1" and "TERM2" and multiply selected elements by the appropriate gaussian weights and abscissae. Due to the similarity of terms 3, 4 and 5 in the transmission coefficient and of terms 2, 3 and 4 in the reflection coefficient, the higher order terms can be evaluated in the same subroutines. Utilizing the same array several times and continually updating the elements has led to a more efficient use of workspace and this contributed to a faster execution time. Performing the initial layer calculation in "ILAYER" is simple, though caution needs to be exercised when adding the various fourier components of the terms. This subroutine also takes into account the turbidity of the medium to calculate the extinction of the direct components. The results of the first double layer are passed into the datafile "MSDUMP" for further processing.

8.3.5 To check the results of the program

The biggest single problem with a program of this size and complexity is how to check the results effectively and to prove that the program subroutines are performing correctly. This is an essential step if the program is to be used to compare its own results with experimental data. The first test is to plot out the first terms of the transmission and reflection coefficients for the first single layer. They should, of course, be equivalent to the single scattering phase function as computed by "TSCAT", in form at least. Program "MS/PHASEPLOT" combines the transmission and reflection terms for the initial layer to form a single polar plot from $\theta=0 \rightarrow 180^0$. Only the first term is used and so here is a direct means of comparing the single scattering phase function to the simulated phase function given by the first terms. Figure 8.10 shows a block diagram of how the plotting routines function. Two different particle distributions were tried of the form described in Section (7.3.4.3). Both distributions had the values of their constants chosen to approximate as closely as possible to a monodispersal, though for the purpose of comparison, this was not essential. One of the distributions was a standard atmospheric haze type of aerosol, the exact form being known as the "Haze-H" distribution well documented by Deirmendjian (20) and McCartney (64). The second distribution is a model wet steam particle distribution based upon a simulated

GAMMA DISTRIBUTION PARAMETERS	DISTRIBUTION TYPE	
	MODEL WET STEAM	HAZE-M
N	$10^{14}{}_m{}^{-3}$	$10^{11}{}_m{}^{-3}$
rp	0.14μm	0.05μm
a	1.18×10^{73}	5.3×10^{4}
α_d	57.6	1
b	12707.0	8.94
γ	3	0.5

Table 8.1 WET STEAM MODEL/HAZE-M DISTRIBUTION PARAMETERS

2.8	6.5	10.2	13.9	17.6	21.3
25.0	28.7	32.4	36.1	39.9	43.6
47.3	51.0	54.7	58.4	62.1	65.8
69.5	73.2	77.0	80.7	84.4	88.1

Table 8.2 ANGLES AVAILABLE IN 48-STEP GAUSSIAN INTEGRATION

5.6	12.9	20.2	27.5	34.9	42.2
49.6	56.9	64.2	71.6	78.9	86.3

Table 8.3 ANGLES AVAILABLE IN 24-STEP GAUSSIAN INTEGRATION

monodispersal of water droplets of 1μm in diameter. The essential parameters of these two test distributions are shown in Table 8.1. Figures 8.11 and 8.12 show the single scattering phase functions for the Haze model and wet steam model respectively. A slight displacement of about 10% is imposed upon the predicted single scattering phase function (as derived from the first terms of the transmission and reflection coefficients) to facilitate a comparison. Both these polar plots show that the multiple scattering programs "MS/LOOKUP" and "MS/TRANSM" are capable of reproducing the single phase scattering function. This not only implies that the curve fitting routines are behaving correctly but that the generation of the ordinary and associated legendre polynomials and their combination with the weighting functions are accurate. Thus equation (8.25) and (8.26) have been computed accurately.

The second test concerns the evaluation of the tranmission and reflection terms for the initial double layer. With such a small optical depth of the initial layer ($2\tau_o \sim 2^{-24}$), little diffuse scattering of the incident light can be expected and hence the coefficients should be negligibly small. This implies that the extinction of the incident beam is negligible, which, for this optical depth is going to be the case and figures 8.13 and 8.14 illustrate this. The form of the plots is still representative of the single scattering phase function. The angle convention used throughout the calculations in "MS/TRANSM" is shown in

figure 8.15.

If the angle of incidence of the direct beam is changed in accordance with figure 8.15, then the peak of the diffuse intensity distribution should shift by an equal amount. Figures 8.16 and 8.17 show the transmission coefficient for the first layer shifted by an angle of 32.4 and 62.1 degrees respectively. As can be seen the program satisfies this condition. Table 8.2 shows the total possible discrete angles that can be computed by the suite of multiple scattering programs for a 48-step gaussian integration. Table 8.3 shows the same for a 24-step integration routine showing the greater difference between the individual angles which leads to a lower resolution of the programs and ultimately to a less accurate result. As a matter of interest here, the comparisons of figure 8.12 are repeated but for a 24-step and 12-step gaussian rule in figures 8.18 and 8.19 respectively. Although the form of the distributions is still in agreement, the function does not vary as much and the resolution is greatly reduced.

The third test refers to the proportion of directly and diffusely transmitted light passing through the turbid medium. As the optical depth of the medium increases, the proportion of the incident light diffusely transmitted (and reflected) by multiple scattering increases but the directly transmitted (i.e. unscattered) light will be increasingly extinguished in accordance with equation (7.7). Consequently, as the number of doublings increases, the

effect of the diffuse components of the scattered light is to smooth out any rapidly varying polar intensities in the phase function. As has already been explained the effect of multiple scattering can be thought of as a cumulative overlapping of the peaks of the single scattering phase functions of each individual scattering particle. It is for precisely this reason that angular scattering measurements of light passing through a particulate medium are inaccurate when multiple scattering is taking place within the medium. Some of the very prominent features may, however, still be preserved particularly for smaller optical depths.

Figures 8.20 and 8.21 show the transmission and reflection coefficient developing after 10 doublings of the initial layer. Whilst the form of the distribution still resembles that of the single scattering phase function, it is increasing in magnitude. Some smoothing is taking place in figures 8.22 and 8.23 after 20 doublings where here the only remaining prominent feature in the transmission coefficient is the highly developed forward lobe which can be expected, since the mean particle radius for the model wet steam distribution is equal to the wavelength of the incident light. The scattering particle distribution used to compute figures (8.16 - 8.25) is that of the wet steam Gamma distribution whose parameters are shown in Table 8.1.

The fourth and final test is concerned with what happens when the number of doublings becomes very large. Theory (51) suggests that at very large optical depths

($\tau >> 1$), the proportion of diffusely reflected light from a turbid medium rapidly reaches the level of diffusely transmitted light through the same medium. In this instance the direct incident beam is completely extinguished. More formally as the number of doublings increases and τ becomes very large, then:

$$S(\tau;\ \mu,\phi;\ \mu_o,\phi_o) \simeq T(\tau;\ \mu,\phi;\ \mu_o,\phi_o) \simeq 0.5$$

Due to some of the large exponential terms in the transmission equations, this condition cannot be simulated because of exponent overflow within these routines as the programs are being executed. But figures 8.24 and 8.25 show respectively that for 30 initial layer doublings, the intensity distributions of the transmission and reflection coefficients are not significantly different from those of figures 8.22 and 8.23 which have been plotted for 20 initial layer doublings. The rate of increase in magnitude of the transmission coefficient is dramatically reduced with increasing optical depth, as prediced by the theory (51).

In conclusion, therefore, the results of these tests show that for the optical depths considered in this work, at least, the suite of multiple scattering programs are performing satisfactorily. A complete assessment of the performance of these programs together with a more exhaustive testing procedure has been described in (39).

8.4 To estimate the SNR for a two phase medium

8.4.1 Derivation of the general signal-to-noise formula

8.4.1.1 Noise mechanisms in photomultipliers

At lower light levels and wider bandwidths, the photomultiplier becomes superior as a light detector for LDA work. This is due to its inherently high sensitivity as compared with a photodiode, and its high gain. When deriving a general relationship for the signal-to-noise ratio (SNR) at the output of a photomultiplier it is highly desirable to consider the noise mechanisms which exist in the tube and account must be taken of these. Any random fluctuations observed in the photomultiplier output are usually due to two dominant noise mechanisms. These are the cathode shot noise and the dynode shot noise.

Cathode shot noise is dependent upon the bandwidth of the tube and its rms value is given by (91).

$$(i_{N1}^2) = G^2 2e(i_c+i_d)\,\Delta f \qquad (8.39)$$

where i_c is the average current emitted by the photocathode due to the signal power incident upon it and i_d is the dark current of the tube. This current is due to the random thermal excitation of electrons from the surface of the photocathode as well as excitation by cosmic rays and radioactive bombardment. It typically constitutes a background count of ~100's per second.

Dynode shot noise, on the other hand, is due entirely to the random nature of the secondary emission process at

the dynodes of the tube. A photomultiplier tube contains a chain of dynodes, each dynode maintained at a potential slightly higher than the previous one. The dynode chain provides the progressive amplification of electrons that are emitted from the photocathode and previous dynodes by secondary emission. The magnitude of this noise relative to the cathode shot noise is small and can be neglected.

8.4.1.2 The basic SNR relationship

This relationship, although general in nature, will be adapted for use in an LDA application.

The heterodyne current in a photomultiplier tube is given by (8):

$$i = i_1 + i_2 + 2\varepsilon\sqrt{i_1 . i_2}\ \cos \nu_D t \qquad (8.40)$$

where i_1 and i_2 are the currents produced by the two beams alone,

ν_D is the doppler frequency to be detected and,

ε^2 is the heterodyning efficiency and takes into account any degradation of the a.c. term due to misalignment of the beams or distortion suffered through the transmission optics. $0 \leqslant \varepsilon^2 \leqslant 1$.

The individual currents in equation (8.40) are related to each of the incident beams by the following:

$$i_1 = \frac{P_1 . \eta e}{h\nu} \quad \text{and} \quad i_2 = \frac{P_2 . \eta e}{h\nu} \qquad (8.41)$$

The cathode shot noise is given by equation (8.39) as

$$(i_{N1}^2) = 2G^2e\,(i_c + i_d)\,\Delta f$$

$$= 2G^2e\left(\frac{P_1.\eta e}{h\nu} + \frac{P_2.\eta e}{h\nu} + i_d\right)\Delta f$$

Now Johnson Noise is given by

$$(i_{N2}^2) = 4kT\Delta f/R_L \tag{8.42}$$

The mean square value of the signal current is given by

$$(\overline{i_s^2}) = \frac{1}{2\pi}\int_0^{2\pi}\left\{2\varepsilon^2 \cdot P_1P_2 \cdot \frac{G^2\eta^2\lambda^2e^2}{h^2c^2} \cdot \cos^2\nu_D t\right\} d\nu_D t \tag{8.43}$$

$$(\overline{i_s^2}) = 2\varepsilon^2P_1P_2 \cdot G^2\left[\frac{\eta^2e^2\lambda^2}{h^2c^2}\right] \tag{8.44}$$

The SNR is therefore given by:

$$SNR = \frac{(\overline{i_s}^2)}{(\overline{i_{N1}}^2) + (\overline{i_{N2}}^2)}$$

which on substitution for the individual terms becomes:

$$SNR = \frac{2\varepsilon^2P_1P_2G^2 \cdot \left[\frac{\eta e\lambda}{hc}\right]^2}{2G^2e(P_1+P_2+i_D\frac{hc}{\eta e\lambda})\ hc \cdot \Delta f + 4KT\Delta f/R_L}$$

$$SNR = \frac{2P_1P_2\left[\frac{\eta e\lambda}{hc}\right]\varepsilon^2}{2(P_1+P_2+i_D\cdot\frac{hc}{\eta e\lambda})\,\Delta f + \frac{4KT\Delta f/R_L}{G^2\left[\frac{\eta e\lambda}{hc}\right]}} \tag{8.45}$$

High photomultiplier gain, G, reduces the importance of the Johnson noise from the input circuit following the anode of the tube. The power SNR will increase linearly with laser power and depends upon the quantum efficiency when the dark current and Johnson noise are negligible.

Two modes of LDA are commonly used. For the reference beam mode, if P_1 is identified with the scattered light power and P_2 with the reference beam power, then the SNR can be increased by increasing the reference beam power. In the limit, however, $P_2 >> P_1$ and so equation (8.45) reduces to:

$$(SNR)_{power} = \frac{\eta \epsilon^2}{h\nu \Delta f} \cdot P_1 \qquad (8.46)$$

In practice, there exists an upper limit to the average photomultiplier current and this should not be exceeded. This limit will in any case be reached before the limit given above.

In the differential mode, let P_1 and P_2 be the light power scattered by each of two incident light beams. Usually $P_1=P_2=P_s$, the total scattered light power and so equation (8.45) reduces to:

$$SNR = \frac{\frac{2\eta\epsilon^2\lambda}{hc} \cdot P_s}{2\Delta f\left(2+\frac{hc}{\eta e\lambda}\cdot(i_D/P_s)\right) + \frac{4hcKT\cdot\Delta f}{G^2 e^2 \lambda \eta R_L \cdot P_s}} \qquad (8.47)$$

By increasing the tube gain, G, the Johnson noise term becomes insignificant. With sufficiently low dark current, then the above can be written as:

$$(SNR)_{power} \approx \frac{\eta \epsilon^2}{2h\nu . \Delta f} . P_s \qquad (8.48)$$

Using a high gain photomultiplier with negligible dark current the maximum SNR that is possible for the differential mode is half that obtainable in the reference beam mode.

The SNR of the detector current is very important for the operation of the signal processing electronics. It determines the velocity resolving power and upper frequency limit of the system. A low SNR may be improved by reducing the bandwidth of the electronics through successive filtering. The disadvantages of this are that the upper limit of the frequency fluctuation is reduced and this automatically restricts the range of velocity fluctuation that can be measured.

8.4.2 Adaptation of the scattering geometry for the experimental rig.

The transmission and reflection coefficients for a

given optical depth have been computed and the results displayed in accordance with the scattering geometry of figure 7.3.

The multiple scattering program "MS/TRANSM" computes the diffusely scattered intensity in the following form:

$I(\mu,\phi:\mu_o,\phi_o)$ where for convenience $\mu_o=\cos\theta_o$, $\mu=\cos\theta$. While retaining the essential features of this geometry it is necessary to re-define it for the purposes of a general two beam LDA configuration. In this context it is proposed that the modified geometry of figure 8.26 be adopted. For two laser beams whose bisector is perpendicular to the direction of the flow the beam angles may be defined as:

$$\mu_1 = \cos [45 - \alpha/2] \qquad (8.49)$$

$$\mu_2 = \cos [45 + \alpha/2] \qquad (8.50)$$

The geometry may be made more general by including the option of tilting the bisector of the two beams at γ to the perpendicular, whence :

$$\mu_1 = \cos [45 - \alpha/2 + \gamma]$$

$$\mu_2 = \cos [45 + \alpha/2 + \gamma] \qquad (8.51)$$

A sign convention for γ is required for accurate computation. γ is defined as negative if the value of γ moves μ_1 or μ_2 nearer towards $\mu = 1$. Conversely γ is positive if its value moves μ_1 or μ_2 towards $\mu = 0$.

On inspection of the modified geometry of figure 8.26, it will be seen that only the transmission coefficients

computed by the program are of any direct use. They occupy the first and third quadrants of figure 7.3 and as such coincide with the incident and emergent laser beams according to figure 8.26. In practice this is of little consequence since the reflection coefficient is not relevant for detection in forward scatter LDA systems. If detection in backscatter was a requirement in this work the computational geometry would have to be further modified to suit, though this would not be trivial. As discussed earlier the values of μ are discrete, their values being determined by the number of steps chosen in the gaussian numerical integration routines. However, the azimuth dependence of equation (8.26) is continuous. This may be represented in the complete LDA geometry of figure 8.27. The ϕ dependence of the two scattered intensities is shown. All angles for the arrangement are measured from the z ordinate.

Each light beam incident upon the medium scatters light from each particle independently given by

$$I_1 (\mu_1', \phi_1' : \mu_{o1}, \phi_{o1})$$

and

$$I_2 (\mu_2', \phi_2' : \mu_{o2}, \phi_{o2}) \qquad (8.52)$$

Which proportion of the scattered light is detected will depend upon the physical geometry and position of the detector optics.

The detection optics may be included in the geometry

in the manner given in figure 8.28. When these geometries are analysed by the computer program the detector aperture may be centred on any of the discrete values of μ set by the number of gaussian steps for the integration routines. In practice the user will be able to position the detector anywhere over a spherical surface within the boundaries of the third quadrant of figure 8.26. The program will then determine the nearest value of μ that is available provided that a large (at least 48 in practice) number of gaussian steps are chosen, and the actual error involved will be small.

8.4.3 Derivation of the practical formulae for the SNR in an LDA system.

In section 8.4.1 an expression was derived for the SNR of a detection system employing a photomultiplier tube. It was based principally upon a quantity of signal power from each incident laser beam and the total available light power arriving at the tube surface. It does not, however, include any parameters related to the actual physical geometry such as in figure 8.28. In this sense equation (8.48) is an ideal relationship. It is the purpose of this section to include those parameters necessary to make the formula of some practical use in this LDA application.

The ideal SNR for a detection system is given by:

$$(SNR)_{power} = \frac{\lambda \eta \varepsilon^2 Psig^2}{2hc\, P_T \,.\, \Delta f} \qquad (8.53)$$

Immediately this equation can be related to a practical situation if Psig is considered to be Psig (μ, ϕ) and P_T given by P_T (μ, ϕ). These power levels would have to be integrated over a solid angle defined by the physical geometry of the detector optics. Further P_T (μ, ϕ) is the total scattered light arriving at the photodetector aperture and may thus be written as:

$$P_T(\mu,\phi) = Psig(\mu,\phi) + P_{diffuse}(\mu,\phi) \qquad (8.54)$$

The program "TSCAT" is capable of computing the necessary components to yield $Psig(\mu,\phi)$ and "MS/TRANSM" will produce information to calculate the distribution of diffusely scattered light power.

The phase function computed by "TSCAT" has been normalised according to Deirmendjian (20) where:

$$\frac{2(i_1(\Theta) + i_2(\Theta))}{k^2 \circ rp^2 \circ Q_{scat}} = \frac{1}{2}(P_1(\Theta) + P_2(\Theta)) \qquad (8.55)$$

whence using the square law dependence of radiation propagating over a distance R gives:

$$I_s(\Theta,\phi) = \frac{1}{4} \circ k^2 \circ rp^2 \circ Q_{scat} \circ (P_1(\Theta) + P_2(\Theta)) \circ I_o \qquad (8.56)$$

for a monodispersal illuminated by white light. For Argon-ion laser light, equation (8.55) reduces to:

$$I_s(\Theta,\phi) = \frac{1}{4} \cdot k^2 \cdot rp^2 \cdot Q_{scat} \cdot P_1(\Theta) \cdot I_o \qquad (8.57)$$

According to the detector geometry of figure 8.27, the proportion of scattered light reaching the detector aperture is given by:

$$I_s(\Theta,\phi) = \int_{\Omega_D} \frac{1}{4} \cdot k^2 \cdot rp^2 \cdot Q_{scat} \cdot P_1(\Theta) \cdot I_o \cdot d\Omega_D \qquad (8.58)$$

where $d\Omega_D = \sin \theta_D d\theta_D d\phi_D$, the incremental solid angle element.

However, since both programs "TSCAT" and "MS/TRANSM" yield a discrete distribution for the direct and diffusely scattered light, the more practical form of equation (8.58) would be:

$$P_{sig}(\Theta,\phi) = \frac{\Omega_D}{4\pi} \cdot \frac{A}{4} \cdot k^2 \cdot rp^2 \cdot Q_{scat} \cdot \sum_{i=1}^{n_p} P_{1i}(\Theta_i) \cdot I_o \qquad (8.59)$$

where n_p is the number of intensity points lying within the solid angle of detection defined by the position and size of the detector aperture.

Including the turbidity term, representing the turbidity of the medium over a distance to the measuring volume, τ_1, and from the measuring volume to the detector,

τ_2, gives:

$$P_{sig}(\Theta,\phi) = \frac{\Omega_D}{4}\circ\frac{A}{4}\circ K\circ rp^2\circ Q_{scat}\circ\sum_{i=1}^{n_p} P_{1i}(\Theta_i)\circ I_o\circ e^{-(\tau_1+\tau_2)} \quad (8.60)$$

The expression is valid for the directly scattered light given by the Mie formulae. For the diffusely transmitted light, the summation term need only be replaced by an equivalent summation of the discrete transmission coefficient terms. The expression in equation (8.53) for the SNR of the medium may then be written as:

$$SNR = \frac{\eta\mathcal{E}^2}{2hc\Delta f}\circ\frac{\Omega_D}{4\pi}\circ A\circ\frac{P'^2_{sig}}{P_T'} \quad (8.61)$$

where

$$P'^2_{sig} = \frac{1}{4}\circ k^2 rp^2\circ A\circ Q_{scat}\circ\sum_{i=1}^{np}\circ P_1(\Theta_i)\circ I_o\circ e^{-(\tau_1+\tau_2)} \quad (8.62)$$

and

$$P_T' = P'_{sig} + A\circ\sum_{i=1}^{np}\circ T_i(\tau_1+\tau_2;\mu_i,\phi_i;\mu_o,\phi_o)\circ I_{AV} \quad (8.63)$$

Equation (8.61) is the final form of the expression and is the practical formula used in the next section.

8.4.4 Computation of the SNR and results.

The process of calculating the SNR is shown in the flow diagram of figure 8.29. Essentially once the required geometrical data has been requested and entered the program proceeds to calculate two intensity distributions. One of

these distributions is the signal strength in any given direction as computed by "TSCAT". The other is the diffusely transmitted distribution of laser light. These two distributions can be combined in the way suggested by equation 8.63.

The intensity distribution given by "TSCAT" has 96 discrete intensity points between 0^0 and 180^0. The corresponding number in "MS/TRANSM" depends uon the gaussian steps chosen for the numerical intergration routines but typically is 48. The position of the detector optics defines a solid angle of detection as shown in figure 8.30. All of the scattered light which is scattered into that cone should, in theory, be integrated to give the total intensity of light incident upon the detector surface.

This would certainly be true if the intensity distributions were continuous. For simplicity and reasonable accuracy the discrete intensity points in each distribution that lie within the detector cone of collection were added. The azimuth, ϕ_o, term is continuous and the dependence is integrated in the usual gaussian numerical integration routine. It must be emphasized that this technique is only intended to provide an estimate of the SNR of the medium. In particular it is useful to provide some indication of whether a good signal is available from a given turbid medium. Figure 8.31 gives an example of the sort of distribution for the SNR that is given by the program. Arbitrary conditions have been chosen but in

Chapter 9 an attempt has been made to simulate actual steam conditions and to compare the predicted SNR with the general ability to obtain signals from the steam with a counter based LDA system.

9. RESULTS AND DISCUSSION

9.1 The form of the results

This research was concerned chiefly with the assessment of the viability of the laser Doppler technique for making velocity measurements in a wet steam flow using the water droplets naturally present in the flow as seeding particles. A turbid medium such as wet steam presents a number of complications to an instrumentation technique such as laser Doppler anemometry which are inherent characteristics and which each warrant an investigation. What began as a piece of research dedicated to the potential use of LDA in wet steam very quickly broadened into an experimental program concerned with the fundamental process of light scattering. For example, the manner in which a laser beam propagates through the wet steam and the effect of single and multiple scattering events upon its strength led to the development of a computer program which would predict the polar distribution of diffusely transmitted light due to scattering in any particulate medium. This work in itself was a significant part of the overall development of the LDA technique and this forms a large proportion of the results. The results of this research then are not only concerned with the use of LDA in wet steam but also a fundamental approach to the study of the non-trivial light scattering processes involved. Comparisons are made between experimental quantities and those values predicted by several computer simulation programs developed as part of

this research.

It is for these reasons that this Chapter will be split into three main sections, each section covering completely that particular subject of experimentation. The previous Chapters have been concerned with the design and development of the experimental facility. This Chapter will present and discuss all the results that were obtained during this research using the experimental facility.

The results obtained can be grouped into three main subject areas. The first is concerned with the determination of the number concentration and size of the nucleated water droplets in the wet steam flow. This information is vital if the full investigation of the light scattering processes is to be undertaken. The extinction method described in Chapter 2 was used in conjunction with the steam wetness to calculate the mean droplet size. It should be emphasized here that only the droplet size that has produced the bulk extinction could be estimated. Other sizes of water droplets clearly present in the steam flow could not be sized by this method. The values for the number concentration and mean size of the water droplets providing the bulk extinction, which were estimated from a knowledge of the steam wetness, were checked with some predicted values. Despite the fact that the wetness of the steam itself was subject to a degree of uncertainty, it will be shown that there was a close agreement between these two results.

In Chapter 8 a method was evolved which could determine the transmission and reflection coefficients for the diffusely transmitted and reflected components of the incident light due to scattering through a turbid medium. As will now be appreciated, the optical depth of a particulate medium is an indication of the nature of the light scattering process involved. As the optical depth increases, the likelihood of multiple scattering becomes greater and for an extinction coefficient of above about 0.3, it is widely accepted (50) that the effects of multiple scattering are dominant. During the experimental work it had been assumed that the bulk extinction of light propagating through a turbid medium is independent of the effects of any multiple scattering. The limitations of this assumption will be discussed.

The values of N and rp, from the extinction measurements, have been used to calculate the parameters of a Gamma type size distribution of the form used for atmospheric clouds. An equivalent Gamma distribution has been produced for each discrete condition of wet steam generated. The function parameters in each case were then used as input to compute the scattering phase function. This function was processed by the multiple scattering simulation programs to yield a polar intensity distribution for the diffusely transmitted light generated by any given turbid medium.

The second section of results is therefore concerned with the generation of these polar plots for different wet steam conditions. A technique was developed to make measurements of the intensity of the diffuse light using a photomultiplier tube and a comparison made between the predicted and measured results. The method of predicting this distribution for the scattering and detection geometry existing in the measuring section will be described in detail. A very good agreement was obtained with this method and the computer simulation generally performed well. There were, however, some severe limitations which will be discussed. The third and final set of results are intended to completely define the suitability of LDA in wet steam. Some good results were obtained but more importantly, the potential to make velocity measurements in the wet steam was evident from the results. Consequently the discussion of results in this section is directed towards the acceptance of this technique and a recommendation for further development.

It should be emphasized also that it is the viability of the LDA technique that was under investigation in this research rather than the implications of the individual measurements themselves. The LDA measurements were confined to the determination of the velocity profile across the measuring section at a pre-selected number of measuring stations. Nevertheless a simple pipe flow analysis was carried out in order to confirm the validity of the

individual values of mean velocity over the profile. This proved to be quite satisfactory and constituted a theoretical fit of a developing turbulent velocity profile over a range of Reynolds numbers. A velocity profile was obtained for each wet steam condition.

Throughout the discussions, particular emphasis will be placed upon the reasons why the anemometer developed in this work was quite successful for the flow of wet steam produced by the experimental facility. The wet steam conditions prevailing in the measuring section were rather different from those that exist in a wet steam turbine. Bulk extinction was provided by nucleated water droplets of about 0.1μm in radius, the scattering from which was small enough to allow the two laser beams to penetrate the fog even under the wettest conditions generated. Larger droplets were relatively very few in number and it was these droplets that provided the seeding for the instrument. The source of the larger water droplets is thought to be as a consequence of deposition, and tearing off or drooling of quantities of water from the walls and leakage from the turbine bearings. Due to their very small numbers, their effect upon the transmission of the laser beams was therefore small. This observation will be discussed in more detail in the appropriate section.

When measuring the velocity profiles, a point was reached at which no useful signal was obtained from the measuring volume. Despite efforts to optimize the

collection optics, no further improvement in the signal strength was obtained. This situation occured at wetness values of greater than 3%. The computer simulation program developed for the prediction of the diffuse components of the scattered light was adapted to yield an estimate of the SNR obtainable from the medium at the photodetector itself. It will be shown that the station at which measurements became unobtainable corresponded to a significant drop in the predicted SNR.

9.2 Measurements of the light extinction to determine N & rp values.

9.2.1 Outline of the method

When measurements of light extinction are to be made, an appreciation of the manner in which a laser beam is extinquished as it propagates through a turbid medium is essential. As has already been discussed in Chapter 7, it is the particles suspended in an atmosphere that cause the scattering and so as the optical depth through that atmosphere increases, so does the degree of attenuation experienced by the direct beam given by the Lambert-Beer Law expressed in equation (7.1). In this application the water droplets constituting the wet steam dictate the extent to which a laser beam will be extinguished. The number of water droplets present for given thermodynamic conditions is a function of the steam quality, namely the wetness fraction. Therefore any extinction measurements that are performed on a laser beam emerging from a turbid wet steam

volume require a knowledge of the steam quality and the amount by which the laser beam has been attenuated. An expression is now sought which has a practical use in linking the above quantitites, and such a relationship will be presented.

From a geometrical consideration, it has been shown in Chapter 5 that the specific number of water droplets can be related to the steam quality as in equation (5.5). For convenience this equation is repeated here. It has already been shown that:

$$Y = \frac{4}{3} \pi rp^3 \rho_f \cdot N_{kg}$$

and so

$$Y = \frac{4}{3} \pi rp.^3 \frac{\rho_f}{\rho_s} \cdot N \qquad (9.1)$$

since $\nu_s'' \approx X\nu_g''$ (9.2)

and

$$\rho_s = \frac{\rho_g}{(1-Y)} \qquad (9.3)$$

rearranging equation (9.1) gives:

$$N = \frac{3}{4} \cdot Y \cdot \frac{\rho_s}{\rho_f} \cdot \frac{1}{\pi rp^3} \qquad (9.4)$$

The Lambert-Beer Law expresses the amount by which a light beam is attenuated by a particulate medium and is given by

$$\frac{I}{I_o} = \exp\left[-N \cdot Q_{scat} \cdot \pi rp^2 . \ell\right] \qquad (9.5)$$

On substituting for N in equation (9.5) from equation (9.4) gives the following:

$$\frac{I}{I_o} = \exp\left[-\left(\frac{3}{4} \cdot \frac{Q_{scat}}{rp} \cdot \frac{\rho_s}{\rho_f} \cdot Y \cdot \ell\right)\right]$$

or

$$\frac{I}{I_o} = \exp\left[-\left(\frac{3}{2} \cdot \frac{Q_{scat}}{dp} \cdot \frac{\rho_s}{\rho_f} \cdot Y \cdot \ell\right)\right] \qquad (9.6)$$

This may also be written as:

$$\frac{I}{I_o} = \exp\left[-\frac{3\ell}{2} \cdot \frac{Q_{scat}}{dp} \cdot \frac{\rho}{\rho_f} \cdot \frac{Y}{1-Y}\right] \qquad (9.7)$$

which agrees with the expression quoted in (71).

A second useful relationship is obtained if equation (9.5) is rearranged to give:

$$Nrp^2 = \frac{-\log(I/I_o)}{Q_{scat} \cdot \pi \cdot \ell} \qquad (9.8)$$

It will now be shown how equations (9.7) and (9.8) can be used to make an estimate of N and rp.

A technique for measuring the strength of the laser beam both on entering the steam rig and on emerging was simply to use a good quality power meter. The power meter used here was a Spectra-Physics 404 capable of measuring direct laser beam powers of up to 5W over a range of wavelengths of 0.45-0.9μm. It was particularly sensitive to green (514 nm) light. The detector head of the meter was clamped firmly in a specially adapted grip and mounted on a sturdy tripod. The laser and optical system were adjusted

until the intersection of the two beams was approximately incident on the centre of the window. The beamsplitter cube was removed from the beamsplitter assembly and the three beam conditioning lenses L1, L2 and L3 removed from the bench. The detector head was positioned on the emergent side of the measuring section as shown in figure 9.1. The figure shows the layout of the optics and detector head in relation to the steam rig. With the laser set to deliver 400mW, the position of the head could now be adjusted by means of the clamp until the meter registered as close to 400mW as possible. No steam was flowing through the measuring section at this stage. With the laser on and warmed up (hence power output remained steady throughout the taking of readings), and the detector head of the power meter firmly locked in position, the rig was ready for the steam.

For the range of turbine speeds that had been set for the wet steam calibration, the power meter reading was taken. As expected the reading dropped dramatically as the turbine speed (and hence wetness) increased above 1500rps. Since power is proportional to the intensity equation (9.6) may be written as:

$$\frac{P_m}{P_{mo}} = \exp\left[-\frac{3}{2} \cdot \frac{Q_{scat}}{d} \cdot \frac{\rho_s}{\rho_f} \cdot Y \cdot \ell\right] \qquad (9.9)$$

9.2.2 Results of the extinction measurement

The variation of P_m/P_{mo}, expressed as a percentage, with turbine speed is shown in figure 9.2. The readings were

repeated three times and averaged. It was important that the readings taken were reliable and this was judged by their repeatability. In any case the individual readings for each particular condition never differed by more than 5%. In figure 9.2 bands have been superimposed upon the characteristic to indicate the observable state of wetness in the measuring section. As would be expected for the densest fog at 4.7%, the transmission was very low and was less than 1%.

Equations (9.7) and (9.8) contain three unknown variables, namely N, rp and Q_{scat}. They can not be solved directly. Since Q_{scat} is in itself a very complicated function of rp involving the Mie amplitude functions an alternative method was required to solve for N and rp. McCartney (64) has published a comprehensive table of the Mie scattering efficiency for a very wide range of size parameter. It is with the aid of these tables that an iterative solution to obtain N and rp was evolved. For the purpose of illustration these tables have been reproduced in Table 9.1. The basis of this iterative solution is shown in the flow chart of figure 9.3. This flow chart may be used to give an illustrative example of the process, the results of which are shown in Table 9.2.

Turbine Speed = 1700rps

Wetness Fraction = 0.023 as estimated from thermodynamic measurements

Density of steam = 0.557 kgm^{-3}

	Refractive index			Refractive index	
α	1.33	1.50	α	1.33	1.50
0.1	0.000011090	0.000023084	3.0	1.7534	3.4181
0.2	0.00017704	0.00037007	3.1	1.8769	3.4581
0.3	0.00089246	0.0018787	3.2	1.9900	3.5317
0.4	0.0028019	0.0059551	3.3	2.0909	3.6733
0.5	0.0067731	0.014567	3.4	2.1833	3.8788
0.6	0.013847	0.030183	3.5	2.2747	4.0785
0.7	0.025151	0.055609	3.6	2.3726	4.1849
0.8	0.041764	0.093635	3.7	2.4811	4.1842
0.9	0.064544	0.14648	3.8	2.5979	4.1264
1.0	0.093924	0.21510	3.9	2.7142	4.0671
1.1	0.12977	0.29869	4.0	2.8197	4.0525
1.2	0.17138	0.39496	4.1	2.9089	4.1187
1.3	0.21771	0.50159	4.2	2.9845	4.2555
1.4	0.26786	0.61897	4.3	3.0545	4.3593
1.5	0.32171	0.75282	4.4	3.1283	4.3326
1.6	0.38045	0.91435	4.5	3.2125	4.2025
1.7	0.44654	1.1142	4.6	3.3070	4.0413
1.8	0.52306	1.3489	4.7	3.4034	3.8997
1.9	0.61213	1.5901	4.8	3.4878	3.8191
2.0	0.71295	1.7984	4.9	3.5502	3.8381
2.1	0.82096	1.9553	5.0	3.5910	3.9278
2.2	0.92912	2.0753	5.1	3.6200	3.9325
2.3	1.0312	2.1916	5.2	3.6505	3.7832
2.4	1.1252	2.3383	5.3	3.6935	3.5683
2.5	1.2135	2.5395	5.4	3.7535	3.3567
2.6	1.3023	2.7924	5.5	3.8238	3.1816
2.7	1.3985	3.0512	5.6	3.8868	3.0835
2.8	1.5068	3.2510	5.7	3.9241	3.1101
2.9	1.6270	3.3648	5.8	3.9295	3.1905

Table 9.1 THE MIE SCATTERING EFFICIENCY FOR A RANGE OF α (McCartney(64))

ATTEMPT NO.	Q_{SCAT}	rp	$\alpha = \frac{2\pi rp}{\lambda}$	REQUIRED VALUE OF FROM TABLES FOR Q_{SCAT} (74)
1	0.17138	0.07 μm	0.89	1.2 (Not acceptable)
2	0.21771	0.192 μm	1.13	1.3 (Not acceptable)
3	0.26786	0.114 μm	1.39	1.14 (Acceptable)
TURBINE SPEED = 1700 rps WETNESS FRACTION = 0.023 DENSITY OF STEAM = 0.557 kgm^{-3}				

Table 9.2 ITERATIVE PROCEDURE FOR CALCULATING N AND rp

$$I/I_o = 0.0107 = Pm/Pmo$$

and hence in equation (9.9) this gives

$$rp = 0.43 \cdot Q_{scat} \cdot \mu m \qquad (9.10)$$

No more than three attempts were ever required to reach a satisfactory solution using this technique.

Now in equation (9.8)

$$N\,rp^2 = \frac{-\log (0.0107)}{0.26786 . \pi . 0.557} = 9.68$$

$$N = 8 \times 10^{14}\ m^{-3} \text{ for } rp = 0.11\mu m \qquad (9.11)$$

Table 9.3 lists all the values of N and rp estimated in this way, for the range of running conditions.

Due to the way in which values of Q_{scat} have been tabulated for different α, the value of α(rp) may not exactly correspond to that listed. But this would have had little effect upon the results of the simulation programs.

The estimation of N and rp relied upon the knowledge of the steam wetness, which was known to within 10%. In Chapter 5 a characteristic was produced which showed the variation of water droplet concentration in nucleated steam with mean droplet radius for a range of pressures and a given wetness fraction. This characteristic was essentially plotted by means of equation (9.1).

It can be shown from equation (9.1) that there are at least two sets of values of N and r_p that can be obtained by this method although only one is shown in figure 9.4. In Appendix C, the uniqueness of this solution has been defined and the result of figures 9.12(c),(d) - figures 9.15(c),(d) do in fact show that the values of N and r_p are

TURBINE SPEED (rps)	ESTIMATED WETNESS FRACTION	Q_{SCAT}	$N(m^{-3})$	rp(μm)	$\alpha(rp)$	P_M/P_{MO}
1500	$0.01 \pm 10\%$	1.0312	7.36×10^{13}	0.187	2.28	0.0146
1600	$0.019 \pm 10\%$	0.38065	4.36×10^{14}	0.135	1.65	0.0140
1700*	$0.023 \pm 10\%$	0.26786	8×10^{14}	0.11	1.39	0.0107
1800	$0.030 \pm 10\%$	0.2286	1.035×10^{15}	0.11	1.39	0.0079
1850	$0.04 \pm 10\%$	0.2286	2.0×10^{15}	0.11	1.39	0.004
1900	$0.047 \pm 10\%$	0.13786	3.088×10^{15}	0.09	1.1	0.00195

*Worked example - see Table 9.2

Table 9.3 CALCULATION OF THE SCATTERING PROPERTIES OF THE WET STEAM FOR A GIVEN EXTINCTION

correct. This is because if another solution had been used, the polar extinction plots produced by "MS/TRANSM" would have been more peaked for larger r_p .

9.2.3 Discussion of the results

The last section has shown that direct light extinction measurements of a laser beam propagating directly through a wet steam atmosphere are a valid method of predicting the number concentration and mean radius of the water droplets providing the bulk extinction of the beam. It is important to emphasize the term "bulk extinction" here because it was impossible to discriminate between different sizes of water droplets using only one wavelength of the light source as explained in Chapter 2. (c.f. (62) with (75)).

One of the main criticisms made by authors recently (81) (82) of original work is that it is not unusual to see that the Lambert-Beer Law of extinction is used without proper justification both for the interpretation of experimental results and the application of transmission data to make estimates of atmospheric parameters. Indeed this criticism can be equally levelled at the method of obtaining the estimates of N and rp in this work. What is meant by the above statement is that very often not enough thought is given to the fundamental use of the law and to its limitations which can be quite severe in some applications. It is intended therefore to explain this

* There are in fact several values of r_p that can be obtained from equation (9.10) in conjunction with figure 7.5. However the experimental results of figure 9.12 (c),(d) - figure 9.15 (c),(d) suggest that the values of r_p chosen were correct.

statement more clearly and to explain why the estimates of N and rp were relatively successful under the experimental conditions. Tam (81) has suggested that corrections to the law should be incorporated to compensate for the effect of single scattering, primarily in the forward direction, and for the effects of multiple scattering. The forwardscatter correction refers to the correction that must be made to the optical extinction measurements carried out in a scattering medium, due to the fact that along with the direct light, some forward scattered light inevitably enters the finite aperture of the detector. The author knows of no light measuring device that can distinquish between the intensity of the direct beam of light and the light scattered in the forward direction. Either the forward scattered contribution is so small that it can be neglected or, it is significant, in which case some compensation is required. It is the effect of single and multiple scattering on the measurement of extinction of laser beams through known fogs that has prompted some very recent research (19). The outcome of this research has been the prediction of a wide range of correction factors that may be universally applied and the error likely to be encountered under given conditionsif no correction factor is used.

The approach adopted by Tam (81) was to develop an additional relationship which took into account the effect on the transmission if a portion of the laser beam undergoes m scatterings. This factor was a modification to the

original Lambert-Bouguer law, viz:

$$\frac{I}{I_o} = e^{-\sigma_{ext} \cdot l} \cdot \left(1 + \sum_{m=1}^{\infty} \frac{\tau^m}{m!} \cdot \frac{1-S(m)}{1-\exp(-\gamma l) dp^2}\right) \qquad (9.13)$$

where the factor S(m) is a term analogous to the transmission coefficient computed in Chapter 8 to describe the portion of the direct laser light which has been diffusely transmitted due to having been scattered m times.

Equation (9.13) does not include the effects of absorption, which are neglected in this work, but they could be included if required. The first term on the right hand side corresponds to the Lambert-Bouguer law, while the terms under the summation sign are the corrections for various orders of scattering. Tam has computed the correction factor C_{fac} for all orders of scattering, given by:

$$C_{fac} = \sum_{m=1}^{\infty} \cdot \frac{\tau^m}{m!} \cdot \frac{1-S(m)}{1-\exp(-\gamma l) dp^2} \qquad (9.14)$$

as well as the single scattering correction factor defined as:

$$C_S = \tau \cdot \frac{1-S(1)}{1-\exp(-\gamma l) dp^2} \qquad (9.15)$$

Figure 9.5 shows the correction factors for laser propagation in fogs with liquid water content of 0.1, 0.5 and 1.0 gm^{-3}. The computations have been carried out for a

laser beam of wavelength 1.06μm. Hence although not directly relevant to this work, the three figures here indicate that the single scattering correction factor remains very nearly constant for all optical depths. However, there is a very rapid departure from this for the correction factor for multiple scattering as would be expected. Some very significant errors can result.

The work of Deepak and Box (17) (18) provides the best evidence for the validity of the extinction measurements made here. These authors have treated the single and multiple scattering corrections as two different problems. The term forwardscattering used in the earlier statement, is considered a single, not multiple, scattering phenomenon in which scattered light reaches the detector after being scattered only once by scatterers situated within the path of direct light. The case of multiple scattering requires additional corrections to the optical extinction measurements. All of the work published on this subject to date confines any treatment to homogeneous spherical aerosols, having uniform size distribution, concentration and composition.

Again Deepak (17) considered the limitations of the Lambert-Bouguer law and concluded that because of the detectors finite field of view, invariably some forwardscattered light enters into the detectors cone of view along with the direct beam. This law, strictly speaking, cannot be used to obtain the true optical depth,

τ, of a turbid medium from extinction measurements. What is really obtained is the apparent optical depth τ' related to the apparent efficiency factor Q_{scat}'. Q_{scat} as defined in Chapter 7, is based upon the total amount of light lost from the laser beam due to scattering by a particle in all directions. Q_{scat}', on the other hand refers to the amount of light lost due to scattering in all directions except within a cone of half-angle θ in the forward direction. From the formal definition of the Mie theory using the notation of Chapter 7, Q_{scat} is defined as follows:

$$Q_{scat} = \frac{1}{\alpha^2} \int_0^{\pi} (i_1 + i_2) \sin\theta \, d\theta \qquad (9.16)$$

The difference between Q_{scat} and Q_{scat}' may then be expressed by the following:

$$Q_{scat} - Q_{scat}' = \frac{1}{\alpha^2} \int_0^{\theta} (i_1 + i_2) \sin\theta' \, d\theta' \qquad (9.17)$$

A correction factor due to forwardscattering may be defined as

$$C_{fac} = \frac{Q'_{ext}}{Q_{ext}} = 1 - E \qquad (9.18)$$

where E, the error factor is

$$E = \frac{1}{\alpha^2 Q_{ext}} \int_0^{\theta} (i_1 + i_2) \sin\theta' \, d\theta' \qquad (9.19)$$

Figure 9.6 shows the variation of the correction factor with size parameter α for different refractive indices of the scattering particles and angle of detection. Only those features relating to a refractive idex of 1.33-j(0.0) are of interest in this application. Water droplets of 0.1μm in radius have a size parameter of 1.22. From figure 9.6, the correction factor required for the Lambert-Bouguer law is very close to unity in all cases. In figure 9.7, the variation of error in the use of the basic form of the transmission law, is also shown plotted against size parameter. For the 0.1μm radius water droplets, an error of no greater than about 4% is likely in the use of the transmission law as a means of estimating the optical depth of a turbid medium from extinction measurements. From this discussion, it is apparent that the transmission law cannot be used except in the case of small particles, for which it is a good approximation only. The effect of not only the particles size and composition, but also the geometry of the optical system, on the apparent volume scattering and extinction coefficients must be considered.

The results published by Deepak and Box (17) for Argon-ion laser beams propagating through atmospheric fogs help to explain why use of the simple uncorrected version of the transmission law is successful in estimating the optical depth of the wet steam. They give some credibility to the technique used and place some confidence upon the estimates of N and rp obtained in this work. Clearly, however, if the

nucleated droplets in the wet steam had grown appreciably in size by the time they had reached the measuring section, to beyond 0.1μm, then use of a correction factor in the extinction measurements would have been essential.

Referring back to the conditions in the measuring section, it was evident from observations in the flowing wet steam and from the nature of the Doppler signals received, that some very large water droplets were flowing through the rig. It was beyond the scope of this research work to make estimates of the size, by measurement, suffice to say that they were certainly of the order of 50μm in diameter a size of which, and greater, could be resolved by the human eye. Due to large number densities of the order of 10^{13} - 10^{15} water dropletsm^{-3} in the wet steam fog, then clearly it was the nucleated water droplets themselves which constituted the bulk extinction.

9.3 Prediction of the polar distribution of diffuse light intensity.

9.3.1 Introduction

The experimental work covered by this section provided the ultimate proving ground for the multiple scattering simulation program developed in Chapter 8. Making precise measurements of the diffusely scattered light from a laser beam enabled a comparison to be made between the experimental values and the predicted polar distribution. The purpose of this section is to describe a method used quite successfully to measure the intensity of the diffusely

scattered light produced by a laser beam propagating through the wet steam. As in section 9.2.2, the procedure was repeated for each of the six known wet steam conditions but in addition, the method has also been applied to the two beams forming an intersection in the measuring section. The multiple scattering program has been used to predict the diffuse light distribution in the forward direction, given by the transmission coefficient. It used the values of N and rp calculated earlier to generate a particle size distribution of the Gamma type as described in Chapter 8. The calculation of the Gamma distribution parameters for each of the known wet steam conditions will be described.

A close prediction of the diffuse light intensity distributions for both one beam and two beams will show that the diffuse light distribution computed for each individual beam at its angle of incidence has been added correctly to produce the combined distribution.

It was important to be able to make consistent measurements of the diffuse light and to be able to model the detection system as closely as possible. Some difficulty was experienced in matching the geometry of the beam passing through the medium, and that of the detection optics, with the angle geometry used in the simulation programs to compute the transmission and reflection coefficients. A technique used to overcome this difficulty will also be presented.

9.3.2 Measurement of the diffuse light intensity

To measure the extinction of the laser beam passing through varying conditions of wet steam, a good quality power meter was used as before. An active device such as a photomultiplier tube would not have been entirely suited to the detection of a laser beam incident directly upon the photocathode surface. The risk of burning a hole in the photocathode itself or passing too much current through the dynodes were too great.

However for detection of very weak or low level light off the axis of propagation of the laser beam, the photomultiplier (PM) tube was superior. Since a PM tube converts light energy into electrical energy at an efficiency of up to about 15%, the only measure of the light intensity is the anode current. Using a microammeter the anode current could be read for a given detector position. The multiple scattering program predicted the transmission coefficient for an incident light beam at a chosen angle of emergent angle. What was required of the experiment was a polar distribution of PM tube current in μA for the same values of emergent angle used by the simulation routines. The geometry shown in figure 9.8 was used for modifying the simulation and it is to this that the detection optics must correspond. Figure 9.9 shows the physical layout of this experiment, the plane of the paper indicating the plane of detection of the scattered light. The inset shows how the detection optics were positioned in

order to link in with the geometry of the scattering process. Since the PM tube averages the scattered light that it receives, it was not absolutely critical that the photocathode surface be located in the exact position. Nevertheless, considerable care was taken to ensure that it was as close as was possible under the experimental conditions. As shown in figure 9.9, polar angles up to 45^0 either side of the line of direct transmission were marked upon an adjacent wall and the detector assembly was positioned as closely in line with these marks as was practicable. The image in the pinhole mount was a line of light, this being the entire length of the laser beam in the turbid atmosphere. The pinhole itself was adjusted so as to be midway along the image at all times. This was really the only way in which focusing upon the same area in the measuring section could be made with reasonable consistency.

The PM tube current was taken at every 5^0 across the measuring section for each of the six wet steam conditions. Provided that the plane of detection could be maintained as shown in figure 9.9, then ϕ, the azimuth angle of detection could be assumed to be 90^0.

9.3.3 Method of predicting the diffuse light intensity using the multiple scattering simulation program

The multiple scattering computer simulation makes use of the single scattering phase function. This section will describe the method of predicting the transmission

coefficient for the diffusely scattered light for the geometry of figure 9.8. It was mentioned in Chapter 7 that the program written to compute the phase function for single scattering could cope with any particle size distribution of scattering particles of any refractive index illuminated by light of any wavelength. The Gamma type size distribution is normally used for atmospheric aerosols where the values of N and rp are considerably different from those in wet steam. Wet steam presents a new dimension to the Gamma parameters as the water droplet number concentrations are so much higher than that of atmospheric scattering particles. The wide range of values for N and rp that the Gamma function has been used for by previous authors (20) is shown in Table 7.2. Also included is the equivalent typical wet steam condition and as can be seen the difference is more than several orders of magnitude. Nevertheless the Gamma distribution coped with all of the wet steam conditions met in this work, albeit only just.

The parameters of the gamma Distribution described in Chapter 7 need to be calculated before executing the simulation program.

The relevant parameters are shown in Table 9.4 and the significance of each will now be explained. The first four columns of Table 9.4 list respectively, the turbine speed, mean particle radius and number concentration as predicted by the extinction measurements and the corresponding scattering efficiency listed in Table 9.1. These require

no further explanation. The remaining eight columns refer to the form of the Gamma distribution itself. As discussed in Chapter 7, this particle size distribution was originally conceived with a polydispersal in mind but as also explained, may be adapted to fit a monodispersal if the range of particle sizes is reduced to give a very peaked and narrow particle size distribution. This could be done by a careful manipulation of the formulae which must be used to calculate the parameters. They are reproduced as follows:

For a distribution of the form:

$$n(rp) = a r_p^{\alpha_d} \exp(-b r_p^{\gamma}) \tag{9.20}$$

then

$$\alpha = \frac{\gamma rp^{\gamma} \ln(R)}{\gamma rp^{\gamma} \ell n (rp/r_1) + r_1^{\gamma} - rp^{\gamma}} \tag{9.21}$$

$$b = \frac{\alpha_d}{\gamma rp^{\gamma}} \tag{9.22}$$

$$a = \frac{n(rp)}{rp^{\alpha} \exp(-\alpha_d/\gamma)} \tag{9.23}$$

and

$$\gamma = 3 \text{ (usually)} \tag{9.24}$$

The derivation and meaning of the above formulae is discussed in Appendix B.

The particle sizes r_1 and r_2 refer to the two extremes of the size distribution and are listed in column 5 of Table 9.4 for each wet steam condition. Since this type of distribution was originally developed for atmospheric

SPEED (rps)	rp (μm)	N(rp) (m^{-3})	$Q_{SCAT(rp)}$	SIZE RANGE (μm)	ALPHA (α_d)	GAMMA	a	b	X1	X2	DX
1500	0.187	7.36×10^{13}	1.0312	$0.096 \leq rp \leq 0.285$ $(0.1 \leq rp \leq 0.28)$	64.96 (58.65)	3	3.73×10^{70} (1.58×10^{65})	3311.31 (2989.66)	1.1 (1.2)	3.484 (3.42)	0.01
1600	0.135	4.36×10^{14}	0.38065	$0.062 \leq rp \leq 0.21)$ $(0.056 \leq rp \leq 0.22)$	57.6 (44.5)	3	3.73×10^{70} (6.048×10^{59})	7803.68 (6028.9)	0.73 (0.61)	2.57 (2.69)	0.01
1700	0.11	8×10^{14}	0.26786	$0.045 \leq rp \leq 0.175$ $(0.05 \leq rp \leq 0.17)$	50.74 (43.53)	3	7.73×10^{70} (1.108×10^{63})	12707.24 (10900)	0.55 (0.61)	2.14 2.08	0.01
1800	0.11	1.035×10^{15}	0.2286	$0.045 \leq rp \leq 0.175$ $(0.05 \leq rp \leq 0.17)$	47.34 (43.53)	3	1.0×10^{71} (8.55×10^{62})	12707.24 (10900)	0.55 (0.49)	2.14 (2.08)	0.01
1850	0.11	2.0×10^{5}	0.2286	$(0.045 \leq rp \leq 0.17)$ $(0.05 \leq rp \leq 0.17)$	47.34 (43.53)	3	1.93×10^{71} (1.62×10^{63})	12707.24 (10900)	0.55 (0.49)	2.14 (2.08)	0.01
1900	0.09	3.088×10^{5}	0.13786	$0.035 \leq rp \leq 0.145$ $(0.03 \leq rp \leq 0.15)$	47.34 (39.53)	3	7.063×10^{71} $3.47 \times 10^{62})$	21560.0 (18000)	0.43 (0.37)	1.77 (1.83)	0.01

Table 9.4 GAMMA DISTRIBUTION PARAMETERS FOR EACH WET STEAM CONDITION

aerosols, some problems arose when fitting it to the wet steam conditions. One major problem arises when the size range is made as narrow as possible to accommodate a near monodispersal. As r_1 (or r_2) tends to r_p, the magnitude of α in equation (9.21) increases quite rapidly. The variation of α with r_1/r_p is shown in figure 9.10. Similarly as α increases so does the size of the coefficient "a" in equation (9.23). Due to the number concentration of droplets encountered in wet steam, this coefficient can very quickly assume very large values as shown in figure 9.11. Here the variation of "a" is plotted against the range of values for α depicted in figure 9.10. The IBM mainframe computer used for the numerical work could cope with real numbers up to 10^{76}. The fundamental limit was imposed upon the extent to which a monodispersal could be approximated. The parameters for the distribution were therefore chosen so that the coefficient "a" did not exceed 10^{75}. It was found that a very good approximation to a monodispersal could be achieved despite the limitations. Figures in brackets in this table indicate an earlier attempt at optimizing the approximation to a monodispersal which was in any case largely achieved by trial and error. The next four columns list respectively the parameters ALPHA, GAMMA, a and b for each wet steam condition. The two penultimate columns list the size parameters X1 and X2 corresponding to the two extremes of the size range given in column 5. GAMMA here has been set equal to 3 throughout because this figure is

typical of a symmetrical distribution. In this work there appeared to be no requirement to deviate from this general rule.

Finally DX is the size parameter increment used in the numerical routines. In all cases this was set to 0.01 and with the particular wavelength of laser light, represented a water droplet size increment of 0.0008μm (= DX.λ/π) and so was extremely sensitive to any variation in water droplet size. The program "TSCAT" effectively samples the particle size distribution at this increment and, for each size, calculates the single scattering phase function. The final phase function is the summation of the effects of every individual phase function, the influence of each being weighted by their relative number concentration. As will be seen in the next section, a near monodispersion was achieved and the main influence in the scattering phase function is from water droplets of the mean radius r_p. This was absolutely essential because throughout the numerical treatment of the size distribution only one value of Q_{scat} has been assumed, this being the one corresponding to the value of r_p. Strictly speaking the scattering efficiency of each droplet size should have been taken into account. In reality however, the relative number concentration of the other particles in the distribution were so small that any errors introduced by this action would also be small.

The parameters used in the Gamma distribution may be checked by a substitution into equation (9.20). For example

consider the distribution corresponding to a turbine speed of 1700 rps, the relevant parameters for which are shown on row 3 of Table 9.4.:

Here $a = 7.73 \times 10^{70}$

$b = 12707.24$

ALPHA = 50.74

GAMMA = 3

Hence in equation (9.20)

$n(r_p) = 7.73 \times 10^{70} \times 0.11^{50.74} \times \exp[-12707.24 \times 0.11^3]$

$= 8.0 \times 10^{14} m^{-3}$ which is the required value.

9.3.4 A comparison between experimental and predicted distributions of diffuse light intensity

The main objective was to establish whether the diffuse light distribution formed as a laser beam passes through a known atmosphere of wet steam can be predicted.

In section 9.3.2, the experimental method of obtaining the polar distribution of diffusely transmitted light has been described. In order to predict this, the Gamma size distribution function, well known and widely applied in atmospheric physics, was used. The parameters for this distribution function depend closely upon the water droplet size and number concentrations in the wet steam and these have been given in section 9.3.3. The results of the comparison between experimental values and the computer simulation will now be presented.

The results have been placed into six groups represented by consecutive figures 9.12 to 9.17,

respectively. Each individual group consists of four plots, (a), (b), (c) and (d). Consider as an example the results of figure 9.12. Figure 9.12 (a) shows the single scattering phase function for a mean particle radius of r_p = 0.187 μm, as computed by the simulation program "TSCAT". The plot of figure 9.12(b) shows the variation in number concentration of the scattering particles with particle radius as assumed by "TSCAT". It is the information contained in figures 9.12(a) and 9.12(b) that contain the raw data for the multiple scattering programs. The third plot, in figure 9.12(c) shows the experimental values plotted as a polar distribution with $\phi=90^0$ in accordance with the scattering and detection geometry of figure 9.8. This polar plot is for one beam only, passing through the wet steam in the measuring section. The theoretical plot of the distribution of diffusely transmitted light is given by the solid line of figure 9.12(c). The comparison made in figure 9.12(d) is as for figure 9.12(c) but in this case it is performed for two laser beams passing through the wet steam. In summary, then, the following figures give the complete results of these comparisons described above for the following wet steam conditions:

(i) Figure 9.12 (a)-(d) - polar plots for a wetness value of 1%

(ii) Figure 9.13 (a)-(d) - polar plots for a wetness value of 1.9%

(iii) Figure 9.14 (a)-(d) - polar plots for a wetness value of 4.0%

(iv) Figure 9.15 (a)-(d) - polar plots for a wetness value of 4.7%

9.3.5 A discussion of the predicted and experimental distributions

There are basically two comments that can be made about the polar plots.

(i) No direct component has been measured. The PM tube was at no time positioned directly in the path of the laser beam. In the single beam case, it is the direct component along 45^0 which is missing whereas in the two beam case, measurements along the beam at 43.6^0 and 47.3^0 are omitted,

(ii) Only the form of the diffuse light distribution has been compared here. No measurement of the direct light has been attempted with the PM tube and therefore no reference light intensity is available. What has been measured is the variation of PM anode current for a given detector position. Whilst it is accepted that the current will vary in sympathy with the level of scattered light intensity, only the relative shape of the distributions can be compared.

It may have been possible to take a measurement of the intensity of the direct light beam. When taking measurements of the diffuse light components, the tube voltage was kept constant. In order to measure any direct light components, the tube voltage would have to have been

reduced significantly. This would have changed the sensitivity of the device so a voltage/gain or voltage/sensitivity characteristic would have been required. However, it was decided intially that only the form of the distribution would have been useful and, in any case, due to the time limitations imposed upon the experimental work there would have been an enormous and unjustifiable risk of damage to the PM tube if the intensity of the direct light was measured in this way.

The very fact that the form of the two distributions conpares very favourably is of some importance. It means that the raw scattering data for the multiple scattering program was accurate. Since the input parameters for the Gamma function used were obtained empirically, this in turn implies that the determination of N and r_p and their estimates were reasonable.

The polar plots are then a valid means of estimating the wetness of the steam optically without resort to the more traditional method using a throttling calorimeter. Since the program "TSCAT" is very sensitive to scattering particle size then if the estimates of r_p were in great error, the form of the scattering phase function would be very different. This would have had a knock on effect upon all the successive processing in the multiple scattering programs with the result that the polar distribution of scattered light would not have been so slowly varying. In figure 9.12(a) showing the phase function for r_p = 0.187μm,

this is more rapidly varying than that for r_p = 0.11μm in figure 9.14(a). In fact water droplets of 0.11μm in radius providing the bulk extinction are just in the Mie scattering regime. It was mentioned in Chapter 7, that the computer program "TSCAT", providing the scattering phase function uses on algorithm which reduces to that of Rayleigh scattering when the mean scattering particle radius falls below about 0.08μm. Otherwise, of course, it allows for the computation of the full Mie solution. Figure 9.16 shows the single scattering phase function for r_p = 0.05μm and figure 7.6 shows the corresponding size distribution. It can be seen here that the ratio of forward to backscattered intensity is unity. This is a typical feature of Rayleigh type scattering. The phase functions shown in figures 9.13(a), 9.14 (b) and 9.15(a) represent those of scattering particles which may be thought of as the transition size between Rayleigh and Mie size regimes. When these are compared with figure 9.16, it can be seen that the forward scattered intensity is beginning to develop a prominent lobe with an increase of mean scattering particle size of only 0.05μm.

9.4 Using LDA to obtain velocity profiles across the flow of wet steam

9.4.1 Outline of the method

The main objective of this research was to assess the viability and suitability of LDA as an instrument for measuring the velocity of wet steam flows using the water

droplets present in the flow as seeding. If this could be achieved with a counter type processor, then the possibility of extending the current research to measuring local turbulence intensities and ultimately to sizing the water droplets, becomes a proposition. This section describes how a velocity profile was constructed across the flow of wet steam in the measuring section of the rig.

The actual bore of the five way crosspiece was about 165 mm in diameter. Starting at a point just within the window opening, local velocities were measured at 17 individual stations evenly spaced by 10 mm as shown in figure 9.17. A metric rule was glued to the lead screw housing of the optics bedplate and this was positioned such as to read 0 mm against a pointer when the intersection of the two laser beams was located at the front surface of the first window. The dimensions of the measuring section were known and it was a relatively simple task to position the intersection at any given point by moving the bedplate towards the rig at the required distance given by the position of the pointer on the metric rule.

At every measuring station across the flow, the detection optics had to be moved accordingly. Due to the fact that they were at least 0.8m away from the beam intersection at any given measuring station (0.8 m was the minimum focusing distance for the camera zoom lens) only a fine adjustment of the angle of the zoom lens relative to the horizontal was required. Thereafter optimizing the

signal by means of finely adjusting the position of the pinhole relative to the crossover was simple. This procedure avoided the need for a complete realignment every time.

In order to assess whether the velocity profiles were meaningful, a theoretical fit was tried based upon a simple pipe flow analysis and quite a good agreement was obtained. The mean velocity required to obtain this agreement was well within the 10% error band of the predicted mean velocity of the wet steam.

9.4.2 The velocity profiles and a theoretical fit using simple pipe flow analysis.

A total of six velocity profiles were produced, one for each wet steam condition. These profiles are shown in figure 9.18 (a)-(f). In all of the figures the turbine speed, steam wetness and the important parameters of the detection optics and counter processor settings were recorded.

With the DISA type LDA counter, a good indication of the SNR of the signal entering the counter circuits from the filter board was given by the data rate and the percentage of those signals that were validated by the counter circuits. Wet steam is a very difficult medium in which to make any measurements and as far as LDA is concerned is far from ideal. This is due to the severe attenuation imposed upon the signal from the measuring volume of the instrument by successive scattering and the glare produced by the diffuse

light which is detected as noise. The difficulty with which the velocity measurements were made can be realised when these two readings are compared with those obtained from a flow of clean drinking water used to check the optics in Chapter 4. In this situation the data rate was as high as 2-3 kHz with a 50% validation. Up to and including a turbine speed of 1800 rps a complete velocity profile was produced though with increasing difficulty. Thereafter only a limited number of measuring stations nearest the detection optics yielded good enough signals to be detected. This situation is shown in figure 9.18(e) and figure 9.18(f).

In all the measuring situations encountered in this research, the optimum laser power was about 400mW. Lower laser powers, down to about 200mW, were permissible with wetness fractions below 0.02 but with the higher values up to about Y = 0.03, more laser power was required (in conjunction with a greater degree of spatial filtering) to yield a signal of sufficient strength to initiate the electronic counting circuits of the counter processor. For wetness fractions about 0.03, any increase in laser power above 400 mW reduced the quality of the Doppler signal and increased the amount of background noise to a level at which no Doppler signal was detectable. Crane et al (1975) pointed out that for the particular conditions under investigation, 60mW appeared to be the optimum laser power. However in this work, water droplets with mean diameters of between 1 and 2 μm were present in the flow as nucleated

droplets. The scattering efficiency for droplets of this size is of the order of 5 times greater than that for droplets of mean radius 0.1 μm encountered in this research. (α ($=\pi d_p/\lambda$) = 1.22 for r_p = 0.1μm and α = 6.0 for r_p = 0.5μm). The laser beams of the anemometer will therefore have been subjected to a greater level of extinction due to scattering as they passed through the wet steam. In the work of Crane et al. an increase in laser power above 60 mW would have yielded no further improvement in Doppler signal quality due to the effects of multiple scattering and the influence of the reflection coefficient. The amount of light diffusely reflected becomes significant at higher laser powers when the optical depth of the turbid medium is such that multiple scattering is an important influence in itself. However, if the mean size of the nucleated droplets acting as light scatterers is smaller, then this effect does not become apparent until higher laser powers are used. Furthermore for a size parameter of α = 6.0, figure 7.6 shows that the extinction from particulate media is most severe when the mean size is of the order of 0.5μm. It is hardly surprising therefore that Crane could not manage to obtain good enough signals with higher laser powers.

The variation in the counter readings shown in the profiles in figure 9.18 will be discussed more fully in section 9.4.3.

In order to assess whether the velocity profiles

obtained are representative of the flow of steam under these experimental conditions, a simple theoretical analysis was performed based upon the flow of fluid through smooth walled pipes. The theory is based upon investigations into the laws of friction and velocity profiles in smooth pipes over a wide range of Reynolds numbers $4 \times 10^3 \leqslant Re \leqslant 3.2 \times 10^6$.
The well known work of Nikuradse may be represented by the empirical equation:

$$\frac{c}{c_4} = \left(\frac{y}{R}\right)^{1/n} \qquad (9.25)$$

This relation is valid for the experimental conditions under investigation here, as illustrated by the values of Re in Table 9.5, given for each of the operating conditions of wet steam. A further expression is useful relating the mean velocity to the maximum velocity for a flow situation as given by:

$$\frac{c}{c_4} = \frac{2n^2}{(n+1)(2n+1)} \qquad (9.26)$$

The value of the exponent n in equation (9.25) is n=6 at the lowest Reynolds number of 4×10^3, it increases to n=7 at $Re = 100 \times 10^3$ and n=10 at the highest Re of 10^6.

In order to provide a theoretical fit to the profiles in figure 9.19, the degree of fit depended upon the values of mean velocity down the pipe that were taken. Since there was an experimental tolerance on the predicted mean velocity of

N_T (rps)	Y	Predicted $\bar{c}$ (ms^{-1})	ρ_{st} (Kgm^{-3})	μ (Nms^{-2})	Re
1500	0.01	15.4	0.51	14.6×10^6	8.8×10^4
1600	0.019	16.3	0.53	17.1×10^6	8.4×10^4
1700	0.023	16.9	0.56	18.3×10^6	8.5×10^4
1800	0.03	19.9	0.57	20.3×10^6	9.3×10^4
1850	0.04	20.0	0.57	22.3×10^6	8.5×10^4
1900	0.047	20.8	0.58	25.1×10^6	7.9×10^4

Table 9.5 RANGE OF REYNOLDS NUMBERS FOR EACH WET STEAM CONDITION

N_T (rps)	Predicted $\bar{c}$ ±10% (ms^{-1})	$\bar{c}$ taken to give good fit	C_4 (ms^{-1})	Percentage error in $\bar{c}$
1500	15.4	13.9	17.0	-7.0%
1600	16.3	15.0	18.36	-8.0%
1700	16.9	15.3	18.73	-9.5%
1800	19.9	18.0	22.0	-9.5%
1850	20.0	18.2	22.3	-9.0%
1900	20.8	[illegible]	23.2	-8.6%

Table 9.6 MEAN VELOCITY REQUIRED TO GIVE GOOD AGREEMENT WITH THE EXPERIMENTAL DATA

±10%, then the degree of fit to the experimental data of figure 9.18, could be varied. Table 9.6 shows the values of the maximum velocity calculated from equation (9.26) given a value of mean velocity within the tolerance and taking an index of n=7. The results of the theoretical fit to the experimental data for the velocity profiles are shown in the plots of figure 9.19.

9.4.3 Discussion

The main objective of this research was concerned with the general problem of the applicability of LDA to wet steam flows, and specifically the determination of those steam qualities in which a counter based LDA system could be expected to operate. It has already been established that wet steam is a highly turbid medium in which the scattering of laser light is complicated by the effects of multiple scattering. This feature prompted further research into the processes of scattering and, ultimately, to the development of a computer program to model a polar distribution of the scattered intensity by considering both single and multiple scattering events. Simple methods of proving the program have been described in Chapter 8 and the experimental work of the last section has established that, under the operating conditions of wet steam experienced by the author, the model can accurately predict the diffuse components of the scattered light from a turbid medium.

The main objective of this section was to assess the

performance of a counter processor with Doppler signals obtained from wet steam flows of variable quality. Velocity profiles have been produced across the wet steam flow in the measuring section for each wet steam condition. A theoretical profile based upon a simple pipe flow analysis was applied to establish whether the velocity profiles were realistic. In figures 9.19(a)-(d), the fit is reasonable particularly near the walls of the measuring section. Some departure, of a varying degree, is noticeable in the central regions of the flow and a possible explanation for this is as follows.

The steam on leaving the turbine exhaust is subjected to a sudden expansion before entering the measuring section of the rig. The abrupt change in area ratio at this point induces large scale turbulence through the flow. The effect of this turbulence is to even out the energy distribution and, aided by fluid turning back to provide entrainment flow, to induce a flow reattachment. Following reattachment the large scale turbulence decays rapidly. This should have occured within four diameters of the measuring section downstream of the sudden expansion. The expansion chamber of the experimental facility is only 0.8 m long and it is unlikely that, after six diameters downstream of the

expansion to the measuring section. In figure 9.20 sudden expansion process is shown. Only after about 6-8 diameters of the measuring section (67) will a fully developed turbulent velocity profile be present. The 1/n power law is not suitable as a model for this flow

PLEASE NOTE:

Whilst the 1/n power law is not suitable for the centre of the flow, it does give an indication as to the validity of the velocity measurements near the walls of the test section.

and will only serve as an approximation for the velocity profile near the walls of the section.

For $Re \approx 10^6$, fully turbulent flow is produced after about 30 diameters downstream of attachment. This is shown in region 3 of figure 9.20. However within region 2, the core of nearly constant total pressure will tend to flatten the velocity profile across the flow as shown. It is possible that this process was responsible for the nearly flat topped velocity profiles produced for the wet steam flows. It must also be borne in mind that the model used to fit the velocity profile was not perfect and it would be rather surprising if the fit was very close across the entire profile. Earlier it was stated that the actual velocities of the flow as measured with the LDA were not as important as the ability to achieve measurements at all. Despite this it is useful to attach some meaning to those velocities in order to obtain information about the state of the development of the steam flow.

On each of the figures showing the velocity profiles across the steam flow, the corresponding counter readings are shown. The optimum laser power appeared to be about 400 mW and this power level was maintained throughout the readings. The counter was operated in the COMBINED mode when the 5/8 comparison was performed to an accuracy of within 1.5%. Basically this means that the processing unit

of the counter counts the number of peaks in the signal in such a way that it counts the first 5 and the first 8. The velocity computed from the first count is compared with that of the comparator accuracy set, then the signal is validated. This was probably the most accurate way of making velocity measurements with the counter. The velocities were measured directly from the mean velocity computer module.

It can be seen from figures 9.19 (a)-(d) that the data rate and number of validated signals are decreasing as the percentage wetness of the steam increases. Plate (viii) shows a typical filtered Doppler signal obtained from the wet steam flow. This signal was stored on a digital storage oscilloscope and the time base expanded twice as shown. The first trace is that of the filtered signal in its unexpanded form. In order to observe the signal more closely the trace was expanded by two levels. As can be seen there is a relatively clean Doppler frequency present. One interesting feature is the presence of a continuous background signal of very low amplitude, less than 0.05 V which would not have been detected by the counter as a minimum amplitude of 0.2V was required to trigger the counting circuits. Basically the Doppler signals of Plate (viii) can be summarized by the following:

(i) There is without doubt a Doppler frequency present in the signal traces,

(ii) There is a continuous background signal of low amplitude superimposed upon which are discrete bursts of larger amplitude and it is these signals that are being detected by the processing electronics,

(iii) In these traces which were obtained in the steam flow of 3% wetness it can be seen why the percentage validation of the Doppler signals in the COMBINED mode of operation of the counter was so low. From the moment that the amplitude of discrete signals exceeds 0.2V, the counting process was initiated. However, although 5 counts are available it was not always possible to perform the 8 counts as the signal amplitude dips due to the influence of a second water droplet of comparable size present simultaneously in the measuring volume. This can be seen in Plate (ix).

The presence of a very much smaller number of discrete Doppler bursts superimposed upon the continuous background signal is worthy of further investigation. Plate (x) shows an expanded Doppler signal trace obtained at 2.3% wetness. The presence of two amplitudes of discrete bursts are very clear. The question arises as to the source of these water droplets because they are providing the seeding for the laser anemometer. The continuous background signal is that

due to the 0.1μm nucleated water droplets naturally occurring in the steam. The laser light scattered by these droplets is of such small amplitude that it is undetectable using the counter. Plate (xi) shows the steam conditions from which these signals were obtained. The light scattered by these small water droplets is providing the diffuse light in the photograph. Extensive spatial filtering in the detection optics was necessary to improve the quality of the signal. A 50μm pinhole was used with an aperture of f16 on the zoom lens. The intensity of the cross beams in the eyepiece of the photodetector was very low under these conditions which is why alignment and focusing were carried out with full aperture. Only when a signal trace was produced, was the lens aperture stopped down gradually and the supply voltage increased to the PM tube from about 800 V to 1100V. The PM tube current increased as the supply voltage was increased but a situation was quickly reached when the noise in the signal, due to multiple scattering by the 0.1μm water droplets, swamped the Doppler signal. A compromise had to be reached, therefore, between increasing the supply voltage to increase the level of signal current and stopping the lens down to improve the quality of the Doppler signal.

The source of the water droplets providing the detectable Doppler signals now needs to be established. Plate (iii) shows the beam passing through the measuring section with the turbine running at about 1200 rps. At this

speed the steam in the exhaust was dry as can be seen from the photograph. Extremely good Doppler signals were obtained under these conditions and water droplets were visibly flowing through the measuring section, the bulk of which appeared to be the same size, as far as the eye could tell. In addition to these there were a number of much larger water drops which were not always flowing with the main body of steam. The source of the smaller droplets was most likely to have been due to water being sprayed out of the turbine bearings, which has further broken up downstream of the turbine wheel. The amplitude of the signals produced by these drops coincided very closely to those discrete signals of smaller size obtained under the wet steam conditions. The smaller number of larger discrete droplets is thought to be as a result of water drooling from the walls of the measuring section. Rivulets of water were seen flowing around the window openings and if these were any indication of the conditions upstream in the expansion chamber, then this was most likely. The size of these droplets appeared to vary considerably but in any case were greater than 500 μm in diameter. This assessment of their minimum size could easily be made from observations of the flow conditions through the windows when running dry.

It is interesting to note from the results in Table 9.6, that the mean velocity required to yield a good theoretical model to fit the experimental velocity data was always less than the predicted mean velocity. Whilst there

is error in the estimate of the mean velocity of the steam flow in the measuring section, this result highlights the possibility that the water droplets that yielded the good quality Doppler signals, were travelling with the flow streamlines with little or even negligible slip. According to the literature (71), this is the case for water droplets up to 5μm in diameter (i.e. $r_p \leq 2.5\mu m$).

So far in this discussion attention has been drawn to the fact that detectable signals have been produced from the seeding droplets in the steam. Mention has also been made of the compromise between supply voltage to the PM tube and the spatial filtering required to yield the better quality signal. What is really at issue here is the SNR of the signals obtained from the steam. The next section will concentrate upon this aspect and attempt to compare the SNR with the estimated size of the water droplets in the wet steam providing the seeding for the laser anemometer.

9.5 A Prediction of the SNR at the photodetector and a comparison with experimental results.

9.5.1 Introduction

Any observation of the extinction of laser light by a wet steam fog and its transformation to a general, even level of illumination leads to the inescapable conclusion that a great enough optical depth of that turbid medium will reduce the SNR of the laser anemometry system to below its operational threshold. It has been established in the last section that it is the SNR which determines whether a

detected Doppler signal is of sufficient quality to yield the required information reliably. Here the signal is the laser light scattered and Doppler shifted in frequency, by the water droplets in the measuring volume, travelling directly to the photodetector and the noise is the integration of the diffuse light, generated by the beams of the LDA system, arriving at the photodetector. If the noise generated internally by the photodetector is included then an expression can be obtained for the SNR at the processor's electronic signal input. This formed the basis of the derivation of such an expression in section 8.4.3. All signal processors used in laser Anemometry applications have a minimum SNR at which they can be expected to operate. The range of operation of a specific processor can be expressed in terms of the turbidity of the wet steam (here proportional to steam wetness) and the distances through the medium from the entry port to the measuring volume and from the measuring volume to the exit port and then to the photodetector.

The results of section 9.4 have revealed that at a steam wetness of 4% and above, no Doppler signals can be obtained from the steam flow at depths of greater than 60 mm. This was not only due to the very low amplitude signal present, but to the fact that the level of noise just cannot be reduced sufficiently to yield a good SNR. At 4.7% wetness, this problem worsened considerably when only very poor signals were detected at depths of up to 30 mm, which

are not considerable. This section describes the attempt made by the author to compute the SNR at the photodetector output and to relate this to the ability of the laser anemometer system to make velocity measurements of the wet steam flows at given depths and under varying conditions of operation. It will be shown that quite a good agreement is obtained between the predicted SNR at a given measuring station and the point after which no useful signal is detected. Of importance here are the relative values of SNR computed. It is very difficult to assess the actual SNR of the photodetector output as processed by the counter as the noise figures of the individual stages of processing, including filtering are not known. The SNR has been computed from a very simple consideration of the "signal" and "noise" components generated in the steam and the noise generated by the photodetector. Any additional sources of light constituting noise have been neglected.

The results will show that the suite of computer programs developed to compute the polar distribution of diffusely scattered light from within turbid medium have proved to be a very useful tool in assessing the applicability of LDA measurement techniques to two-phase flows. The computation of the SNR is not perfect, however, and there are some limitations to its use but with further development it can be improved.

9.5.2 Results

Doppler signals obtained from the 0.1μm radius droplets in the steam are visible on the signal trace under conditions of high SNR as shown in Plate (viii). The SNR figure for these water droplets may be relatively high but the actual signal amplitude is too low to be detected. Increasing the laser power only aggravates the situation as the much increased noise levels reduce the effective SNR figure.

The program computes the noise contribution from the diffusely scattered light generated by the 0.1μm radius water droplets in the steam. This is effectively a 'background' noise. The signal on the other hand is generated by water droplets that are somewhat larger than these. Four sizes of these seeding droplets have been considered as potential sources of good signal. These are water droplets of radius r_p = 1μm, 2μm, 5μm and 10μm. It is accepted that for the latter two sizes some slip, albeit small, would be evident in the velocity measurements. It will nevertheless be interesting to see how this size would affect the computed values of the SNR figure. In order to perform the computation some knowledge of the droplet number density and radius dispersion is required. No technique was actually available to do this directly since these droplets did not constitute a bulk extinction and so a light extinction method could not be employed. There was a means, however, of making an estimate of their relative numbers.

It will be assumed in the following analysis that the water droplets of the above sizes are as a result of water leakage from the turbine bearings into the rig and that only a monodispersion exists.

It was found that water was being 'lost' from the sump. Neglecting evaporation this water was assumed to be that water producing the seeding droplets for the LDA system.

The amount of loss was measured to be approximately one litre every three hours of constant running. It was measured at a speed of 1850 rps giving a predicted mean velocity of wet steam in the measuring section of the rig of $20ms^{-1}$.

The rate of water loss from the sump can be calculated as

$$\frac{1000}{3x3600} = 0.093\ cm^3\ s^{-1} \text{ i.e. } 0.093g\ s^{-1}$$

which, as a proportion of the corresponding steam mass flow rate of $0.27\ kgs^{-1}$, is less than 0.04%!

The velocity occupied by a water droplet of radius r_p is $4/3\ \pi\ r_p^3$. Thus the total volume occupied by N_p is given by $4/3\ N\pi\ r_p^3$. Equating this to the volumetric rate of water lost from the sump gives:

$$\frac{4}{3}N_p . r_p^3 = 0.093x10^{-6} \qquad (9.27)$$

The values of N_p for r_p = 1, 2, 5 and 10μm were calculated

from the above relationship as 2.2×10^{10}, 2.8×10^{9}, 1.8×10^{8} and 2.2×10^{7} droplets m^{-3} respectively. The corresponding number concentration of 0.1μm droplets under the same conditions was $2.0 \times 10^{15} m^{-3}$ from Table 9.4. In Chapter 4 the measuring volume produced by the LDA system was estimated to be about $10^{-12} m^{3}$. The number of droplets likely to be present simultaneously in the measuring volume of radii r_p = 0.1μm, 1.0μm, 2.0μm, 5.0μm and 10μm are, respectively, 2000, 0.022, 0.0028, 1.0×10^{-4} and 2.2×10^{-5}. It is of no surprise, therefore, that a continuous background signal produced by light scattered from the 0.1μm droplets was present in the oscilloscope traces.

Knowing the relative number concentrations of the seeding droplets allows a Gamma type size distribution to be calculated for each particle size in a similar manner to that shown in Appendix B. Table 9.7 lists the Gamma parameters for each case as used to generate the single scattering phase function "TSCAT". The scattering phase functions as computed by "TSCAT" are shown in figures 9.21(a) - 9.21(c) together with their corresponding number and size distributions in figures 9.22(a) - 9.22(c), for r_p = 2, 5 and 10μm. As the scattering particle radius increases to beyond the wavelength of the illuminating light, so the intensity distribution becomes more complex. In Table 9.7, all the parameters of the Gamma distribution are decreasing with an increase in scattering particle size. In fact as the particle size increases, the narrowest

rp (μm)	N(rp) (m^{-3})	Q_{SCAT}	SIZE RANGE (μm)	ALPHA α_d	GAMMA	a	b	X1	DX	X2
1	2.2×10^{10}	1.7847	$0.75 \leq rp \leq 1.25$	292.0	3	4.38×10^{32}	97.3	9.16	0.1	15.28
2	2.8×10^{9}	2.3286	$0.5 \leq rp \leq 3.5$	30.9	3	1.48×10^{5}	1.29	6.11	0.1	42.8
5	1.8×10^{8}	2.0	$0.1 \leq rp \leq 10.0$	13.73	3	19.5	0.037	1.22	0.1	122.0
10	2.2×10^{7}	2.0	$1.0 \leq rp \leq 30.0$	8.96	2	9.67	0.045	12.2	1.0	428.0
25	1.42×10^{6}	2.0	$1.0 \leq rp \leq 60$	3.85	4	152.0	2.46×10^{-6}	12.2	1.0	733.5
50	1.67×10^{5}	2.0	$10.0 \leq rp \leq 150$	5.83	2.2	97.5	1.32×10^{-4}	122.0	10.0	1833.6
100	2.22×10^{4}	2.0	$50 \leq rp \leq 1000$	44.4	0.2	9.22×10^{11}	88.4	610.0	10.0	12200.0

Table 9.7 THE GAMMA DISTRIBUTION PARAMETERS FOR THE SEEDING WATER DROPLETS (N_T = 1850 rps)

particle size range that can be modelled by this type of distribution for the number concentrations involved becomes wider. Consequently the approximation of what is essentially a polydispersion to a monodispersion by means of choosing a very narrow distribution no longer becomes possible. To illustrate this point, rows 5-7 of Table 9.7 contain the distribution parameters for r_p = 25, 50 and 100μm. Use of any of these parameters to model a monodispersion would have resulted in large inaccuracies in the computation of the phase function making the suite of multiple scattering programs very unreliable. In fact a mean scattering particle size of 5.0μm represents the limit to which the Gamma type distribution may be used to model a monodispersion of wet steam droplets.

In the velocity profiles of figure 9.18(e) and figure 9.18(f), no LDA signals were obtained at depths of greater than 60 mm and 30 mm respectively. These two cases will be used to compare the acquisition of experimental data with the computed SNR. In each figure the computed SNR is shown on a logarithmic scale with those velocity readings obtained at the stated steam quality. Figures 9.23(a) - 9.23(b) show the comparison for a turbine speed of 1850 rps (wetness = 4%) for r_p = 1.0μm and 2.0μm and for r_p = 5μm and 10μm respectively and figures 9.24(a) - 9.24 (b) show the corresponding plots for a turbine speed of 1900 rps (wetness = 4.7%). As can be seen for r_p = 1.0μm and r_p = 2.0μm, the cut-off point for obtaining Doppler signals occurs at a

value of SNR of the order of the minimum operating value for a DISA 55L90a counter processor. The same cannot be said for $r_p = 5.0\mu m$ and $r_p = 10.0\mu m$, however, where a cut off occurs at a value of SNR of about 10. This discrepancy with the other radii could be due to the following factors:

(i) These water droplets have been assumed to be monodispersed and that their source was leakage of lubricant from the turbine bearings. In reality, however, the dispersion of the droplets providing the seedingmay be skewed and have several mode radii, and

(ii) The parameters of the Gamma distribution for scattering particles whose radii are greater than $2.5\mu m$ define a distribution which can no longer be regarded as a good approximation to a monodispersion. The suite of multiple scattering programs are designed to handle a monodispersion only. Although the routines will function with a polydispersion the computed results will be inaccurate.

With these two points in mind the plots for $r_p = 5.0\mu m$ and $10\mu m$ must be regarded with caution. The program can, of course, be modified but the execution of such modifications would have exceeded the time scale for this research. Any worker wishing to do this would find that the necessary theory is documented in Deirmendjian (20).

9.5.3 Discussion

The computation of the SNR was performed using the formulae derived in Chapter 8. The noise generating light has been scattered from the entire length of the beams to the photodetector and is indpendent of the position of the crossover depending only upon the angles of the beams entering the steam, the distance through the steam, the collection angle of the photodetector and the scattering properties of the steam.

The signal light is scattered from the water droplets present in the LDA measuring volume. A change in the SNR is therefore experienced when the position of the probe volume in the steam is moved. Since the solid angle subtended by the photodetector at the measuring volume decreases with increasing distance from the measuring volume to the photodetecotr, it would be expected that the SNR would be higher for measuring sections nearest to the photodetector. Thus when a steam condition was reached which gave a large enough optical depth to reduce the SNR below the required threshold, measurements would first become imposs ble with the measuring volume in the half of the measuring section nearest to the detection optics. This was borne out as shown in figures 9.23 and 9.24. In each figure the SNR is shown on a logarithmic scale with those velocity readings obtainable at the stated steam quality.

Despite the apparent usefulness of the multiple scattering programs to predict the SNR of the two phase

medium, the results have also highlighted some deficiencies , particularly in "LDA/PLOT" which computed the SNR for a given wet steam conditions. They may be summarized as follows:

(i) The program "TSCAT" was written to compute the single scattering phase function for any distribution of particle sizes. Reliable results could only be obtained from the multiple scattering programs if a good approximation to a monodispersion was used as input data for "TSCAT". Modification of these programs to handle a polydispersion would not be difficult.

(ii) The main limitation, however, is that no account has been taken of the so called visibility factor (24). Although increasing the seeding particle size generally increases the scattered light received by the detector, this does not necessarily improve the LDA signal. With the differential Doppler mode there is a degradation of signal quality when the diameter of the scattering particle becomes large compared to the fringe spacing seen by the detector. If the anemometer has not been designed accoridng to equation (4.5), then the modulation of a Doppler signal form

the passage of the particle will be reduced. The visibility factor may be defined by

$$\text{Visibility factor} = \frac{\text{a.c. amplitude}}{\text{d.c. amplitude}} \qquad (9.27)$$

for the signal. In other words the ratio of the depth of modulation to the pedestal amplitude. This is shown plotted in figure 8.25 having been obtained by integrating the area of illumination of a fringe pattern over a scattering particle. Clearly there are certain particle sizes for which little or no signal would be obtained. This must be allowed for in the program. Equation (9.27) and figure 9.25 have formed the basis for particle sizing (3) (4) and many practical experiments have been performed (5) (35).

(iii) The third limitation arises due to the fact that any photodetector is an integrating device. The total number of scattered photons that are detected will depend upon the residence time of particles through the measuring volume. The SNR expression does not include a velocity term. Durao and Whitelaw (25) have demonstrated that the visibility of Doppler signals is very much influenced by the velocity of the particle

under investigation. It has been shown that for a given laser anemometer system, the amplitude and visability of a detected Doppler signal decreased with increasing velocity. A residence time term (i.e. reciprocal of velocity) needs to be incorporated into the expression.

Time did not permit these additional influences to be developed into the multiple scattering programs. The programs were, however, moderately successful due to the fact that the laser anemometer was geometrically matched to the size of the water droplets and a mean low velocity flwo - ($<25\ ms^{-1}$) was under investigation.

Of great practical interest to NEI Parsons Ltd would be the ability of a laser anemometer to make velocity measurements in backscatter. This was not possible in the experimental facility because insufficient light was scattered in this direction even at maximum laser power. The programs used to computer the SNR to provide some theoretical evidence to support this. Figure 9.26 shows the ratio of the SNR in forward to backscatter for a range of water droplet sizes. As before these droplets were assumed to be flowing in a steam flow containing nucleated water droplets of $0.1\mu m$ in radius.

In this plot the reflection coefficient was used to provide the noise generating scattered light in the backscatter direction. Despite the limitations (ii) and

(iii) above, the plot does show that for water droplets of less thatn 1.0μm in radius, the SNR is substantially higher for forward detection systems. The ratio $SNR_F : SNR_B$ for the larger droplets should be treat with caution but it does suggest that in the presence of a very large number of nucleated water droplets, only detection of the forward scattered light should be attempted. Clearly a further development of these programs to include the visability factor and residence time terms would provide a more accurate characteristic. Considering the single scattering phase function for the larger particles, the ratio of forwardscattered to backscattered light can be several to five orders of magnitude (c.f. figure 7.4 with figure 9.21 (a)-(c)). Even though the noise generating light, given by the reflection coefficient, can be lower in backscatter by as much as two orders of magnitude (compared to the transmission coefficient), there is still a net reduction in the SNR figure for detection systems deployed in backscatter. This requires further investigation.

10. CONCLUSIONS

10.1 The design of a laser Doppler anemometer

A laser Doppler anemometer was designed (3ℰ) with a very small probe volume. The beam diameter at the intersection was designed to be 40μm although in practice it was about twice this due to the effects of spherical aberation at the outer edge of the large transmitting lens. It has been demonstrated that this instrument was capable of yielding good Doppler signals from the wet steam flow up to about 3% wetness. Classical Doppler signals were obtained from a filtered water flow and this was used as a means of finely adjusting the optical system before moving the probe volume into the steam flow.

The design of the optical system was based upon the waist-waist relations developed by Dickson for a laser beam propagating along an optical axis. A computer program was written to predict the behaviour of a laser beam passing through various lens systems and it has been shown how the program was used to design a beam expander. Beam expansion was one of the essential features of the optical system and without it the small probe volume would not have been achieved.

There was, however, a severe limitation to the use of this program. It was written to compute the size and location of the focused beam waist for a given lens based upon the relationships reviewed in Chapter 3. It did not consider the effect of a surface of different optical

constant or geometry upon the laser beam. A beam profile was drawn within the e^{-2} intensity points for a given lens system and the appropriate lens profile was inserted afterwards. Originally the program was only intended as a design tool for a simple LDA optical system and for this purpose, it was successful. It would have been useful to have considered the physical effect of any surface, placed in the path of the beam, upon the beam parameters.

10.2 The generation of wet steam using a turbocharger.

The objective of this work was the investigation of the applicability of LDA to wet steam flows and a determination of those steam qualities in which a counter based LDA system could be expected to operate. In order to establish this, a wet steam flow of a known and variable quality was required to be consistently produced. An optical system capable of yielding good quality Doppler signals had to be designed and proven.

To the best of the author's knowledge, no work has yet been published which concerns the use of a commerical engine turbocharger as a means of generating a wet steam flow of variable quality. A wet steam flow was generated by extracting enthalpy from superheated steam, of known thermodyanmic state, carrying it down into the vapour dome of the Mollier chart. This has been shown for all the wet steam conditions under investigation. The homogeneous generation of a wet steam flow via a turbomachine was preferred as this avoided the separated phases of the heat

exchanger and the non-nucleated water droplets of water spray injection. The compressor stage of the turbocharger was used to brake the turbine and measurements of the mass flow of air through the compressor and its temperature and pressure before and after the compressor served to give a measure of power output. The compressor and turbine efficiencies were given by manufacturers performance maps, obtained with air and exhaust gases respectively. It has been shown how those performance maps constructed for the turbine in exhaust gases were transformed to a working medium of superheated steam by the use of the true non-dimensional plots.

For technical reasons, the bearings of the turbocharger were lubricated, and cooled, with water instead of the recommended grade of turbine oil. It was estimated that the bearing efficiency as a result of using water as the lubricant was no more than ~~two~~ six points lower than that with oil. This figure was, in any case, sufficiently close to unity to have had negligible effect upon the calculations. Using the efficiencies for the compressor, turbine and bearings and having measured the mass flow rate of the steam and its temperature and pressure at the inlet to the turbine, it was possible to estimate the quality of the steam at the turbine exhaust. The wet steam from the turbine exhaust passed into the circular test section of the steam tunnel via a sudden expansion.

It has been shown for a speed range of 1500 - 1900 rps, the speed being increased in discrete steps, that altogether six states of wet steam could be reliably and repeatedly generated. These states were estimated as having a wetness fraction of 1.0, 1.9, 2.3, 4.0 and 4.7% respectively to within an accuracy of 9%.

The running conditions mapped on the compressor performance chart were matched to within 5% of the actual running conditions, establishing that the methods of calculating the essential parameters from the thermodynamic measurements were correct. Due to the nature of the operating conditions of the turbine, namely those of running with dry superheated steam at inlet and a two phase mixture of water and steam at the exhaust, some departure from the turbine performance characteristics was expected. This was indeed the case and the anomalies have been explained.

10.3 The optical extinction method of determining the scattering characteristics of wet steam.

It has been demonstrated that the well known optical extinction method of determining the number concentration and mean radius of the nucleated water droplets in the wet steam flow, is effective. The droplets that are sized are those that constitute the so called bulk scattering of the turbid medium. Previous investigations into the use of the optical extinction method have used a range of wavelengths of light traversing the turbid medium and the light attenuation is measured for each wavelength. A plot of

attenuation with wavelength is matched to a plot of the Mie scattering efficiency curve and the point at which perfect coincidence is achieved gives the size parameter and hence mean scattering particle size at the particular wavelength. However, in this work, only one wavelength is employed and the attenuation is measured directly along the beam under each operating condition. The variation of the attenuation (or extinction) of the laser light with turbine speed is shown in figure 9.2. The values of N and r_p so produced correspond very closely to those values predicted from theoretical conditions given the operating pressure (and hence temperature).

The amount of extinction was calculated by means of the simplest form of the Lambert-Bouguer law. Recent literature has suggested that significant departures can be expected in very turbid media (and hence large optical depths) due to the effects of multiple scattering. However, according to the results of the extinction measurements, use of this law in its classical form was adequate. This was due to the fact that the mean size of the scattering particles in the steam was of such size that no noticeable departure from the law was observed at this wavelength of λ = 514.5 mm. This view is in agreement with the observations made in the literature for particles of the order of 0.1μm in radius.

Any estimation of N and r_p also depends upon the water content in the steam, i.e. the wetness fraction, though not

to a very large extent. However, the very fact that the estimates of N and r_p agree closely with theory suggest that the values of the wetness fraction as calculated from thermodynamic measurements were accurate to within ±9%.

10.4 The polar variation of the diffusely scattered light intensity by multiple scattering.

On the basis of the Mie scattering theory and the Mie scattering functions derived therefrom, a computer program was written by Brinkman which calculates the polar intensity distribution around a scattering particle of any size and refractive index, illuminated by light of any wavelength. However, the program is limited to single scattering events. In order to be any practical use in highly turbid media, the program must be extended to take into account the full effects of multiple scattering. A suite of programs has been written which takes the analysis of the scattering process one stage further and which predicts the polar distribution for the diffusely scattered light. In particular, it computed the transmission and reflection coefficients for the medium. These coefficients refer to the proportion of the incident light diffusely scattered in the forward or backward directions by the effects of multiple scattering alone, respectively.

The analysis used to develop the computer programs was based upon the doubling method of Hansen (48) which has been shown to be ideal for use in turbid media which can be approximated by parallel sided atmospheres. The basic form

of the transmission and reflection coefficients was adapted from che text of Chandrasekhar (10) and the complicated functions reduced into a more manageable form. The method of computing these coefficients has been described in detail and techniques for reducing the amount of running time discussed. Due to the large number of numerical integration routines used in evaluating the individual terms of the coefficients, there was ample scope to make use of redundancy and so make the program faster in its execution of these terms.

However, having written a computer simulation program of a very complicated scattering process, the program needed to be proven against experimental data obtained from the actual conditions of the wet steam. An experiment was performed very carefully in which for each wet steam condition, the diffuse light intensity was measured by means of a photomultiplier tube positioned at a range of polar locations. The distribution of the photomultiplier current with angle was plotted. Using the results of the extinction measurements made in the wet steam, a Gamma distribution of scattering particles was calculated, this distribution being used as the input data for the suite of multiple scattering programs. A comparison of the predicted polar distribution of the diffusely scattering light intensity with the form of the distribution of the photomultiplier current was shown to be very encouraging in almost all the operating conditions. These results lend further weight to the conclusion that the

extinction method used was valid. If the scattering properties of the wet steam had not been correctly determined initially, the form of the Gamma distribution would have been inaccurate with the result that there would have been a considerable mismatch in the comparison of theoretical and experimental data. It has been shown that the program used to predict the single scattering phase function was very sensitive to a change in the scattering properties of the individual water droplets. A corresponding change in the form of the distribution of diffusely scattered light would then be expected.

10.5 The use of laser Doppler anemometry in wet steam

The method used to assess the performance of the LDA in wet steam was to predict the velocity profile across the flow in the measuring section at each of the six operating conditions of wetness. It has been shown that a counter based system was capable of making velocity measurements under certain conditions of wet steam with a high degree of accuracy. This was indicated by a comparison of the measured velocity profile and a general theoretical model. The velocity profile was predicted by measuring the mean velocity at 17 stations across the flow. The velocity at each station was computed by the mean velocity computer on board the DISA 55L90a counter processor. There were, however, very severe limitations to the use of this type of LDA system and these have been shown to be due to the following factors.

It has been shown that the Doppler signal traces obtained from the wet steam consist of a continuous low amplitude signal generated by the nucleated water droplets in the flow. These signals were not sufficiently large to be detected by the processing electronics. Superimposed upon this were discrete Doppler bursts which appeared to be of two discrete amplitudes. The source of the smaller of these bursts was thought to be as a result of water being lost into the measuring section from the turbine bearings. This was unavoidable with the exhaust being under a partial vacuum. Water lost in this way would break up in the wake of the blades of the turbine wheel. The droplets constituted the seeding particles for the laser anemometer and followed the flow quite reasonably. The larger water drops which generated bursts of the order of 1 V in magnitude were thought to originate from water film formed on the walls of the measuring section by deposition and condensation. These water films were drooled off into the flow passing by. In any case these droplets were unimportant to the performance of the instrument since the signals generated were of such a large amplitude as to be rejected by the electronics. It is the nature of the Doppler bursts upon the continuous signal as shown in Plate (x) which helps to illustrate the limitations of this LDA system in wet steam.

A counter processor generally requires discrete bursts of high quality (i.e. good SNR to function correctly. As

the steam wetness, and hence number density of the equilibrium water droplets, increases so does the level of noise. As has been shown in Chapter 8, the intensity of the diffusely scattered light, due to the multiple scattering effects, increases dramatically as the optical depth increases. The result is that the signals generated by the seeding particles are subjected to a greater level of extinction and at the same time the noise level can become comparable in magnitude to the peak amplitude of the discrete signals. At a wetness fraction of 4.7% no signals were obtained at all beyond a depth of 30 mm into the flow, but the noise level exceeded 0.2V despite extensive spatial and analogue filtering. Under these conditions the intensity of diffuse light was very high and the two laser beams were hardly distinguishable against the high background illumination.

At wetness fractions of greater than 0.03, no complete velocity profile across the flow was produced and the data rate and validation percentages were very poor. Between 2% and 3% wetness the signals that were detected produced a velocity reading but their quality was poor and could not be improved. Up to 2% steam wetness, however, the signals were generally good and easily detectable. The use of a small probe volume was an advantage since even at wetness fractions of 4 and 4.7% sufficient direct light was able to reach the cross over region to illuminate the seeding particles sufficiently to yield visibly discrete bursts on

an oscilloscope. They were, in most cases, undetectable as bursts by the processing electronics. An ensemble width of 4096 was used to maintain accuracy and this meant gathering data over several hours in the cases of very low data rates. It would have been useful to have compared the performance of a counter based LDA system with a correlator based system. A photon correlator was available throughout the course of the work but at the time it was required, was not functioning properly. Such a comparison would have yielded much general information about the viability of LDA systems in wet steam flows.

10.6 The prediction of the SNR of the Doppler signals obtained from the wet steam.

It has been demonstrated that the diffuse light intensity generated by a laser beam passing through wet steam can be predicted quite accurately for the geometry of the measuring section. The simulation was performed by means of a suite of multiple scattering programs which acted upon the scattering information of the single scattering phase function. The diffuse light produced by a beam does not contain signal due to the incoherent nature of the multiple scattering process and as such acts as a source of noise. Due to the high turbidity levels experienced in wet steam flows, the amplitude of this noise is often significant and can be greater than the signal itself. One program "TSCAT" can predict the signal strength at the detector for any angular position when used in conjunction

with the Lambert-Beer transmission law. The multiple scattering programs "MS/TRANSM" and "MS/PLOTLOG" can predict the optical noise component of the detected light and if the characteristics of the photodetector are known, then an expression for the SNR of the Doppler signals can be derived. Such an expression has been proposed and it has been shown that, when used with an appropriate LDA geometry, it has yielded some convincing results.

The expression for the SNR was not intended to serve as an all embracing formula to be applicable to any two phase flow but was simply an exercise to investigate whether the single scattering information could be used with the diffuse components to yield a useful relationship. It was not expected to be accurate to any high degree for any turbid medium. However, it has been demonstrated that the point at which LDA signals are no longer obtained from the flow consistently correspond to a SNR figure of less than 10.

Detectable Doppler signals were not produced by the naturally occuring seeding particles present in the steam flow but rather by those water droplets present as a result of water being ejected out of the turbine bearings and then breaking up in the wake of the turbine. No velocity slip was evident and this being the case, scattering particles of up to 5μm in radius could be present (71). It has been shown that the degree of velocity slip by particles up to this size was negligible for all the wet steam operating

conditions investigated.

It has further been shown that a distribution containing water droplets of up to 10μm in radius could be used to predict the SNR. However for mean particle size greater than 10μm, the program breaks down. This could have been due to the following:

(i) The scattering program "TSCAT" was written for a polydispersion. Good results were only obtained for the wet steam by choosing the distribution parameters to simulate a near monodispersion. The Gamma distribution function allowed this for very small particle sizes only. However, as the particle size increased beyond a radius of 10μm, the number density distribution became very polydispersed. The multiple scattering programs could not have been expected to perform adequately with this input data.

(ii) No account has been taken of the relationship between the SNR and the flow velocity, nor has the effect of the scattering particle size in relation to the apparent fringe spacing been considered. The visibility function has been discussed in detail in (24) and an adaptation for this work has been briefly described in section 9.5.3.

The results do show that the program "LDA/PLOT" offers potential for further development. In its present form it was only suitable for low velocity two phase flows containing scattering particles of small mean radius (i.e < 0.5μm).

10.7 Suggestions for further research

The results of this research have shown that a counter based LDA technique has demonstrated potential as an effective instrument for making velocity measurements in a wet steam flow. The feasibility study originally proposed by NEI Parsons Ltd has been completed satisfactorily. The objectives, however, have only been partially fulfilled. As part of the original proposal, LDA measurements were to be carried out on an experimental facility and then repeated on one of the experimental turbines operated by the company. Delays in completing the rig at Durham University and technical problems did not allow time for this.

The ground work has now been done by the author in establishing the counter processor in this application. The technique has shown scope for further development and it is recommended that it be conducted along the following guidelines.

(j) The wet steam flows under investigation were generated by a supposedly homogeneous extraction of enthalpy by means of a turbo-charger. The effect of the sudden expansion upon the nucleated water droplets in steam

is unknown. As a further investigation it would be useful to mount two optical windows into the adaptor of the exhaust. Optical extinction measurements would quickly establish the mean scattering particle size in this part of the flow. This would enable this distribution and the known water droplet distribution in the measuring section to be directly compared, and would promote a greater understanding of the operation of the rig.

(ii) The water droplet concentration in the steam depended upon the exhaust pressure for a given wetness fraction. In order to reduce this the pressure needs to be reduced proportionally. Despite a condenser pressure of 0.2 bar (absolute), the lowest pressure achieved in the measuring section was about 0.6 bar (at 1% wetness). There were significant pressure losses along the inlet supply pipe from the superheater and along the exhaust section to the condenser. In any further development, the measuring section must be moved nearer to the condenser as suggested in Chapter 6. The effect of a lower water droplet concentration upon the performance of the

anemometer could then be investigated.

(iii) The process of droplet nucleation in the steam has not been relevant to this work directly since the objective was to assess the performance of the LDA system in a wet steam flow. The subject of nucleation received a very low priority. In any further investigation this subject deserves further attention particularly regarding the location of the turbocharger at, or near, which nucleation was taking place.

(iv) From the trace of the Doppler signal shown in Plate (ix), it is evident that very low amplitude signals are present. A counter based LDA system would not detect these. A different processing technique such as a correlator with amplitude discrimation could be tried and if successful, only then could an LDA technique be said to work in its true capability in wet steam flows. A correlator would also function better with poorer quality signals and does not rely upon discrete bursts for optimum performance.

(v) Due to the high turbidity of wet steam flows, the number of scattering water droplets present simultaneously in the measuring volume could be as high as 10^3.

The limit of non-coherent detection (23) would have been reached very quickly at which point a dual beam laser anemometer is of little use. All previous research in the use of LDA in wet steam (14), (15) and (89) has concentrated upon the application of the dual beam technique but it is recommended that a reference beam technique be investigated. It has been widely predicted that this alternative type of laser anemometer is superior in flows containing very high concentrations of scattering particles. The reference beam anemometer has not yet been tried in wet steam flows.

(vi) The next obvious step after velocity measurements in a flow is the determination of the scattering water droplet size by means of analysis of the form of the Doppler burst. Various well established techniques for particle sizing have been demonstrated (29), (35) and (53) and it would be of great benefit to NEI Parsons Ltd if the laser anemometer system were developed to perform simultaneous velocity and particle size measurements.

(vii) The computer models could be developed further, particularly the distribution

function used to model wet steam. The Gamma particle distribution function was originally conceived as a very general atmospheric distribution upon which a great variety of specific distributions have been based. The only real way in which this function can be used with accuracy for larger scattering particles (i.e. $r_p > 10\mu m$) is to reduce the value of "a". In practice this can only be achieved by working at a lower pressure in the measuring section and thereby lowering the concentrations of scattering particles.

(viii) The program developed as a design aid for the tracing of a gaussian beam through a lens system is not really satisfactory as a general tool. The precise physical effect of placing a surface in the path of a propagating laser beam needs to be analysed. One method of doing this would be to consider the beam as a series of wavefronts moving from the beam waist. By treating a number of discrete points on the wavefront as a point source of light then to each point can be applied the laws of refraction when incident upon a surface. Plotting out the wavefronts at discrete optical distances will trace the development and deformation

of the wavefronts as they move through a lens. This idea has, however, not been tried.

The list of further work is quite extensive but from an industrial viewpoint there is one aspect of further development which is very important. The development of a probe, using a laser source and fibre optics, is the next stage prior to making actual measurements in a turbine. High power fibre optic systems for LDA have been developed (52) and ideally fibre optic transmitters and receivers could be mounted into the hollow stationary (stator) blades of an experimental machine to make velocity measurements between the blade passages. It has been shown that the extinction encountered in a flow of wet steam containing coarse water droplets would be excessively high precluding the possibility of simply pointing the beams and detector into the wet steam flow. Results have shown that as small an optical depth as possible is desirable.

REFERENCES

1. ABRAMOWITZ, M., STEGUN, I.A. "Handbook of Mathematical Functions", ISBN: 486-61272-4, 1982.

2. ADRIAN, R.J., EARLEY, W.L., "Evaluation of LDV Performance using Mie Scattering Theory", Proceedings of the Minnesota Symposium for Laser Anemometry. University of Minnesota, 1976, pp. 426-454.

3. ATAKAN, M.S., JONES, A.R., "Measurement of Particle Size and Refractive Index using Crossed Beam Laser Anemometry", Journal of Physics D : Applied Physics 1982, Vol. 15, pp. 1-13.

4. BACHALO, W.D., "Method for Measuring the Size and Velocity of Spheres by Dual Beam Light-Scatter Interferometry", Applied Optics 1980, Vol. 19, No. 3, pp. 363-370.

5. BACHALO, W.D., HESS, C.F., HARTWELL, C.A., "An Instrument for Spray Droplet Size and Velocity Measurements", Transactions of the ASME, 1980, Vol. 102, pp. 798-806.

6. BORN, M., WOLF, E., "Principles of Optics", Pergamon Press, London 1959.

7. BRINKMAN, A.W. (1984), Private Communication, Department of Applied Physics and Electronics, University of Durham.

8. BUCHAVE, P., "Light Collecting System and Detector in a Laser Doppler Anemometer", DISA Information No. 15, Measurement and Analysis, Oct. 1973.

9. BURSCAGLIONI, P., ISMAELII, A., ZACCANTI, G., PANTAWI, C., "Modified Monte Carlo Method to Evaluate Multiple Scattering Effects on Lightbeam Transmission Through a Turbid Atmosphere", SPIE 1983, Vol. 369 Max Born, pp. 164-173.

10. CHANDRASEKHAR, S., "Radiative Transfer", Dover Publications, New York 1960.

11. CHIN, J.H., SLIEPCEVICH, C.M., TRIBUS, M., "Particle Size Distributions from Angular Variations of Intensity of Forward Scattered Light a very Small Angles", Journal of Physical Chemistry 1955, Vol. 59, pp. 841-847.

12. CHU, W.P., ROBINSON, D.M., "Scattering from a Moving Spherical Particle by two crossed coherent plane Waves", Applied Optics 1977, Vol. 16, No. 3, pp. 619-626.

13. COPSON, E.T., "An Introduction to the Theory of Functions of a Complex Variable", Oxford University Press 1935.

14. CRANE, R.I., MELLING, A., "Velocity measurement in Wet Steam Flows by Laser Anemometry and Pitot Tube", Journal of Fluids Engineering, March 1975, pp. 113.

15. DECUYPERE, R., ARTS, A., "Some Aspects Concerning the use of a Laser-Doppler Velocimeter in Steam Expanding at Supercritical Pressure Ratios". International Symposium on Applications of LDA to Fluid Mechanics - Conference Proceedings 1981, Lisbon, Portugal.

16. DEEPAK, A., "Computer Modelling of Laser Doppler Velocimeter (LDV) Systems and the Performance of CO_2-LDV in Fogs and Comparison with Experimental Results", Proceedings of the 2nd International Workshop on Laser Velocimetry, Purdue University 1974, Vol. 1.

17. DEEPAK, A., BOX, M.A., "Forward Scattering Corrections for Optical Extinction Measurements in Aerosol Media - 1:Monodispersions", Applied Optics 1978, Vol. 17, No. 18.

18. DEEPAK, A., BOX, M.A., "Forward Scattering Corrections for Optical Extinction Measurements in Aerosol Media - 2:Polydisperions", Applied Optics 1978, Vol. 17, No. 19.

19. DEEPAK, A., FARRUKH, U.O., ZARDECKI, A., "Significance of Higher Order Multiple Scattering for Laser Beam Propagation Through Hazes, Fogs and Clouds", Applied Optics, February 1982, Vol. 21, No. 3, pp. 439-447.

20. DEIRMENDJIAN, D., "Electromagnetic Scattering on Spherical Polydispersions", Elsevier Publications, New York 1969.

21. DICKSON, L.D., "Characteristics of a Propagating Gaussian Beam", Applied Optics 1970, Vol. 9, No. 8, pp. 1854-1861.

22. DOBBINS, R.A., "A Theory of the Wilson Line for Steam at Low Pressures", Transactions of the ASME, Vol. 105, December 1983, pp. 414-422.

23. DRAIN, L.E, "Coherent and Non-Coherent Methods in Doppler Optical Beat Velocity Measurement", Journal of Physics D: Applied Physics, Vol. 5, 1972, pp. 481-495.

24. DRAIN, L.E., "The Laser Doppler Technique", Wiley Publications 1980, ISBN 0-471-27627-8.

25. DURAO, D.F.G., WHITELAW, J.H., "Relationship Between Velocity and Signal Quality in Laser Doppler Anemometry", Journal of Physics E: Scientific Instruments 1979, Vol. 12, pp. 47-50.

26. DURRANI, T.S., GREATED, C.A., "Laser Systems in Flow Measurements", Plenum Press, New York 1977, ISBN: 0-306-30857-6.

27. DURST, F., RUCK, B., "Influence of Signal Detection and Signal Processing Electronics on Mean Property Measurements of LDA Frequencies", International Symposium on Applications of LDA to Fluid Mechanics - Conference Proceedings 1984, Lisbon, Portugal.

28. DURST, F., "Studies of Particle Motion by Laser Doppler Techniques", Proceedings of the Dynamic Flow Conference 1978.

29. DURST, F., "REVIEW - Combined Measurements of Particle Velocities, Size Distribution and Concentrations", Transactions of the ASME, Vol. 104, September 1982, pp. 284-295.

30. DURST, F., MELLING, A., WHITELAW, J.H., "Principles and Practice of Laser Doppler Anemometry", Academic Press, 2nd Edition, 1972.

31. DURST, F., STEVENSON, W.H., "Influence of Gaussian Beam Properties on Laser Doppler Signals", Applied Optics 1979, Vol. 18, No. 4, pp. 516-524.

32. DURST, F., WHITELAW, J.H., "Integrated Optical Units for Laser Anemometry", Journal of Physics E: Scientific Instruments, Vol. 4, 1971, pp. 804-808.

33. DURST, F., WHITELAW, J.H., "Light Source and Geometrical Requirements for the Optimization of Optical Anemometry Signals", Opto-Electronics, Vol. 5, 1973, pp. 137-151.

34. DURST, F., ZARE, M., "Bibliography of LDA Literature", Report SFB80/M/44, Nov. 1974, Sonderforschungsbereich 80, Universitat Karlsruhe, West Germany.

35. FARMER, W.M., "Measurement of Particle Size, Number Density and Velocity using a Laser Interferometer", Applied Optics, Vol. 11, No. 11, November 1972, pp. 2603-2611.

36. FOSTER, S.J. "LDA in Wet Steam Turbines - Design of Optical System", Report, Department of Engineering, University of Durham, August 1983.

37. FOSTER, S.J., KING, C.F., "Some Predictions of the Laser Power Requirements for Making Measurements of Droplet Velocity in a Wet Steam Flow", Applications of LDA Counter Systems, LDA Counter Users Group, University of Durham, December 1983.

38. FOSTER, S.J., KING, C.F., "Using the Theory of the Propagation of Gaussian Beams to Design a Dedicated Optical System", Applications of LDA Counter Systems, LDA Counter Users Group, University of Durham, December 1983.

39. FOSTER, S.J., "The Determination of the Multiple Scattering of Radiation by the Doubling Method", Report, Department of Engineering, University of Durham, September 1984.

40. FOSTER, S.J., "Using the Mie Theory to Make Some Predictions of the Minimum Laser Power Requirements for Making Measurements in Wet Steam", Report, Department of Engineering, University of Durham, September 1984.

41. FOSTER, S.J., KING, C.F., "Signal-to-Noise Ratio of LDA Signals Obtained in Two Phase Flows", Paper to be presented at the International Conference on Laser Anemometry - Advances and Applications, University of Manchester, December 1985.

42. FOWLES, G.R., "Introduction to Modern Optics", Holt, Reinhardt and Winston, New York, 1968.

43. GARDAVSKY, J., BOK, J., "Scattering of Circularly Polarised Light in Laser Doppler Anemometry", Applied Optics, 1982, Vol. 21, No. 1, pp. 158-165.

44. GOLDSCHMIDT, V.W., "Measurements in Two Phase Flow", Proceedings of the Dynamic Flow Conference 1978, pp. 289-319.

45. GRADSHTEYN, I.S., RYZHIK, I.M., "Tables of Integrals, Series and Products, Corrected and Enlarged Edition", Academic Press, New York, 1980.

46. GUCKER, F.T., EGAN, J.J., "Measurement of the Angular Variation of Light Scattered from Single Aerosol Droplets", Journal of Colloidal Science, 1961, Vol. 16, pp 68-84.

47. GYARMATHY, G., LESCH, F., "Fog Droplet Observations in Laval Nozzles and in an Experimental Turbine", Proceedings of the Institute of Mechanical Engineers 1969-70, Vol. 184, Pt. 3G(iii), Paper 12.

48. HANSEN, J.E, "Radiative Transfer by the Doubling of Very Thin Layers", The Astrophysical Journal 1969, Vol. 155.

49. HONG, N.S., JONES, A.R., "Light Scattering by Particles in Laser Doppler Velocimeters Using Mie Theory", Applied Optics 1976, Vol. 15, No. 12, pp. 2951-2953.

50. HULST van de, H., "Light Scattering by Small Particles", John Wiley & Sons, New York, 1957.

51. IRVINE, W.M., "Multiple Scattering by Large Particles - II. Optically Thick Layers", The Astrophysical Journal, 1968, Vol. 152, pp. 823-834.

52. JACKSON, D.A, JONES, J.D.C., CHANN, R.K.Y., "A High Power Fibre-Optic Laser Doppler Velocimeter", Journal of Physics E: Scientific Instruments, Vol. 17, 1984, pp. 977-980.

53. JONES, A.R., "Light Scattering by a Sphere Situated in an Interference Pattern, with Relevance to Fringe Anemometry and Particle Sizing", Journal of Physics D: Applied Physics 1974, Vol. 7, pp. 1369-1376.

54. KERKER, M., "The Scattering of Light and Other Electromagnetic Radiation", Acadmic Press, New York, 1969.

55. KOGELNIK, H., LI, T., "Laser Beams and Resonators", Applied Optics, 1966, Vol. 5, No. 10.

56. KONIUTA, A., DUDERMEL, M.T., ADLER, P.M., "A Laser Doppler Anemometer with Microscopic Intersection Volume", Journal of Physics E: Scientific Instruments, Vol. 12, 1979.

57. LADING, L., "Analysis of the Signal-to-Noise Ratio of the Laser Doppler Velocimeter", Opto-Electronics 5, 1973, pp. 175-187.

58. LANGDON, P., Private Communication. Chief Aerodynamicist, Holset Engineering, Huddersfield, England.

59. LIOU, Kuo-Non, "An Introduction to Atmospheric Radiation", Academic Press, New York, 1980.

60. McALLISTAIR, D.H., "Visibility Through Wet Steam", Technical Memorandum No. LP68-16, 1968, NEI Parsons Ltd., Heaton Works, Newcastle upon Tyne, NE6 2YL.

61. McALLISTAIR, D.H., "Measurement of Steam Wetness and Droplet Diameter in HP Wet Steam Experimental Turbine using Light Extinction Techniques", Technical Memorandum No. ME 72-242, 1972, NEI Parsons Ltd., Heaton Works, Newcastle upon Tyne, NE6 2YL.

62. McALLISTAIR, D.H., "Steam Wetness in Experimental HP Wet Steam Turbine, Determined by Optical Extinction Method", Technical Memorandum No. ME 73-97 1973, NEI Parsons Ltd., Heaton Works, Newcastle upon Tyne, NE6 2YL.

63. McALPINE, R., (1982), Private Communication, Chief Electrical Engineer, THORN-EMI Electron Tubes Ltd., Ruislip, Middlesex.

64. McCARTNEY, E.J., "Optics of the Atmosphere", Wiley Publications, 1976, ISBN 0-471-01526-1.

65. MEYERS, J.F., WALSH, M.J., "Computer Simulation of a Fringe Type Laser Velocimeter", Proceedings of the 2nd International Workshop on Laser Velocimetry, Purdue University 1974, Vol. I, pp. 471-510.

66. MIDDLETON, W.E.K., "Vision Through the Atmosphere", University of Toronto Press, 1952.

67. MILLER, D.S., "Internal Flow Systems", Vol. 5 in the BHRA Fluid Engineering Series, 1978, ISBN: 0-900983-78-7.

68. MOORE, M.J., LANGFORD, T.W., TIPPING, J.C., "Wet Steam Research at CERL on Turbine Blade Erosion", Wet Steam Conference 2, Bristol 1968, pp. 1-8.

69. MOORE, M.J., SCULPHER, P., "Conditions Producing Concentrated Erosion in Large Steam Turbines", Proceedings of the Institution of Mechanical Engineers 1969-70, Vol. 184, Pt. 3G(iii), p. 45.

70. MOORE, M.J., WALTERS, P.T., CRANE, R.I., DAVIDSON, B.J., "Predicting the Fog-Drop Size in Wet Steam Turbines", Paper C37/73, Conference Publication 3, Institution of Mechanical Engineers, London 1973.

71. MOORE, M.J., SIEVERDING, C.H., "Two-Phase Flow in Turbines and Separators", Theory, Instrumentation, Engineering, Hemisphere Publishing Corporation, 1976, ISBN 0-07-042992-8.

72. NEGUS, C.R., DRAIN, L.E., "Mie Calculations of the Scattered Light from a spherical particle traversing a fringe pattern produced by two intersecting Light Beams", Journal of Physics D: Applied Physics 1982, Vol. 15, pp. 375-402.

73. OW, C.S., CRANE, R.I., "On the Critical Weber Number for Coarse Water Formation in Steam Turbines", Journal of Mechanical Engineering Science, 1979, Vol. 21, No. 5, pp. 353-356.

74. PENNDORF, R.B., "New Tables of Total Mie Scattering Coefficients for Spherical Particles of Real Refractive Indexes ($1.33 \leqslant n \leqslant 1.50$)", Journal of the Optical Society of America, Nov. 1957, Vol. 47, No. 11.

75. PETR, V., "Measurement of an Average Size and Number of Droplets During Spontaneous Condensation of Supersaturated Steam", Proceedings of the Institute of Mechanical Engineers, 1969-70, Vol. 184, Pt. 3G(iii), Paper 10.

76. POOLE, L.R., VENABLE, D.D., CAMBELL, J.W., "Semianalytic Monte Carlo Radiative Transfer Model for Oceanographic Lidar System", Applied Optics, 1981, Vol. 20, No. 20, pp. 3653-3656.

77. RYLEY, C.J., "Condensation Fogs in Low Pressure Steam Turbines", International Journal of Mechanical Science, Pergamon Press Ltd., 1967, Vol. 9, pp. 729-741.

78. SOMM, E., "A Means of Estimating the Erosion Hazard in Low Pressure Steam Turbines", Brown Boveri Review No. 10, 1971.

79. STEAM TABLES IN SI UNITS (U.K.) 1970, Arnold Publishers Ltd., London, ISBN: 0-7131-3239-6.

80. TABLES OF SCATTERING FUNCTIONS FOR SPHERICAL PARTICLES, National Bureau of Standards - Applied Mathematics Series 4, US Government Printing Office, Washington, 1948.

81. TAM, W G., "Multiple Scattering Corrections for Atmospheric Aerosol Extinction Measurements", Applied Optics, 1980, Vol. 19, No. 13.

82. TAM, W.G., "Aerosol Backscattering of a Laser Beam", Applied Optics, 1983, Vol. 22, No. 19, pp. 2964-2968.

83. TRIDIMAS, Y., LALOR, M.J, WOOLLEY, N.H., "Beam Waist Location and Measurement in a Dual-Beam Laser Doppler Anemometer",Journal of Physics E: Scientific Instruments, 1978, Vol. 11.

84. TRIDIMAS, Y., LALOR, M.J., WOOLLEY, N.H., "Criteria for Achieving coincidence of beam waist and crossover region in a Dual Beam Laser Doppler Anemometer", Journal of Physics E: Scientific Instruments, 1979, Vol. 12.

85. WALTERS, P.T., "Optical Measurements of Water Droplets in Wet Steam Flows", Paper C32/73, Conference Publication 3, Institution of Mechanical Engineers, London, 1973.

86. WALTERS, P.T., SKINGLEY, P.C., "An Optical Instrument for Measuring the Wetness Fraction and Droplet Size of Wet Steam Flows in LP Turbines", Paper C141/79, Design Conference on Steam Turbines for the 1980's.

87. WIGLEY, G., "The Sizing of Large Droplets by Laser Anemometry", Journal of Physics E : Scientific Instruments, 1978, Vol. 11, pp. 639-643.

88. WILLIAMS, G.J., GREGORY, B., LORD, M.J., "Instrumentation for Wet Steam Measurements" Sixth Thermodynamics and Fluid Mechanics Convention", Institution of Mechanical Engineers, University of Durham, 1976.

89. WITTIG, S.L.K., STEVENSON, W.H., WHIRLOW, D.K., STEWART, W.A., "Laser Doppler Studies in the Westinghouse Steam Cascade", Proceedings of the 2nd International Workshop on Laser Velocimetry, Purdue University, March 1974, Vol. II, pp. 182-198.

90. WOOD, B., "Wetness in Steam Cycles", Proceedings of the Institution of Mechanical Engineers, 1960, Vol. 174, No. 14, pp. 491-570.

91. YARIV, A., "An Introduction to Optical Electronics", Holt, Reinhardt & Winston, 1976, 2nd edition.

92. YOUNG, J.B., "Critical Conditions and the Choking Mass Flow Rate in Nonequilibrium Wet Steam Flows", Transactions of the ASME, December 1984, Vol. 106.

93. ZARDECKI, A., GERSTL, S.A.W., EMBURY, J.F., "Application of the 2-D Discrete-Ordinates Method to Multiple Scattering of Laser Radiation, Applied Optics 1983, Vol. 22, No. 9, pp. 1346-1352.

APPENDIX A - LISTING OF PROGRAM "TSCAT"

```
C     PROGRAM CALCULATES THE SCATTERING PHASE FUNCTIONS FOR ANY
C     POLYDISPERSE AEROSOL. (The computer algorithm presented by
C     Deirmendjian is used to manipulate the Mie functions)
C
      REAL TH(96),THE(96),W(96),PP(96,51),LCOEF(5,51),SCAT(5,96),
     &ANUM(999),AKEX(999),AKSC(999),ASYM(999),KSC,KEX,I1,I2,I3,I4,
     &ITHETA,MODEL(2)
      COMPLEX A(200),B(200)
      REWIND 4
C
      CALL INST(ACOEF,BCOEF,ALPHA,GAMMA,RIR,RII,WAVL,X1,DX,X2,MODEL)
C
      PI = 2.0*ACOS(0.0)
      DO 29 III=1,96
      READ(4,*) TH(III)
   29 CONTINUE
      DO 31 III=1,48
      THE(III) = TH(49-III)
      THE(48+III) = -TH(III)
      W(III) = TH(97-III)
      W(III+48) = TH(III+48)
   31 CONTINUE
      Z = WAVL**3/8.0/PI/PI
      DXINV = 1.0/DX
      WAVLPI = WAVL/2.0/PI
      IS = X1*DXINV+.0001
      IE = X2*DXINV+.001
      BASYM = 0.0
C      Calculate the size parameter range.....
      DO 40 IXI=1,96
      ITHETA = ACOS(THE(IXI))
      P1 = 0.0
      P2 = 0.0
      P3 = 0.0
      P4 = 0.0
      BSC = 0.0
      BEX = 0.0
      DO 30 I=IS,IE
      X = I
      X = X*DX
C      Calculate the MIE coefficients An & Bn .....
      CALL CROSSS(RIR,RII,X,KSC,KEX,N,A,B)
C      Calculate the intensity for any state of polarization.....
      CALL INTENS(A,B,N,ITHETA,I1,I2,I3,I4)
C      Calculate number concentration of each particle size.....
      R = X*WAVLPI
      RNX = ACOEF*R**ALPHA*EXP(-BCOEF*R**GAMMA)*DX/1000.0
      ANUM(I) = RNX*10000.0
      P1 = P1 + I1*RNX
      P2 = P2 + I2*RNX
      P3 = P3 + I3*RNX
      P4 = P4 + I4*RNX
      RX = Z*X*X*RNX
      BSC = BSC + KSC*RX
      BEX = BEX + KEX*RX
   30 CONTINUE
```

```
      SCAT(1,IXI) = ITHETA
      ZPIBSC = Z/PI/BSC
      SCAT(2,IXI) = ZPIBSC*P1
      SCAT(3,IXI) = ZPIBSC*P2
      SCAT(4,IXI) = ZPIBSC*P3
      SCAT(5,IXI) = ZPIBSC*P4
      OMEGA = BSC/BEX
      BASYM = BASYM + COS(ITHETA)*SIN(ITHETA)*(P1+P2)/
     &ZPIBSC/4.0*W(IXI)
   40 CONTINUE
C      Generate the angular coefficients using Legendre polynomials.....
      DO 79 II=1,96
      PP(II,1) = 1.0
      PP(II,2) = THE(II)
      DO 79 NN=3,51
      NN1 = NN-1
      NN2 = NN-2
      PP(II,NN) = (2.0*NN - 3.0)*THE(II)*PP(II,NN1)
      PP(II,NN) = PP(II,NN) - (NN-2.0)*PP(II,NN2)
      PP(II,NN) = PP(II,NN)/FLOAT(NN1)
   79 CONTINUE
      DO 83 IN=2,5
      DO 83 NN=1,51
      LCOEF(IN,NN) = 0.0
      DO 84 II=1,96
      LCOEF(IN,NN) = LCOEF(IN,NN) + W(II)*PP(II,NN)*SCAT(IN,II)
   84 CONTINUE
      LCOEF(IN,NN) = LCOEF(IN,NN) * (2.0*NN-1.0)/2.0
   83 CONTINUE
      DO 95 NN=1,51
      ALC = 0.0
      DO 96 II=1,96
      SCA = (SCAT(2,II)+SCAT(3,II))/2.0
      ALC = ALC + W(II)*PP(II,NN)*SCA
   96 CONTINUE
      LCOEF(1,NN) = ALC*(2.0*NN-1.0)/2.0
   95 CONTINUE
      DO 32 I=IS,IE
      X = I
      X = X*DX
C
      CALL CROSSS(RIR,RII,X,AKSC(I),AKEX(I),N,A,B)
      CALL ASSYM(AKSC(I),N,A,B,ASYM(I),X)
C
   32 CONTINUE
C
      AA=ACOEF
      BB=BCOEF
C
C      Plot out the phase function and corresponding number.....
      CALL GRAF(SCAT,MODEL,RIR,RII,WAVL,AA,BB,ALPHA,GAMMA,X1,DX,X2,
     &IS,IE,ANUM,WAVLPI)
C
      CALL DSTORE(IS,IE,X1,X2,DX,MODEL,WAVL,RII,RIR,LCOEF,
     &SCAT,AKEX,AKSC,ASYM,BEX,BSC,OMEGA,BASYM)
C
      STOP
      END
C
C
```

```
      SUBROUTINE INST(A,B,ALPHA,GAMMA,RIR,RII,WAVL,X1,DX,X2,MODEL)
      REAL MODEL(2),ALP(10),GAM(10),AM(10),BM(10),M(11,2)
      DATA ALP/1.0,1.0,2.0,2.0,2.0,2.0,6.0,8.0,8.0,8.0/
      DATA GAM/0.5,0.5,0.5,0.5,1.0,1.0,1.0,3.0,3.0,3.0/
      DATA AM/5.3333E4,5.3333E5,4.9757E6,4.9757E7,4.0E5,
     &4.0E4,2.373,1.0851E-2,5.5556,5.5556/
      DATA BM/8.9443,8.9443,15.1186,15.1186,20.0,20.0,1.5,
     &0.0416667,0.333333,0.333333/
      DATA M(1,1),M(1,2),M(2,1),M(2,2),M(3,1),M(3,2),M(4,1),
     &M(4,2),M(5,1),M(5,2)/
     &4HHAZE,4H M  ,4HRAIN,4H M  ,4HHAZE,4H L  ,4HRAIN,4H L
     &,4HHAZE,4H H  /
      DATA M(6,1),M(6,2),M(7,1),M(7,2),M(8,1),M(8,2),M(9,1),
     &M(9,2),M(10,1)
     &,M(10,2)/4HHAIL,4H H  ,4HCLOU,4HD C1,4HCLOU,4HD C2,
     &4HCLOU,4HD C3,4HCLOU,4HD C4/
      DATA M(11,1),M(11,2)/4HGAMM,4HA   /
      WRITE(6,100)
    1 READ(5,101) MODEL(1),MODEL(2)
      DO 2 I=1,11
      IF (MODEL(1) .NE. M(I,1) .OR. MODEL(2) .NE. M(I,2)) GO TO 2
      IF (I .EQ. 11) GO TO 4
      A = AM(I)
      B = BM(I)
      ALPHA = ALP(I)
      GAMMA = GAM(I)
      GO TO 3
    2 CONTINUE
      WRITE(6,102)
      GO TO 1
    3 WRITE(6,103)
      READ(5,*) X1,DX,X2
      WRITE(6,104)
      READ(5,*) WAVL
      WRITE(6,105)
      READ(5,*) RIR,RII
      RETURN
    4 WRITE(6,106)
      READ(5,*) A,B,ALPHA,GAMMA
      GO TO 3
  100 FORMAT('SCATTERING PHASE FUNCTIONS PROGRAM.',/,
     &'INPUT TYPE OF MODEL')
  101 FORMAT(2A4)
  102 FORMAT('MISTAKE: TRY AGAIN.')
  103 FORMAT('INPUT: SIZE PARAMETER LIMITS ; X1,DX,X2')
  104 FORMAT('INPUT: WAVELENGTH IN MICRONS.')
  105 FORMAT('INPUT: REAL & IMAG.PARTS OF REFRACTIVE INDEX.')
  106 FORMAT('INPUT: A,B,ALPHA & GAMMA.')
      END
C
C
      SUBROUTINE CROSSS(RE,IM,X,KSC,KEX,N,A,B)
      REAL RE,IM,KEX,KSC,IWN,IWNM1,IWNM2
      COMPLEX M,ANM1,AN,CA,CB
      COMPLEX A(200),B(200)
      KEX = 0.0
      KSC = 0.0
      M = CMPLX(RE,-IM)
C      Generate the circular functions to give the
C      BESSEL functions for any real argument.....
```

```
      ANM1 = CCOS(M*X)/CSIN(M*X)
      RWNM2 = COS(X)
      IWNM2 = -SIN(X)
      RWNM1 = -IWNM2
      IWNM1 = RWNM2
      XSQ = X*X
      DO 10 N=1,200
      QQ = (2.0*N - 1.0)/X
      RWN = QQ*RWNM1 - RWNM2
      IWN = QQ*IWNM1 - IWNM2
      XN = N/X
      AN = -XN/M + 1.0/(XN/M - ANM1)
      CA = AN/M + XN
      CB = AN*M + XN
C      Compute the MIE coefficients An & Bn .....
      A(N) = (CA*RWN-RWNM1)/(CA*CMPLX(RWN,IWN)-CMPLX(RWNM1,IWNM1))
      B(N) = (CB*RWN-RWNM1)/(CB*CMPLX(RWN,IWN)-CMPLX(RWNM1,IWNM1))
      ANM1 = AN
      RWNM2 = RWNM1
      IWNM2 = IWNM1
      RWNM1 = RWN
      IWNM1 = IWN
      TT = (4.0*N + 2.0)/XSQ
      TSC = TT*(CABS(A(N))*CABS(A(N)) + CABS(B(N))*CABS(B(N)))
      TEX = TT*REAL(A(N)+B(N))
      KSC = KSC+TSC
      KEX = KEX+TEX
      IF(ABS(TSC/KSC) .LT. 1E-10 .AND. ABS(TEX/KEX) .LT. 1E-10
     &.AND. N .GT. 10) RETURN
   10 CONTINUE
      RETURN
      END
C
C
      SUBROUTINE INTENS(A,B,N,ITHETA,I1,I2,I3,I4)
      REAL I1,I2,I3,I4,ITHETA
      COMPLEX A(200),B(200)
      COMPLEX S1,S2,SC2
      THETA = ITHETA
      PI0 = 0.0
      PI1 = 1.0
      T0 = 0.0
      CT = COS(THETA)
      T1 = CT
      ST = SIN(THETA)
      S1 = 1.5*(A(1)*PI1 + B(1)*T1)
      S2 = 1.5*(B(1)*PI1 + A(1)*T1)
      DO 20 L=2,N
      R = L
      PI = (2.0*R - 1.0)/(R-1.0) * CT * PI1 - PI0*R/(R-1.0)
      T = CT*(PI-PI0) - (2.0*R - 1.0)*ST*ST*PI1 + T0
      ZZ = (2.0*R + 1.0)/R/(R+1.0)
      S1 = S1 + ZZ*(A(L)*PI + B(L)*T)
      S2 = S2 + ZZ*(B(L)*PI + A(L)*T)
      PI0 = PI1
      T0 = T1
      PI1 = PI
      T1 = T
   20 CONTINUE
      SC2 = CONJG(S2)
```

```
      I1 = REAL(S1*CONJG(S1))
      I2 = REAL(S2*SC2)
      I3 = REAL(S1*SC2)
      I4 = -AIMAG(S1*SC2)
      RETURN
      END


      SUBROUTINE ASSYM(KSC,N,A,B,ASYM,X)
      REAL KSC
      COMPLEX A(200),B(200)
      ASYM = 0.0
      N1 = N-1
      DO 30 I=1,N1
      R = I
      II1 = I+1
      ASYM = ASYM + (R*(R+2.0)/(R+1.0)*REAL(A(I)*CONJG(A(II1))
     &+ B(I)*CONJG(B(II1))) + (2.0*R + 1.0)/R/(R+1.0) * REAL(A(I)
     &*CONJG(B(I))))
   30 CONTINUE
      ASYM = ASYM * 4.0/X/X/KSC
      RETURN
      END


      SUBROUTINE GRAF(SCAT,MODEL,RIR,RII,WAVL,A,B,ALPHA,GAMMA,X1,DX,X2,
     &IS,IE,NUM,WAVLPI)
      REAL NUM(999),PF(96),SCAT(5,96),MODEL(2),RADIUS(999)
      REAL LOGNUM(999)
      PI = 4.0*ATAN(1.0)
      DO 1 I=1,96
      PF(I) = (SCAT(2,I)+SCAT(3,I))/2.0
    1 CONTINUE
      CALL PAPER(1)
      CALL PSPACE(0.15,0.9,0.2,0.95)
      YMIN = PF(1)
      YMAX = PF(1)
      DO 20 I=2,96
      IF (PF(I) .LT. YMIN) YMIN = PF(I)
      IF (PF(I) .GT. YMAX) YMAX = PF(I)
   20 CONTINUE
      Y = 10**(FLOAT(INT(ALOG10(ABS(YMIN)))))
      IF (YMIN .LT. 1.0) Y = Y/10.0
      YMIN = Y
      Y = 10**(FLOAT(INT(ALOG10(ABS(YMAX)))))
      IF (YMAX .GT. 1.0) Y = Y*10.0
      YMAX = Y
      CALL MAPYL(0.0,180.0,YMIN,YMAX)
      CALL SCAYLI(20.0)
      CALL BORDER
      X = SCAT(1,1)*180.0/PI
      CALL POSITN(X,PF(1))
      DO 2 I=2,96
      X = SCAT(1,I)*180.0/PI
      CALL JOIN(X,PF(I))
    2 CONTINUE
      CALL PSPACE(0.05,0.9,0.05,0.2)
      CALL MAP(0.0,10.0,0.0,2.0)
      CALL CTRSIZ(0.2)
      CALL CTRSLP(100.0)
```

```
      CALL POSITN(0.05,5.0)
      CALL TYPECS('PHASE FUNCTION P(cosO)',22)
      CALL CTRSLP(0.0)
      CALL POSITN(0.2,0.78)
      CALL TYPECS('SCATTERING PHASE FUNCTION. - ',29)
      CALL TYPECS(MODEL(1),4)
      CALL TYPECS(MODEL(2),4)
      CALL CTRSIZ(0.14)
      CALL POSITN(0.2,0.35)
      CALL TYPECS('REF.INDEX =  ',13)
      CALL TYPENF(RIR,3)
      CALL TYPECS(' + j',4)
      CALL TYPENF(RII,3)
      CALL POSITN(4.8,0.35)
      CALL TYPECS('WAVELENGTH = ',13)
      CALL TYPENF(WAVL,3)
      CALL TYPECS(' ',1)
      CALL CTRFNT(2)
      CALL TYPENC(109)
      CALL CTRFNT(1)
      CALL TYPECS('m',1)
      CALL CTRFNT(1)
      CALL POSITN(0.2,0.0)
      CALL TYPECS('LIMITS:X1,DX,X2; ',17)
      CALL TYPENF(X1,2)
      CALL TYPECS(',',1)
      CALL TYPENF(DX,3)
      CALL TYPECS(',',1)
      CALL TYPENF(X2,2)
      CALL POSITN(4.8,0.0)
      CALL TYPECS('A,B,ALPHA,GAMMA= ',17)
      CALL TYPENE(A,3)
      CALL TYPECS(',',1)
      CALL TYPENF(B,3)
      CALL TYPECS(',',1)
      CALL TYPENF(ALPHA,3)
      CALL TYPECS(',',1)
      CALL TYPENF(GAMMA,2)
      CALL CTRSIZ(0.2)
C
C      NOW PLOT OUT THE ACTUAL GAMMA DISTRIBUTION.....
C      (Number density against particle radius)
      CALL FRAME
C
      DO 100 I=IS,IE
      X=FLOAT(I)*DX
      RADIUS(I)=X*WAVLPI
  100 CONTINUE
C
C      NOW FIND THE MINIMUM AND MAXIMUM VALUES OF ARRAYS "NUM" AND
C      "RADIUS".....
C
      N=(IE-IS)+1
      IS2=1
      IE2=N
      CALL MINMAX(RADIUS,IS,IE,RMIN,RMAX)
C
      DO 110 I=IS,IE
      XVAL=NUM(I)
      IF(XVAL.LE.1.0) GO TO 113
```

```
      GO TO 114
  113 LOGNUM(I)=0.0
      GO TO 110
  114 LOGNUM(I)=ALOG(XVAL)/ALOG(10.0)
  110 CONTINUE
C
      CALL MINMAX(LOGNUM,IS,IE,YMIN,YMAX)
      YNEW=YMIN+1.0
      YMAX=YMAX+2.0
      CALL PSPACE(0.15,0.9,0.23,0.95)
      CALL MAPXL(0.1,600.0,YMIN,YMAX)
      CALL SCAXLI(1.0)
      CALL BORDER
      YMIN=3.0
      CALL WINDOW(RMIN,RMAX,YNEW,YMAX)
      XP=RADIUS(IS)
      YP=LOGNUM(IS)
      ISS=IS+1
      DO 119 I=ISS,IE
      II=ISS-IS+1
      XP=RADIUS(I)
      YP=LOGNUM(I)
      CALL JOIN(XP,YP)
  119 CONTINUE
      CALL WINDOW(RMIN,RMAX,YMIN,YMAX)
C
C      NOW LABEL THE AXES.....
      CALL PSPACE(0.05,0.9,0.1,0.95)
      CALL MAP(0.0,1.0,0.0,1.0)
      CALL CTRSLP(100.0)
      CALL CTRMAG(16)
      CALL POSITN(0.05,0.4)
      CALL TYPECS('LOG.',4)
      CALL SUFFIX
      CALL TYPECS('10',2)
      CALL NORMAL
      CALL TYPECS(' PART. CONCENTRATION (',22)
      CALL SUFFIX
      CALL TYPECS('-3',2)
      CALL NORMAL
      CALL TYPECS(')',1)
      CALL CTRSLP(0.0)
      CALL PSPACE(0.1,0.9,0.05,0.2)
      CALL MAP(0.0,10.0,0.0,2.0)
      CALL CTRSIZ(0.2)
      CALL POSITN(0.2,0.78)
      CALL TYPECS('PART. DISTRIB. - ',17)
      CALL TYPECS(MODEL(1),4)
      CALL TYPECS(MODEL(2),4)
      CALL POSITN(6.5,0.78)
      CALL TYPECS('PART. RADIUS (',14)
      CALL CTRFNT(2)
      CALL TYPENC(109)
      CALL CTRFNT(1)
      CALL TYPECS('m)',2)
      CALL CTRSIZ(0.13)
      CALL POSITN(0.2,0.35)
      CALL TYPECS('REF.INDEX =  ',13)
      CALL TYPENF(RIR,3)
      CALL TYPECS(' + j',4)
```

```
      CALL TYPENF(RII,3)
      CALL POSITN(4.85,0.35)
      CALL TYPECS('WAVELENGTH = ',13)
      CALL TYPENF(WAVL,3)
      CALL TYPECS(' ',1)
      CALL CTRFNT(2)
      CALL TYPENC(109)
      CALL CTRFNT(1)
      CALL TYPECS('m',1)
      CALL CTRFNT(1)
      CALL POSITN(0.2,0.0)
      CALL TYPECS('LIMITS:X1,DX,X2; ',17)
      CALL TYPENF(X1,2)
      CALL TYPECS(',',1)
      CALL TYPENF(DX,3)
      CALL TYPECS(',',1)
      CALL TYPENF(X2,2)
      CALL POSITN(4.85,0.0)
      CALL TYPECS('A,B,ALPHA,GAMMA= ',17)
      CALL TYPENE(A,3)
      CALL TYPECS(',',1)
      CALL TYPENF(B,3)
      CALL TYPECS(',',1)
      CALL TYPENF(ALPHA,3)
      CALL TYPECS(',',1)
      CALL TYPENF(GAMMA,2)
      CALL GREND
      RETURN
      END
C
C
      SUBROUTINE MINMAX(A,IS,IE,XMIN,XMAX)
      DIMENSION A(IE)
      XMIN=A(IS)
      XMAX=A(IS)
      IS2=IS+1
      DO 10 I=IS2,IE
      IF(A(I).LT.XMIN) XMIN=A(I)
      IF(A(I).GT.XMAX) XMAX=A(I)
   10 CONTINUE
      RETURN
      END
C
C
      SUBROUTINE DSTORE(IS,IE,X1,X2,DX,MODEL,WAVL,RII,RIR,LCOEF,
     &SCAT,KEX,KSC,ASYM,BEX,BSC,OMEGA,BASYM)
C
C      STORES DATA ON FILE 2.
C
      REAL LCOEF(5,51),SCAT(5,96),KEX(999),KSC(999),ASYM(999),MODEL(2)
      REWIND 2
      WRITE(2,100) MODEL(1),MODEL(2),RIR,RII,WAVL
      WRITE(2,101) X1,DX,X2,BEX,BSC,BASYM,OMEGA
      DO 1 I=1,96
      WRITE(2,*)(SCAT(J,I),J=1,5)
    1 CONTINUE
      WRITE(2,102)
      DO 2 I=1,51
      WRITE(2,*)(LCOEF(J,I),J=1,5)
    2 CONTINUE
```

```
      WRITE(2,103)
      DO 3 I=IS,IE
      WRITE(2,*) KEX(I),KSC(I),ASYM(I)
    3 CONTINUE
      RETURN
  100 FORMAT('SINGLE PARTICLE SCATTERING DATA FOR ',2A4,/,
     &'REFRACTIVE INDEX = ',F8.5,' + J',F8.5,/,
     &'WAVELENGTH = ',F6.3)
  101 FORMAT('X1,DX,X2 = ',3F9.4,/,'BULK.PAR. EXT.,SCAT.,ASYM.,'
     &'& SCAT.ALB. = ',4G15.6,/,'SCAT.ARRAY.')
  102 FORMAT('LEGENDRE COEFFICIENTS.')
  103 FORMAT('SINGLE PARTICLE SCATTERING CHARACTERISTICS.',/,
     &'EXT.EFF.,SCAT.EFF., & ASSYM.')
      END
```

APPENDIX B

The form of the distribution function

A family of distribution functions are chosen having the general form:

$$n(r) = a r_p^{\alpha_d} \exp\left(-b r_p^{\gamma}\right) \qquad \text{(B.1)}$$

This function vanishes as r=0 and r=∞. It is referred to as the modified Gamma distribution in analogy with the so called Gamma distribution to which it reduces when $\gamma = 1$. The four constants, a, α_d, b and γ are positive and real. They are not independent of each other and are related to quantities in a given frequency distribution which can be determined by measurements.

Basically the constants may be defined as follows:

a is a scaling coefficient

r is the particle radius

α_d is a factor controlling the narrowness of the distribution. The larger the value of α_d, the narrower the distribution.

γ controls the skewness. Typically $\gamma = 3$ for a symmetric distribution.

and

$b = \alpha_d / \gamma r_p^{\gamma}$ where rp is mode particle radius .

To find the constant of the Gamma distribution

B.1 To find γ

Two radii either side of rp at which n(rp) is the same are chosen. If those radii are r_1 such that $r_1 > rp$ and r_2

where $r_2 < r_p$ then the condition to be fulfilled is given by

$$n(r_1) = n(r_2) \tag{B.2}$$

On substituting for n(r) from equation (B.1) gives:

$$n(r_1) = a r_1^{\alpha_d} \exp(-b r_1^{\gamma}) = a r_2^{\alpha_d} \exp(-b r_2^{\gamma}) = n(r_2)$$

Now divide through by a and take natural logs whence

$$\alpha \ln r_1 - b r_1^{\gamma} = \alpha \ln r_2 - b r_2^{\gamma}$$

$$\therefore \alpha \ln(r_1/r_2) = b(r_1^{\gamma} - r_2^{\gamma}) \tag{B.3}$$

Differentiating equation (B.1) with respect to r yields:

$$\frac{d}{dr} n(r) = a r^{\alpha_d - 1} (\alpha_d - \gamma b r^{\gamma}) \exp(-b r^{\gamma}) \tag{B.4}$$

which has three zeros at r=0 (for $\alpha_d > 1$) and at $r=\infty$. If $\alpha_d = 1$, the derivative at the origin is equal to a. The third and important zero is found by putting the last factor in equation (B.4) equal to zero. This determines the absolute maximum value of the function. Thus it is required that:

$$(\alpha_d - \gamma b r^{\gamma}) \exp(-b r^{\gamma}) = 0$$

$$\therefore b = \frac{\alpha_d}{\gamma r_p^{\gamma}} \tag{B.5}$$

Now substitute equation (B.5) for b in equation (B.3) to give

$$\alpha_d \ln(r_1/r_2) = \frac{\alpha_d}{\gamma r_p^{\gamma}} \cdot (r_1^{\alpha_d} - r_2^{\alpha_d})$$

or

$$\ln(r_1/r_2) = \frac{1}{\gamma} \frac{(r_1^{\gamma} - r_2^{\gamma})}{r_p^{\gamma}}$$

rearranging

$$\frac{1}{\ln(r_1/r_2)} = \frac{\gamma}{(r_1/r_p)^{\gamma} - (r_2/r_p)^{\gamma}} \qquad \text{(B.6)}$$

This is solved by trial and error basically but typically $\lambda=3$ for a symmetrical distribution.

B.2 To find α

The ratio $n(r_1)/n(rp)$ is required. α is essentially a measure of how sharp the Gamma distribution is.

Let $$\frac{n(r_p)}{n(r_1)} = R$$

on substitution from equation (B.1) gives

$$R = \frac{r_p^{\alpha_d} \exp(-b r_p^{\gamma})}{r_1^{\alpha_d} \exp(-b r_1^{\gamma})}$$

$$= (r_p/r_1)^{\alpha_d} \exp\left[b(r_1^{\gamma} - r_p^{\gamma})\right]$$

and on substitution for b from equation (B.5) gives

$$R = (r_p/r_1)^{\alpha_d} \exp\left[\frac{\alpha_d}{\gamma r_p^{\gamma}} \cdot (r_1^{\gamma} - r_p^{\gamma})\right]$$

$$\therefore \ln R = \alpha_d \ln(r_p/r_1) + \alpha_d \left(\frac{r_1^{\gamma} - r_p^{\gamma}}{\gamma r_p^{\gamma}}\right)$$

rearranging

$$\alpha_d = \frac{\gamma r_p^{\gamma} \ln(R)}{\gamma r_p^{\gamma} \ln(r_p/r_1) + r_1^{\gamma} - r_p^{\gamma}} \qquad \text{(B.7)}$$

B.3 To find B

Simply substitute for rp, α_d and γ in equation (B.1) to give $$b = \frac{\alpha_d}{\gamma r_p^{\gamma}}$$

B.4 <u>To find a</u>

If n(rp) or $n(r_1)$ is known then substitute known values into equation (B.1) to give:

$$a = \frac{n(r_p)}{r_p^{\alpha_d} \exp(-\alpha_d/\gamma)} \quad \text{or} \quad \frac{n(r_1)}{r_1^{\alpha_d} \exp(-\alpha_d/\gamma)} \qquad \text{(B.8)}$$

The results of this section have shown, however, that the program can be used effectively to determine the scattering properties of any turbid medium provided that a light beam can be directed through that medium.

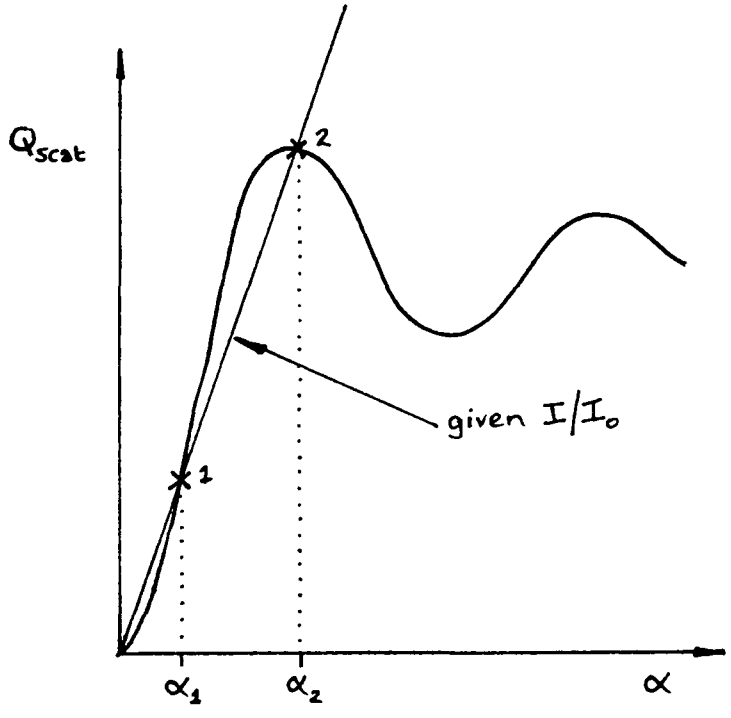

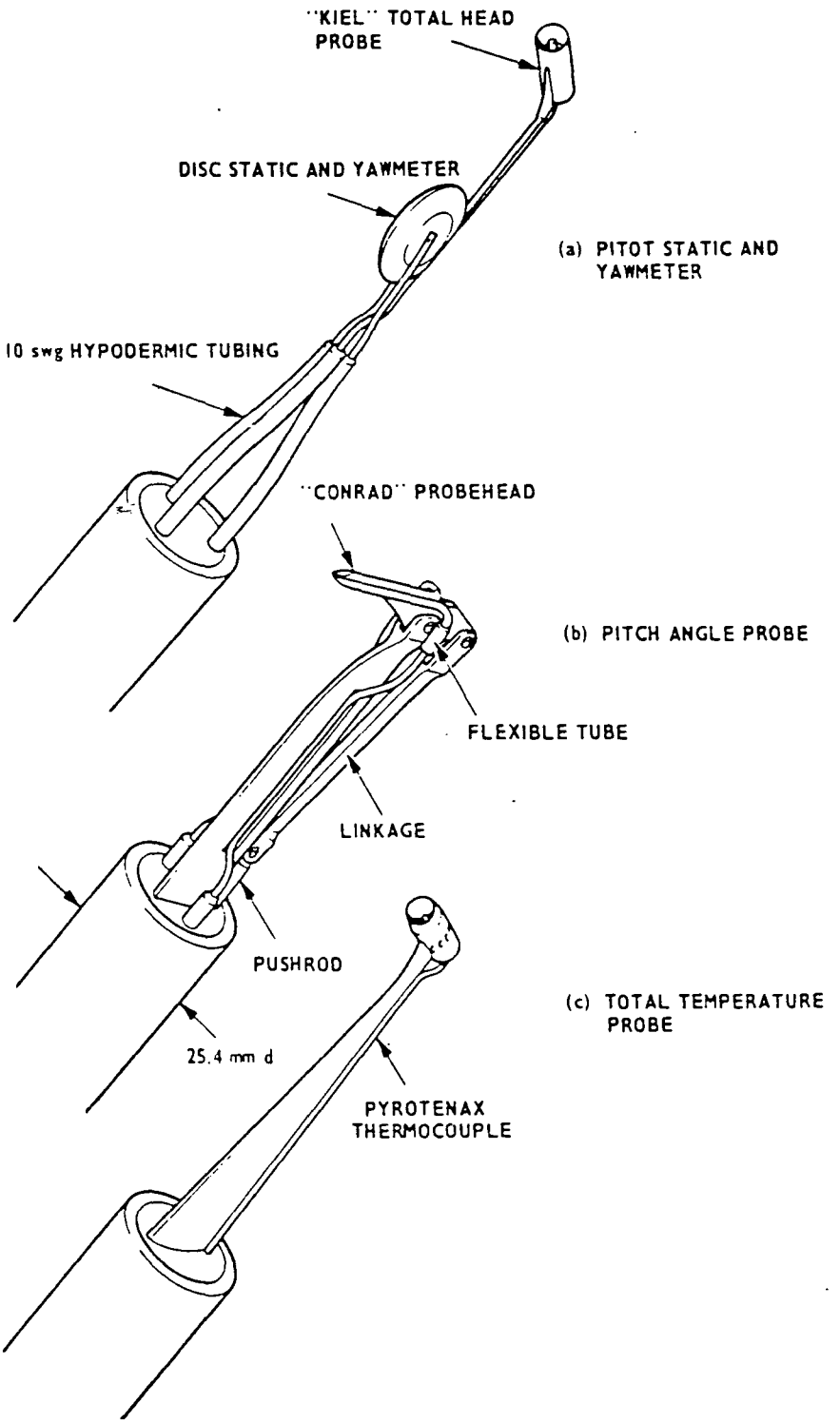

Figure 2.1 TYPICAL TURBINE PROBES

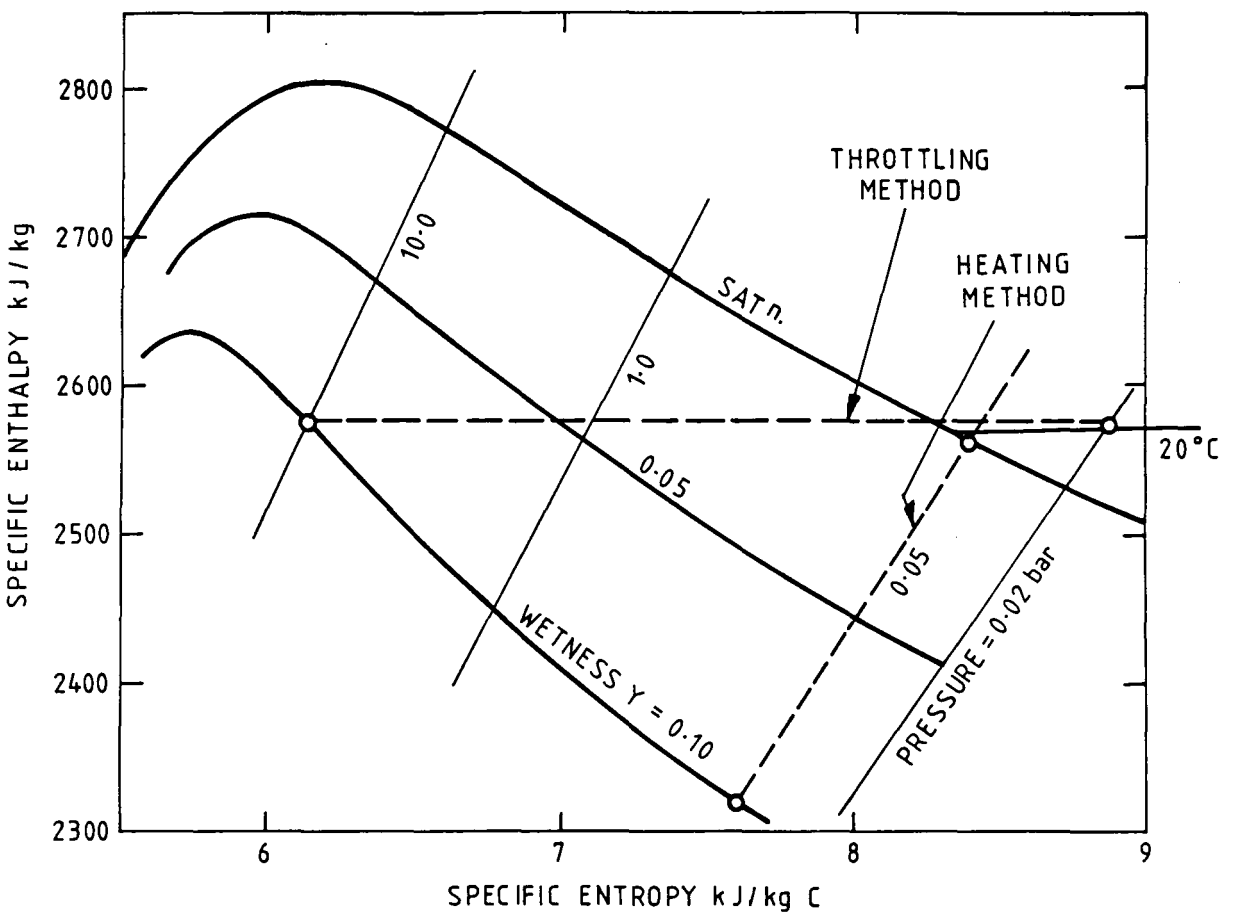

Figure 2.2 METHODS OF WETNESS FRACTION MEASUREMENT

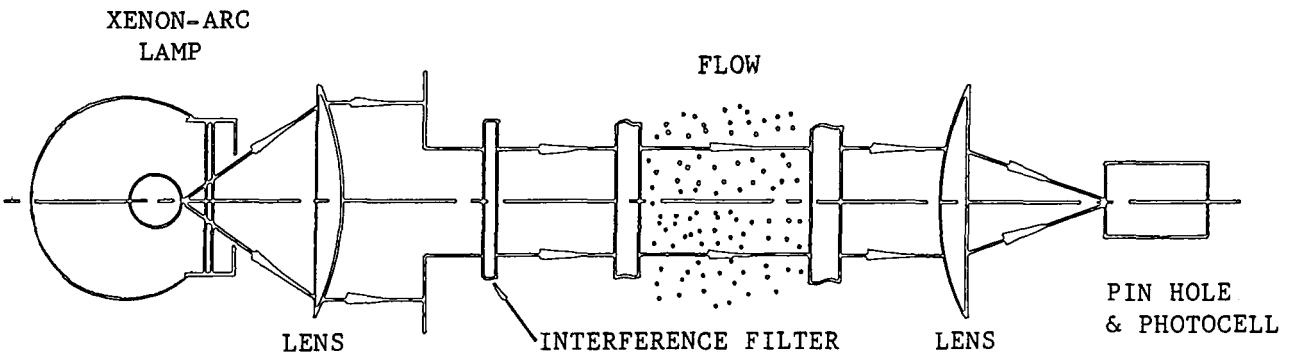

Figure 2.3 BASIC LIGHT EXTINCTION APPARATUS - Walters (85)

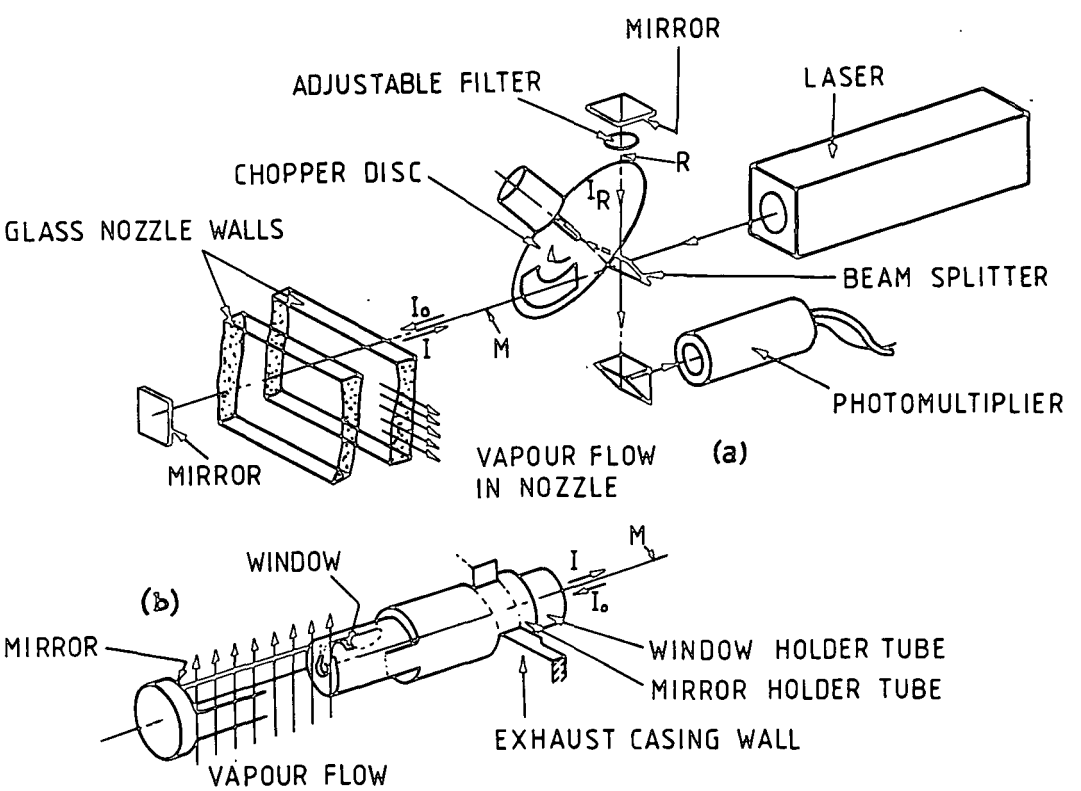

Figure 2.4 LAYOUT OF LIGHT EXTINCTION METHOD - Gyarmathy (47)

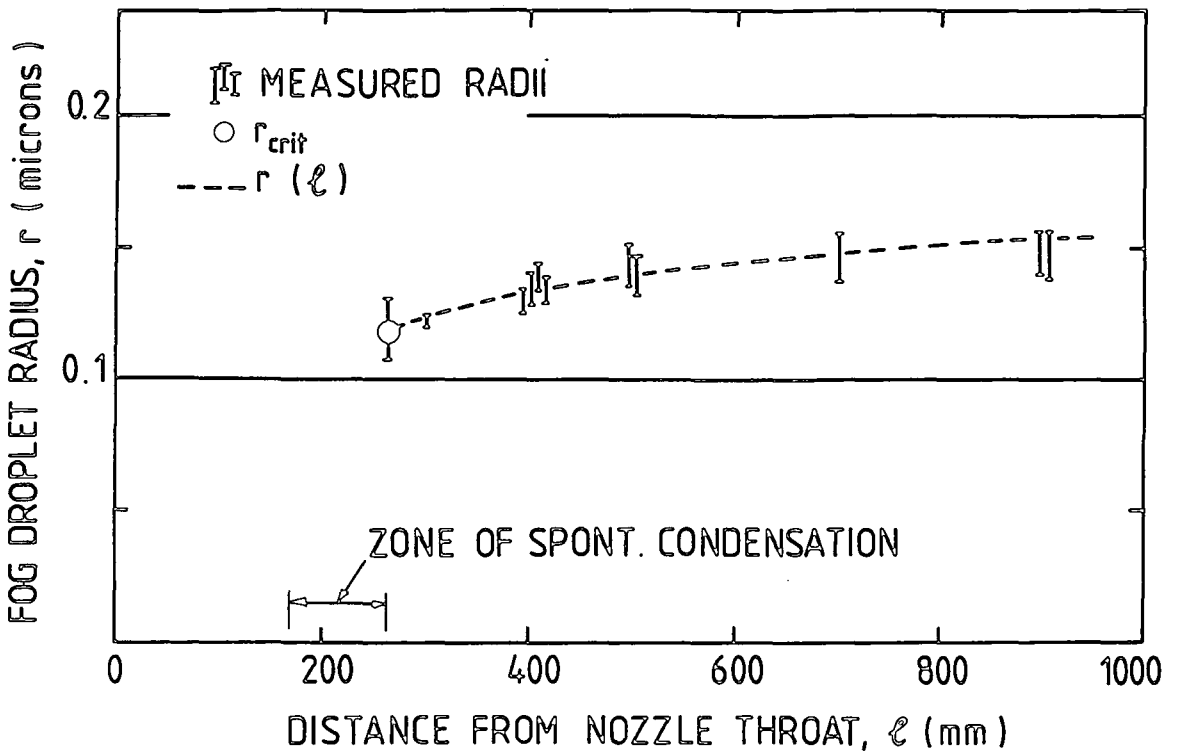

Figure 2.5 GROWTH OF WATER DROPLET RADIUS - Gyarmathy(47)

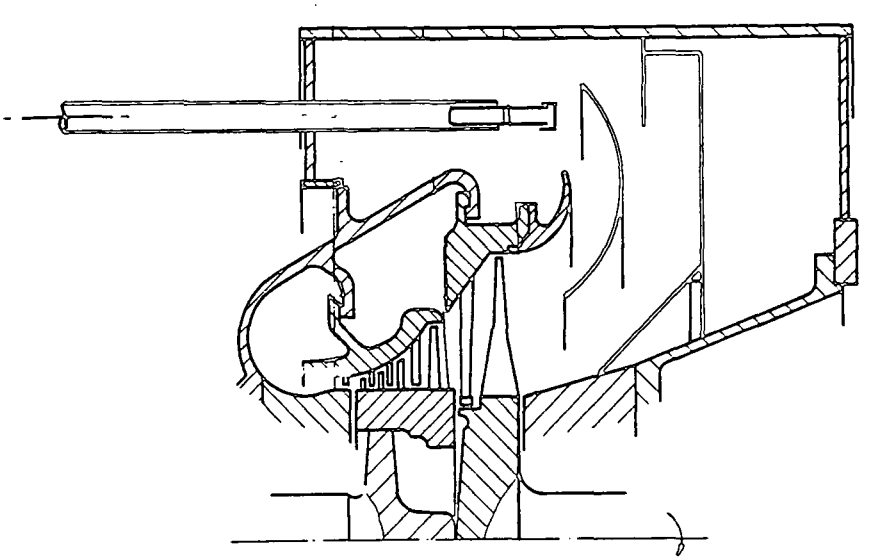

Figure 2.6 LOCATION OF OPTICAL PROBE IN MODEL TURBINE EXHAUST

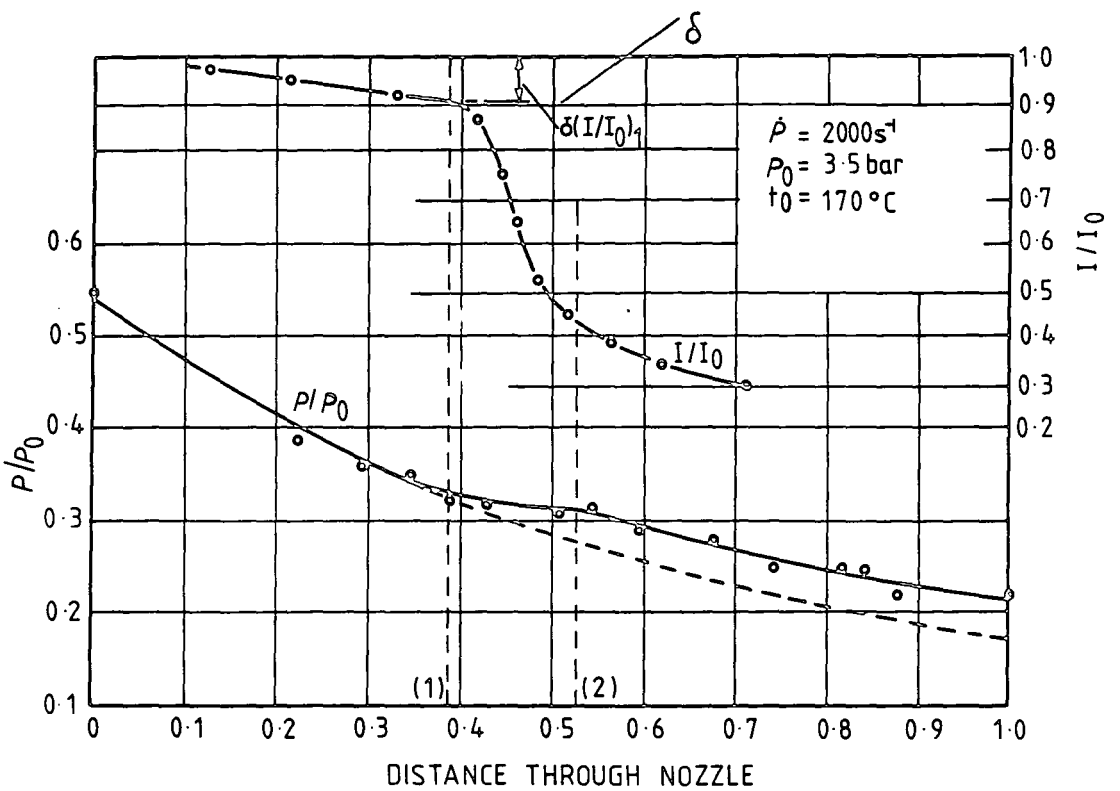

Figure 2.7 MEASURED LIGHT ATTENUATION THROUGH A NOZZLE

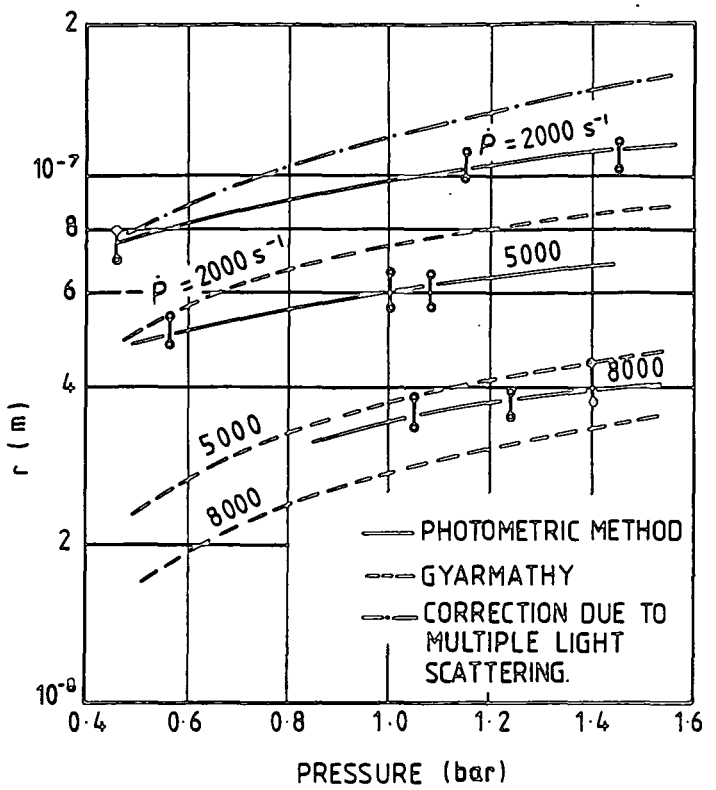

Figure 2.8 DROPLET RADII VARIATION WITH PRESSURE AND EXPANSION RATE - Petr(75)

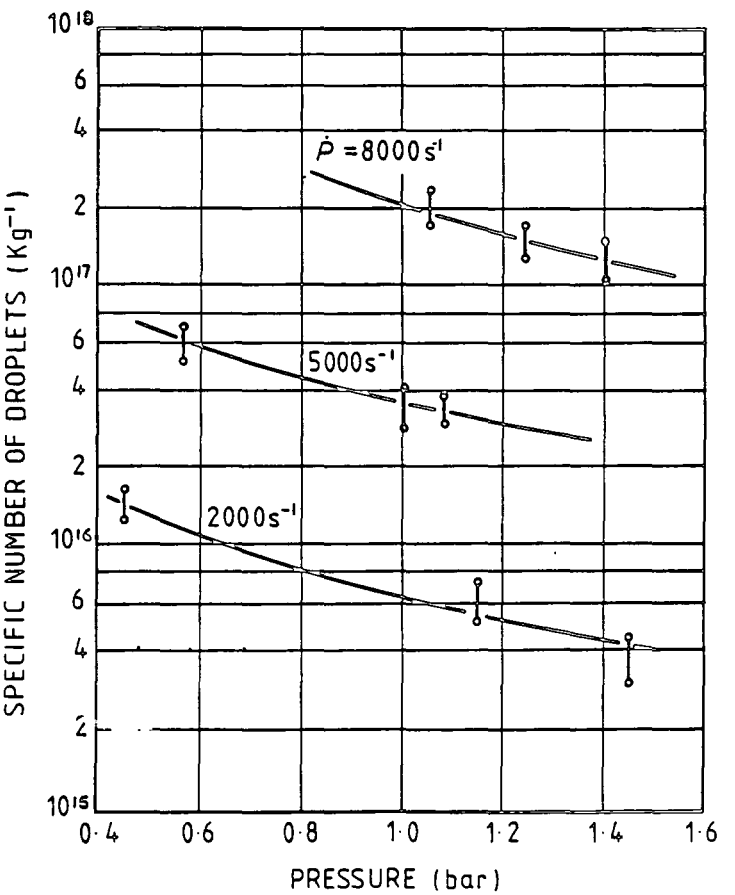

Figure 2.9 VARIATION IN THE NUMBER OF DROPLETS WITH PRESSURE - Petr(75)

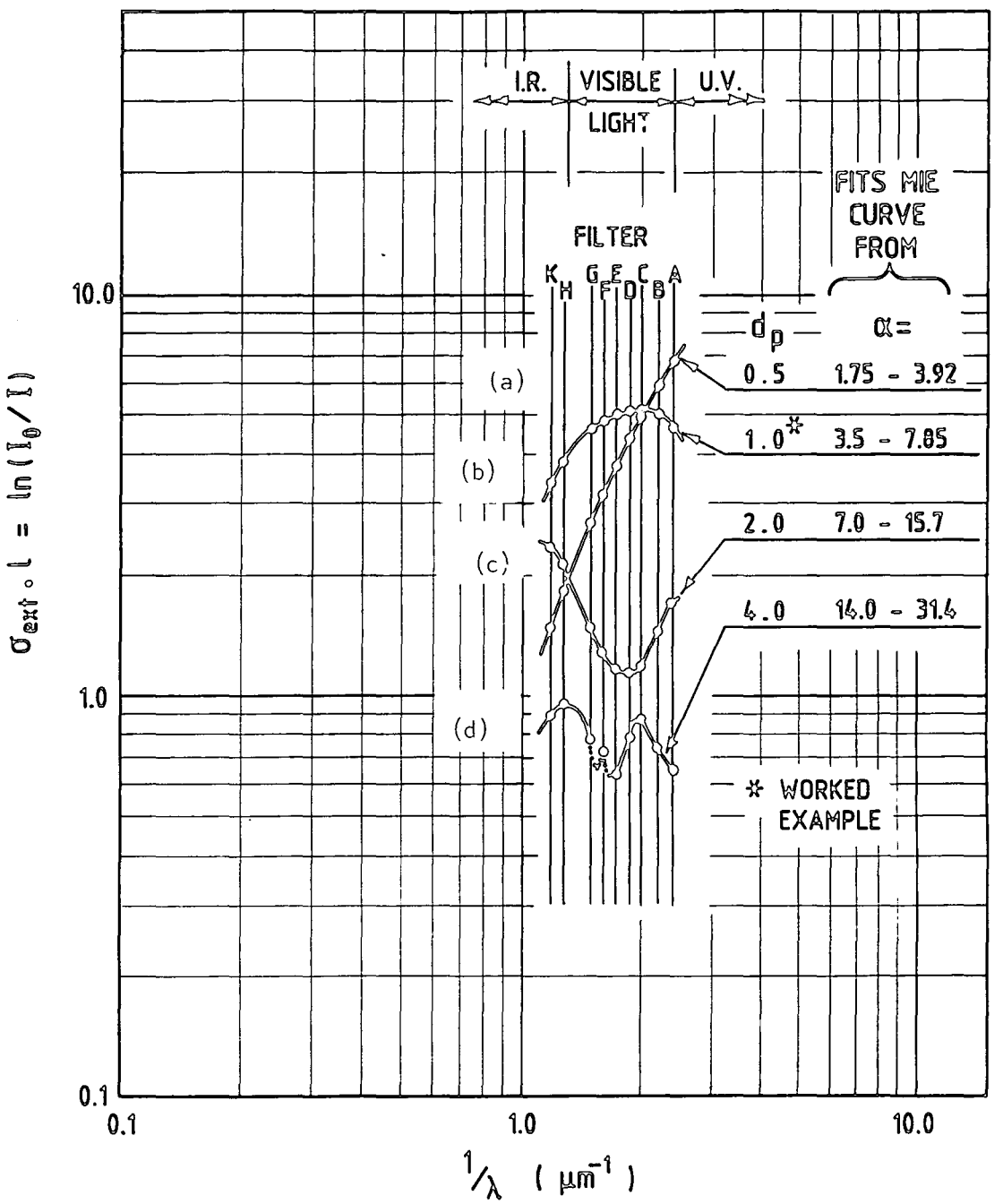

Figure 2.10 MEASUREMENTS OF WATER DROPLET SIZE USING THE MIE THEORY - McAllistair (61)

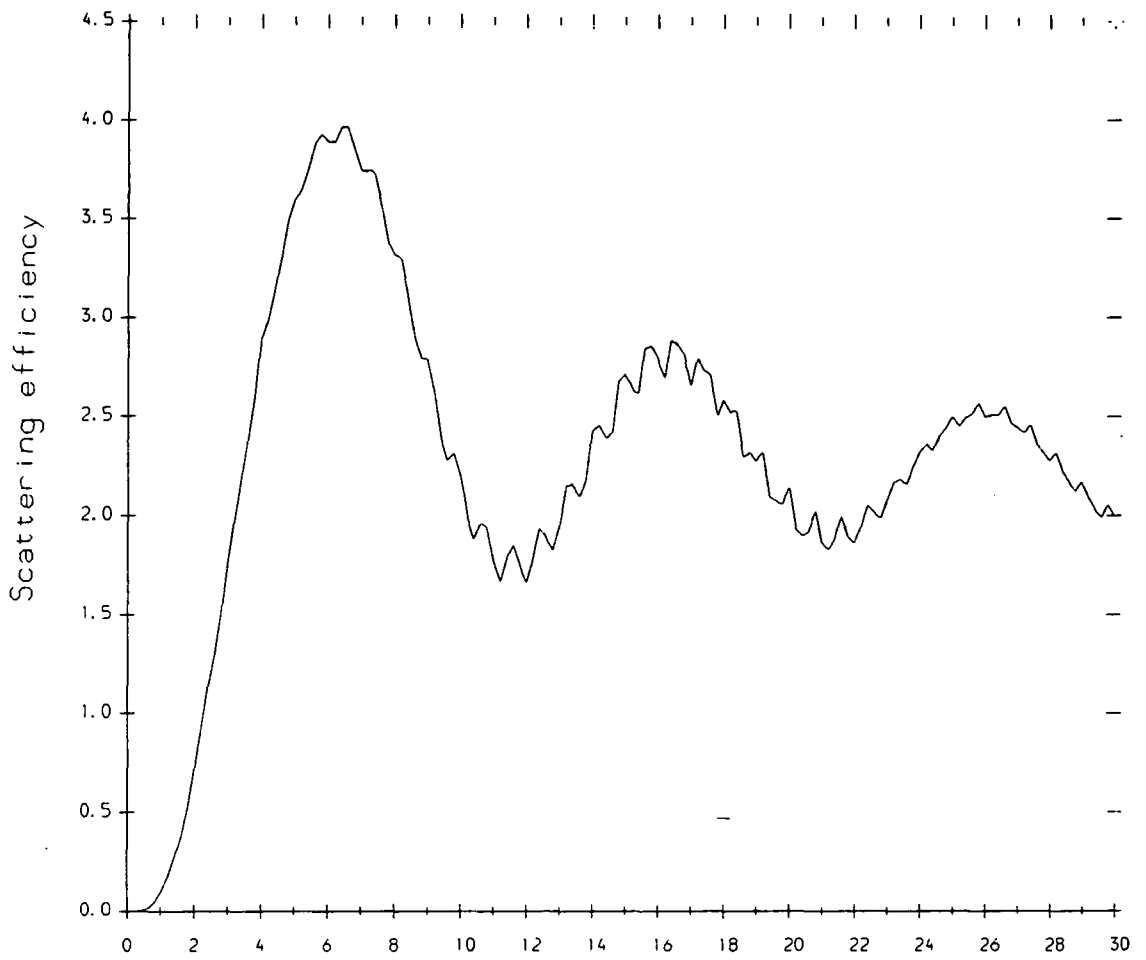

SCATTERING EFFICIENCY FACTOR AGAINST SIZE PARAMETER

Figure 2.11

1. XENON ARC LAMP
2. HEAT FILTER
3. INTERFERENCE FILTER
4. PLANO CONVEX LENS
5. BI-CONCAVE LENS
6. LIGHT GUIDE
7. COOLING AIR INLET
8. P.T.F.E. INSULATION
9. SPHERICAL MIRROR

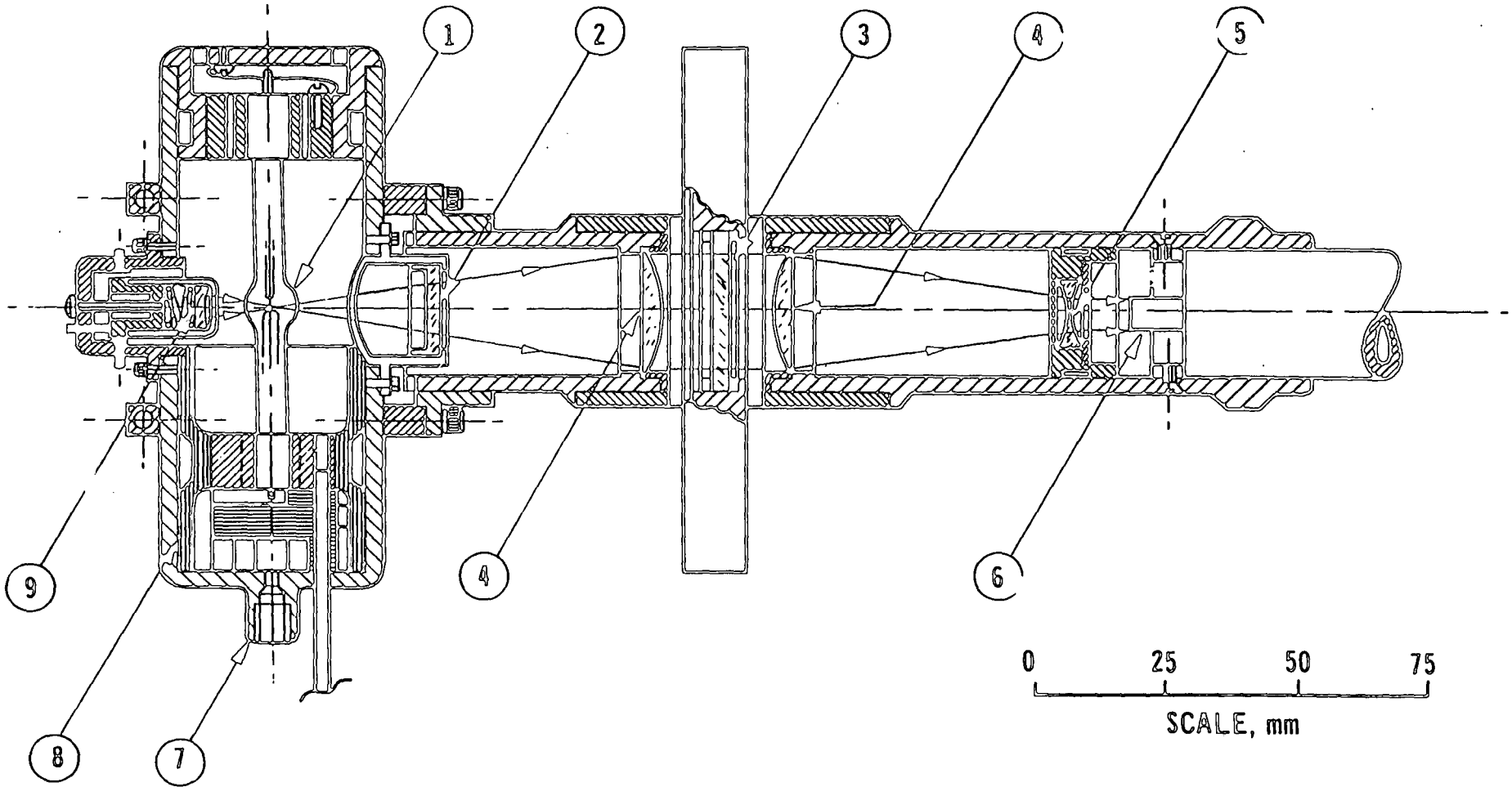

Figure 2.12 LAYOUT OF OPTICAL PROBE - Walters(86)

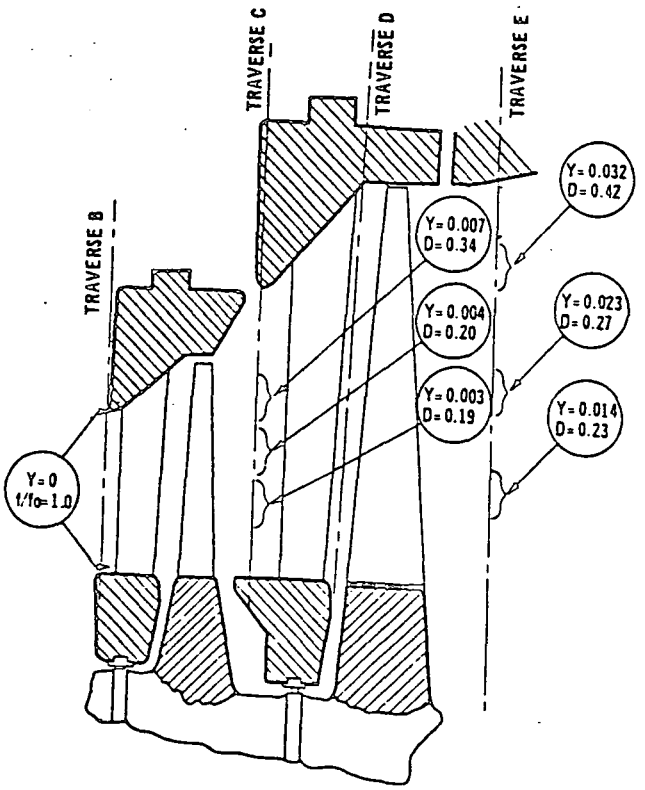

Figure 2.13 MEASURING STATIONS FOR PROBE TRAVERSES - Walters(86)

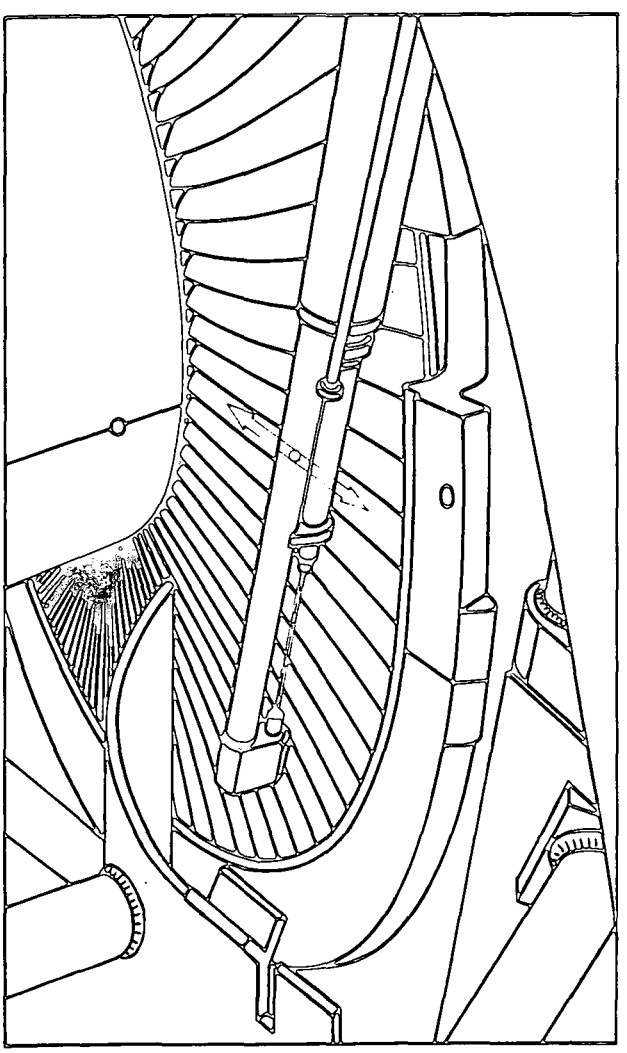

Figure 2.14 LOCATION OF LIGHT EXTINCTION PROBE AT EXIT OF FINAL STAGE

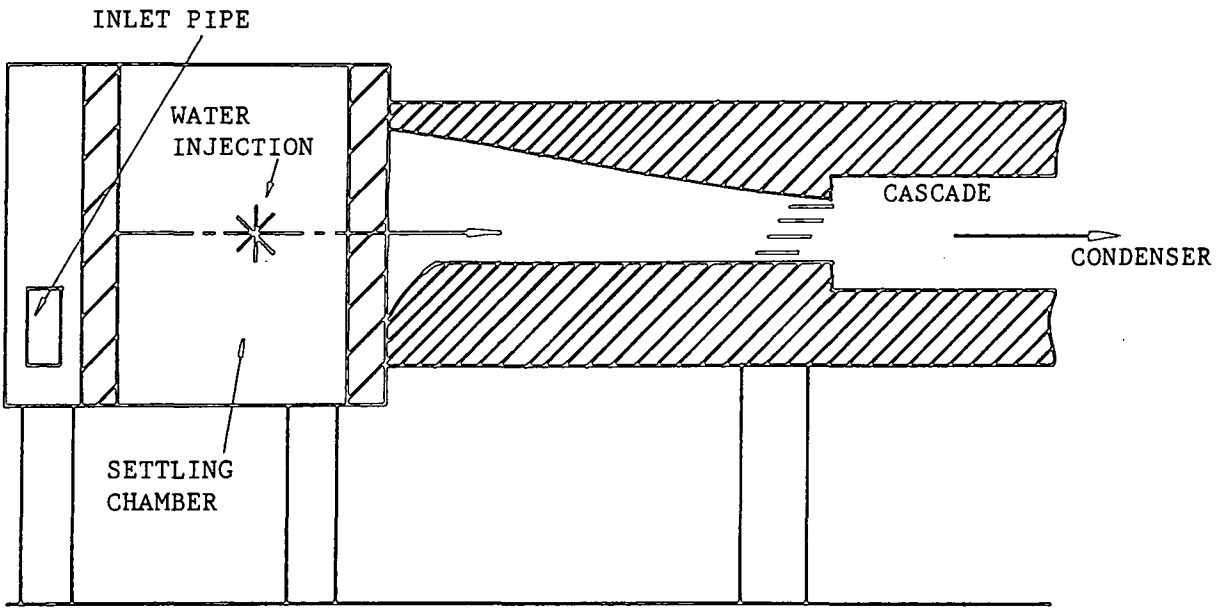

Figure 2.15 LAYOUT OF STEAM TUNNEL - Decuypère(15)

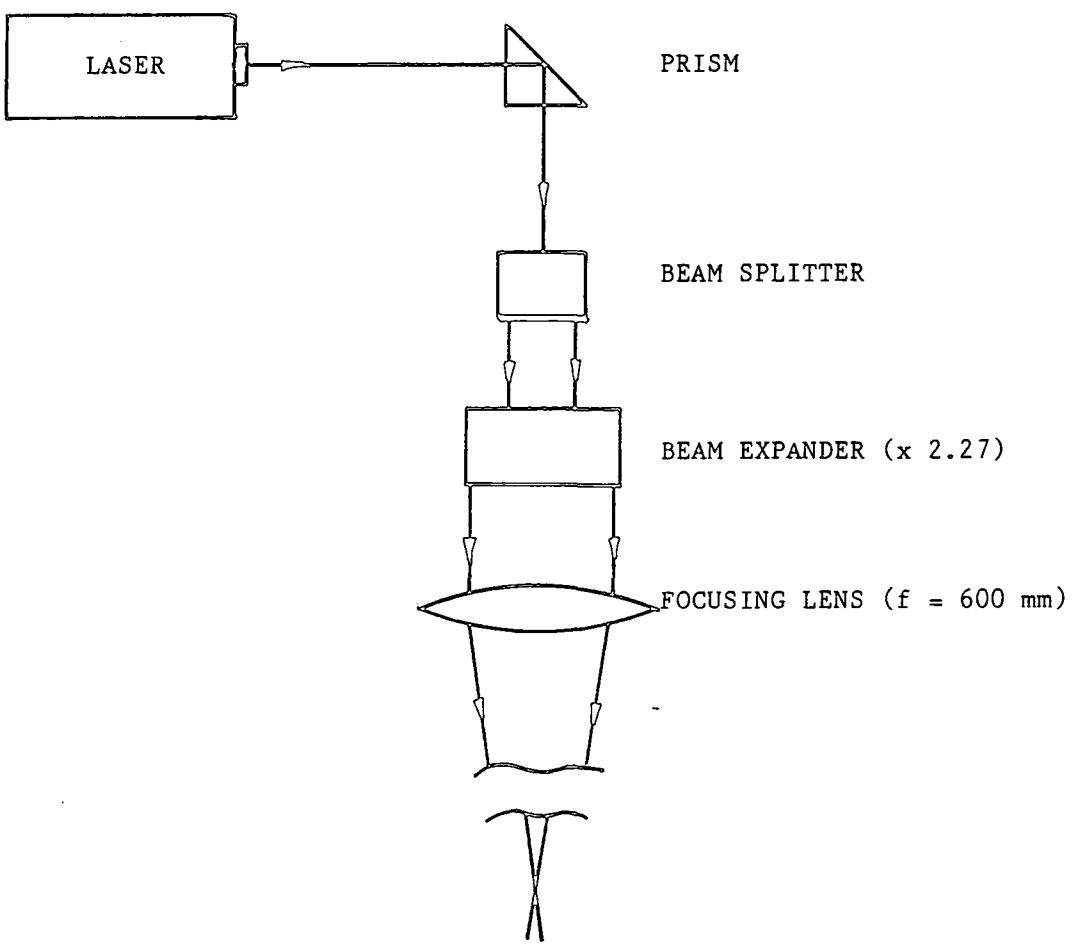

Figure 2.16 LAYOUT OF LDA OPTICAL SYSTEM - Decuypère (15)

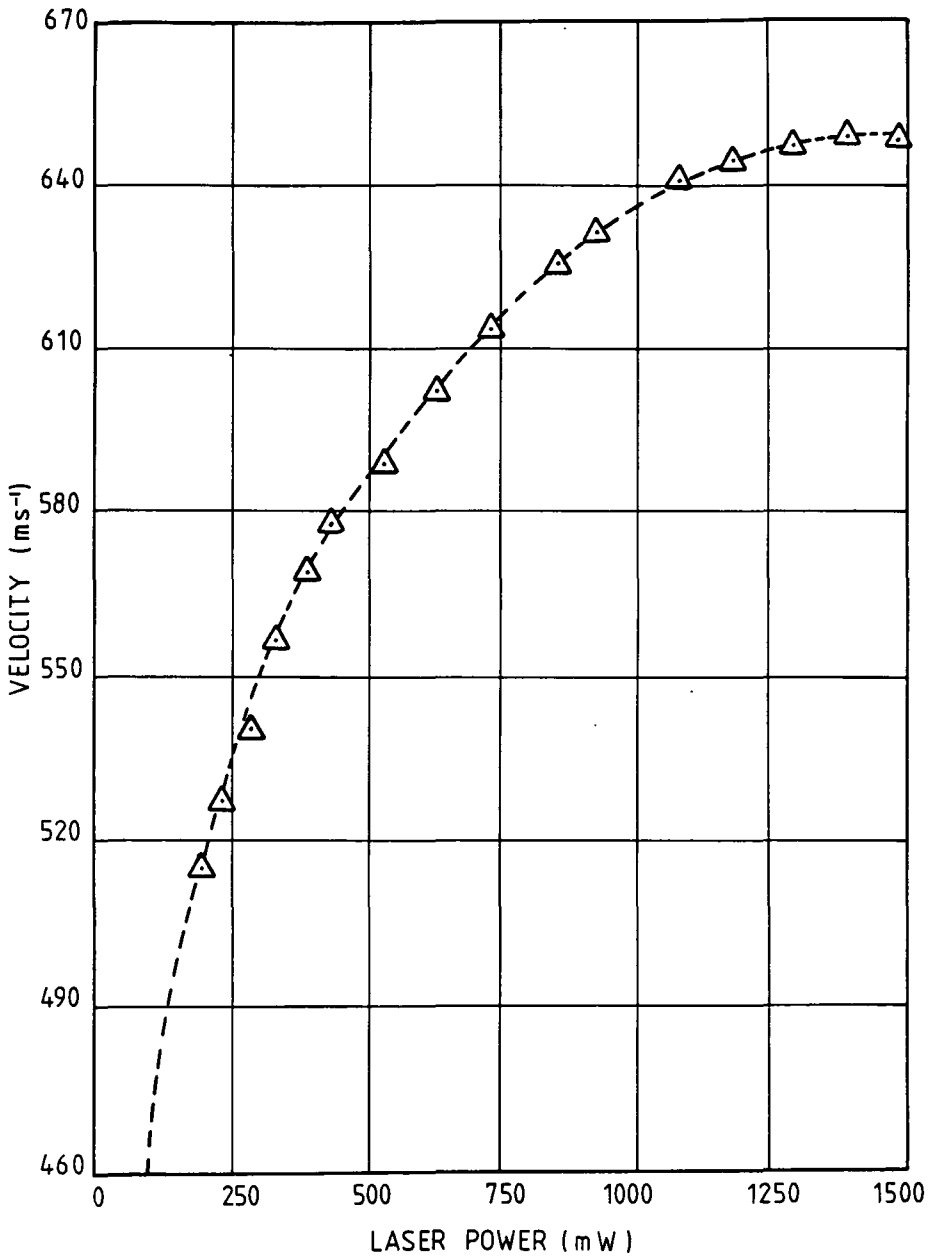

Figure 2.17 RELATIONSHIP BETWEEN MEAN VELOCITY AND LASER POWER - Decuypère(15

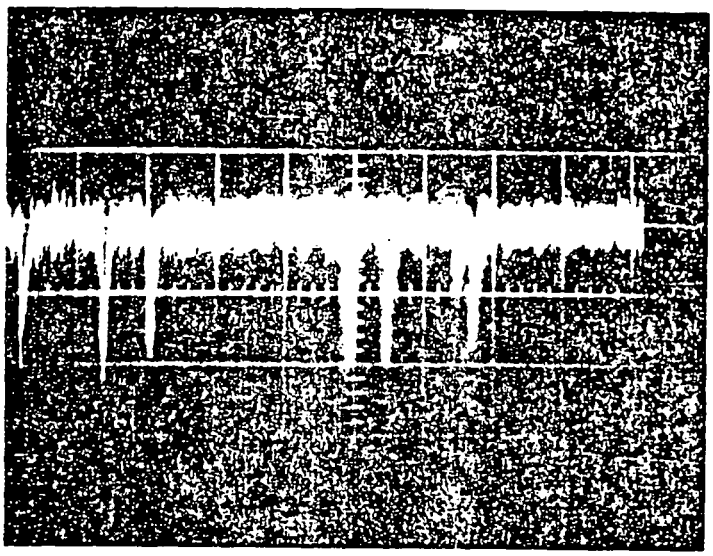

Figure 2.18 TYPICAL DOPPLER SIGNAL TRACE(1) -Wittig(89)

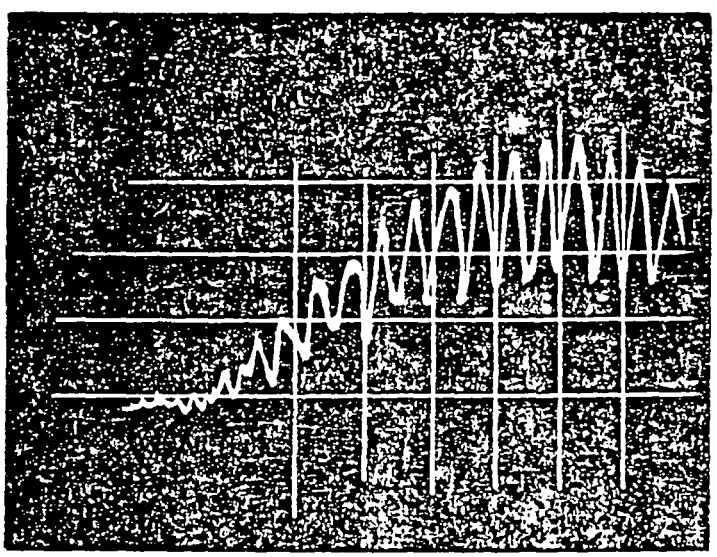

Figure 2.19 TYPICAL DOPPLER SIGNAL TRACE(2) - Wittig(89)

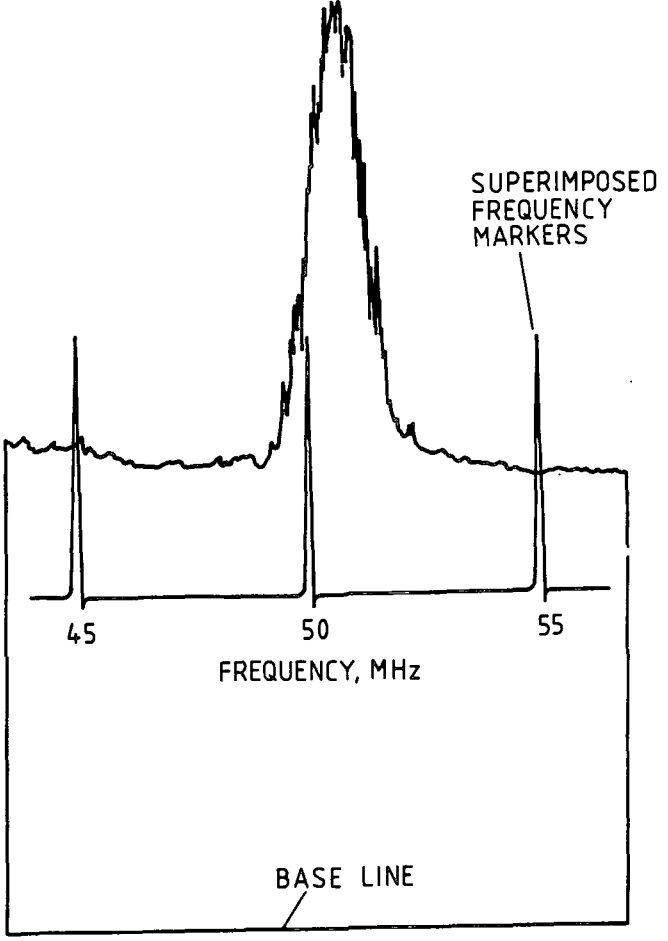

Figure 2.20 SPECTRUM OF DOPPLER SIGNAL - Crane(14)

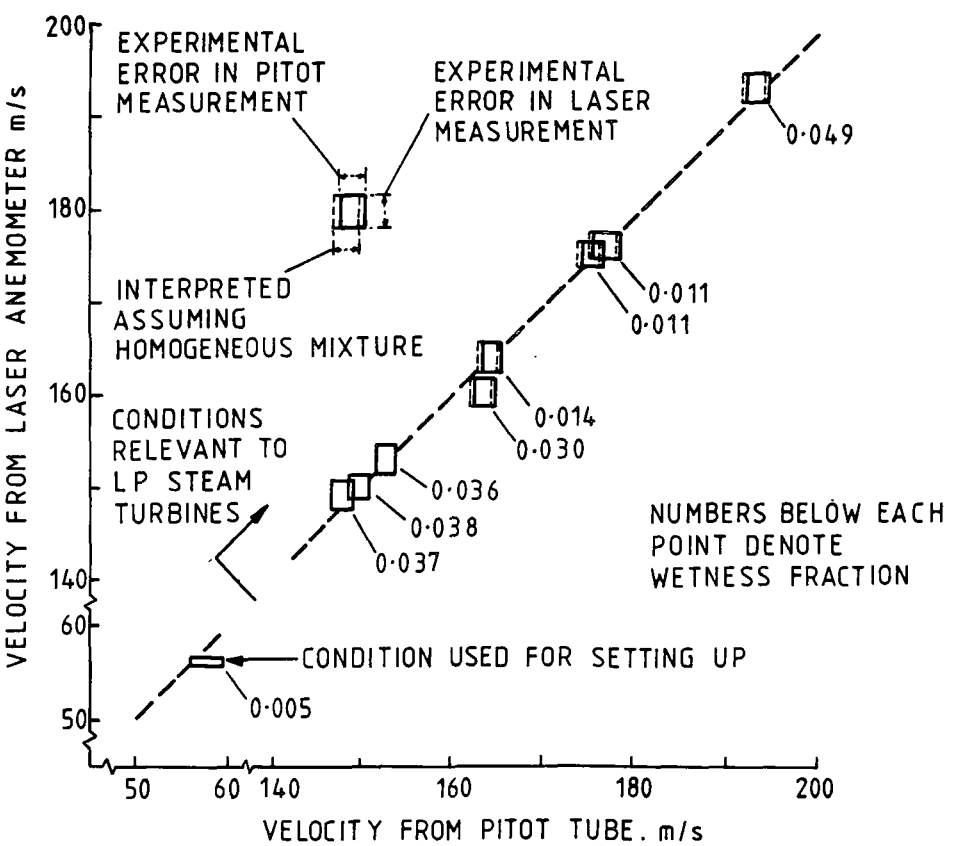

Figure 2.21 COMPARISON OF VELOCITIES DERIVED FROM PITOT TUBE AND LASER ANEMOMETER - Crane(14)

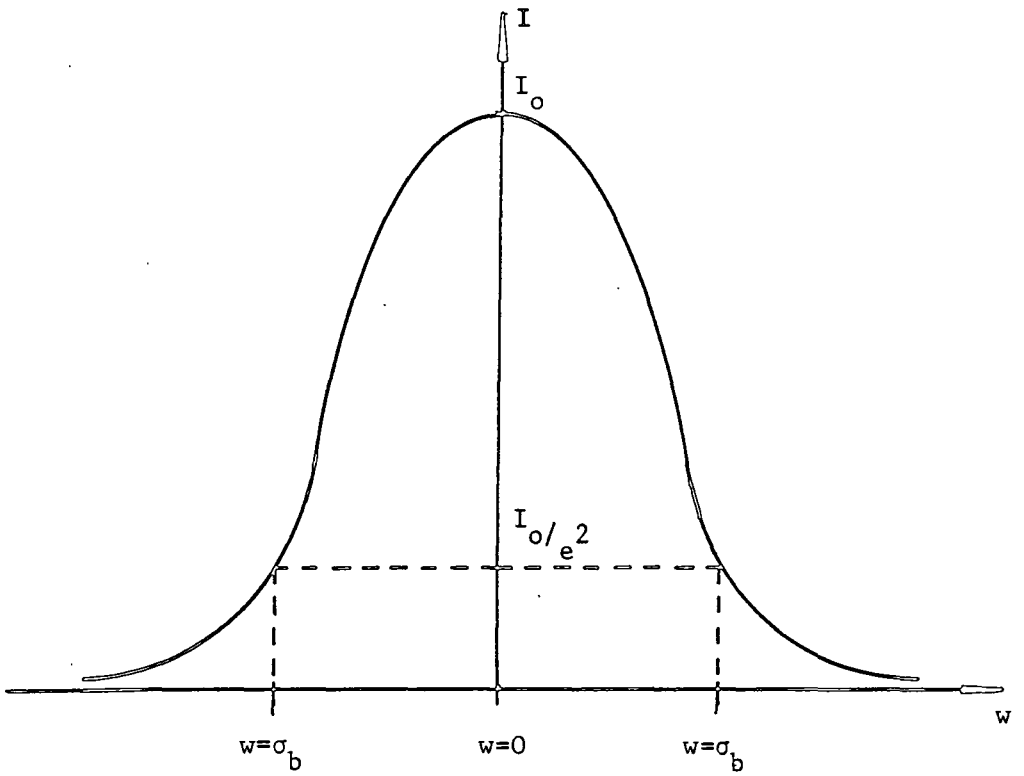

Figure 3.1 THE GAUSSIAN INTENSITY DISTRIBUTION FOR A TEM_{oo} LASER.

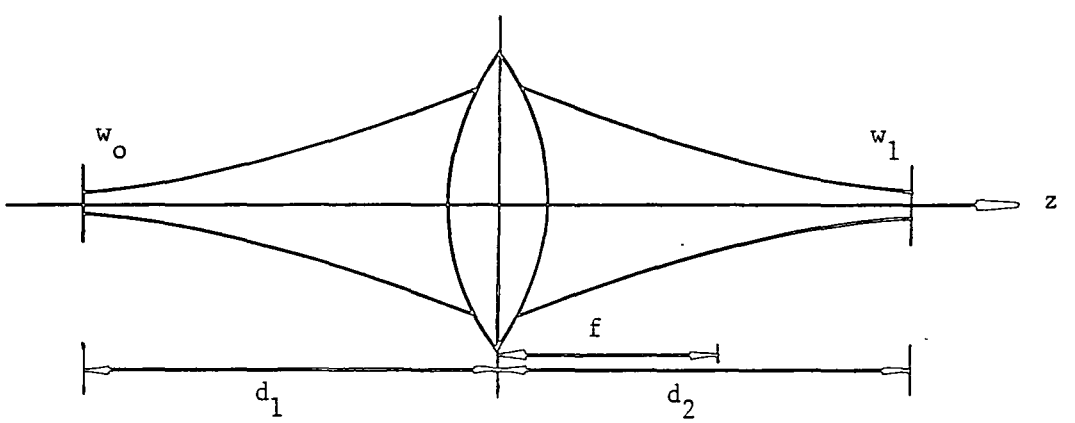

Figure 3.2 NOTATION USED FOR THE FOCUSING OF A LASER BEAM THROUGH A SINGLE LENS.

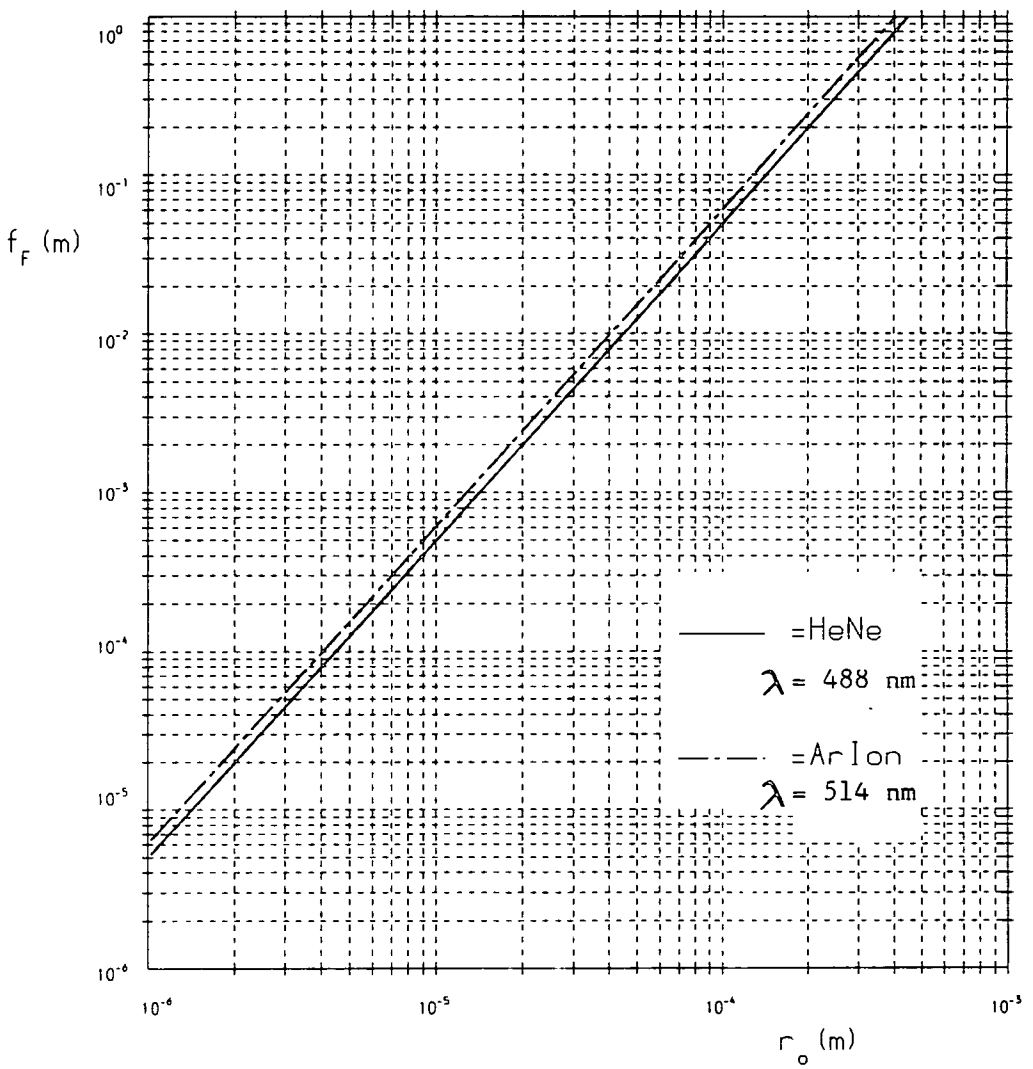

Figure 3.3 VARIATION OF THE BEAM PARAMETER WITH BEAM RADIUS

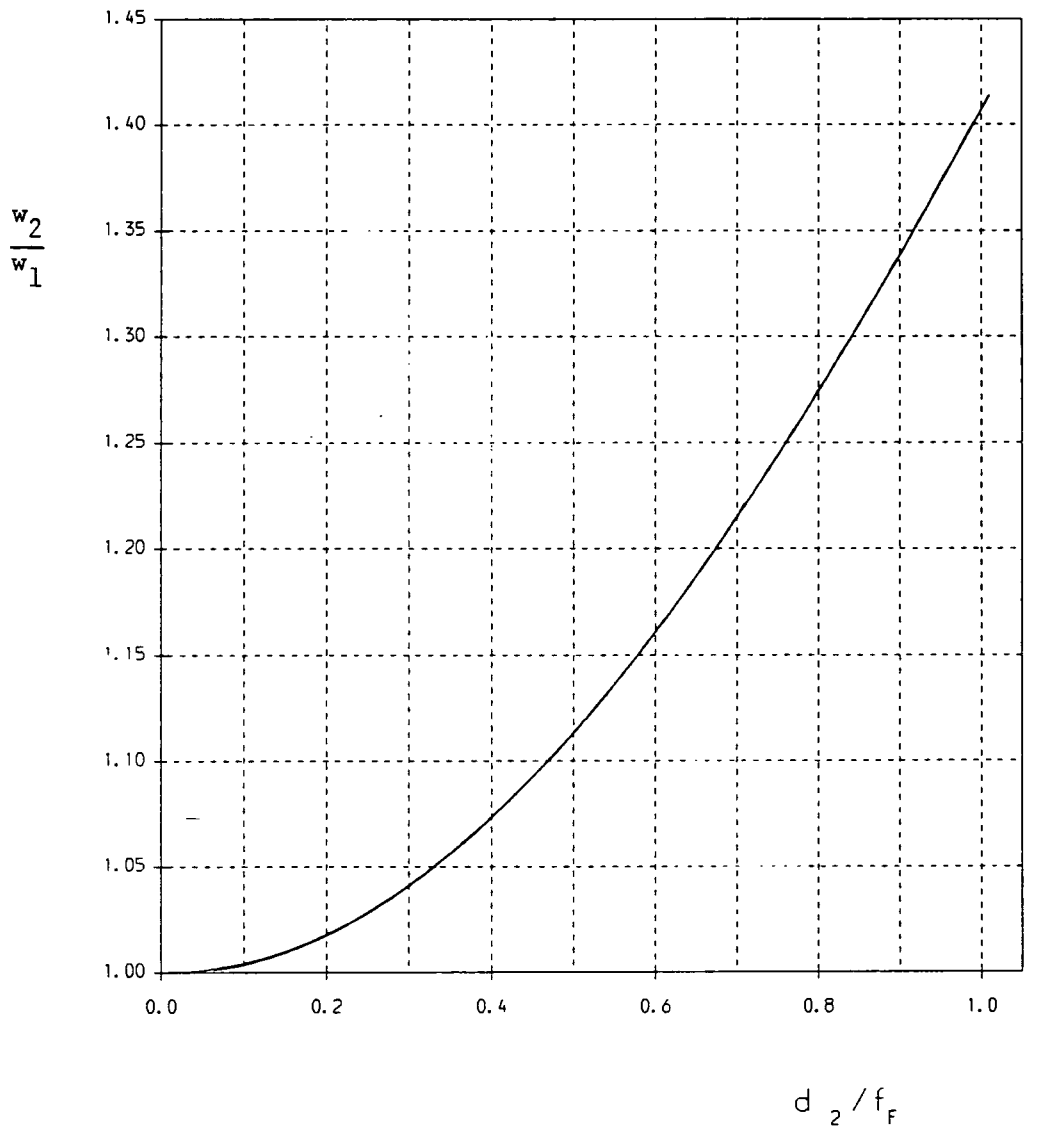

Figure 3.4 GROWTH OF BEAM RADIUS AS A FUNCTION OF d_2/f_F

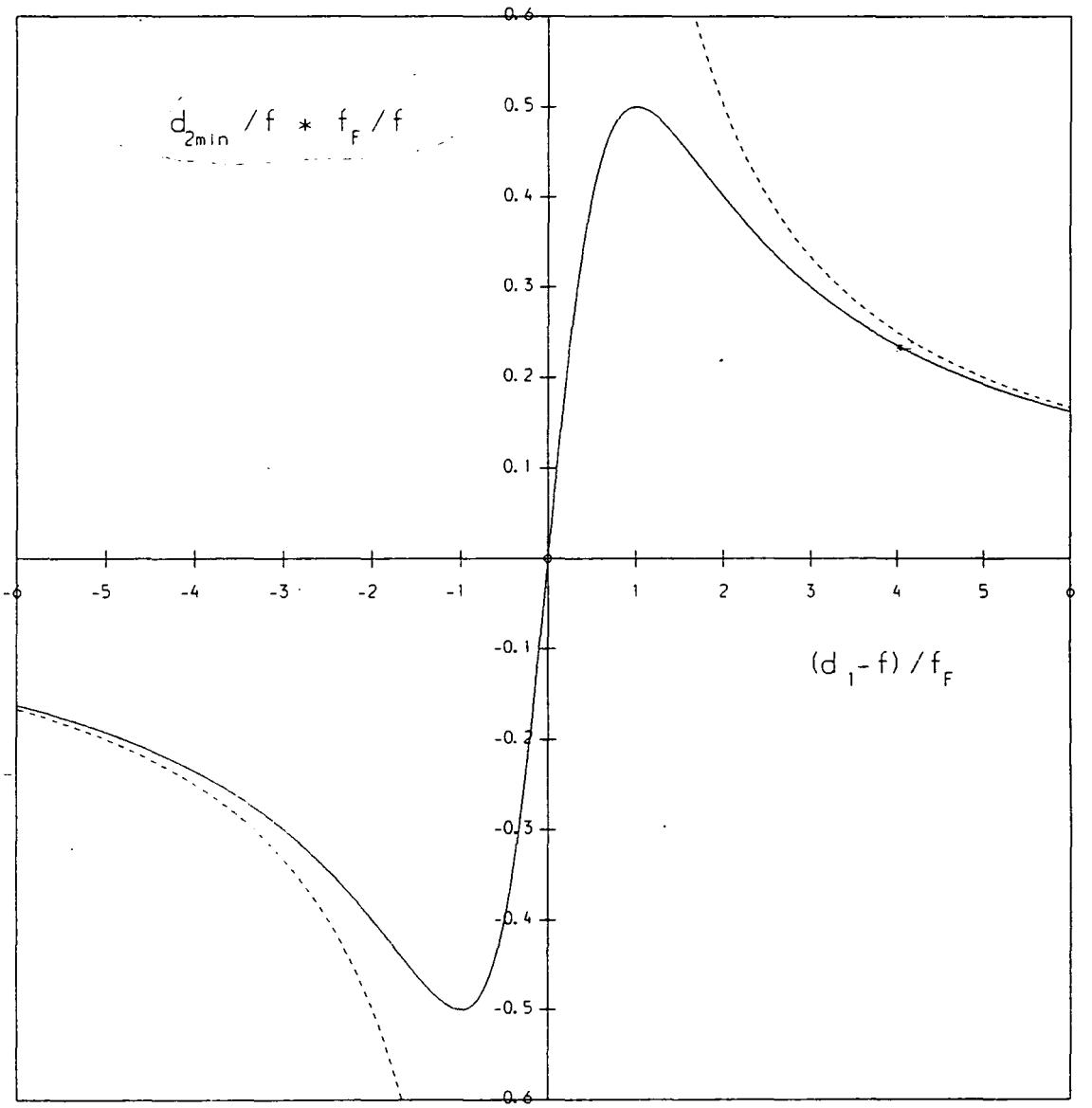

Figure 3.5 THE WAIST-WAIST RELATIONSHIP FOR A GIVEN LENS SYSTEM

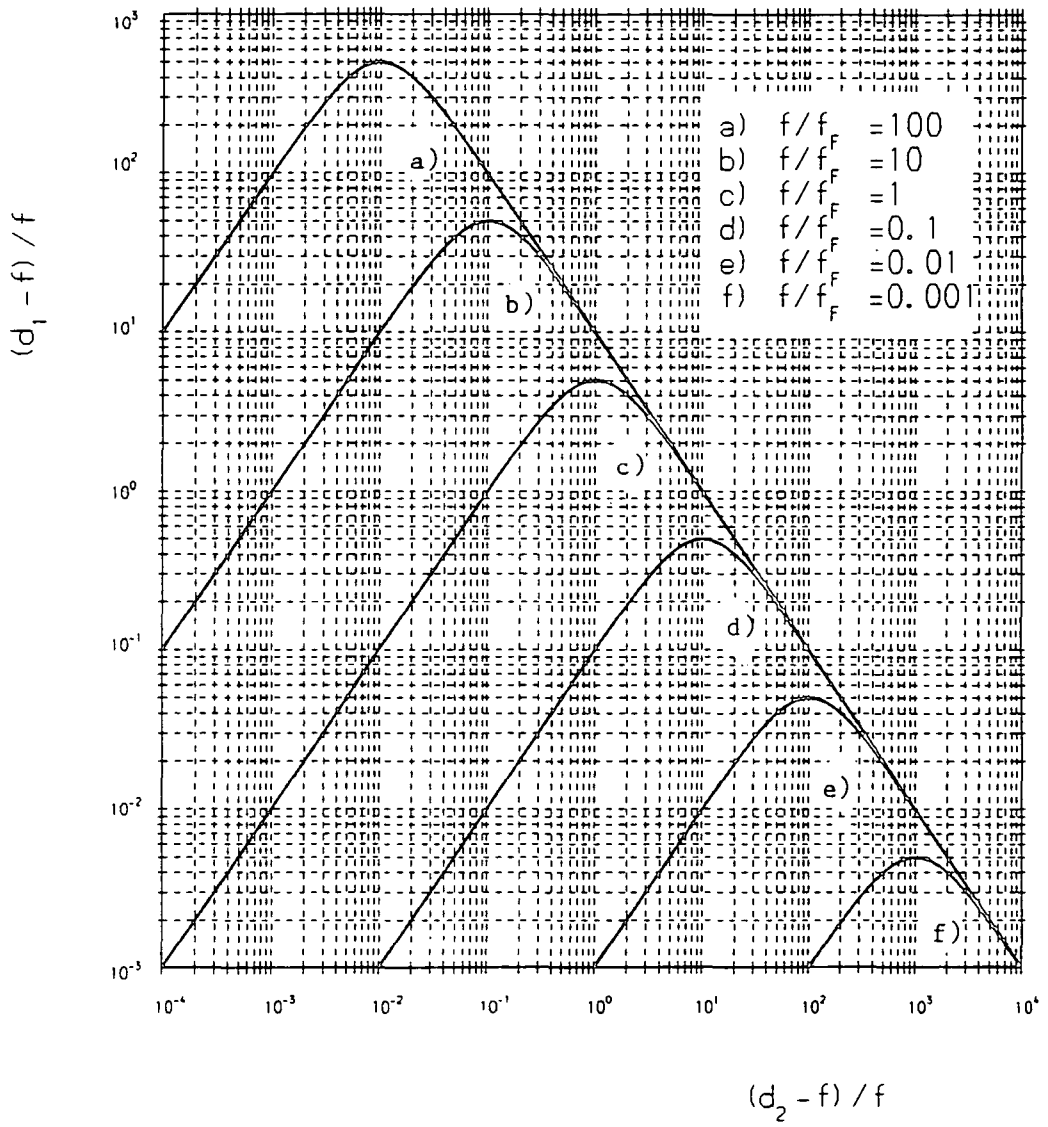

Figure 3.6 VARIATION OF INPUT WAIST POSITION WITH OUTPUT WAIST POSITION FOR A GIVEN BEAM PARAMETER

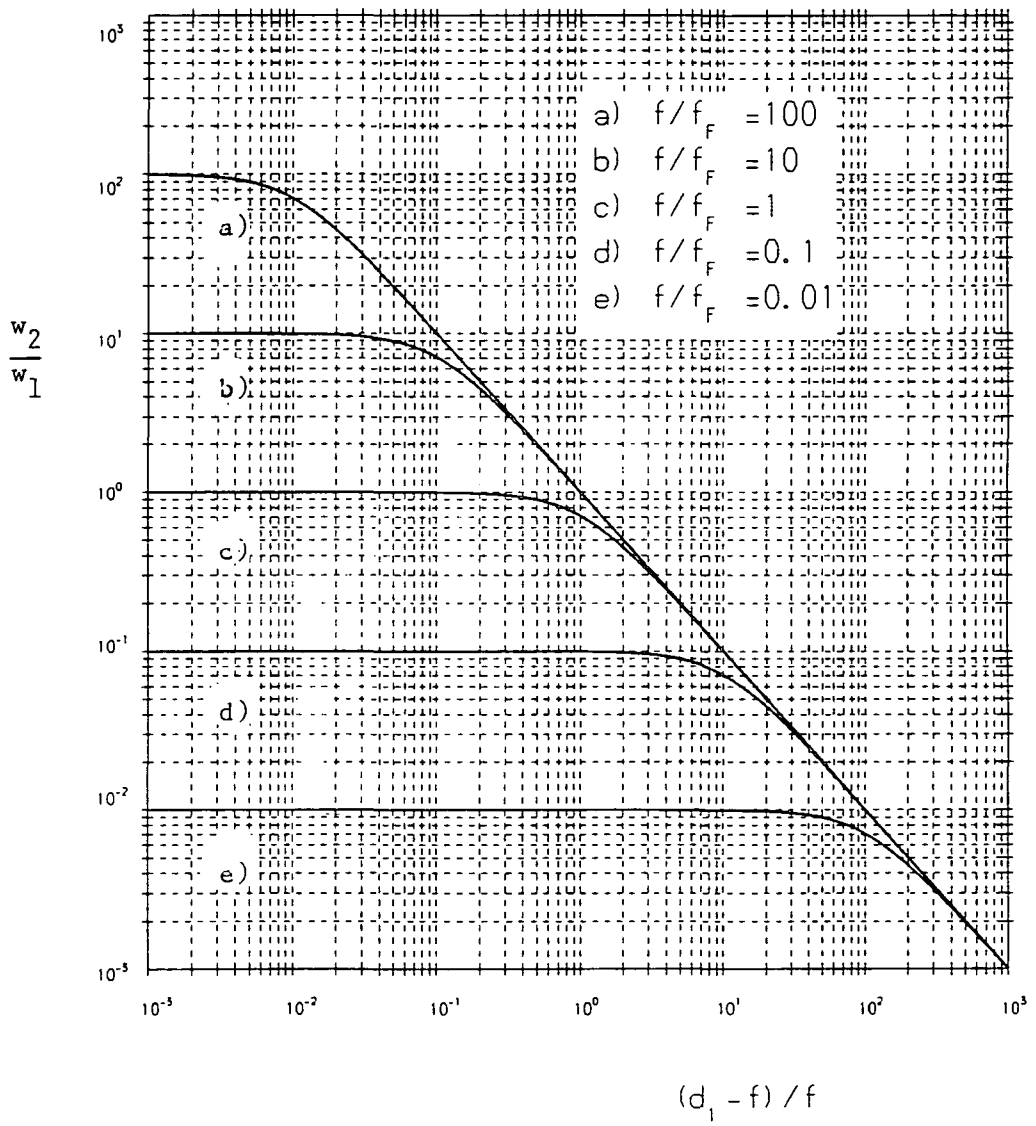

Figure 3.7 BEAM EXPANSION AS A FUNCTION OF WAIST TO LENS SPACING FOR A GIVEN BEAM PARAMETER AND LENS

BEAM DIVERGENCE AT INPUT (rads) =0.001
BEAM DIVERGENCE AT OUTPUT (rads) =0.020
VALUE OF FF (mm) = 1528.01221
LENS FOCAL LENGTH = -50.
INPUT WAIST DISTANCE = 80
VIRTUAL WAIST DISTANCE= -49
INPUT WAIST SIZE=0.500

BEAM DIVERGENCE AT INPUT (rads) =0.020
BEAM DIVERGENCE AT OUTPUT (rads) =0.000
VALUE OF FF (mm) = 1.62435
LENS FOCAL LENGTH = 100.
INPUT WAIST DISTANCE = 100
OUTPUT WAIST DISTANCE= 100
INPUT WAIST SIZE=0.016

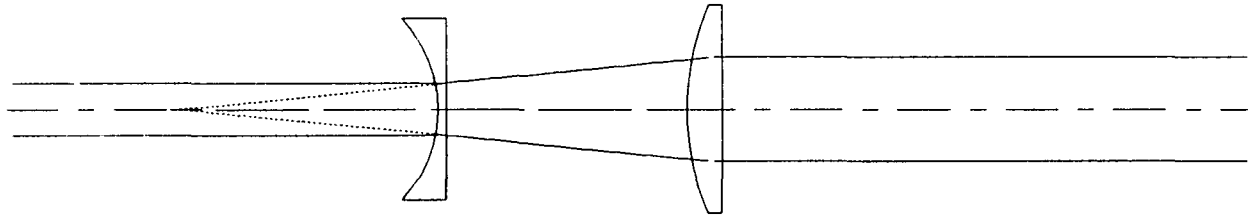

OUTPUT WAIST SIZE= 0.016
RADIUS OF BEAM AT LENS= 0.501
GEOMETRICAL IMAGE DISTANCE= -30
BEAM MAGNIFICATION= 10

OUTPUT WAIST SIZE= 1.004
RADIUS OF BEAM AT LENS= 1.004
GEOMETRICAL IMAGE DISTANCE=INFINITY
BEAM MAGNIFICATION= 10

Figure 3.8 A SIMPLE 2:1 BEAM EXPANDER USING A DIVERGING AND CONVERGING LENS

BEAM DIVERGENCE AT INPUT (rads) =0.001
BEAM DIVERGENCE AT OUTPUT (rads) =0.064
VALUE OF FF (mm) = 2503.49341
LENS FOCAL LENGTH = 20.
INPUT WAIST DISTANCE = 120
OUTPUT WAIST DISTANCE= 20
INPUT WAIST SIZE=0.640

BEAM DIVERGENCE AT INPUT (rads) =0.064
BEAM DIVERGENCE AT OUTPUT (rads) =0.000
VALUE OF FF (mm) = 0.15952
LENS FOCAL LENGTH = 250.
INPUT WAIST DISTANCE = 250
OUTPUT WAIST DISTANCE= 250
INPUT WAIST SIZE=0.005

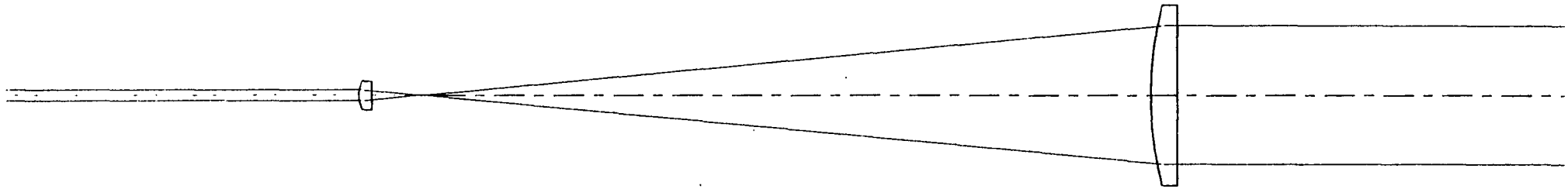

OUTPUT WAIST SIZE= 0.005
RADIUS OF BEAM AT LENS= 0.641
GEOMETRICAL IMAGE DISTANCE= 24
BEAM MAGNIFICATION= 3

OUTPUT WAIST SIZE= 8.006
RADIUS OF BEAM AT LENS= 8.006
GEOMETRICAL IMAGE DISTANCE=INFINITY
BEAM MAGNIFICATION= 3

Figure 3.9 THE BEAM EXPANDER USED IN THIS RESEARCH

TWO COMMON TYPES OF LASER DOPPLER ANEMOMETER

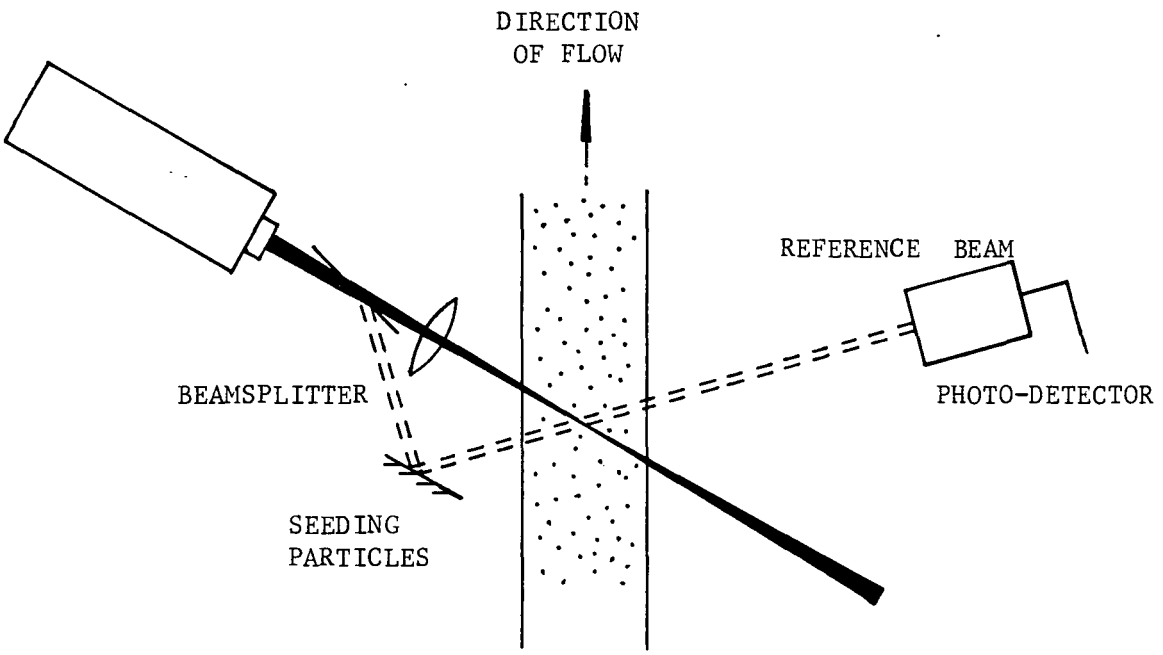

Figure 4.1 SIMPLE REFERENCE BEAM ARRANGEMENT

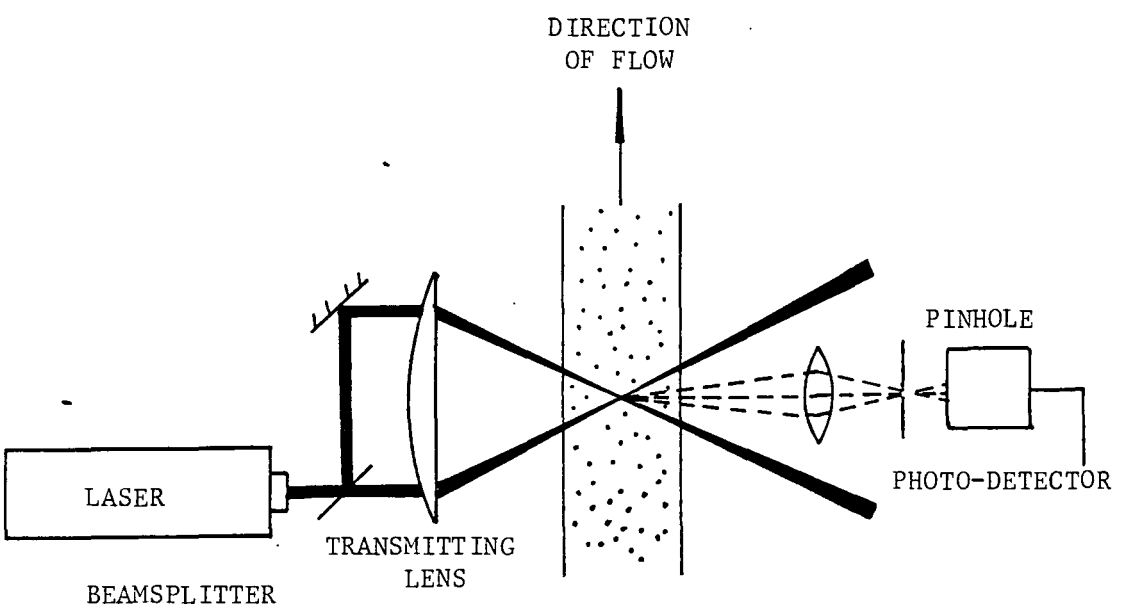

Figure 4.2 SIMPLE DUAL BEAM ARRANGEMENT

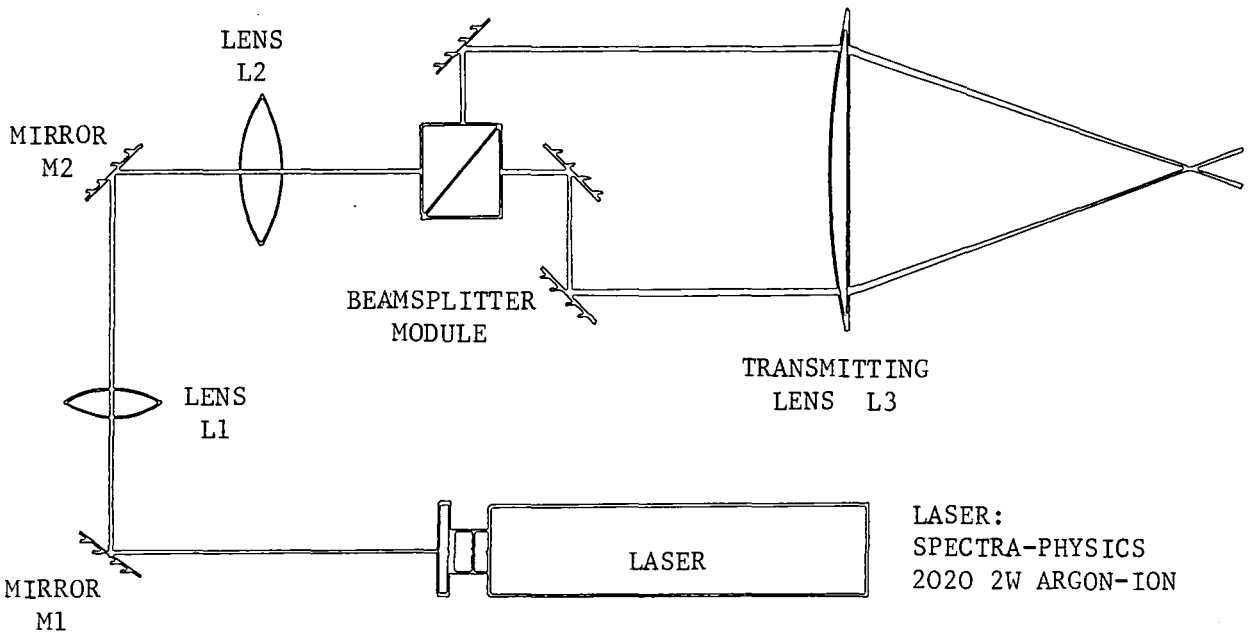

Figure 4.3 VIEW OF LDA SYSTEM USED IN THIS RESEARCH

MIRRORS M1 & M2 ARE FULLY ADJUSTABLE

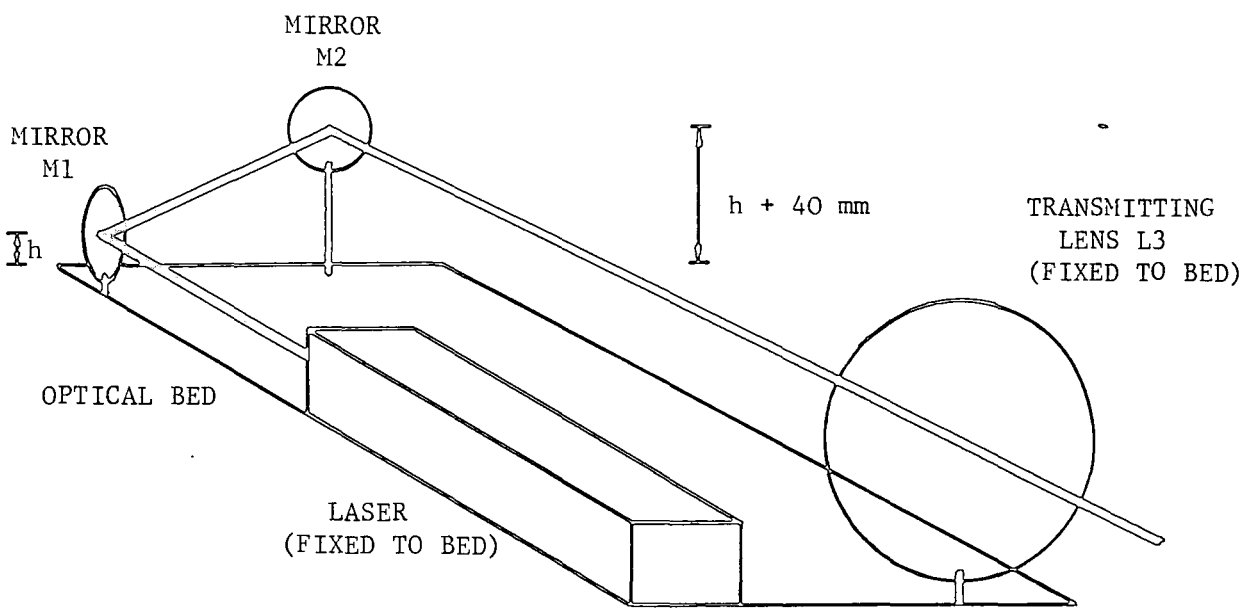

Figure 4.4 VIEW OF THE OPTICAL SYSTEM SHOWING THE FOLDING OF THE LASER BEAM

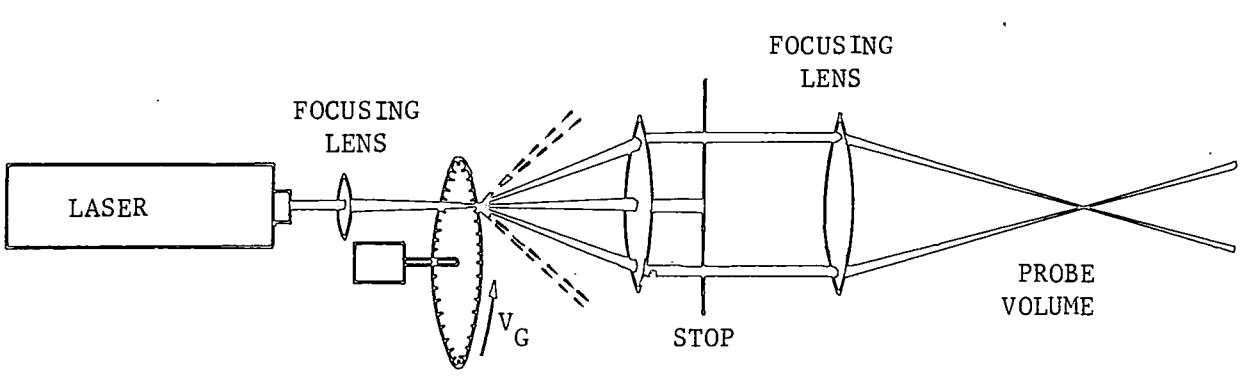

Figure 4.5 A DUAL BEAM ANEMOMETER USING A DIFFRACTION GRATING

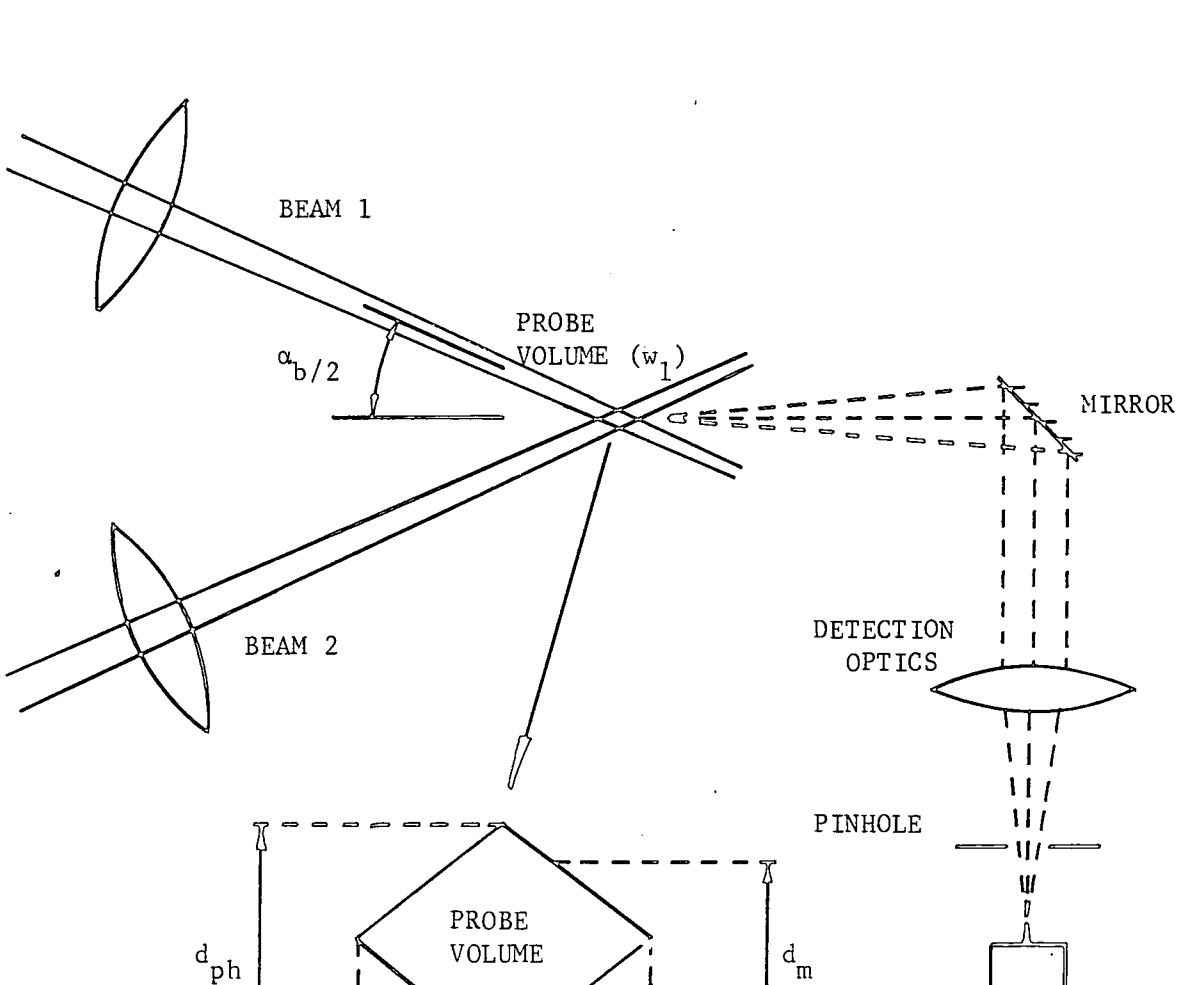

Figure 4.6 PRINCIPLE OF DETECTING THE SCATTERED LIGHT FROM THE PROBE VOLUME

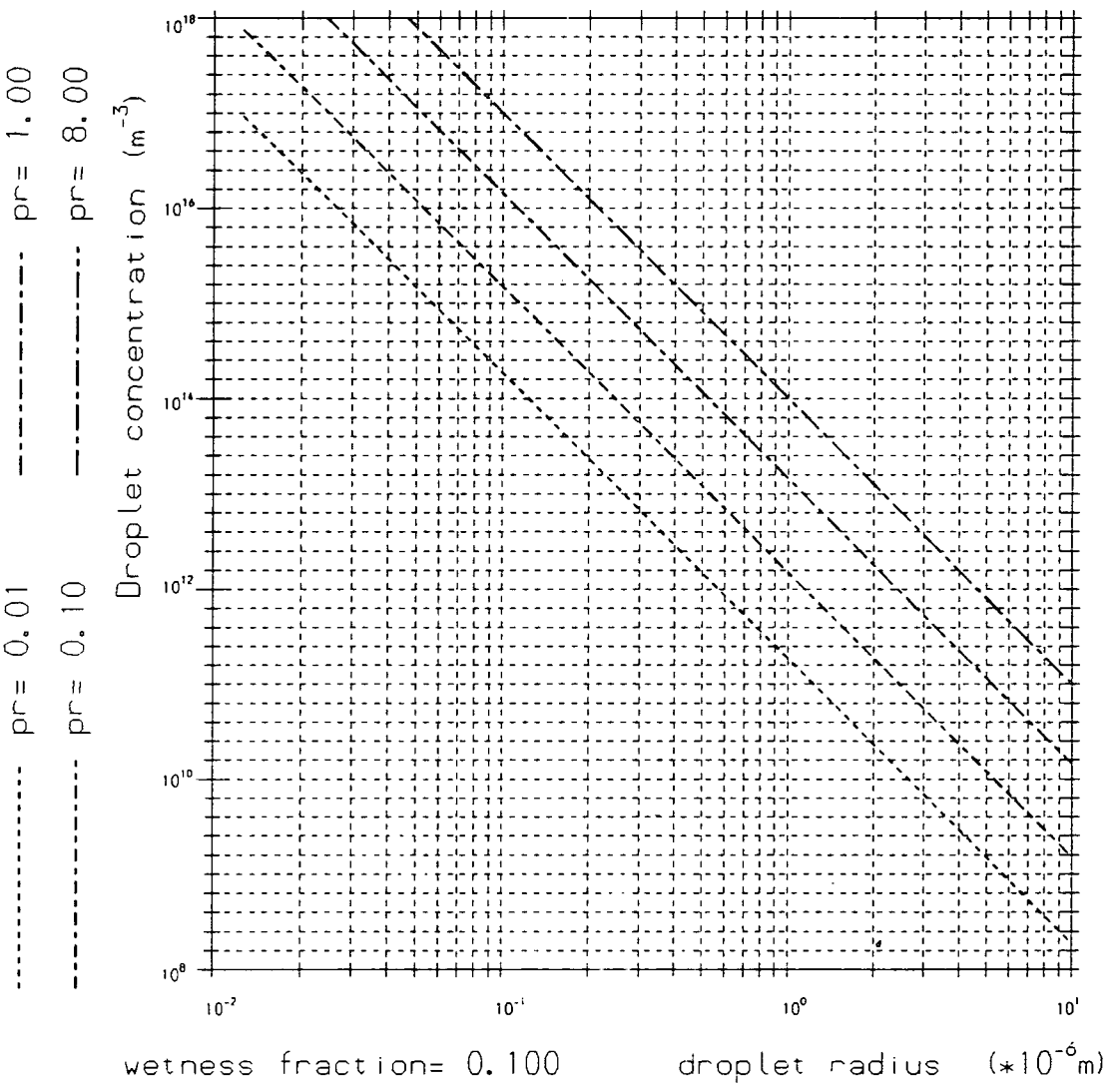

Figure 4.7 WATER DROPLET CONCENTRATION IN WET STEAM FOR A RANGE OF PRESSURES

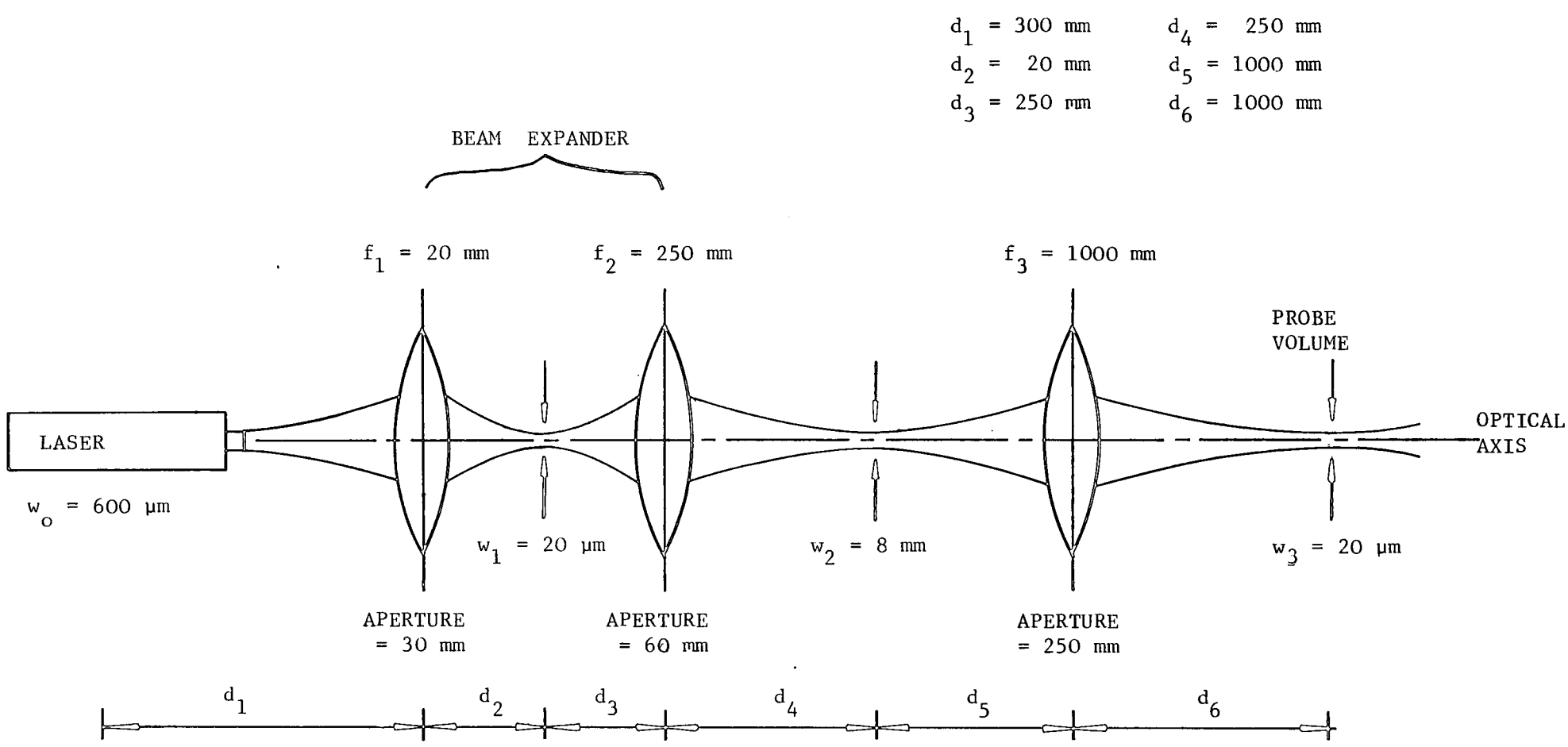

Figure 4.8 THE PATH OF THE LASER BEAM THROUGH THE THREE LENS SYSTEM

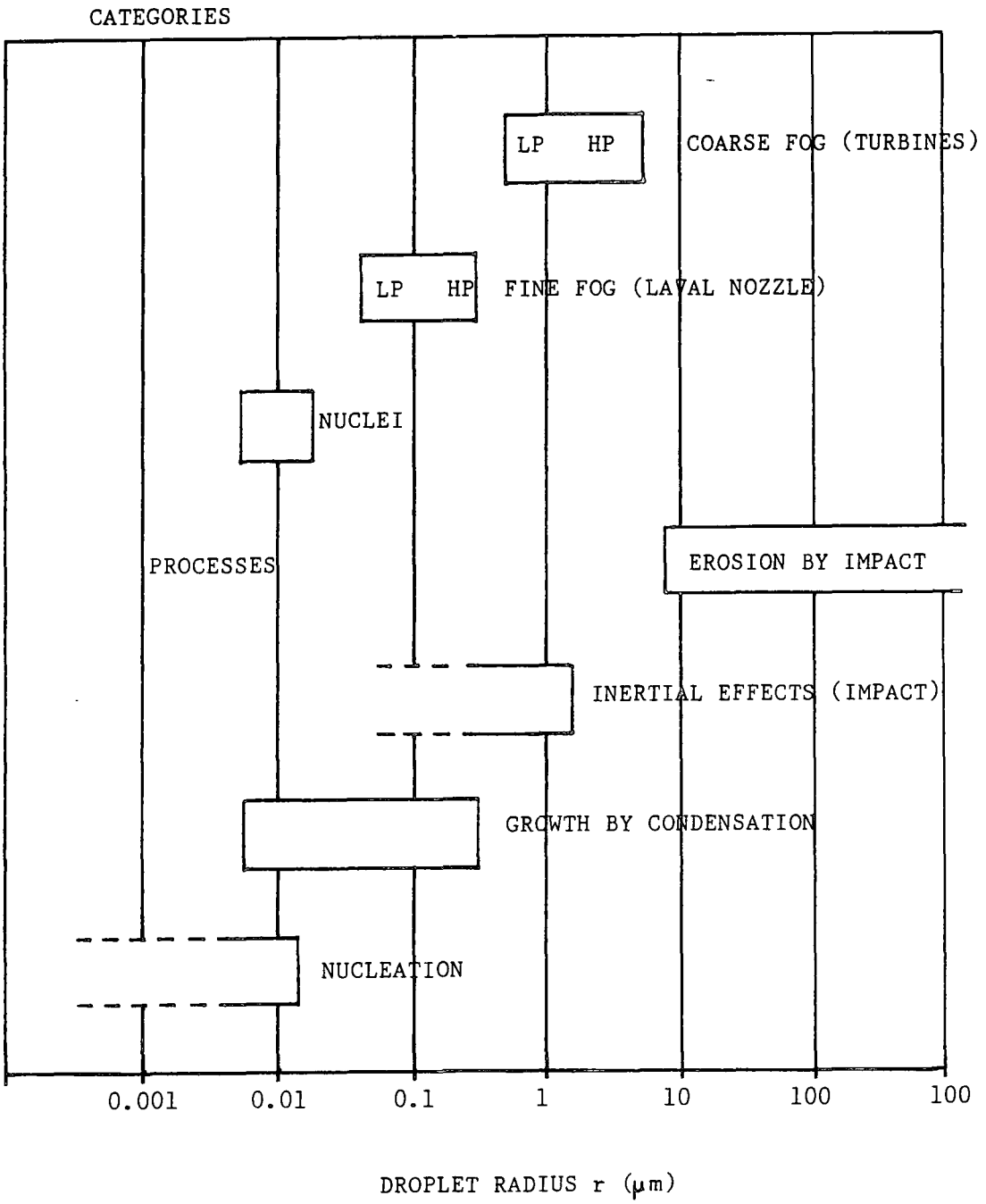

Figure 5.1 SIZE CATEGORIES OF WATER DROPLETS AND PROCESSES THEY ARE INVOLVED IN.

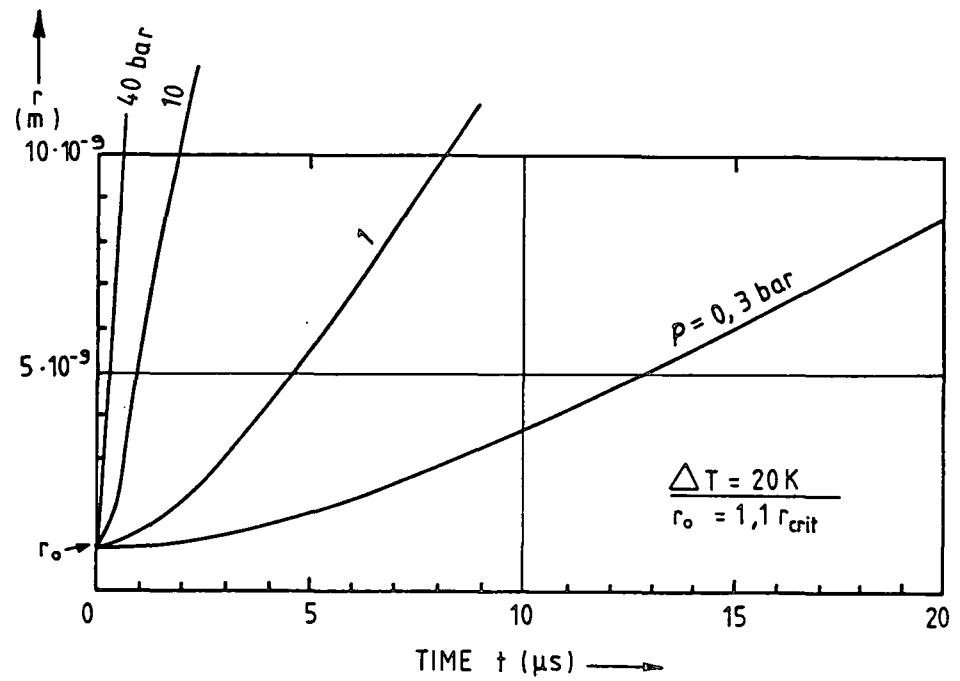

Figure 5.2 GROWTH OF A NEAR-CRITICAL WATER DROPLET AT VARIOUS PRESSURE LEVELS

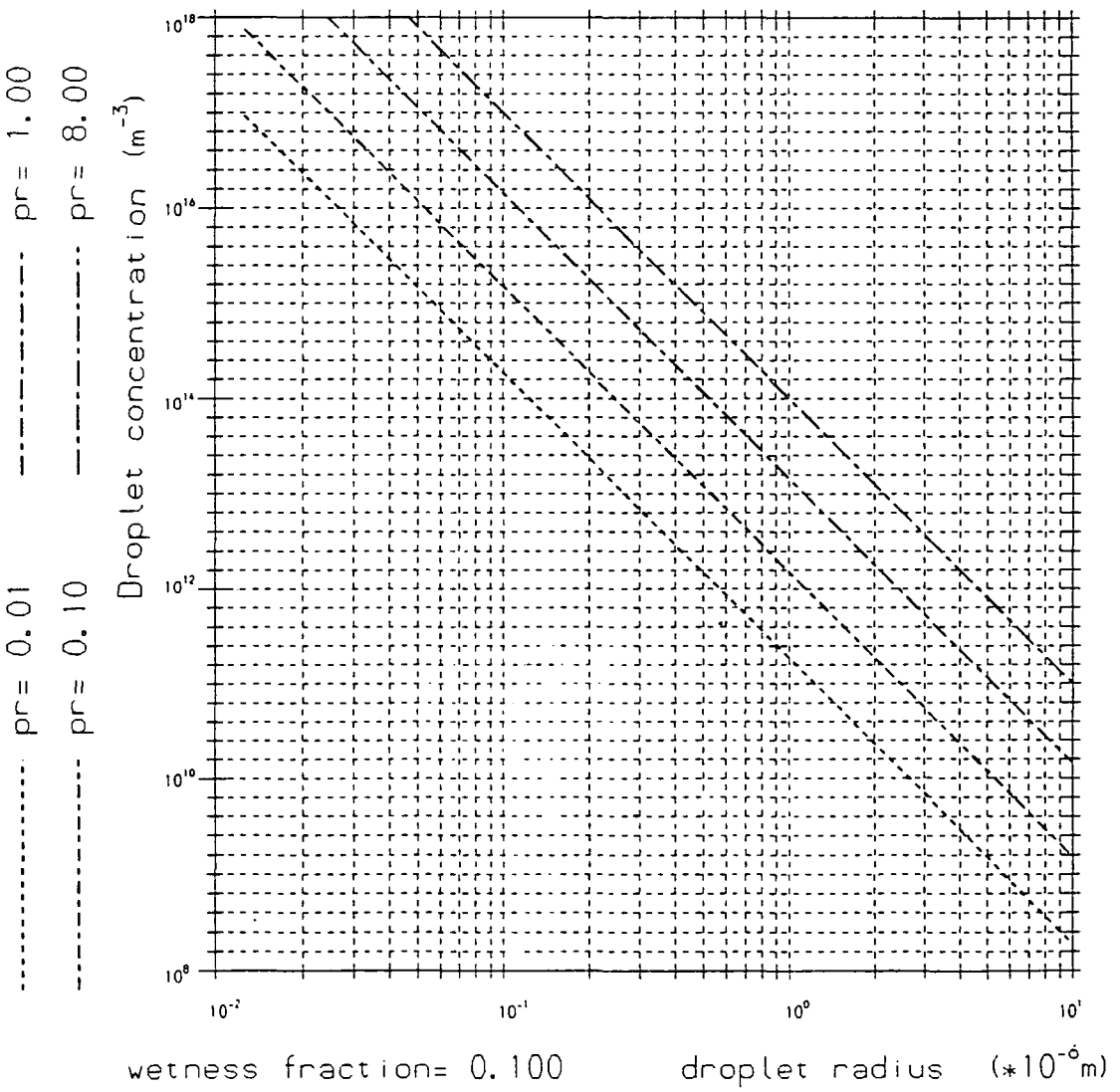

Figure 5.3 WATER DROPLET CONCENTRATION IN WET STEAM FOR A RANGE OF PRESSURES

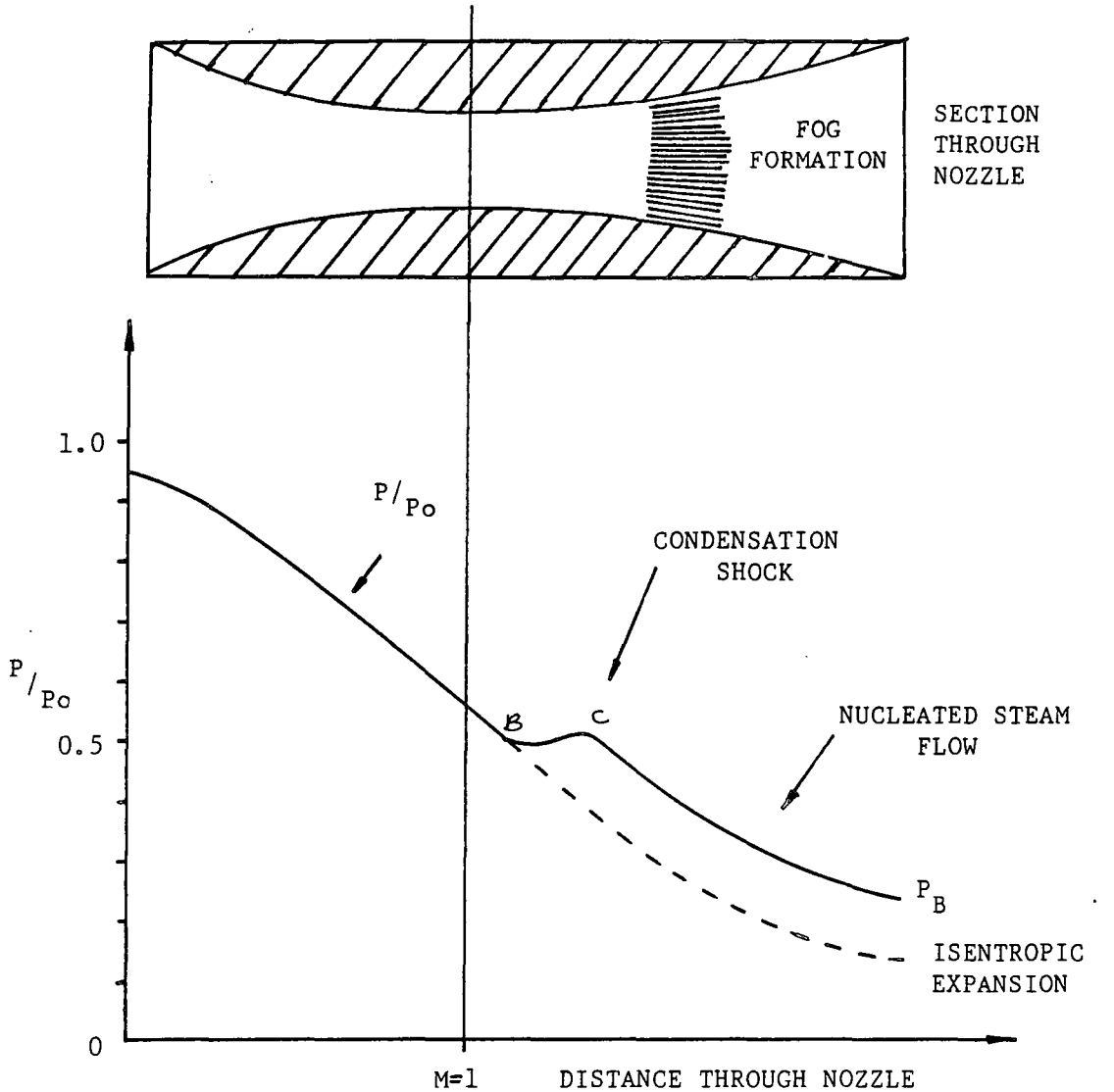

Figure 5.4 PRESSURE DISTRIBUTION ACROSS A LAVAL NOZZLE

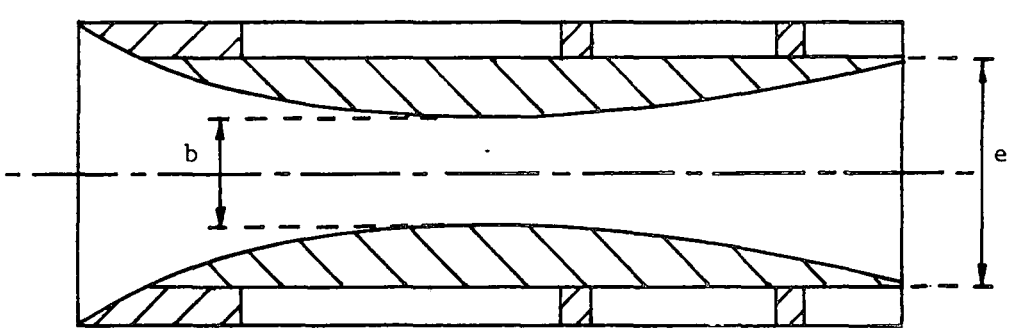

NOZZLE	A	B	C	D	E
b(mm)	63	100	120	127	140
e(mm)	114	144	150	148	157

Figure 5.5 GEOMETRY OF THE EXPERIMENTAL LAVAL NOZZLE - MOORE(70)

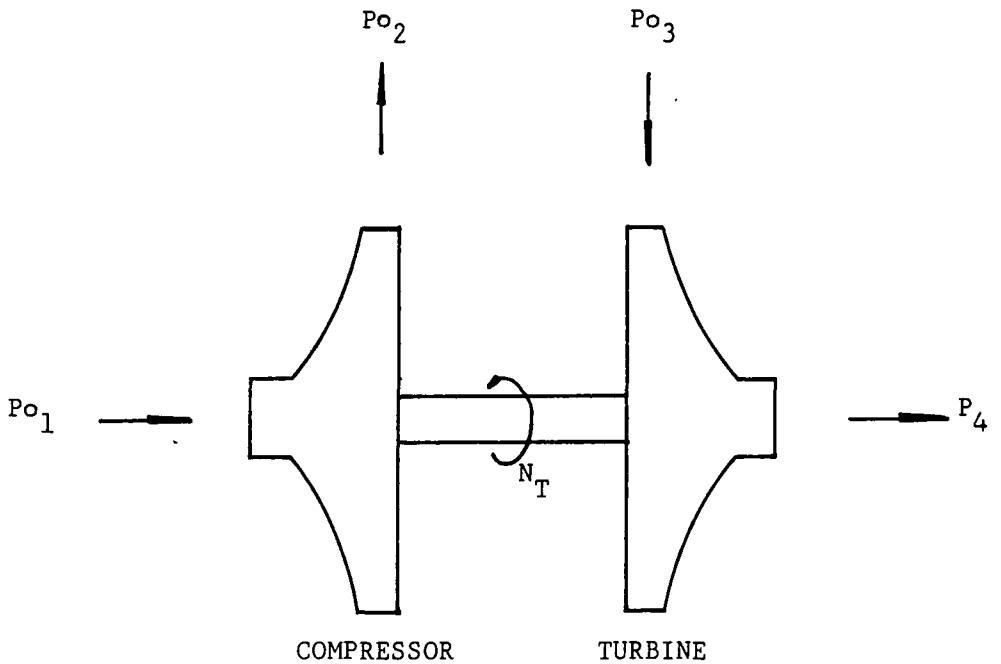

Figure 5.6 NOTATION USED FOR A TURBOCHARGER

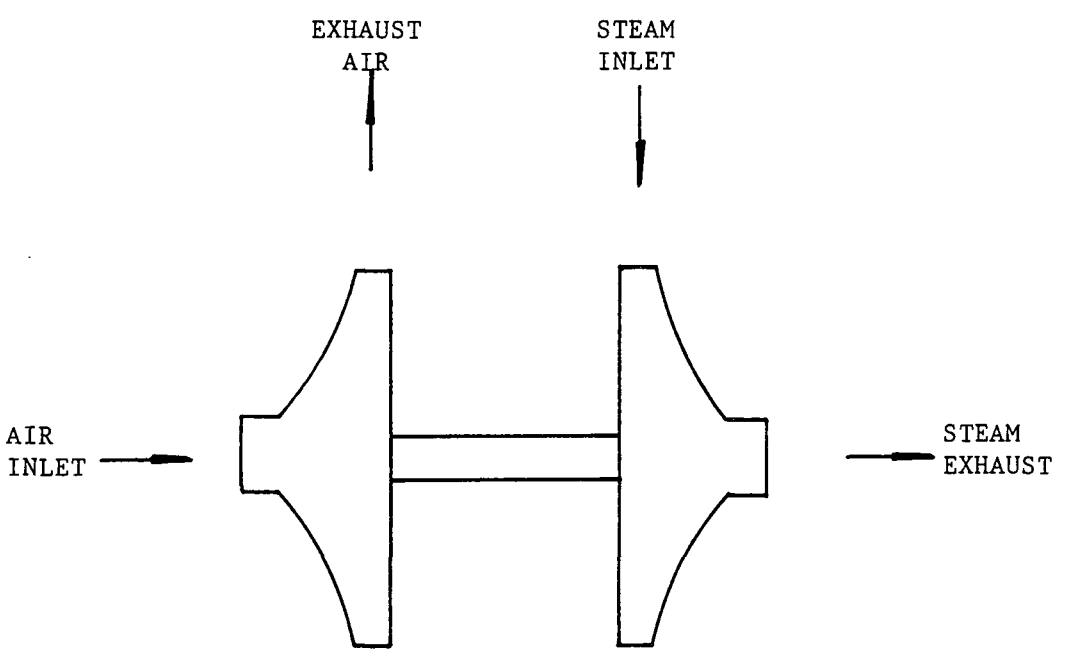

Figure 5.7 USE OF A TURBOCHARGER ON THE EXPERIMENTAL RIG

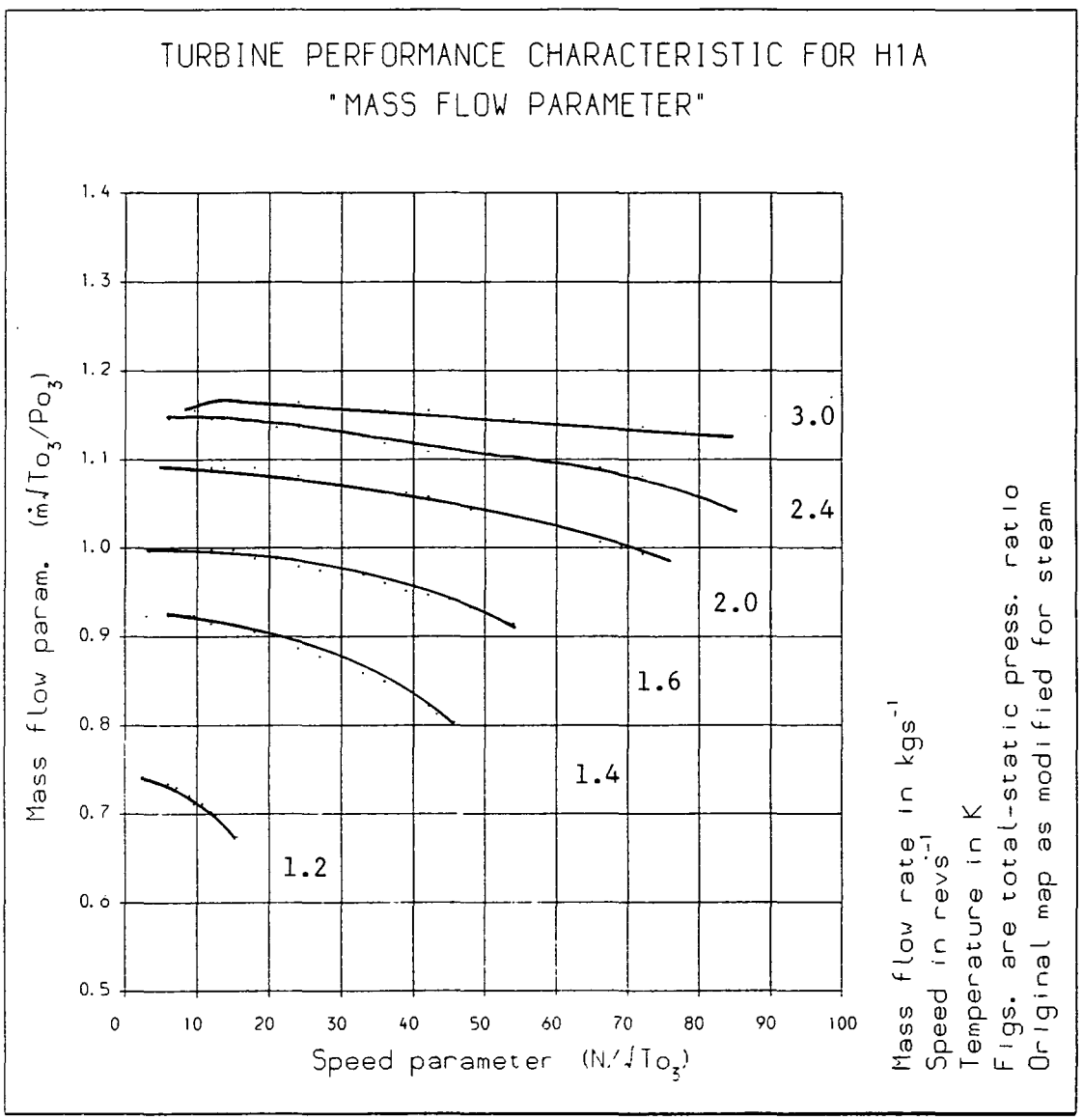

Figure 5.8

(REPRODUCTION OF ORIGINAL MAP BY COURTESY OF HOLSET ENGINEERING LTD)

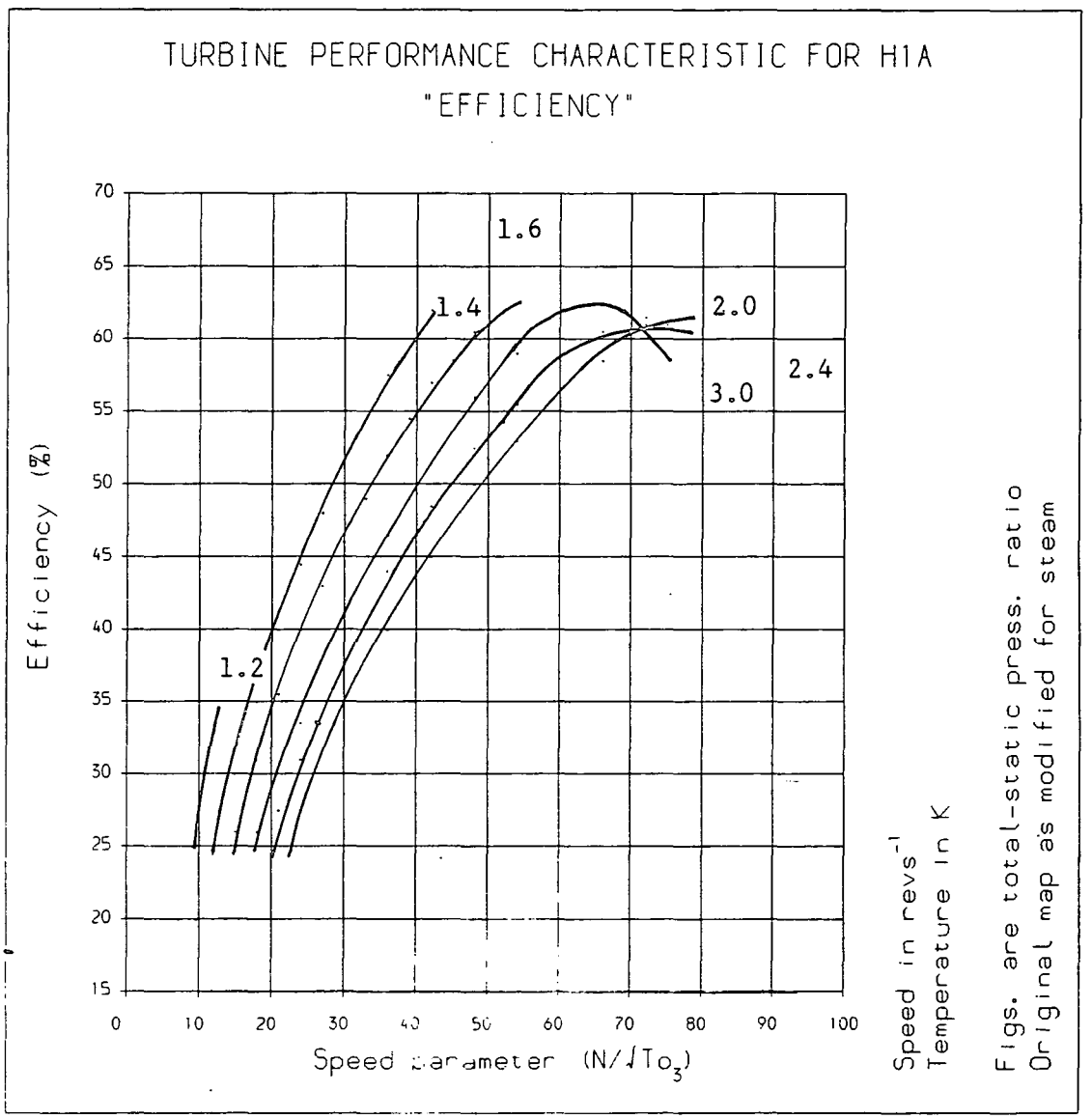

Figure 5.9

(REPRODUCTION OF ORIGINAL MAP BY COURTESY OF HOLSET ENGINEERING LTD)

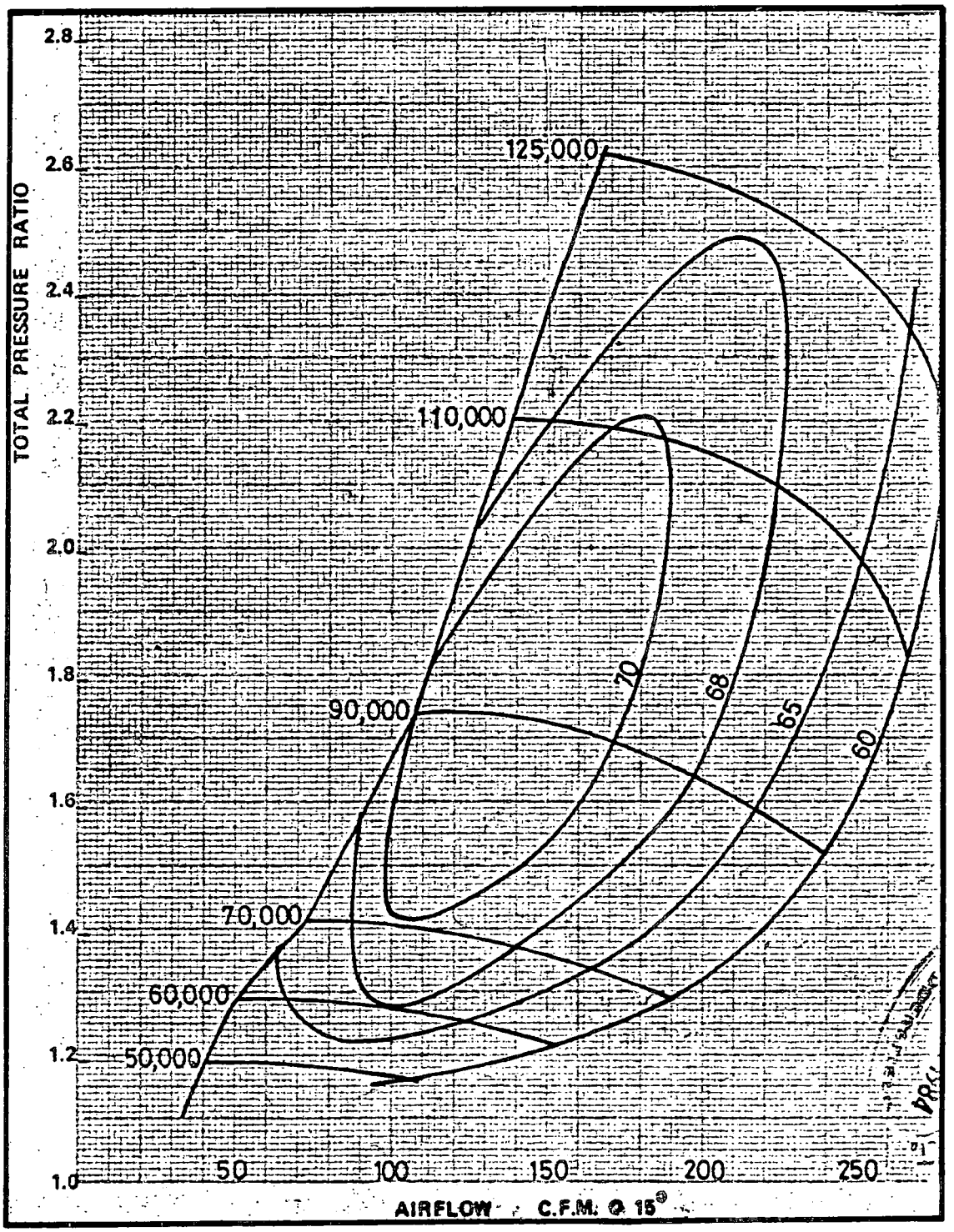

Figure 5.10 COMPRESSOR PERFORMANCE MAP FOR H1a TURBOCHARGER (SPEED AND EFFICIENCY)

(REPRODUCTION BY COURTESY OF HOLSET ENGINEERING LTD)

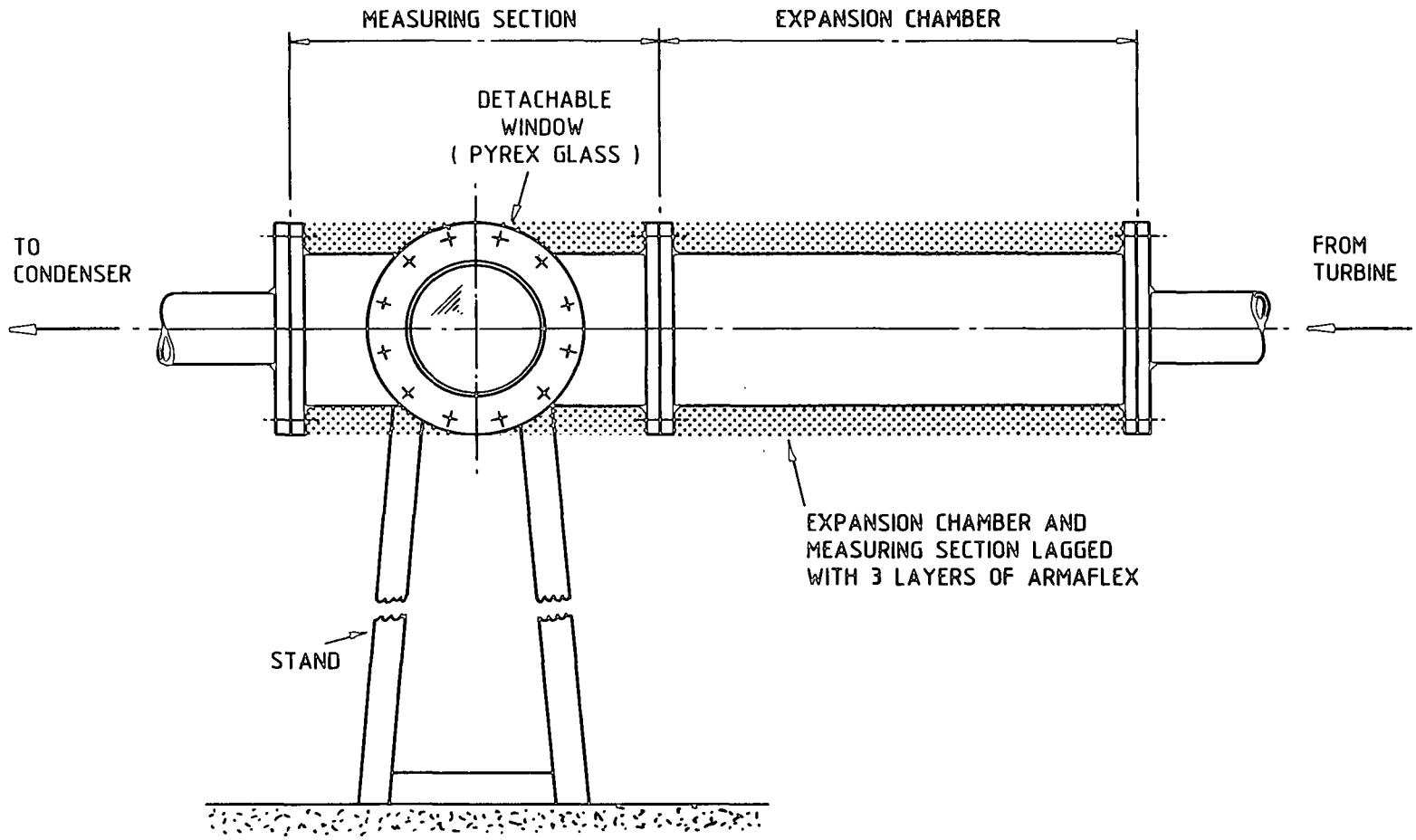

Figure 6.1 LAYOUT OF EXPERIMENTAL STEAM FACILITY

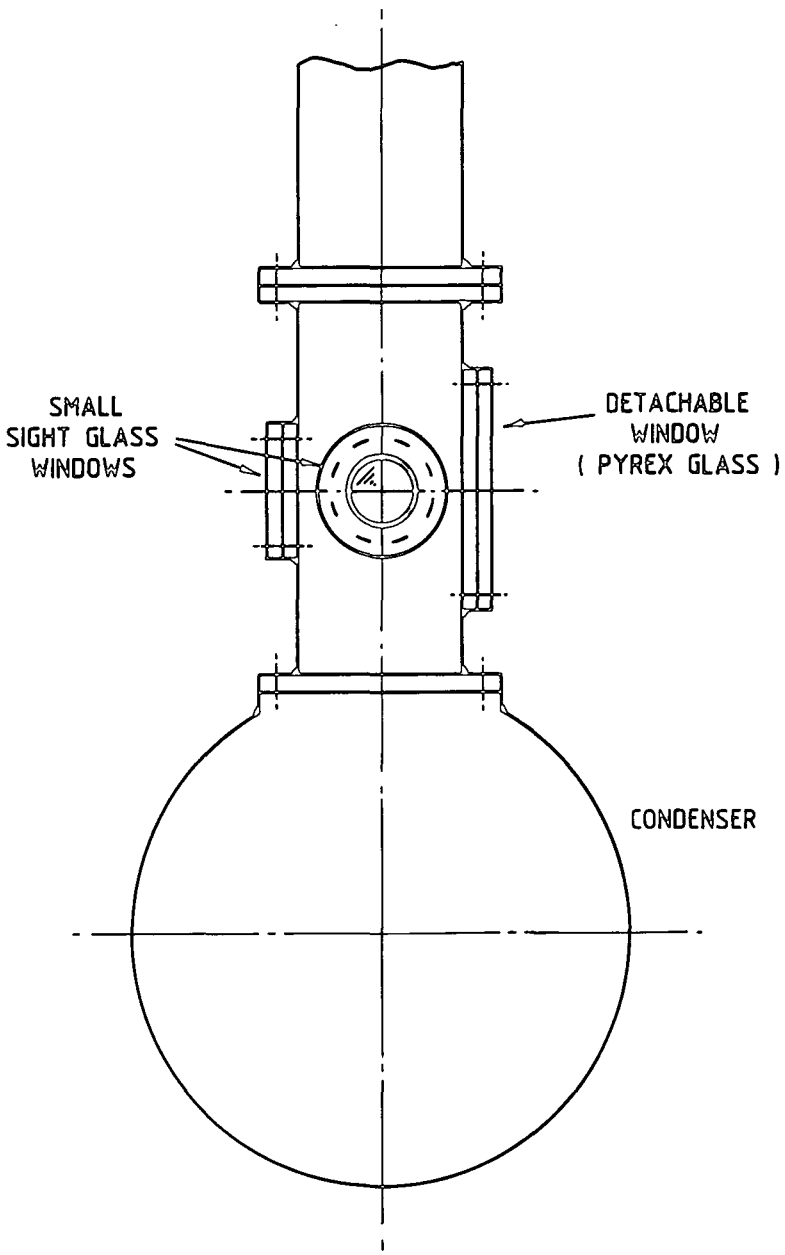

Figure 6.2 PROPOSED LOCATION ON TOP OF CONDENSER

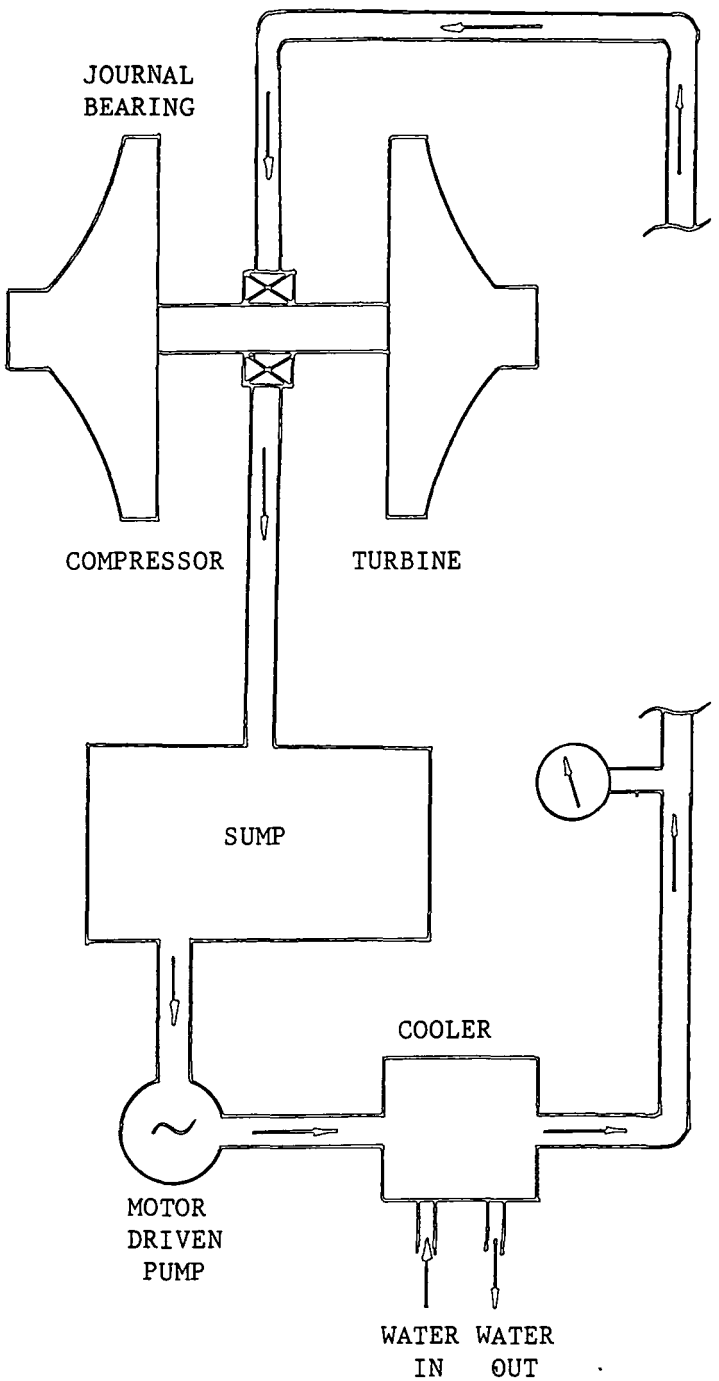

Figure 6.3 ESSENTIAL FEATURES OF THE LUBRICATION SYSTEM

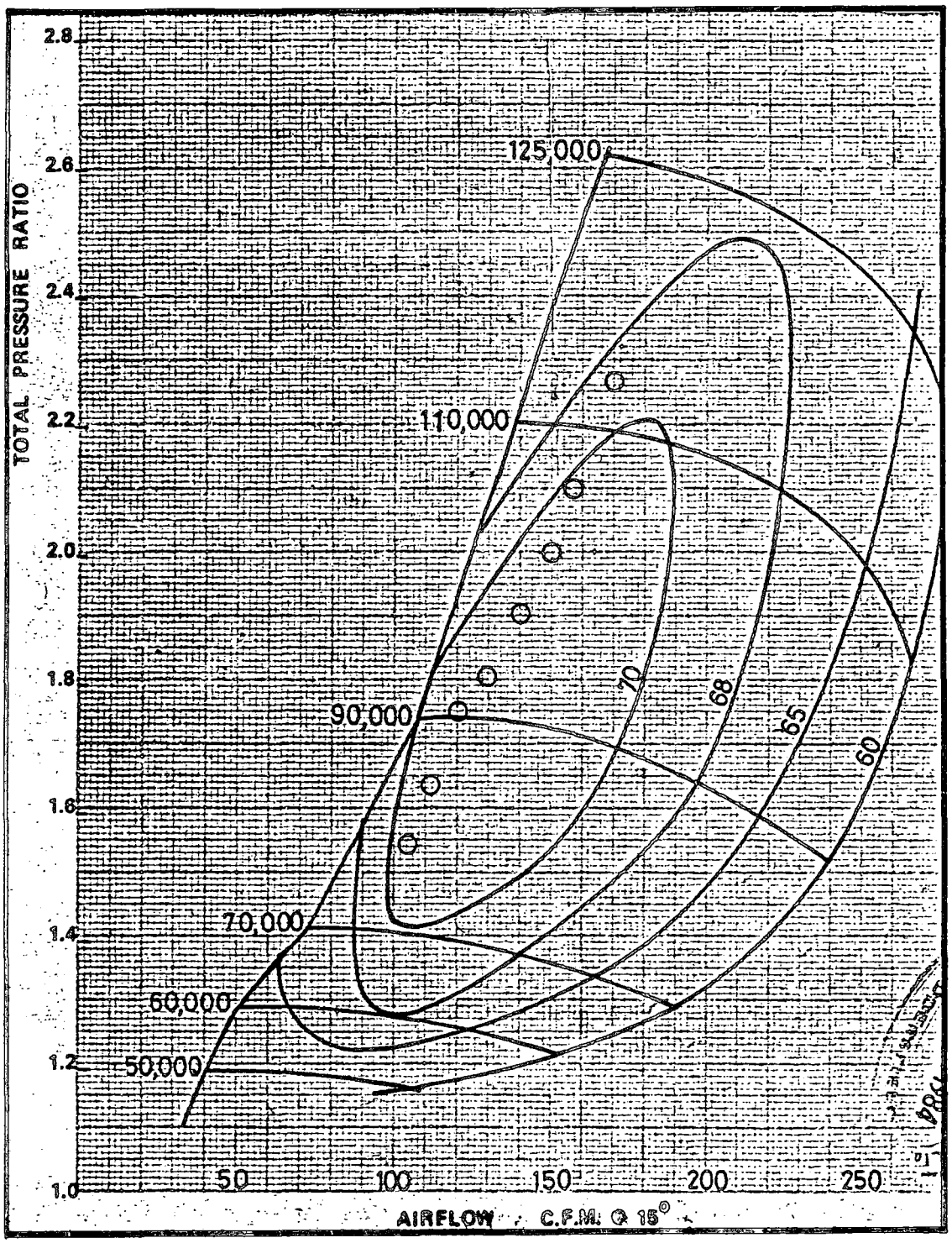

○ = RUNNING CONDITION

Figure 6.4 COMPRESSOR PERFORMANCE MAP FOR Hla SHOWING THE RUNNING CONDITIONS

(Reproduction of original by courtesy of Holset Engineering Ltd)

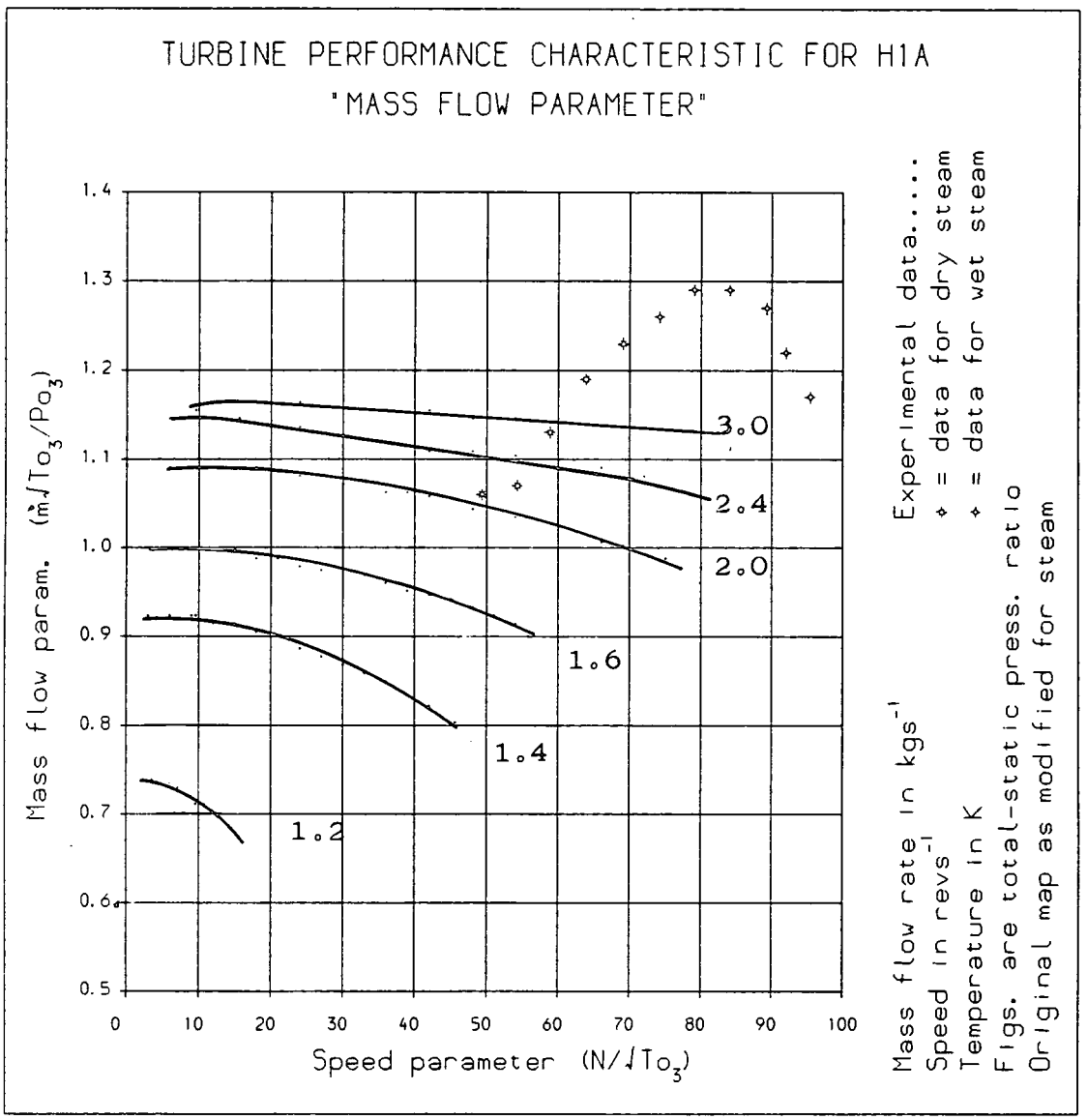
TURBINE PERFORMANCE CHARACTERISTIC FOR H1A
"MASS FLOW PARAMETER"
Mass flow param. ($\dot{m}\sqrt{To_3}/Po_3$)
Speed parameter ($N/\sqrt{To_3}$)
1.4
1.3
1.2
1.1
1.0
0.9
0.8
0.7
0.6
0.5
0
10
20
30
40
50
60
70
80
90
100
3.0
2.4
2.0
1.6
1.4
1.2
Experimental data.....
+ = data for dry steam
+ = data for wet steam
Mass flow rate in kgs^{-1}
Speed in $revs^{-1}$
Temperature in K
Figs. are total-static press. ratio
Original map as modified for steam

Figure 6.5

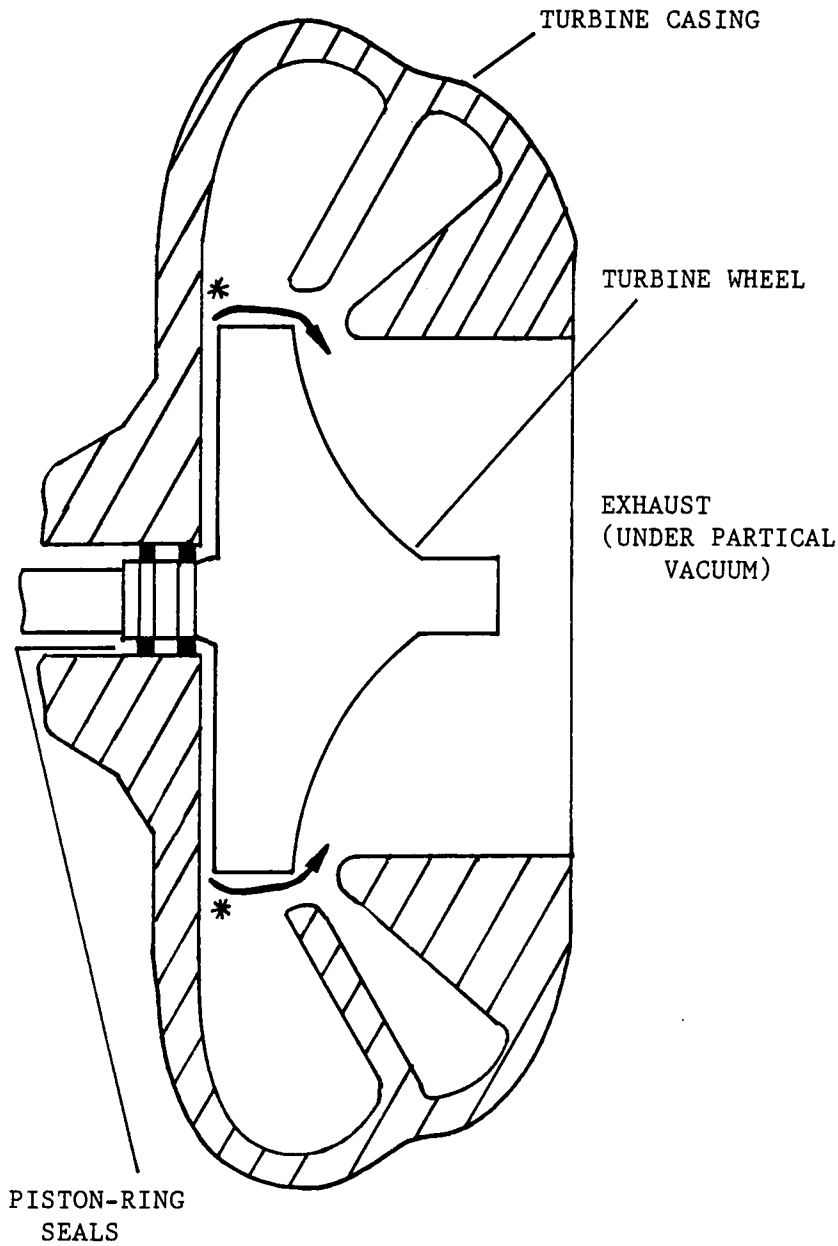

Figure 6.6 THE POSSIBLE PASSAGE OF OIL FROM THE JOURNAL BEARINGS INTO THE EXHAUST

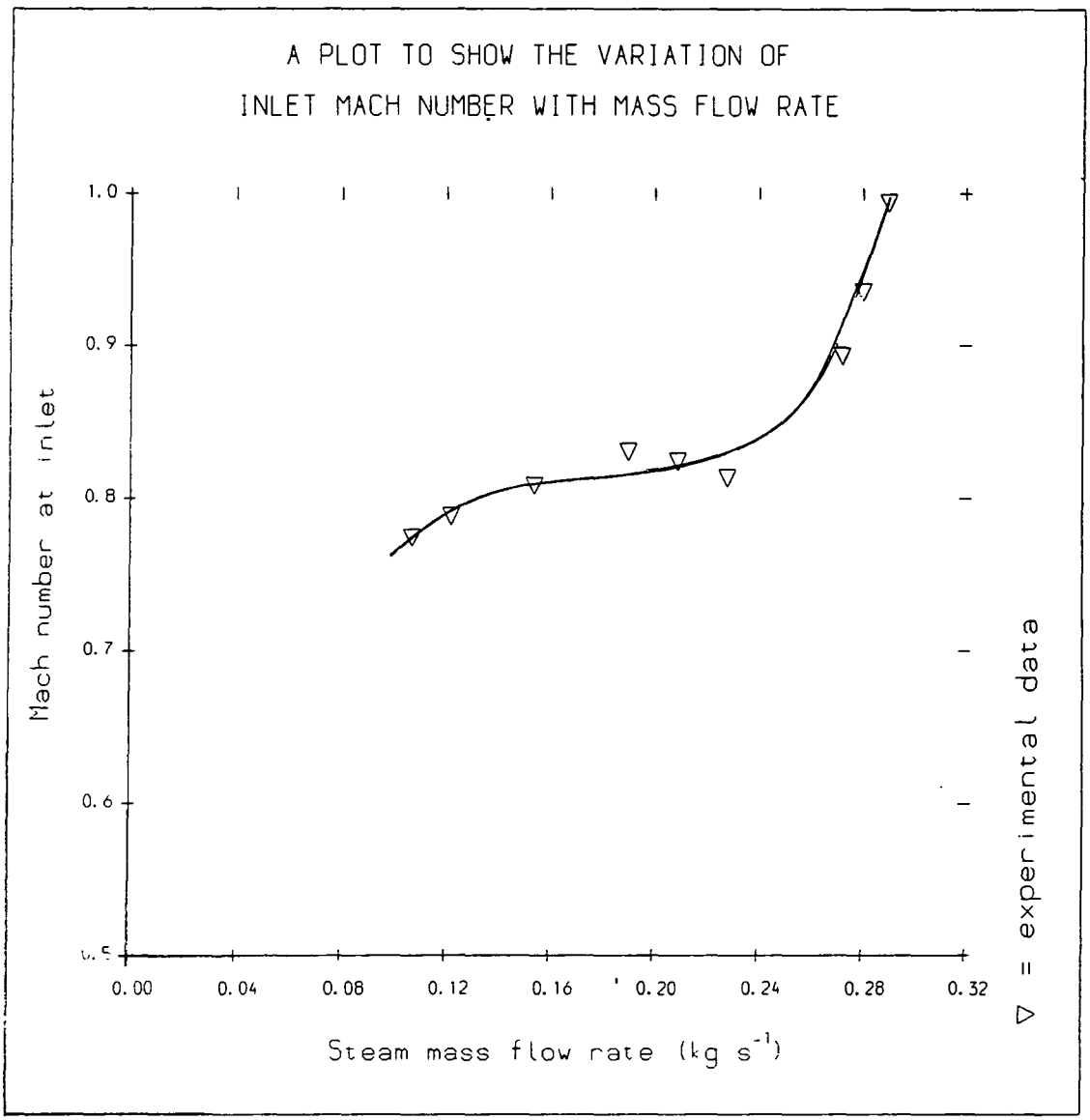
A PLOT TO SHOW THE VARIATION OF
INLET MACH NUMBER WITH MASS FLOW RATE
Mach number at inlet
1.0
0.9
0.8
0.7
0.6
0.5
0.00
0.04
0.08
0.12
0.16
0.20
0.24
0.28
0.32
Steam mass flow rate (kg s⁻¹)
▽ = experimental data

Figure 6.7

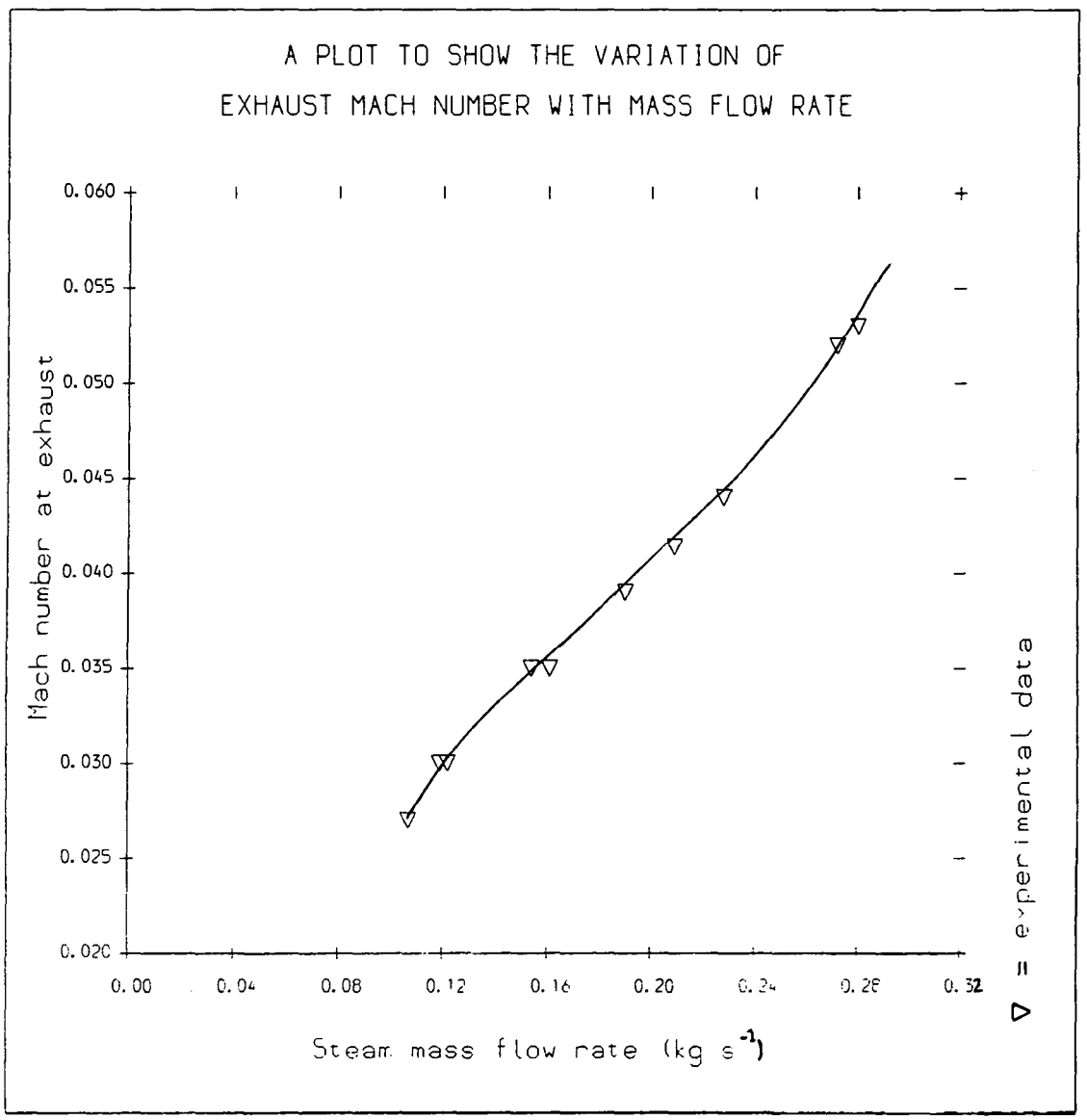
A PLOT TO SHOW THE VARIATION OF
EXHAUST MACH NUMBER WITH MASS FLOW RATE
Mach number at exhaust
0.060
0.055
0.050
0.045
0.040
0.035
0.030
0.025
0.020
0.00
0.04
0.08
0.12
0.16
0.20
0.24
0.28
0.32
Steam mass flow rate (kg s-1)
▽ = experimental data

Figure 6.8

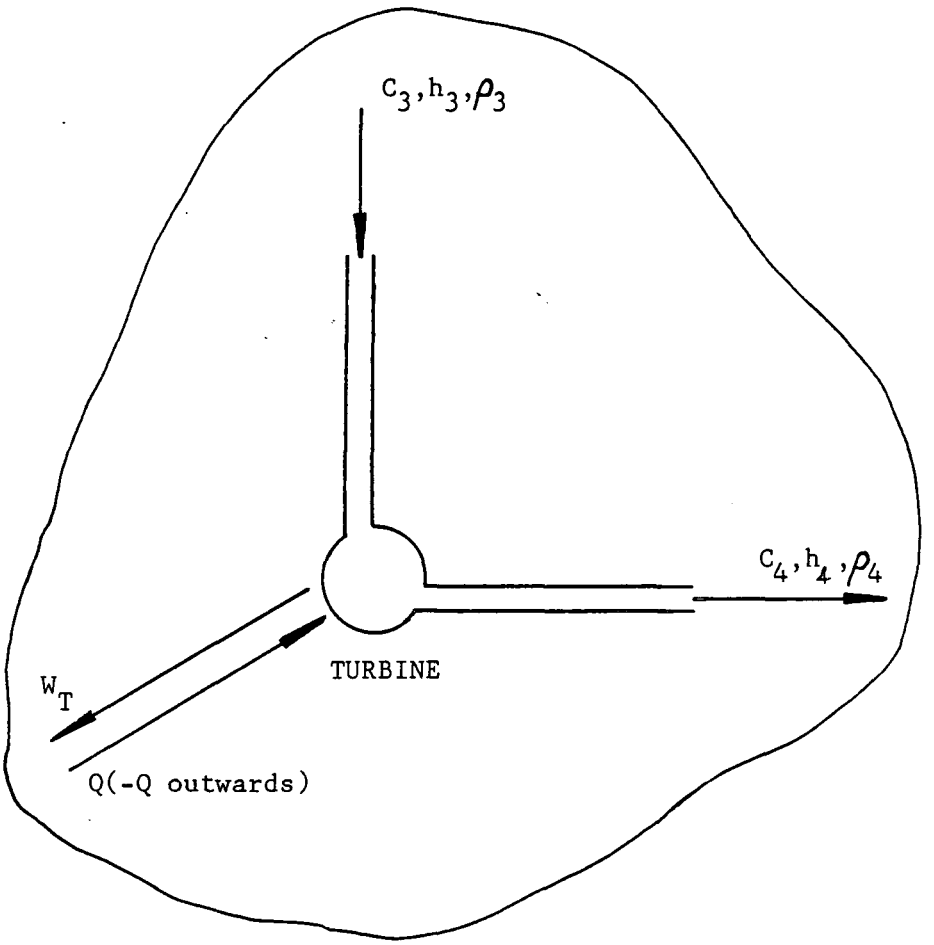

Figure 6.9 THE STEADY FLOW ENERGY EQUATION

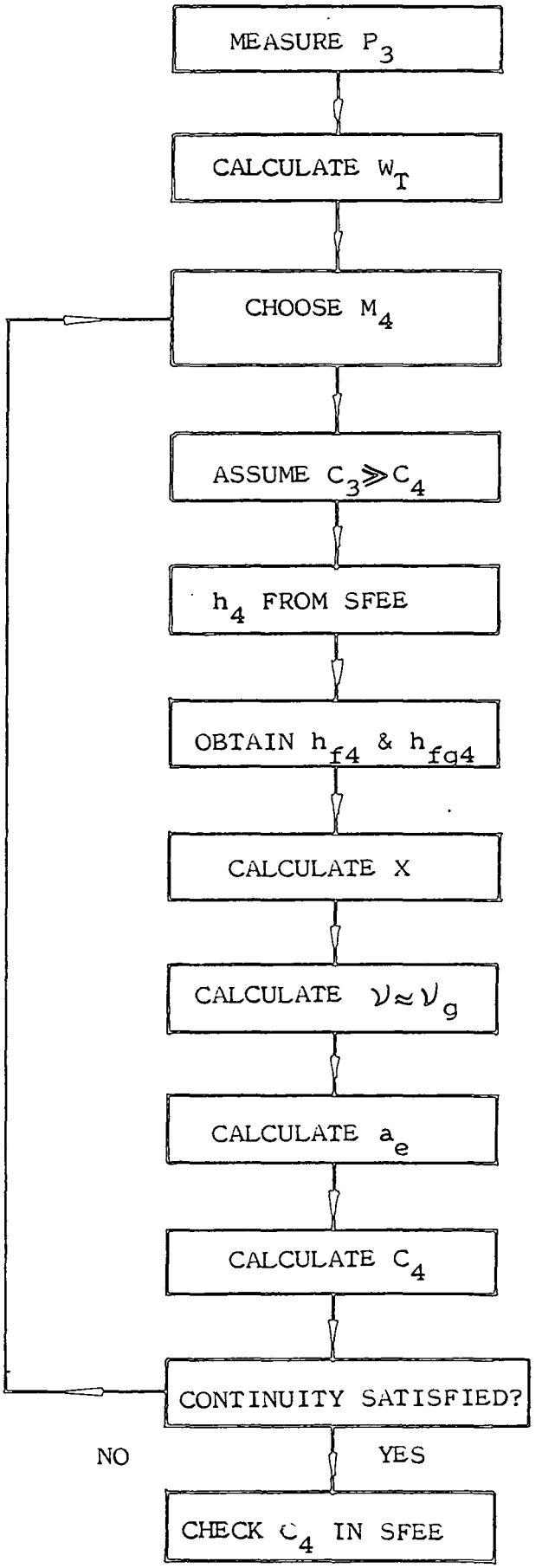

Figure 6.10 FLOW CHART FOR CALCULATING THE DRYNESS FRACTION

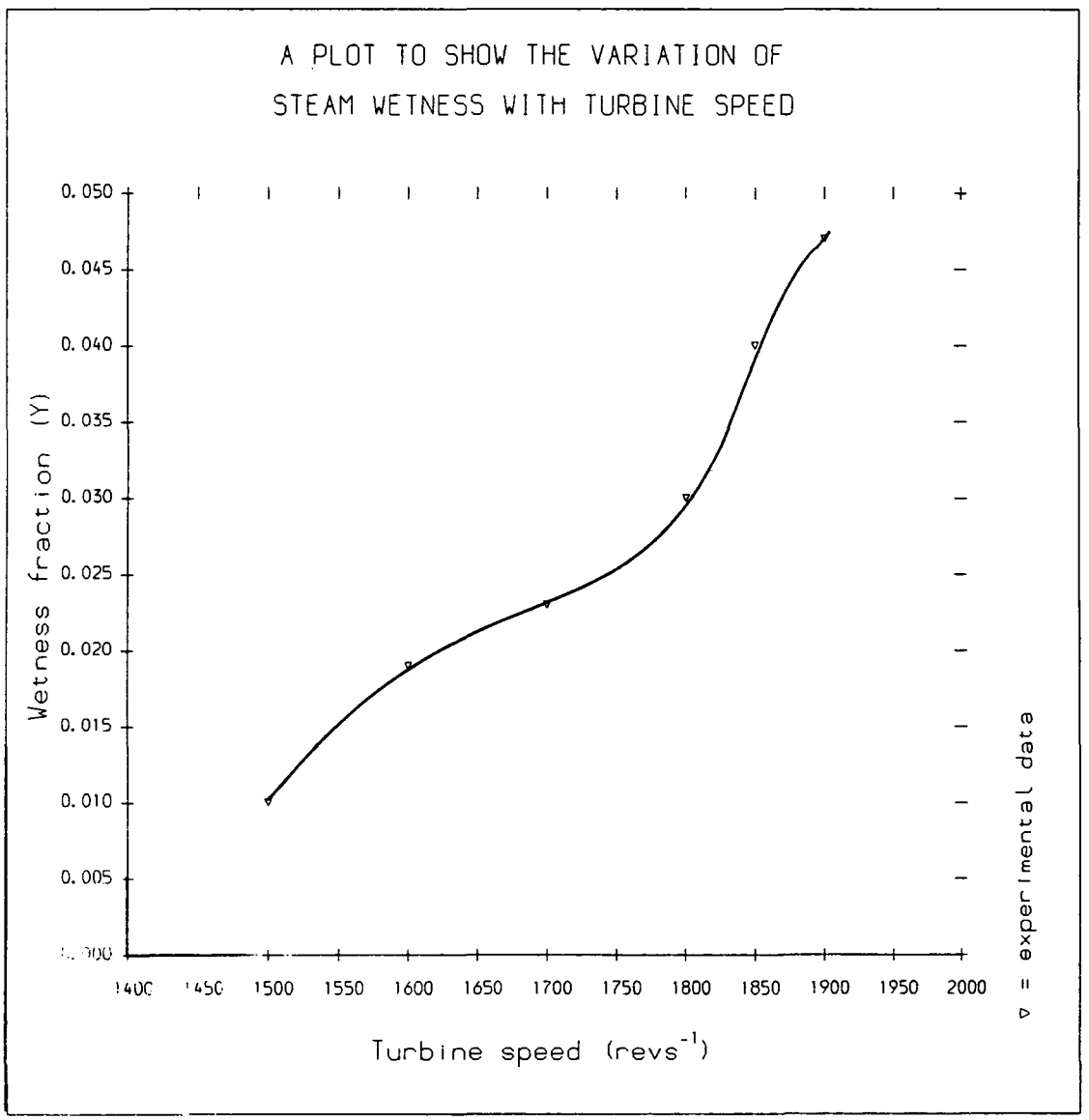
A PLOT TO SHOW THE VARIATION OF
STEAM WETNESS WITH TURBINE SPEED
Wetness fraction (Y)
0.050
0.045
0.040
0.035
0.030
0.025
0.020
0.015
0.010
0.005
1400
1450
1500
1550
1600
1650
1700
1750
1800
1850
1900
1950
2000
Turbine speed (revs^{-1})
▽ = experimental data

Figure 6.11

TURBINE SPEED = 1500 rps
SUPPLY PRESSURE = 4.7 bar
SUPPLY TEMPERATURE = 187°C

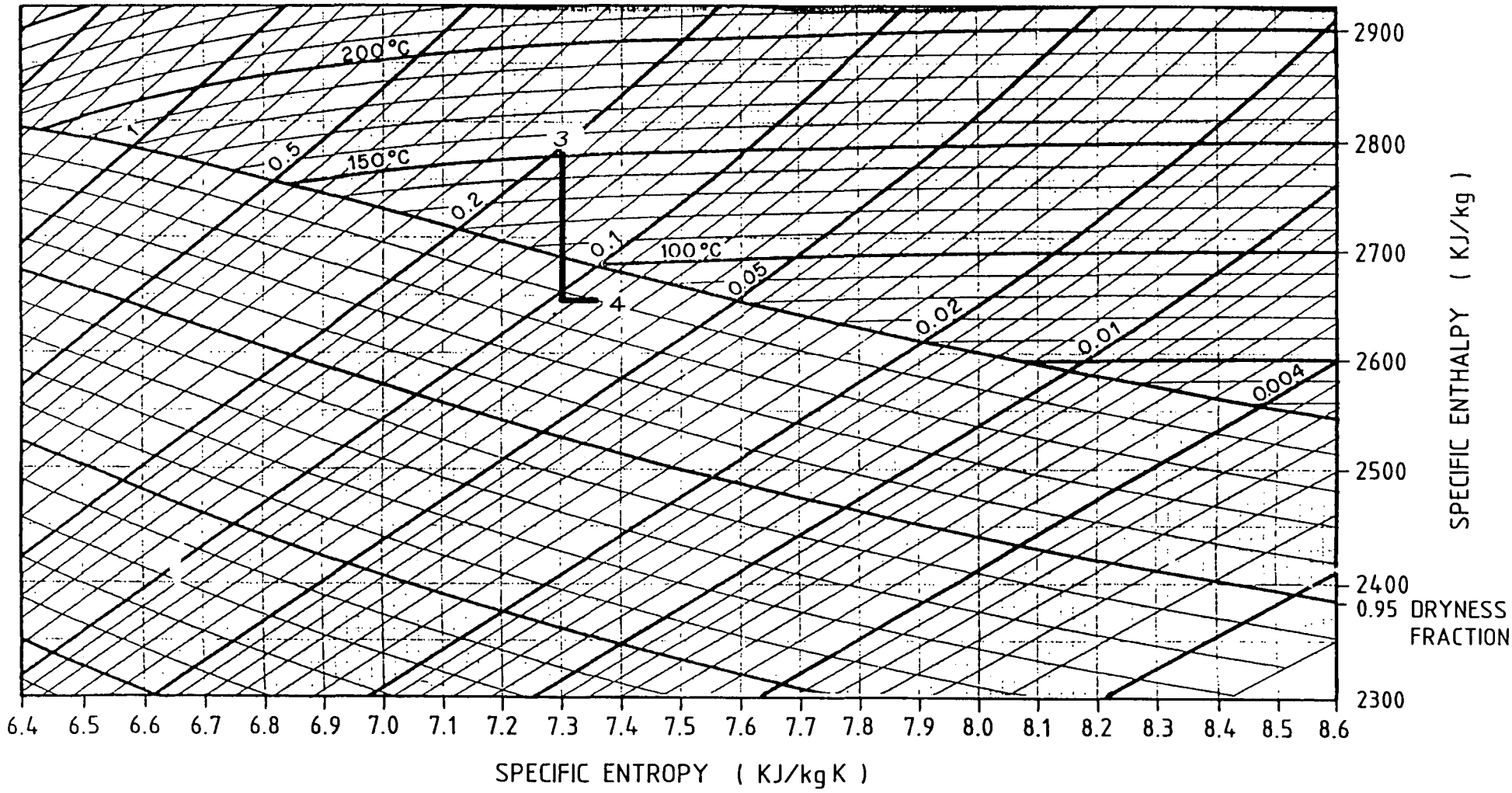

Figure 6.12(a) EXPANSION ACROSS THE TURBINE SHOWN ON A MOLLIER CHART FOR Y = 0.01

TURBINE SPEED = 1600 rps
SUPPLY PRESSURE = 4.7 bar
SUPPLY TEMPERATURE = 187°C

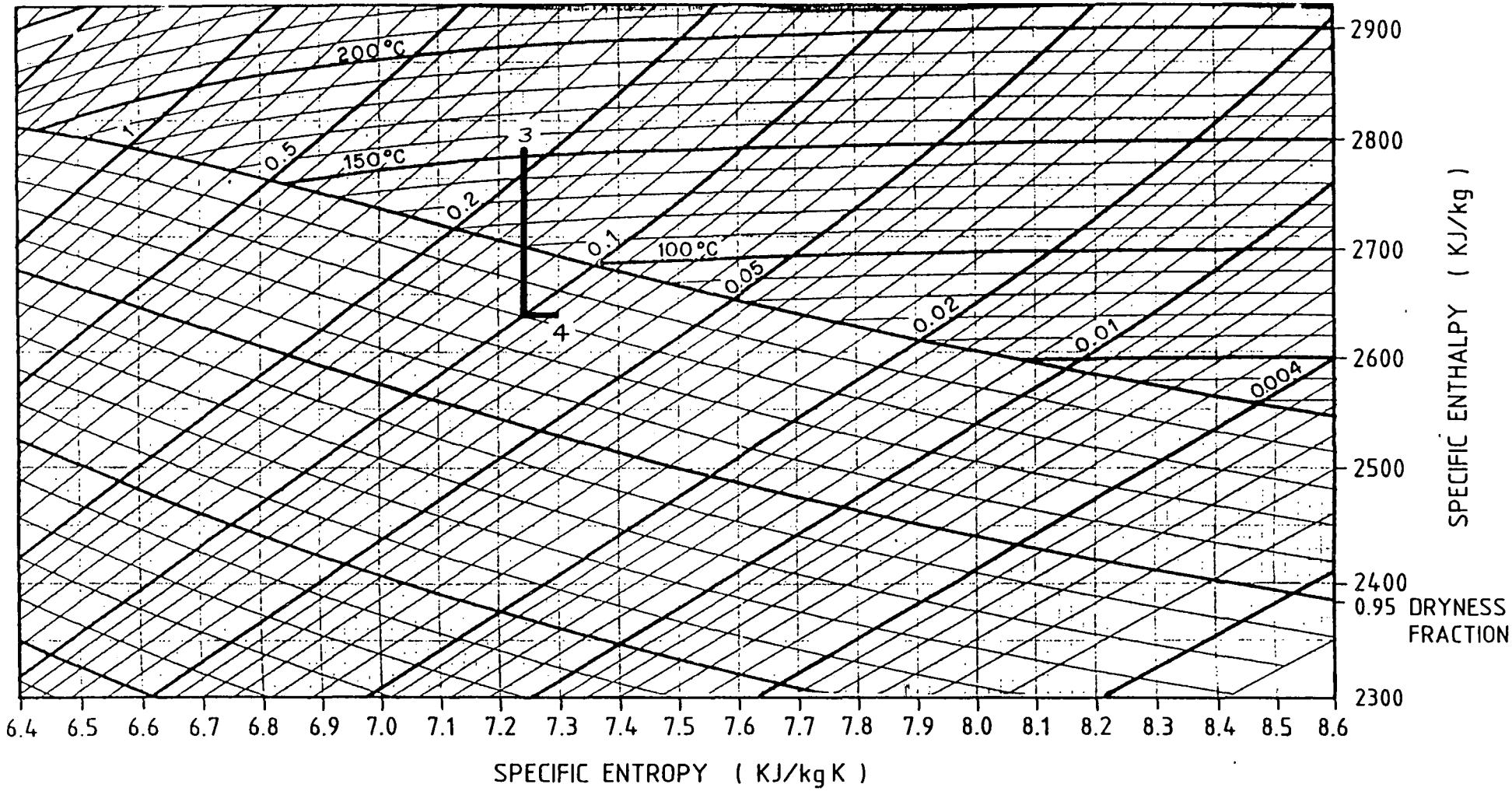

Figure 6.12(b) EXPANSION ACROSS THE TURBINE SHOWN ON A MOLLIER CHART FOR Y = 0.019

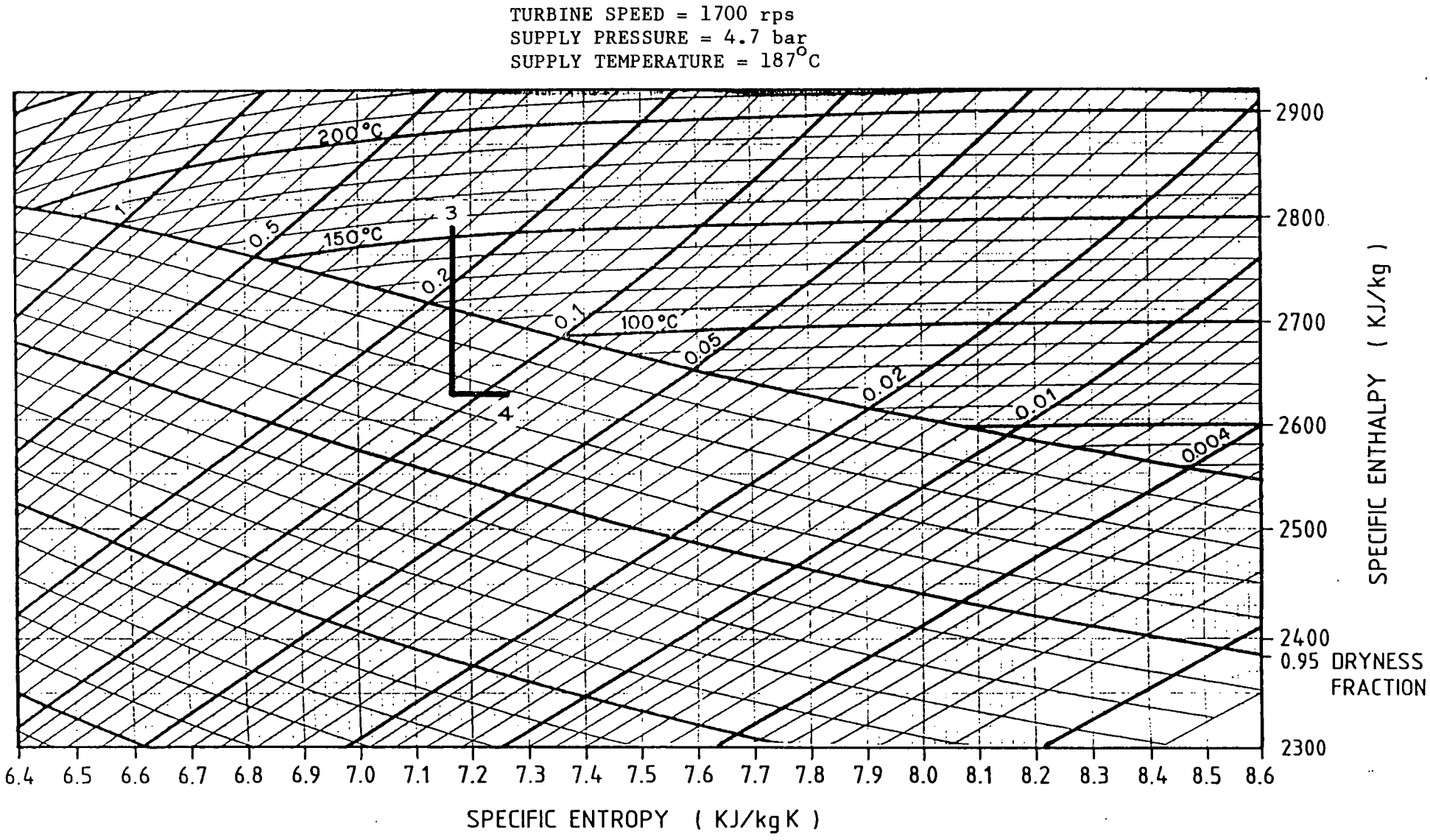

Figure 6.12(c) EXPANSION ACROSS THE TURBINE SHOWN ON A MOLLIER CHART FOR Y = 0.023

TURBINE SPEED = 1800 rps
SUPPLY PRESSURE = 4.7 bar
SUPPLY TEMPERATURE = 187°C

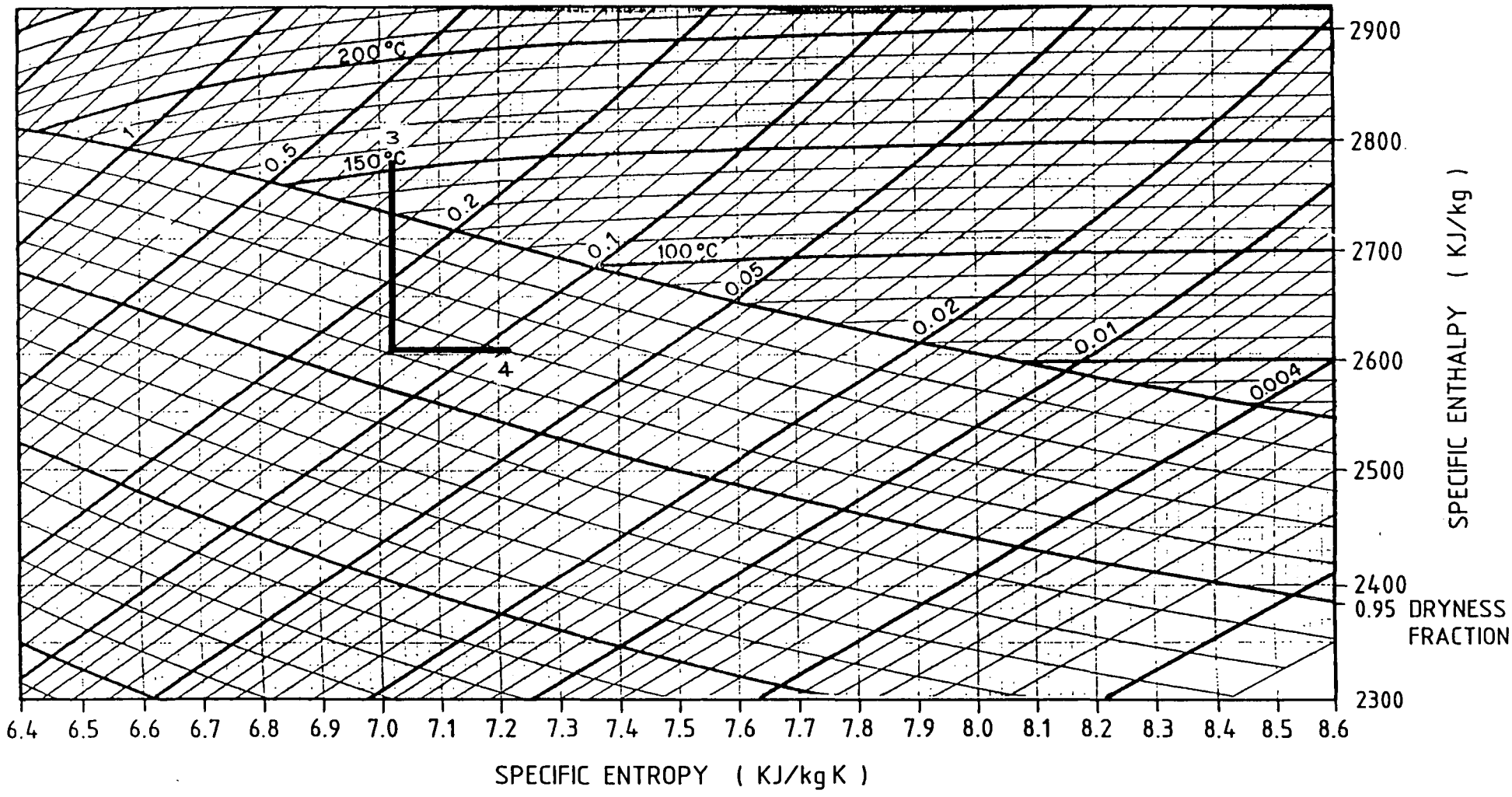

Figure 6.12(d) EXPANSION ACROSS THE TURBINE SHOWN ON A MOLLIER CHART FOR Y = 0.03

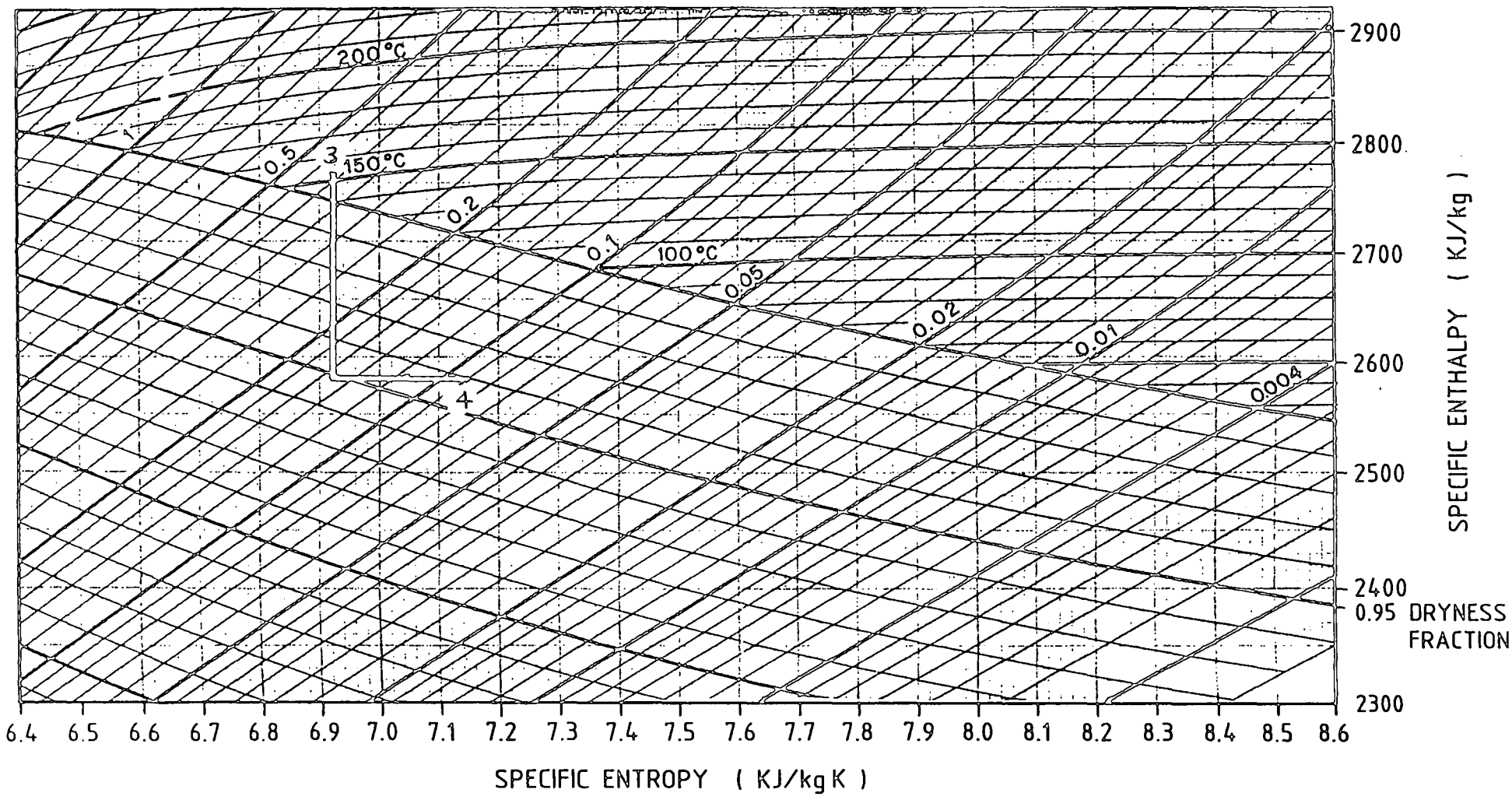

Figure 6.12(e) EXPANSION ACROSS THE TURBINE SHOWN ON A MOLLIER CHART FOR Y = 0.04

TURBINE SPEED = 1900 rps
SUPPLY PRESSURE = 4.7 bar
SUPPLY TEMPERATURE = 187°C

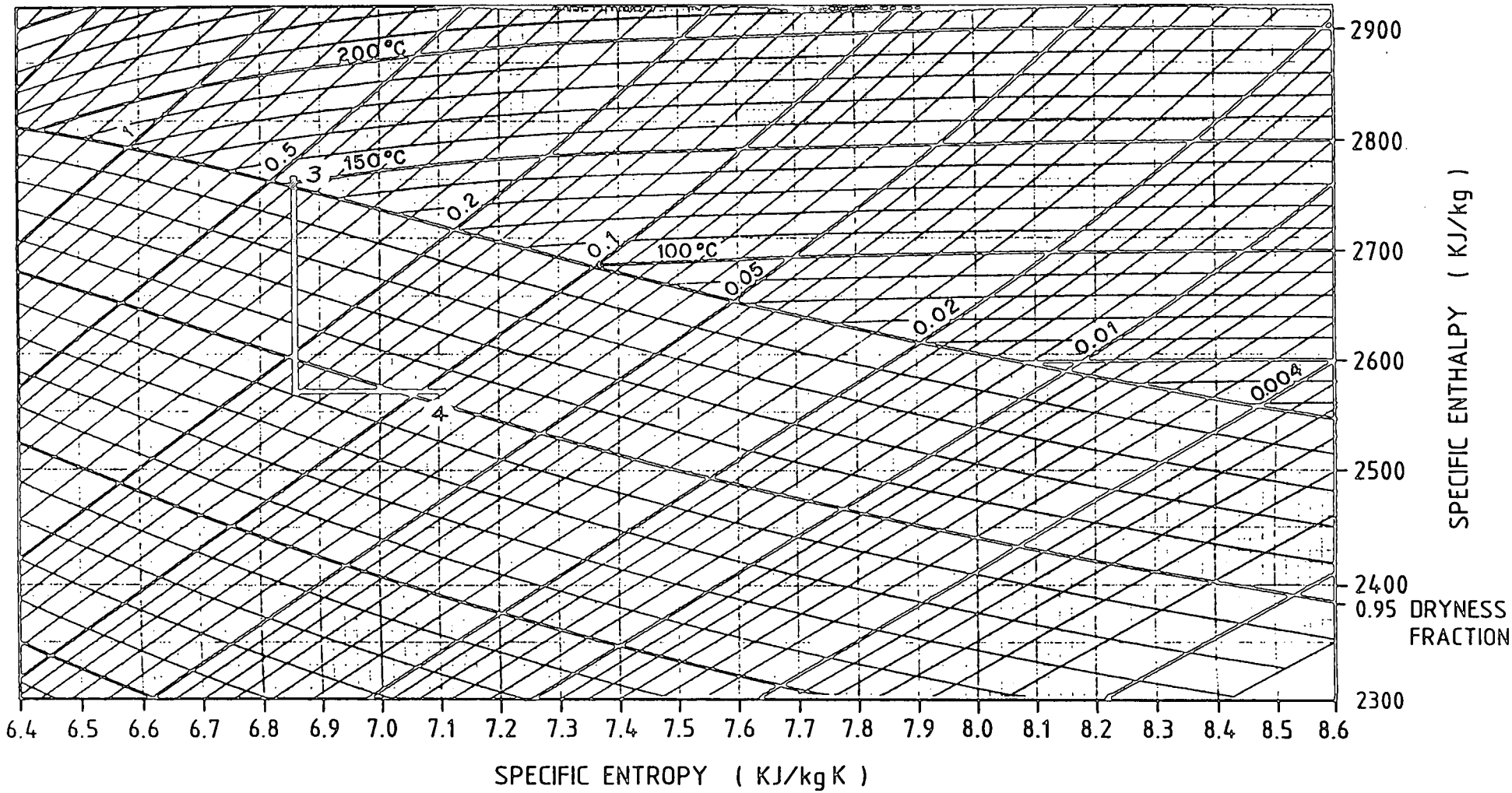

Figure 6.12(f) EXPANSION ACROSS THE TURBINE SHOWN ON A MOLLIER CHART FOR Y = 0.047

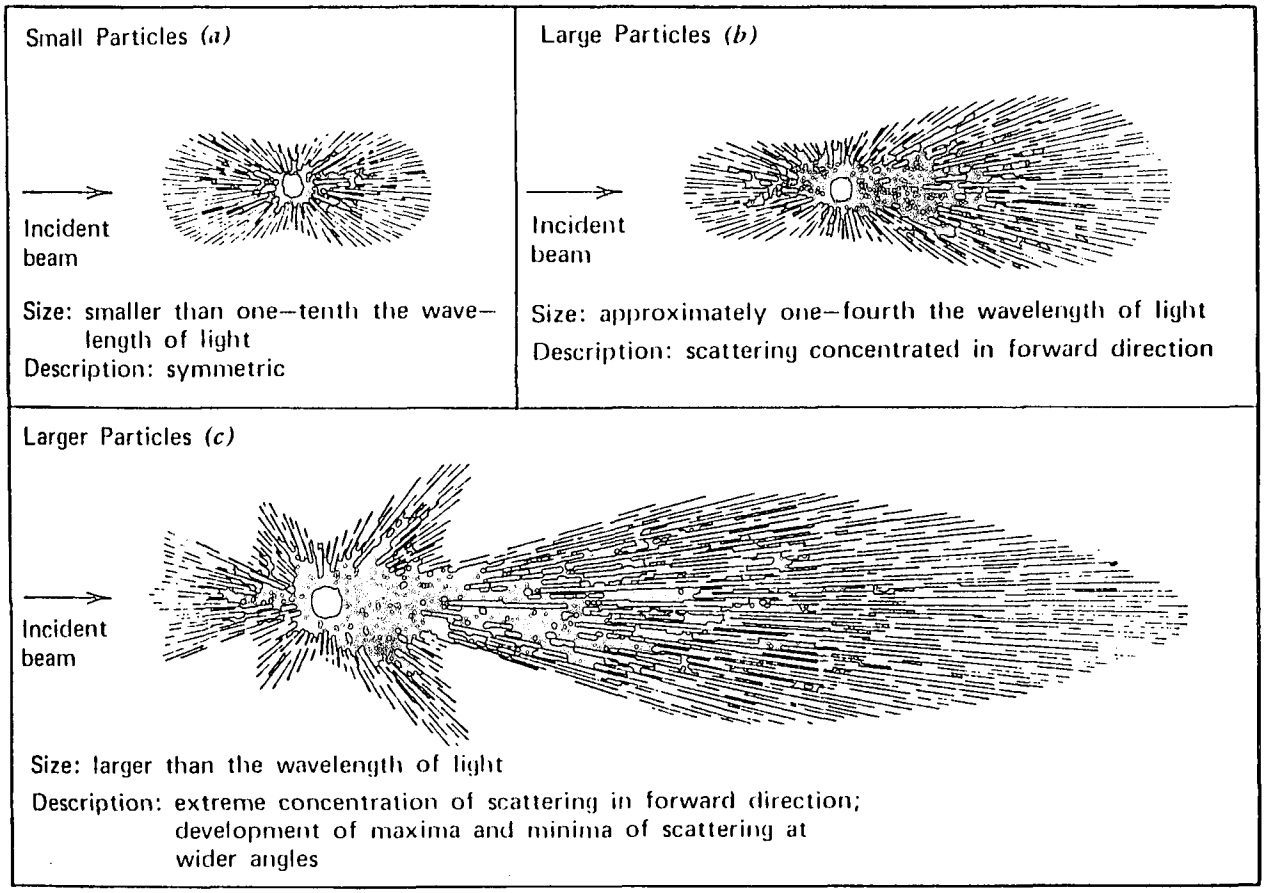

Figure 7.1 ANGULAR PATTERNS OF SCATTERED INTENSITY FROM PARTICLES OF THREE SIZES

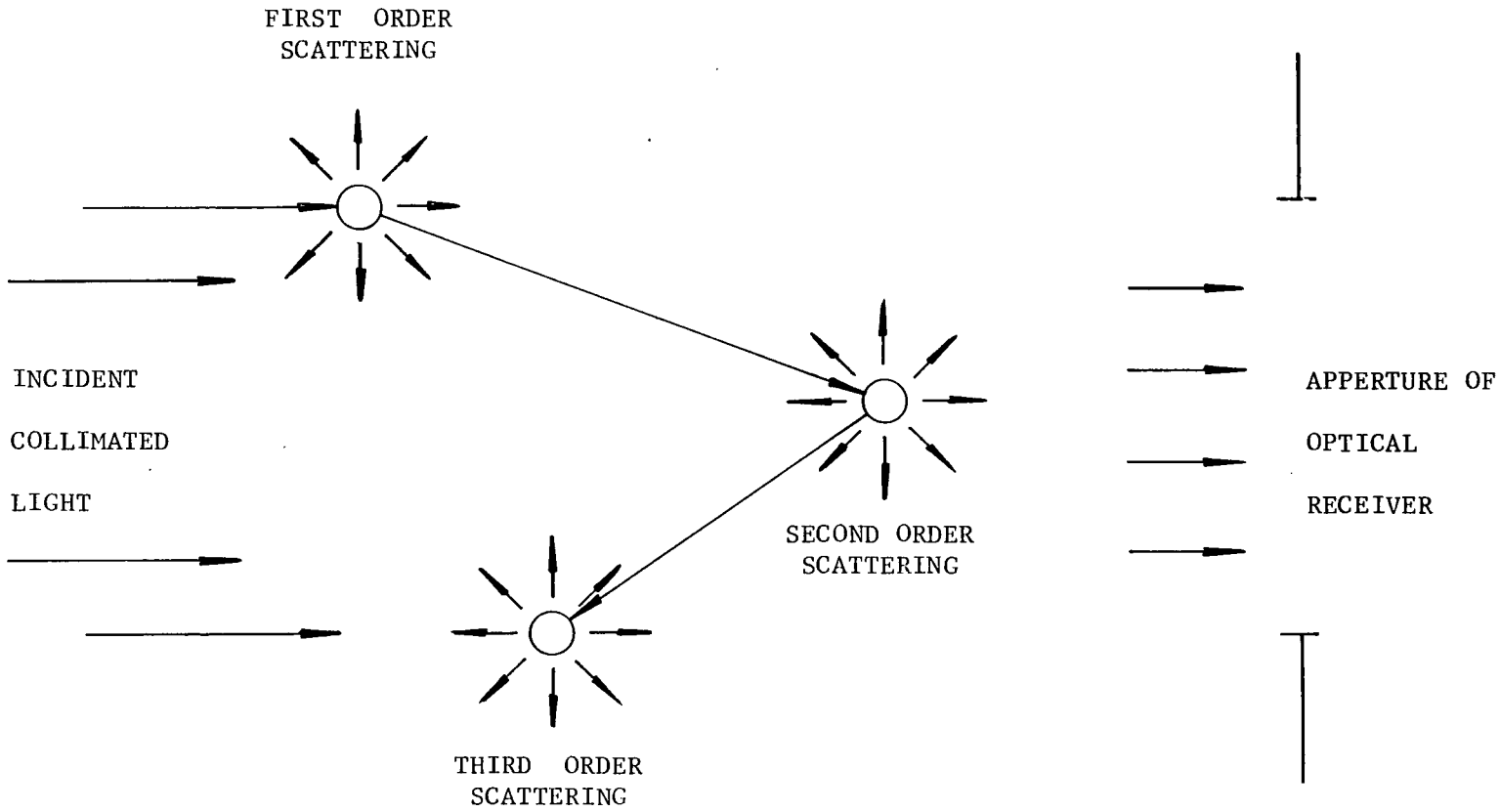

Figure 7.2 MULTIPLE SCATTERING, OR RESCATTERING OF ONCE SCATTERED LIGHT. THE LIGHT FROM ALL ORDERS OF SCATTERING ARE INCIDENT UPON ALL PARTICLES FROM ALL DIRECTIONS.

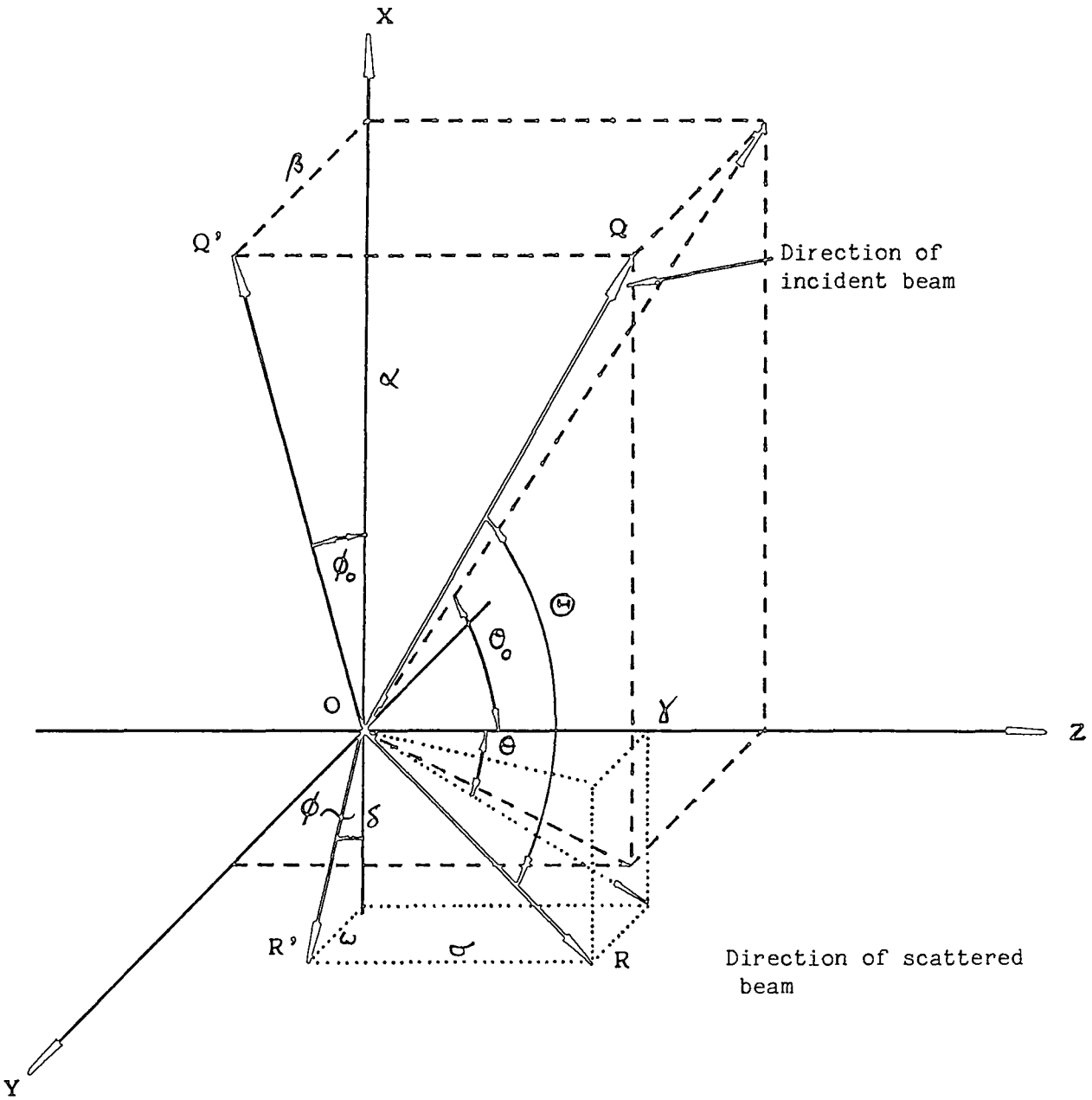

Figure 7.3 THE SCATTERING GEOMETRY IN THREE DIMENSIONS

Please note: The scattering geometry above is an adaptation by the author of a standard atmospheric scattering geometry (van de Hulst(50)) to suit the requirements of this research

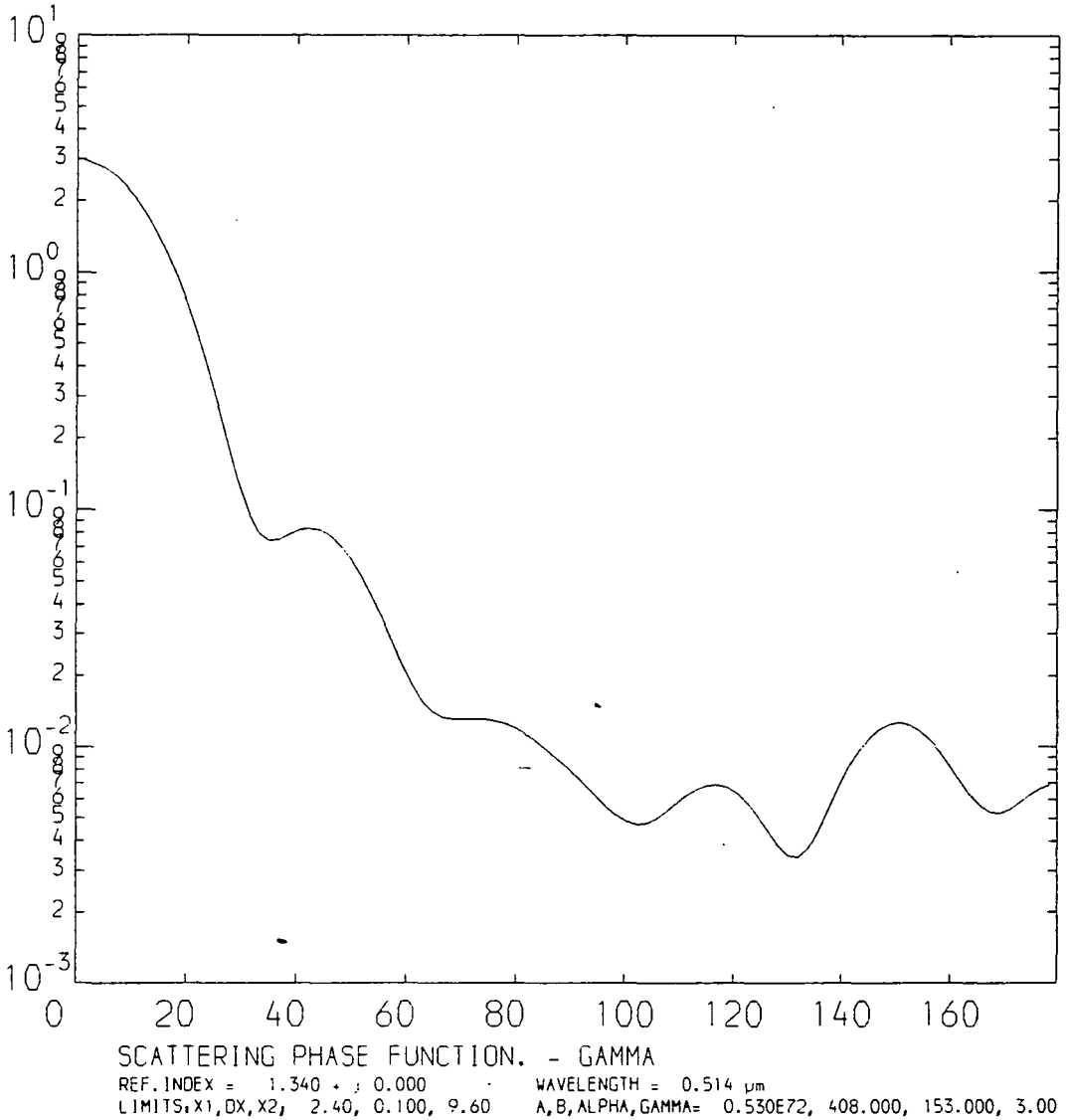

Figure 7.4 EXAMPLE OF COMPUTED SINGLE SCATTERING PHASE FUNCTION

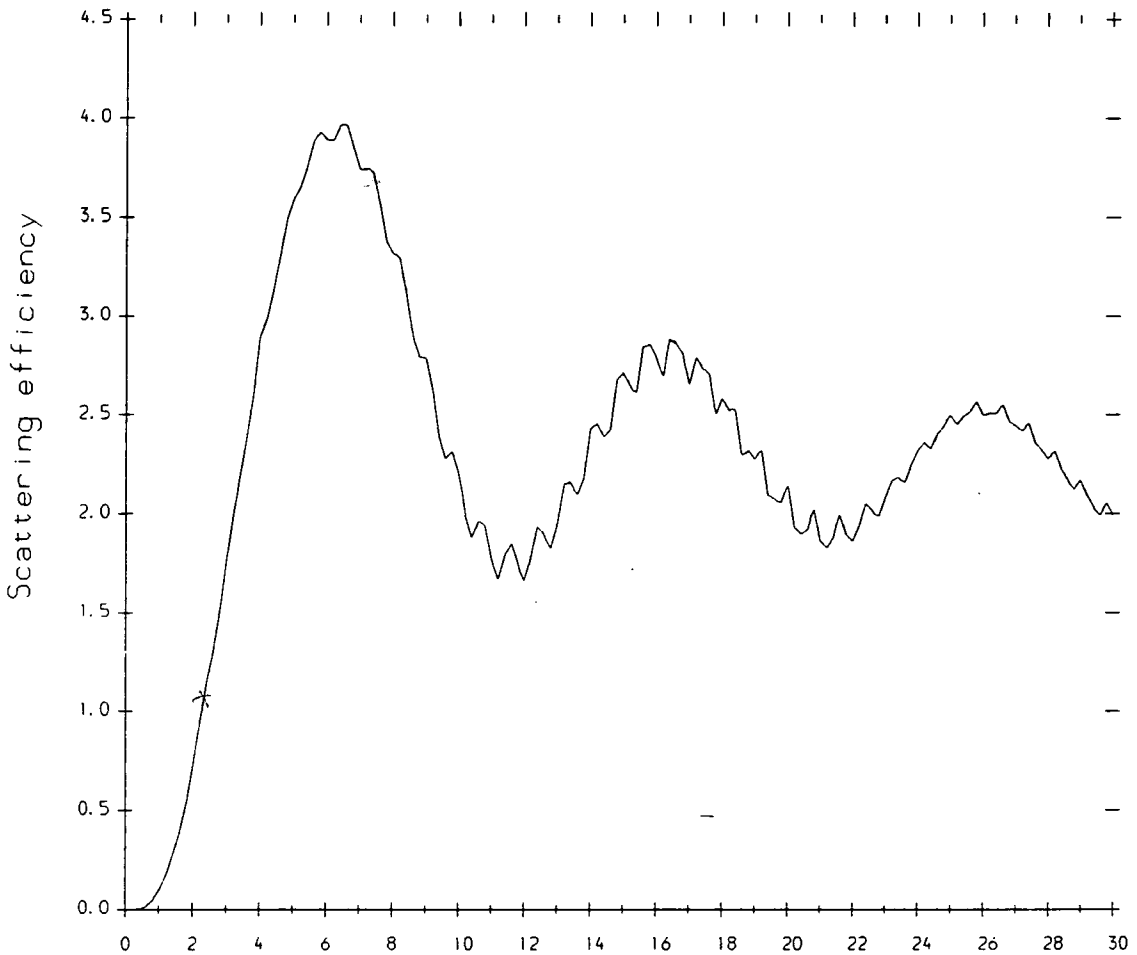

SCATTERING EFFICIENCY FACTOR AGAINST SIZE PARAMETER

Figure 7.5

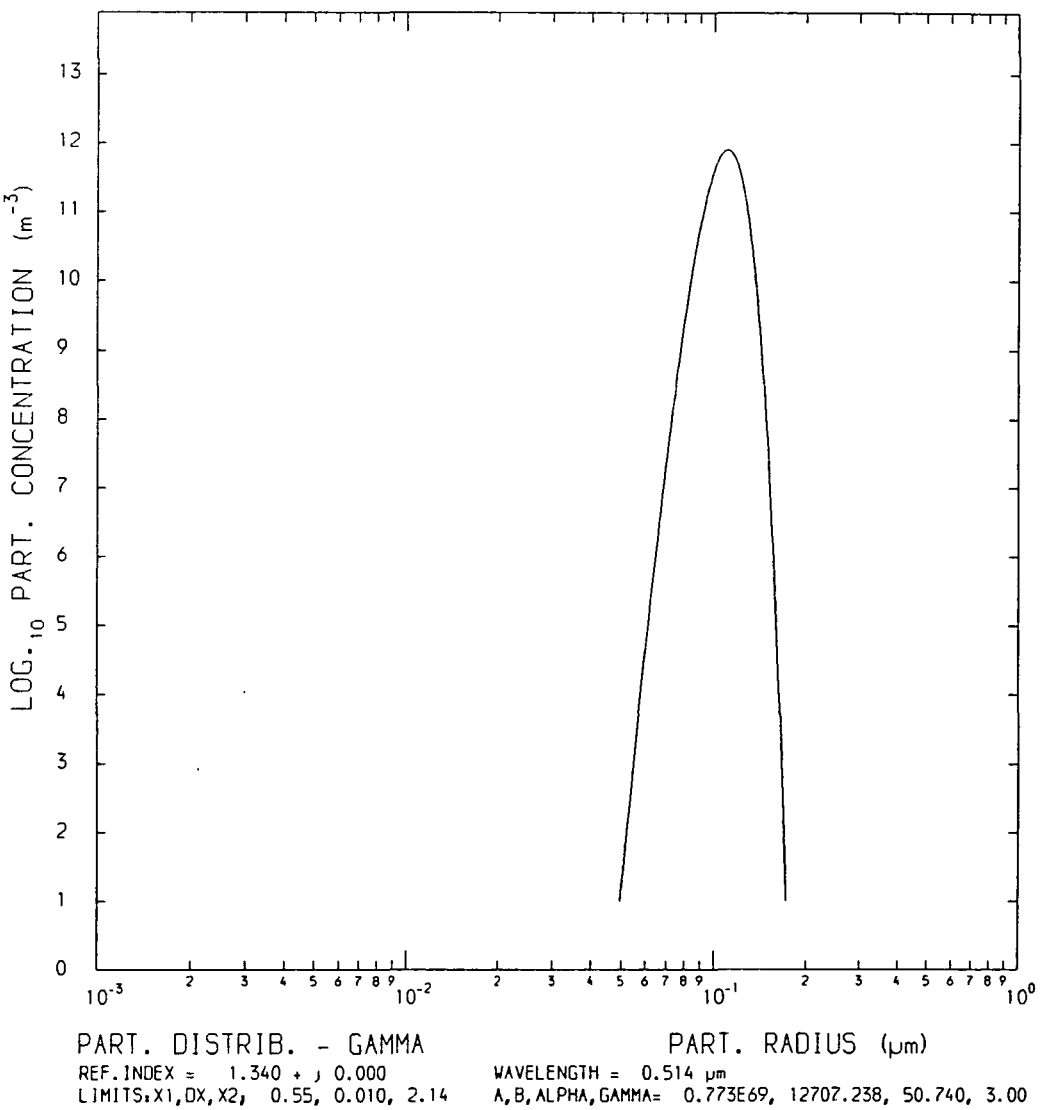
LOG.10 PART. CONCENTRATION (m-3)
13
12
11
10
9
8
7
6
5
4
3
2
1
0
10-3
10-2
10-1
100
PART. DISTRIB. - GAMMA
REF. INDEX = 1.340 + j 0.000
LIMITS: X1, DX, X2, 0.55, 0.010, 2.14
PART. RADIUS (μm)
WAVELENGTH = 0.514 μm
A, B, ALPHA, GAMMA= 0.773E69, 12707.238, 50.740, 3.00

Figure 7.6

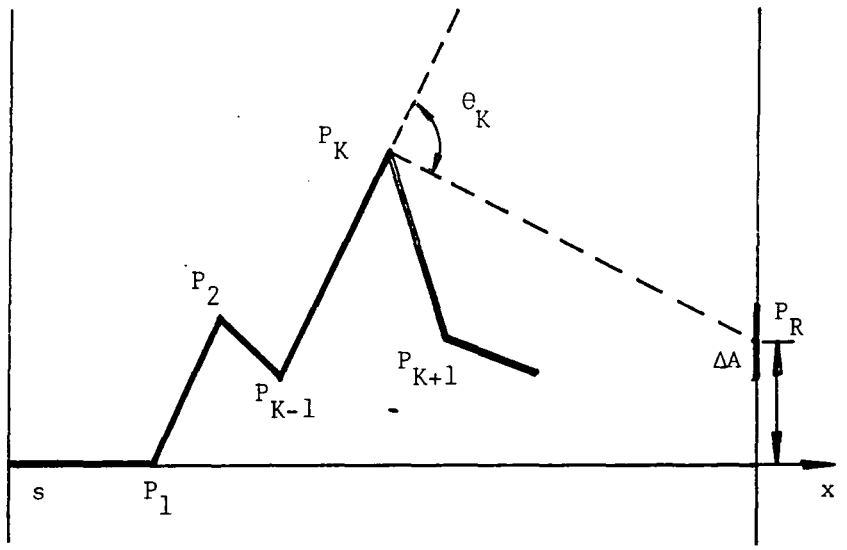

Figure 8.1 THE MONTE CARLO TECHNIQUE

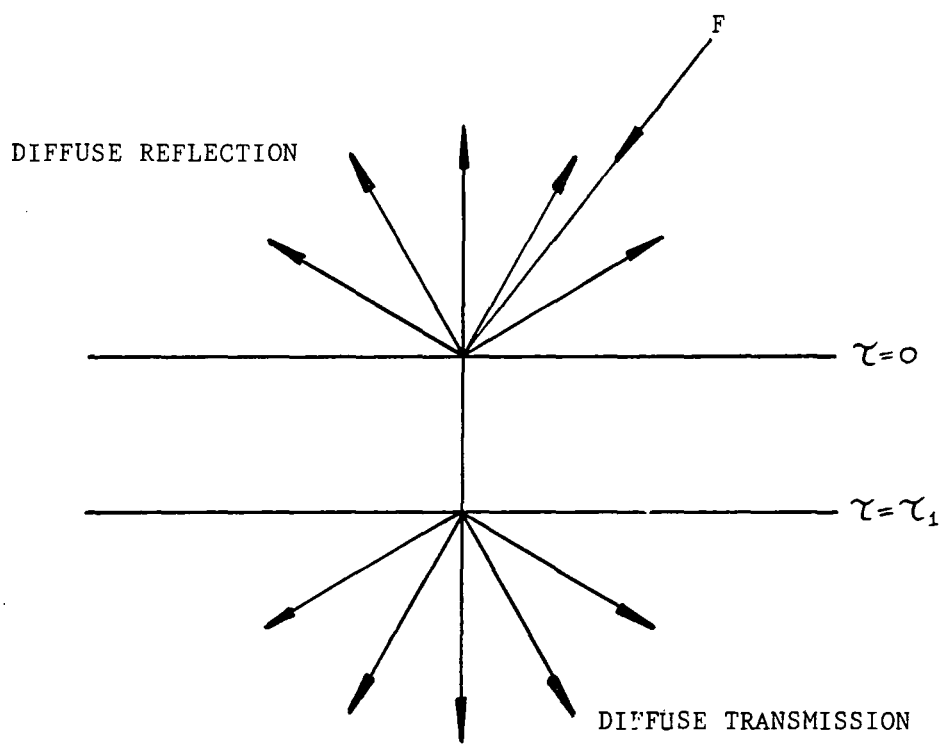

Figure 8.2 A SIMPLE PLANE-PARALLEL ATMOSPHERE

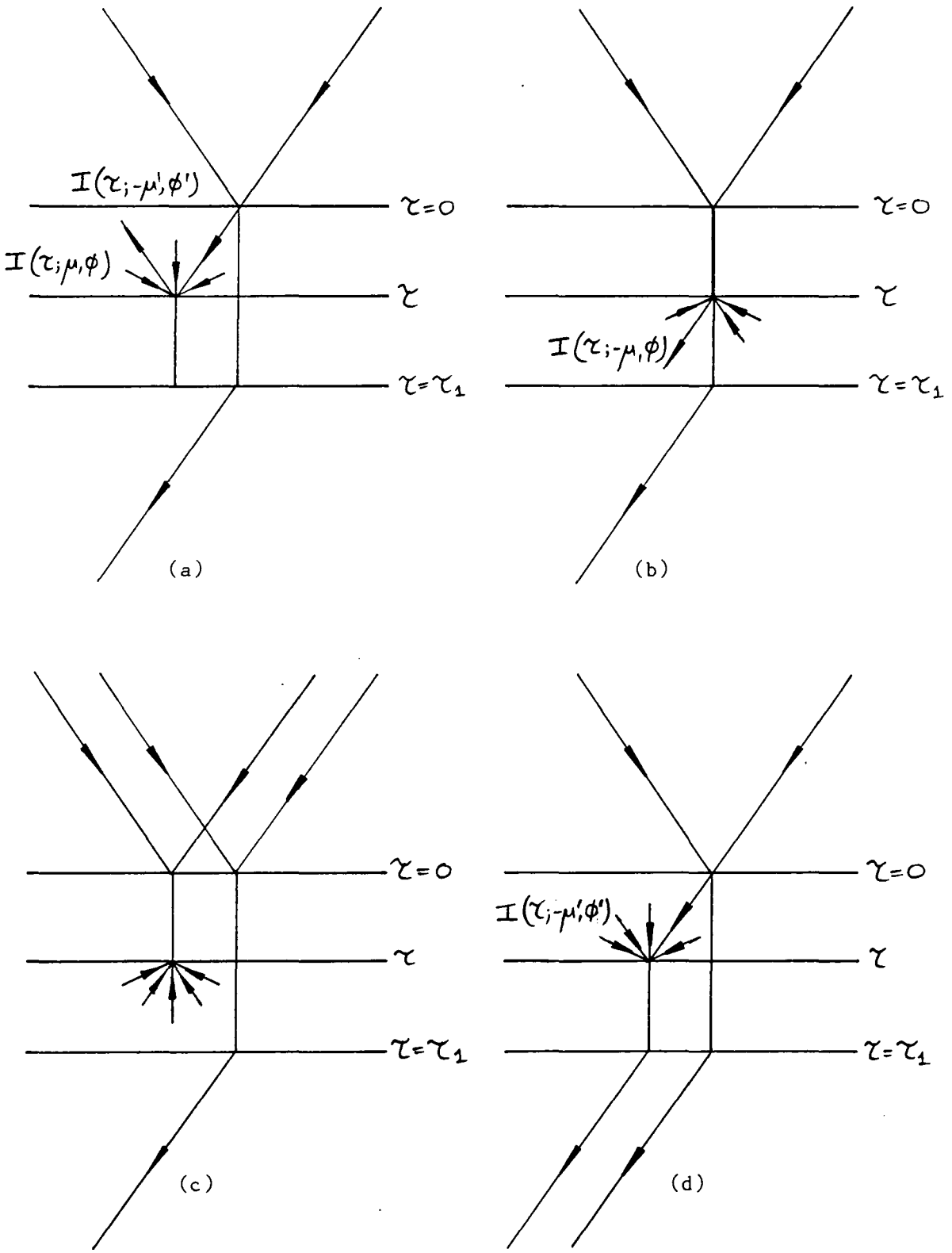

Figure 8.3 ILLUSTRATING THE PRINCIPLES OF INVARIANCE

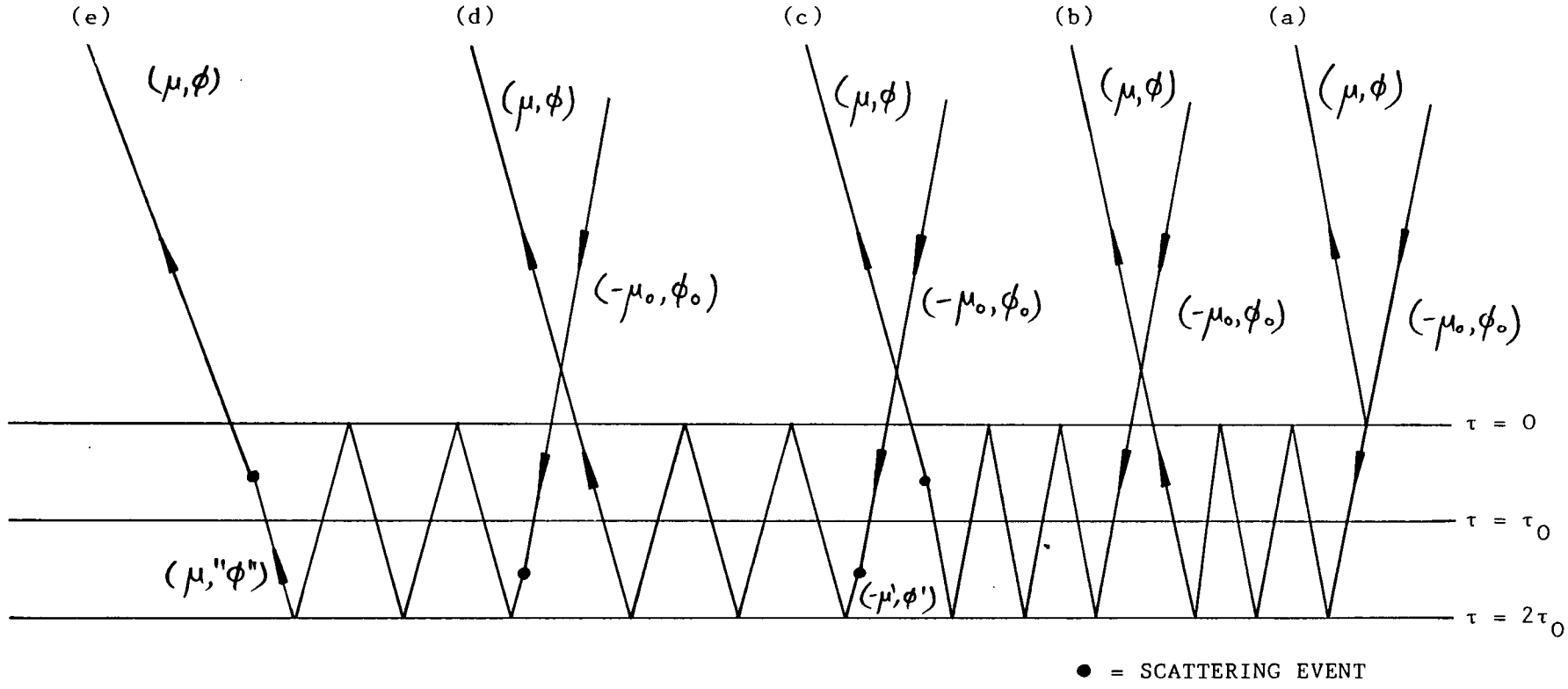

Figure 8.4 ILLUSTRATING ALL THE TERMS OF THE REFLECTION COEFFICIENT

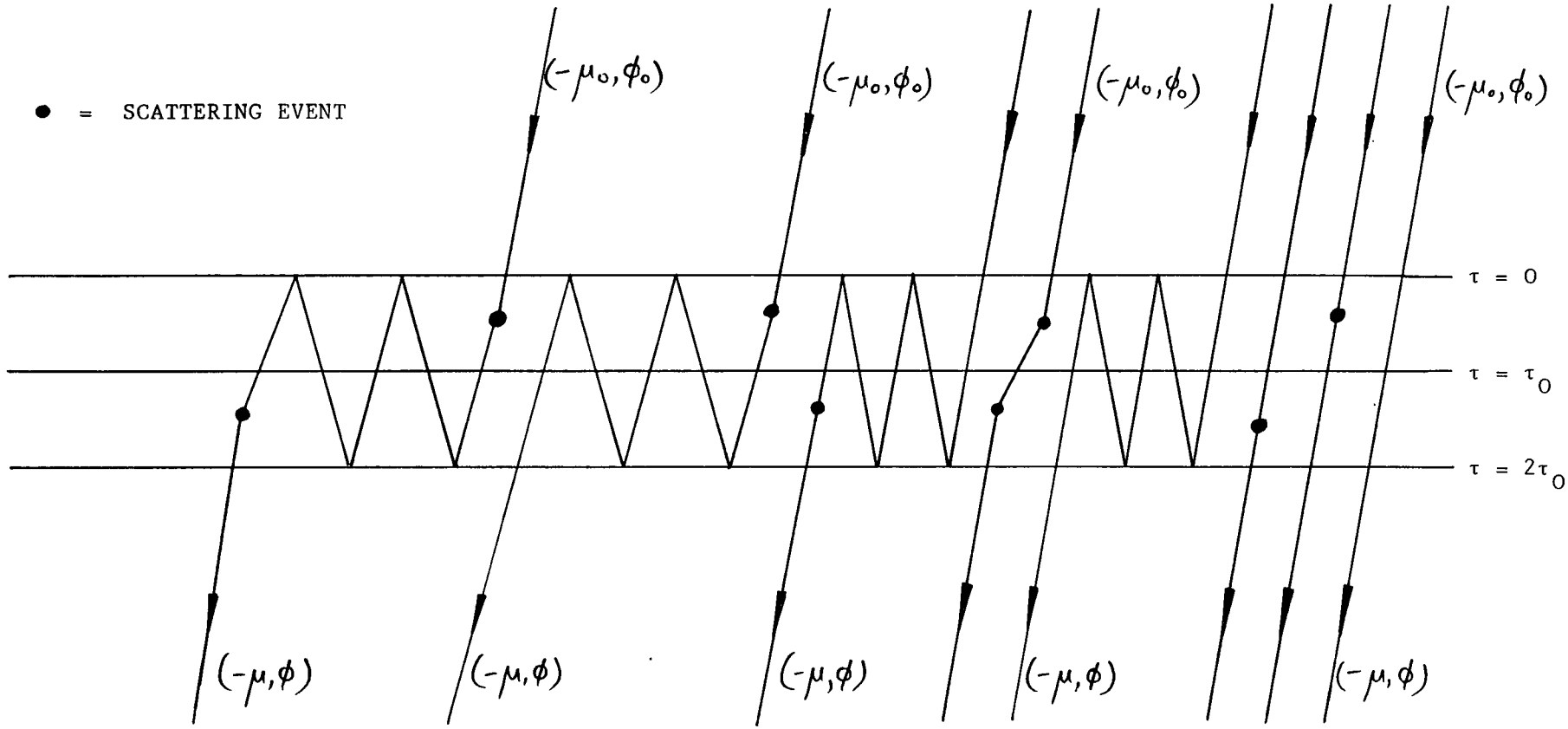

Figure 8.5 ILLUSTRATING ALL THE TERMS OF THE TRANSMISSION COEFFICIENT.

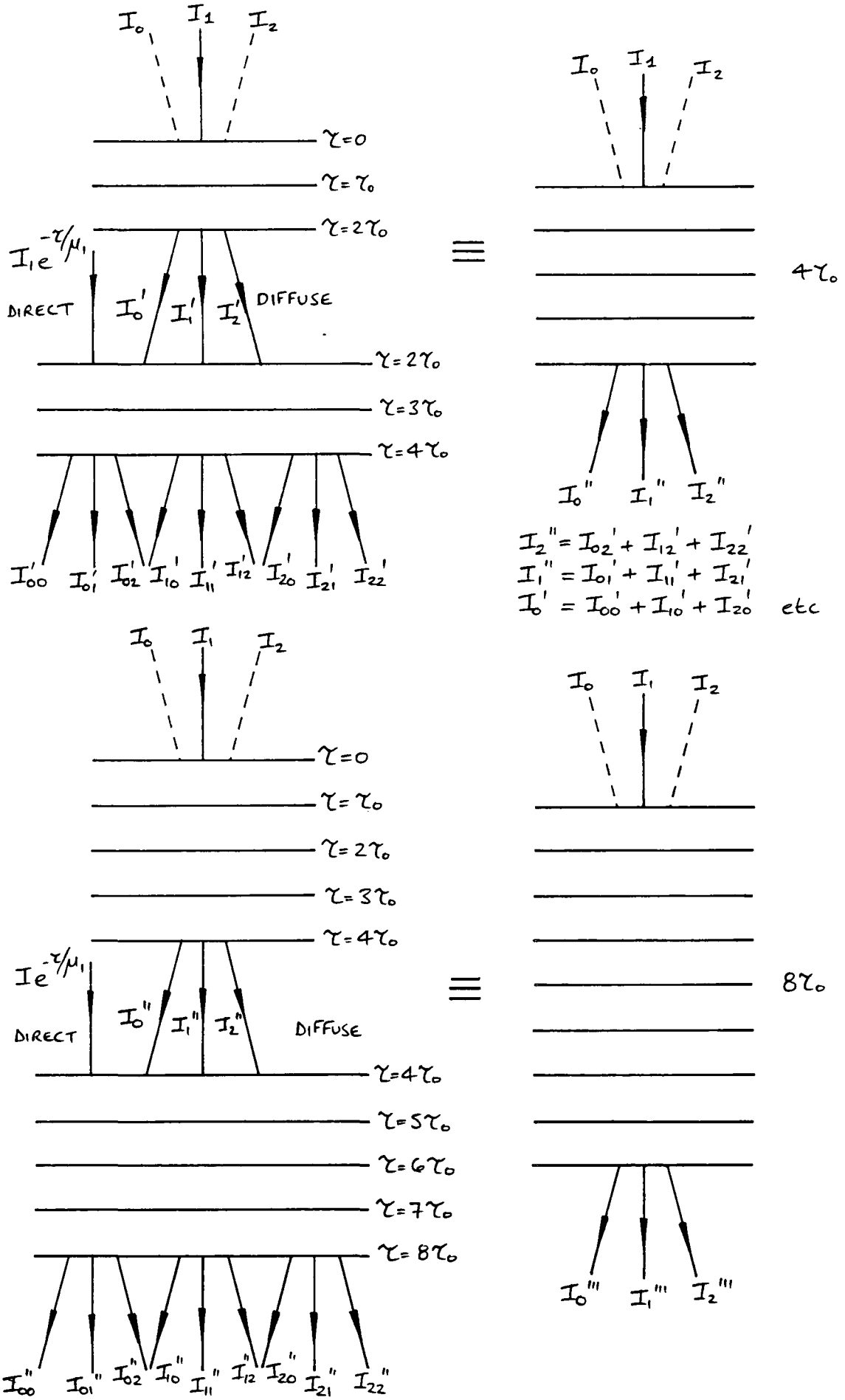

Figure 8.6 METHOD OF DOUBLING FOR THE TRANSMISSION COEFFICIENT

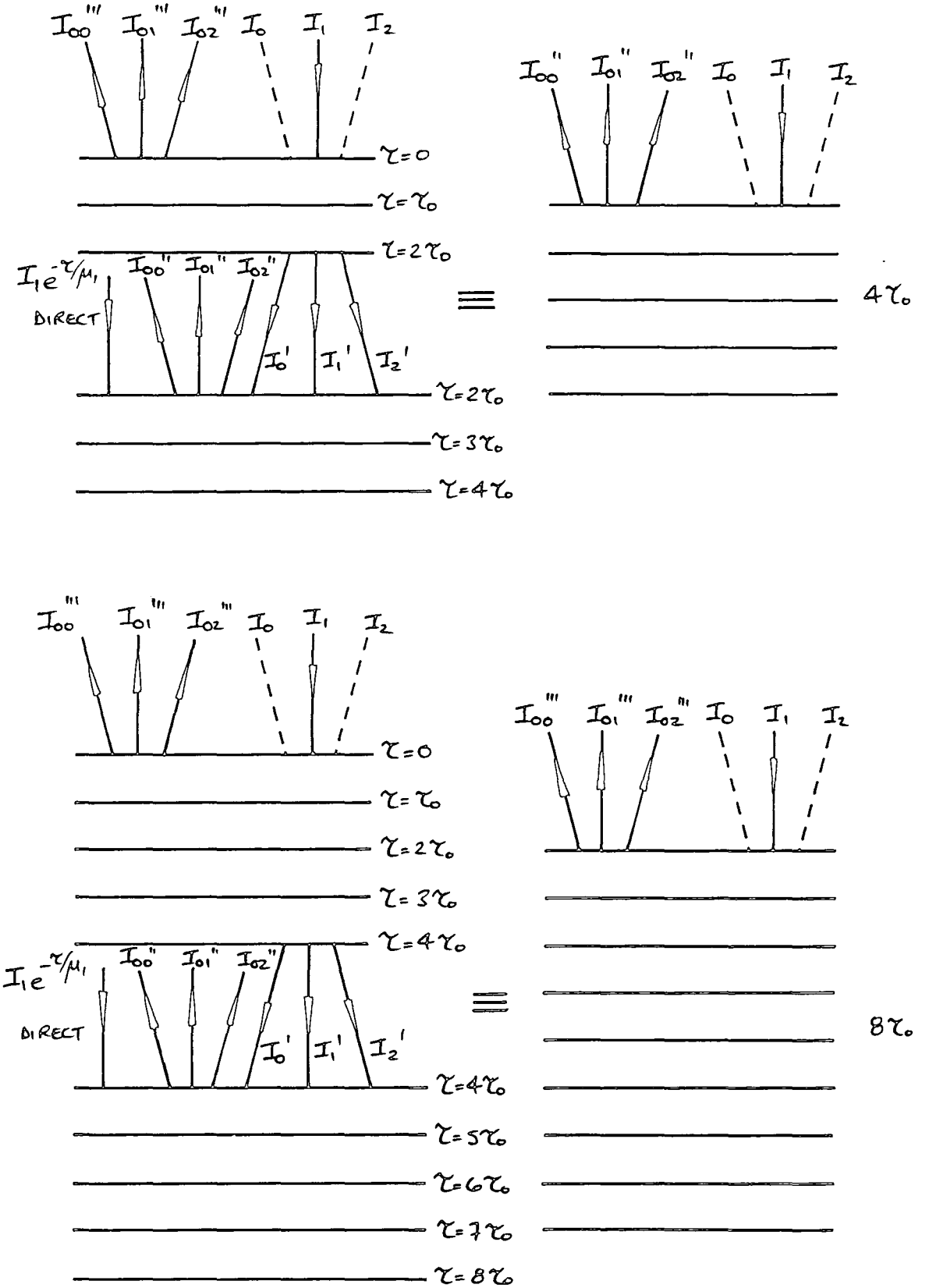

Figure 8.7 METHOD OF DOUBLING THE REFLECTION COEFFICIENT

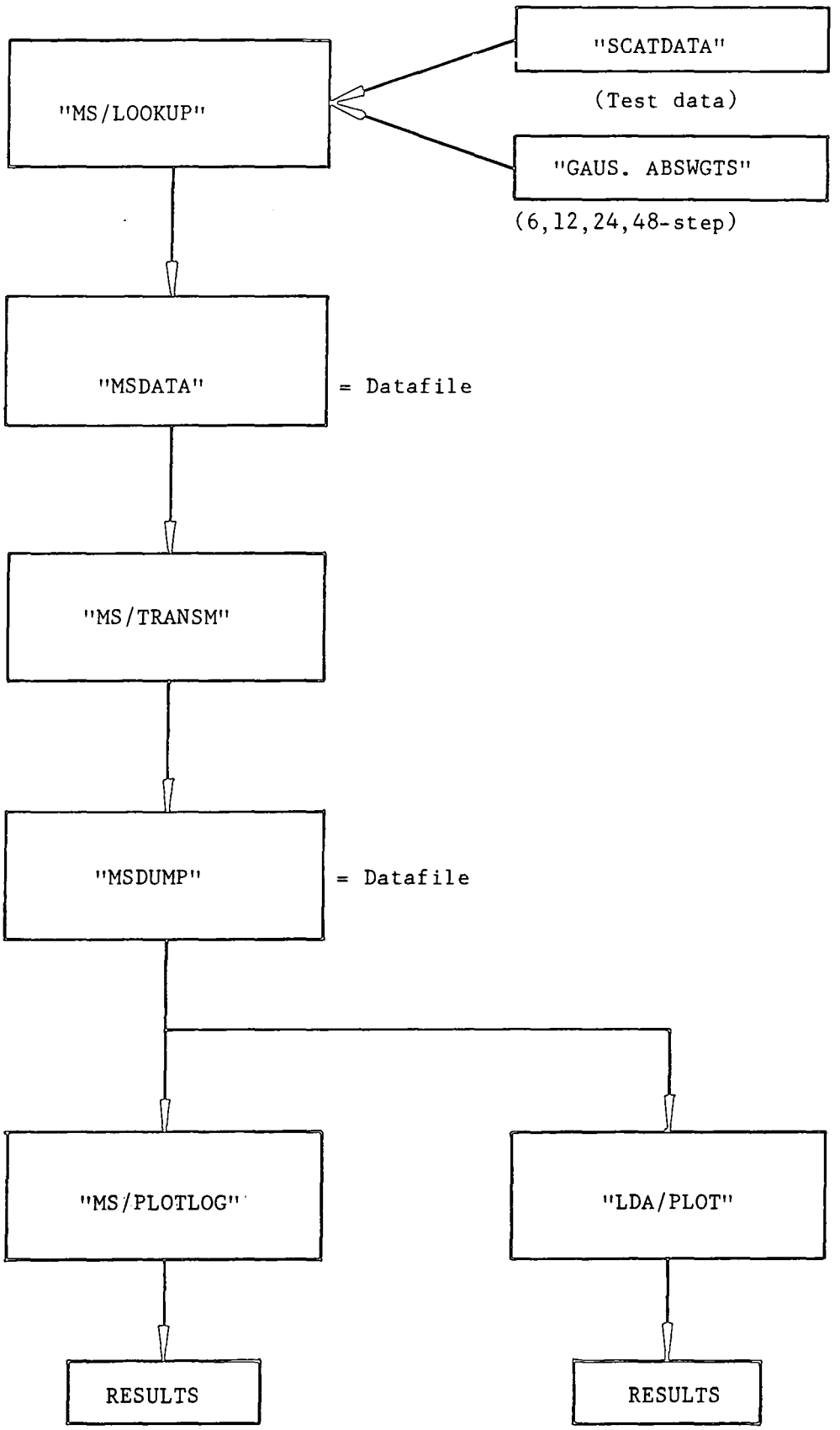

Figure 8.8 THE SUITE OF MULTIPLE SCATTERING PROGRAMS

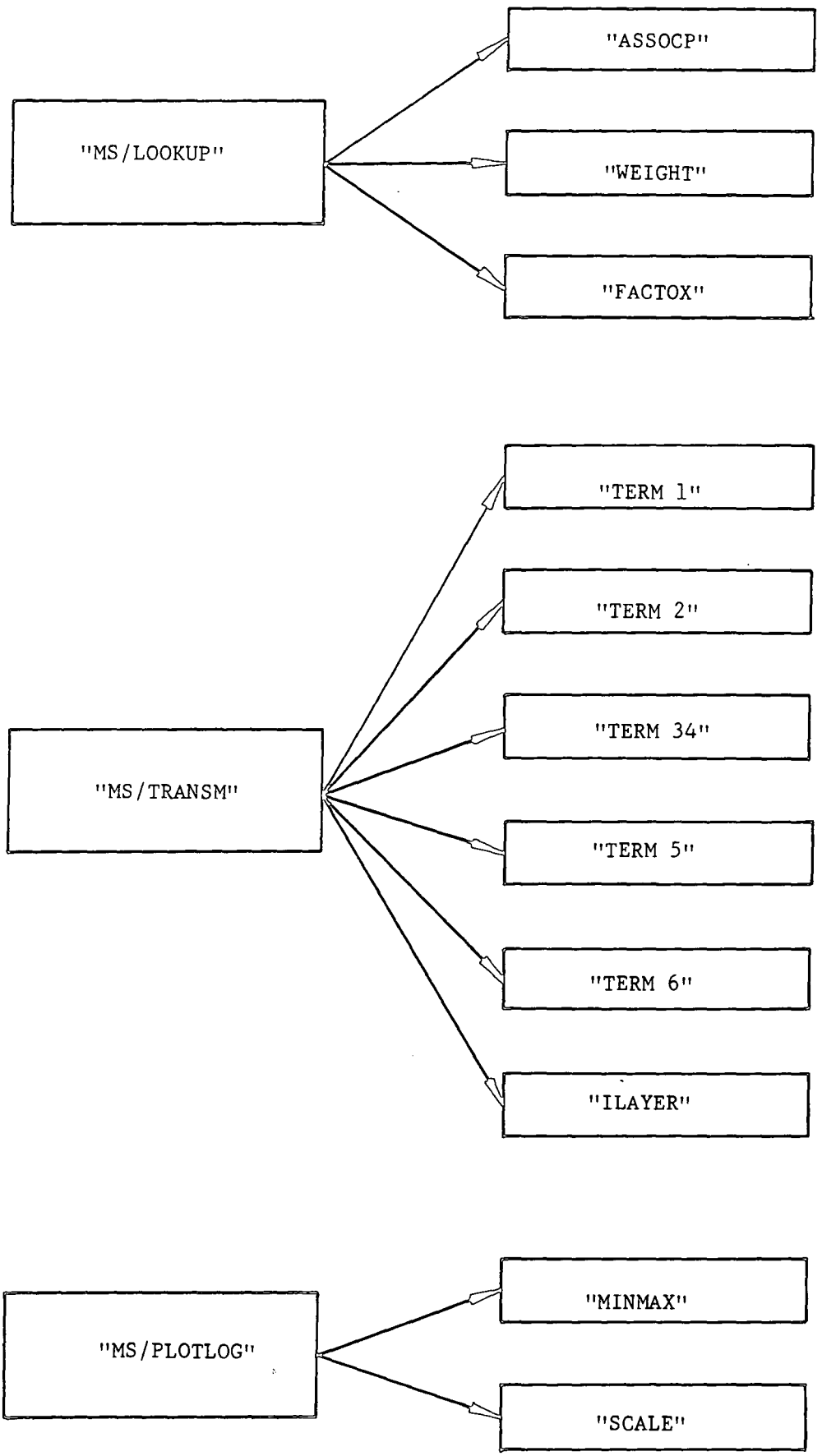

Figure 8.9 BREAKDOWN OF THE MAIN PROGRAMS

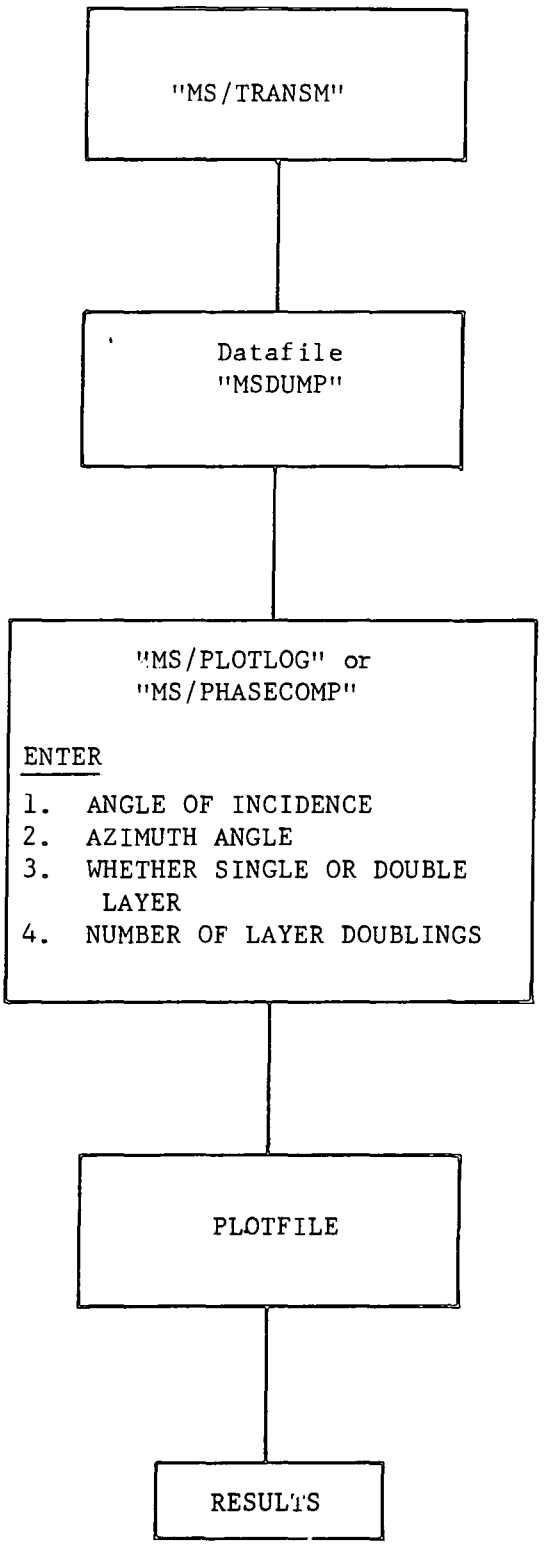

Figure 8.10 GENERATION OF THE PLOTFILES

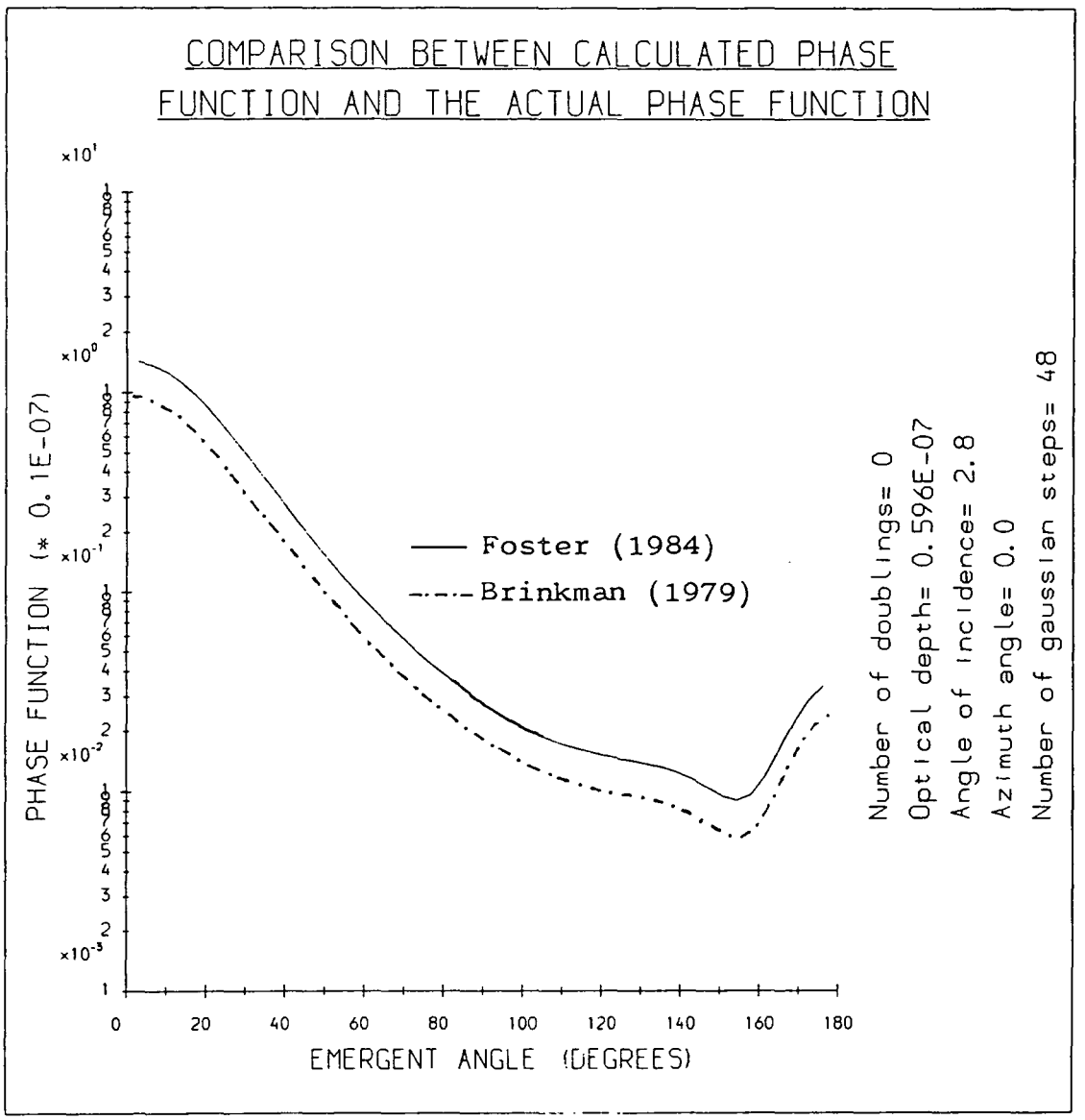
COMPARISON BETWEEN CALCULATED PHASE FUNCTION AND THE ACTUAL PHASE FUNCTION
PHASE FUNCTION (* 0.1E-07)
EMERGENT ANGLE (DEGREES)
Foster (1984)
Brinkman (1979)
Number of doublings= 0
Optical depth= 0.596E-07
Angle of incidence= 2.8
Azimuth angle= 0.0
Number of gaussian steps= 48

Figure 8.11

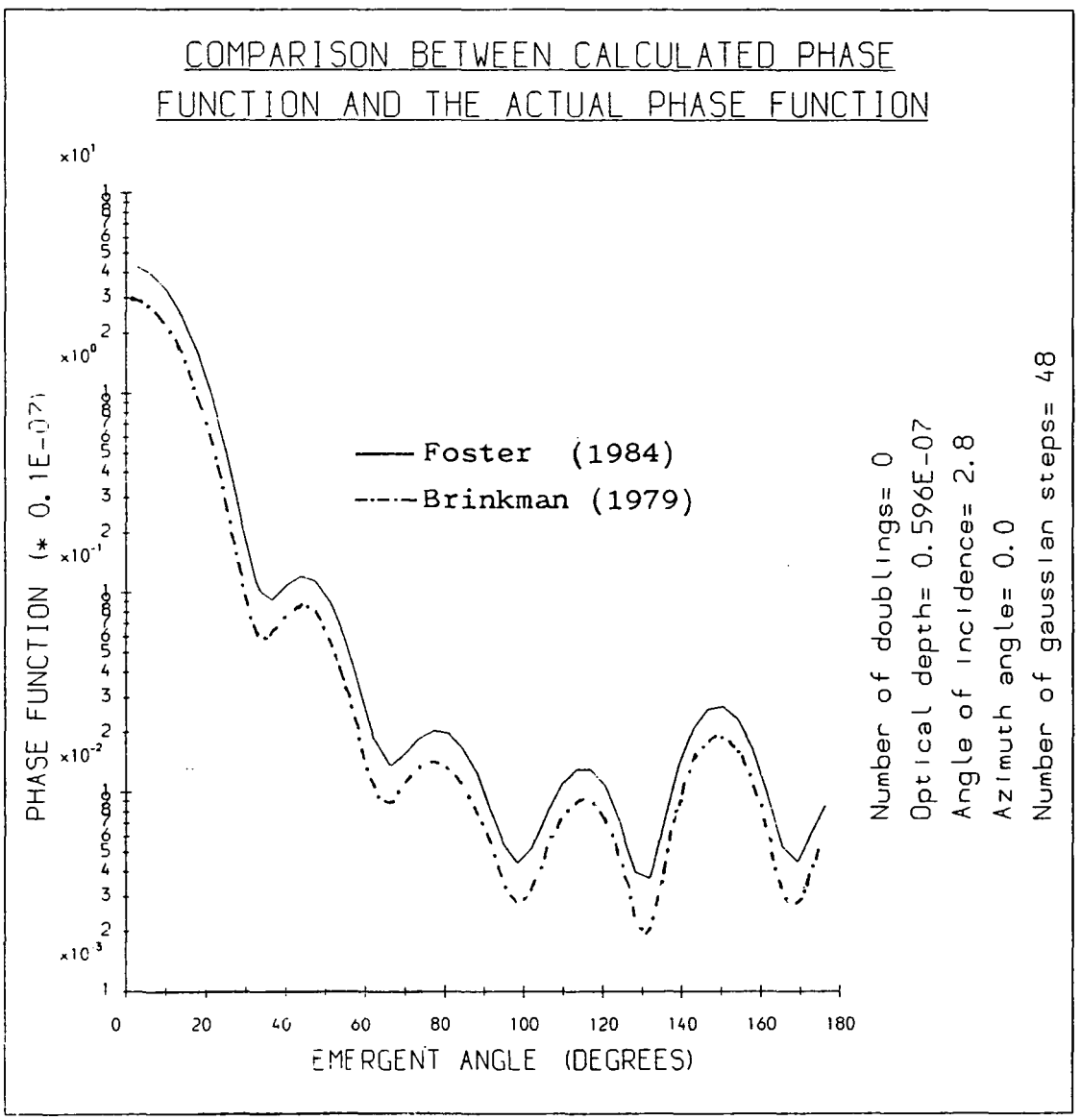
COMPARISON BETWEEN CALCULATED PHASE FUNCTION AND THE ACTUAL PHASE FUNCTION
PHASE FUNCTION (* 0.1E-07)
EMERGENT ANGLE (DEGREES)
Foster (1984)
Brinkman (1979)
Number of doublings= 0
Optical depth= 0.596E-07
Angle of incidence= 2.8
Azimuth angle= 0.0
Number of gaussian steps= 48

Figure 8.12

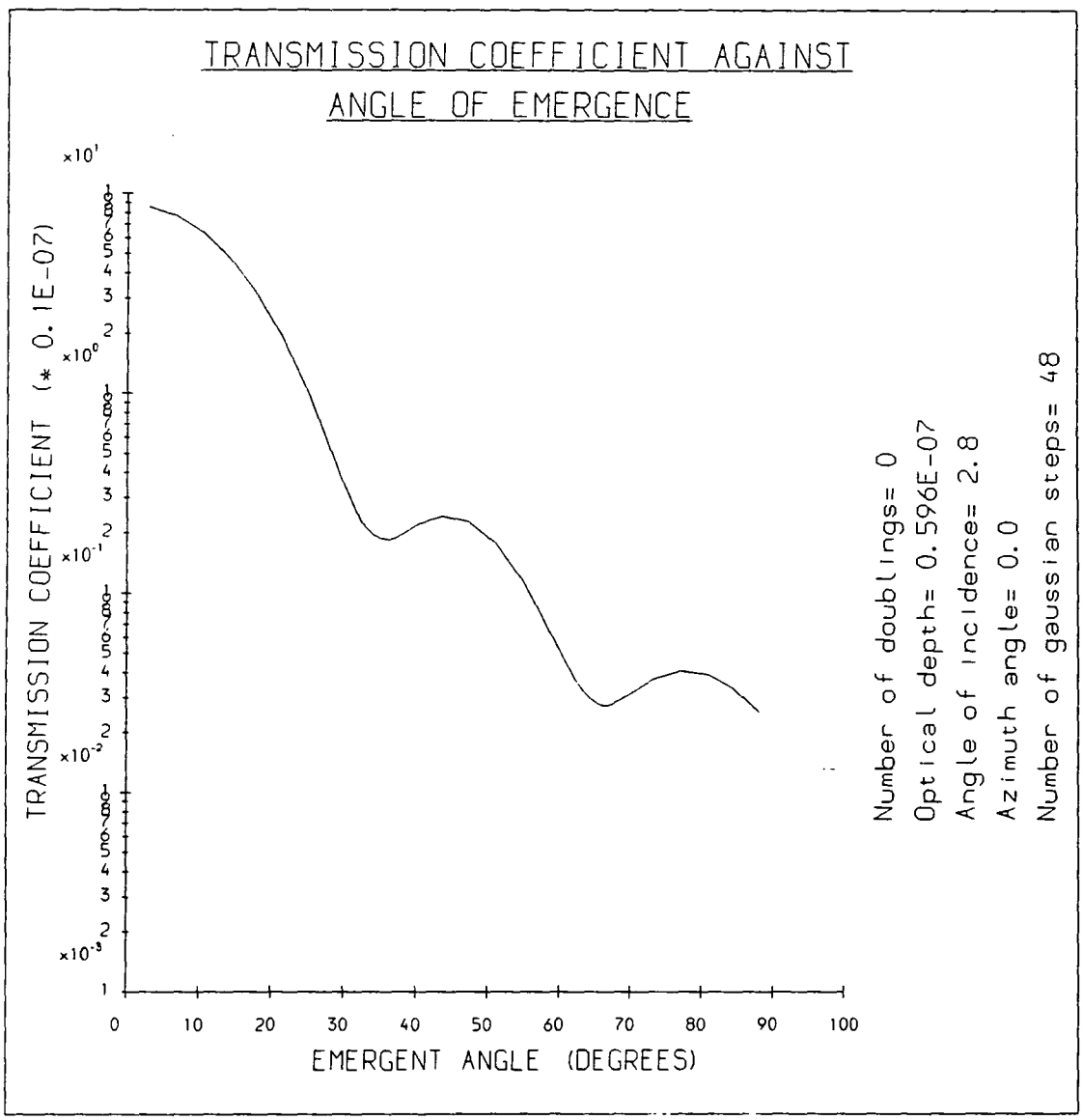
TRANSMISSION COEFFICIENT AGAINST
ANGLE OF EMERGENCE
TRANSMISSION COEFFICIENT (* 0.1E-07)
EMERGENT ANGLE (DEGREES)
0
10
20
30
40
50
60
70
80
90
100
Number of doublings= 0
Optical depth= 0.596E-07
Angle of incidence= 2.8
Azimuth angle= 0.0
Number of gaussian steps= 48

Figure 8.13

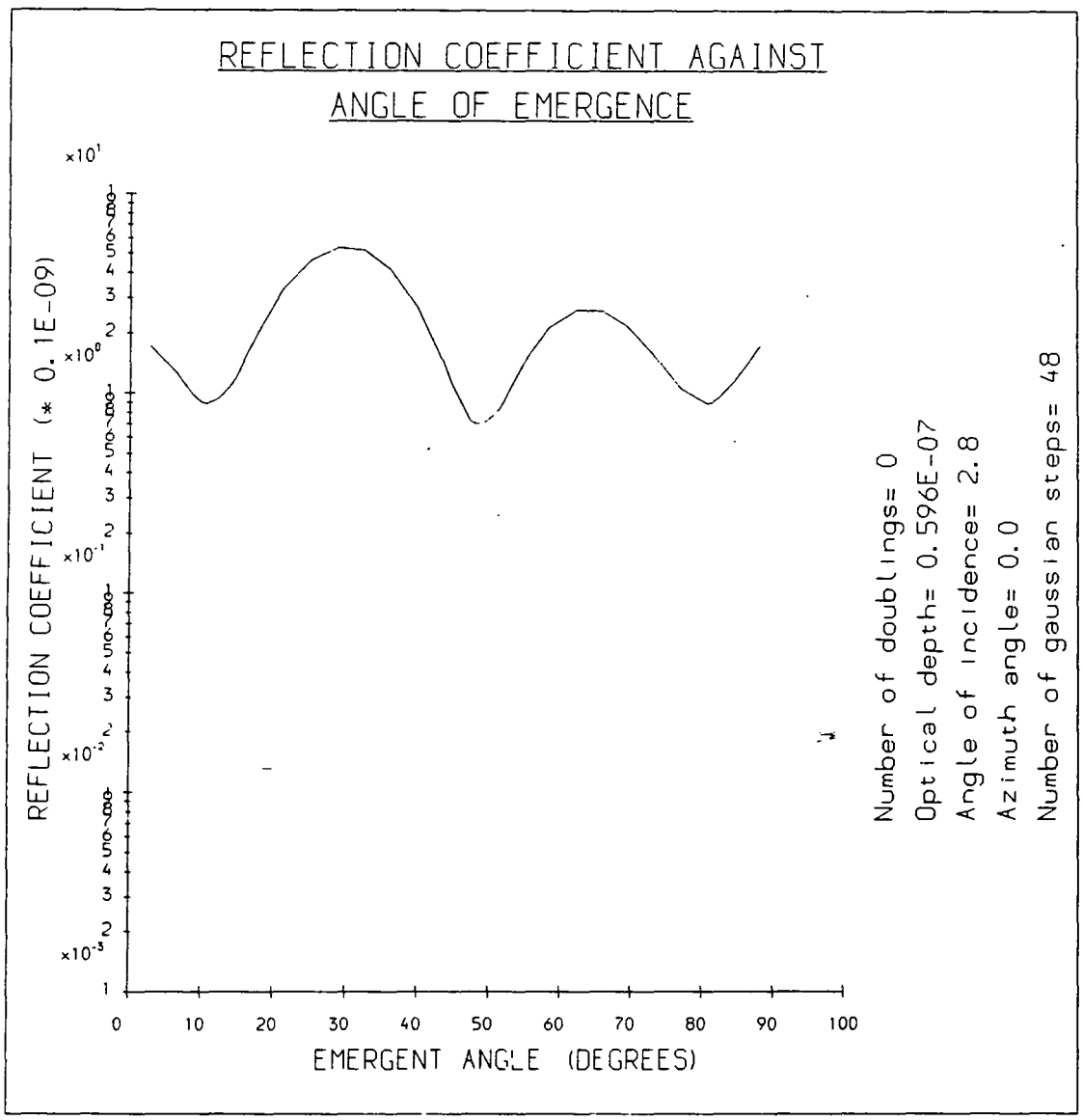
REFLECTION COEFFICIENT AGAINST
ANGLE OF EMERGENCE
REFLECTION COEFFICIENT (* 0.1E-09)
EMERGENT ANGLE (DEGREES)
0
10
20
30
40
50
60
70
80
90
100
Number of doublings= 0
Optical depth= 0.596E-07
Angle of incidence= 2.8
Azimuth angle= 0.0
Number of gaussian steps= 48

Figure 8.14

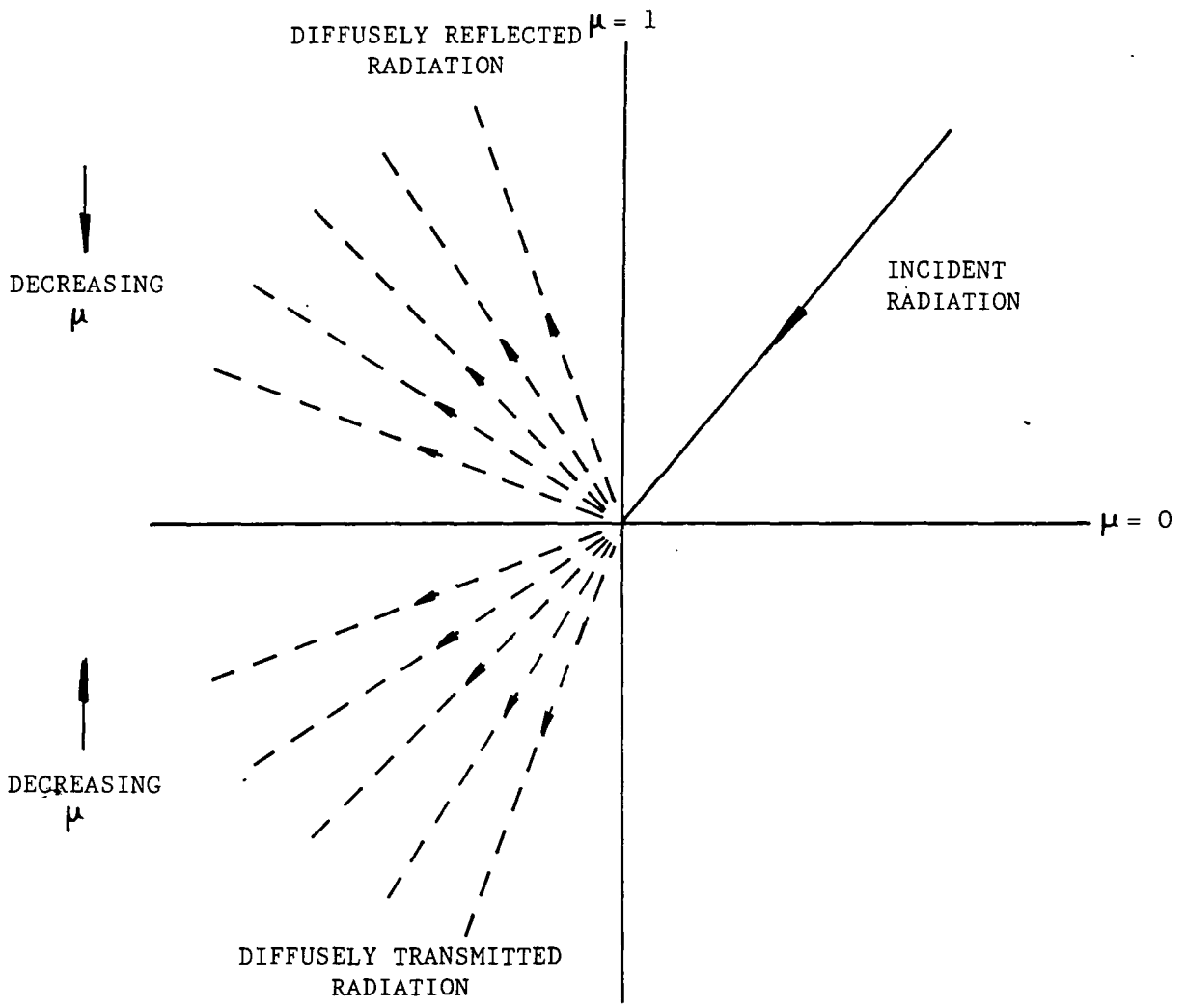

Figure 8.15 ANGLE CONVENTION USED FOR COMPUTING THE TRANSMISSION AND REFLECTION COEFFICIENTS

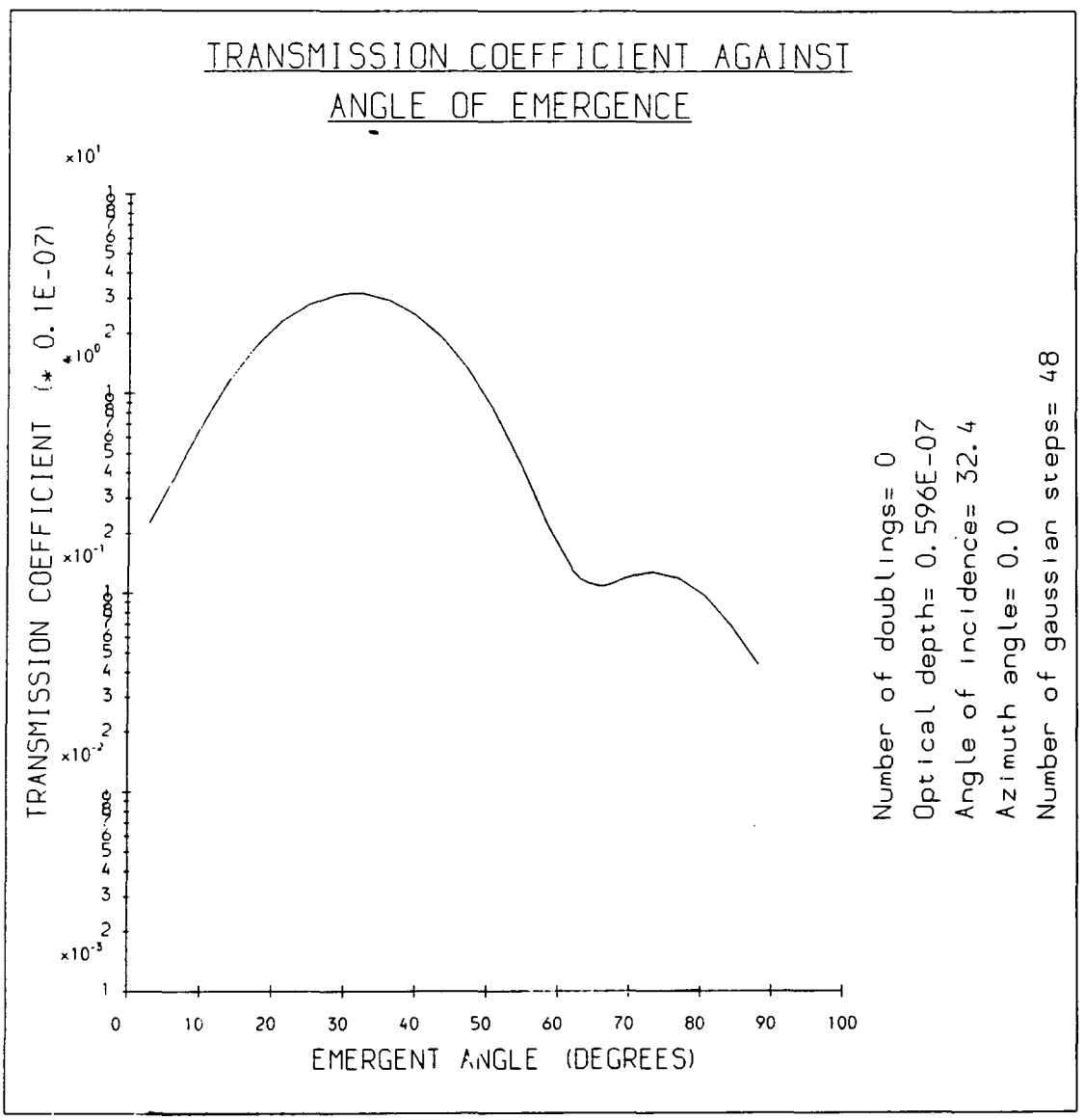
TRANSMISSION COEFFICIENT AGAINST
ANGLE OF EMERGENCE
TRANSMISSION COEFFICIENT (* 0.1E-07)
EMERGENT ANGLE (DEGREES)
Number of doublings= 0
Optical depth= 0.596E-07
Angle of incidence= 32.4
Azimuth angle= 0.0
Number of gaussian steps= 48

Figure 8.16

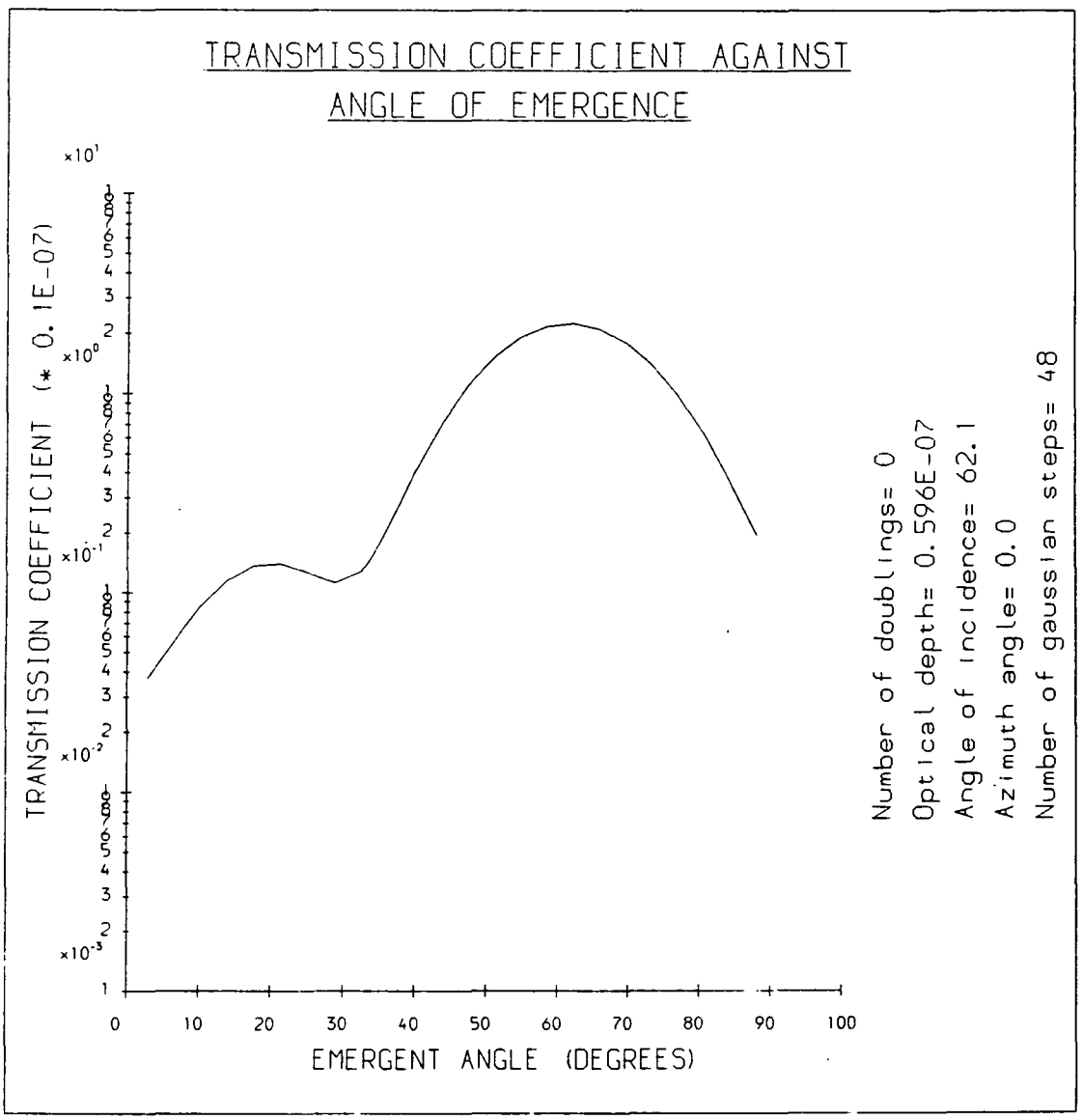
TRANSMISSION COEFFICIENT AGAINST
ANGLE OF EMERGENCE
TRANSMISSION COEFFICIENT (* 0.1E-07)
EMERGENT ANGLE (DEGREES)
0
10
20
30
40
50
60
70
80
90
100
Number of doublings= 0
Optical depth= 0.596E-07
Angle of incidence= 62.1
Azimuth angle= 0.0
Number of gaussian steps= 48

Figure 8.17

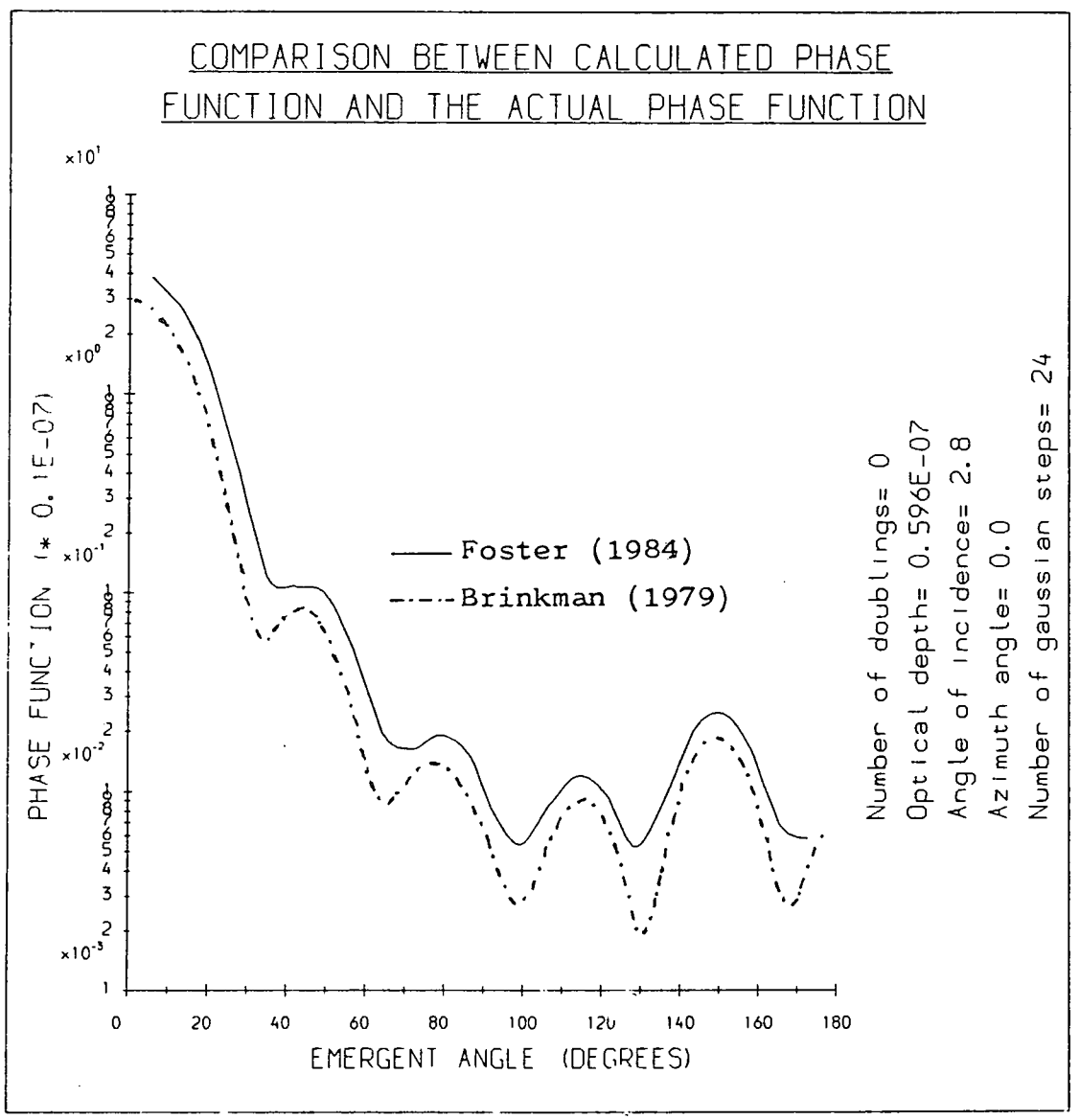
COMPARISON BETWEEN CALCULATED PHASE FUNCTION AND THE ACTUAL PHASE FUNCTION
PHASE FUNCTION (* 0.1E-07)
EMERGENT ANGLE (DEGREES)
Foster (1984)
Brinkman (1979)
Number of doublings= 0
Optical depth= 0.596E-07
Angle of incidence= 2.8
Azimuth angle= 0.0
Number of gaussian steps= 24

Figure 8.18

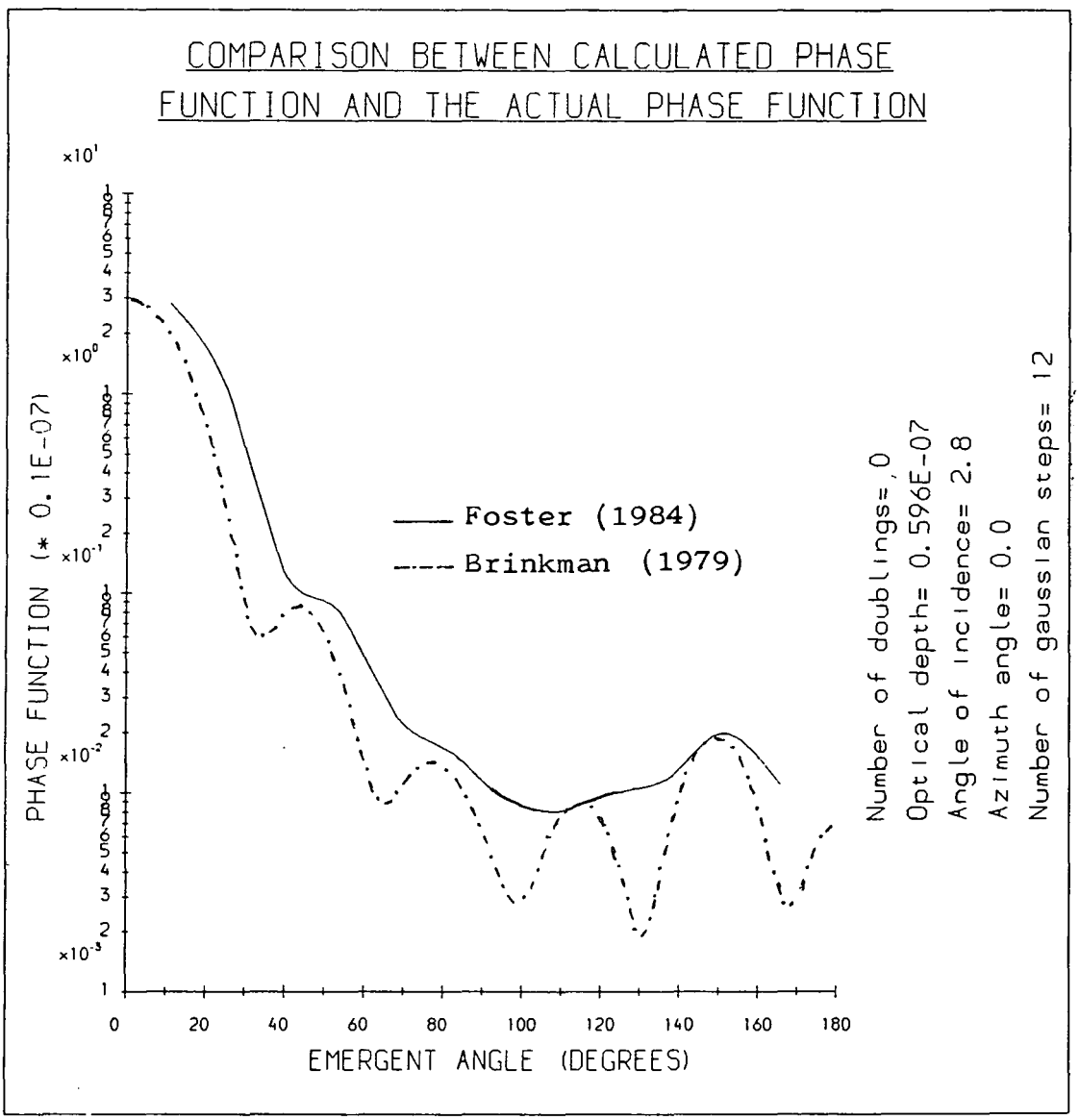
COMPARISON BETWEEN CALCULATED PHASE FUNCTION AND THE ACTUAL PHASE FUNCTION
PHASE FUNCTION (* 0.1E-07)
EMERGENT ANGLE (DEGREES)
Foster (1984)
Brinkman (1979)
Number of doublings= 0
Optical depth= 0.596E-07
Angle of incidence= 2.8
Azimuth angle= 0.0
Number of gaussian steps= 12

Figure 8.19

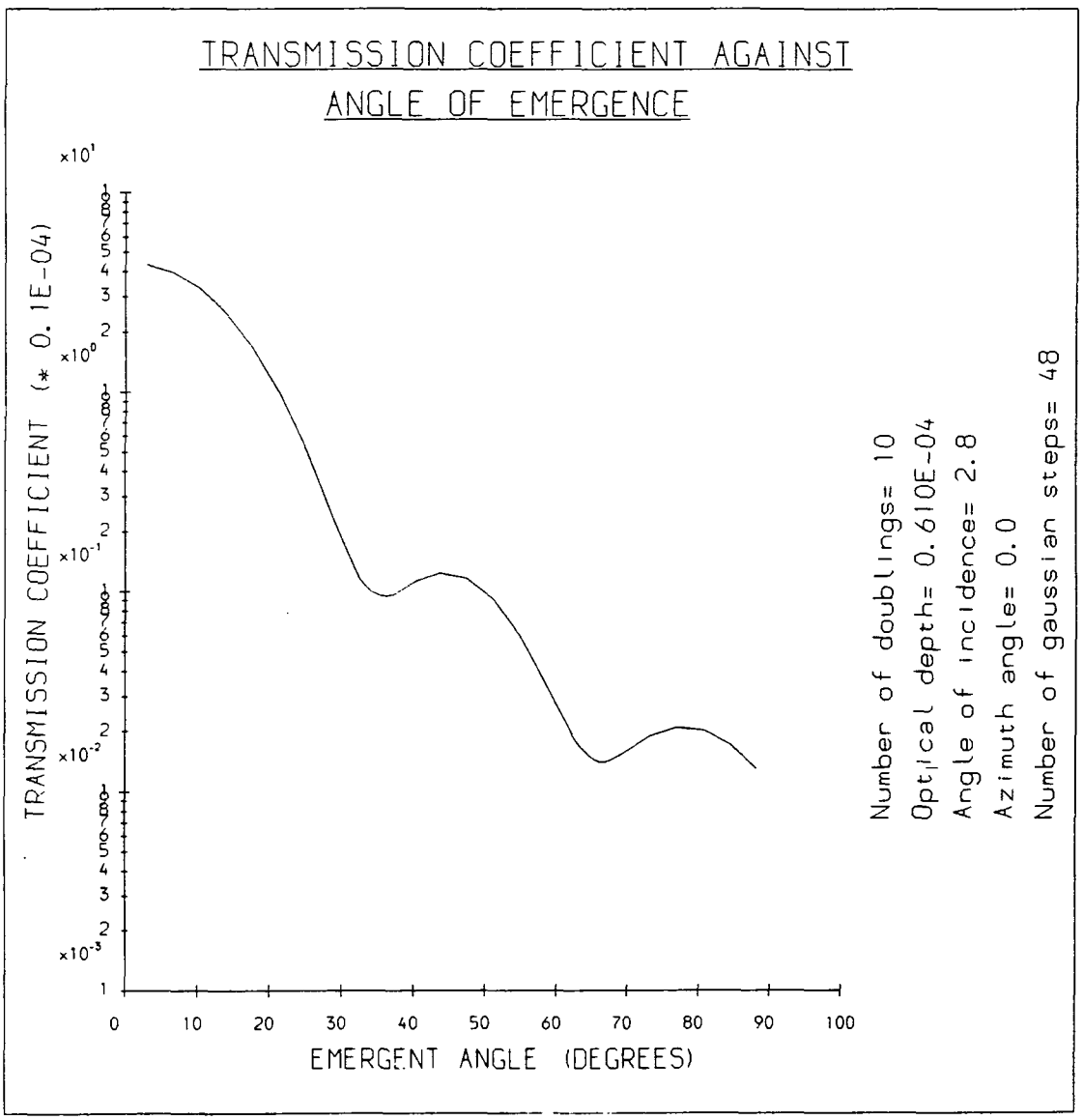
TRANSMISSION COEFFICIENT AGAINST
ANGLE OF EMERGENCE
TRANSMISSION COEFFICIENT (* 0.1E-04)
EMERGENT ANGLE (DEGREES)
Number of doublings= 10
Optical depth= 0.610E-04
Angle of incidence= 2.8
Azimuth angle= 0.0
Number of gaussian steps= 48

Figure 8.20

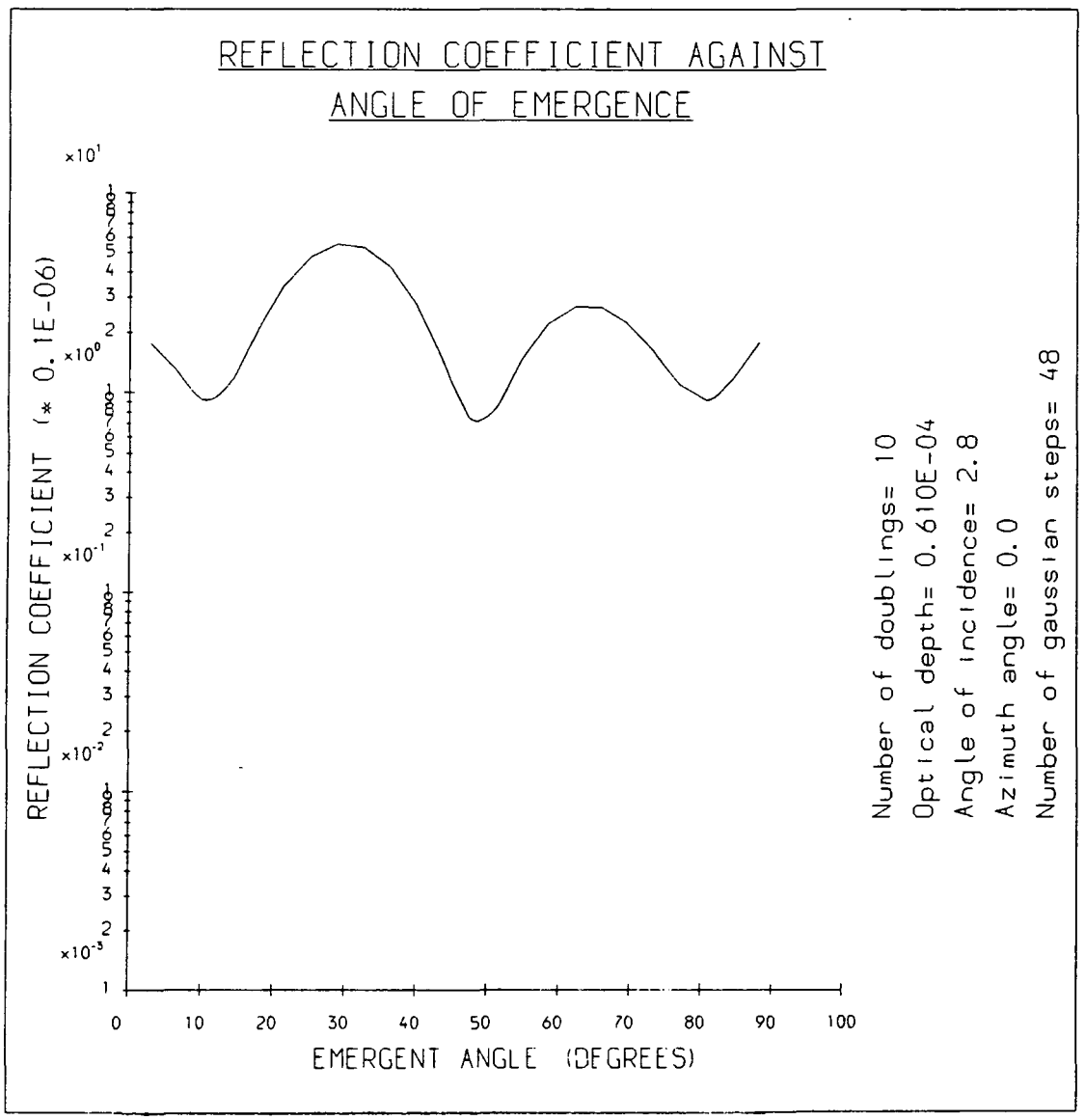
REFLECTION COEFFICIENT AGAINST
ANGLE OF EMERGENCE
REFLECTION COEFFICIENT (* 0.1E-06)
EMERGENT ANGLE (DEGREES)
0
10
20
30
40
50
60
70
80
90
100
Number of doublings= 10
Optical depth= 0.610E-04
Angle of incidence= 2.8
Azimuth angle= 0.0
Number of gaussian steps= 48

Figure 8.21

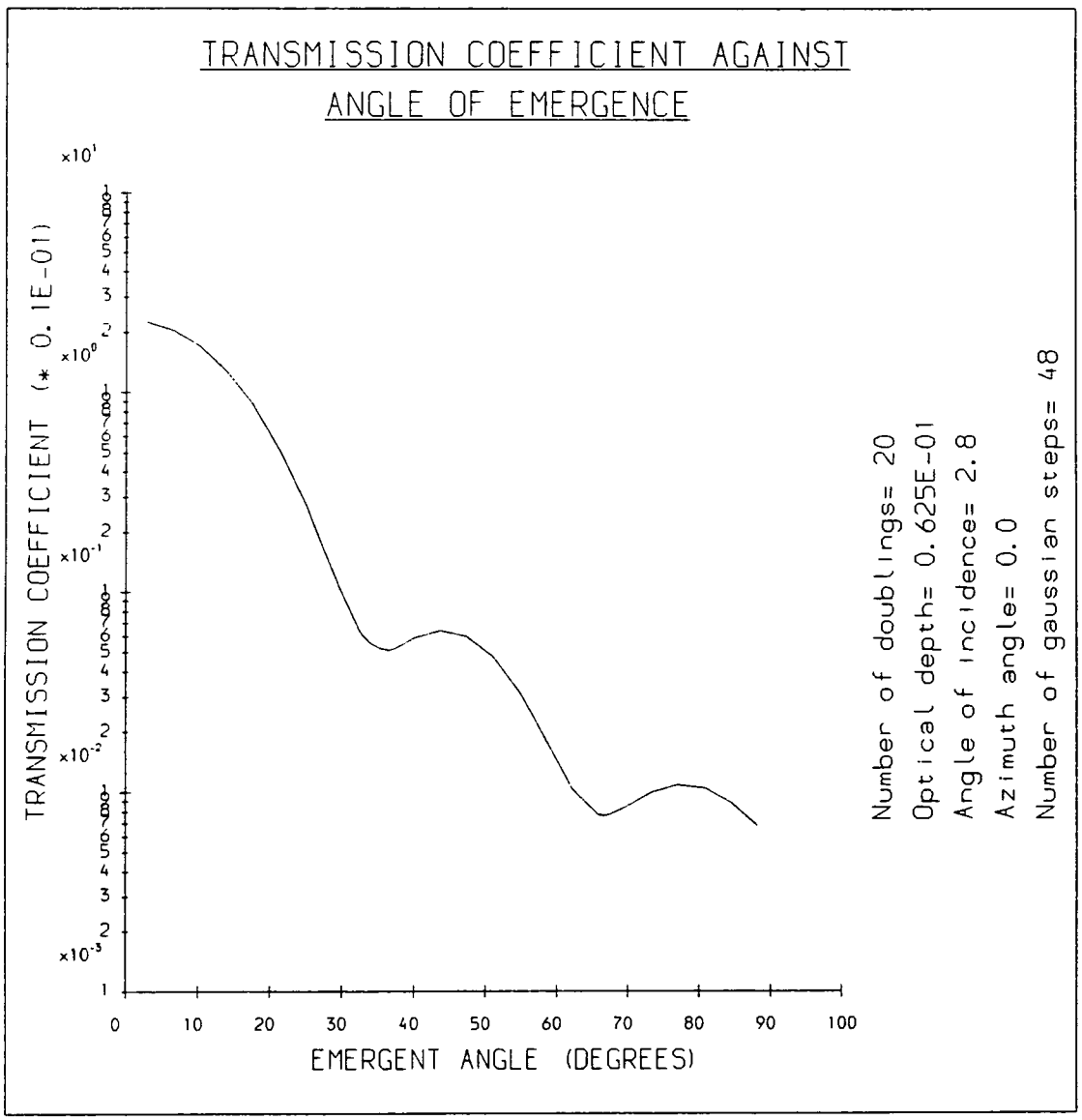
TRANSMISSION COEFFICIENT AGAINST
ANGLE OF EMERGENCE
TRANSMISSION COEFFICIENT (* 0.1E-01)
EMERGENT ANGLE (DEGREES)
0
10
20
30
40
50
60
70
80
90
100
Number of doublings= 20
Optical depth= 0.625E-01
Angle of incidence= 2.8
Azimuth angle= 0.0
Number of gaussian steps= 48

Figure 8.22

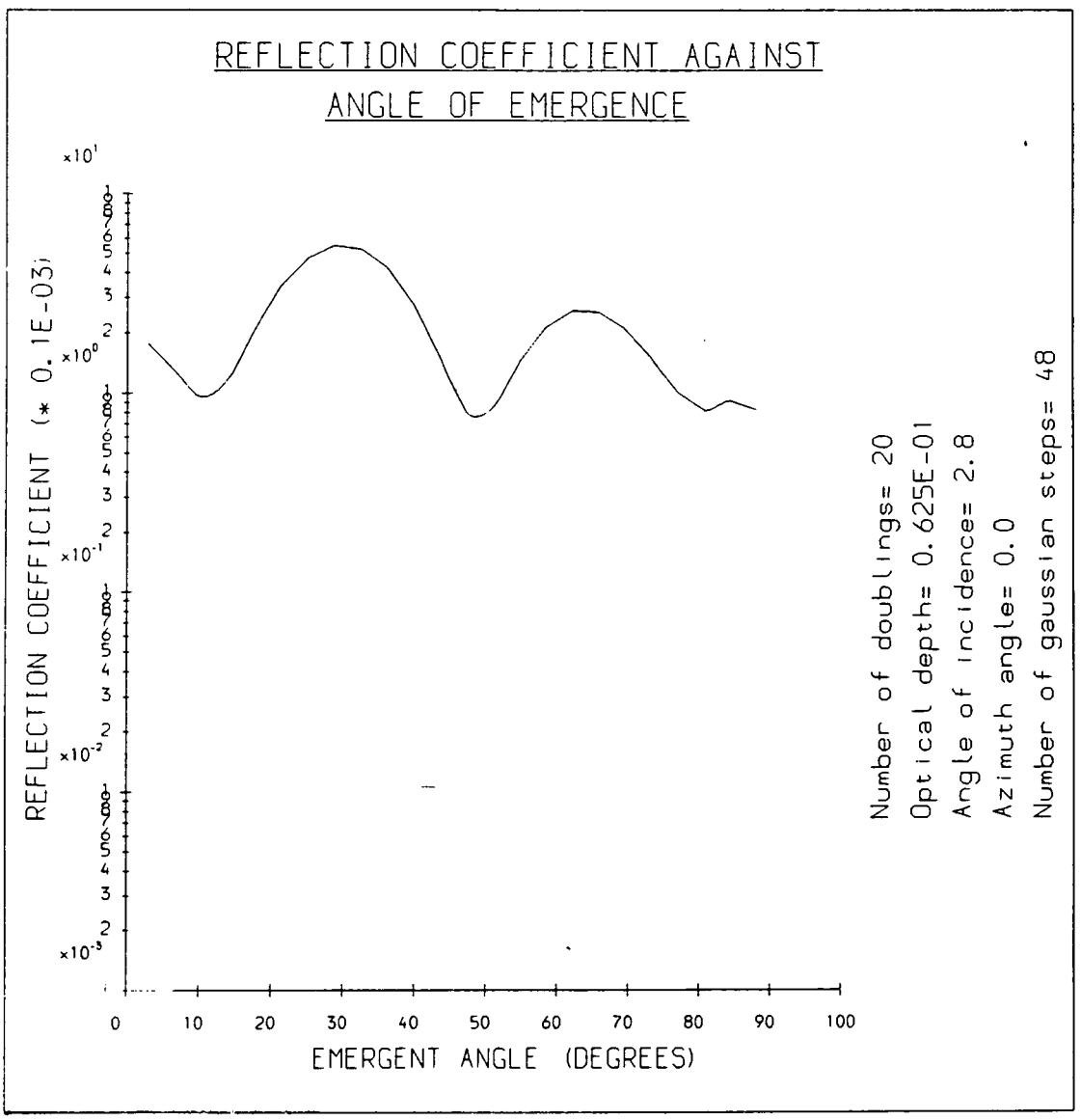
REFLECTION COEFFICIENT AGAINST
ANGLE OF EMERGENCE
REFLECTION COEFFICIENT (* 0.1E-03)
EMERGENT ANGLE (DEGREES)
0
10
20
30
40
50
60
70
80
90
100
Number of doublings= 20
Optical depth= 0.625E-01
Angle of incidence= 2.8
Azimuth angle= 0.0
Number of gaussian steps= 48

Figure 8.23

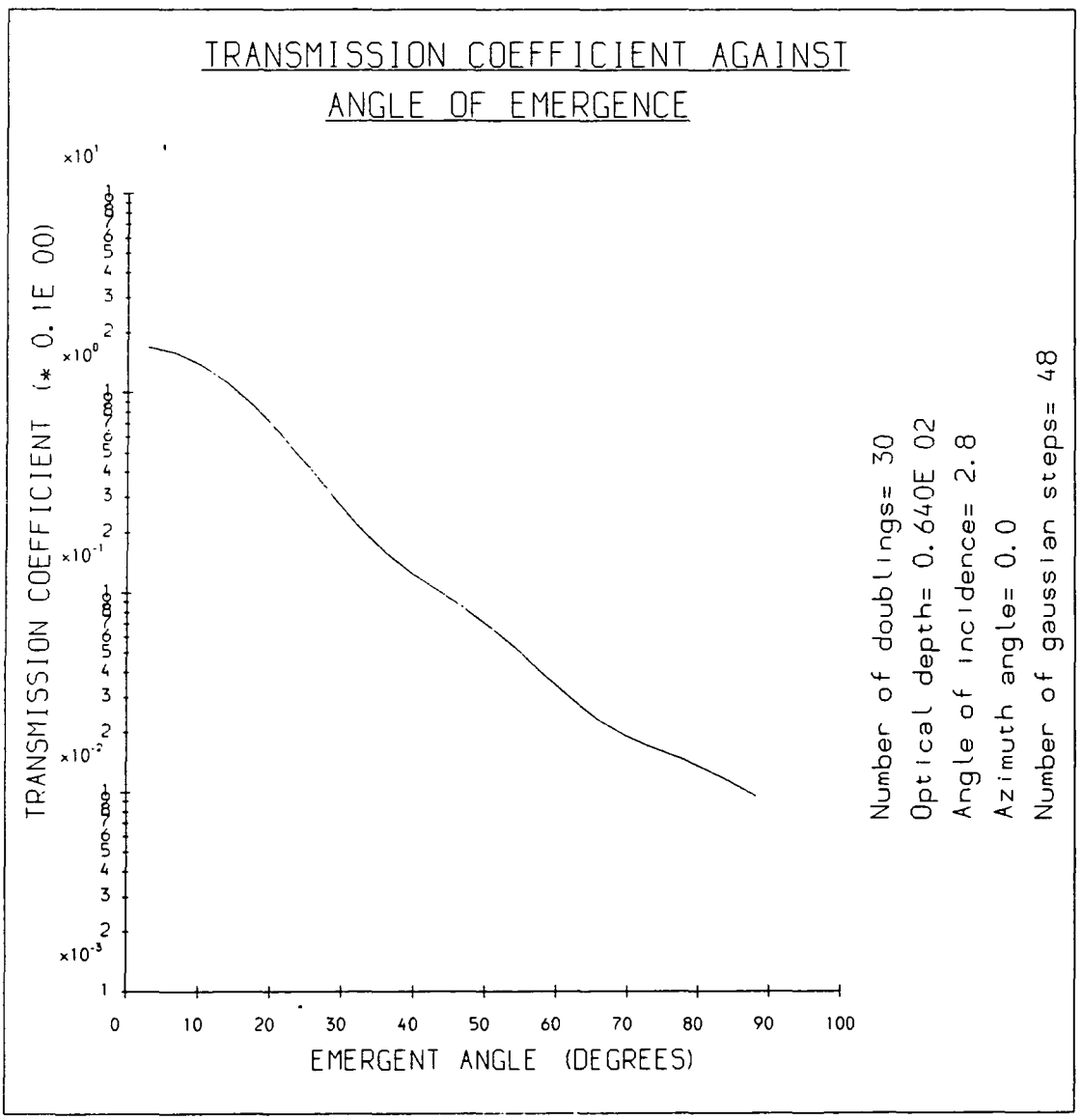
TRANSMISSION COEFFICIENT AGAINST
ANGLE OF EMERGENCE
TRANSMISSION COEFFICIENT (* 0.1E 00)
EMERGENT ANGLE (DEGREES)
0
10
20
30
40
50
60
70
80
90
100
Number of doublings= 30
Optical depth= 0.640E 02
Angle of incidence= 2.8
Azimuth angle= 0.0
Number of gaussian steps= 48

Figure 8.24

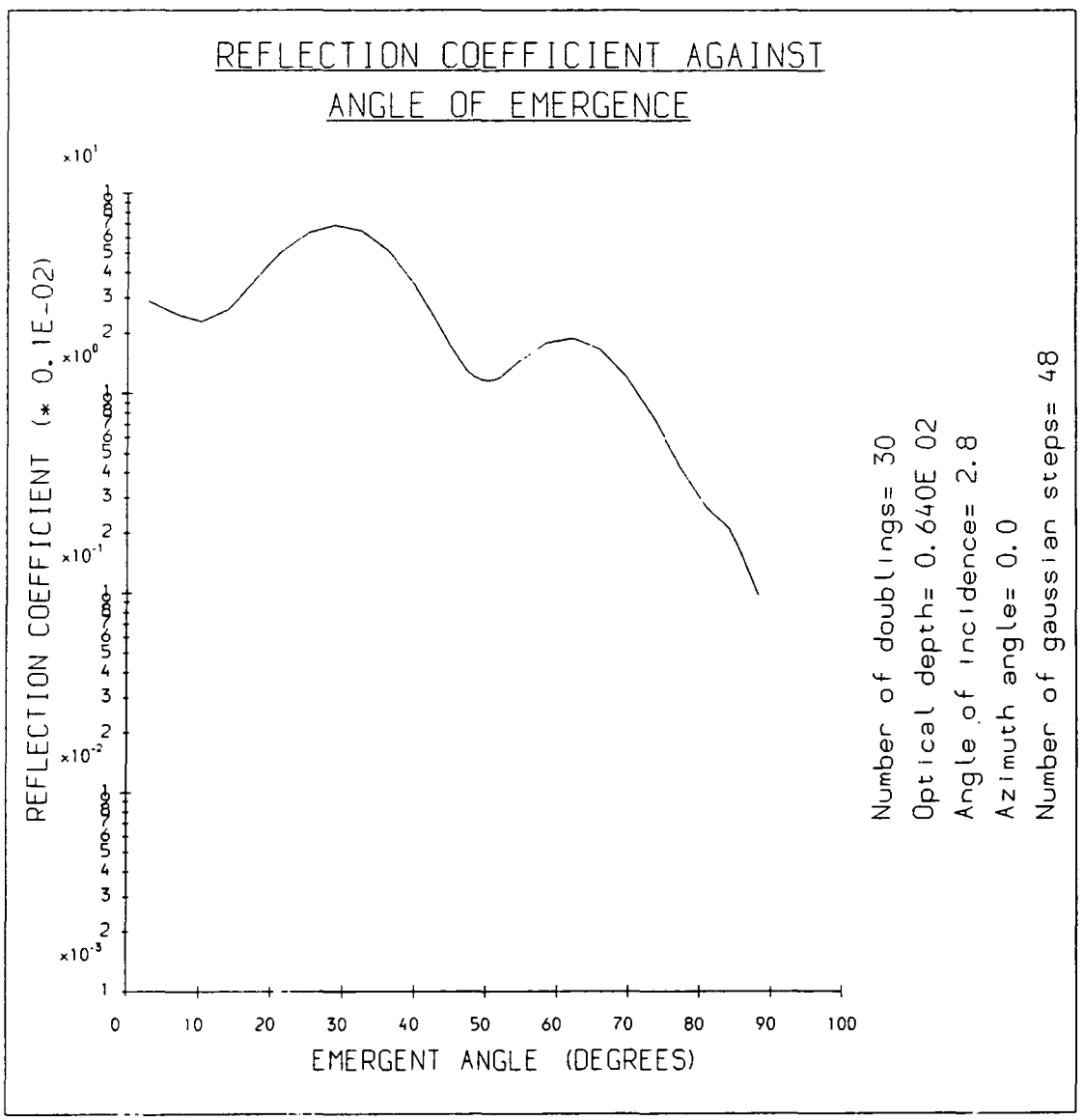
REFLECTION COEFFICIENT AGAINST
ANGLE OF EMERGENCE
REFLECTION COEFFICIENT (* 0.1E-02)
EMERGENT ANGLE (DEGREES)
0
10
20
30
40
50
60
70
80
90
100
Number of doublings= 30
Optical depth= 0.640E 02
Angle of incidence= 2.8
Azimuth angle= 0.0
Number of gaussian steps= 48

Figure 8.25

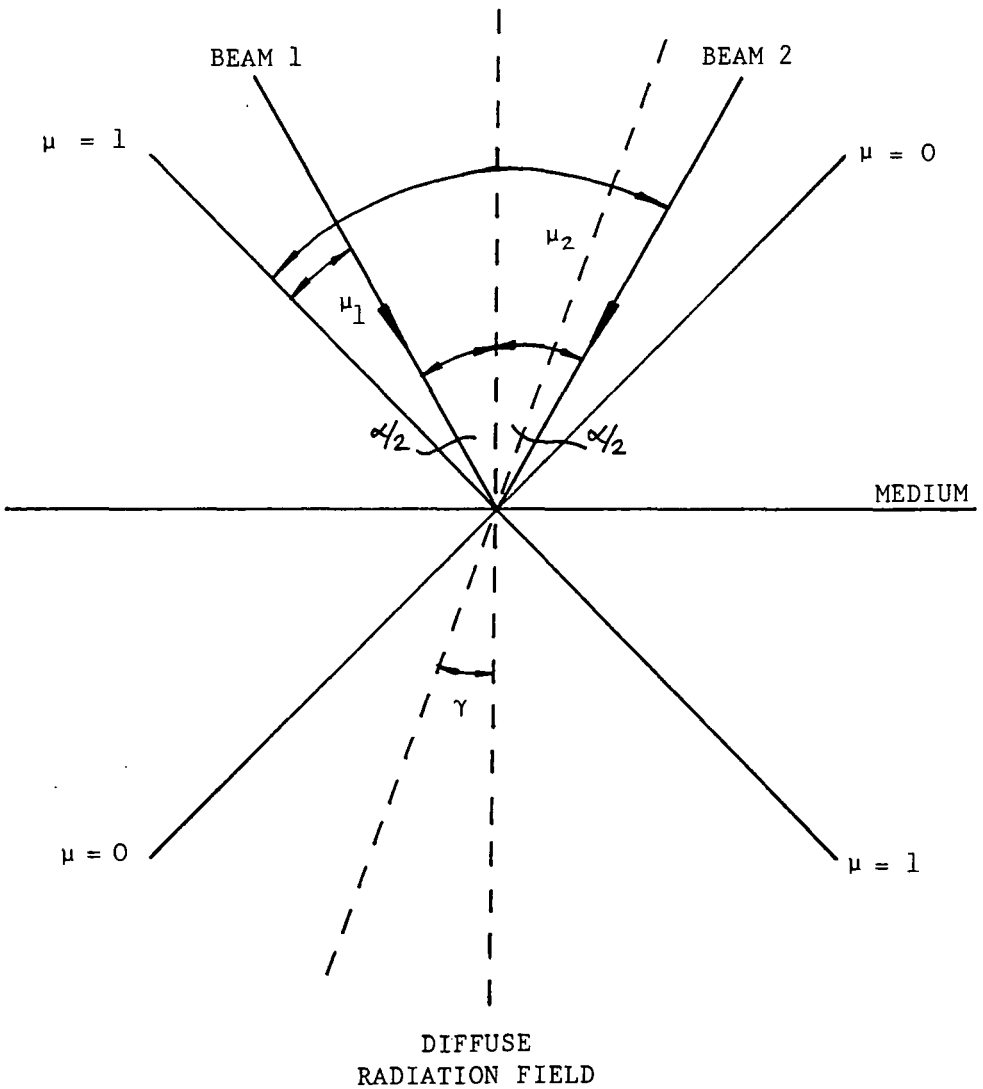

Figure 8.26 MODIFIED GEOMETRY FOR THE LDA COMPUTATIONS

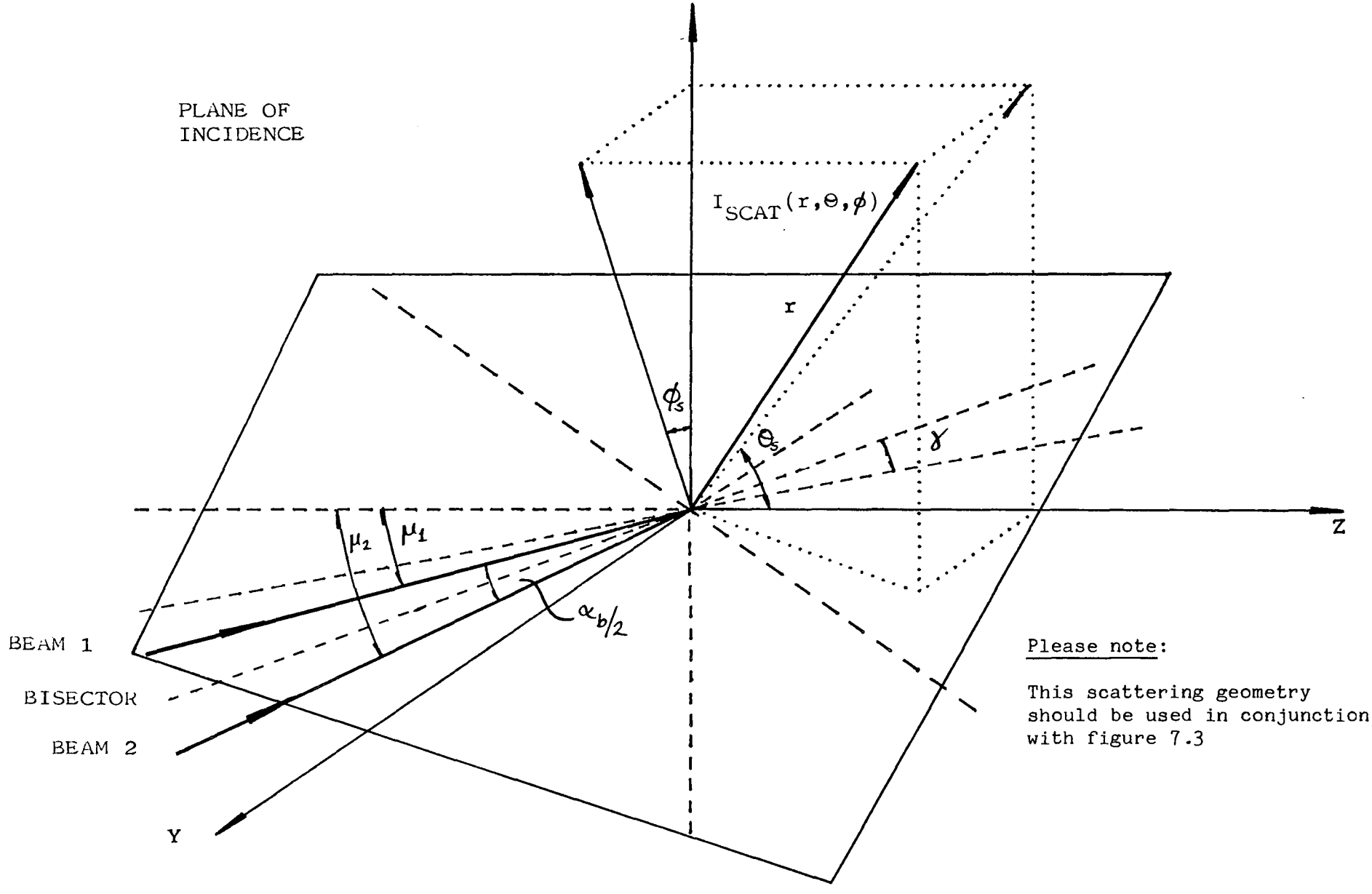

Figure 8.27 GEOMETRY USED TO COMPUTE THE SNR

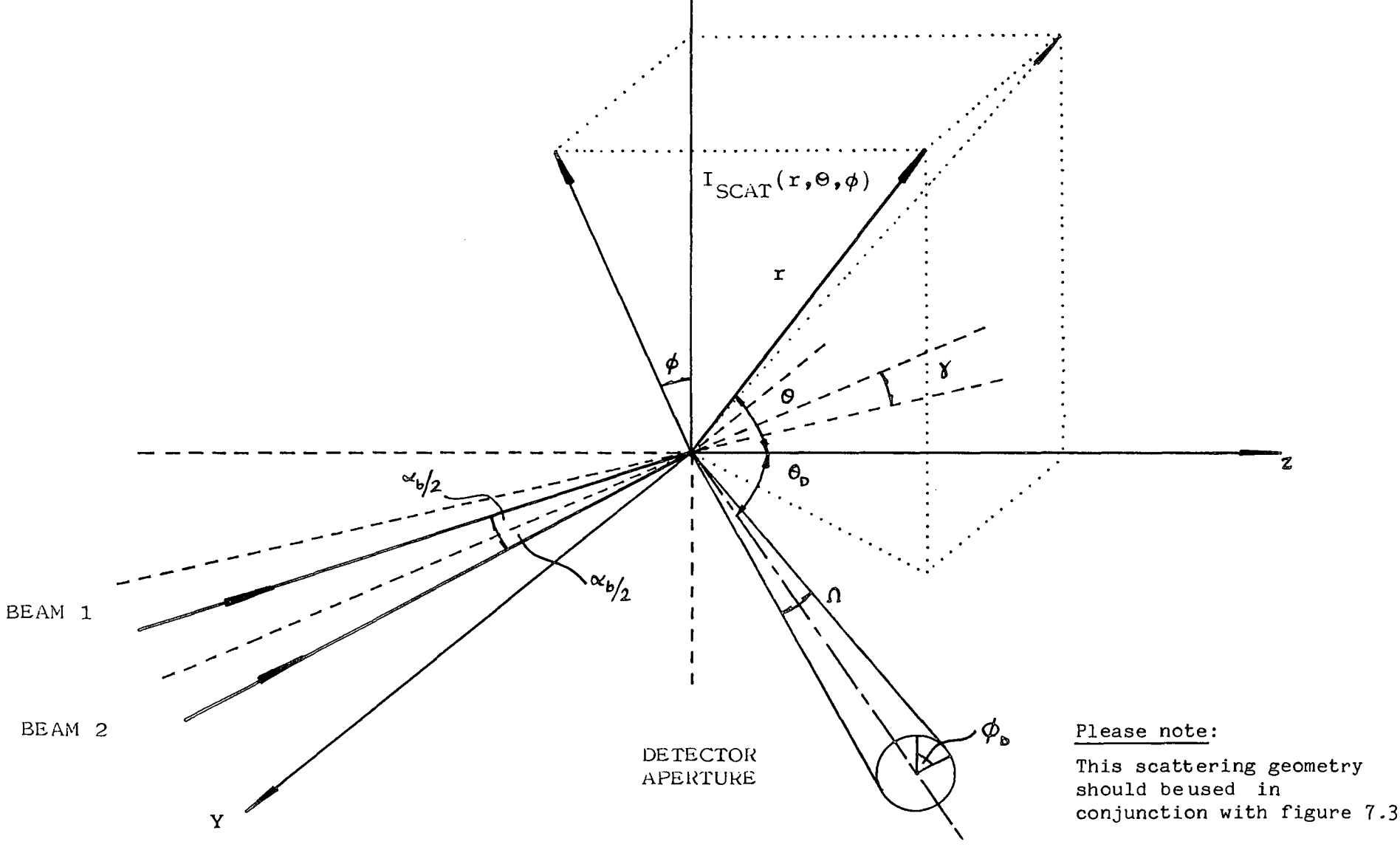

Please note:

This scattering geometry should be used in conjunction with figure 7.3

Figure 8.28 SCATTERING GEOMETRY TO INCLUDE THE DETECTION OPTICS

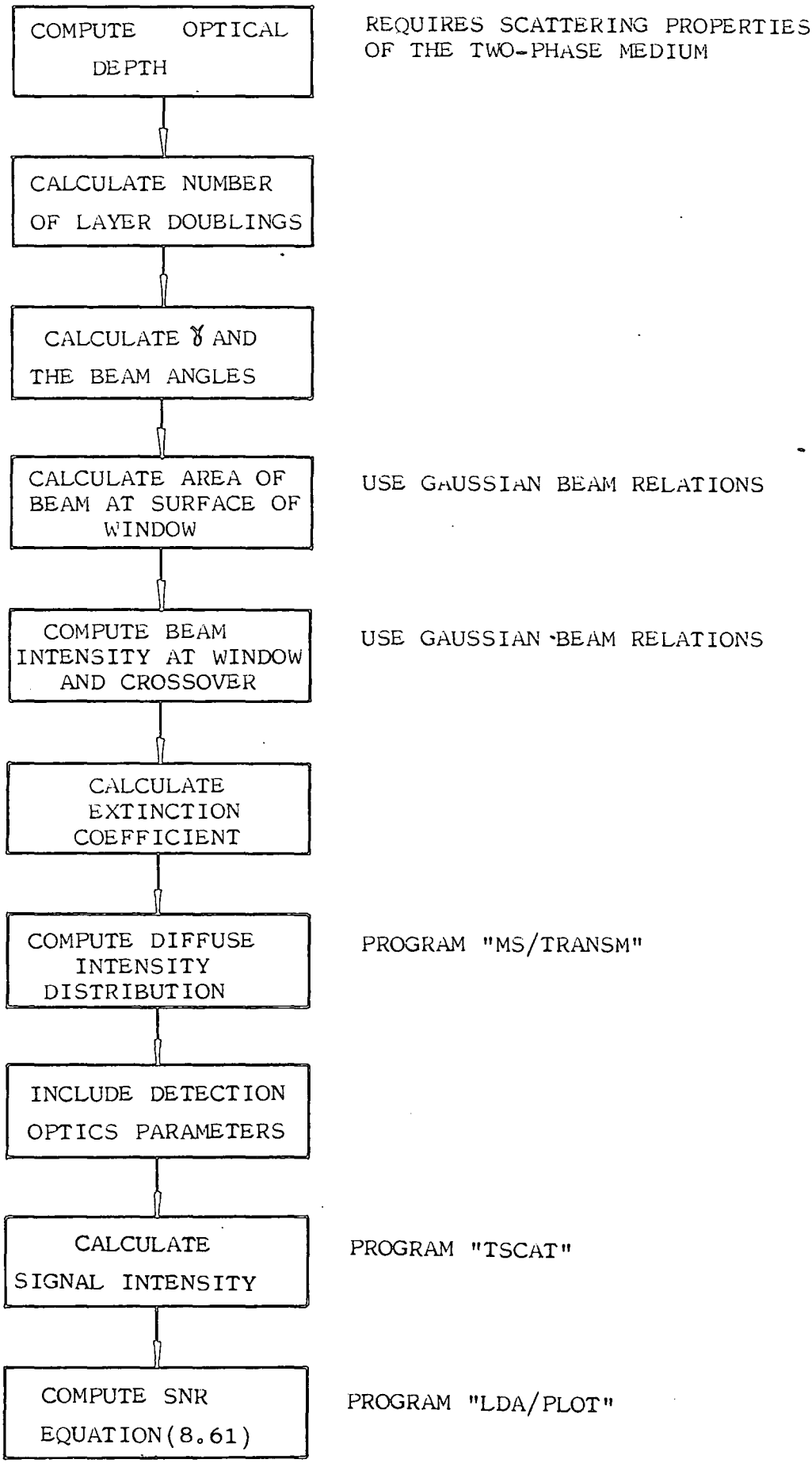

Figure 8.29 FLOW CHART TO CALCULATE THE SNR

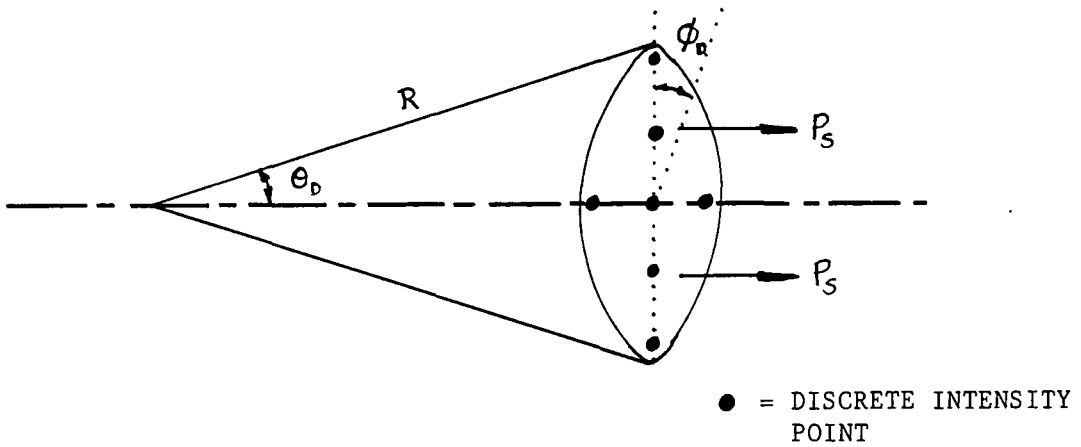

Figure 8.30 CONE OF DETECTION

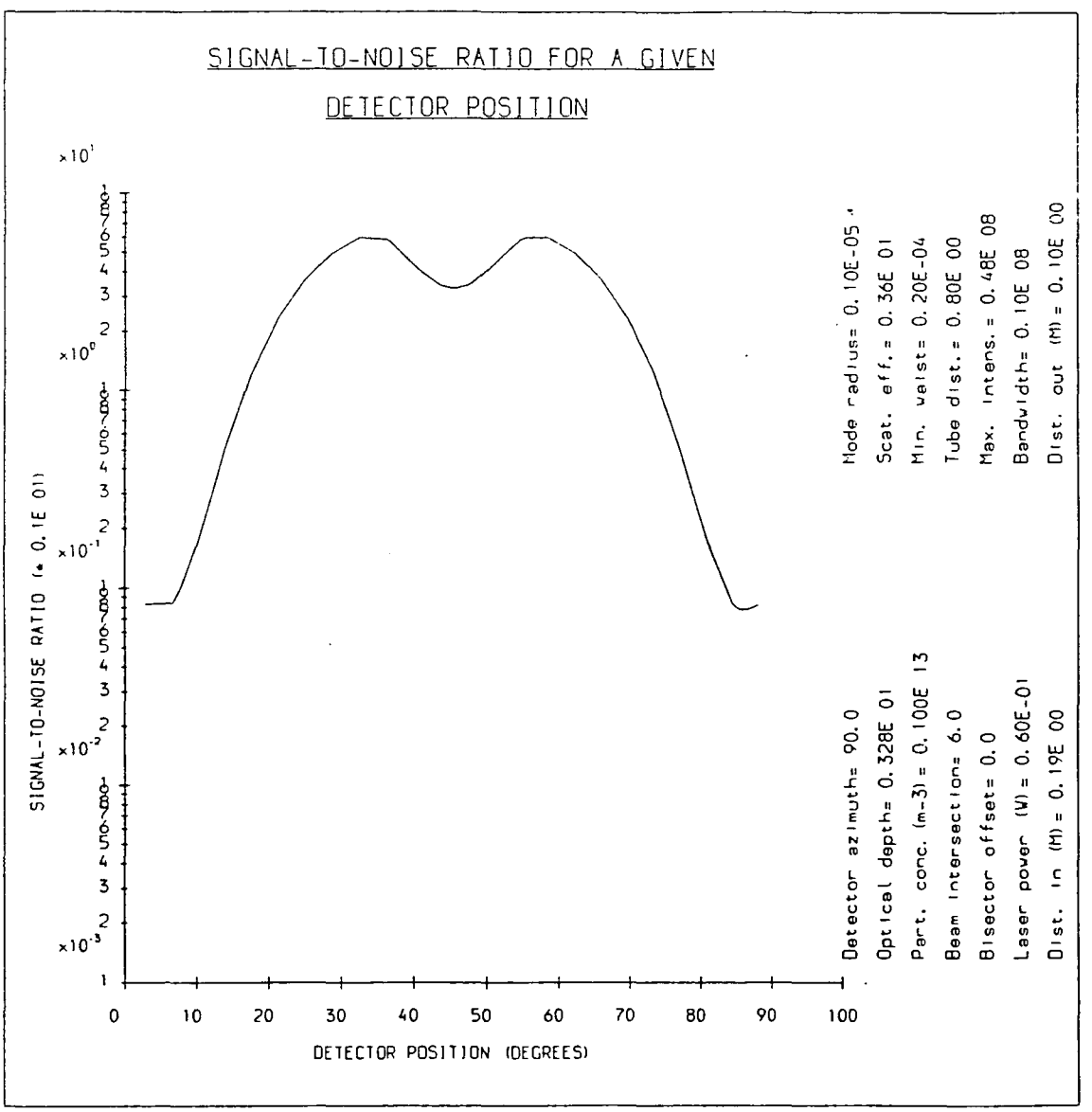

Figure 8.31

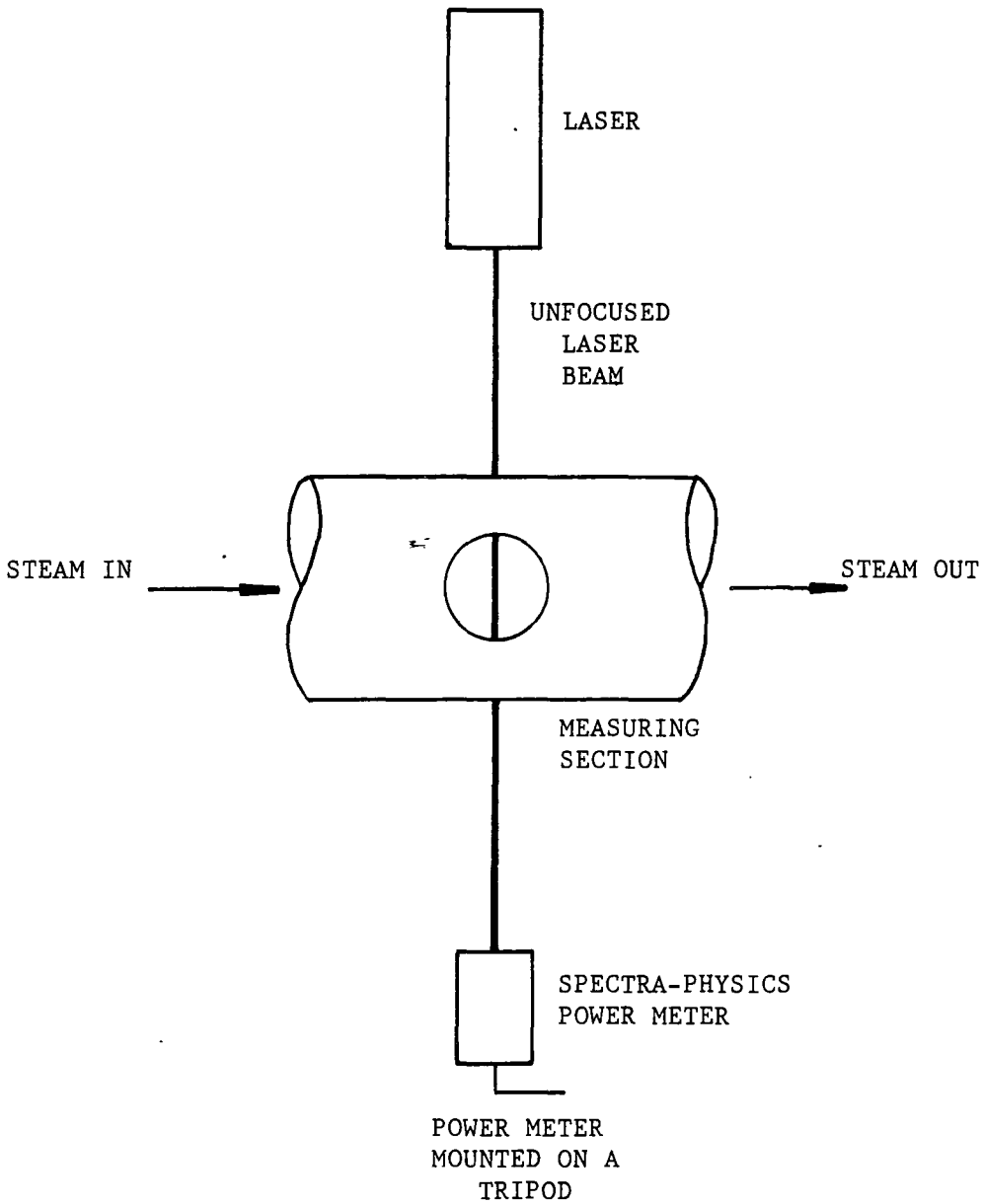

Figure 9.1 PRINCIPLE OF MEASURING THE EXTINCTION OF THE LASER BEAM

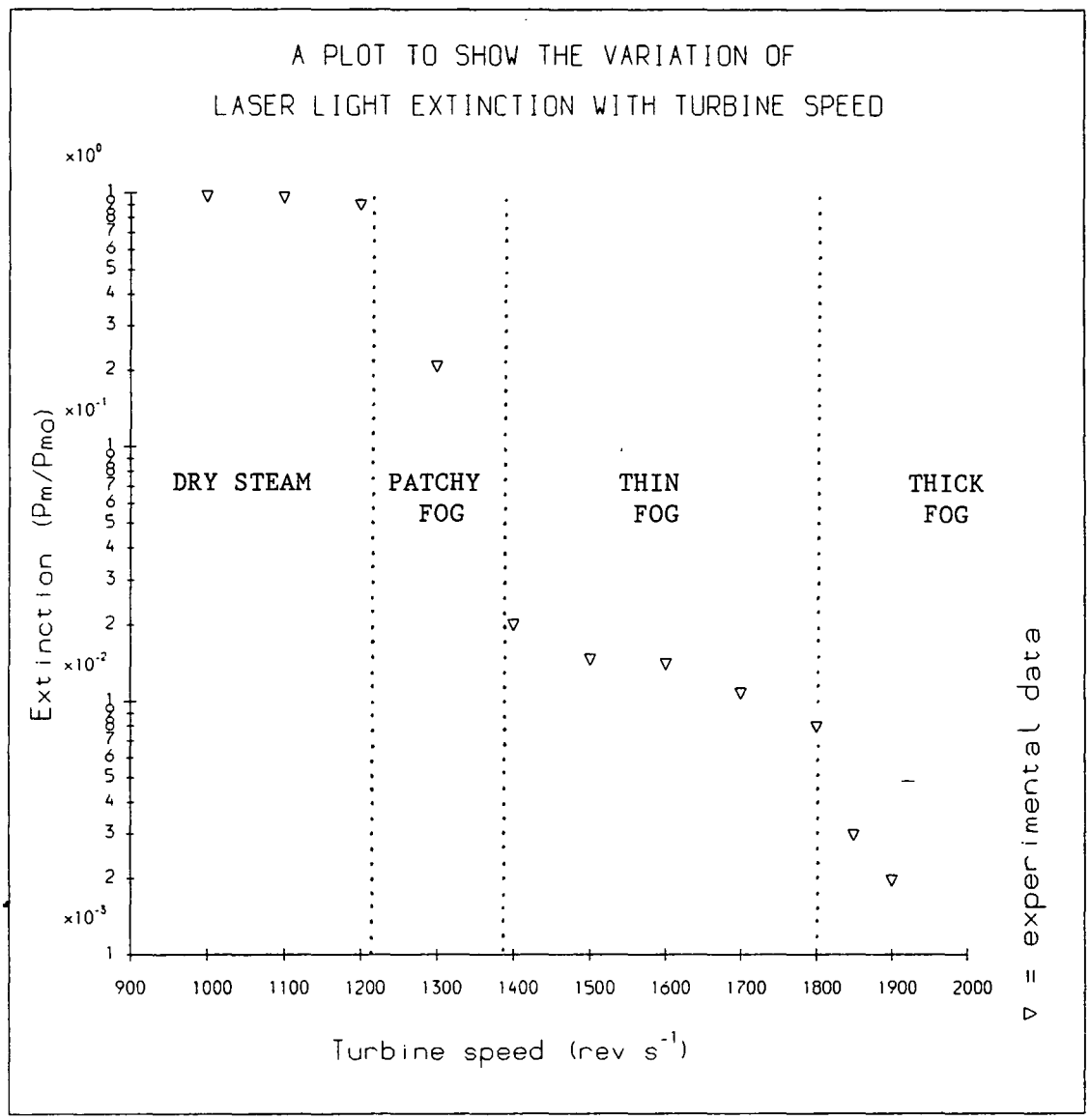
A PLOT TO SHOW THE VARIATION OF
LASER LIGHT EXTINCTION WITH TURBINE SPEED
Extinction (Pm/Pmo)
Turbine speed (rev s-1)
DRY STEAM
PATCHY FOG
THIN FOG
THICK FOG
∇ = experimental data
900
1000
1100
1200
1300
1400
1500
1600
1700
1800
1900
2000

Figure 9.2

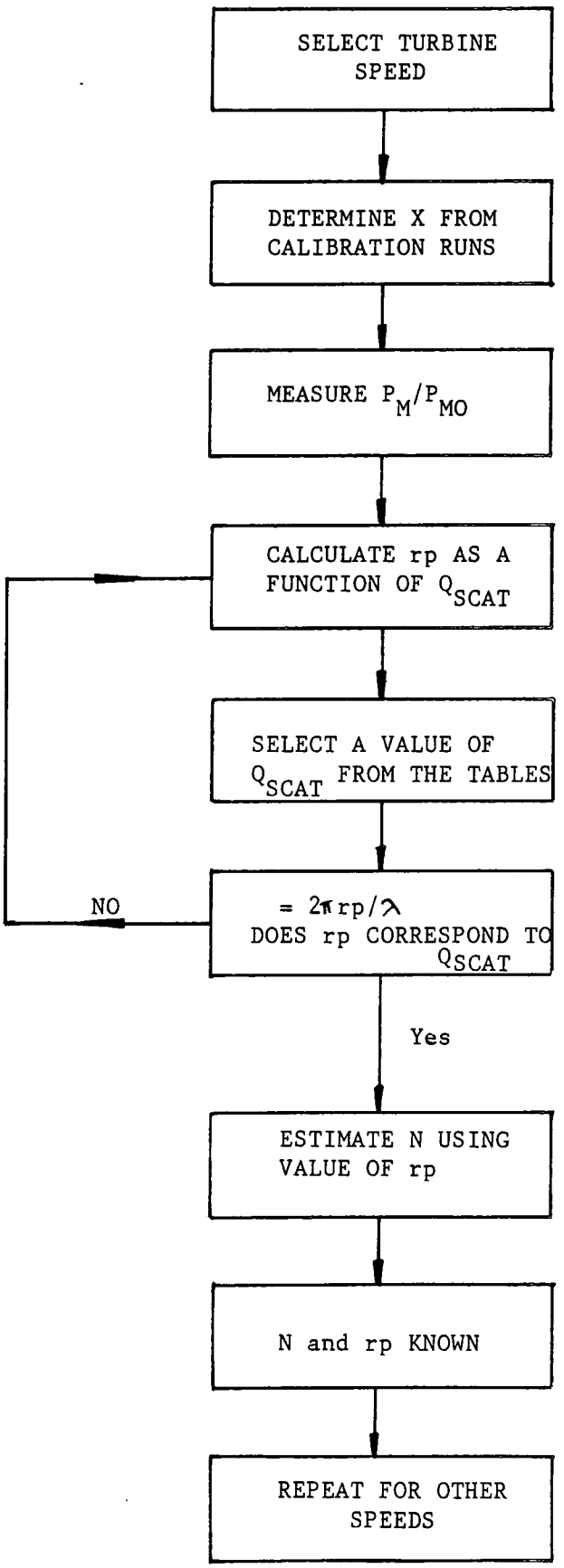

Figure 9.3 FLOW CHART TO CALCULATE N and rp FROM THE EXTINCTION MEASUREMENTS

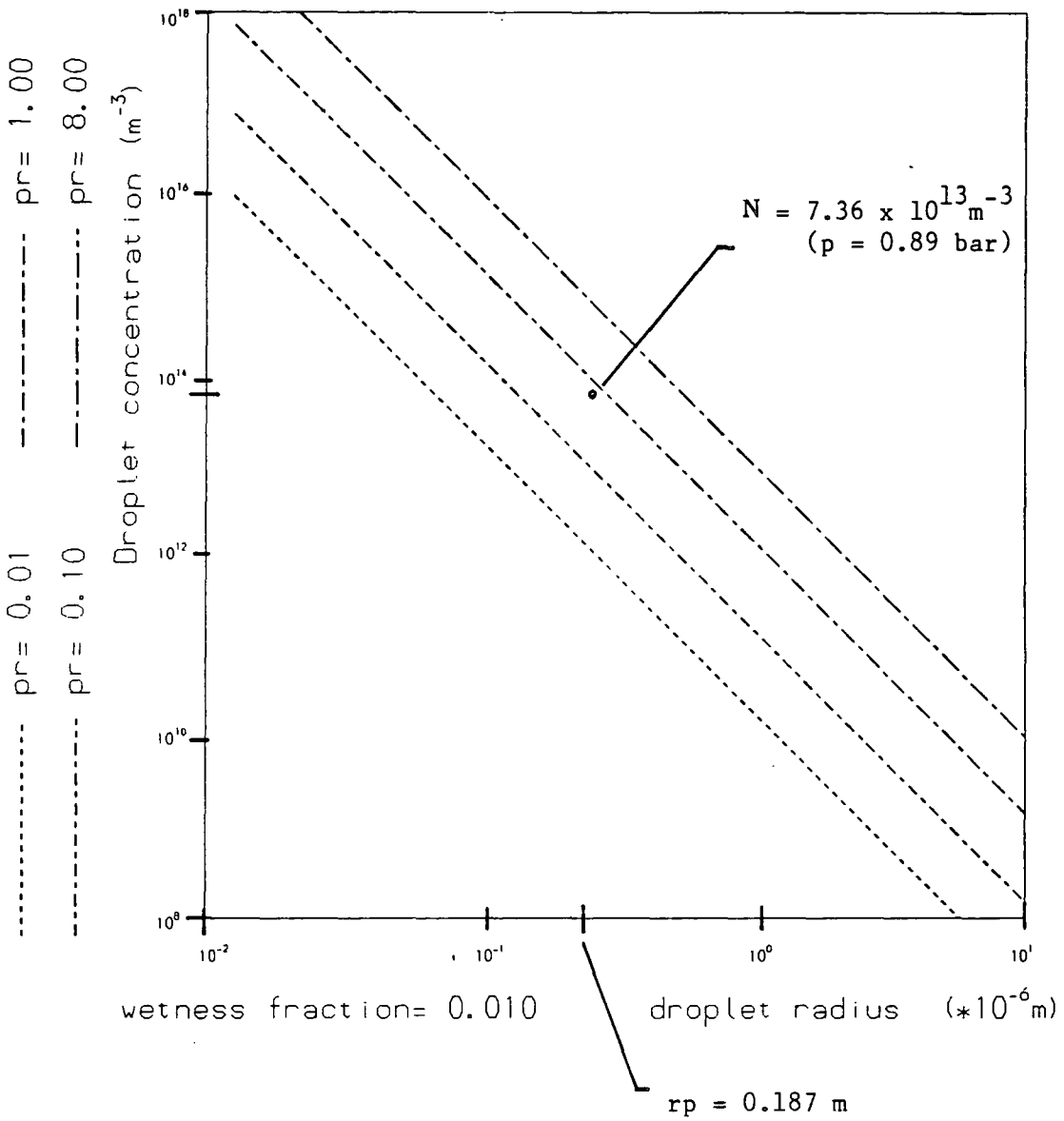

Figure 9.4 PLOT TO SHOW THE COINCIDENCE OF MEASURED N and rp WITH THE THEORETICAL VALUES

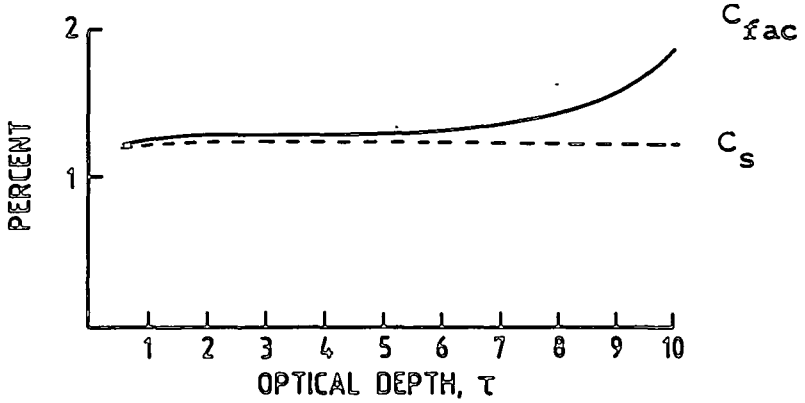

(a) WATER CONTENT = 0.1 gcm^{-3}

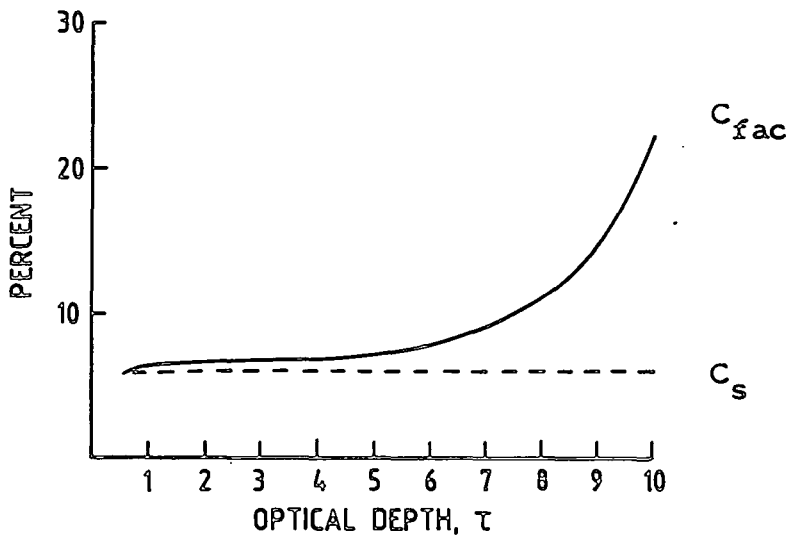

(b) WATER CONTENT = 0.5 gcm^{-3}

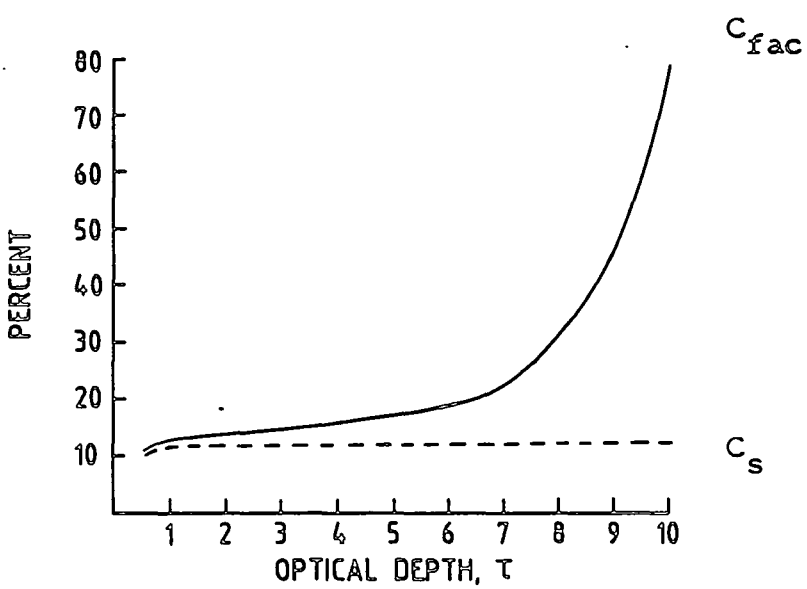

(c) WATER CONTENT = 1.0 gcm^{-3}

FIGURE 9.5 CORRECTION FACTORS FOR THE TRANSMISSION LAW AGAINST OPTICAL DEPTH

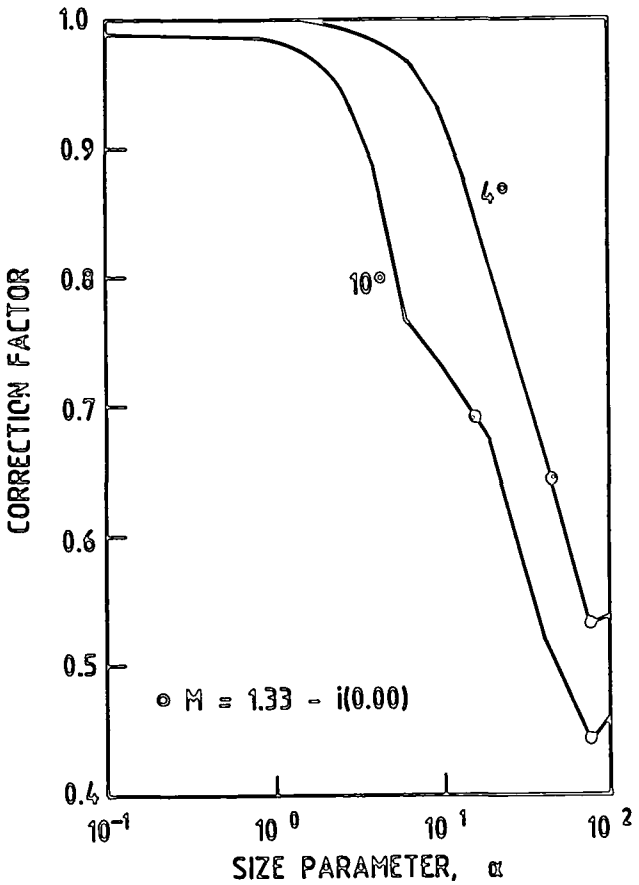

Fig. 9.6 VARIATION OF CORRECTION FACTOR WITH SIZE PARAMETER

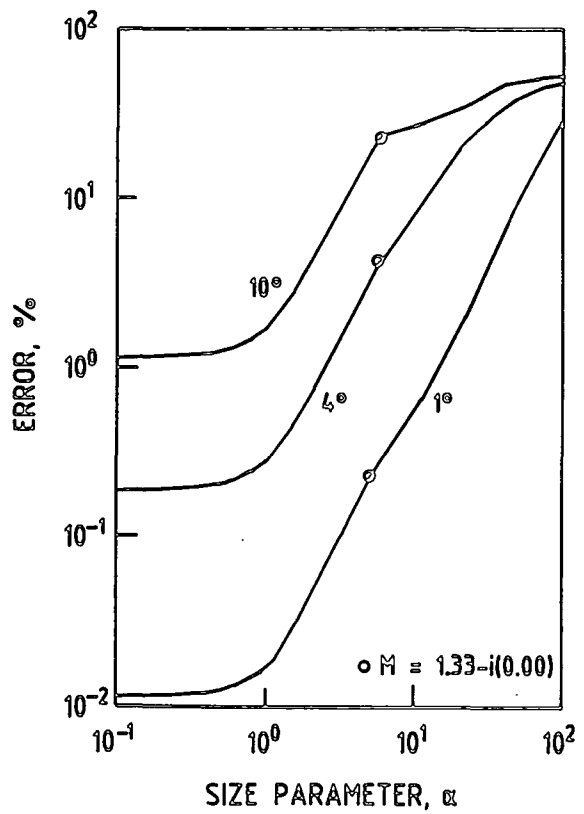

Figure 9.7 VARIATION OF ERROR IN THE USE OF THE TRANSMISSION LAW WITH SIZE PARAMETER

Note: In both figures the angles represent the angle of detection

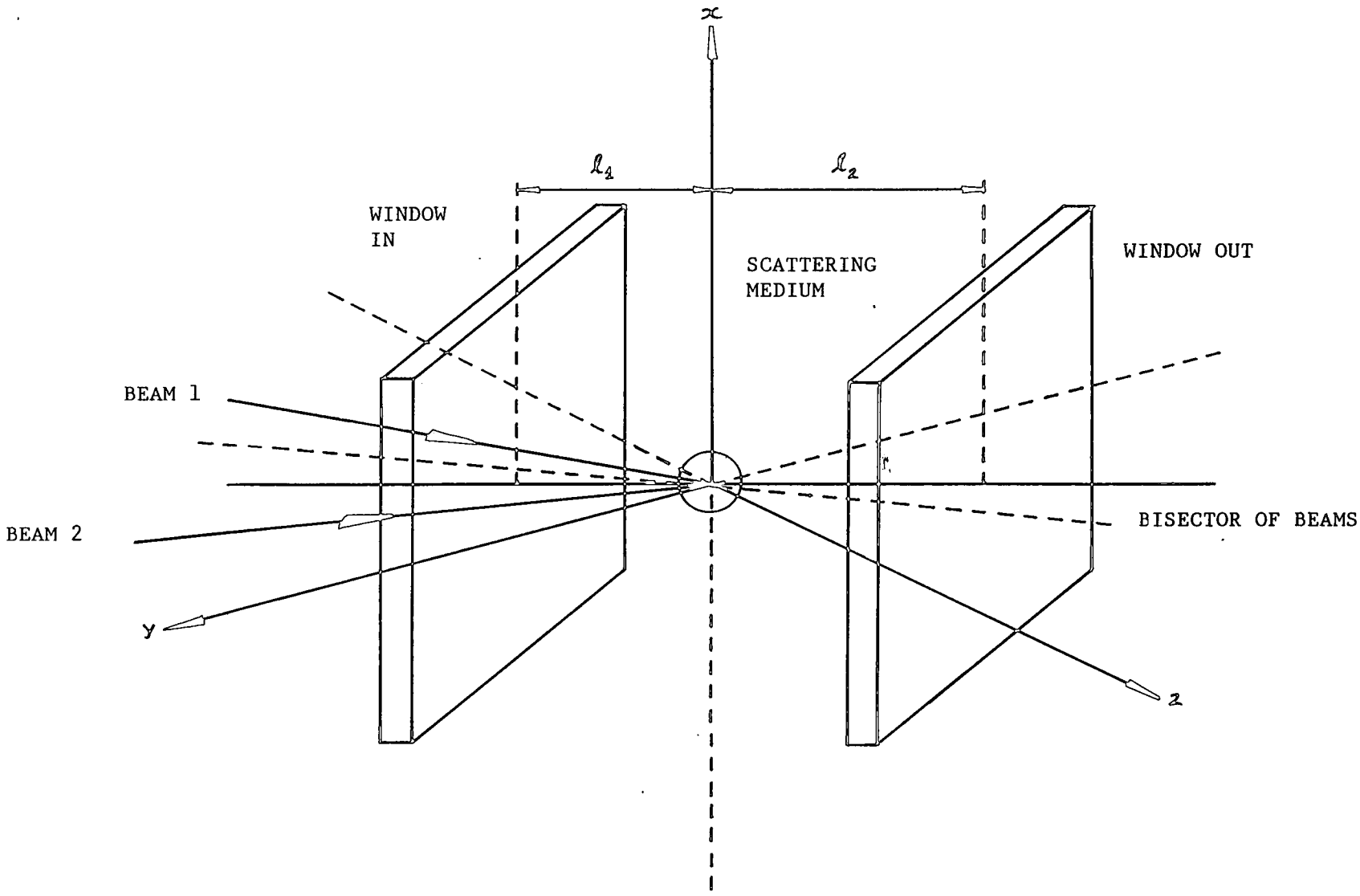

Figure 9.8 GEOMETRY FOR PREDICTING THE DISTRIBUTION OF DIFFUSELY TRANSMITTED LASER LIGHT (see also Figure 8.27)

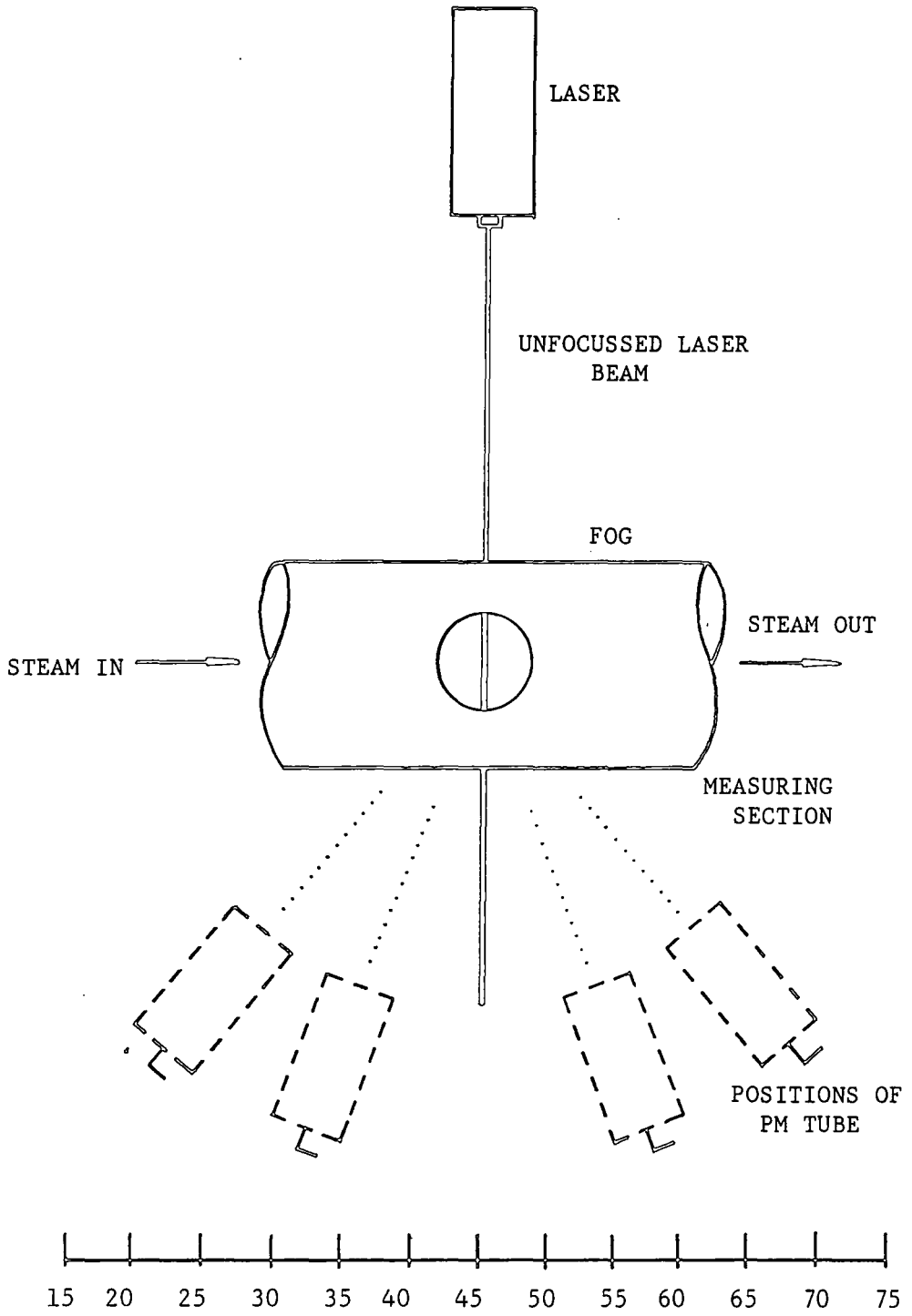

Figure 9.9 LAYOUT OF EXPERIMENT TO MEASURE THE DIFFUSELY SCATTERED LASER LIGHT

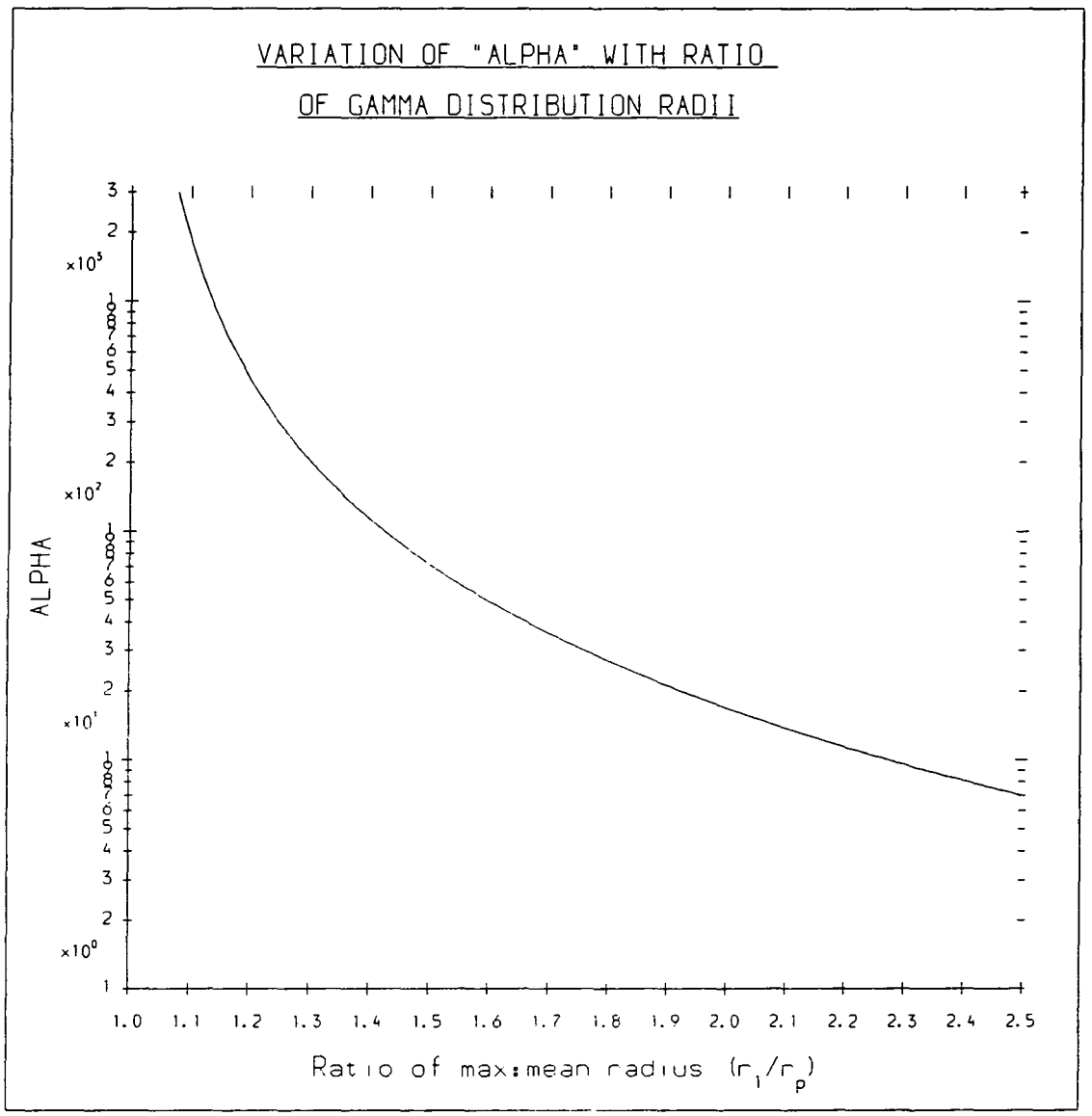
VARIATION OF "ALPHA" WITH RATIO
OF GAMMA DISTRIBUTION RADII
ALPHA
×10⁵
×10⁴
×10³
×10²
×10¹
×10⁰
1.0 1.1 1.2 1.3 1.4 1.5 1.6 1.7 1.8 1.9 2.0 2.1 2.2 2.3 2.4 2.5
Ratio of max:mean radius (r1/rp)

Figure 9.10

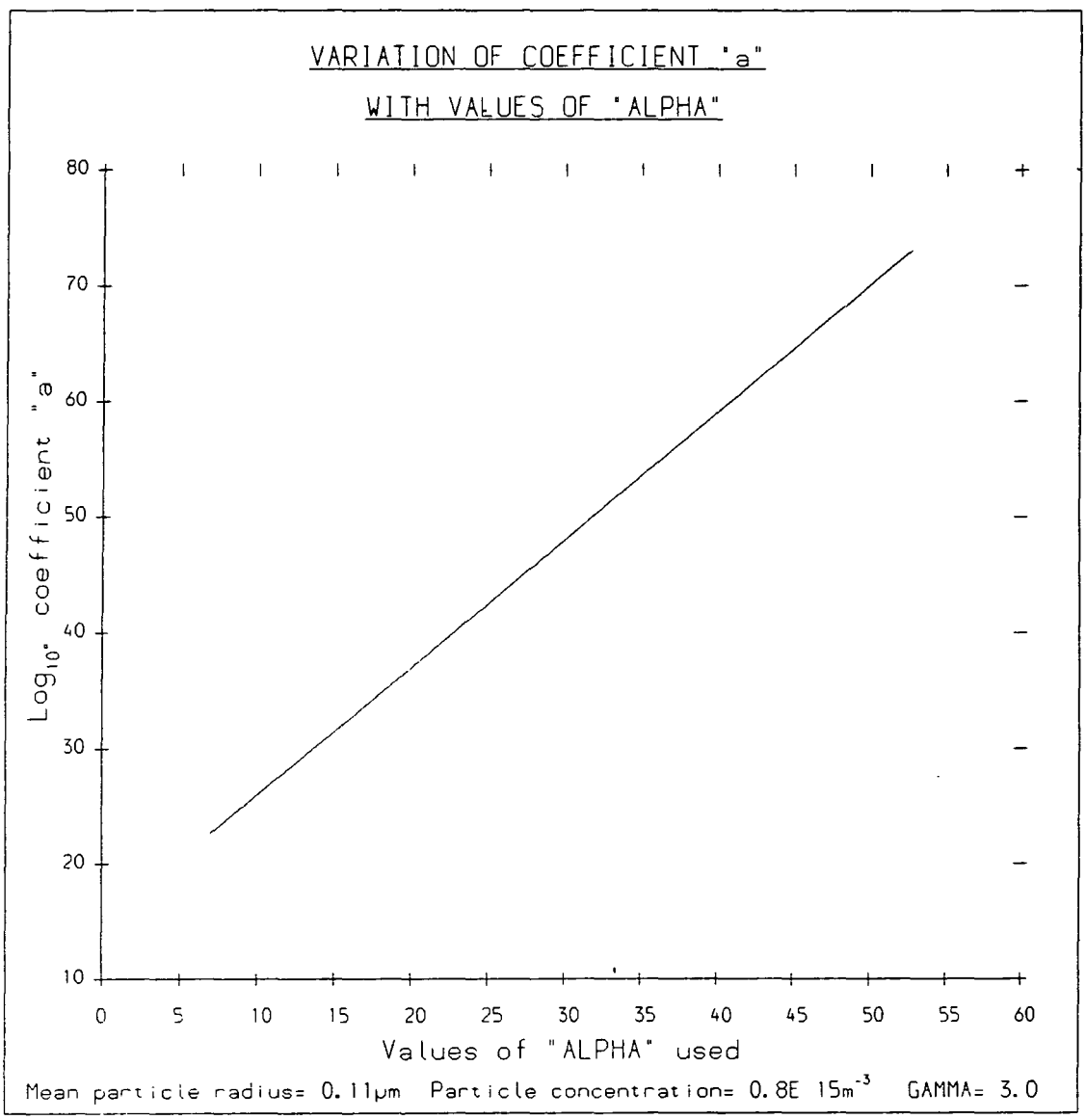
VARIATION OF COEFFICIENT "a"
WITH VALUES OF "ALPHA"
80
70
60
50
40
30
20
10
Log10 coefficient "a"
0
5
10
15
20
25
30
35
40
45
50
55
60
Values of "ALPHA" used
Mean particle radius= 0.11μm Particle concentration= 0.8E 15m-3 GAMMA= 3.0

Figure 9.11

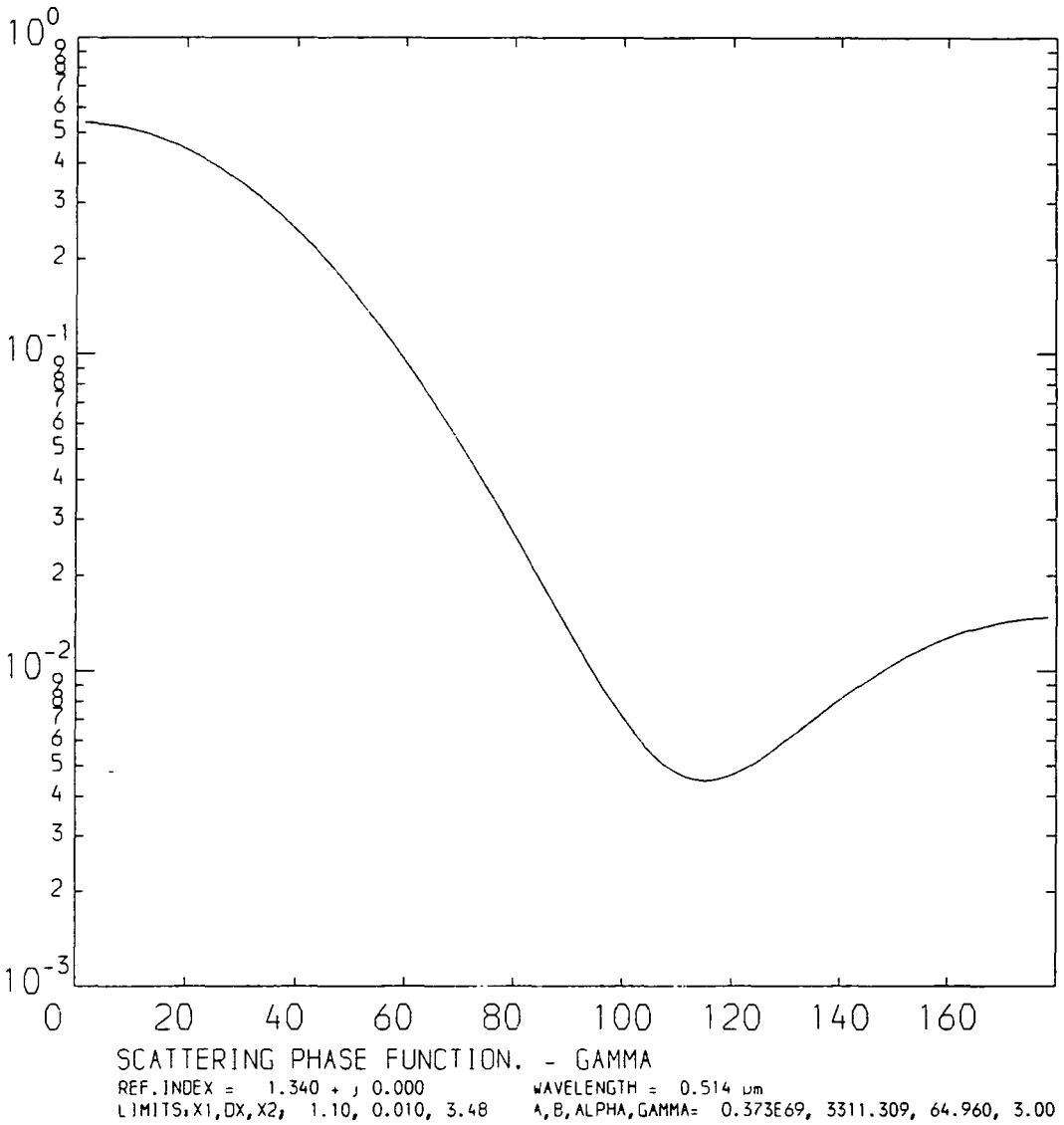
SCATTERING PHASE FUNCTION. - GAMMA
REF. INDEX = 1.340 + j 0.000
WAVELENGTH = 0.514 μm
LIMITS; X1, DX, X2, 1.10, 0.010, 3.48
A, B, ALPHA, GAMMA= 0.373E69, 3311.309, 64.960, 3.00

Figure 9.12(a)

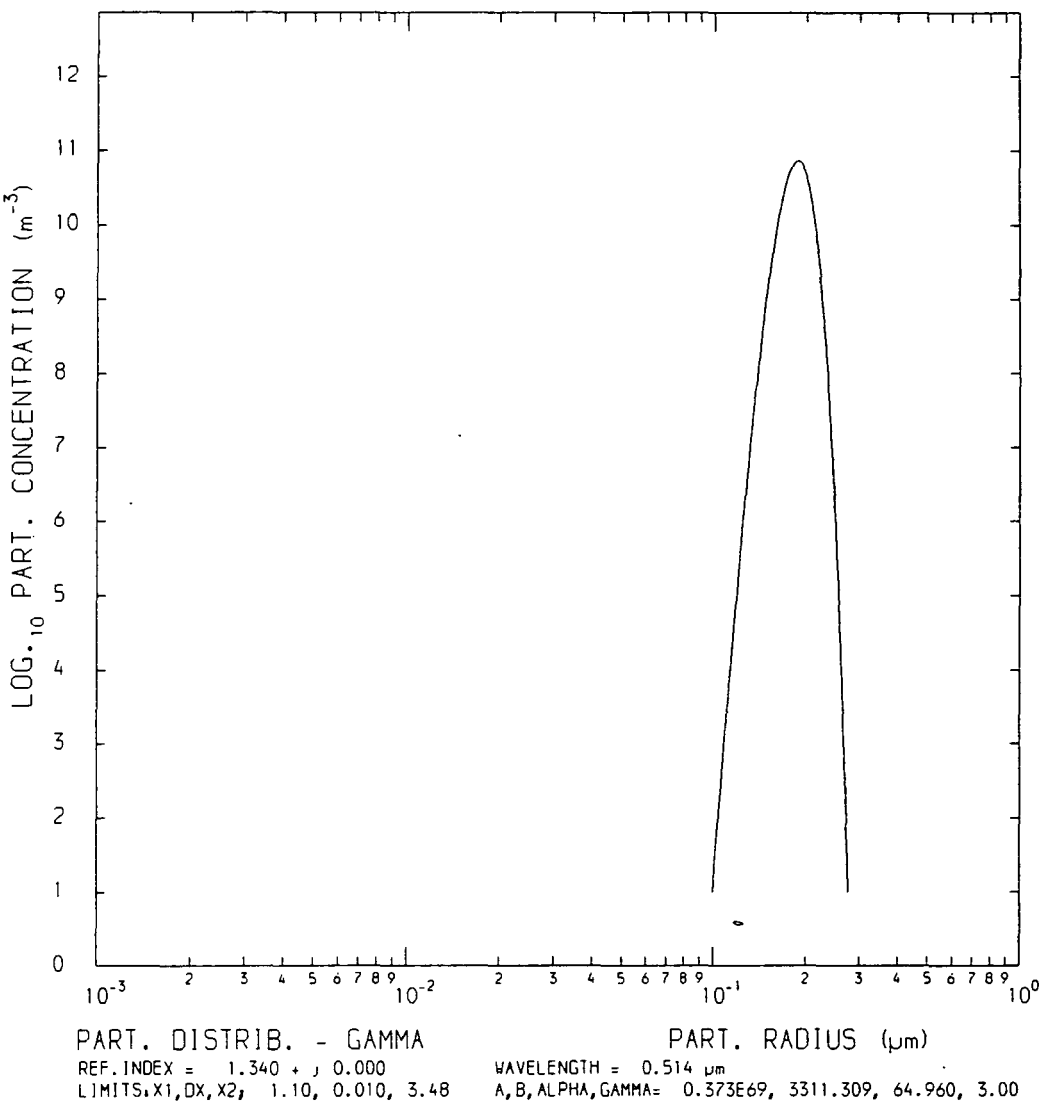
LOG.10 PART. CONCENTRATION (m-3)
12
11
10
9
8
7
6
5
4
3
2
1
0
10-3
10-2
10-1
100
PART. DISTRIB. - GAMMA
REF. INDEX = 1.340 + j 0.000
LIMITS, X1, DX, X2, 1.10, 0.010, 3.48
PART. RADIUS (μm)
WAVELENGTH = 0.514 μm
A, B, ALPHA, GAMMA= 0.373E69, 3311.309, 64.960, 3.00

Figure 9.12(b)

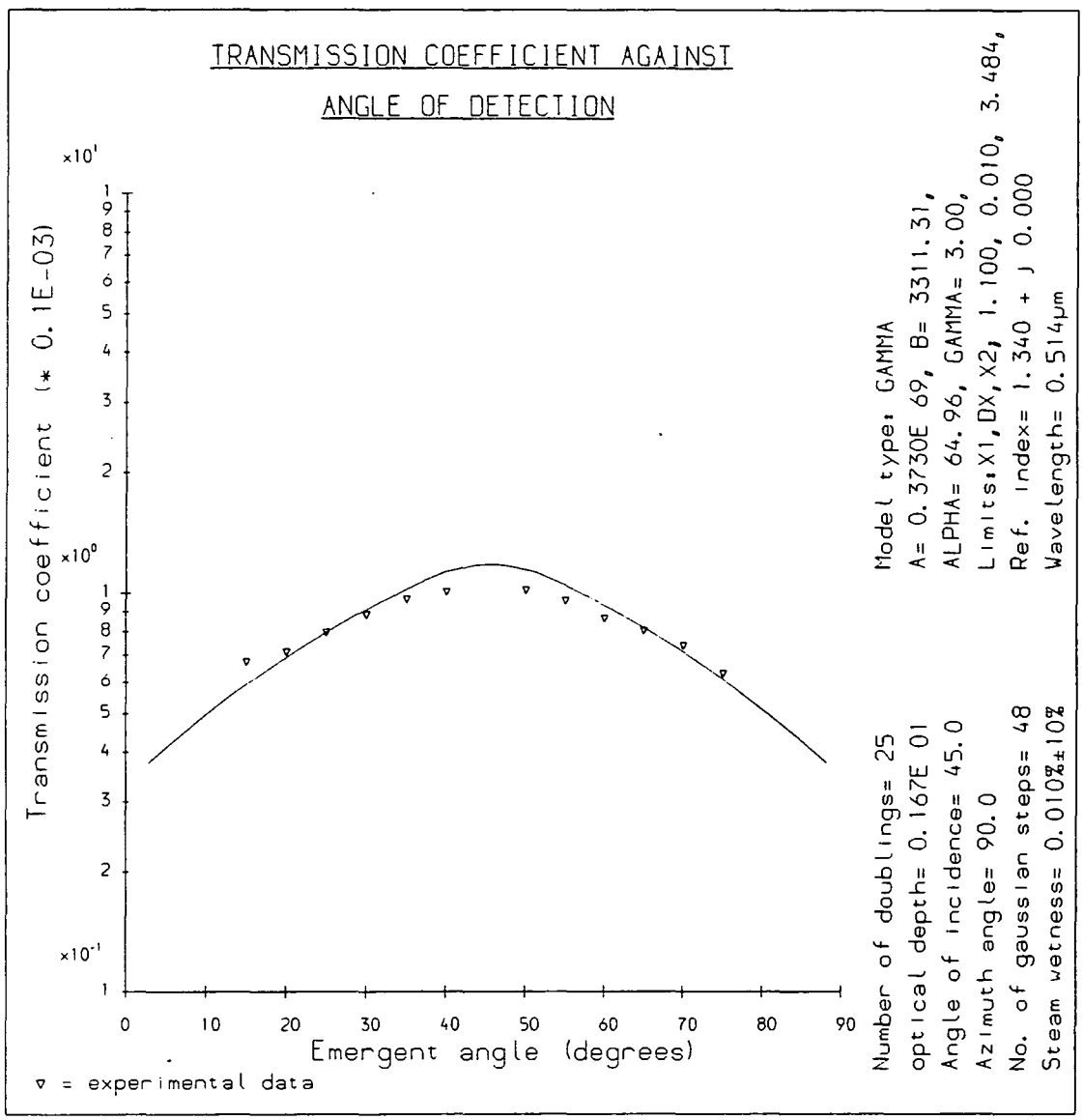
TRANSMISSION COEFFICIENT AGAINST
ANGLE OF DETECTION
Transmission coefficient (* 0.1E-03)
Emergent angle (degrees)
▽ = experimental data
Model type: GAMMA
A= 0.3730E 69, B= 3311.31,
ALPHA= 64.96, GAMMA= 3.00,
Limits:X1,DX,X2, 1.100, 0.010, 3.484,
Ref. Index= 1.340 + j 0.000
Wavelength= 0.514μm
Number of doublings= 25
optical depth= 0.167E 01
Angle of incidence= 45.0
Azimuth angle= 90.0
No. of gaussian steps= 48
Steam wetness= 0.010%±10%

Figure 9.12(c)

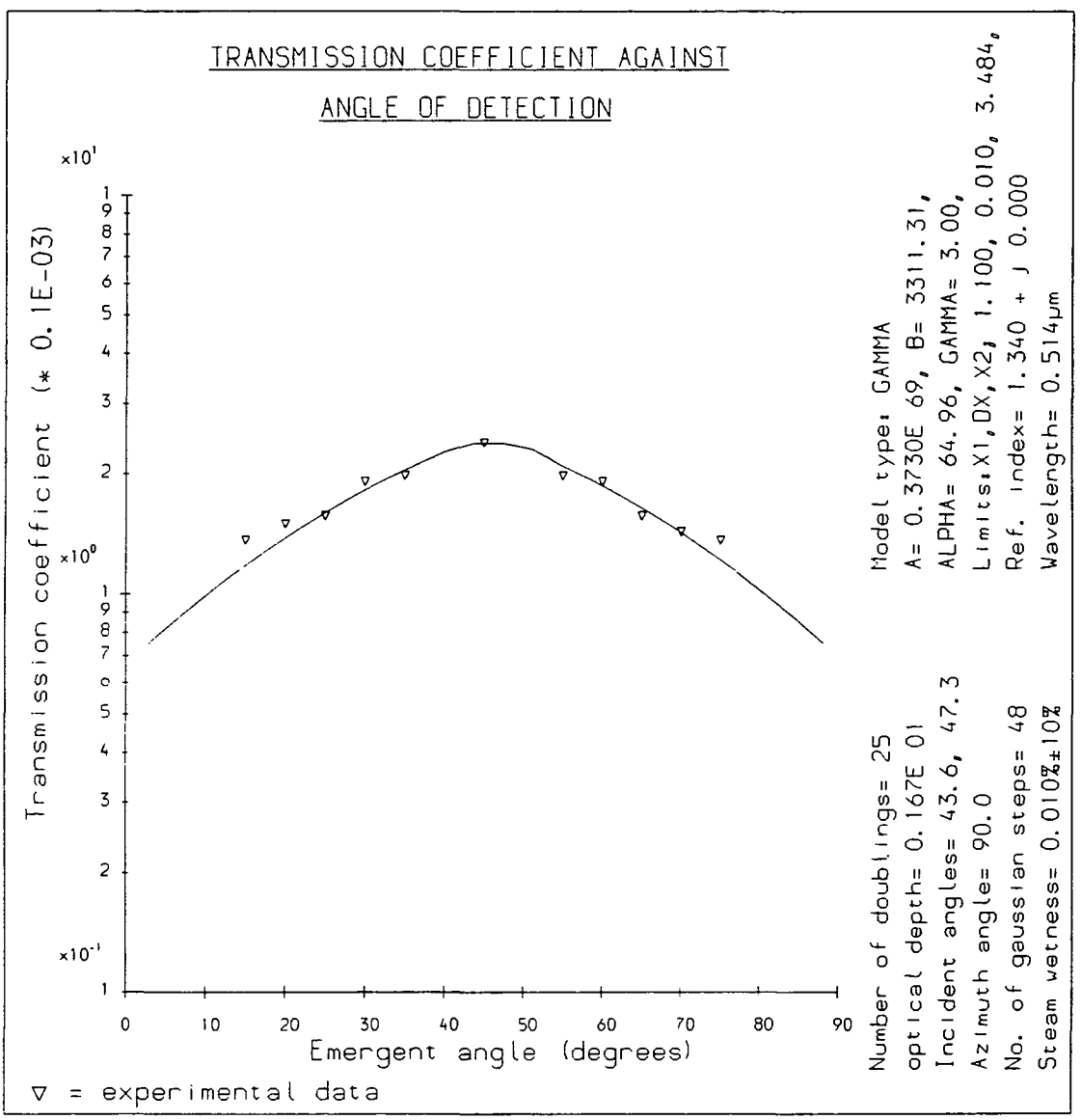
TRANSMISSION COEFFICIENT AGAINST
ANGLE OF DETECTION
Transmission coefficient (* 0.1E-03)
Emergent angle (degrees)
∇ = experimental data
Model type: GAMMA
A= 0.3730E 69, B= 3311.31,
ALPHA= 64.96, GAMMA= 3.00,
Limits:X1,DX,X2, 1.100, 0.010, 3.484,
Ref. index= 1.340 + i 0.000
Wavelength= 0.514μm
Number of doublings= 25
optical depth= 0.167E 01
Incident angles= 43.6, 47.3
Azimuth angle= 90.0
No. of gaussian steps= 48
Steam wetness= 0.010%±10%

Figure 9.12(d)

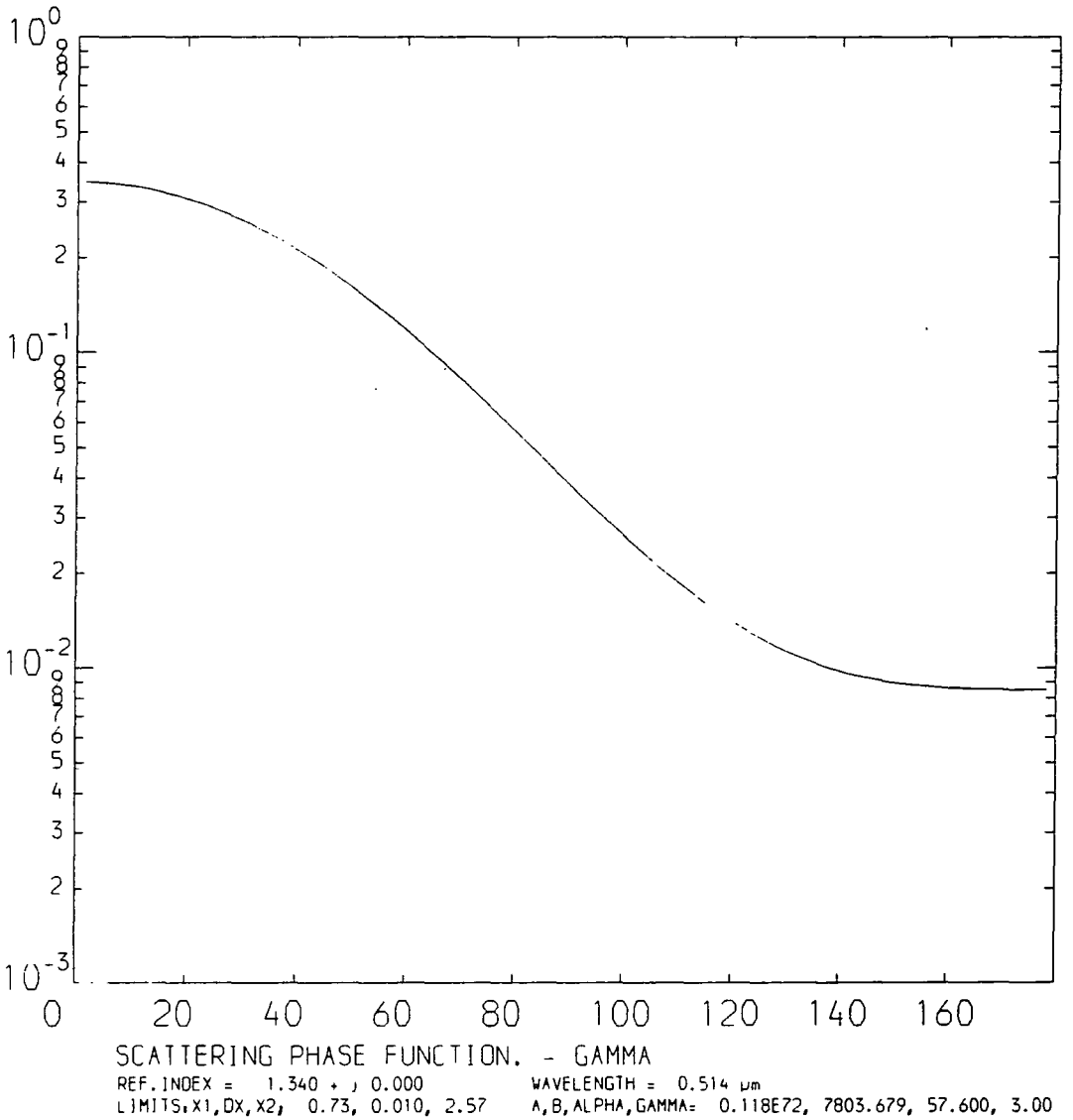
10^0
10^{-1}
10^{-2}
10^{-3}
0
20
40
60
80
100
120
140
160
SCATTERING PHASE FUNCTION. - GAMMA
REF. INDEX = 1.340 + j 0.000
WAVELENGTH = 0.514 μm
LIMITS, X1, DX, X2, 0.73, 0.010, 2.57
A, B, ALPHA, GAMMA= 0.118E72, 7803.679, 57.600, 3.00

Figure 9.13(a)

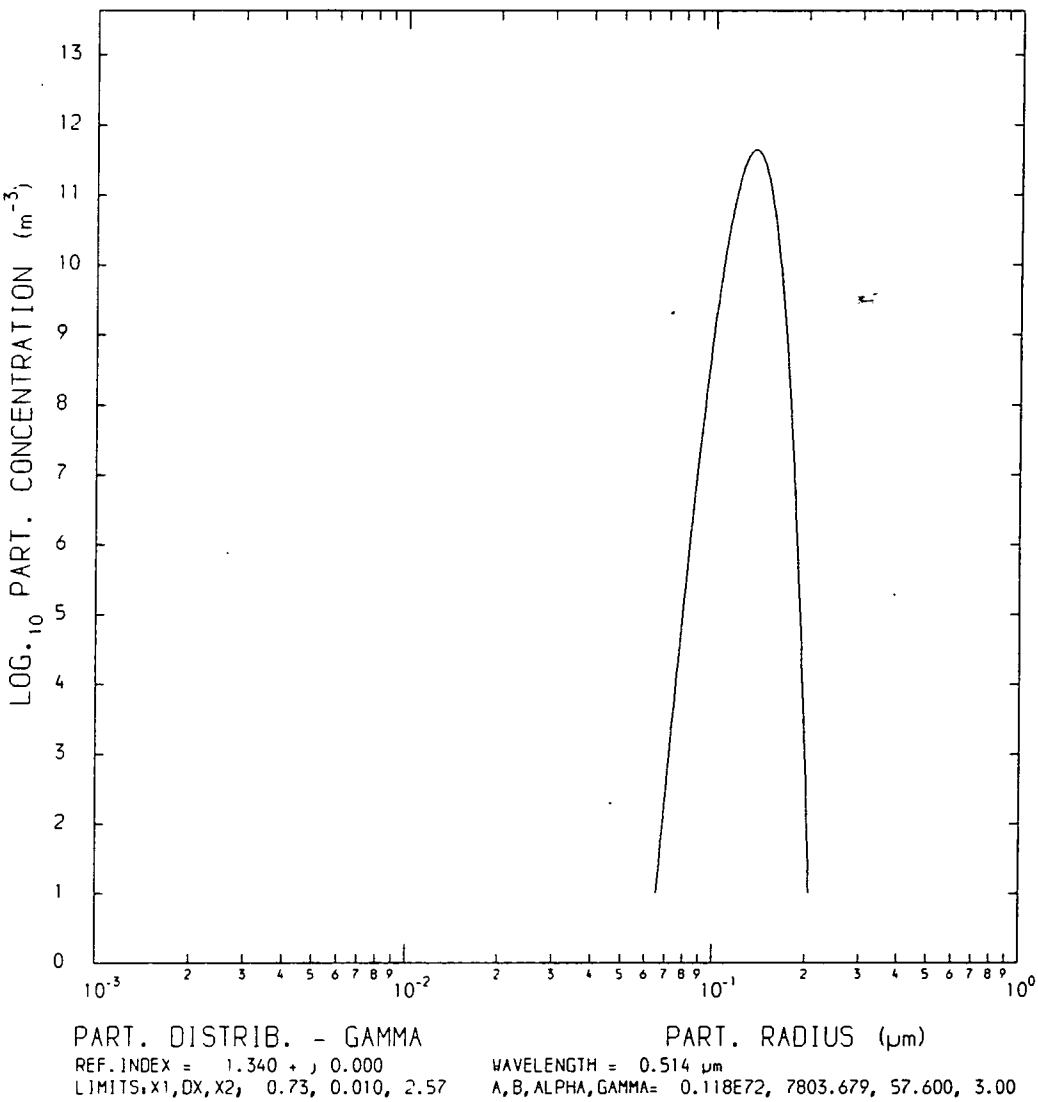
LOG.10 PART. CONCENTRATION (m-3)
0
1
2
3
4
5
6
7
8
9
10
11
12
13
10-3
10-2
10-1
100
PART. RADIUS (μm)
PART. DISTRIB. - GAMMA
REF. INDEX = 1.340 + j 0.000
LIMITS: X1, DX, X2, 0.73, 0.010, 2.57
WAVELENGTH = 0.514 μm
A, B, ALPHA, GAMMA= 0.118E72, 7803.679, 57.600, 3.00

Figure 9.13(b)

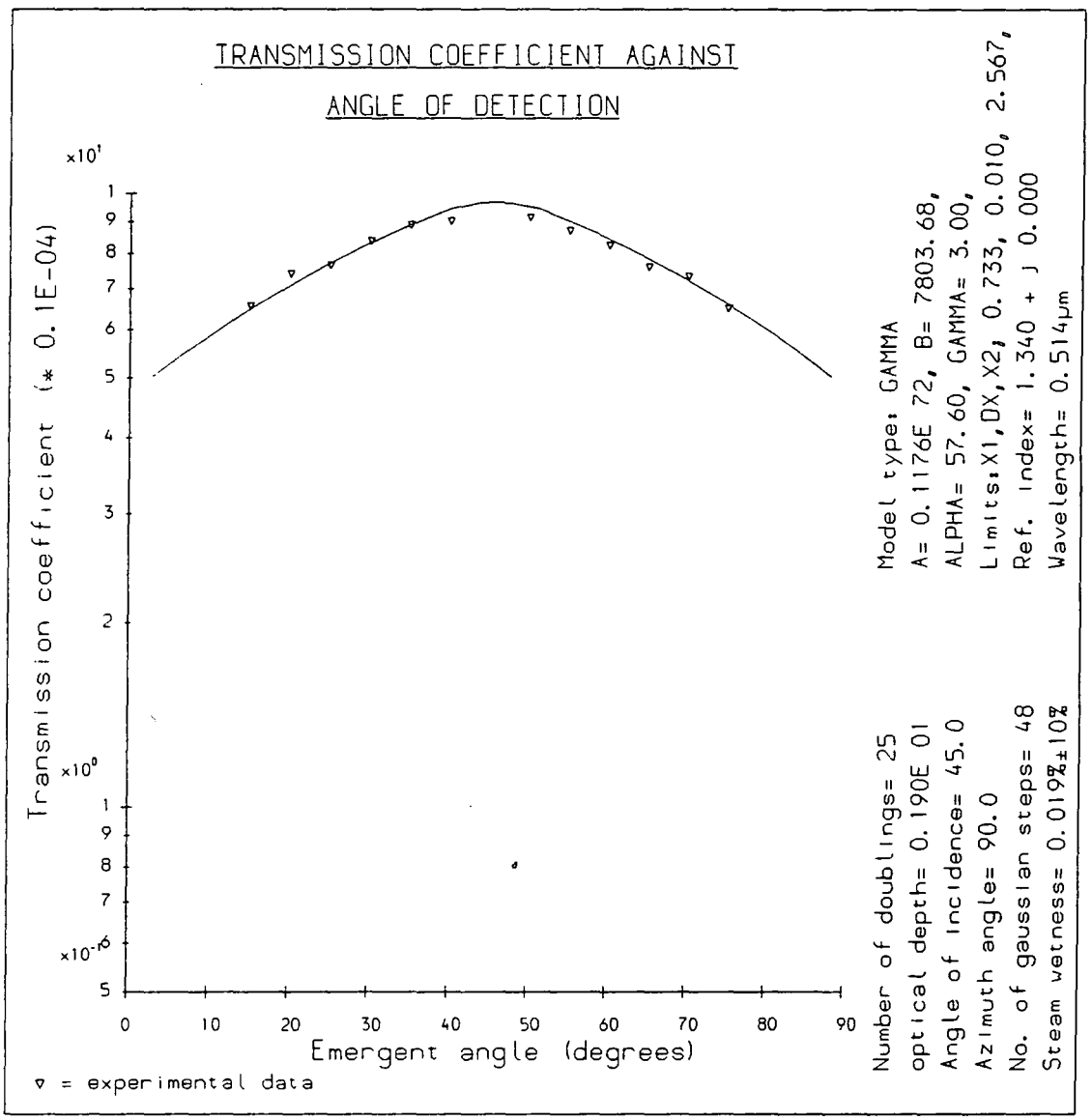
TRANSMISSION COEFFICIENT AGAINST
ANGLE OF DETECTION
Transmission coefficient (* 0.1E-04)
x10¹
x10⁰
x10⁻¹
1
9
8
7
6
5
4
3
2
0
10
20
30
40
50
60
70
80
90
Emergent angle (degrees)
▽ = experimental data
Model type: GAMMA
A= 0.1176E 72, B= 7803.68,
ALPHA= 57.60, GAMMA= 3.00,
Limits:X1,DX,X2; 0.733, 0.010, 2.567,
Ref. index= 1.340 + j 0.000
Wavelength= 0.514μm
Number of doublings= 25
optical depth= 0.190E 01
Angle of incidence= 45.0
Azimuth angle= 90.0
No. of gaussian steps= 48
Steam wetness= 0.019%±10%

Figure 9.13(c)

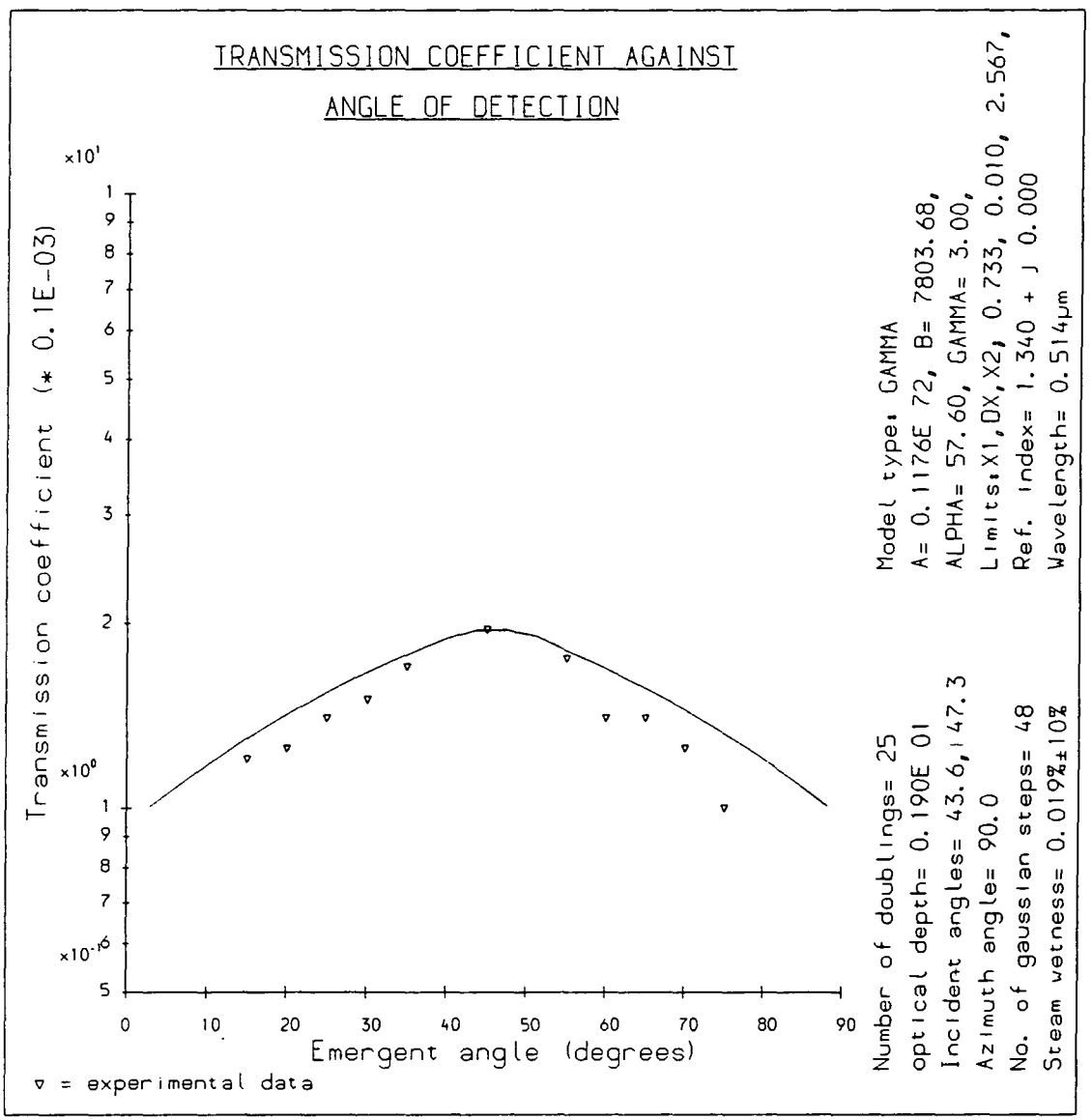
TRANSMISSION COEFFICIENT AGAINST
ANGLE OF DETECTION
Transmission coefficient (* 0.1E-03)
Emergent angle (degrees)
▽ = experimental data
Model type: GAMMA
A= 0.1176E 72, B= 7803.68,
ALPHA= 57.60, GAMMA= 3.00,
Limits:X1,DX,X2; 0.733, 0.010, 2.567,
Ref. index= 1.340 + i 0.000
Wavelength= 0.514μm
Number of doublings= 25
optical depth= 0.190E 01
Incident angles= 43.6,147.3
Azimuth angle= 90.0
No. of gaussian steps= 48
Steam wetness= 0.019%±10%

Figure 9.13(d)

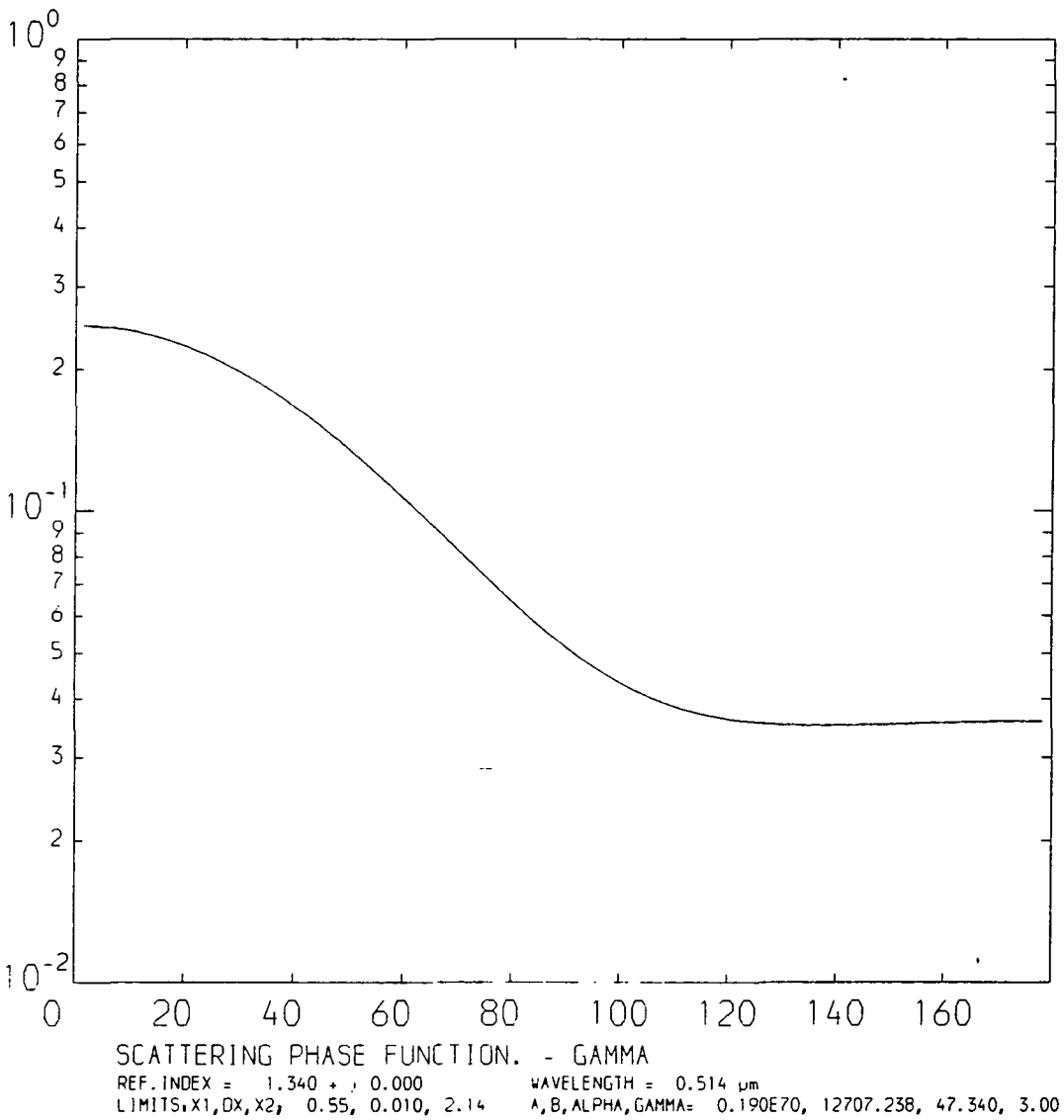
10^0
9
8
7
6
5
4
3
2
10^{-1}
9
8
7
6
5
4
3
2
10^{-2}
0
20
40
60
80
100
120
140
160
SCATTERING PHASE FUNCTION. - GAMMA
REF. INDEX = 1.340 + i 0.000
WAVELENGTH = 0.514 μm
LIMITS, X1, DX, X2, 0.55, 0.010, 2.14
A, B, ALPHA, GAMMA= 0.190E70, 12707.238, 47.340, 3.00

Figure 9.14(a)

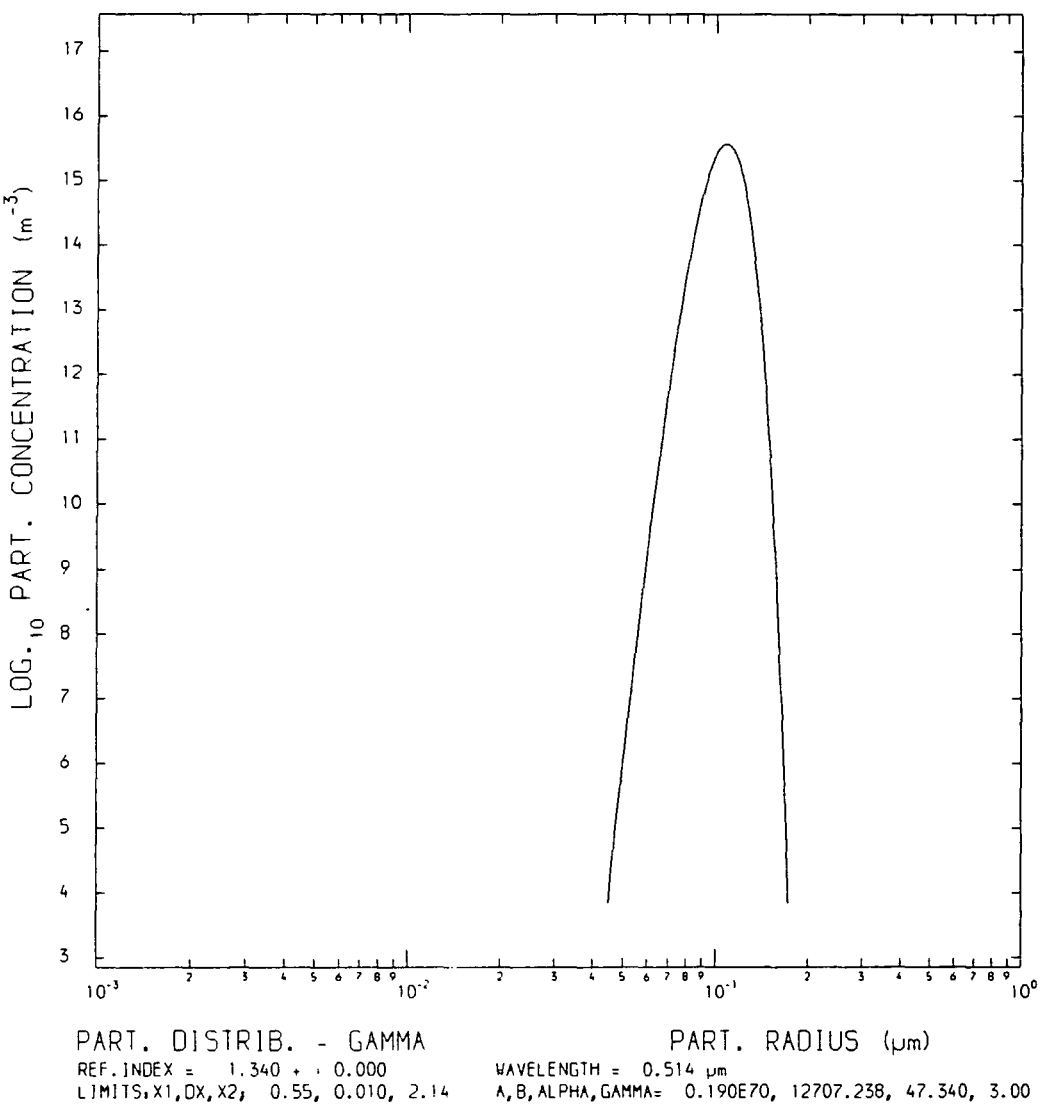
LOG.10 PART. CONCENTRATION (m-3)
17
16
15
14
13
12
11
10
9
8
7
6
5
4
3
10-3
10-2
10-1
100
PART. DISTRIB. - GAMMA
PART. RADIUS (μm)
REF. INDEX = 1.340 + i 0.000
LIMITS, X1, DX, X2; 0.55, 0.010, 2.14
WAVELENGTH = 0.514 μm
A, B, ALPHA, GAMMA= 0.190E70, 12707.238, 47.340, 3.00

Figure 9.14(b)

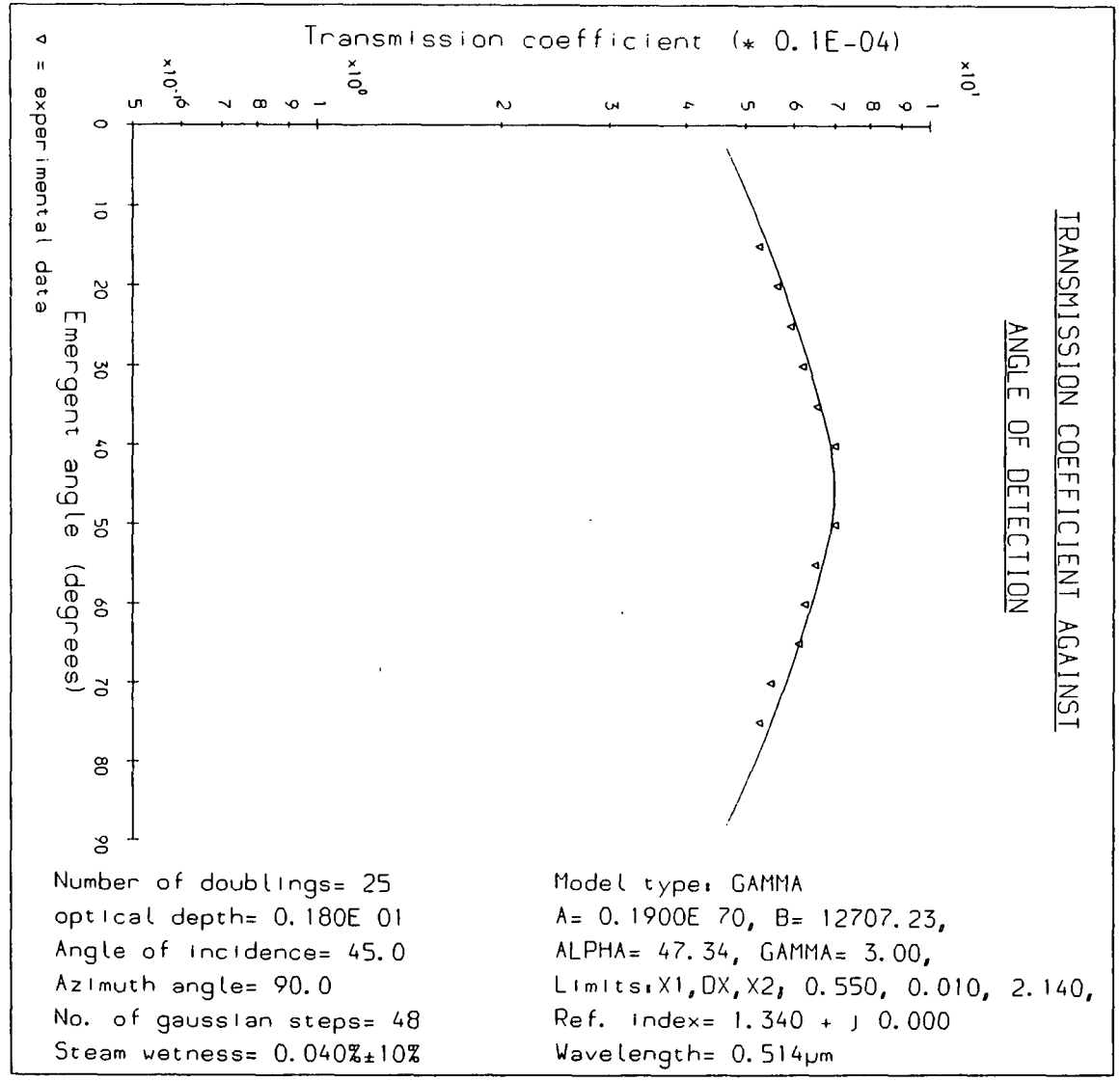
TRANSMISSION COEFFICIENT AGAINST
ANGLE OF DETECTION
Transmission coefficient (* 0.1E-04)
Emergent angle (degrees)
▽ = experimental data
Number of doublings= 25
optical depth= 0.180E 01
Angle of incidence= 45.0
Azimuth angle= 90.0
No. of gaussian steps= 48
Steam wetness= 0.040%±10%
Model type: GAMMA
A= 0.1900E 70, B= 12707.23,
ALPHA= 47.34, GAMMA= 3.00,
Limits:X1,DX,X2; 0.550, 0.010, 2.140,
Ref. index= 1.340 + j 0.000
Wavelength= 0.514μm

Figure 9.14(c)

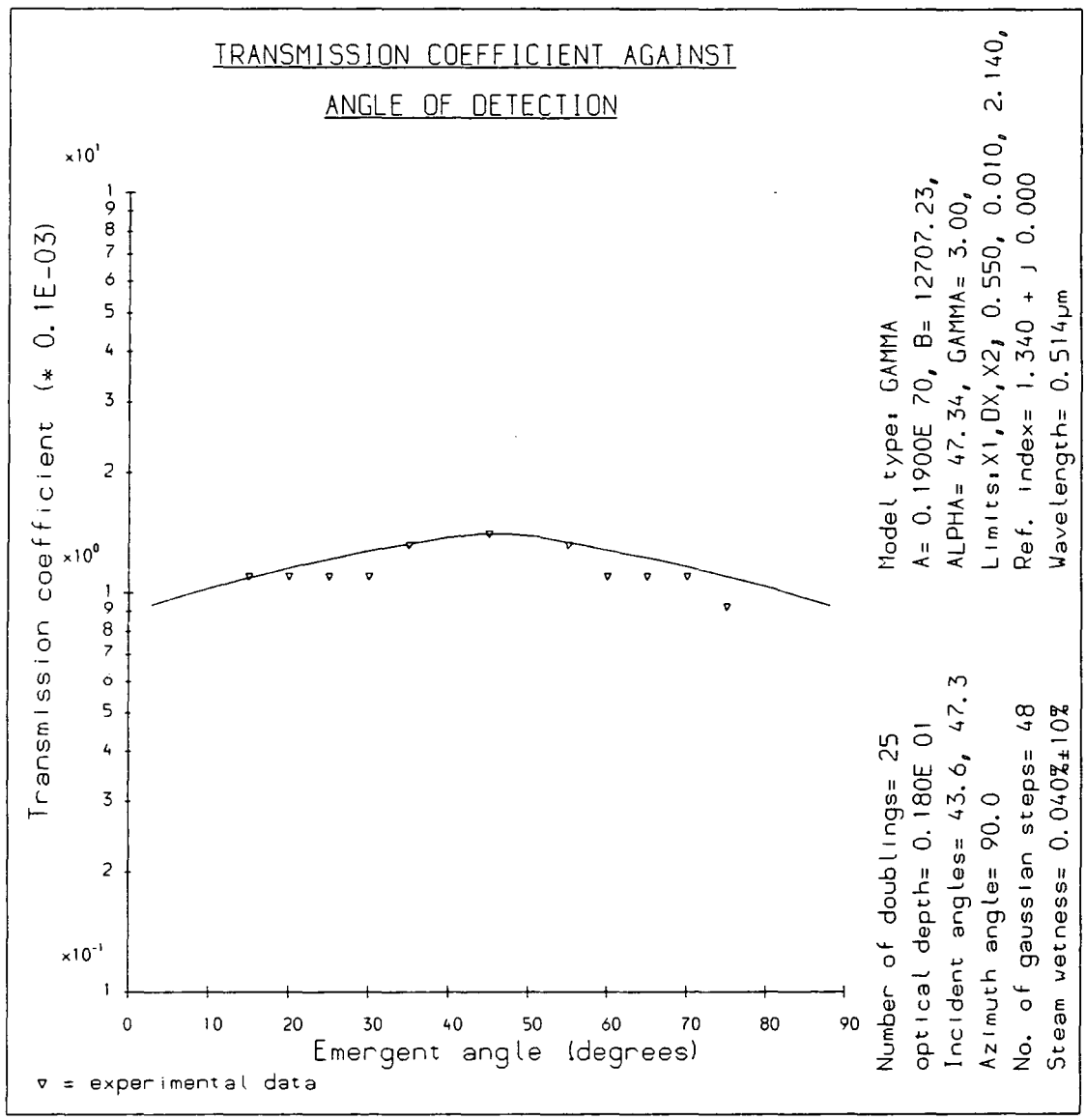
TRANSMISSION COEFFICIENT AGAINST
ANGLE OF DETECTION
Transmission coefficient (* 0.1E-03)
Emergent angle (degrees)
▽ = experimental data
Model type: GAMMA
A= 0.1900E 70, B= 12707.23,
ALPHA= 47.34, GAMMA= 3.00,
Limits:X1,DX,X2, 0.550, 0.010, 2.140,
Ref. index= 1.340 + i 0.000
Wavelength= 0.514μm
Number of doublings= 25
optical depth= 0.180E 01
Incident angles= 43.6, 47.3
Azimuth angle= 90.0
No. of gaussian steps= 48
Steam wetness= 0.040%±10%

Figure 9.14(d)

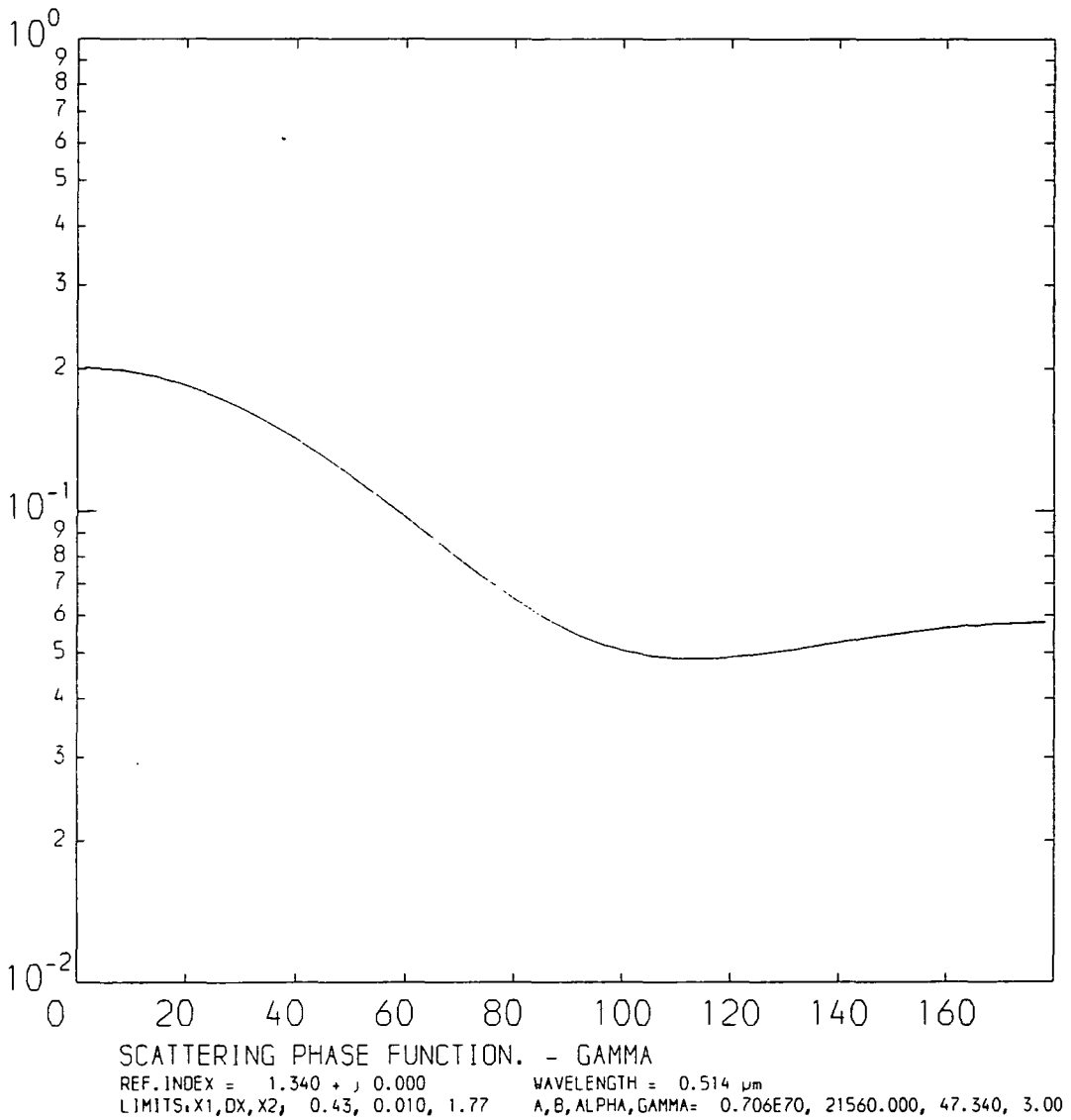
10^0
9
8
7
6
5
4
3
2
10^{-1}
9
8
7
6
5
4
3
2
10^{-2}
0
20
40
60
80
100
120
140
160
SCATTERING PHASE FUNCTION. - GAMMA
REF. INDEX = 1.340 + j 0.000
WAVELENGTH = 0.514 μm
LIMITS.X1,DX,X2, 0.43, 0.010, 1.77
A,B,ALPHA,GAMMA= 0.706E70, 21560.000, 47.340, 3.00

Figure 9.15(a)

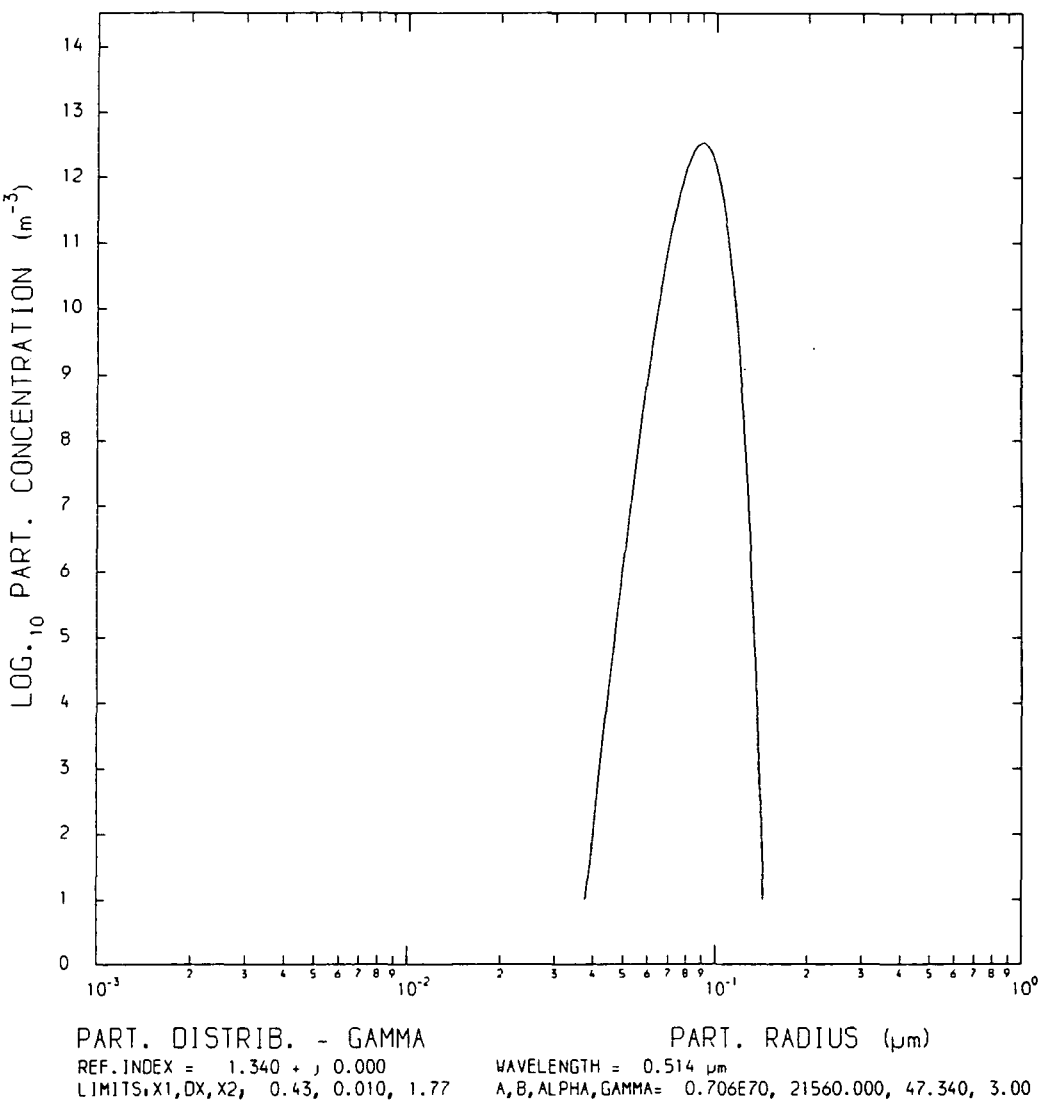
LOG.10 PART. CONCENTRATION (m-3)
14
13
12
11
10
9
8
7
6
5
4
3
2
1
0
10-3
10-2
10-1
100
PART. DISTRIB. - GAMMA
PART. RADIUS (μm)
REF. INDEX = 1.340 + j 0.000
LIMITS, X1, DX, X2, 0.43, 0.010, 1.77
WAVELENGTH = 0.514 μm
A, B, ALPHA, GAMMA= 0.706E70, 21560.000, 47.340, 3.00

Figure 9.15(b)

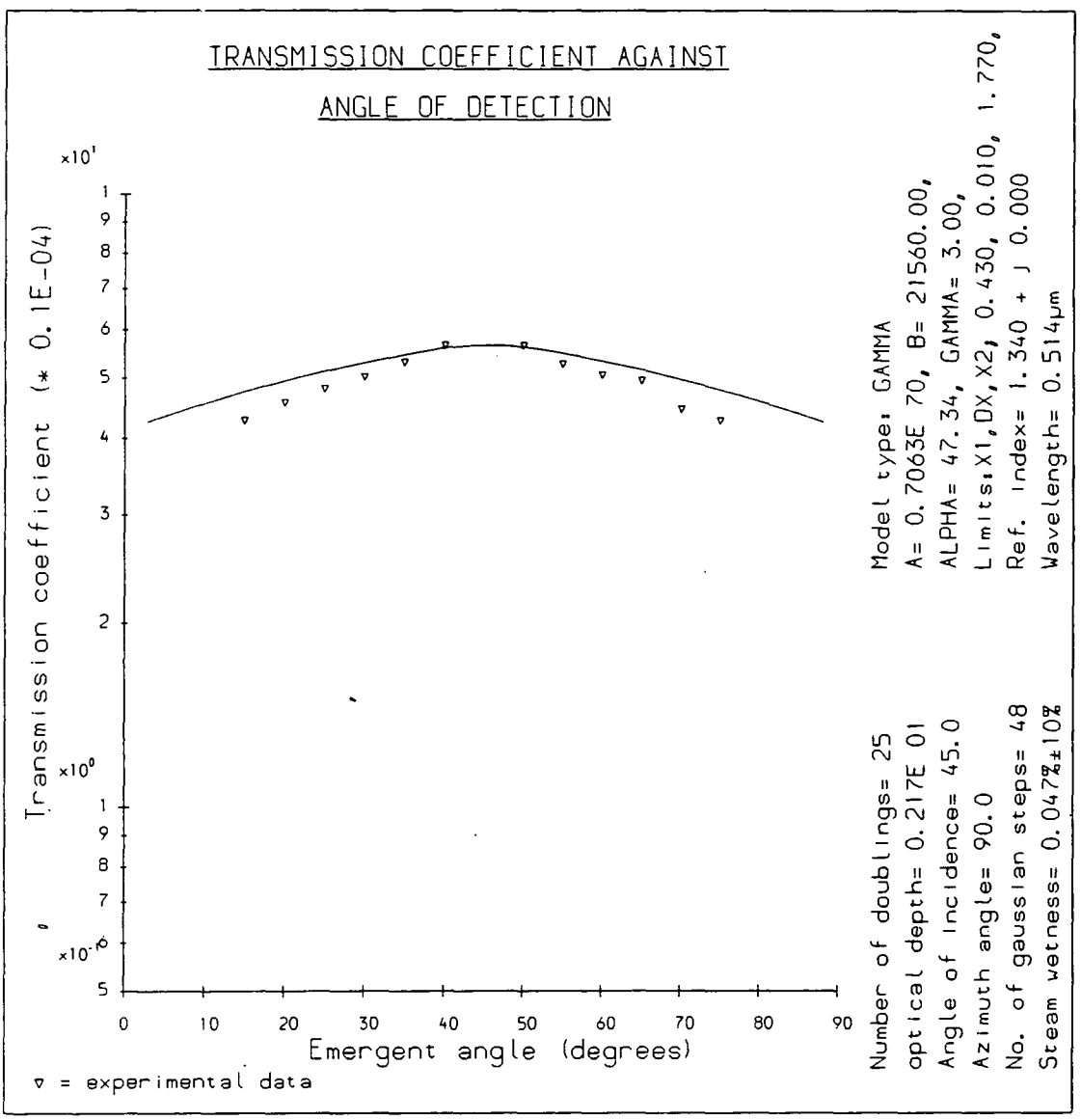
TRANSMISSION COEFFICIENT AGAINST
ANGLE OF DETECTION
Transmission coefficient (* 0.1E-04)
Emergent angle (degrees)
▽ = experimental data
Model type: GAMMA
A= 0.7063E 70, B= 21560.00,
ALPHA= 47.34, GAMMA= 3.00,
Limits:X1,DX,X2; 0.430, 0.010, 1.770,
Ref. index= 1.340 + i 0.000
Wavelength= 0.514μm
Number of doublings= 25
optical depth= 0.217E 01
Angle of incidence= 45.0
Azimuth angle= 90.0
No. of gaussian steps= 48
Steam wetness= 0.047%±10%

Figure 9.15(c)

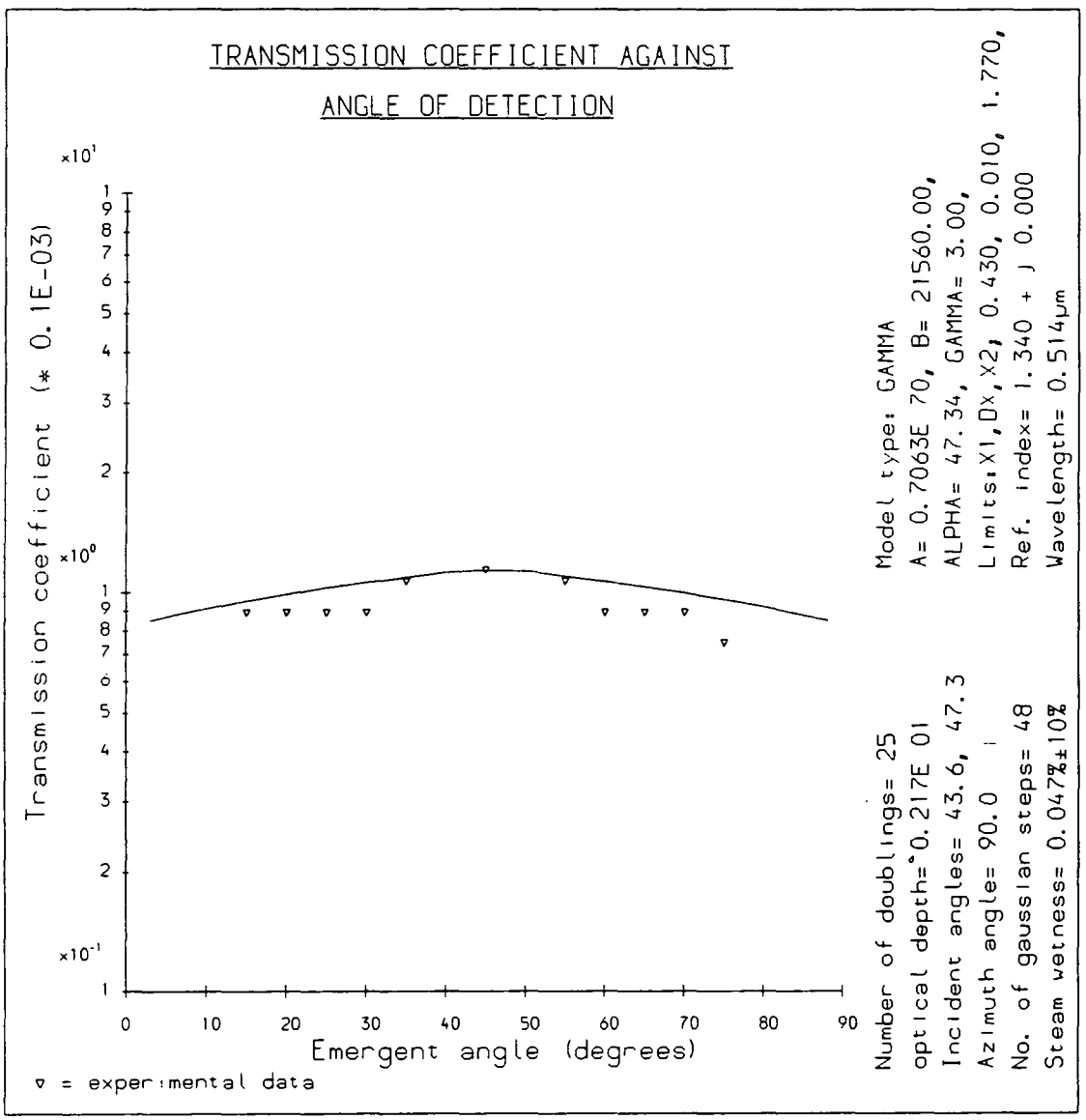
TRANSMISSION COEFFICIENT AGAINST
ANGLE OF DETECTION
Transmission coefficient (* 0.1E-03)
Emergent angle (degrees)
▽ = experimental data
Model type: GAMMA
A= 0.7063E 70, B= 21560.00,
ALPHA= 47.34, GAMMA= 3.00,
Limits:X1,DX,X2; 0.430, 0.010, 1.770,
Ref. index= 1.340 + j 0.000
Wavelength= 0.514μm
Number of doublings= 25
optical depth=°0.217E 01
Incident angles= 43.6, 47.3
Azimuth angle= 90.0
No. of gaussian steps= 48
Steam wetness= 0.047%±10%

Figure 9.15(d)

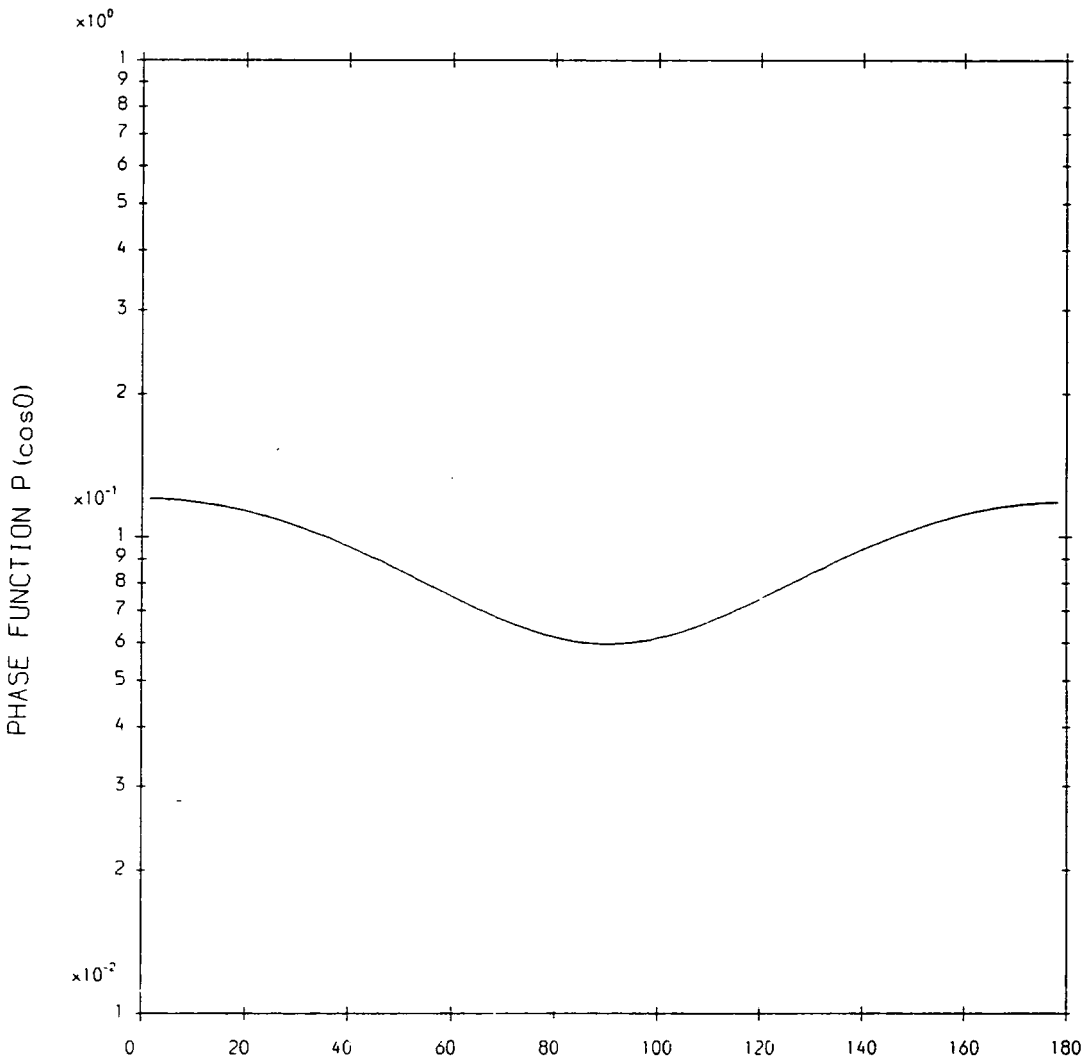

SCATTERING PHASE FUNCTION. - GAMMA

REF. INDEX = 1.340 + j 0.000 WAVELENGTH = 0.514 μm

LIMITS, X1, DX, X2, 0.11, 0.001, 0.15 A, B, ALPHA, GAMMA= 0.373E 60, 311.310, 6.960, 3.00

Figure 9.16

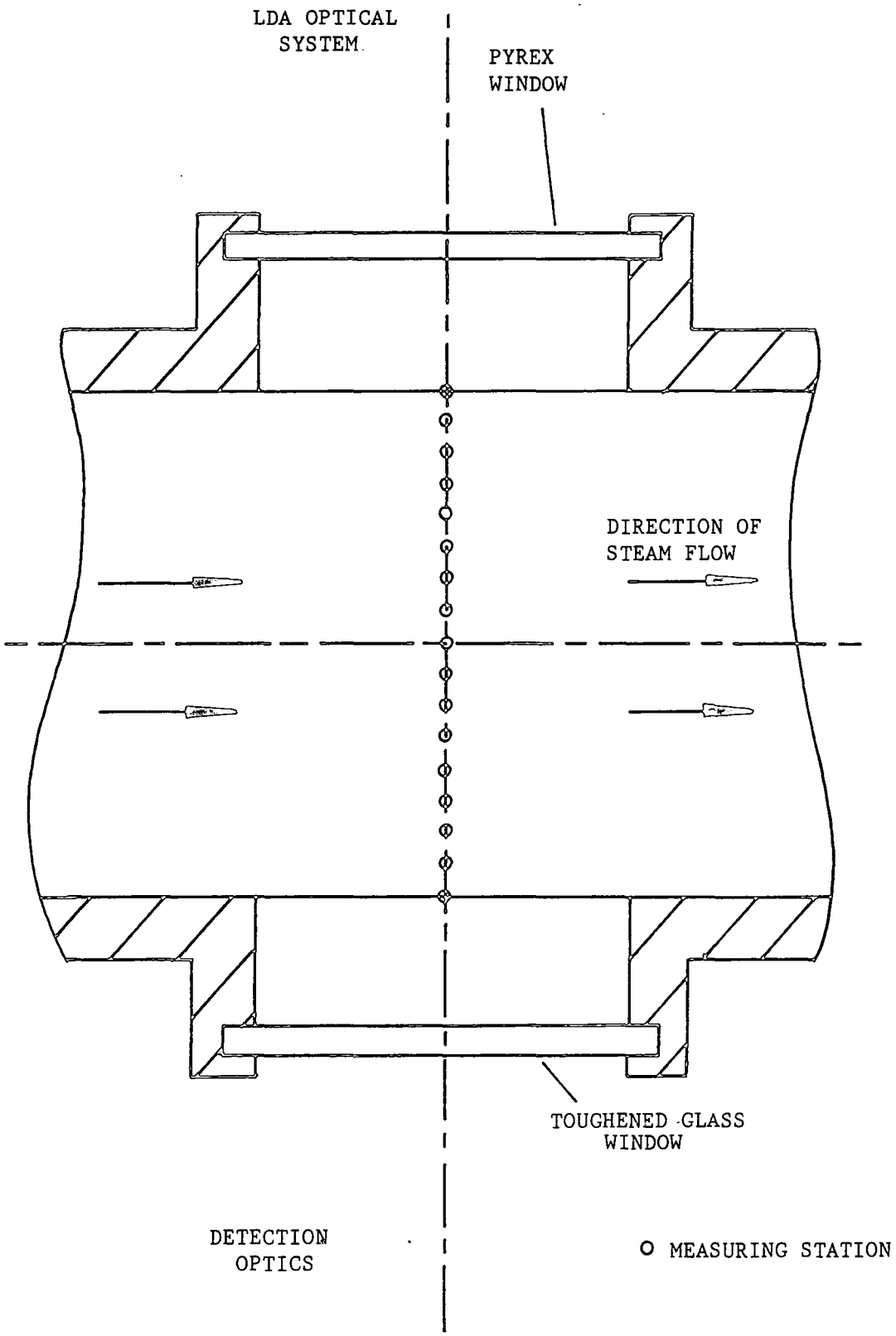

Figure 9.17 LOCATION OF VELOCITY MEASURING STATIONS IN THE RIG

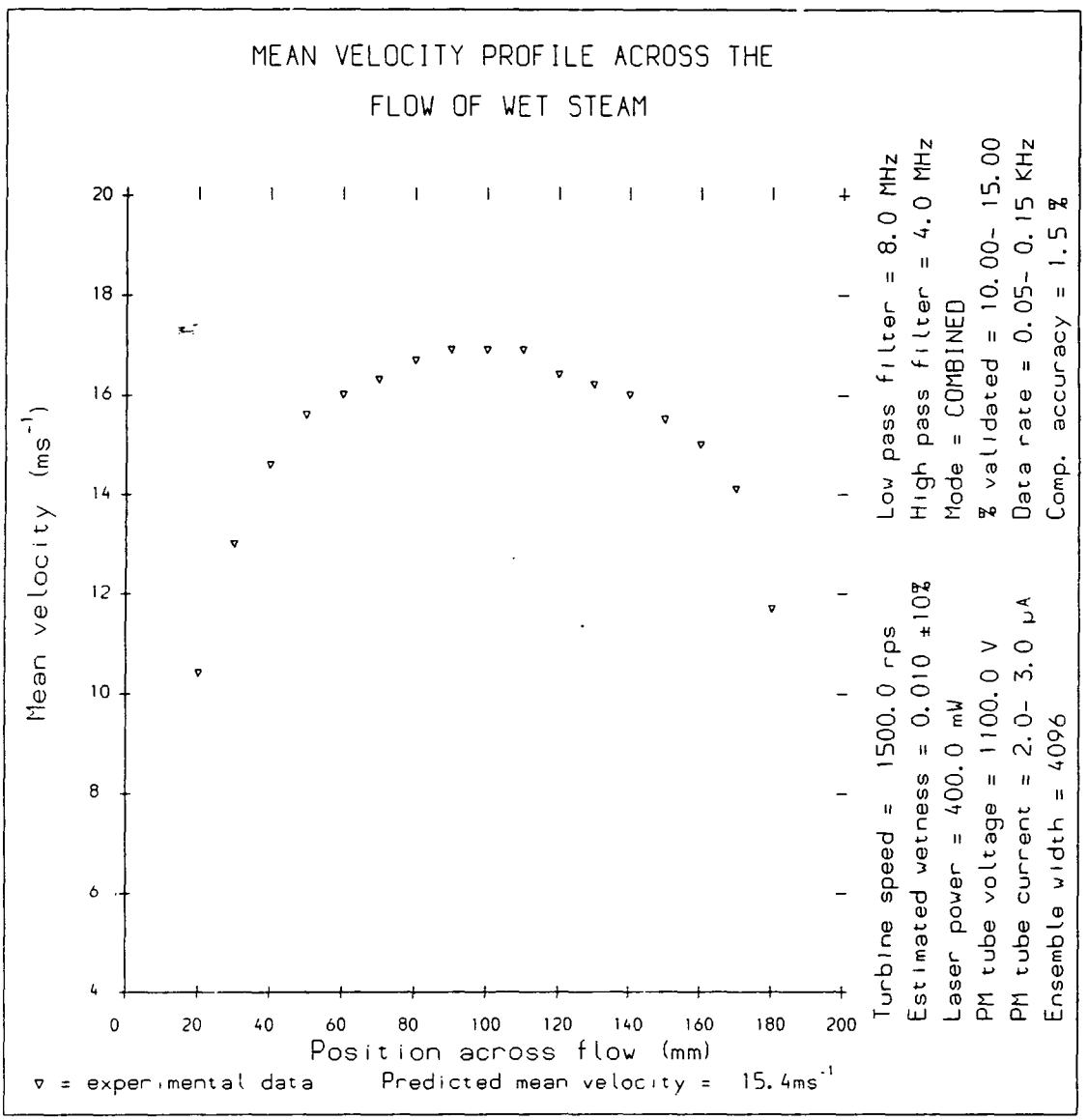
MEAN VELOCITY PROFILE ACROSS THE
FLOW OF WET STEAM
Mean velocity (ms-1)
20
18
16
14
12
10
8
6
4
0
20
40
60
80
100
120
140
160
180
200
Position across flow (mm)
▽ = experimental data
Predicted mean velocity = 15.4ms-1
Turbine speed = 1500.0 rps
Estimated wetness = 0.010 ±10%
Laser power = 400.0 mW
PM tube voltage = 1100.0 V
PM tube current = 2.0- 3.0 μA
Ensemble width = 4096
Low pass filter = 8.0 MHz
High pass filter = 4.0 MHz
Mode = COMBINED
% validated = 10.00- 15.00
Data rate = 0.05- 0.15 KHz
Comp. accuracy = 1.5 %

Figure 9.18(a)

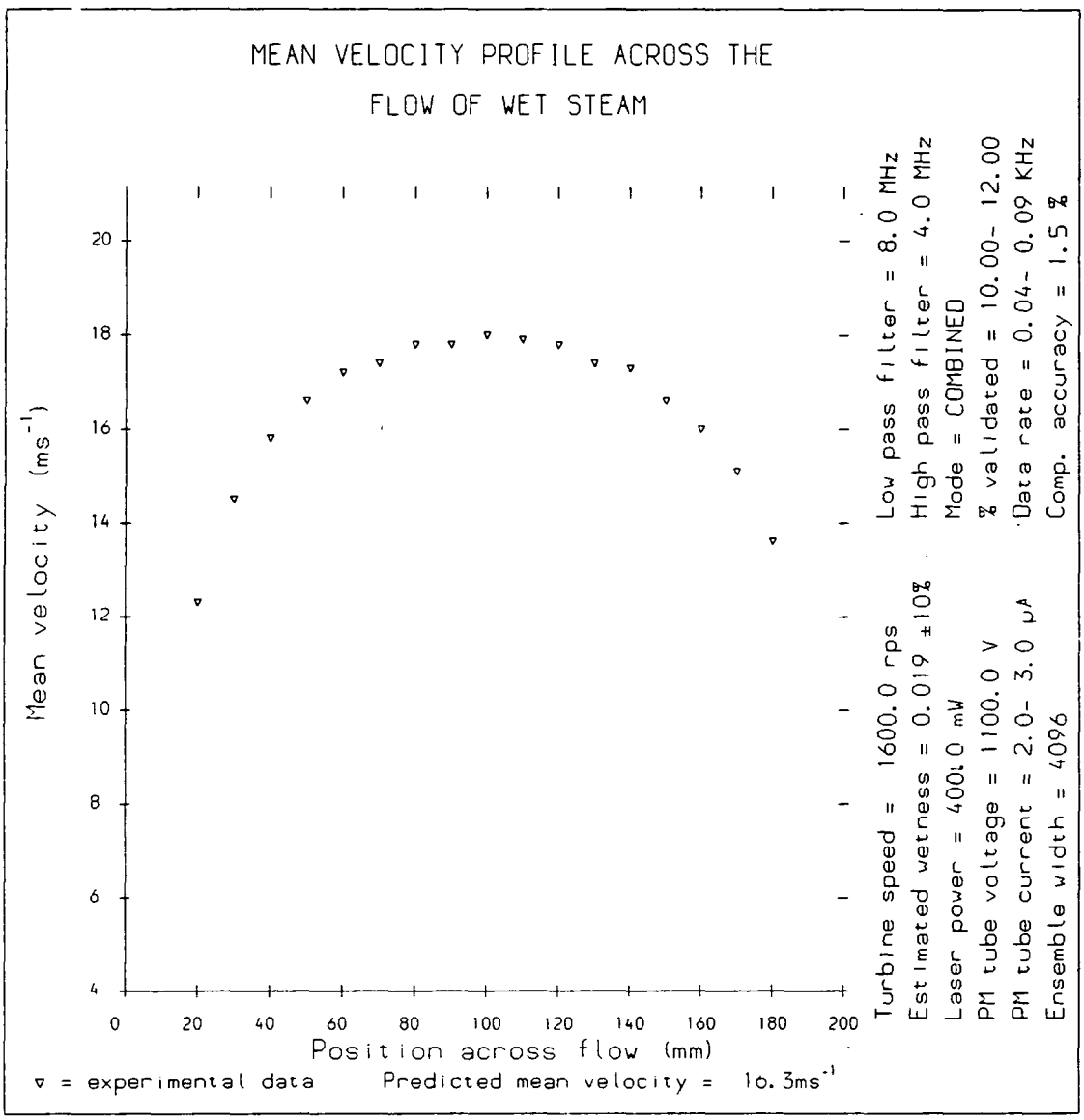
MEAN VELOCITY PROFILE ACROSS THE
FLOW OF WET STEAM
Mean velocity (ms-1)
20
18
16
14
12
10
8
6
4
0
20
40
60
80
100
120
140
160
180
200
Position across flow (mm)
▽ = experimental data
Predicted mean velocity = 16.3ms-1
Turbine speed = 1600.0 rps
Estimated wetness = 0.019 ±10%
Laser power = 400.0 mW
PM tube voltage = 1100.0 V
PM tube current = 2.0- 3.0 μA
Ensemble width = 4096
Low pass filter = 8.0 MHz
High pass filter = 4.0 MHz
Mode = COMBINED
% validated = 10.00- 12.00
Data rate = 0.04- 0.09 KHz
Comp. accuracy = 1.5 %

Figure 9.18(b)

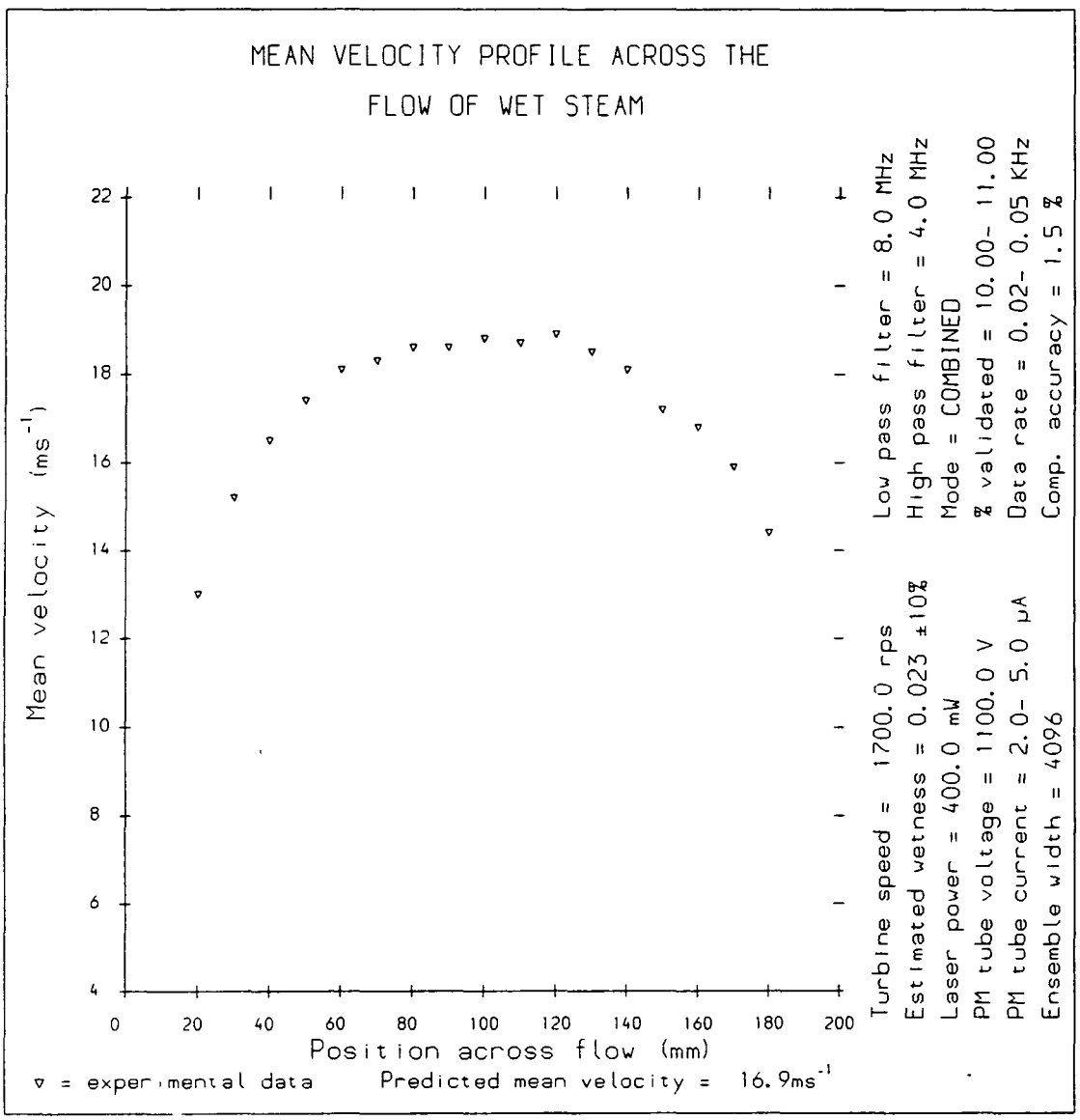
MEAN VELOCITY PROFILE ACROSS THE
FLOW OF WET STEAM
Mean velocity (ms-1)
22
20
18
16
14
12
10
8
6
4
0
20
40
60
80
100
120
140
160
180
200
Position across flow (mm)
▽ = experimental data
Predicted mean velocity = 16.9ms-1
Turbine speed = 1700.0 rps
Estimated wetness = 0.023 ±10%
Laser power = 400.0 mW
PM tube voltage = 1100.0 V
PM tube current = 2.0- 5.0 μA
Ensemble width = 4096
Low pass filter = 8.0 MHz
High pass filter = 4.0 MHz
Mode = COMBINED
% validated = 10.00- 11.00
Data rate = 0.02- 0.05 KHz
Comp. accuracy = 1.5 %

Figure 9.18(c)

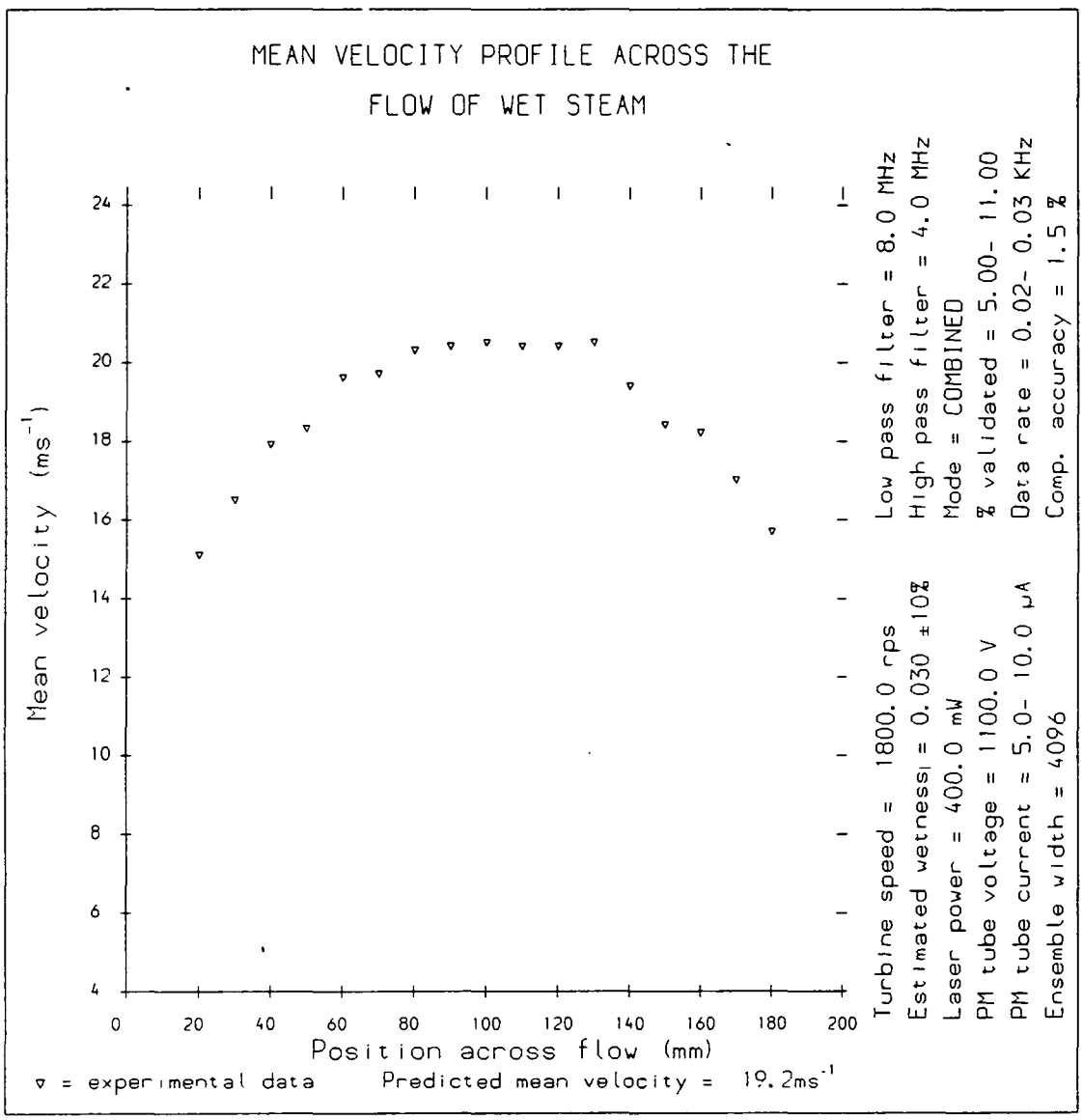
MEAN VELOCITY PROFILE ACROSS THE
FLOW OF WET STEAM
Mean velocity (ms-1)
24
22
20
18
16
14
12
10
8
6
4
0
20
40
60
80
100
120
140
160
180
200
Position across flow (mm)
▽ = experimental data
Predicted mean velocity = 19.2ms-1
Turbine speed = 1800.0 rps
Estimated wetness = 0.030 ±10%
Laser power = 400.0 mW
PM tube voltage = 1100.0 V
PM tube current = 5.0- 10.0 μA
Ensemble width = 4096
Low pass filter = 8.0 MHz
High pass filter = 4.0 MHz
Mode = COMBINED
% validated = 5.00- 11.00
Data rate = 0.02- 0.03 KHz
Comp. accuracy = 1.5 %

Figure 9.18(d)

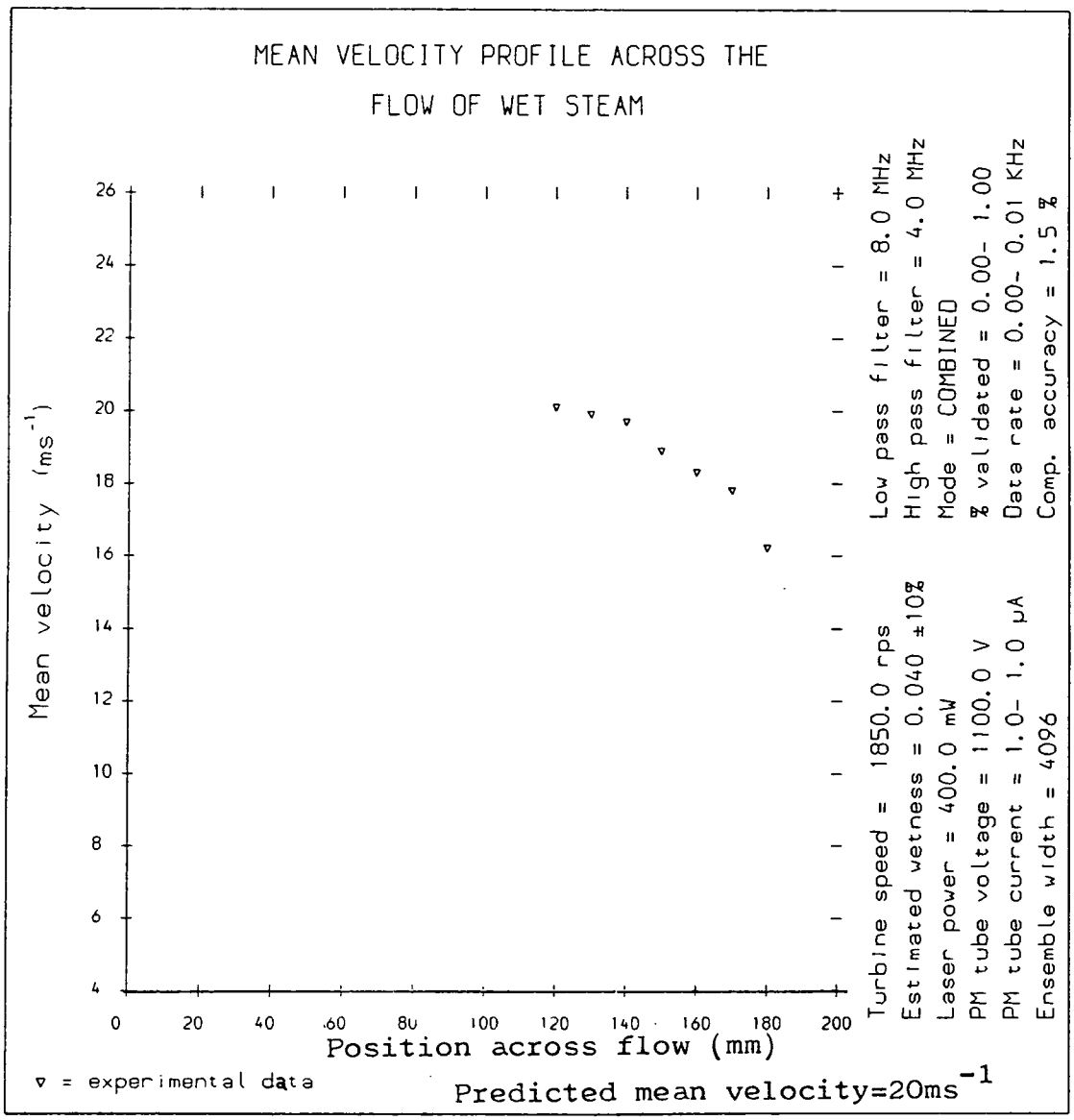
MEAN VELOCITY PROFILE ACROSS THE
FLOW OF WET STEAM
Mean velocity (ms-1)
26
24
22
20
18
16
14
12
10
8
6
4
0
20
40
60
80
100
120
140
160
180
200
Position across flow (mm)
▽ = experimental data
Predicted mean velocity=20ms-1
Turbine speed = 1850.0 rps
Estimated wetness = 0.040 ±10%
Laser power = 400.0 mW
PM tube voltage = 1100.0 V
PM tube current = 1.0- 1.0 μA
Ensemble width = 4096
Low pass filter = 8.0 MHz
High pass filter = 4.0 MHz
Mode = COMBINED
% validated = 0.00- 1.00
Data rate = 0.00- 0.01 KHz
Comp. accuracy = 1.5 %

Figure 9.18(e)

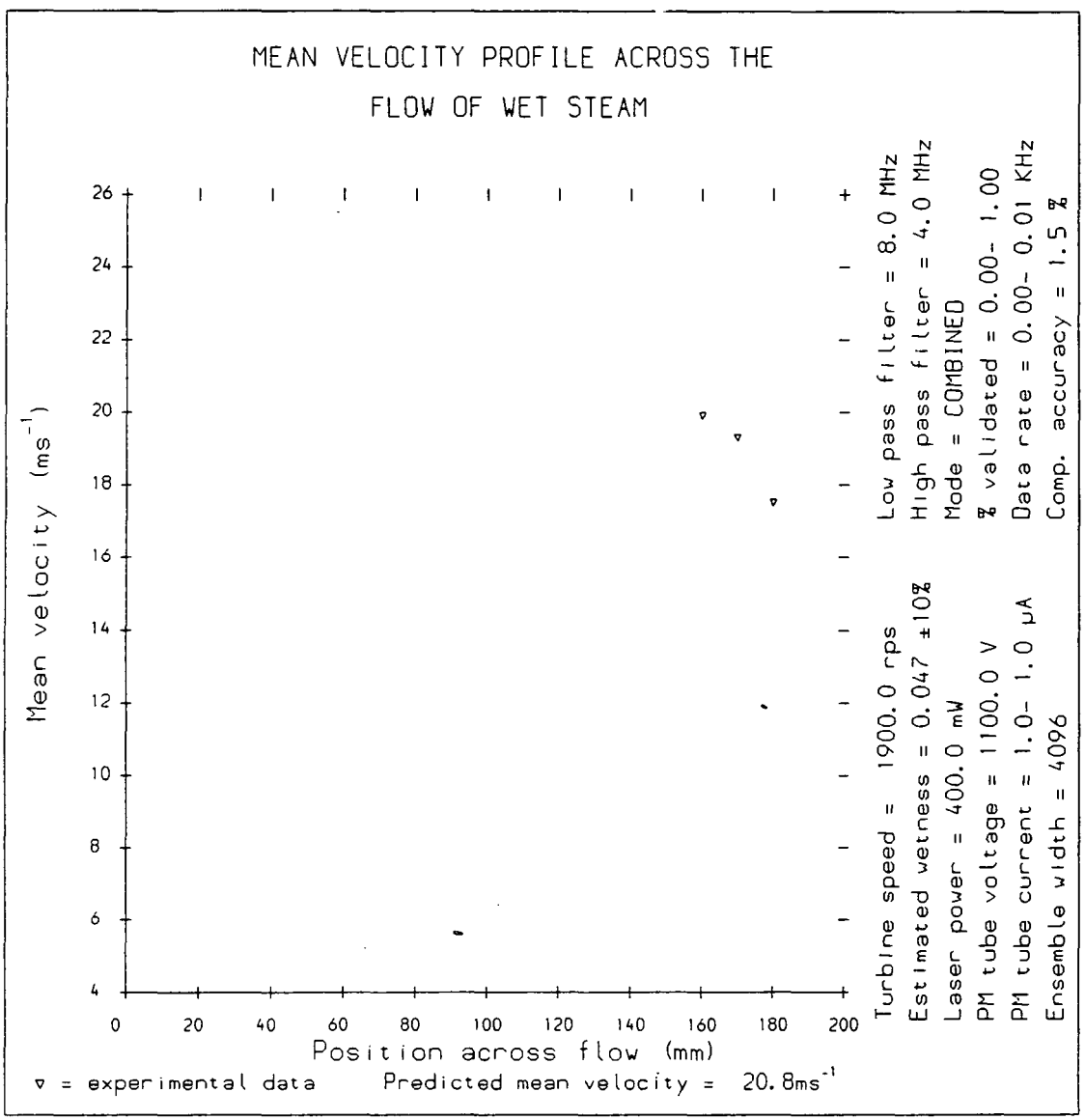
MEAN VELOCITY PROFILE ACROSS THE
FLOW OF WET STEAM
Mean velocity (ms^{-1})
26
24
22
20
18
16
14
12
10
8
6
4
0
20
40
60
80
100
120
140
160
180
200
Position across flow (mm)
▽ = experimental data
Predicted mean velocity = 20.8ms^{-1}
Turbine speed = 1900.0 rps
Estimated wetness = 0.047 ±10%
Laser power = 400.0 mW
PM tube voltage = 1100.0 V
PM tube current = 1.0- 1.0 μA
Ensemble width = 4096
Low pass filter = 8.0 MHz
High pass filter = 4.0 MHz
Mode = COMBINED
% validated = 0.00- 1.00
Data rate = 0.00- 0.01 KHz
Comp. accuracy = 1.5 %

Figure 9.18(f)

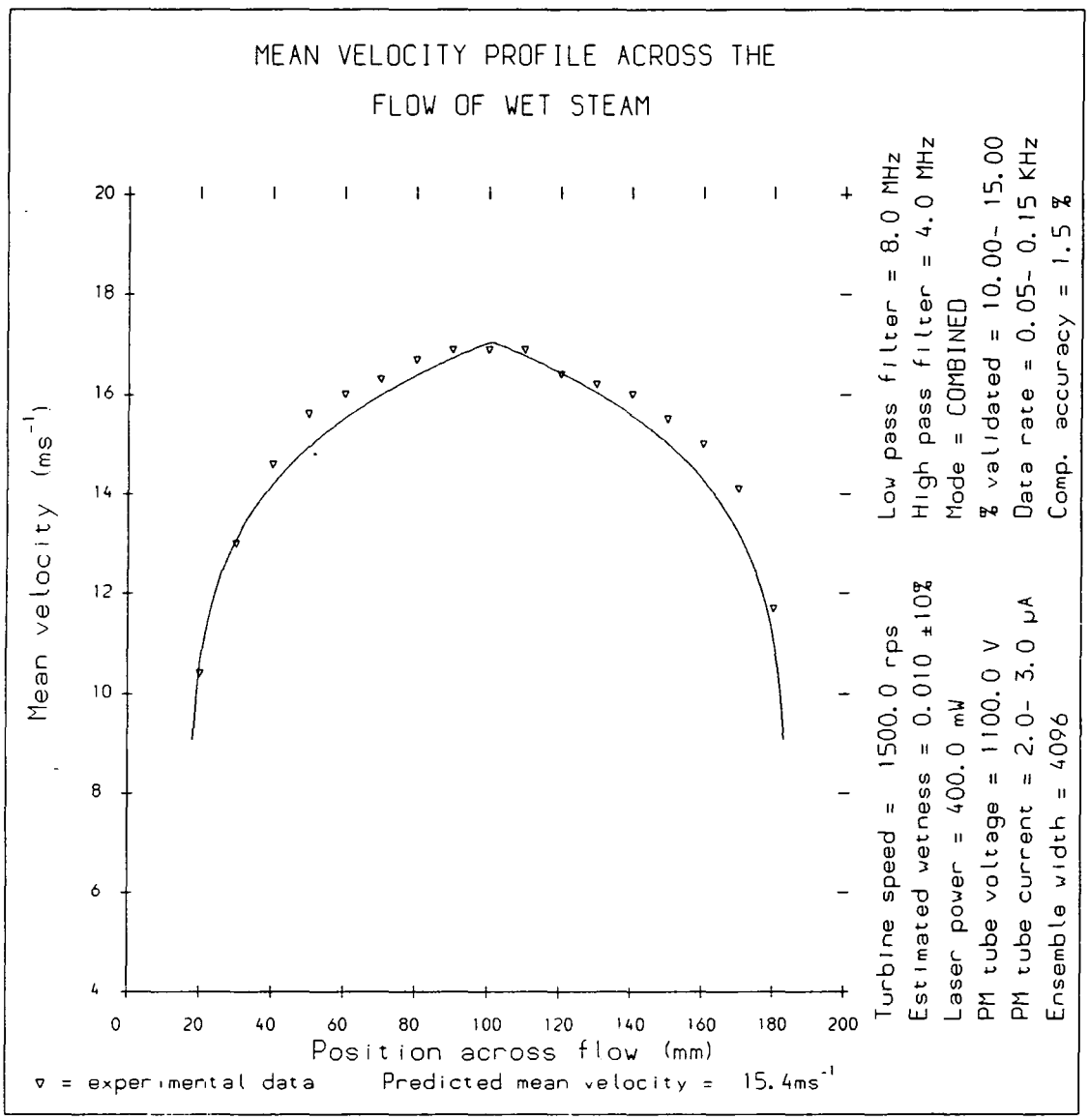
MEAN VELOCITY PROFILE ACROSS THE
FLOW OF WET STEAM
Mean velocity (ms-1)
20
18
16
14
12
10
8
6
4
0
20
40
60
80
100
120
140
160
180
200
Position across flow (mm)
▽ = experimental data
Predicted mean velocity = 15.4ms-1
Turbine speed = 1500.0 rps
Estimated wetness = 0.010 ±10%
Laser power = 400.0 mW
PM tube voltage = 1100.0 V
PM tube current = 2.0- 3.0 μA
Ensemble width = 4096
Low pass filter = 8.0 MHz
High pass filter = 4.0 MHz
Mode = COMBINED
% validated = 10.00- 15.00
Data rate = 0.05- 0.15 KHz
Comp. accuracy = 1.5 %

Figure 9.19(a)

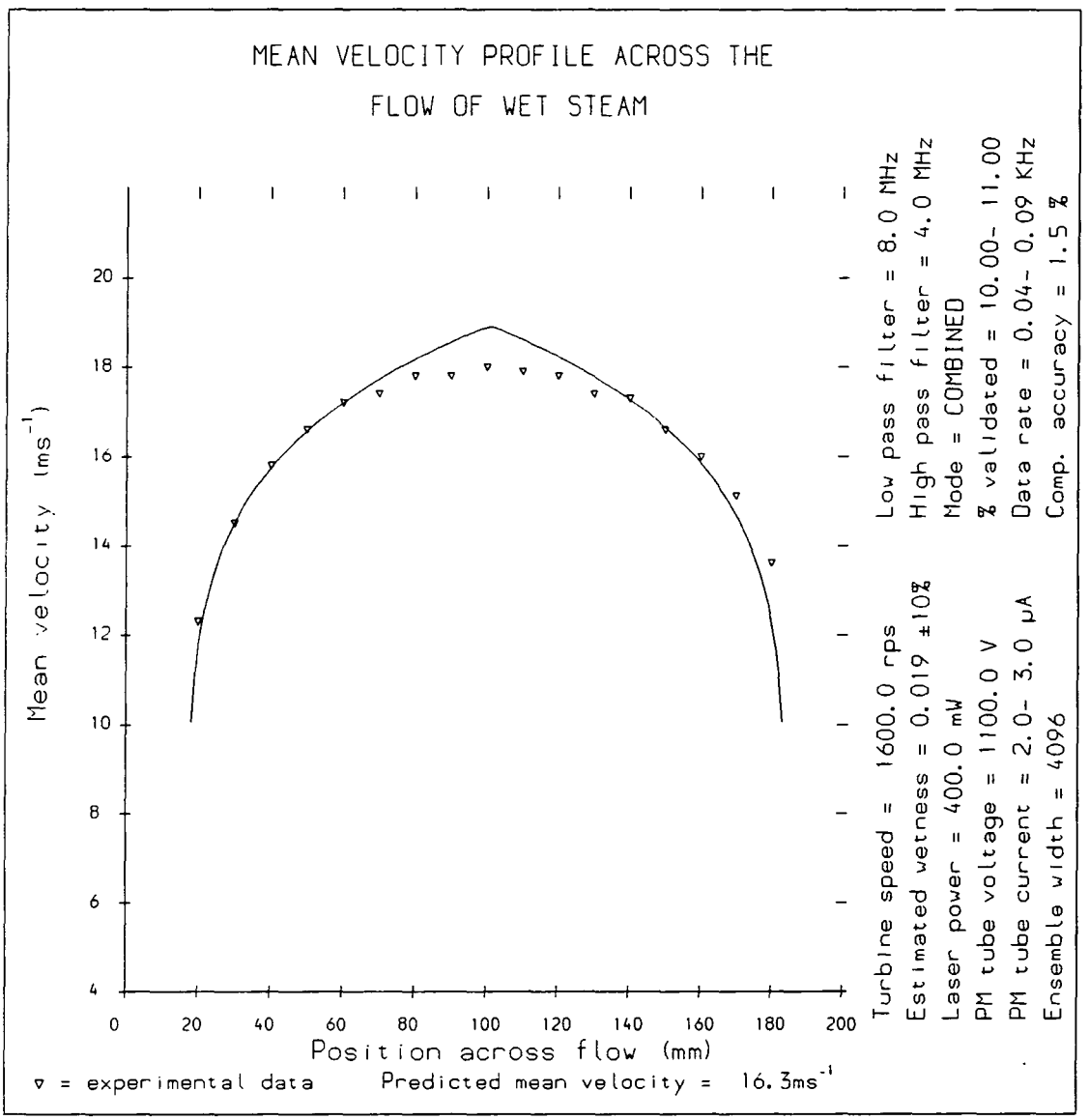
MEAN VELOCITY PROFILE ACROSS THE
FLOW OF WET STEAM
Mean velocity (ms^{-1})
20
18
16
14
12
10
8
6
4
0
20
40
60
80
100
120
140
160
180
200
Position across flow (mm)
▽ = experimental data
Predicted mean velocity = 16.3ms^{-1}
Turbine speed = 1600.0 rps
Estimated wetness = 0.019 ±10%
Laser power = 400.0 mW
PM tube voltage = 1100.0 V
PM tube current = 2.0- 3.0 μA
Ensemble width = 4096
Low pass filter = 8.0 MHz
High pass filter = 4.0 MHz
Mode = COMBINED
% validated = 10.00- 11.00
Data rate = 0.04- 0.09 KHz
Comp. accuracy = 1.5 %

Figure 9.19(b)

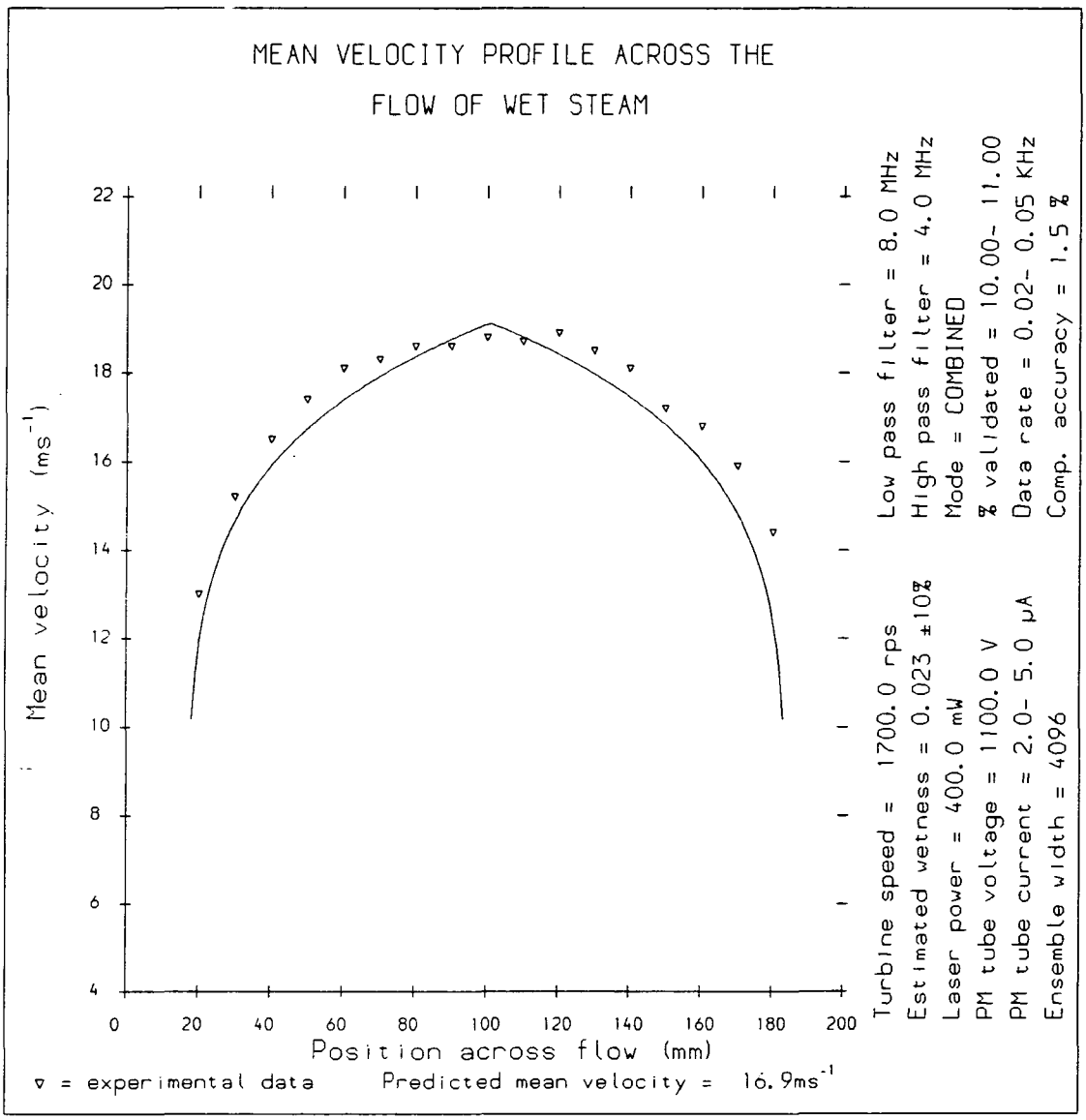
MEAN VELOCITY PROFILE ACROSS THE
FLOW OF WET STEAM
Mean velocity (ms⁻¹)
22
20
18
16
14
12
10
8
6
4
0
20
40
60
80
100
120
140
160
180
200
Position across flow (mm)
▽ = experimental data
Predicted mean velocity = 16.9ms⁻¹
Turbine speed = 1700.0 rps
Estimated wetness = 0.023 ±10%
Laser power = 400.0 mW
PM tube voltage = 1100.0 V
PM tube current = 2.0- 5.0 μA
Ensemble width = 4096
Low pass filter = 8.0 MHz
High pass filter = 4.0 MHz
Mode = COMBINED
% validated = 10.00- 11.00
Data rate = 0.02- 0.05 KHz
Comp. accuracy = 1.5 %

Figure 9.19(c)

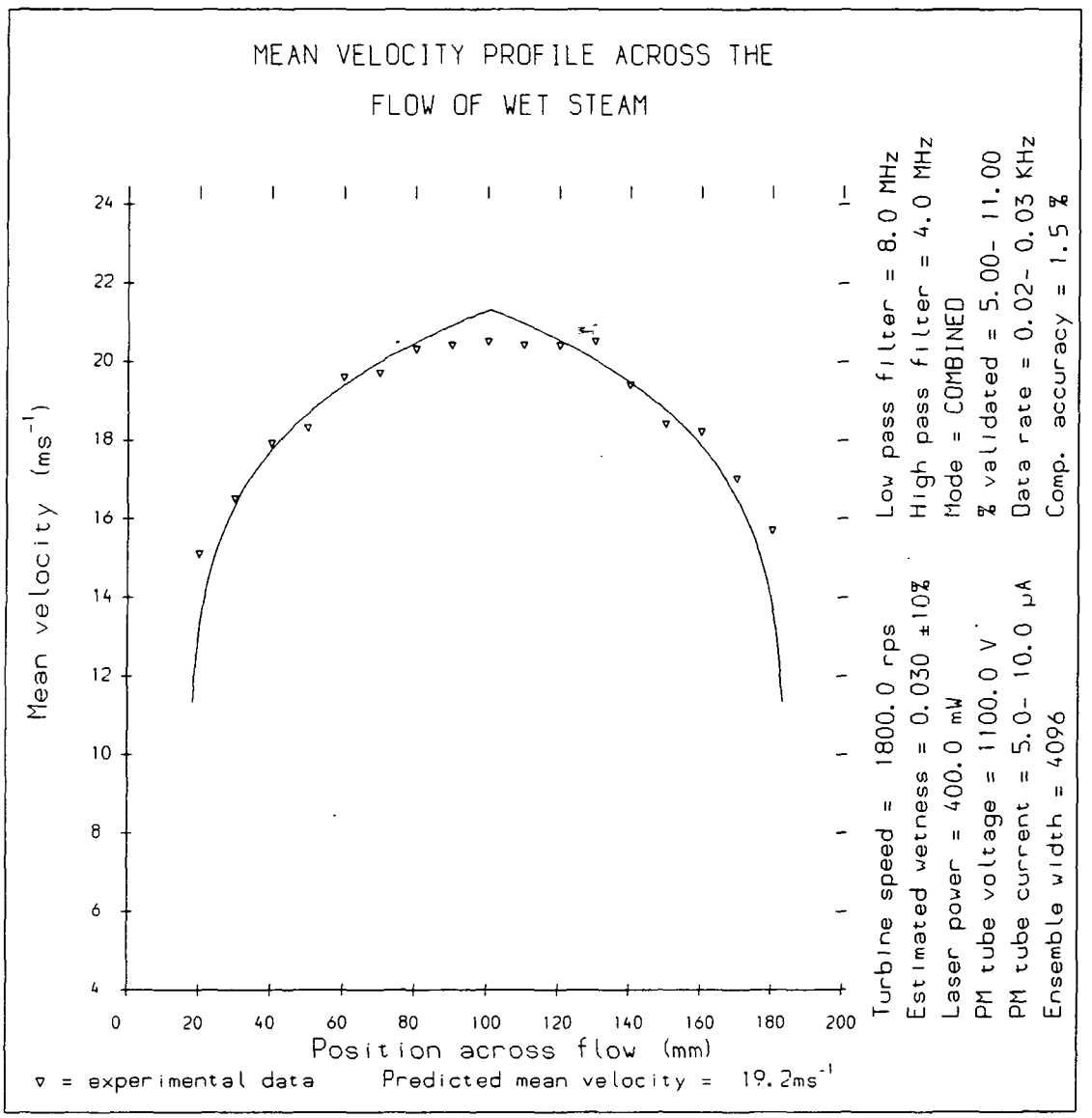
MEAN VELOCITY PROFILE ACROSS THE
FLOW OF WET STEAM
Mean velocity (ms^{-1})
24
22
20
18
16
14
12
10
8
6
4
0
20
40
60
80
100
120
140
160
180
200
Position across flow (mm)
▽ = experimental data
Predicted mean velocity = 19.2ms^{-1}
Turbine speed = 1800.0 rps
Estimated wetness = 0.030 ±10%
Laser power = 400.0 mW
PM tube voltage = 1100.0 V
PM tube current = 5.0- 10.0 μA
Ensemble width = 4096
Low pass filter = 8.0 MHz
High pass filter = 4.0 MHz
Mode = COMBINED
% validated = 5.00- 11.00
Data rate = 0.02- 0.03 KHz
Comp. accuracy = 1.5 %

Figure 9.19(d)

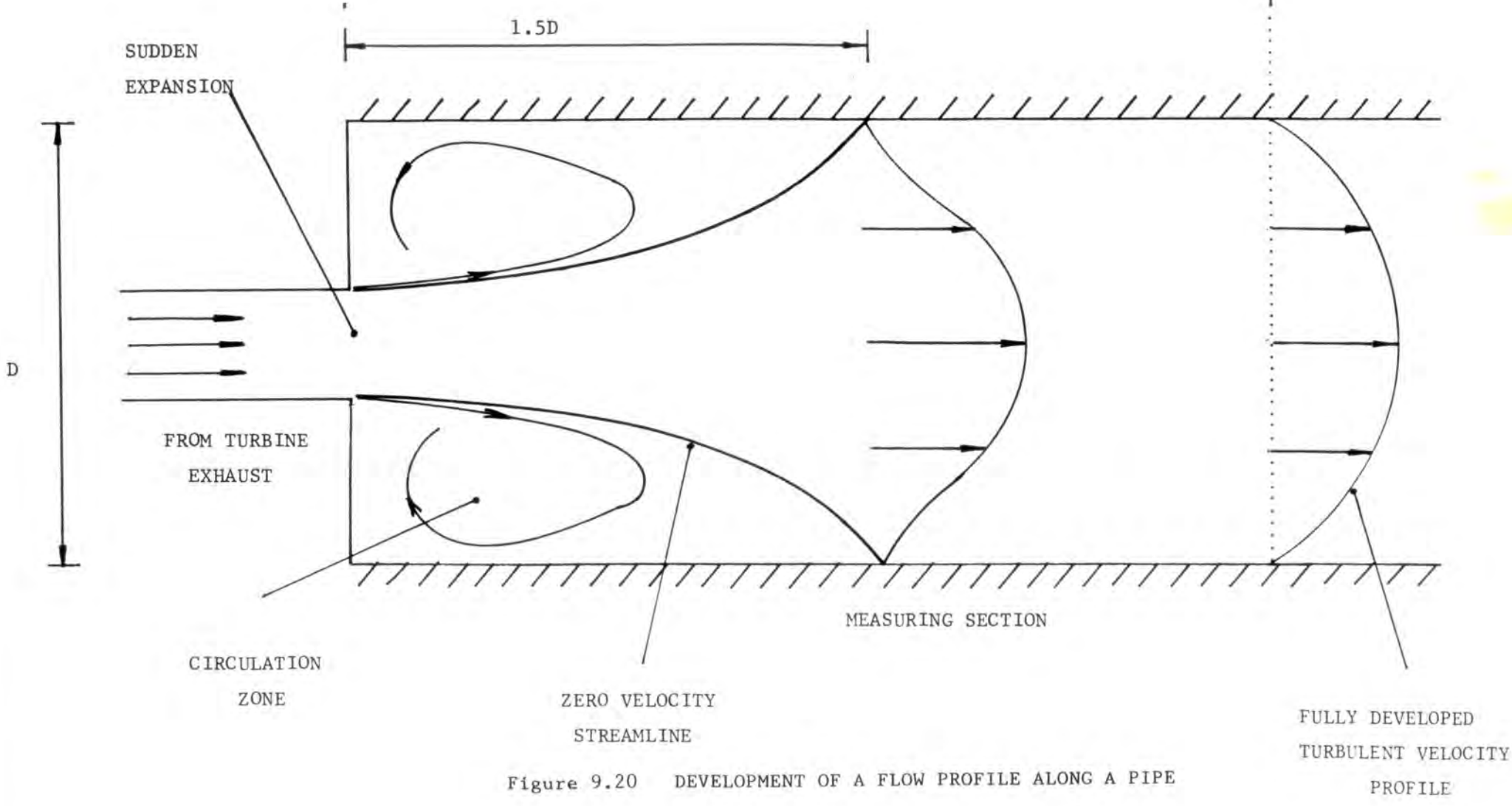

Figure 9.20 DEVELOPMENT OF A FLOW PROFILE ALONG A PIPE

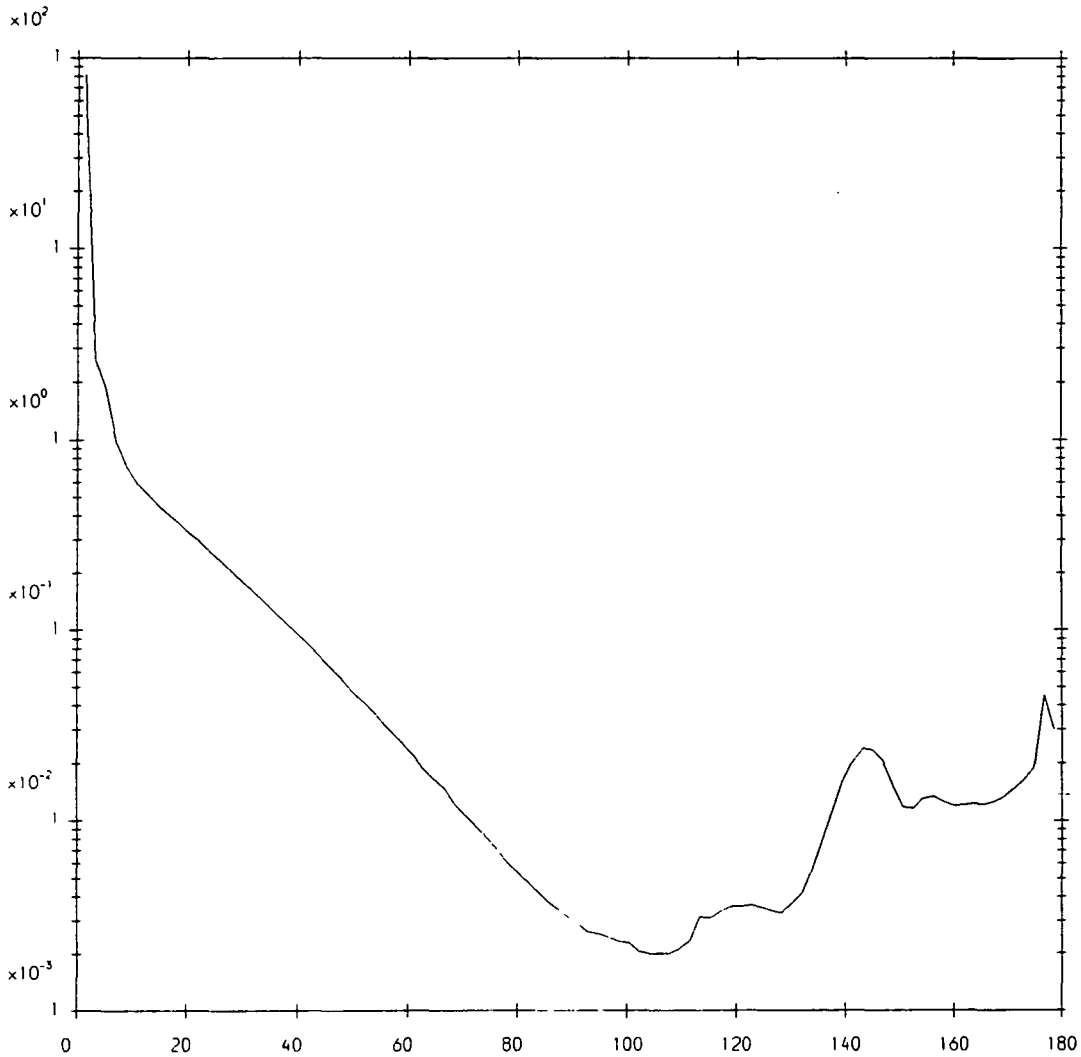

SCATTERING PHASE FUNCTION. - GAMMA

REF. INDEX = 1.340 + j 0.000 WAVELENGTH = 0.514 μm

LIMITS.X1,DX,X2, 1.22, 0.500, 122.00 A,B,ALPHA,GAMMA= 0.195E 02, 0.037, 13.730, 3.00

Figure 9.21(a)

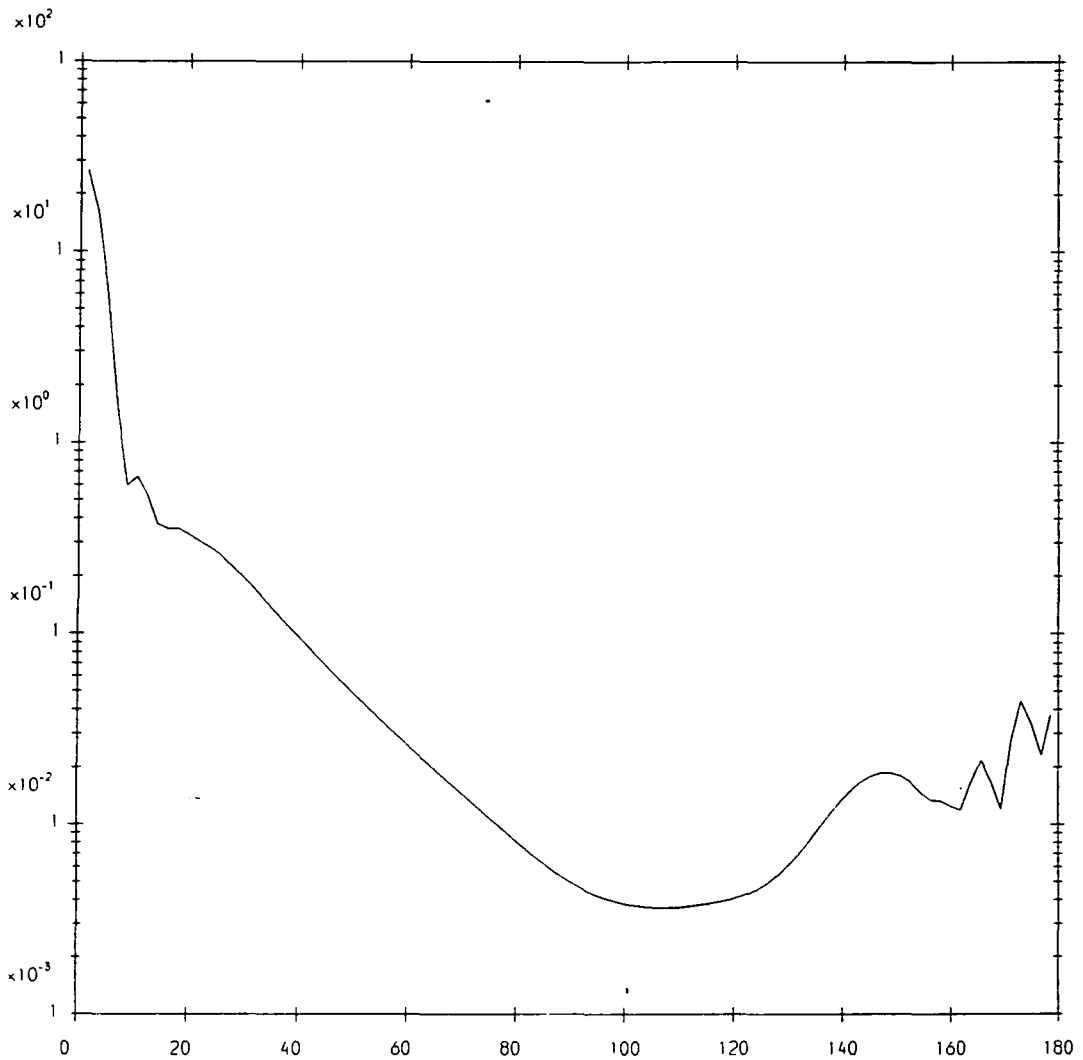

SCATTERING PHASE FUNCTION. GAMMA

REF. INDEX = 1.340 + j 0.000 WAVELENGTH = 0.514 μm

LIMITS, X1, DX, X2, 6.11, 0.100, 42.80 A, B, ALPHA, GAMMA= 0.148E 06, 1.290, 30.900, 3.00

Figure 9.21(b)

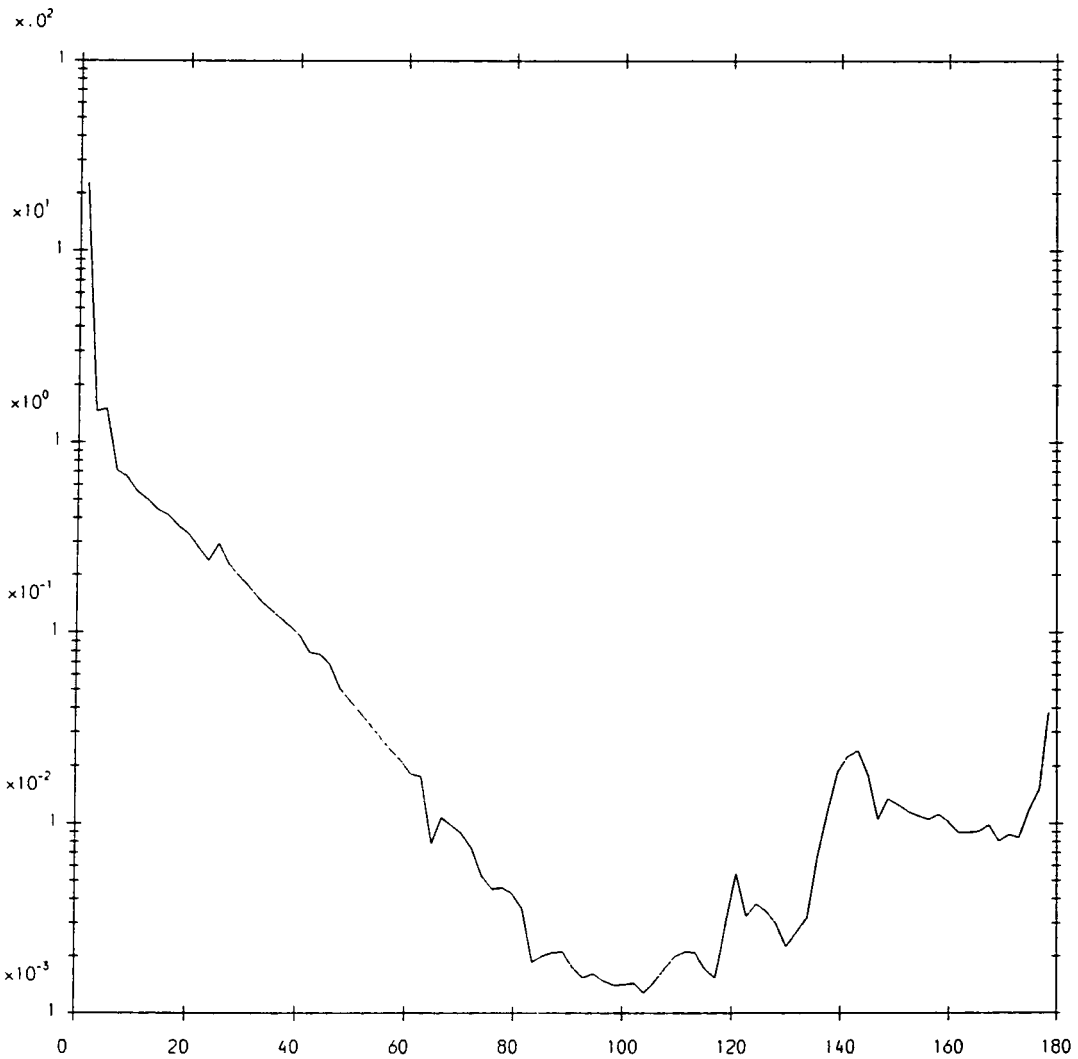

SCATTERING PHASE FUNCTION. - GAMMA

REF. INDEX = 1.340 + · 0.000 WAVELENGTH = 0.514 μm

LIMITS,X1,DX,X2, 12.20, 10.000, 428.00 A,B,ALPHA,GAMMA= 0.967E 01, 0.045, 8.960, 2.00

Figure 9.21(c)

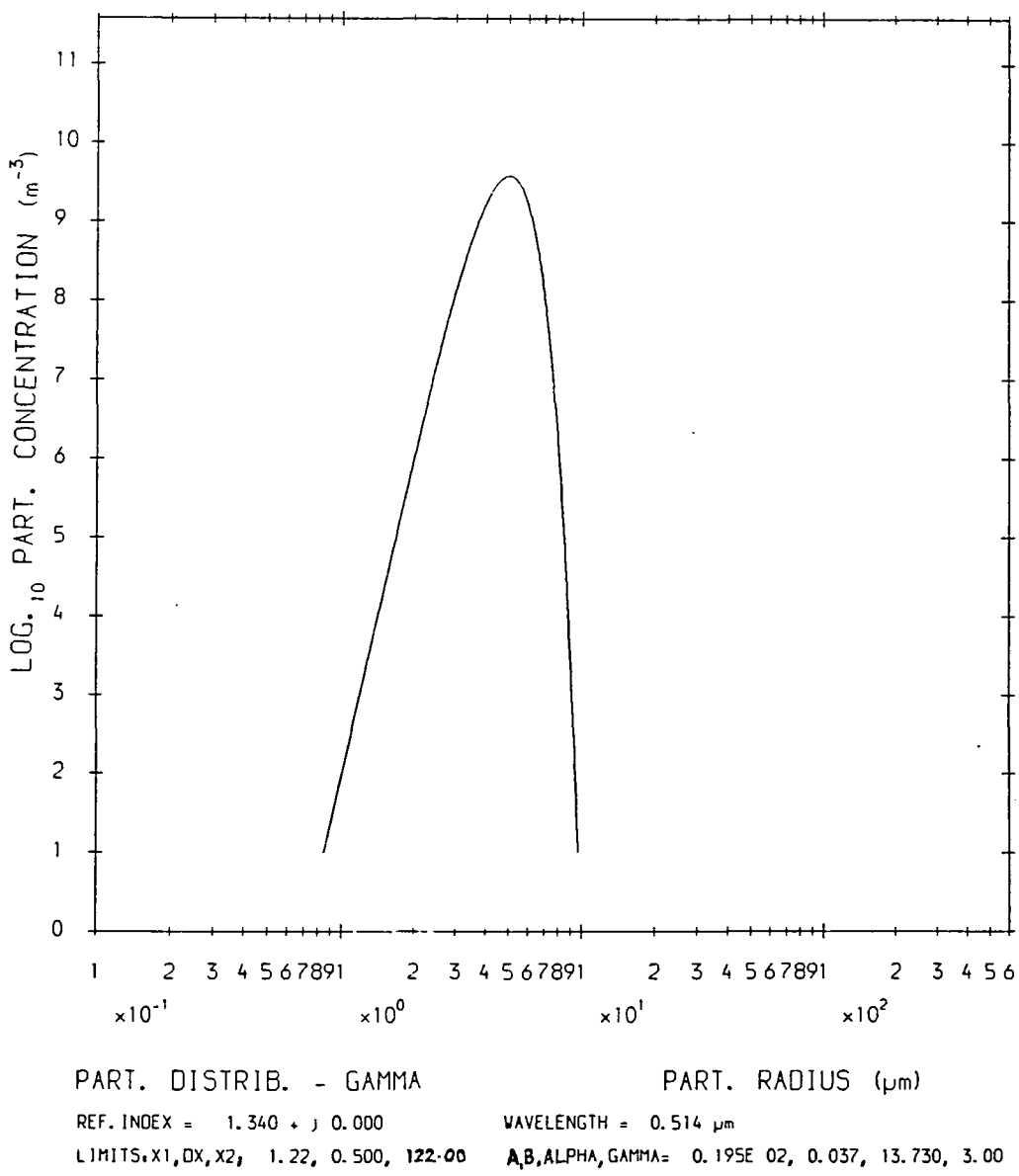
LOG.10 PART. CONCENTRATION (m-3)
0
1
2
3
4
5
6
7
8
9
10
11
1 2 3 4 5 6 7 8 9 1 2 3 4 5 6 7 8 9 1 2 3 4 5 6 7 8 9 1 2 3 4 5 6
×10-1
×100
×101
×102
PART. DISTRIB. - GAMMA
PART. RADIUS (μm)
REF. INDEX = 1.340 + j 0.000
WAVELENGTH = 0.514 μm
LIMITS,X1,DX,X2, 1.22, 0.500, 122.00
A,B,ALPHA,GAMMA= 0.195E 02, 0.037, 13.730, 3.00

Figure 9.22(a)

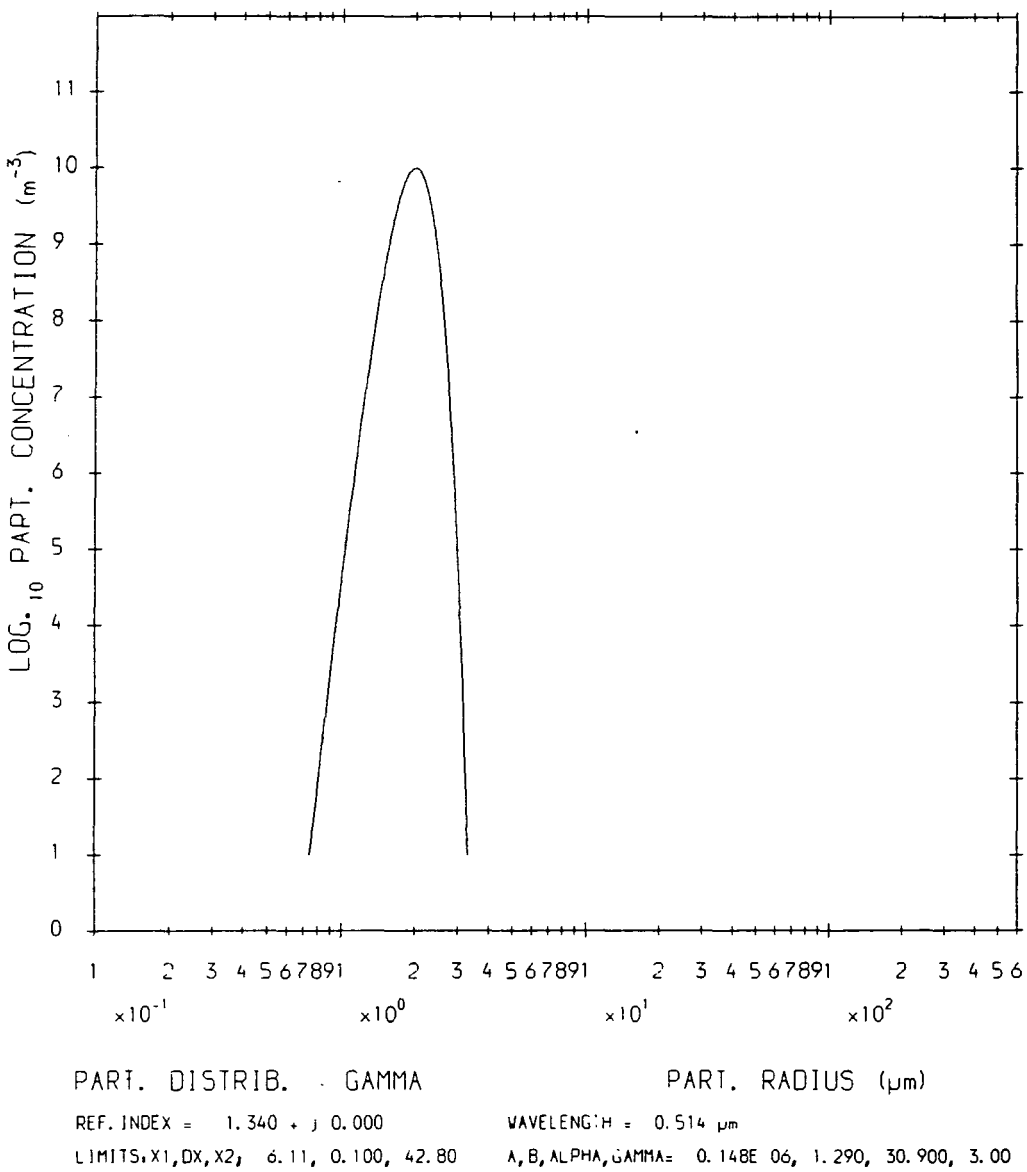
LOG.10 PART. CONCENTRATION (m-3)
0
1
2
3
4
5
6
7
8
9
10
11
1 2 3 4 5 6 7 8 9 1 2 3 4 5 6 7 8 9 1 2 3 4 5 6 7 8 9 1 2 3 4 5 6
×10-1
×100
×101
×102
PART. DISTRIB. - GAMMA
PART. RADIUS (μm)
REF. INDEX = 1.340 + j 0.000
WAVELENGTH = 0.514 μm
LIMITS, X1, DX, X2, 6.11, 0.100, 42.80
A, B, ALPHA, GAMMA= 0.148E 06, 1.290, 30.900, 3.00

Figure 9.22(b)

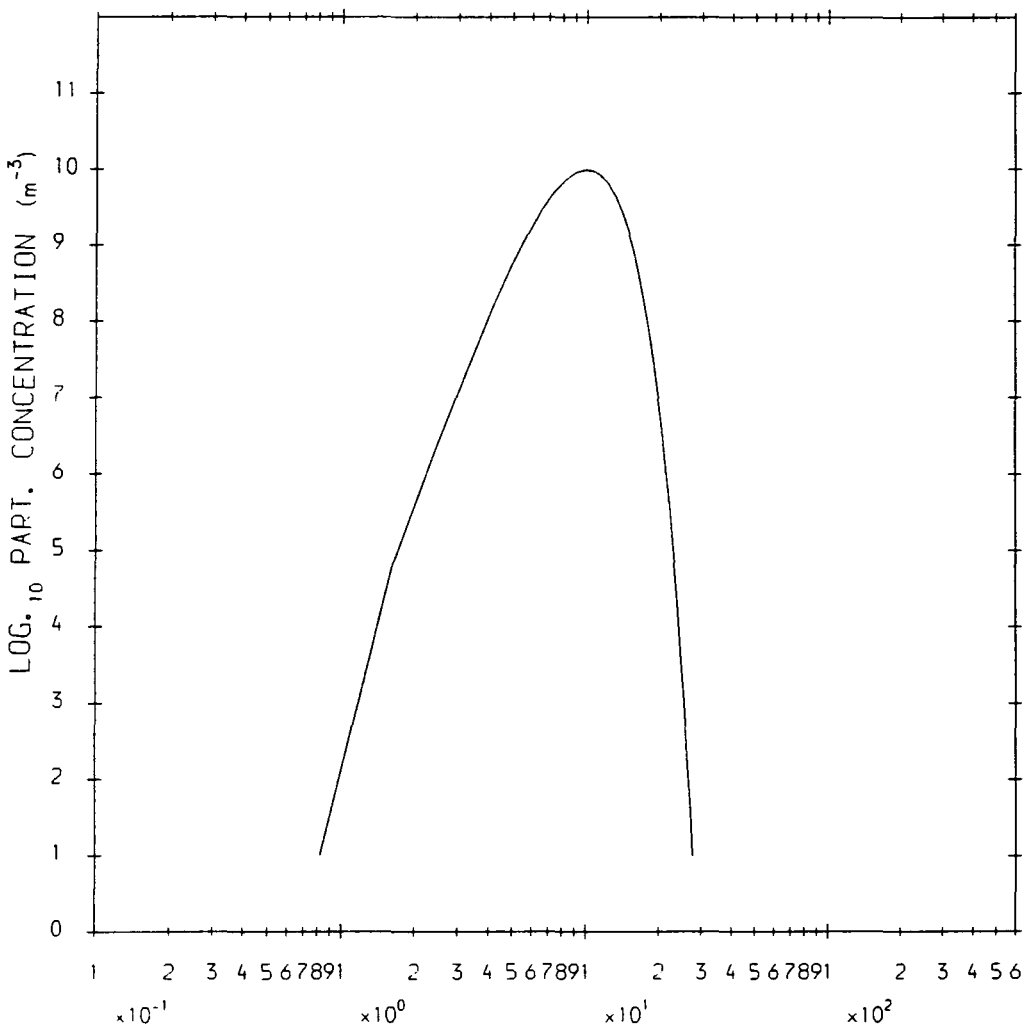
LOG. 10 PART. CONCENTRATION (m-3)
0
1
2
3
4
5
6
7
8
9
10
11
1 2 3 4 5 6 7 8 9 1 2 3 4 5 6 7 8 9 1 2 3 4 5 6 7 8 9 1 2 3 4 5 6
×10-1
×100
×101
×102
PART. DISTRIB. - GAMMA
PART. RADIUS (μm)
REF. INDEX = 1.340 + j 0.000
WAVELENGTH = 0.514 μm
LIMITS, X1, DX, X2, 12.20, 10.000, 428.00
A, B, ALPHA, GAMMA= 0.967E 01, 0.045, 8.960, 2.00

Figure 9.22(c)

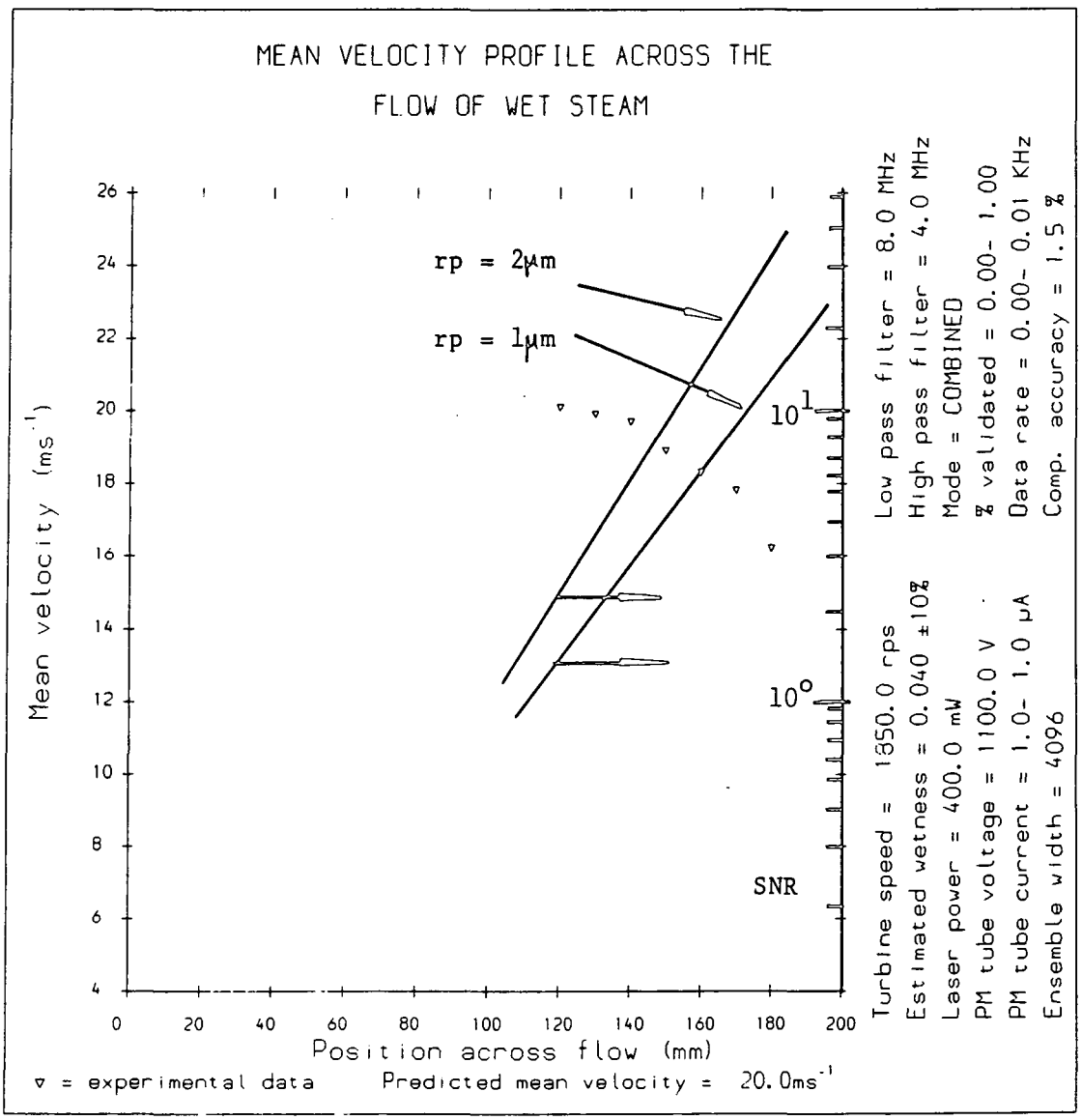

Figure 9.23(a) THE VARIATION OF PREDICTED SNR ACROSS THE STEAM FLOW FOR rp = 1μm and rp = 2μm AT 4% WETNESS

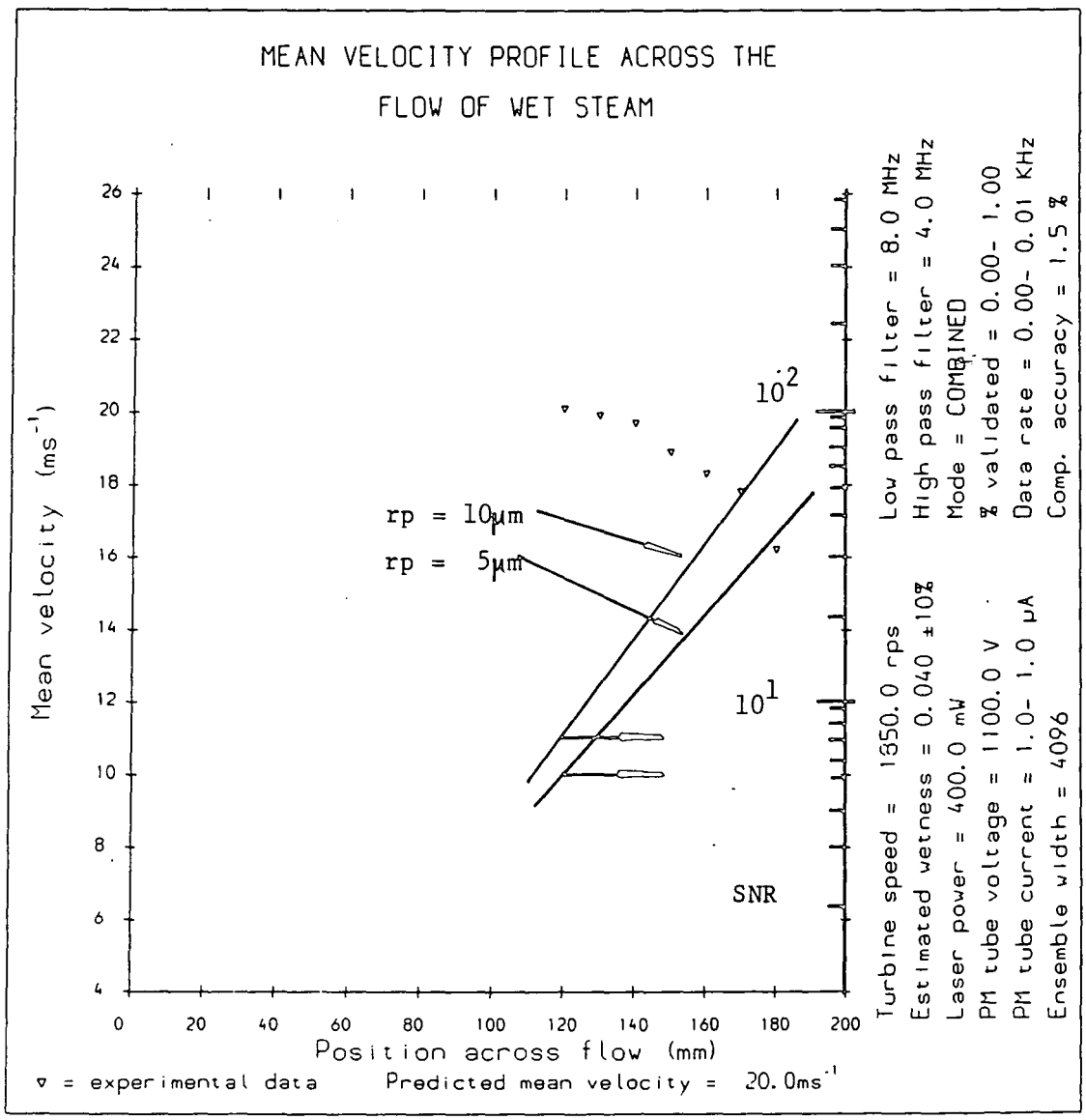

Figure 9.23(b) THE VARIATION OF PREDICTED SNR ACROSS THE STEAM FLOW FOR rp = 5μm and rp= 10μm AT 4% WETNESS

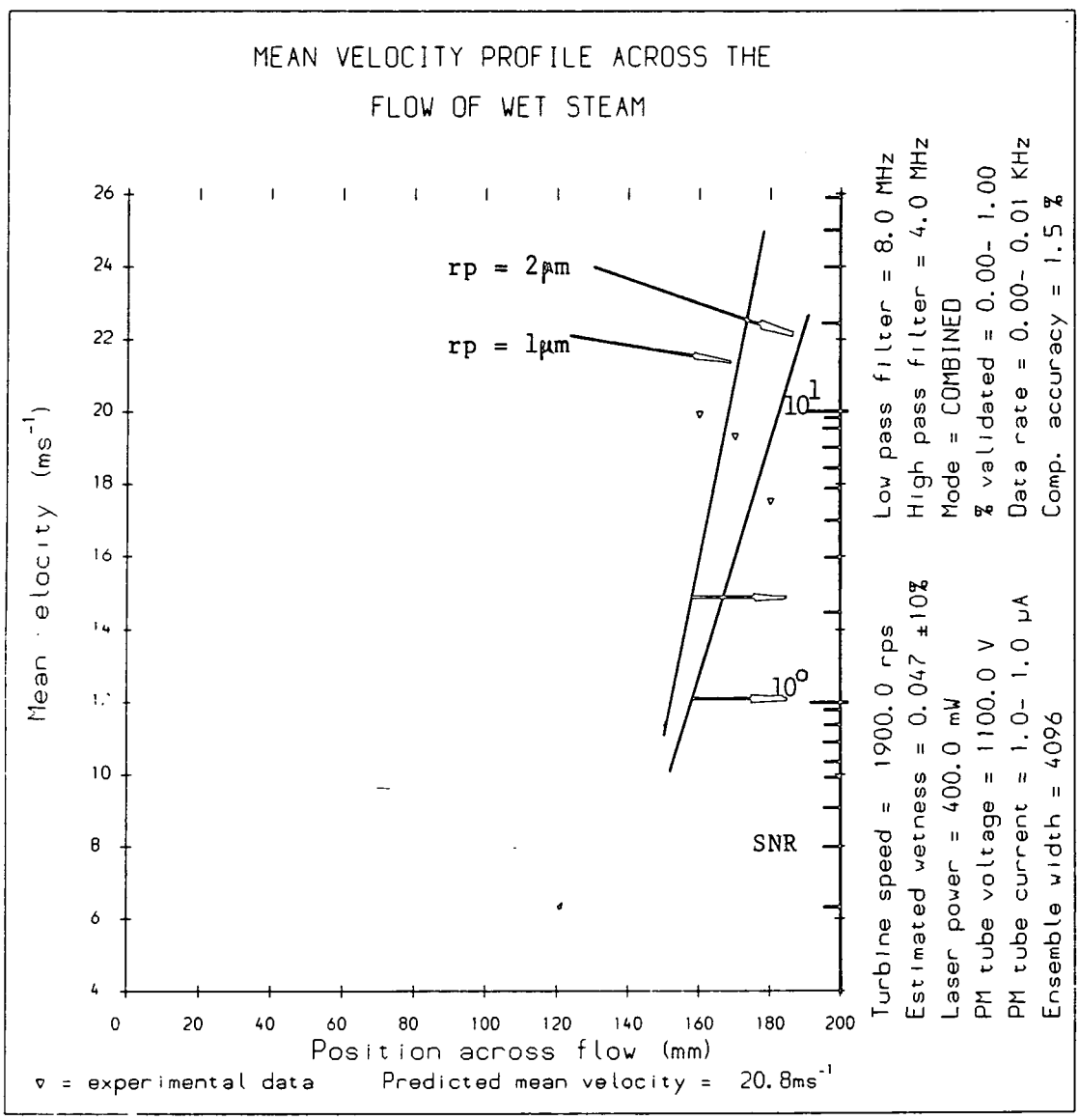

Figure 9.24(a) VARIATION OF PREDICTED SNR ACROSS THE STEAM FLOW FOR rp = 1μm AND rp = 2μm AT 4.7% WETNESS

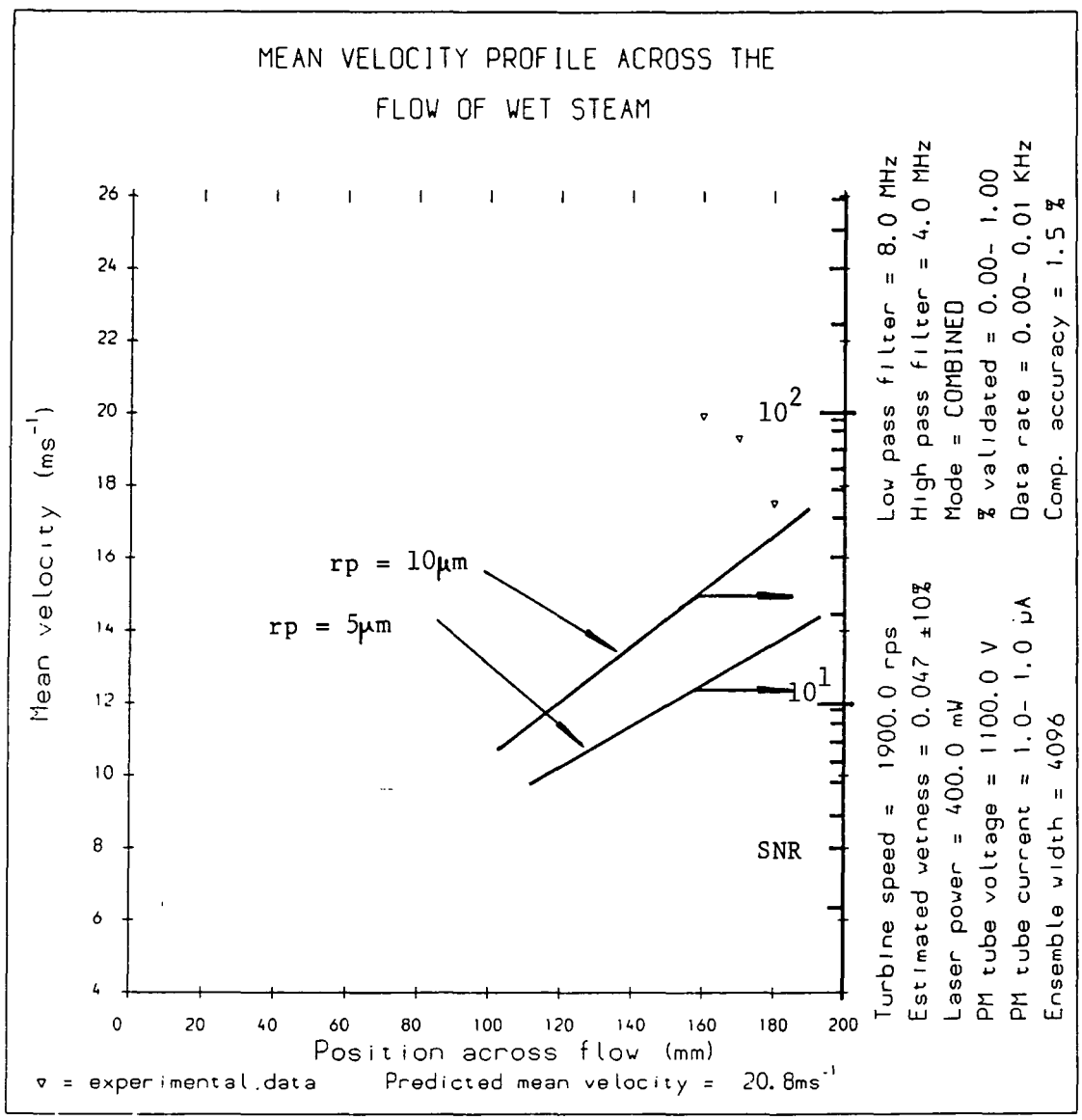

Figure 9.24(b) THE VARIATION OF PREDICTED SNR ACROSS THE STEAM FLOW FOR rp = 5μm AND rp = 10μm AT 4.7% WETNESS

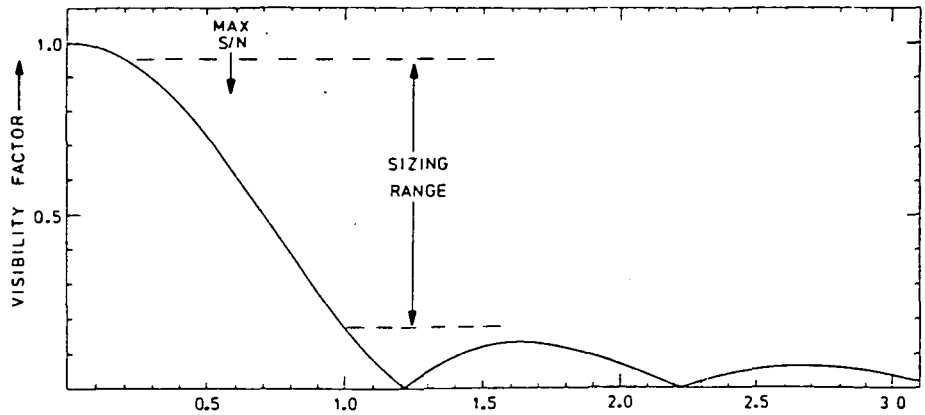

RATIO OF PARTICLE DIAMETER TO FRINGE SPACING

FIGURE 9.25 THE VISIBILITY FACTOR WITH PARTICLE SIZE

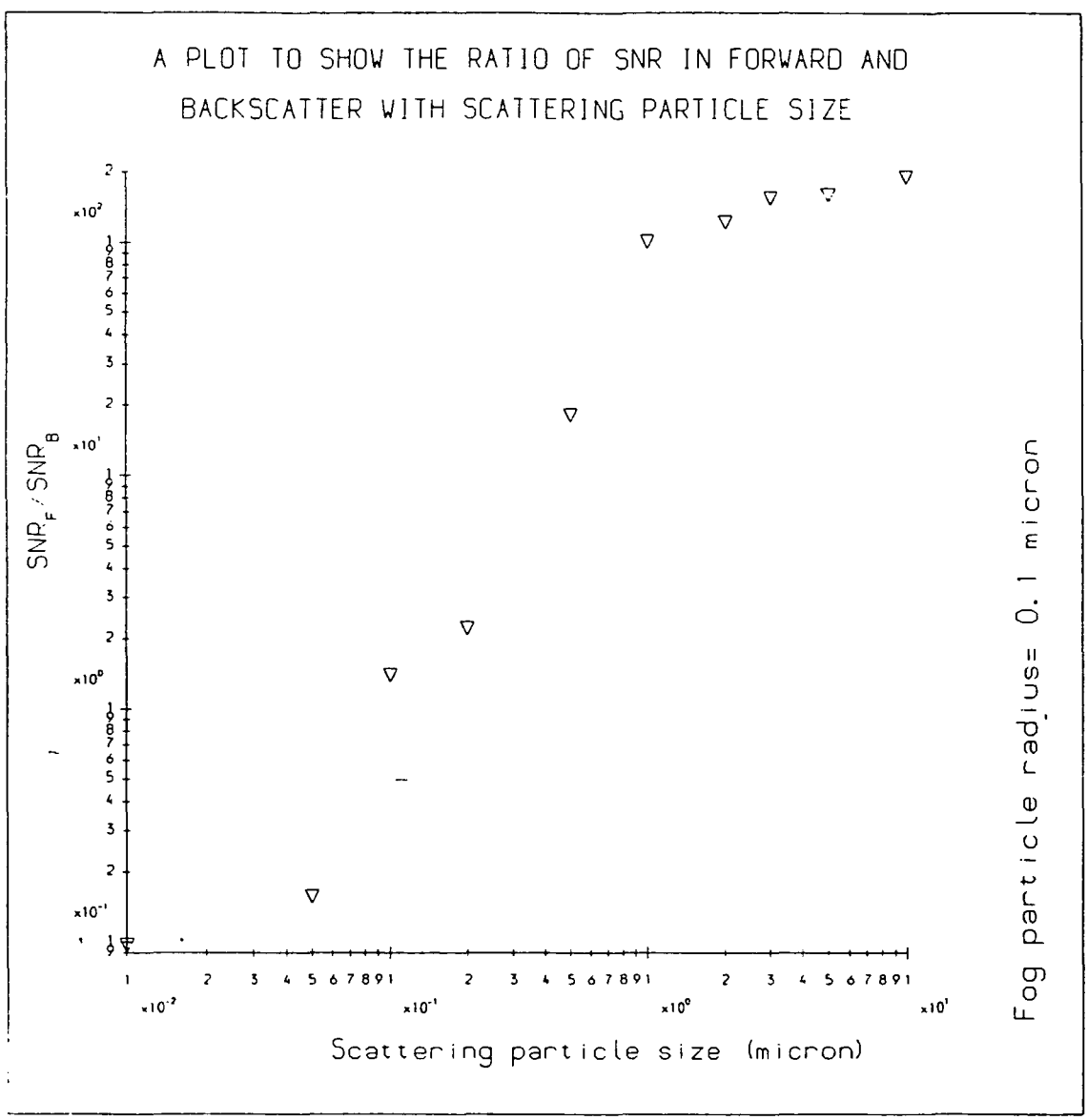

Figure 9.26

LDA IN WET STEAM - LAYOUT OF THE EXPERIMENTAL FACILITY

PLATE (i)

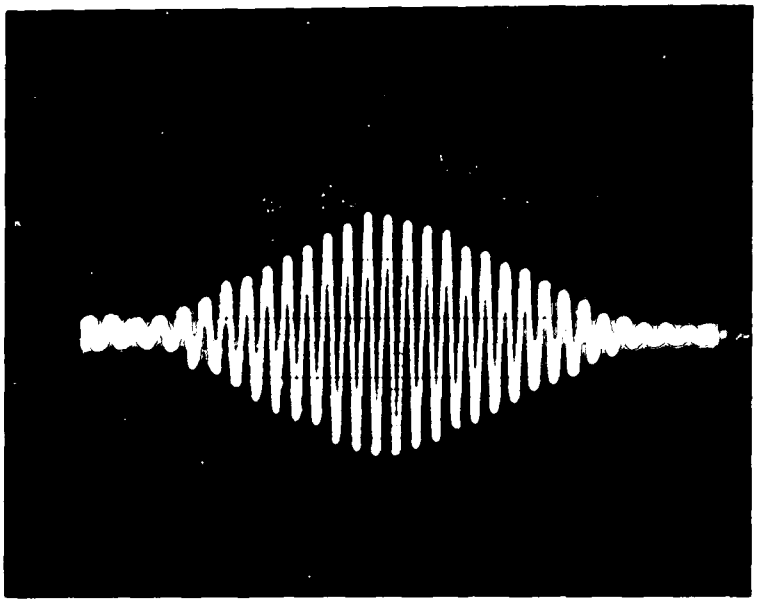

ν_D = 64 kHz
50μs/cm
0.2 V/cm

(a) SINGLE BURST

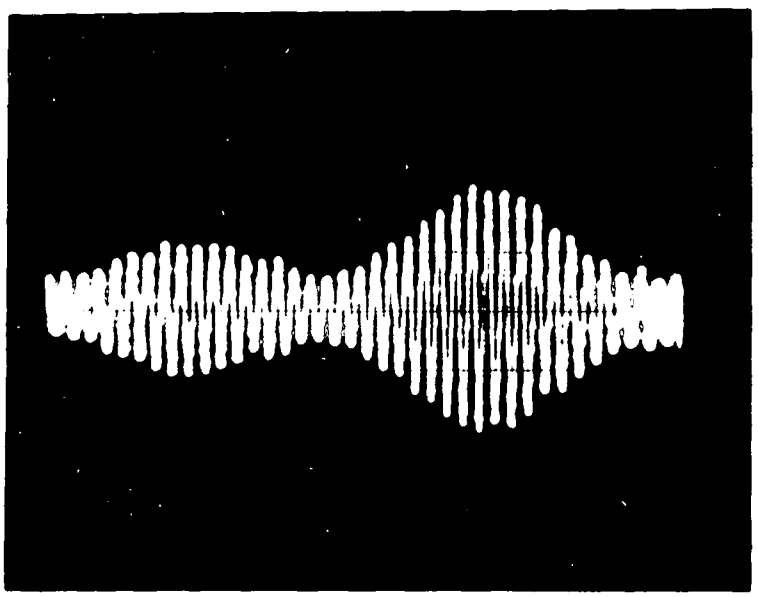

ν_D = 76 kHz
50μs/cm
0.2 V/cm

(b) MULTIPLE BURST

TYPICAL DOPPLER SIGNALS OBTAINED FROM A WATER FLOW
(MEAN VELOCITY = 0.25 m s^{-1})

PLATE (ii)

SHOWING THE PROBE VOLUME FORMED BY THE FOCUSED LASER BEAMS IN A FLOW OF DRY STEAM

TURBINE SPEED = 1200 rev s^{-1}

PLATE (iii)

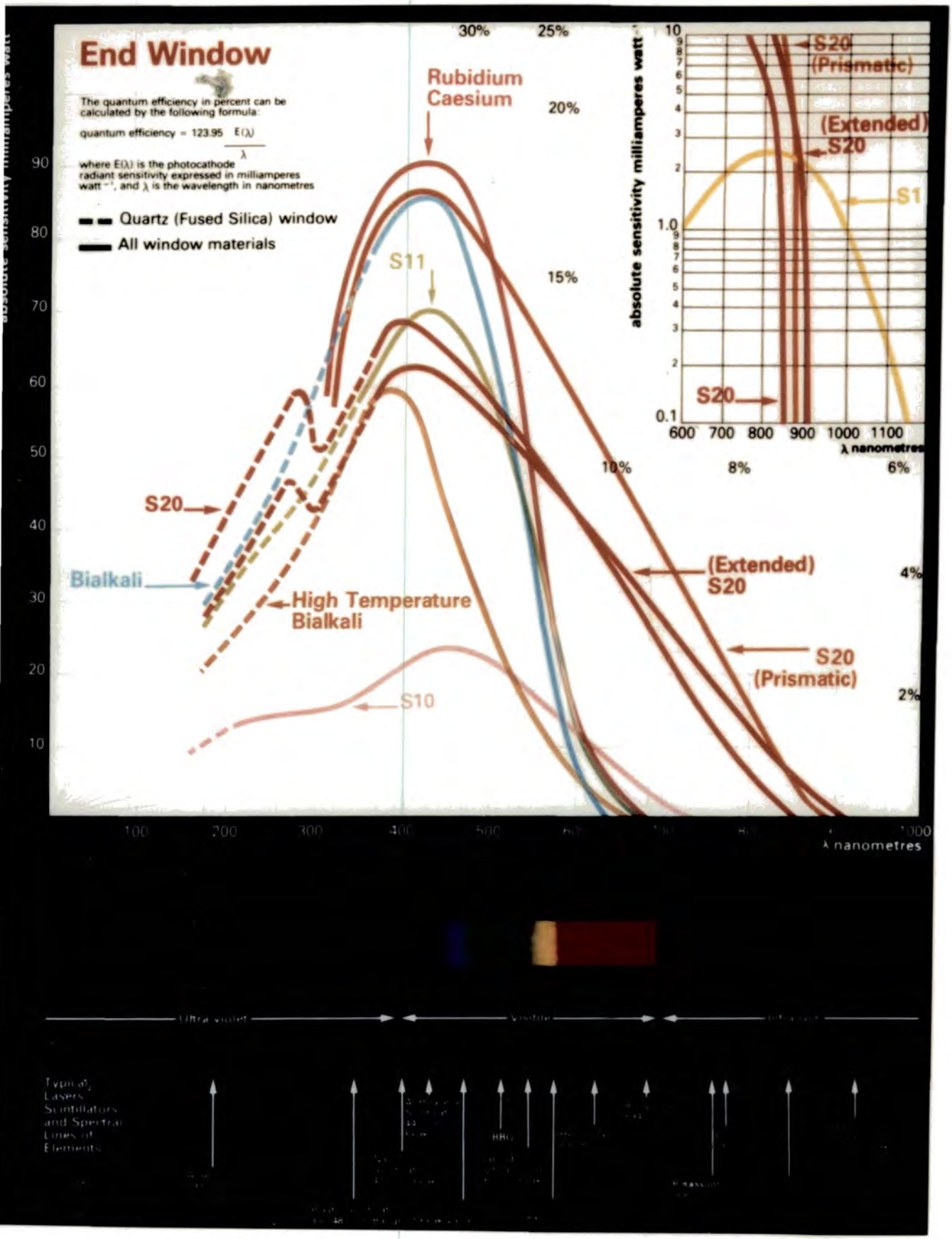

THE SPECTRAL RESPONSE CHARACTERISTICS FOR VARIOUS TYPES OF PHOTOCATHODE (Reproduction by courtesy of THORN EMI ELECTRON TUBES Ltd.)

PLATE (iv)

THE LDA OPTICAL SYSTEM - BEAMSPLITTER MODULE

PLATE (v)

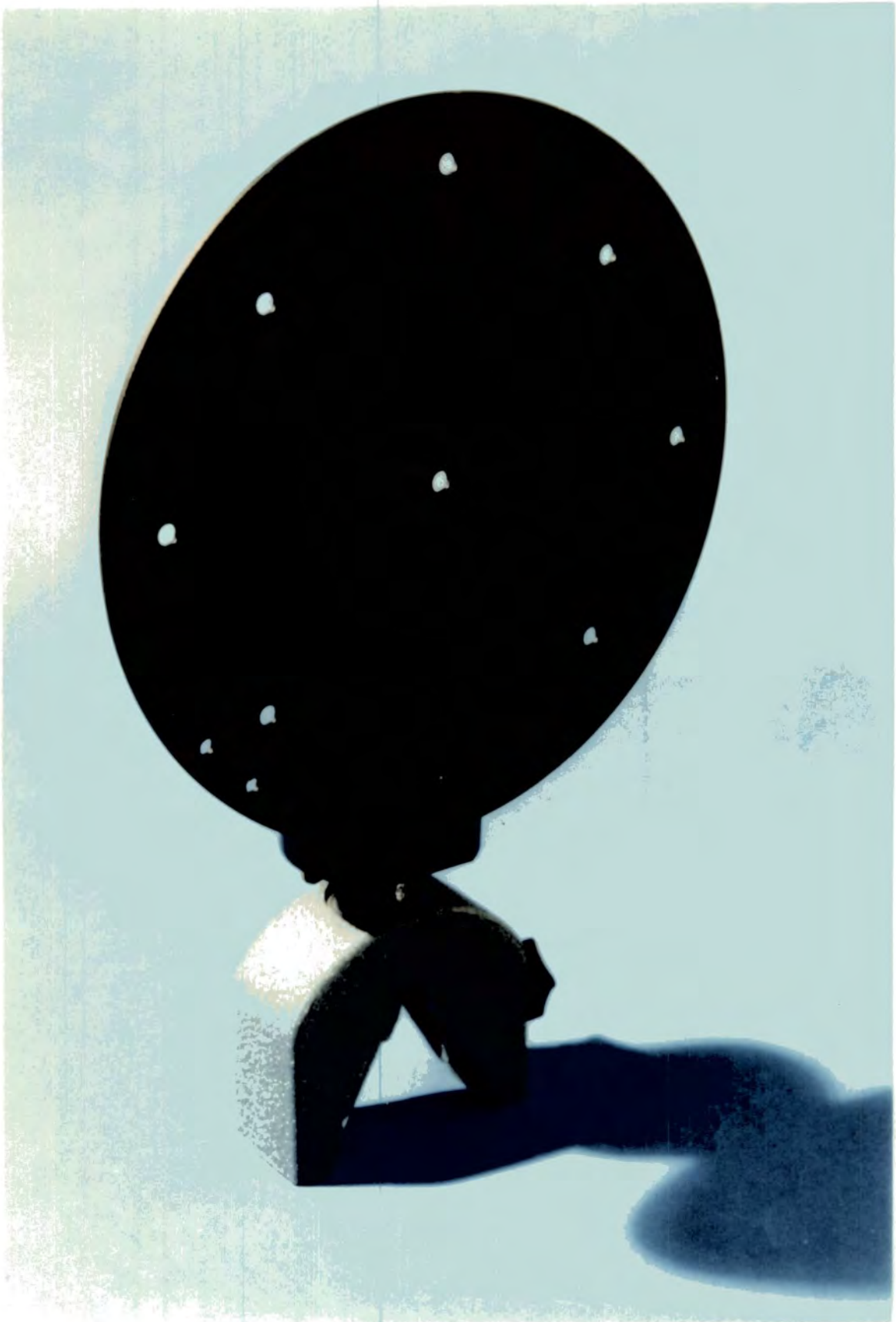

THE LDA OPTICAL SYSTEM - MASK USED FOR THE COARSE ALIGNMENT OF THE BEAMSPLITTER

PLATE (vi)

THE LDA OPTICAL SYSTEM - DETECTION OPTICS AND PHOTOMULTIPLIER TUBE ASSEMBLY

PLATE (vii)

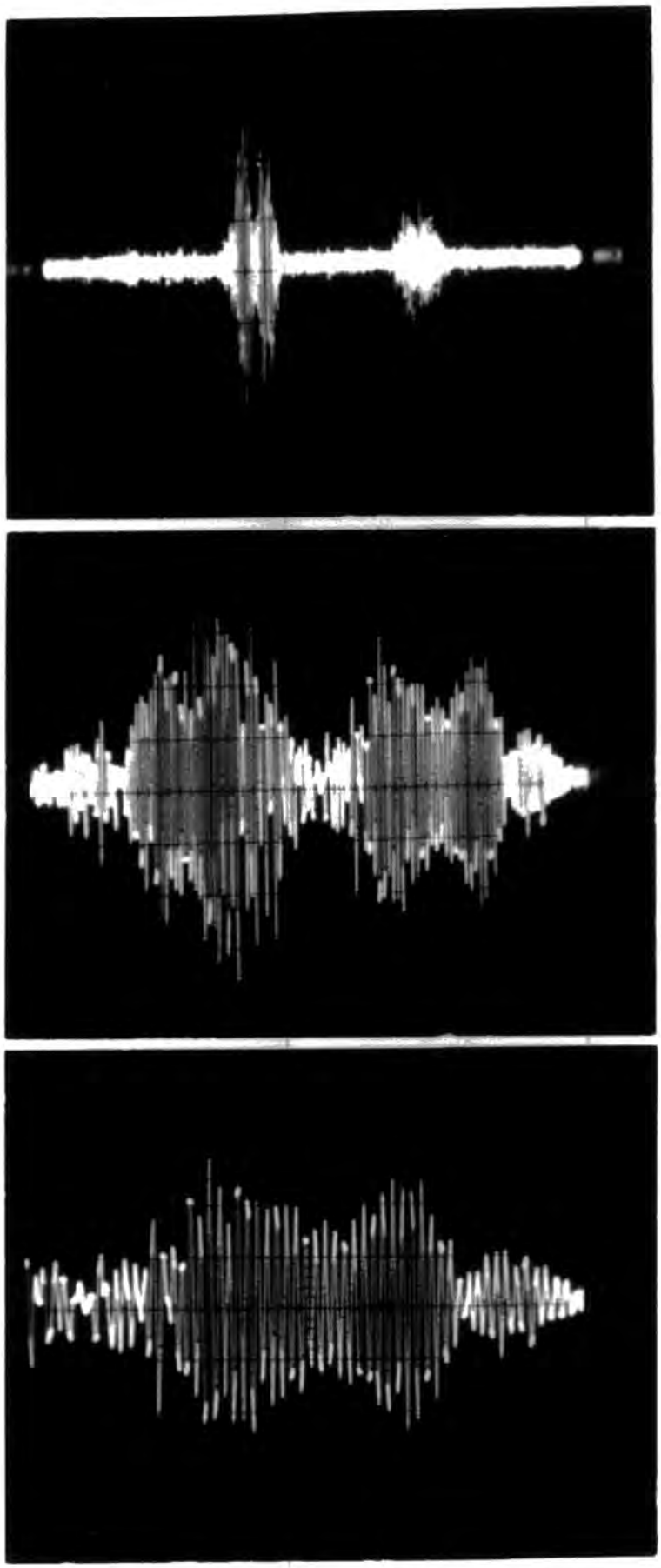

MULTIPLE BURSTS ν_D = 5.5 MHz

TYPICAL DOPPLER SIGNALS OBTAINED FROM A FLOW OF WET STEAM OF 3% WETNESS
(MEAN EXHAUST VELOCITY = 17.6 $m\,s^{-1}$)

PLATE (viii)

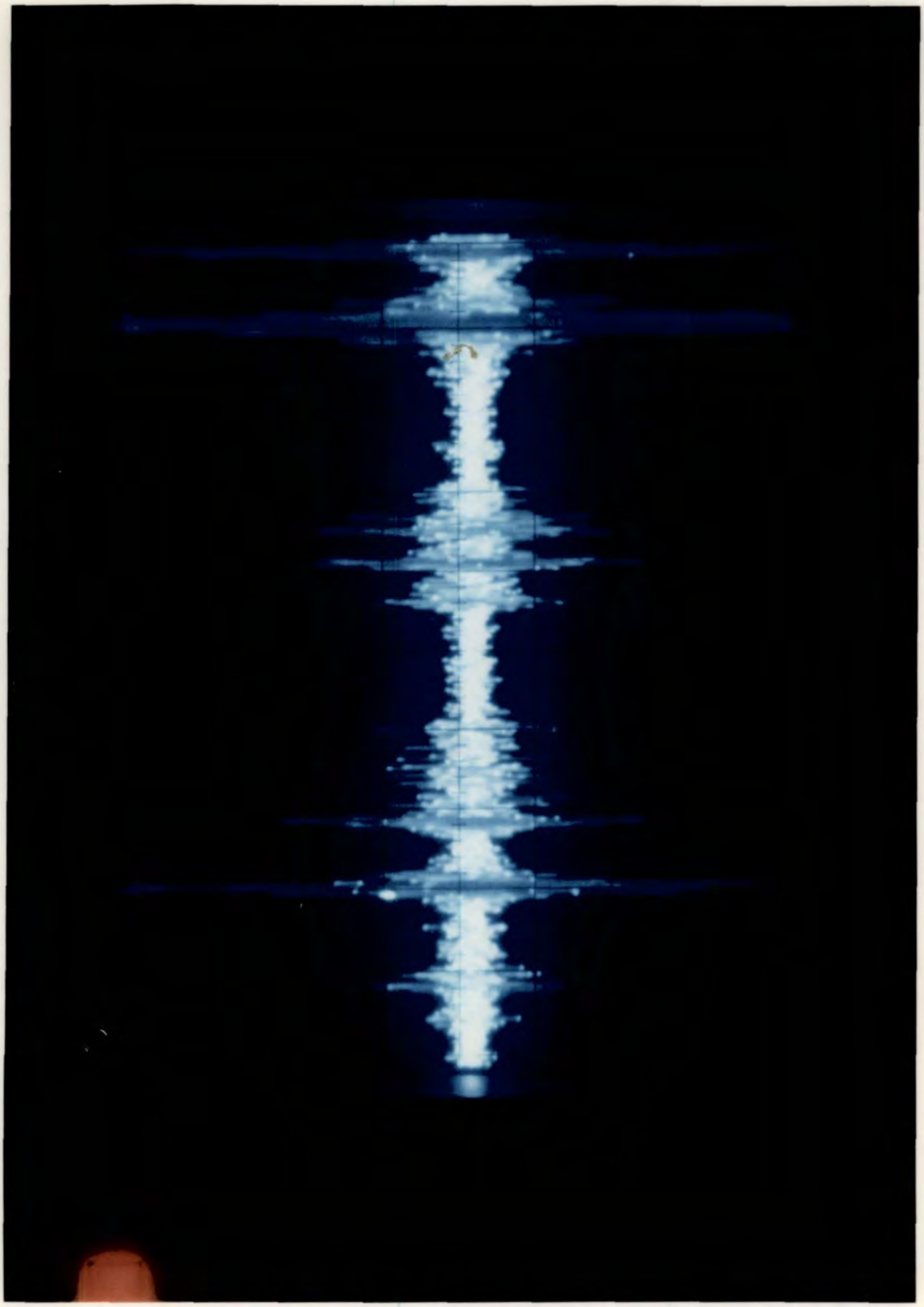

ν_D = 4.85 MHz , 10 μs/cm , 0.2 V/cm

TYPICAL DOPPLER SIGNAL OBTAINED FROM A WET STEAM FLOW OF 2.3% WETNESS (MEAN EXHAUST VELOCITY = 15.5 $m s^{-1}$)

PLATE (ix)

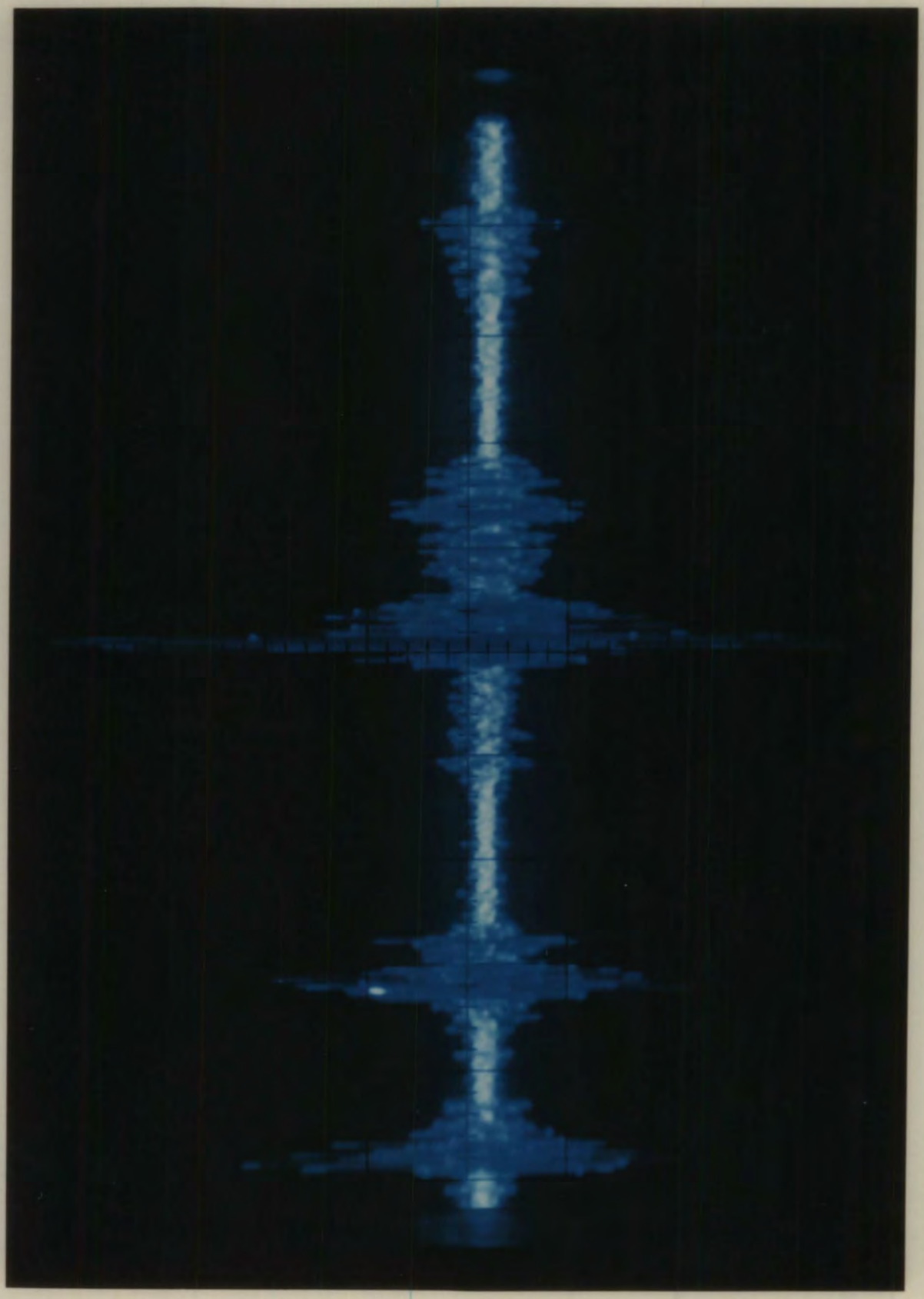

ν_D = 4.85 MHz , 5 μs/cm , 0.2 V/cm

TYPICAL DOPPLER SIGNAL OBTAINED FROM A WET STEAM FLOW OF 2.3% WETNESS

PLATE (x)

SHOWING THE INTERSECTION OF THE LASER BEAMS IN A FLOW OF WET STEAM OF 3% WETNESS

TURBINE SPEED = 1800 rev s^{-1}

PLATE (xi)